STUDIES OF SPIN-ORBIT COUPLING PHENOMENA IN MAGNETIC SEMICONDUCTORS

Thesis submitted to the University of Nottingham for the degree of Doctor of Philosophy

BRYN HOWELLS, MPhys

May 2015

Abstract

Hard disk drives (HDDs) have been the dominant secondary memory device in computing for over 50 years, while more recently magnetoresistive random access memory (MRAM) has emerged as a candidate for primary computing memory. Both HDDs and MRAM store information in the polarity of a magnetic layer, which is written and read by non-relativistic mechanisms. There is now gathering interesting in using relativistic mechanisms whose origins lie with spin-orbit coupling (SOC) for MRAM writing because of potential benefits in terms of scalability, device design, and efficiency. This thesis investigates the fundamental physics of SOC phenomena that can write (spin-orbit torque (SOT), Néel order SOT) or read (anisotropic magnetoresistance (AMR), magnetic gating) the magnetic state by the application of electrical current. These phenomena are studied in semiconducting materials that offer a relevant electrical conductivity for integration into commercial electronic devices.

Effective magnetic fields which parametrise the SOT phenomenon are measured in the diluted magnetic semiconductor (Ga,Mn)As using a technique based upon experimental planar Hall effect measurements and analytical fitting with a free energy equation for coherent magnetization rotation. It is found that effective magnetic fields which originate from Dresselhaus SOC increase in magnitude with increasing temperature, whereas those originating from Rashba SOC have no significant temperature dependence within experimental uncertainty. The size of the measured effective fields per unit of current density, as well as the ratio of Dresselhaus to Rashba effective field magnitudes averaged over all temperatures are comparable to previous experimental measurements.

Evidence for electrical switching of the antiferromagnet CuMnAs via the Néel order SOT (NSOT) mechanism is presented. Pulses of current density of the order of a few MA/cm^2 are applied along orthogonal directions of a CuMnAs Hall cross device at room temperature in order to set its antiferromagnetic (AF) spin-axis orientation via NSOT effective magnetic fields. DC longitudinal and transverse probe measurements subsequent to each setting pulse reveal high and low resistance states for probe geometries that are consistent with a non-crystalline AMR response to the setting pulses switching the AF spin-axis orientation. The results of varying the magnitude and number of setting pulses suggests that the magnetic structure of the CuMnAs sample studied consists of sub-μm AF domains.

Sb-based diluted magnetic semiconductors (Ga,Mn)($As_{0.9}$,$Sb_{0.1}$) and (Ga,Mn)Sb are characterised by magnetic and transport measurements. The Curie temperature (T_c) of (Ga,Mn)($As_{0.9}$,$Sb_{0.1}$) increases from 28K to 55K upon sample annealing. The T_c of as-grown (Ga,Mn)Sb is found to be 34K, and in contrast to (Ga,Mn)($As_{0.9}$,$Sb_{0.1}$) does not change upon annealing, indicating a lack of interstitial Mn in (Ga,Mn)Sb. Field rotation transport measurements for current along various crystalline directions reveal significant crystalline and non-crystalline contributions to the AMR of both as-grown and annealed (Ga,Mn)($As_{0.9}$,$Sb_{0.1}$). An anomalous

temperature dependence of the AMR of the annealed (Ga,Mn)($As_{0.9}$,$Sb_{0.1}$) sample for current along the [110] crystalline direction is accounted for by considering the relative sizes of the individual AMR contributions as a function of temperature.

Results are shown of an attempt to vary the current flow through a non-magnetic GaAs/AlGaAs 2D electron gas (2DEG) by changing the magnetization orientation of an electrically insulated Fe gate layer. Such magnetic gating of electrical current is based upon the principle that, as a result of SOC, the electrochemical potential of a ferromagnet is anisotropic with respect to its magnetization orientation. The magnetic gating experiment proved to be unsuccessful due to an AMR-like signal arising in field rotation measurements of 2DEG samples both with and without the gate layer. The origins of this AMR-like signal are unknown, and it cannot not be accounted for by fitting analysis.

Acknowledgements

First and foremost I would like to thank my supervisor Dr. Kevin Edmonds for his helpfulness, guidance, and hard work in my supervision. The work in this thesis would not have been possible without his ideas and support. My secondary supervisor Prof. Bryan Gallagher provided me with much appreciated advice and suggestions for my work through my PhD for which I am thankful. Dr. Andrew Rushforth helped me on numerous occasions with experimental and theoretical issues which I am grateful for. Thanks to Dr. Richard Campion for growing all the samples I studied in this thesis. I am also appreciative of Prof. Tomas Jungwirth for leading the successful Nottingham-Prague-Cambridge collaboration and hosting Lanna meetings.

I would like to thank all of the technicians in the department who on multiple occasions went above and beyond the call of duty to help me. Special mentions must go to Jaz Chauhan, Dave Taylor, 'Cryogen' Chris Pallander, Dave 'The Man' Holt, Bob Chettle, and Ian Taylor. Dr. Oleg Makarovskiy several times took time out of his own research and teaching commitments to laser anneal my 2DEG contacts which I am grateful for.

Thanks to all the students and postdocs in the Nottingham spintronics group in my 3.5 years here. I would like to especially highlight the following people: Dr. James Haigh spent so much of his time helping me when I was starting my PhD, and I will always remember this. The same can be said of Dr. Mu Wang who continued to help me until he left in 2013. Mu is perhaps the most unreal person I've ever met and also one of the best friends I've ever made. Duncan Parkes has been here throughout my whole PhD and has regularly helped me with computing and clean-room problems. I enjoyed many fruitful discussions with Dr. Jan Zemen and Dr. Peter Wadley about my work throughout my time here. I would also like to thank the members of the department football team which I captained for nearly the entirety of my PhD - there were many hard times so thanks to those who stuck with it.

Finally, no clichéd list of acknowledgements would be complete without thanking my parents.

Contents

Chapter 1

Introduction

1.1 Preface

1.1.1 History of semiconductor electronics and computer technology

Fully automatic and programmable computing machines, i.e. computers in the sense that we know them today, were first successfully produced and demonstrated during the years at the beginning of the second World War (around 1938-1941) by German engineer and inventor Konrad Zuse. Zuse's computers were based upon electromechanical relays which severely limited their operating speed and practical application. The next approach towards building computer was to move away from electromechanical machines and towards all-electrical machines that use vacuum (electron) tubes. Vacuum tube computers (first generation computers) were produced and used towards the end of the war, and their development continued into the early 1950's when commercial machines became available. However, advances in transistor technology meant that by the 1960's vacuum tube computers were no longer considered a competitive route to achieving high-performance computing.

In 1947 John Bardeen, Walter Brattain, and William Shockley of Bell Labs demonstrated the first ever working transistor, a Ge point contact transistor. Over the next decade various forms of field effect and bi-polar transistors were developed, building upon the fundamental understanding gained from the Bell Labs work. A transistor is, in general, a semiconductor device with at least three contact terminals where a current or voltage applied to one set of contacts can amplify or switch an electrical current through another set. Transistors have many advantages over the vacuum tube as the key component upon which to build electronic devices and computers, including their smaller size, manufacturing cost, and power consumption/dissipation, as well as their greater reliability and ease of compatibility in integrated circuits. From the 1960s still to this day, transistors form the basis of the majority of consumer electronics. The invention of the transistor is therefore considered one of the most important of the 20th century, and indeed Bardeen, Brattain, and Shockley shared the 1956 Nobel Prize in recognition for their work.

Early transistor computers (second generation computers) as well as other electronic devices such as car radios were made from germanium in the late 1950's and 1960's.

Advances in the understanding and production of silicon allowed it to replace germanium as the dominant material used in transistor production, and this coincided with the invention of integrated circuits and microprocessors, which are the basis for the third generation of computers which have been in use from the late 1960's to the present day. Silicon remains the semiconductor material of choice for many of today's electronic devices, but other semiconductors such as gallium arsenide (GaAs) are also widely used, finding high frequency applications in communications devices. The explosion in the utilization and commercial success of third generation computers and electronic devices that harness integrated circuits has gone hand in hand with their astonishing rate of development since the mid 1960's, a level of continuing improvements that agrees with the 1965 observation of Gordon Moore ('Moore's law'[1]). Moore's law predicted in 1965 that the number of transistors in an integrated circuit would double approximately every two years, a level of miniaturization that has allowed similar rates of increases in computing power and speed, as well as the development of portable electronics devices such as smart-phones that we are all familiar with today. Moore's law has held for the past 50 years largely due to progress in transistor design, semiconductor processing techniques, and material development. However, as transistor sizes move closer to their ultimate atomic-scale limit and breakthroughs in nano-fabrication become harder to achieve, the rate of miniaturisation is starting to slow down, and the rapid growth in computing technology that has been enjoyed for so long cannot be sustained indefinitely. As a result, researchers are looking at alternative approaches to computing and consumer electronics beyond simply continuing to increase the number of transistors on a chip. Quantum computation has a very distinct methodology compared with classical computing and has immense potential, but is still a field very much in its infancy with everyday applications seemingly a long way away. Spintronics, on the other hand, is less drastic avenue towards future computing and devices that shares many of the features of traditional charge based classical computing, but its advantage beyond classical computing lies with its attempts to simultaneously harness both the charge and spin degrees of freedom of the electron to provide new functionality. Spintronics has been well researched for decades, and many major technology companies continue to pour resources into its development in the hope that in the not too distant future all-spintronic computing and devices will be possible that will allow the continued growth of consumer electronics.

1.1.2 Spintronics

The birth of the field of spintronics is often associated with the discovery of the giant magnetoresistance (GMR) effect in the late 1980's by the groups of Albert Fert[2] and Peter Grunberg[3] (Fert and Grunberg's observations of GMR were independent of one another, and they were both awarded the 2007 Nobel prize for their work). Simplistically, the GMR effect is as follows: a spin-polarised current is generated by passing unpolarised current through a ferromagnetic metal. The spin-polarised current travels through a non-magnetic metal and reaches a second ferromagnetic metal where it experiences spin-dependent scattering, the strength of which depends on the relative alignment of the carrier spins with respect to the magnetization orientation. Therefore, by changing the relative orientation of

the ferromagnetic layers of a GMR device it can take either low or high electrical resistance states. GMR is a prototypical spintronic effect in that it exploits the dependence of the device's charge properties on its spin properties (spin dependent scattering) and vice-versa (spin-polarised current generation). GMR is also perhaps the most successful example of spintronic physics in everyday applications as GMR structures are widely used to make magnetic read-heads in hard disk drives common in today's computers.

Before the discovery of GMR, other magnetoresistance type effects had also previously been reported. Anisotropic magnetoresistance (AMR), which is the dependence of a ferromagnetic material's resistance on its own magnetization orientation, was first observed as far back as the 1850's[4], long before the research area of spintronics began to attempt to use such a phenomenon in devices. The first generation of magnetoresistive read-heads were based upon AMR, before superior performing GMR read-heads began to take over around the year 2000. In 1975 tunnel magnetoresistance (TMR) was discovered[5], a phenomenon similar to GMR in terms of the device structure employed (an insulating tunnel barrier replacing the non-magnetic metal) but with distinct physics. The discovery of TMR was largely unheralded at the time, though eventually in 2005 TMR read-head devices were introduced which began to replace their GMR counterparts. Other types of magnetoresistance effects are still researched by the spintronics community, such as tunnelling anisotropic magnetoresistance (TAMR)[6], coulomb blockade anisotropic magnetoresistance (CBAMR)[7], and spin Hall magnetoresistance (SMR)[8], while the transverse component of the resistance of a ferromagnet can also depend on magnetization orientation in the anomalous Hall effect (AHE)[9]. These magnetoresistance effects can generally be classified into two types; those that don't involve spin-orbit coupling (SOC) (non-relativistic Mott type - GMR, TMR) and those that do involve SOC (relativistic Dirac type - AMR, TAMR, AHE, etc)[10].

Many spintronic phenomena and devices involve, require, or exploit the generation of a spin-polarised current or pure spin-current, and this remains one of the key challenges in spintronics. Spin-polarised current can be generated by passing unpolarised current though a ferromagnetic material[11] or quantum point contacts[12][13], while pure spin current can be generated via the spin Hall effect (SHE)[14]. Spin currents can then be harnessed to efficiently torque magnetic moments which is useful for applications in magnetoresistive random access memory (MRAM) devices. For example spin transfer torque (STT) MRAM has recently become commercially available. MRAM is an important step towards all spintronic computing, offering the non-volatility of flash memory and the potential to match the density and speed of volatile RAM but with a lower energy consumption. Additionally, pure spin current does not generate heat, and this would circumvent one of the major limiting factors in conventional computing.

While the majority of early spintronics devices were metallic, semiconductor spintronics emerged as the most viable route to integrate spintronic devices within the existing electronics hierarchy. Semiconductors have the advantage that their properties can easily be tailored by methods such as electrical gating and doping as is done in conventional electronics today, and so it is desirable to maintain these

properties while also introducing the functionality offered by various spintronic phenomena. One approach is to use the charge degree of freedom for processing and the spin degree of freedom for memory, while another is that control of the spin itself could open up the possibility of a spin transistor. 1990 saw one of the first proposals of a semiconductor spintronic device in the yet to be fully realised Datta Das transistor[15][13], and since then spintronic phenomena have been investigated in a variety of semiconductor materials, notably GaAs[16][17], but also in the more common silicon[18]. Of course, achieving a spin polarised current is easier in magnetic materials than non-magnetic materials, and while some magnetic metals have relatively low spin polarisations, diluted magnetic semiconductors (DMSs), which are non-magnetic semiconductors doped with magnetic ions, have shown high spin polarisations while also maintaining their normal semiconducting properties. For these reasons, DMSs have been among the materials at the forefront of spintronics research for over 20 years and are the major system of study in this thesis.

The field of spintronics continues to develop and evolve in the search for materials and phenomena that can offer applications and performance that betters that of traditional charge based consumer electronics. Recently various spintronic effects have been observed in a variety of other material systems including ferrimagnetic insulators[19], graphene[20], topological insulators[20], organic semiconductors[21], and superconductors[22], while there has also been a great effort towards manipulating single spins, for example in nitrogen vacancy centres in diamond[23], which could have implications for quantum computing. Antiferromagnetic spintronics is beginning to emerge as an exciting alternative to conventional ferromagnetic spintronics in a variety of materials[24][25], with its benefits including room temperature functionality and insensitivity to stray fields. Additionally the research area of spintronics is increasingly expanding to incorporate topics like magnonics and spin-caloritronics that have more overlap with other areas of condensed matter physics. While much has already been achieved in spintronics in the past 25 years or so, including the success of GMR and TMR in everyday devices, there is much work still to do, especially in regard to incorporating more spintronic effects and phenomena into mainstream computing and consumer electronics. The vast potential of spintronics motivates its continuing research and development from both academia and industry alike.

1.1.3 Motivation and organisation of thesis

The general motivation of the work in this thesis is to develop a better fundamental understanding of certain SOC-based phenomena which can either set or detect the magnetic state of a material via the application of an electrical current. Such or similar phenomena may eventually find application in the writing and reading processes for magnetic memory structures. All the materials studied in this thesis are either magnetic, or contain a magnetic element in the specific device structure. In terms of their electronic band structure, the materials under investigation are mostly semiconducting, as is appropriate for the existing commercial electronics architectures.

The thesis is organised into seven chapters. Chapter 1 outlines the key physics of DMSs and introduces the general experimental techniques used for the work within the thesis. Chapter 2 details the characterisation of two types of DMSs containing the element Sb. These DMSs are of interest as the heavy Sb atom should give them larger SOC than (Ga,Mn)As, and therefore possibly also stronger SOC-based phenomena that can set or detect their magnetic state. Chapter 3 investigates AMR in the DMS (Ga,Mn)($As_{0.9}$,$Sb_{0.1}$) (which has unique electronic and magnetic properties) in order to try and gain a greater knowledge of the origin of the various contributions to AMR in DMSs. Chapter 4 details an alternative experimental technique to detecting current induced fields (CIFs) associated with the spin-orbit torque phenomenon in DMSs. The technique is then applied to investigate how the CIFs in (Ga,Mn)As vary with temperature in order to further understand the origins of the SOT effect. Chapter 5 reports on an experimental attempt to magnetically gate a 2D electron gas (2DEG). As no current flows through the magnetic layer of the device (unlike AMR, TMR, GMR etc), the realisation of such an experiment would be a demonstration of a novel approach to varying electric current with magnetic orientation. Chapter 6 presents a preliminary study of attempts to reorientate the spin-axis of an antiferromagnet by applying electrical current. The material investigated in this chapter, CuMnAs, varies from those used in the rest of the thesis in that it is antiferromagnetic and (probably)a semimetal. However the motivation of setting and detecting the magnetic state with electrical current remains the same. Chapter 7 briefly summarises the work of the thesis and the conclusions drawn. Finally, the appendix provides details of three short collaborative side-projects that were also undertaken during the course of the work for this thesis.

1.2 (Ga,Mn)As: The prototypical diluted magnetic semiconductor

1.2.1 Diluted magnetic semiconductors

The terms diluted magnetic semiconductor, ferromagnetic semiconductor, and magnetic semiconductor are all often used interchangeably to describe a material that is both semiconducting and magnetic. DMS is the preferred term for this thesis as the focus will be on materials where a host semiconductor lattice is doped with substitutional magnetic impurities that are commensurate with the lattice and randomly distributed within it, as opposed to ionic ferromagnetic compounds such as EuS or $CdCr_2Se_4$.

Sustained interest in DMSs began in the 1970's with reports of a variety of II-VI semiconductors (such as HgTe, CdTe, and ZnSe) doped with the divalent cations Mn and Co[26][27] which have unfilled d electron shells and thus a finite magnetic moment. In these materials the interaction between the magnetic dopant ions is dominated by antiferromagnetic exchange, and depending on temperature and dopant concentration the II-VI DMS shows either antiferromagnetic, paramagnetic, or spin glass type behaviour. Research into II-VI DMSs continues to make progress, and since the late 1990's there have been observations of carrier-induced ferromag-

netism in II-VI DMSs co-doped with with donor ions which allows the spin and carrier densities to be independently controlled[28][29]. Meanwhile there is much recent interest in oxide based DMSs, including magnetic doping of the wide band gap ZnO where above room temperature ferromagnetism has been reported[30][31]. The carrier induced ferromagnetism in II-VI semiconductors exists only at very low temperatures, while the room temperature ferromagnetic ordering in oxide DMSs is not mediated by itinerant carriers (and is likely to be arise from magnetic clustering) and thus is not easy to control by doping or other conventional means. Therefore, both II-VI and oxide DMSs are perhaps not the most promising class of DMS for use in practical applications.

Since Hideo Ohno's successful non-equilibrium two dimensional growths of (In,Mn)As[32] and (Ga,Mn)As[33] by molecular beam epitaxy (MBE) in the 1990's, III-V semiconductors doped with Mn have become the most widely studied class of DMSs and arguably the flagship spintronic material. The physics behind III-V DMSs is presented in section 1.2.2, but in brief the interest in these materials can be attributed to a number of factors. Firstly, the ferromagnetic ordering between the Mn dopants is mediated by holes provided by the Mn dopants, and therefore the magnetic properties of III-V DMSs are closely linked to their carriers. This allows for novel control of magnetization by various methods besides applying an external magnetic field. Secondly, this type of carrier induced ferromagnetism allows for DMSs with relatively high Curie temperatures (T_c - around 185K for (Ga,Mn)As[34][35]), which is obviously essential for everyday device applications. Thirdly, as III-V semiconductors are used for many traditional charge based electronic applications, III-V DMSs should be able to integrate fairly easily within existing device structures. Finally, as III-V DMSs have strong SOC (and also a broken inversion symmetry) they offer additional potential device functionality that other spintronic materials with weaker SOC cannot match.

Initially there was much hope that III-V DMSs, in particular (Ga,Mn)As, could be used for real world applications. However, it has recently been accepted by some in the III-V DMS community that there is not a great prospect of realising suitable materials with above room temperature T_c[36][10]. Nevertheless, despite their limited practical potential, III-V DMSs are still very much an active part of spintronics research today, often in the role as a test-bed material that is used to explore various emerging spintronic phenomena, owing largely to the tunability of their properties and the relatively good understanding of their underlying physics.

1.2.2 Properties of (Ga,Mn)As

This section reviews the physics of (Ga,Mn)As. (Ga,Mn)As is chosen as it is the most widely studied and well understood III-V DMS, however much of the physics described here applies to other III-V DMSs such as (Ga,Mn)Sb, (Ga,Mn)P, (In,Mn)As (not so much for (Ga,Mn)N which has more distinct structural, electronic, and magnetic properties).

1.2.2.1 Growth by molecular beam epitaxy

Using MBE to grow III-V DMSs was pioneered by Munekata and Ohno in 1989[37] and is now by a long way the most established and widely used method of obtaining high quality III-V DMS samples. MBE itself has been around since the late 1960's[38] and is also commonly used today to manufacture semiconductor devices. All samples studied in this thesis are grown by MBE in the Nottingham MBE machine by Dr Richard Campion.

As the name suggests, MBE is an epitaxial growth technique, i.e. single crystal films are grown layer by layer on top of a single crystal substrate. The basic methodology of MBE growth is as follows: Growth takes places in a chamber that is under ultra high vacuum (UHV - around 10^{-8}Pa). The UHV is essential for the growth of high purity samples with low deposition rates. Elemental sources (e.g. pure Ga) are heated in Knudsen cells outside of the main chamber until their phases change directly from solid to gas. A shutter between the Knudsen cell and the main chamber can then be opened which allows a beam of the gaseous element to be fired into the main chamber where it is targeted at a substrate. Due to the UHV these elemental beams have long mean free paths and do not interact with one another before hitting the substrate. The substrate is heated to an appropriate temperature and rotated to encourage uniform growth across it. The slow deposition rate (around 5nm per minute) allows the various atoms time to react with one another and move about on the surface before the next layer of atoms is deposited on top, which means that the epitaxial layers can adopt the same structure as the substrate. The growth is tracked by reflection high energy electron diffraction (RHEED), a technique that depends largely on the surface layer of atoms but also on thickness, thus allowing the grower to monitor the surface reconstruction and film thickness *in situ*. The relative flux of the elemental beams allows for control of the ratio of atomic composition in the growth of compound materials. Finally, as the shutter speed on the Knudsen cells is much greater than the deposition rate, it is possible to grow samples with atomically sharp interfaces using MBE.

Under thermal equilibrium growth conditions, Mn is found to have a low solubility in GaAs (at most 10^{19}cm^{-3}), beyond which it tends to aggregate on the surface and even combine with As to form separate phases (three-dimensional growth). The breakthrough found by Munekata and Ohno was that by lowering the growth (substrate) temperature to around 200°C - 300°C (low temperature MBE, LT-MBE), non-equilibrium growth can be achieved that allows random incorporation of Mn into the III-V lattice past its solubility limits and yet remains two-dimensional. In practice it is found that the highest quality crystal growth of (Ga,Mn)As takes place on the edge of the two dimensional side of the two-dimensional/three-dimensional growth boundary[39], a boundary that depends upon growth temperature and nominal Mn concentration as shown in figure 1.1.

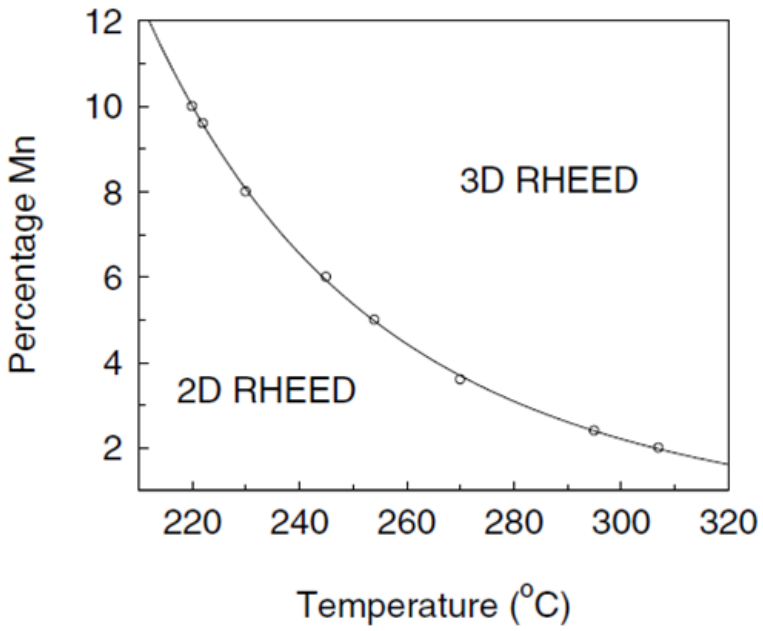

Figure 1.1: Phases of two dimensional and three-dimensional growth of (Ga,Mn)As (as indicated by RHEED) as function of nominal Mn concentration and growth temperature. Plot taken from reference [39]

Due to energetic considerations, nearby Mn atoms attract during growth, and while the LT-MBE growth conditions prevents the formation of Mn clusters, it does not prevent the formation of Mn dimers. At the surface, $[1\bar{1}0]$ and [110] crystalline directions are not equivalent (as shown in figure 1.2), and as the Mn atoms along the $[1\bar{1}0]$ direction are connected to the same As atom they have a lower energy cost, and so dimer formation in the $[1\bar{1}0]$ direction is favoured over the [110] direction. While the Mn distribution remains random on the nm scale[40], the epitaxial growth technique may allow for Mn distribution along preferential directions on the sub-nm scale, and this could be the origin of the observed uni-axial contribution to the magnetic anisotropy (see section 1.2.2.5).

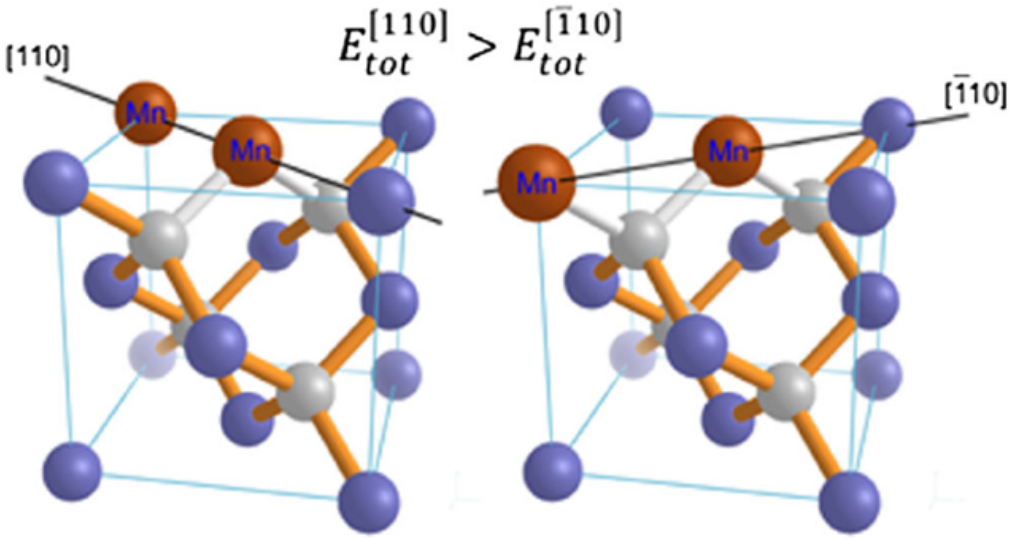

Figure 1.2: Diagram of Mn dimers along the [110] and [1$\bar{1}$0] crystalline directions on the surface of a GaAs lattice. Image taken from reference [41].

1.2.2.2 Structure and defects

The ideal structure of (Ga,Mn)As is that of a zincblende GaAs lattice (interpenetrating Ga and As face centred cubic lattices) with Mn^{2+} ions substituting at random Ga sites by an amount equal to the nominal Mn doping concentration as shown in the left-hand side diagram of figure 1.3.

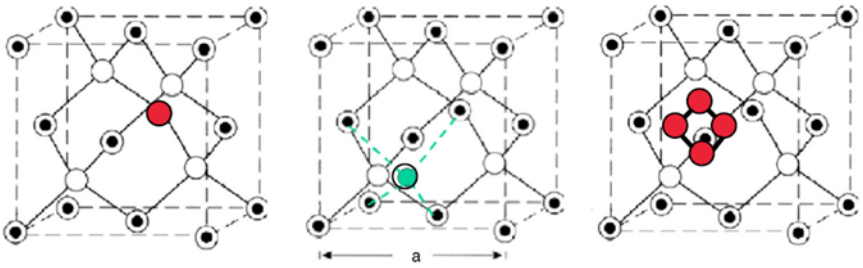

Figure 1.3: Structure of (Ga,Mn)As lattice for substitutional Mn (left-hand side), interstitial Mn (middle), and incommensurate Mn (right-hand side). Ga are circles with dots in the middle, As are open circles, and Mn are filled circles. Image is taken from reference [42].

Mn tends to substitute for Ga as opposed to As atoms as it is energetically more favourable given the respective valencies of the elements: Mn = [Ar]$3d^5 4s^2$, Ga = [Ar]$3d^{10} 4s^2 4p^1$, As = [Ar]$3d^{10} 4s^2 4p^3$. The two $4s$ electrons of Mn take part in the crystal bonding much in the same way as the $4s$ electrons of Ga (and thus the Mn effectively enters the lattice as a Mn^{2+} ion), however, as Mn is missing a single $4p$ electron compared to Ga it needs to accept an electron to fulfil bonding requirements, which therefore introduces a hole into the system that is locally

bound to its substitutional Mn.

Mn has a larger covalent radius than Ga (despite having a smaller atomic radius), and so ideal (Ga,Mn)As has a larger relaxed lattice parameter than GaAs. (Ga,Mn)As is nevertheless most commonly grown on a GaAs substrate as it is the closest lattice match. The nature of the epitaxial growth allows deposited (Ga,Mn)As layers to adopt the in-plane lattice parameter of GaAs, and therefore they are under in-plane compressive strain with a tetragonal distortion along the growth direction. The (Ga,Mn)As layer tends to remain fully strained up to relatively large ($\approx 1\mu$m) film thicknesses. Similarly, (Ga,Mn)As can also be grown on substrates or buffer layers which have a larger lattice parameter than it (e.g. (In,Ga)As), and this puts the (Ga,Mn)As film under tensile strain.

The low growth temperature of (Ga,Mn)As on GaAs prevents the formation of lattice dislocations that would be expected under equilibrium growth conditions, however, several types of other defects are known to occur in (Ga,Mn)As films. The most common defect is Mn taking an interstitial position within the GaAs lattice as opposed to substituting for Ga (see the middle diagram of figure 1.3), and this expands the (Ga,Mn)As lattice[43] and therefore increases its growth strain. Interstitial Mn does not participate in bonding within the lattice and acts as a double donor, contributing its two $4s$ electrons. It is found that as the nominal Mn doping concentration increases, the relative percentage of Mn taking interstitial positions as opposed to substitutional positions increases[44], and this suggests that the formation of interstitial Mn occurs in order to stabilise the hole density and therefore the Fermi level and system energy (self-compensation). The As antisite, another major defect in (Ga,Mn)As (as well as in GaAs), also forms to allow self-compensation. The As antisite defect is an As atom that resides at a Ga lattice site and so the extra two $4p$ electrons it provides to the site also act as donors that reduce the hole density. Interstitial Mn can be largely removed from thin (<100nm)(Ga,Mn)As films by annealing at temperatures just below or around the growth temperature[45], and indeed all annealed samples studied in this thesis are annealed at a temperature of 180°C. Such temperatures are sufficient to overcome the formation energy of interstitial Mn but not substitutional Mn, and so the interstitial Mn, which are relatively mobile due to the number of unoccupied interstitial lattice sites, out-diffuse to the film surface where they become oxidised whereas the substitutional Mn remain in their lattice position. In this thesis, non-annealed and annealed films will be identified by use of the prefixes 'as-grown' and 'annealed' respectively.

Finally, it has previously been shown that in some as-grown (Ga,Mn)As films, up to half of the Mn within the film resides in locations that are incommensurate with the lattice[46]. These incommensurate Mn may take the form of magnetic clusters, as is shown in the right-hand side diagram of figure 1.3, but perhaps more likely is that they reside on the film surface, having out-diffused there during growth. Such surface random Mn can be removed from the film by appropriate etching, for example with HCl.

1.2.2.3 Electronic structure and transport properties

GaAs is a direct gap semiconductor with a band gap of 1.43eV at room temperature[47]. As discussed in section 1.2.2.2, substitutional Mn acts as an acceptor in the GaAs as it introduces locally bound holes into the system, and so (Ga,Mn)As has distinct transport behaviour from un-doped GaAs. At Mn doping concentrations of $<<1\%$, the distance between Mn ions is much greater than the Bohr radius of the bound holes, and so there is no overlap between hole states. These localised holes can be thought of as occupying a narrow impurity band associated with the Mn $3d$ states that is separate from the GaAs valence band and in which the Fermi level resides at such low doping concentrations (see the left-hand side diagram of figure 1.4). As the substitutional Mn concentration increases to $\approx 1\%$, the distance between Mn ions (and their associated bound holes) is sufficiently small that Mn $3d$ states begin to overlap with states at the top of the valence band (which are largely As $4p$) as shown in the middle diagram of figure 1.4. While the system remains insulating at this level of doping, the overlapping of the Mn $3d$ and As $4p$ states is significant for the onset of ferromagnetism, as is discussed in section 1.2.2.5. When the substitutional Mn concentration is increased to beyond $\approx 2\%$, the density of the Mn ions and their holes is sufficient that the hole states overlap and so holes are no longer localised to one lattice site. This delocalisation of hole states at the Fermi level (which now lies within the top of the valence band as shown in the right-hand side diagram of figure 1.4) is accompanied by the system exhibiting metallic behaviour. Further increases in the substitutional Mn concentration push the Fermi level deeper into the valence band where the states are more delocalised, however, as stated in section 1.2.2.2, self-compensation effects limit the lowering of the Fermi level at higher substitutional Mn concentrations.

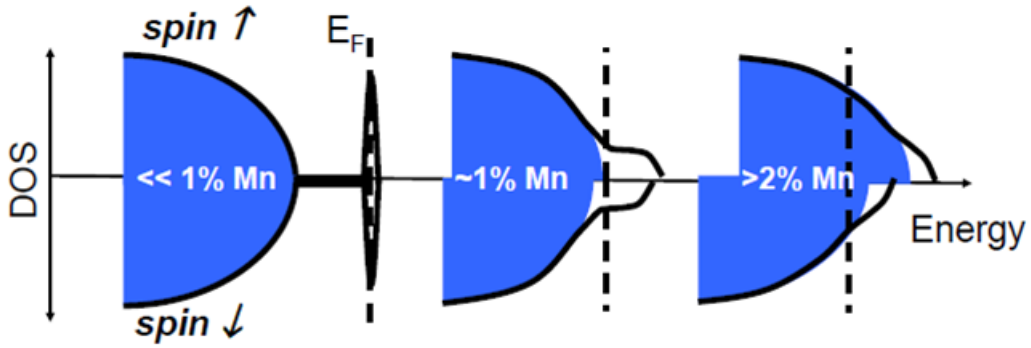

Figure 1.4: Density of states of (Ga,Mn)As for different Mn concentrations. (Left-hand side): Fermi level lies in a narrow impurity band separate from the valence band, insulating behaviour. (Middle): Fermi level lies at top edge of valence band that begins to merge with impurity band, onset of ferromagnetism. (Left-hand side): Fermi level lies within the spin-split valence band that is fully merged with Mn impurity states, metallic conductivity. Diagram taken from reference [42].

As the Mn dopants introduce holes into the system, (Ga,Mn)As exhibits p-type conductivity. Despite each substitutional Mn providing one hole, the hole density of (Ga,Mn)As never corresponds to the nominal Mn concentration due to the

presence of interstitial Mn and As antisite hole compensating defects, as well as incommensurate Mn that do not compensate holes but also do not provide them. The hole density of (Ga,Mn)As largely depends on the factors of Mn doping concentration and annealing conditions, but other factors such as growth conditions, film thickness, choice of substrate, and even the measurement technique used to infer the hole density[48][49][50][51] are likely to also play a role. Therefore, there is no solid quantitative trend as to how hole density varies with nominal Mn concentration, but generally it non-linearly increases from the range of around $0.4\text{x}10^{21}\text{cm}^{-3}$ to $2\text{x}10^{21}\text{cm}^{-3}$ as Mn concentration increases from around 3% to 14% in annealed samples[52][53], and remains fairly constant at a value of around $0.4\text{x}10^{21}\text{cm}^{-3}$ for the same Mn concentration range for as-grown samples[53][42][54]. Mobility tends to decrease with increasing Mn concentration due to increased ionized scattering of holes off impurities[55], and overall for optimally annealed samples the competition between the trends of hole density and mobility with Mn concentration result in the conductivity at 10K only slightly increasing with increasing Mn concentration[55][52], as shown in figure 1.5.

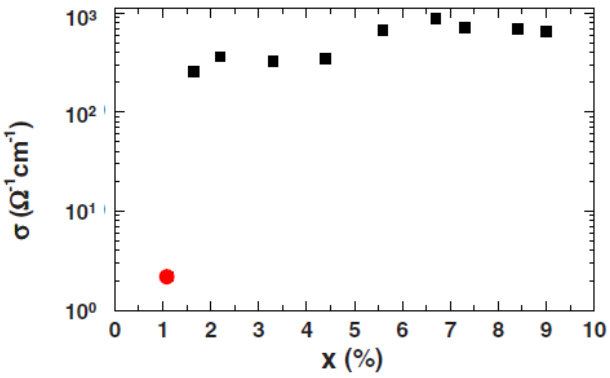

Figure 1.5: Conductivity of optimally annealed (Ga,Mn)As against nominal Mn concentration measured at a temperature of 10K. Red dot indicates insulating sample. Plot taken from reference [55].

1.2.2.4 Spin-orbit coupling

The terms spin-orbit coupling (SOC) and spin-orbit interaction (SOI) are often used interchangeably, and in the context of this thesis both refer to the same mechanism which makes the spin of an electron respond to its orbital environment. At an atomic level, SOC arises as follows: A negatively charged electron will quantum mechanically orbit a positively charged nucleus at relativistic speeds, and in the rest-frame of the electron, the charge of the nucleus is seen as a magnetic field. The electron has finite spin angular momentum and therefore a finite magnetic moment, and so the effective magnetic field from the nucleus acts to reorientate the electron's magnetic moment (in a direction perpendicular to its velocity). The modification in the electron's energy resulting from this SOC is described by the Hamiltonian:

$$H_{SO} = \mathbf{B}_{eff} \cdot \mathbf{S} = (\frac{1}{2m_e^2c^2}\nabla V \times \mathbf{p}) \cdot \mathbf{S} \tag{1.1}$$

where $\mathbf{B}_{eff}$ is the effective magnetic field experienced by the electron, $\mathbf{S}$ is the spin angular momentum of the electron, m_e is the electron mass, V is the electric potential at the position of the electron, and $\mathbf{p}$ is the electron's momentum.

Crystalline solids are made up of individual atoms that electronically bond together to form a periodic lattice, and therefore the atomic energy levels defined by individual electrons orbiting their respective nucleus merge into energy bands that characterise the energy and motion of an electron (or hole) within the solid. Atomic SOC manifests itself in crystalline solids as a splitting of energy sub-bands with different total angular momentum quantum number j at zero wave vector ($k = 0$). This is seen in figure 1.6, where the atomic (also know as fundamental) SOC splits the six-fold degenerate valence band of GaAs into a four-fold degenerate sub-band with $j = 3/2$ and a two-fold degenerate sub-band with $j = 1/2$ (i.e. sub-bands with orbital angular momentum quantum numbers $l = 1$ and $l = 0$), thus introducing a fundamental SOC energy gap at $k = 0$.

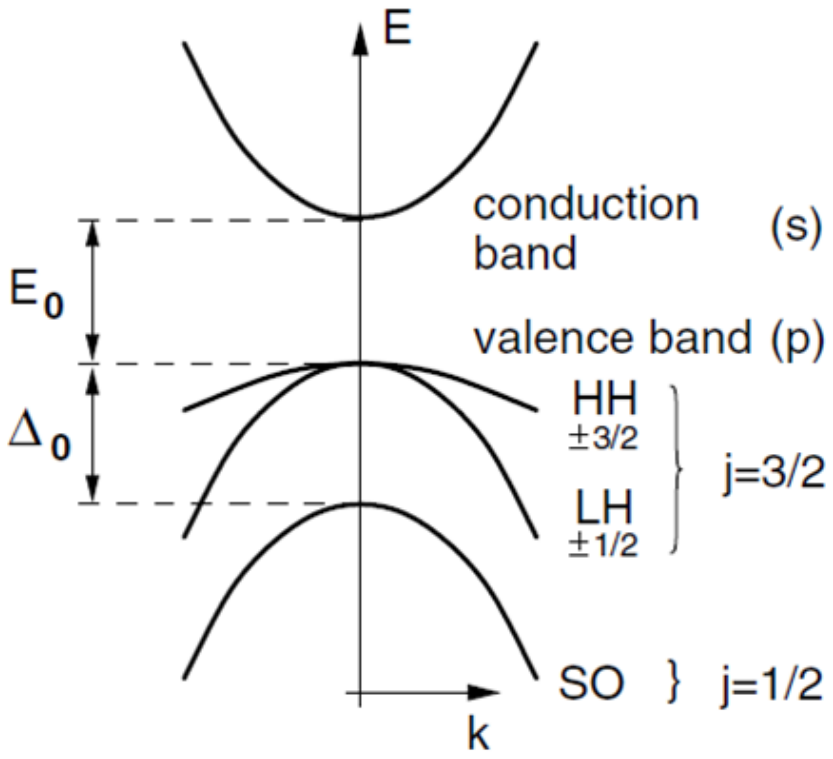

Figure 1.6: Conduction and valence band edges for GaAs (applicable for other III-V semiconductors too). E_0 is the band gap, and Δ_0 is the fundamental spin-split off gap. HH are heavy hole states ($j = 3/2$ states with secondary total angular momentum quantum number $m_j = \pm 3/2$) and LH are light hole states ($j = 3/2$ states with $m_j = \pm 1/2$). Diagram taken from reference [56].

The size of the spin-split off gap varies for different semiconductors. It is usually smaller than the band gap, but can be of a comparable size. Figure 1.7 presents a table of band gaps and spin-split off gaps at 4K for various semiconductors.

Semiconductor	GaAs	GaSb	AlAs	InAs	InSb	Si	CdTe
Band gap (eV)	1.52	0.81	3.13	0.42	0.24	1.17	1.61
Spin-split off gap (eV)	0.34	0.75	0.30	0.38	0.81	0.04	0.95

Figure 1.7: Table of band gaps and energy gaps of various semiconductors at 4K. Values obtained from references [56] and [57].

It is clear from figure 1.6 that fundamental SOC affects the orbital degree of freedom of a carrier in a crystalline solid, but in crystalline solids that lack a centre of inversion symmetry, the spin degree of freedom of a carrier can also be affected by additional forms of SOC, for example Rashba and Dresselhaus SOC. These SOCs lift the degeneracy of the heavy hole, light hole, and spin-split off sub-bands with different spin-orientation at finite wave vectors, even in the absence of a magnetic field. Rashba and Dresselhaus style SOCs are covered in more detail in chapter 4.

The electronic structure of a crystalline lattice essentially arises from hybridisation of the electron orbitals of neighbouring atoms, and so SOC effectively links carrier spin to the lattice, and this gives large contributions to effects such as magnetocrystalline anisotropy and spin relaxation. Furthermore, SOC is at the heart of many relativistic effects in spintronics, and so can be viewed as a desirable property for a spintronic material. In GaAs, the effects of spin-orbit splitting of the conduction band in the gamma valley are relatively weak but are strong at the top of the valence band where the heavy hole states are largely As $4p$ in character. This is beneficial for (Ga,Mn)As where, as a result of doping with the acceptor Mn, the Fermi level lies within these heavy hole states and so the effect of SOC on the carriers is large. SOC scales with atomic number (as the orbiting electron sees the bigger nuclear charge as a bigger magnetic field), and so the heavier As atom gives a bigger fundamental SOC than other semiconductors like Si. Additionally, the zincblende (Ga,Mn)As lattice is strained by its substrate which allows for significant inversion asymmetry SOC effects, again that would not be present in Si. The strong SOC effects at the Fermi level in (Ga,Mn)As therefore make it an ideal test-bed material to understand relativistic spintronic phenomena.

1.2.2.5 Magnetic properties

Ferromagnetism is the spontaneous alignment of the individual magnetic dipole moments of a system which results in a net magnetization. Magnetic dipole moments arise from unpaired electron (or hole) spins (spin magnetic moment) as well as from the orbital motion of electrons (orbital magnetic moment). In (Ga,Mn)As two sources of magnetic moment will be considered, both of which are introduced by the Mn dopants. Firstly, as stated in section 1.2.2.3, the Mn $3d$ electron shell contains 5 electrons and is thus only half filled. In accordance with Hund's rules, the 5 electrons take the same spin state by occupying all five $3d$ sub-orbitals, and therefore the Mn $3d$ shell has a total spin angular momentum $\mathbf{S} = 5/2$ and a total orbital angular momentum $\mathbf{L} = 0$, and so a magnetic moment of $5\mu_B$ (where μ_B is

the Bohr magneton). Secondly, also as stated in section 1.2.2.3, each substitutional Mn introduces a single carrier hole into (Ga,Mn)As, which has a finite magnetic moment due to its uncompensated spin and orbital angular momentum. While GaAs itself can have a diamagnetic response to an external field, such effects are not significant in the discussion of magnetism in (Ga,Mn)As.

Ferromagnetism is a quantum mechanical effect that stems from electron spin, the Pauli exclusion principle, and Coulomb interactions. The interplay between these factors leads to exchange interactions between individual magnetic moments that result in magnetic ordering. There are multiple mechanisms of exchange interactions, and these do not necessarily have to favour neighbouring magnetic moments spontaneously aligning ferromagnetically, for example bulk Mn is either paramagnetic or antiferromagnetic depending on its structural phase[58] (and therefore the strength of the governing exchange interactions). At low doping concentrations ($<<1\%$), the moments of the Mn ions substituted into the GaAs lattice are randomly orientated, and so the (Ga,Mn)As is paramagnetic. At these low doping concentrations not only are Mn ions sufficiently separated to prevent significant direct exchange interaction between themselves, but also their bound holes are sufficiently localised to prevent any significant exchange interaction between a hole localised on one Mn ion with a neighbouring Mn ion (i.e. indirect exchange between Mn ions). Ferromagnetism begins to occur at Mn doping concentrations of $\approx 1\%$. In this regime contributions from a double exchange mechanism where carrier hopping between localised states in a Mn impurity band brings about Mn-Mn interactions may play a role, but the significant source of ferromagnetism for higher Mn concentrations begins to emerge, namely hybridisation of the $4p$ states at the top of the valence band with the Mn $3d$ states. As discussed in section 1.2.2.3, at a Mn concentration of $\approx 1\%$, holes become sufficiently delocalised that they enter the $4p$ states at the top of the valence band, in which the filled Mn $3d$ states lie. Due to the effects of hybridization and repulsion between orbitals of the same spin, spins of the valence band carriers align antiferromagnetically with the local Mn $3d$ spins, and this leads to a net ferromagnetic alignment between the Mn moments. This is a 'Zener kinetic exchange' style interaction[59], but for simplicity the mechanism of ferromagnetism in (Ga,Mn)As is often ascribed to 'carrier mediated ferromagnetism'.

For the ideal case of (Ga,Mn)As with substitutional Mn only, the net moment per Mn atom and acceptor hole has been theoretically predicted[60] and experimentally shown for a range of Mn concentrations[61] to be $\approx 4.5\mu_B$, which reflects the $5\mu_B$ moment of Mn being compensated by its antiferromagnetic alignment with the acceptor hole. The value of the net moment per Mn atom is further reduced in systems where interstitial Mn is present. Interstitial Mn are positively charged and mobile, and during the growth of (Ga,Mn)As this allows them to take up positions next to negatively charged substitutional Mn. Because interstitial Mn do not form on lattice sites, they are in close enough proximity to substitutional Mn that a short-range antiferromagnetic interaction between the interstitial and substitutional Mn moments takes place, i.e. their moments align in opposite directions. This antiferromagnetic alignment lowers the net moment per Mn atom and net magnetization of the system as each interstitial Mn moment approximately

compensates one substitutional Mn moment. Interstitial Mn is also deleterious to ferromagnetism in (Ga,Mn)As as it is a double donor and so compensates the carrier holes required for the carrier mediated ferromagnetic interactions between substitutional Mn ions. The net magnetization of the (Ga,Mn)As sample gets weaker with increasing temperature due to thermal fluctuations, and T_c is defined at the temperature at which the spontaneous net magnetic moment becomes zero. For (Ga,Mn)As, the value of T_c increases approximately linearly with the effective Mn concentration[62] (which is the substitutional Mn concentration minus the interstitial Mn concentration) in accordance with predictions of a modified *p-d* Zener model[63]. This trend deviates slightly at higher Mn concentrations due to the formation of the hole compensating As antisites. Varying the hole density of (Ga,Mn)As, which can be achieved via electrical gating, has also been shown to lead to a change in T_c that is approximately proportional to the hole density to the power of 0.2[64]. Therefore, as T_c scales with both effective Mn concentration and hole density, removing interstitial Mn from (Ga,Mn)As significantly enhances its value. An example of this is reported in reference [65] where T_c of a 12% Mn doped (Ga,Mn)As sample increases by approximately 110K upon annealing from its as-grown state.

(Ga,Mn)As is not a magnetically isotropic material, and so below T_c and in the absence of an external magnetic field its magnetization prefers to align itself along a certain crystalline direction(s), known as an easy axis (axes). Note that in this discussion only single domain magnetic behaviour is considered. In general, magnetic anisotropy can have several sources including magnetocrystalline anisotropy, magnetoelastic anisotropy, shape anisotropy, and exchange anisotropy. The magnetic anisotropy of (Ga,Mn)As is largely dictated by the former two contributions, both of which originate predominantly as a result of SOC. The $3d$ electrons provide (Ga,Mn)As with its magnetic moment, however they have zero total orbital angular momentum and so are not spin-orbit coupled. Therefore, it is the spin-orbit coupled $4p$ valence band holes that are required to bring about the anisotropy of the $3d$ moments. Shape anisotropy is not related to SOC and is often important in dense moment thin ferromagnetic films where it acts to minimise demagnetizing fields by aligning the magnetization in the sample plane. (Ga,Mn)As, however, is a dilute ferromagnet, and so the demagnetizing fields are relatively small and therefore shape anisotropy does not play such a key role in its overall magnetic anisotropy. Exchange anisotropy can be significant in (Ga,Mn)As layers that share an interface with another magnetic layer[66], but as only single (Ga,Mn)As layers are considered in this discussion exchange anisotropy is not relevant.

As stated in section 1.2.2.4, electron orbitals of neighbouring atoms overlap in the formation of a crystalline lattice structure. SOC links spin and orbital angular momentum, and so the preferential alignment of orbitals to form the lattice will therefore also lead to a preferential alignment of spins with respect to the lattice. In the case of (Ga,Mn)As this preferential alignment of the hole spins leads to a preferential alignment of the Mn $3d$ spins due to *p-d* hybridisation. From an alternative viewpoint, if the alignment of the Mn spins (and therefore also the hole spins) is altered, say by an external magnetic field, the hole orbit will also be altered, and this will have an associated energy cost given the electrostatic potential of the periodic

crystalline lattice. This is a simplistic qualitative description of magnetocrystalline anisotropy - magnetoelastic anisotropy is essentially an extension of this where strain alters the shape of a crystalline lattice, thus altering the charge carrier's orbital shape, and so ultimately leads to a change in its preferential spin orientation.

In (Ga,Mn)As there are three major types of magnetic anisotropy: In plane cubic, in plane uni-axial, and out of plane uni-axial.

• **In plane cubic magnetic anisotropy** arises from the strained zincblende lattice structure breaking cubic symmetry[10]. For (Ga,Mn)As the in plane cubic magnetic anisotropy constant (K_C) is positive meaning that the cubic easy axes lie along the <100> directions (i.e. the single domain magnetization will align itself along either of the equivalent [100] or [010] axes), which is in contrast to certain (In,Mn)As[67] and (Ga,Mn)P[68] samples where K_C is negative and so the cubic easy axes lie along the <110> directions. Theoretically the sign of K_C for (Ga,Mn)As has been shown to vary with hole density[69]. The strength of the in plane cubic anisotropy is approximately proportional to the magnetization strength to the power of 4 ($K_C \sim \mathrm{M}^4$), and so K_C falls quickly with increasing temperature.

• **In plane uniaxial magnetic anisotropy** is not expected from the symmetry of the strained zincblende lattice. In plane uniaxial magnetic anisotropy manifests itself as breaking of the symmetry of the $[1\bar{1}0]$ and [110] directions, making it more energetically favourable for the magnetization to align along one compared to the other. Generally for (Ga,Mn)As the $[1\bar{1}0]$ direction tends to be the easier[53], however for high Mn concentration samples the in-plane uniaxial easy direction has been demonstrated to switch from $[1\bar{1}0]$ to [110] at higher temperatures[70]. The strength of the in plane uniaxial magnetic anisotropy is approximately proportional to the square of the magnetization strength ($K_U \sim \mathrm{M}^2$), and so K_U falls less rapidly than K_C with increasing temperature. The origin of the in plane uniaxial magnetic anisotropy is still not clear, but it may be related to the formation of Mn dimers along preferential directions[41] (see section 1.2.2.1). Theoretically it can be modelled by including a shear strain in calculations[71], and it has been shown to also vary with hole density[72].

• **Out of plane uniaxial magnetic anisotropy** is largely dependant on the sign of the growth strain. For samples under tensile growth strain, such as (Ga,Mn)As grown on a (In,Ga)As substrate[73], an out of plane easy axis is favoured. Samples under compressive growth strain, such as (Ga,Mn)As grown on GaAs substrate[53], tend to favour an in plane easy axis/axes. For both tensile and compressive strains, the out of plane magnetic anisotropy changes sign at sufficiently low hole density, e.g. a compressively strained samples favours an out of plane easy axis[74], and in this low hole density regime the out of plane magnetic anisotropy can also change sign with changing temperature[74].

If the out of plane anisotropy is such that an in plane easy axis is favoured (as is the case for all III-V DMS samples in this thesis), the orientation of the magnetization is that which minimises the magnetic anisotropy energy, which is given by the phenomenological expression:

$$E_a = K_U sin^2\theta - \frac{K_C}{4} sin^2 2\theta \tag{1.2}$$

where E_a is the magnetic anisotropy energy and θ is the angle between the magnetization and the $[1\bar{1}0]$ direction. If $K_U \geq K_C$ then the magnetic anisotropy is fully uniaxial and the magnetization lies parallel or antiparallel to the $[1\bar{1}0]$ direction, and if $K_U < K_C$ then the magnetic anisotropy is biaxial, with the magnetization lying along either of the easy axes at the angle $\theta = \frac{1}{2} arcos(K_U/K_C)$.

Some higher Mn doped samples are uniaxial across the temperature range[65], however many (Ga,Mn)As samples have biaxial magnetic anisotropy at low temperatures, but go through a spin reorientation transition (SRT) as temperature increases and the sample becomes magnetically uniaxial as K_U becomes stronger than K_C[75]. As magnetic anisotropy is also sensitive to strain and hole density as well as magnetization strength, SRTs have also been experimentally achieved through modulating strain and carrier density with piezoelectric transducers[76] and electrical gating[77] respectively.

1.3 Experimental measurement techniques

1.3.1 Device fabrication

In order to perform a measurement on a material, it must first be processed into a shape that is appropriate for the given measurement. Materials in this thesis are generally MBE grown onto substrate wafers of around 300μm thickness and typically a few cm^2 in area. For SQUID magnetometry and XMCD measurements the only processing required is scribing the sample wafer along the appropriate crystalline directions to a suitable area. This is done using a scribing tip and applying gentle pressure to break the substrate. For SQUID measurements the wafer is usually scribed along the $[1\bar{1}0]$ and [110] directions into 5mm by 4mm pieces. For transport measurements more sophisticated processing is required to create devices of more complex shapes and of dimensions of the order of tens of μm.

Semiconductor processing has become a major global industry that is of vital importance to consumer electronics. Improvements in processing techniques over the last half century have been a major driving force in the continuation of Moore's law. Many of the general steps involved in fabricating the devices used in this thesis are the same as those used in industry to produce semiconductor components for electronic devices, though obviously the achievable resolution of devices and scale of production differ. The $\approx 10\mu$m resolution of features required for devices studied in this thesis was available to the semiconductor processing industry in the early 1970's, and is achievable through optical lithography and wet etching, which is the device fabrication technique used to make the devices in this thesis.

All fabrication of devices was carried out in the Nottingham cleanroom to prevent contamination from particles of significant dimensions with respect to the device

size. The majority of the devices studied in this thesis are Hall bar structures (see figure 1.8), but Corbino disk and specific gated Hall bars were also processed. To process Hall bars from sample wafer the following multi-step procedure is performed:

1. The sample wafer is scribed into a chip of manageable dimensions for the fabrication procedure, usually around $1cm^2$ - $2cm^2$.
2. The chip is immersed in methanol and gently agitated for 5 minutes to clean dirt from the surface. This step is repeated for immersion in acetone, ethyl lactate, and isopropyl alcohol. Chip is dried with a nitrogen gun.
3. The chip is placed in an oven at 100°C for 2 minutes to remove any remaining solvent from the surface. This step can be skipped if it is not desirable to expose the sample to such a temperature.
4. The chip is covered in photoresist (BPRS 100 or 150) and spun at around 700rpm to ensure a uniform distribution of photoresist across the surface of about 100μm thickness (spin-coating).
5. The chip is baked on a hot plate at 90°C for 2 minutes to remove excess solvent from the photoresist.
6. The chip is placed directly underneath a photomask, which is patterned with Hall bar (or other device structure) shapes. The area of the Hall bar is dark on the mask, the other areas are transparent. The mask is exposed to high intensity UV light, and therefore also the sections of the chip under transparent areas of the mask. Exposure to the UV light chemically alters the photoresist to make it soluble in a developer solution.
7. The chip is immersed in developer solution (usually H_2O and AZ400K in a 7:1 ratio) for around 20s which dissolves all the exposed resit, only leaving resist on the chip in the desired pattern.
8. The thickness of the photoresist is checked using a Dektak surface profiler. This is needed to check the etch depth during the etching process.
9. The chip is etched in a chemical solution. Areas of the chip covered in photoresist are generally unaffected by the etch as the photoresist is immune to the etchant solution. Uncovered areas of the chip are chemically removed by the etchant solution at a rate that depends on the solution and its strength. As a result, the Hall bar pattern becomes defined in the chip. The etch depth can be checked during the etch by removing the chip from the solution and measuring with the surface profiler. For etching (Ga,Mn)As and/or GaAs, a solution of H_2O:H_2SO_4:H_3PO_4:H_2O_2 at a 12:1:1:1 ratio is used, which gives an etch rate of around 100 nm/minute.
10. The chip is immersed in acetone on a hot plate at 90°C and gently stirred to remove the remaining photoresist from the surface.
11. Steps 4-7 are repeated, but this time a photomask is used so that all of the chip is covered in photoresist except for areas where contact pads are to go.
12. The chip is placed in an evaporator system that is pumped down to a vacuum of around 1 x 10^{-3}mbar. Metals to form the contact pad are thermally evaporated onto the chip. 20nm Ti followed by 150nm of Au is the standard recipe for contacts on (Ga,Mn)As.
13. Step 10 is repeated to leave patterned devices with contact pads.
14. The chip is scribed into individual devices.
15. An individual device is mounted onto a non-magnetic sample holder using GE

varnish.
16. Electrical contacts are made between sample header and the device contact pads by wedge bonding with 17.5μm diameter Al wire.

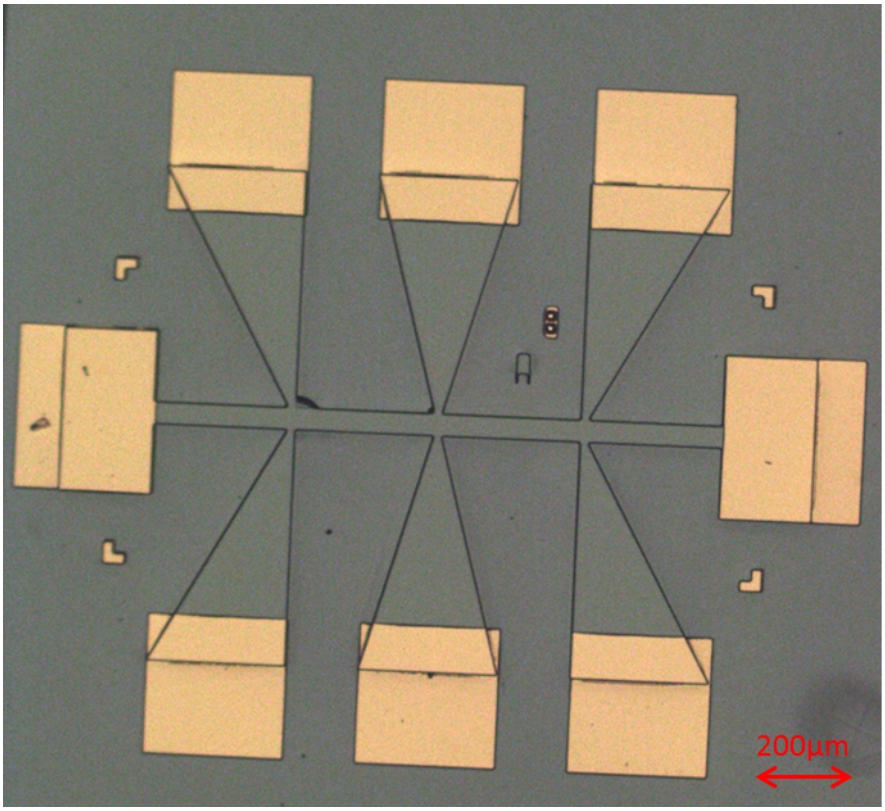

Figure 1.8: Image of processed (Ga,Mn)As Hall bar made from the 'Phillips Hall bar' photomask.

1.3.2 Measurement equipment

1.3.2.1 Small cryostat system

Many of the transport measurements presented in this thesis were carried out in an Oxford Instruments He-4 variox bath cryostat system that has a stable temperature measurement range of 4.2K-400K. A sample mounted on a non-magnetic sample holder is attached to a sample probe which can be electrically connected with various sourcemeters and multimeters. The sample probe is lowered into the cryostat sample space. To cool the sample down, the sample space is pumped and a needle valve connecting the sample space to a liquid He bath is opened allowing He to be drawn into the sample space. The temperature of the sample space is controlled by a heat exchanger positioned at the bottom of the sample space that heats the incoming flow of He. A stable temperature is achieved by a Cerox temperature sensor placed in the sample space and an ITC503 temperature control system together modulating the level of heating via a set of PID parameters. For measurements at 4.2K the sample space is filled with liquid He and no heat or pumping is applied. Boil-off of liquid He from the He bath is minimised by use of inner and outer vacuum shields that reduce heat loss through convection and

conduction, and a nitrogen bath that allows a more gradual (and cost-effective) cooling of the sample space temperature and reduces heat loss through radiative heating. For the Nottingham small cryostat system, an electromagnet is positioned outside of the cryostat surrounding the sample space and can rotate around a 200° range. The electromagnet is powered by a bi-polar power supply that allows for fields of up to +/-4kOe to be generated between the electromagnet poles. The angle of the field with respect to the sample can be altered by rotating the magnet, switching the field polarity, rotating the sample probe, or using a different sample probe that mounts the sample in a perpendicular position.

The advantages of the small cryostat system are the small volume of its He bath (9 litres) which vastly reduces the amount of He needed to run and maintain the system, and the small volume of its sample space, which allows for quick temperature cycling and good temperature stability.

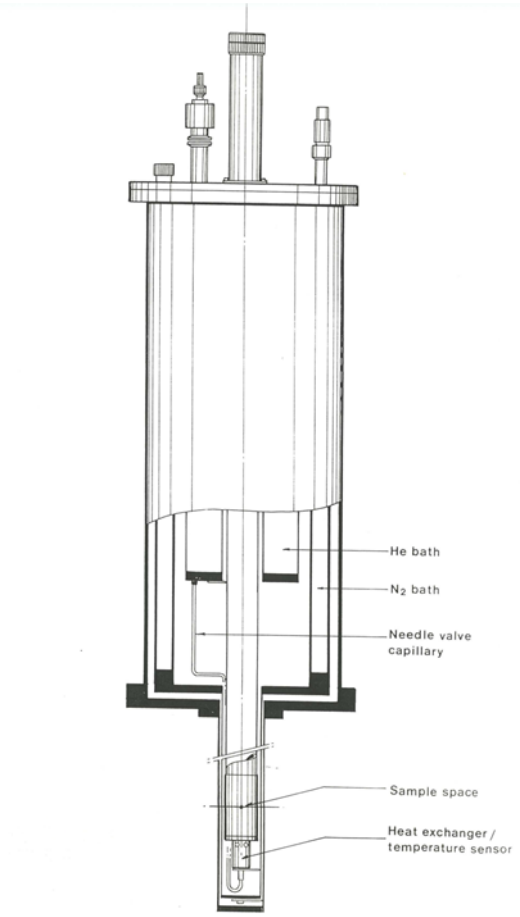

Figure 1.9: Diagram of Oxford Instruments He-4 variox bath cryostat system. Diagram taken from operators handbook for the system.

1.3.2.2 Large vector magnet cryostat system

Measurements in this thesis requiring larger magnetic fields of variable orientation were performed using a Oxford Instruments superconducting vector magnet system. The system is mostly the same as the small vector magnet cryostat described in

section 1.3.2.1, just with a larger He bath (130 litres), and sample space etc. The system is unique in that the sample position sits in between three superconducting coils aligned orthogonal to each other that produce independent magnetic fields along x, y, and z directions. The superconducting magnets lie in the cryostat's He bath, the temperature of which is beneath their critical temperature, and are energised by an external bi-power supply. A field of up to +/-20kOe can be applied in any direction by simultaneously energising all three coils, or for energising the z coil alone a field of up to +/-60kOe can be generated along the z direction.

The advantages of the large cryostat system are its ability to apply large magnetic fields in any direction, and its fully automated operation which allows measurements to be performed without requiring the user to be present.

1.3.2.3 High-field cryostat system

Hole density measurements were made using a uni-axial superconducting vector magnet owned by the Nottingham Semiconductor Quantum Nanostructures Group. The principles of the cryostat operation are again similar to those covered in section 1.3.2.1, though the Lakeshore 340 temperature controller and auto needle valve allow temperature to be controlled by either adjusting the flux of He into the sample space (constant heat) or adjusting the VTI heating (constant flux). A single superconducting magnet sits inside the He bath that can be energised to give fields of up to +/-140kOe along the z direction.

The major advantage of the high-field cryostat system is obviously the magnitude of the field it can apply.

1.3.2.4 SQUID magnetometer

A magnetometer is an instrument used to measure the magnetization of a sample of magnetic material. There are several types of magnetometers commonly used in labs to make magnetization measurements including vibrating sample magnetometers, inductive pick-up coils, Kerr magnetometers etc, but for thin, dilute moment magnetic samples such as (Ga,Mn)As, SQUID magnetometry is often required due to its extreme sensitivity to small magnetic signals.

A superconducting quantum interference device (SQUID) is itself not a magnetometer, but as the name suggests does play a key role in SQUID magnetometry. A SQUID is a ring of superconducting material within which are one or two Josephson junctions (measurements in this thesis were made with the Nottingham SQUID magnetometer which features an RF SQUID, i.e. a SQUID with one Josephson junction). A Josephson junction is a weak link between two superconductors, where the weak link is either an insulating or non-superconducting material, or a physical constriction, and through which superconducting current can tunnel through up to a critical value. A direct voltage appears across the Josephson junction when the current exceeds the critical value, and this leads to a time-varying ac current through the SQUID (ac Josephson effect[78]).

SQUID magnetometry measurements in this thesis were performed in reciprocal sample oscillation (RSO) mode in order to reduce noise and hence improve sensitivity. The basic methodology and principles of an RSO SQUID magnetometry measurement are as follows: The sample to be measured is scribed to appropriate dimensions (around 5mm×4mm) and placed in a drinking straw, either directly for out of plane measurements or attached to a high purity silver wire inside the straw with GE varnish for in-plane measurements. The straw is then attached to the bottom of a sample rod which is mechanically driven by a servo motor. The sample is sinusoidally oscillated up and down through three coils of superconducting wire that are in a second order gradiometer arrangement. It is important that the size of the sample is small with respect to the gradiometer so that it can be approximated as a point dipole. The motion of the sample through the coils generates a persistent current within the coils as the flux going through them changes. The coils are inductively coupled to the SQUID, which sits away from the coils in a shielded environment. To ensure the total flux threading through the SQUID remains constant, screening currents are generated within the SQUID to offset the magnetic fields from the inductively coupled coils. An additional bias current is applied to the SQUID that is slightly greater than the critical current, and due to the properties of the Josephson junction and the fact that only discreet units of flux are allowed through the SQUID, a periodic relationship between the voltage across the SQUID and the flux generated from the gradiometer coils (and therefore the sample magnetization) is established. This allows a voltage to be measured across the SQUID that depends on the position of the sample within the gradiometer coils. This signal can then be analysed by computer software using a non linear least squares fitting routine to fit the data to an ideal dipole response, which allows the magnitude of the sample magnetization to be obtained. The noise on the measurement is reduced by locking in the SQUID signal to the frequency that the sample is driven through the gradiometer coils at.

All measurements were performed in a Quantum Design MPMS XL system. A shown in figure 1.10, all superconducting elements of the system are immersed in liquid He while the sample sits in a central sample space. The sample space temperature can be varied between 2K-400K, and an external magnetic field of up to +/-1T can be applied to the sample by an adjacent superconducting magnet that gives uniformity of 0.01% over the 4cm sample space area.

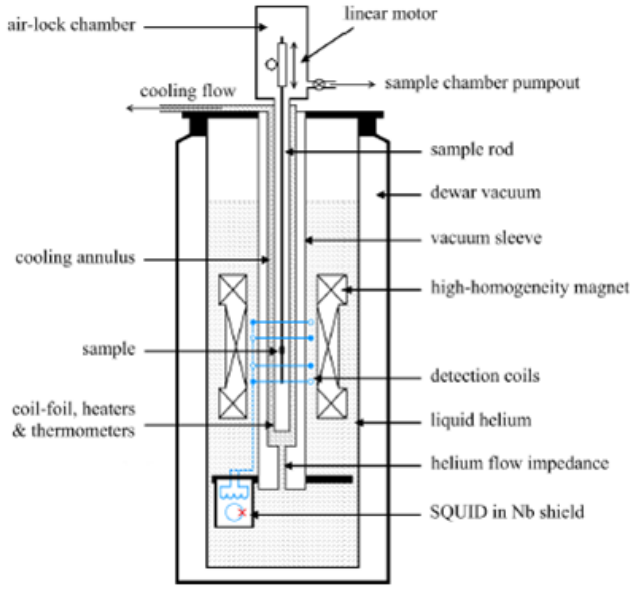

Figure 1.10: Diagram of MPMS SQUID system. Diagram taken from reference [79].

1.3.3 Measurement techniques

The following section presents basic transport, magnetotransport, and magnetometry measurement methods that have been used in this thesis to characterise materials, as well as the underlying physics of the measurement. Some of these experimental techniques are discussed in the context of measurements on (Ga,Mn)As specifically.

1.3.3.1 Sample resistivity

All resistivity measurements in this thesis were made on samples in a Hall bar geometry as shown in figure 1.11. A constant dc current is supplied by a Keithley 2400 sourcemeter that flows between the source and drain contacts of the sample. The resistance of the contacts is small compared to the resistance of the Hall bar channel itself in the materials studied in this thesis. A voltage is sensed between adjacent Hall bar arms (V_{xx}) by a Keithley 2000 multimeter (a 4-point measurement), and is divided by the source current to give a longitudinal resistance (R_{xx}). R_{xx} can then be converted into the sample resistivity (ρ_{xx}) by taking into account the thickness of the sample through which the current flows through (t), the width of the Hall bar channel (W), and the length between contact arms (L) as such:

$$\rho_{xx} = \frac{R_{xx}Wt}{L} = R_s t \tag{1.3}$$

where R_s is the sheet resistivity. Sample resistivity is measured as a function of temperature by putting the sample into a cryostat system and gradually reducing the temperature while continuously recording both R_{xx} and temperature using

Labview software.

The transverse resistance (R_{xy}) is measured in the same 4-point set up, but for a voltage sensed between opposite arms of the Hall bar. For a non-magnetic uniform conductor in the absence of any external fields, R_{xy} should be zero for perfectly aligned Hall bar arms.

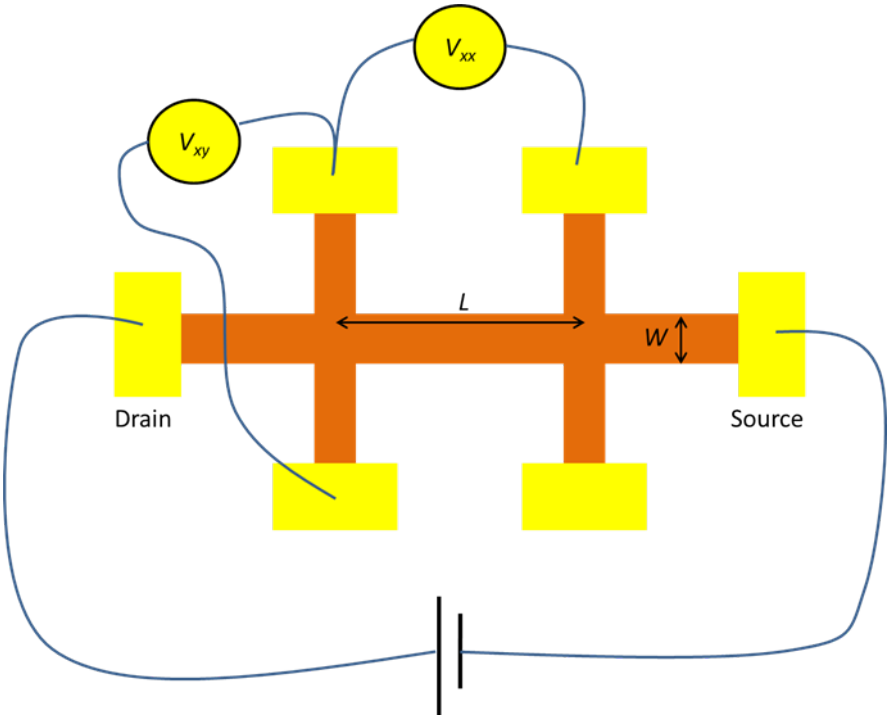

Figure 1.11: Diagram of Hall bar geometry used to make longitudinal and transverse 4-point measurements.

1.3.3.2 Hall measurements

Ordinary Hall effect

Experimentally, a Hall measurement simply involves applying a current to a Hall bar of a sample and measuring R_{xy} while an external magnetic field is applied (usually swept) out of the sample plane. For an ordinary non-magnetic conducting material this generates a finite change in R_{xy} known as the ordinary Hall effect (OHE). The ordinary Hall effect arises as a result of the Lorentz force acting on the charge carriers. The Lorentz force ($\mathbf{F}$) on a charge carrier (q) in a magnetic field ($\mathbf{B}$) in a direction that is orthogonal to its velocity ($\mathbf{v}$) is as given by:

$$\mathbf{F} = q(\mathbf{v} \times \mathbf{B}) \tag{1.4}$$

Therefore, electrons flowing along a Hall bar with an out of plane field applied will deflect towards one edge of the bar. The resultant build up of negative charge along one bar edge (and positive charge along the other) establishes an electric field across the bar width that opposes further charge accumulation, and so therefore there is a measurable voltage between transverse Hall bar arms. R_{xy} as a result of the OHE is given by:

$$R_{xy} = \frac{1}{nqt} B cos(\alpha) \tag{1.5}$$

where n is the carrier density, t is the sample thickness, B is the magnitude of the external magnetic field, and α is the angle it makes with the out of plane axis of the sample. The OHE is therefore antisymmetric with respect to the external magnetic field, and can be used to determine carrier concentrations of samples of known thickness.

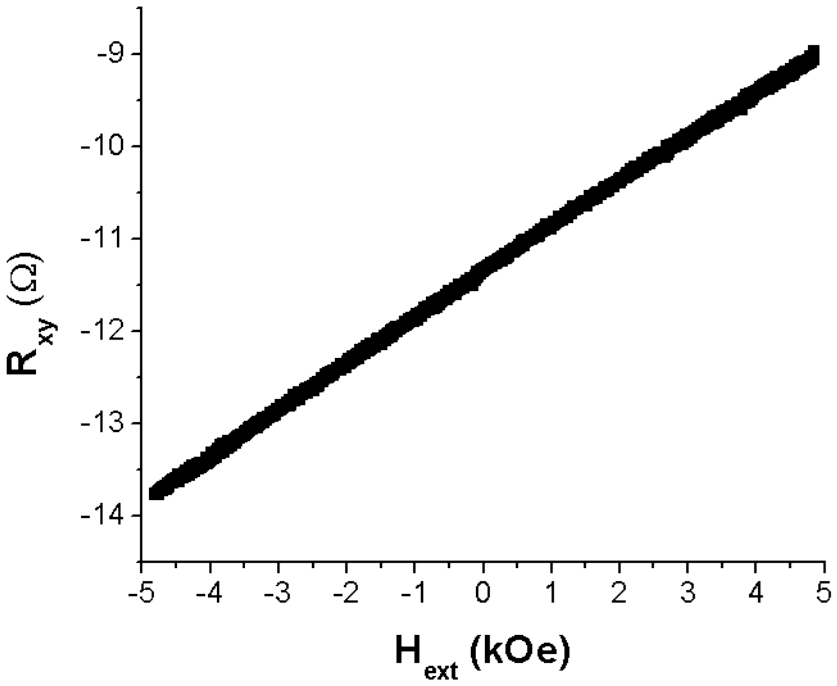

Figure 1.12: Example of a typical OHE dataset plotting R_{xy} against external field applied out of the sample plane. Data is for a GaAs sample at 4K and was taken by Dr. James Haigh. The R_{xy} values are offset from zero due to Hall bar misalignment. Note that the slope would remain linear even if measured over a larger field range.

Anomalous Hall effect

When a ferromagnetic material is measured in the Hall experimental geometry, an additional type of Hall effect named the anomalous Hall effect (AHE) occurs that, at certain field strengths, can be larger in magnitude than the OHE. Due to SOC, charge carriers of opposite spin moving along a bar tend to deflect towards opposite sides of the bar, even in the absence of a magnetic field. In non-magnetic materials such as GaAs, because the spin populations are equal when there is no external magnetic field applied, equal numbers of carriers build up along the bar edges, and thus there is no net charge imbalance across the bar and hence no directly measurable R_{xy} contribution. This phenomenon is known as the spin Hall effect (SHE)[80], and is useful in the generation of spin currents with no net charge

transfer[81].

When current is applied to a bar of ferromagnetic material, the same SOC-induced spin-dependent scattering occurs, however, as the ferromagnet has an intrinsic net carrier spin polarisation, more carriers deflect towards one side of the bar than the other, therefore establishing an electric field across the bar. For the Hall bar geometry, when the ferromagnet's moments and hence its carrier spins are aligned perpendicular to the sample plane, this electric field occurs in the transverse bar direction, and thus generates a finite R_{xy}. Therefore, R_{xy} due to the AHE is proportional to the out of plane component of the magnetization, and so for samples with out of plane magnetic anisotropy no external field is required to generate the AHE R_{xy} whereas for samples with in-plane magnetic anisotropy, an external field is required to align the magnetization out of the plane and hence generate the R_{xy} term.

There are believed to be three main mechanisms which can cause the spin-dependent deflections behind the AHE and SHE. The 'intrinsic deflection' contribution is related to Berry phase curvature, and is dubbed 'intrinsic' as it depends only on band structure and not scattering off impurities. Reference [82] proposed that when an external electric field is applied to a solid, carriers gain an extra component to their group velocity that is perpendicular to the electric field. In ferromagnetic materials, the sum of this additional group velocity over all occupied band states can be non-zero, which therefore leads to a net carrier deflection and thus R_{xy} contribution. The 'side-jump' contribution is classified as an extrinsic contribution, and arises due to backscattering of carriers off a spin-orbit coupled impurity between states with opposite group velocity. Opposite spins scatter in opposite directions as they experience opposite electric fields upon entering and leaving the impurity. Finally the 'skew scattering' contribution, another extrinsic contribution, is an umbrella term for various mechanisms that give asymmetric spin-scattering (note not backscattering) of carriers off an impurity.

Theoretically the three AHE R_{xy} contributions are all predicted to vary with R_{xx}, with $R_{xy} \propto R_{xx}$ for the skew scattering contribution, and $R_{xy} \propto R_{xx}^2$ for both intrinsic deflection and side jump contributions. Therefore, the later two mechanisms cannot be separated by dc Hall measurements, but for (Ga,Mn)As their relative importance can be distinguished by varying the impurity concentration across a range of samples and measuring ac conductivities[83]. For metallic (Ga,Mn)As samples it is found that the intrinsic contribution usually dominates the AHE[83][84][85]. Generally, however, R_{xy} from the AHE can be described by:

$$R_{xy} = CR_{xx}^{n}\mathrm{M}_z \tag{1.6}$$

where n usually (though not always) takes a value between 1 and 2, C is a material specific constant, and M_z is the out of plane component of the magnetization. In samples with out of plane magnetic anisotropy, the dependence of R_{xy} on M_z and weak dependence of R_{xx} on external field at low fields make the AHE a useful tool for measuring coercivity without the need for magnetometry measurements.

In (Ga,Mn)As (as well as other ferromagnets), the AHE R_{xy} contribution can be orders of magnitude larger than the OHE R_{xy} contribution which makes extracting

a carrier density from Hall measurements difficult. In order to try and isolate the OHE R_{xy} contribution, M_z needs to be saturated as best as possible to allow R_{xy} from the OHE to dominate the external field against R_{xy} slope. For samples with in-plane magnetic anisotropy, high magnetic fields and low temperatures are required to saturate M_z, but at these fields R^n_{xx} still varies due to magnetoresistance and so the AHE R_{xy} term still contributes to the slope. Therefore it is difficult to accurately determine carrier density in (Ga,Mn)As through Hall measurements and fitting analysis, with errors typically in the region of 20%[86].

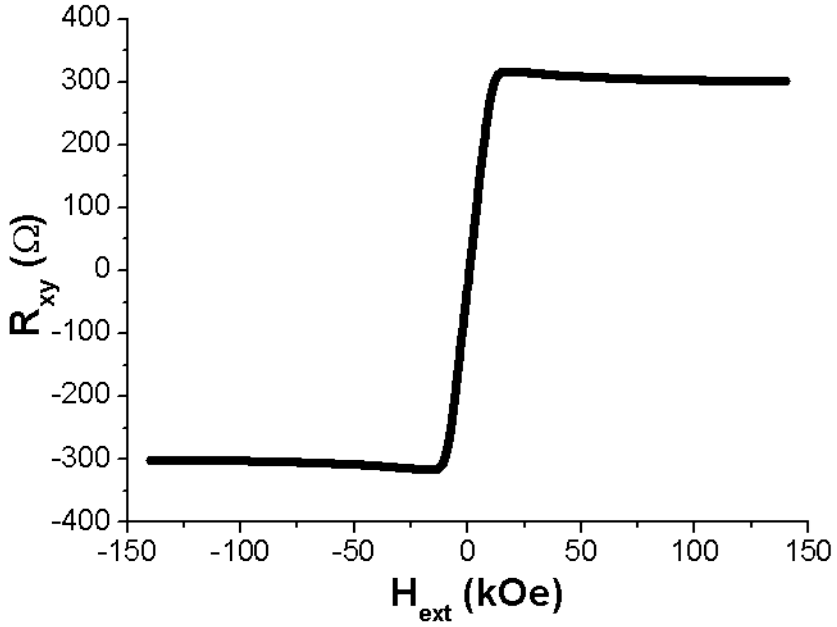

Figure 1.13: Example of a typical AHE dataset plotting R_{xy} against external field applied out of the sample plane. Data is for a (Ga,Mn)($As_{0.9}$,$Sb_{0.1}$) sample at 4K. Unlike the OHE dataset in figure 1.12, the AHE dataset does not have the same slope across the field range. The low field (<15kOe) slope is dominated by the AHE which largely varies with M_z. At high fields (>15kOe) M_z is approximately saturated. In this region the slope is much smaller and determined by a combination of the AHE (which now only varies with R_{xx}) and the OHE.

Quantum Hall effect

When performing a Hall measurement on a two dimensional electron gas (2DEG), at sufficiently low temperatures and high magnetic fields R_{xy} takes quantised values, resulting in a step-like R_{xy} against external field plot, as opposed to the OHE and AHE for which R_{xy} continually increases with increasing field. This is known as the quantum Hall effect (QHE) and is covered in greater detail in chapter 5 where it is observed in a GaAs based 2DEG. As (Ga,Mn)As and the other III-V DMSs investigated in this thesis do not exhibit two dimensional conduction, the QHE does not contribute to their Hall measurements.

1.3.3.3 Magnetoresistance measurements

A magnetoresistance measurement is a measurement where an external magnetic field is applied to a sample and R_{xx} is recorded. Unlike Hall measurements, the external field can be applied and/or swept along any orientation with respect to the sample.

Ordinary and isotropic magnetoresistance
Both ordinary magnetoresistance (OMR) and isotropic magnetoresistance (IMR) can be considered as changes in R_{xx} with the magnitude of an external magnetic field. OMR arises in both non-magnetic and magnetic materials as a result of the deflection of carrier trajectories and tightening of electron orbitals due to the Lorentz force. For OMR, resistance increases with increasing external field ('positive magnetoresistance') and the effect is larger when the external field is perpendicular to the current direction than when it is parallel to the current direction. In magnetic materials IMR also occurs. IMR is independent of the angle of the external magnetic field, and arises due to factors such as suppression of weak localisation and spin-disorder scattering. For IMR, resistance decreases with increasing magnetic field ('negative magnetoresistance'). (Ga,Mn)As, in which both OMR and IMR occur, is generally shown to have an overall negative magnetoresistance.

Anisotropic magnetoresistance
In ferromagnetic materials, R_{xx} varies with the angle of the material's magnetization, which can be controlled by sweeping or rotating an external magnetic field, and this is known as anisotropic magnetoresistance (AMR). AMR arises due to SOC, and is covered in much more depth in chapter 3.

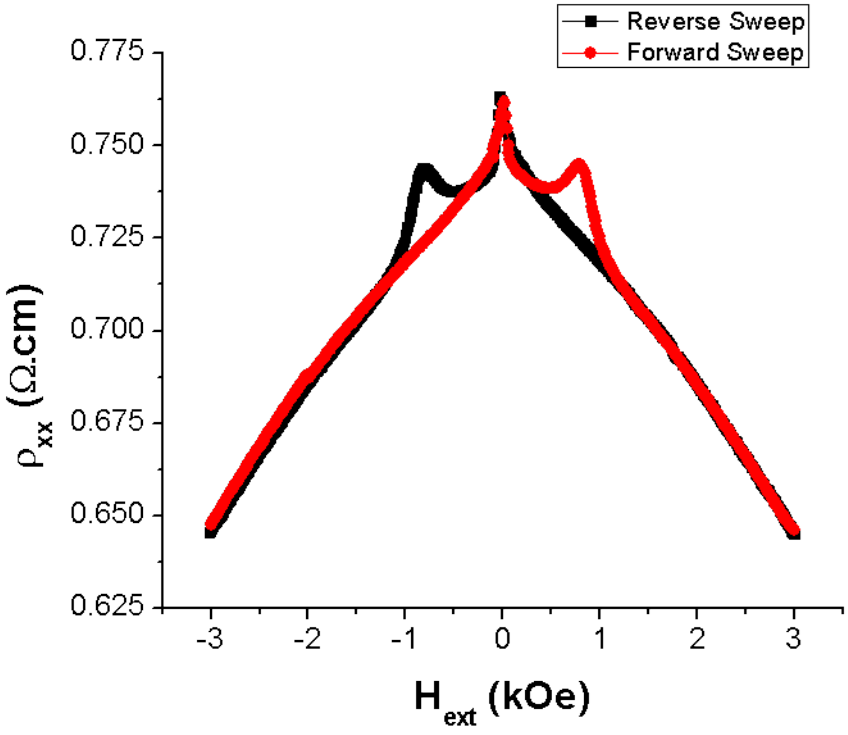

Figure 1.14: R_{xx} as a function of external magnetic field applied in the sample plane for a (Ga,Mn)($As_{0.9}$,$Sb_{0.1}$) sample at 4K. Black data points are for field being swept from 3kOe downwards and red data points for field being swept from -3kOe upwards. The 'jumps' in R_{xx} at around -1kOe (black), 1kOe (red), and 0kOe (both) are due to the AMR contribution to R_{xx} changing as the magnetization switches from one easy axes to another. The general decrease in R_{xx} with increasing field magnitude across the field range is a result of the dominant contribution of IMR.

1.3.3.4 SQUID magnetometry field sweeps

SQUID magnetometry field sweeps measure the projection of the magnetization of a sample along a certain direction in discreet steps as an external magnetic field is swept along the same direction. In this thesis, measurements are performed by sweeping the external field from +10kOe to -10kOe, and then back again from -10kOe to +10kOe in a hysteresis measurement along the $[1\bar{1}0]$, [110], and [001] crystalline directions. For a ferromagnet, the sweeps reveal the saturation magnetization of the sample (M_{sat}), as well as the field needed to reverse the projection of the magnetization along the axis being measured (coercive field).

M_{sat} of a sample is its maximum value of magnetization, i.e. when all the individual moments are aligned along the same direction. The harder an axis is, the larger the magnitude of the external field that is required to saturate the magnetization along it, however M_{sat} itself is approximately the same for all orientations. The field needed to be applied along an easy axis to achieve the maximum magnetization along that direction increases with increasing temperature due to thermal fluctuations.

In the hysteresis sweep measurement, after the magnetization is saturated along a certain direction, the external field is swept down to zero. Unless the sweep direction is 90° away from any easy axis direction, the projection of the magnetization along the sweep axis will be non-zero at zero external field (the remnant magnetization, M_{rem}). For sweeps along easy axes $M_{rem} \approx M_{sat}$. The coercive field (H_c) is defined as the magnitude of the external field, applied along the opposite direction, that is required to reduce M_{rem} to zero. For sweeps along easy axes with square hysteresis loops, H_c can be big or small depending on the 'magnetic hardness' of the material.

For SQUID magnetometry field sweeps of materials grown on III-V substrates, the substrate gives a diamagnetic contribution to the measured magnetization, however this can be separated from the contribution to the measured magnetization from the ferromagnetic layer by a simple linear fitting procedure.

1.3.3.5 SQUID magnetometry remnant measurements

The procedure for SQUID magnetometry remnant measurements in this thesis is as follows. The sample to be measured is heated to above its T_c and then cooled down to 2K in an external magnetic field of 1kOe aligned along the measurement axis. The external field is then removed and the sample is heated up and its magnetization projection along the measurement axis is measured in discreet steps until T_c is passed.

SQUID magnetometry remnant measurements indicate T_c of the sample, which is approximately the temperature where the measured magnetization along an easy direction goes to zero (see reference [87]). In order to accurately measure T_c, measurements in small temperature steps around its approximate value are required.

If SQUID magnetometry remnant measurements are made along orthogonal directions, for example the $[1\bar{1}0]$, [110], and [001] crystalline axes, and assuming that the sample is in a single domain state after each field cool and with its magnetization along the closest easy axis to the measurement axis, M_{sat} at low temperatures can be approximated by:

$$M_{sat} \approx \sqrt{M_{1\bar{1}0}^2 + M_{110}^2 + M_{001}^2} \tag{1.7}$$

where $M_{1\bar{1}0}$ is the remnant magnetization along the $[1\bar{1}0]$ direction following a field cool measurement etc. Additionally, for in-plane magnetic anisotropy, in the case where $K_C > K_U$, the ratio of the in-plane magnetic anisotropy constants can be obtained by:

$$\frac{K_U}{K_C} = cos\left[2tan^{-1}\left(\frac{M_{110}}{M_{1\bar{1}0}}\right)\right] \tag{1.8}$$

Chapter 2

Characterisation of Sb-based diluted magnetic semiconductors

2.1 Introduction

For over two decades now, diluted magnetic semiconductors (DMSs) of the form (III,Mn)V have been the subject of intensive research from various sections of the physics community. In these (III,Mn)V materials, Mn is incorporated into the III-V semiconductor lattice by substituting for the group III cation in the form of Mn^{2+}, introducing both carrier holes and local moments into the semiconductor system (see section 1.2). (Ga,Mn)As is by far and away the most studied (III,Mn)V material as its relatively high Curie temperature (T_c) and compatibility with existing GaAs-based technologies made it a promising candidate for device application, while the reasonably well understood intrinsic link between its electronic and magnetic properties along with its strong spin-orbit coupling (SOC) in the carrier band still make it an ideal test-bed material for exploring spintronic phenomena. One of the properties that make DMSs so appealing is the tunability of both their electrical and magnetic properties by established semiconductor techniques such as doping, electrical gating, annealing, strain-application, and optical irradiation, but it is well known that these properties also vary with the choice of III-V semiconductor host. Additionally, as SOC in (III,Mn)V DMSs largely originates from the III-V semiconductor host rather than the Mn dopant, altering the choice of group III and V elements will also allow a degree of tunability of the strength of SOC in the (III,Mn)V material. Therefore, it is vital to characterise and understand how the choice of III-V semiconductor host material affects all of the DMS properties in order to help identify the (III,Mn)V DMS best suited for device and test-bed applications.

(Ga,Mn)Sb is a DMS that has only been moderately studied in literature, but is an appealing candidate as a spintronic material due to its relatively large SOC brought about by the Sb atom, while its narrow band gap and high conductivity offer alternative optical and transport properties to (Ga,Mn)As. Additionally, there is a lack of published information on quaternary DMSs of the form (III,Mn)(V_A,V_B), where V_A and V_B are different group V elements, to supplement investigations of a variety of (III_A,III_B,Mn)V materials. Varying the relative concentrations of the two group III or V elements allows quaternary DMSs to offer even more freedom when tuning the material properties, which again makes them an interesting class

of materials to study for potential application as well as fundamental understanding. In this chapter, two Sb-based DMSs, (Ga,Mn)Sb and the quaternary DMS (Ga,Mn)($As_{0.9}$,$Sb_{0.1}$), are investigated and characterised by SQUID magnetometry and transport measurements in order to gain insight as to how the incorporation of Sb affects DMS properties.

2.2 Previous experimental and theoretical studies

2.2.1 (Ga,Mn)Sb

To date there have been several experimental studies of MBE-grown (Ga,Mn)Sb, allowing some insight into its fundamental properties. Conductivities of $1000\Omega^{-1}cm^{-1}$[88][89], $700\Omega^{-1}cm^{-1}$[90], and $330\Omega^{-1}cm^{-1}$[91] are reported for (Ga,Mn)Sb samples at temperatures in the range 1.5K-6K with Mn concentration in the range of 2%-3% and of thickness 5nm-200nm. By comparison, optimally annealed (Ga,Mn)As samples with similar Mn concentrations have low temperature conductivities in the range $200\Omega^{-1}cm^{-1}$ - $300\Omega^{-1}cm^{-1}$[55]. The larger conductivity of (Ga,Mn)Sb is assumed to arise due to Mn having a shallower acceptor level in GaSb[92] than GaAs[93]. While there has been no previous measurement of the band gap of (Ga,Mn)Sb it is likely to be very similar to that of GaSb (0.73eV[47] at 300K) which is much narrower than that of GaAs (1.43eV[47] at 300K).

A T_c for (Ga,Mn)Sb of 15K is reported in references [89] and [91], and 25K in references [88] and [90], values that are significantly lower than similarly doped optimally annealed (Ga,Mn)As samples (≈80K[53]). The lower T_c of (Ga,Mn)Sb compared with (Ga,Mn)As is likely to arise due to a weaker p-d exchange energy in (Ga,Mn)Sb as the Sb atom is larger than the As atom; the average length scale between itinerant holes and Mn moments is greater in (Ga,Mn)Sb, meaning a weaker antiferromagnetic coupling between holes and moments, and so a weaker carrier mediated long-range ferromagnetic ordering of Mn moments that requires less energy (temperature) to overcome. SOC effects that may be detrimental to T_c will also be greater in (Ga,Mn)Sb than (Ga,Mn)As[36]. Interestingly an electrical gating study in reference [91] showed that in (Ga,Mn)Sb, T_c is proportional to carrier density to the power of 1.4 ($T_c \propto p^{1.4}$), notably different from (Ga,Mn)As where $T_c \propto p^{0.2}$[94], with the difference in the relations ascribed to carrier holes being accumulated and depleted at the interface between a dielectric gate layer and (Ga,Mn)Sb and (Ga,Mn)As layers respectively as indicated by p-d Zener model calculations. Other observations from previous studies show that (Ga,Mn)Sb behaves similarly to (Ga,Mn)As with regards to some magnetic and magnetotransport properties. Its easy axis lies along an in-plane/out of plane direction for (Ga,Mn)Sb grown on a substrate that applies compressive/tensile strain to the layer[89], it has a negative magnetoresistance suggesting the presence of spin-disorder scattering[88], and also a negative AMR[89].

It is clear from the above referenced previous experimental reports that there are

some key differences in the electrical and magnetic properties between (Ga,Mn)Sb and (Ga,Mn)As. When considering a material for spintronic application, the strength of its SOC is often another vital parameter that should be taken into account. As discussed in sections 1.2.2.4 and 4.2.1, SOC in DMSs has an intrinsic contribution relating to the atomic number of the material involved, as well as a contribution derived from lattice strain. Comparing (Ga,Mn)Sb to (Ga,Mn)As, the larger atomic number of the Sb atom should give it a larger SOC in the carrier bands, which will be mostly Sb 5p-like. Additionally, the larger size of the Sb atom compared with As means that there will be a greater growth strain from lattice mismatch in a (Ga,Mn)Sb layer grown on a GaAs (001) substrate compared with (Ga,Mn)As, often even in the case of buffer layer(s) being grown between substrate and the (Ga,Mn)Sb layer to help relax lattice mismatch. This should lead to a stronger SOC effect. Therefore, through a larger atomic number and strain, (Ga,Mn)Sb should have a stronger SOC than (Ga,Mn)As, which makes it appealing as a spintronic material to investigate phenomena that arise due to SOC.

2.2.2 (Ga,Mn)(As,Sb)

Quaternary Mn doped DMSs can take the form of either (III_A,III_B,Mn)V or (III,Mn)(V_A,V_B), and have been studied for various elemental compositions for over a decade. There has been much attention on the (III_A,III_B,Mn)V class of quaternary DMSs, with extensive investigations into (In,Ga,Mn)As[95][96][97][98], (Al,Ga,Mn)As[99][100][101], (In,Al,Mn)As[102][103][104], and (In,Ga,Mn)N[105]. These studies highlight that changing atomic composition of the group III elements influences the properties of the DMS, such as magnetic anisotropy in (In,Ga,Mn)As and T_c in (Al,Ga,Mn)As. There has been a slightly narrower range of study of the (III,Mn)(V_A,V_B) class of quaternary DMSs. Studies in (Ga,Mn)(As,N)[106][107][108] show that T_c can be increased from that of (Ga,Mn)As for N doping concentrations of up to 1%, and decreased for higher N concentrations, while the metal-insulator transition (MIT) is also be crossed when varying N concentration. (Ga,Mn)(As,P)[109][110][111][112] is an intriguing system to explore the effects of atomic composition variation. P is a smaller atom than As and so on one hand should promote a higher T_c through an increased p-d exchange energy, however, (Ga,Mn)P has a larger band gap than (Ga,Mn)As meaning the effects of hole localisation should be greater which should promote a reduced T_c. Additionally the different sizes of the P and As atoms dictate that the strain of the (Ga,Mn)(As,P) layer varies between tensile and compressive as the atomic composition changes, and this is reflected in the magnetic easy axis transitioning from out of plane to in-plane as the P content is reduced from 9% to 6%. Finally, (Ga,Mn)(As,Bi) is investigated in reference [113] where it is shown, as would be expected, to have an increased strain, reduced T_c, and reduced band gap compared with (Ga,Mn)As.

(Ga,Mn)(As,Sb) is another (III,Mn)(V_A,V_B) DMS material that can offer different properties to (Ga,Mn)As and (Ga,Mn)Sb. Similar to P in (Ga,Mn)(As,P) (but in an opposite manner), Sb in (Ga,Mn)(As,Sb) could, in principle, act to both increase and reduce T_c compared with (Ga,Mn)As as GaSb has a narrower band

gap than GaAs (increased hole delocalisation) and Sb has a larger atomic size than As (weaker p-d exchange). However, the low T_c of (Ga,Mn)Sb suggests the latter mechanism dominates leading to a severely reduced T_c, which begs the question as to whether there is an intermediate level of alloying As and Sb between (Ga,Mn)As and (Ga,Mn)Sb that may increase T_c. Additionally, the incorporation of the differently sized As and Sb atoms into the same lattice structure may promote an increased lattice strain, while the high atomic number Sb may increase SOC strength, and it would be ideal for these properties to emerge while retaining some of the characteristic features of (Ga,Mn)As, namely its high T_c.

After the completion of the work in this chapter, a study was published in reference [114] that investigated the structural, transport, and magnetic properties of MBE grown as-grown and annealed (Ga,Mn)(As,Sb) for Sb concentrations in the range 0% - 2.37%. The lattice constant of (Ga,Mn)(As,Sb) is observed to increase with increasing Sb concentration, as would be expected due to the larger size of the Sb atom. Furthermore the lattice constant is always greater for the as-grown than annealed samples, which is consistent with the out-diffusion of interstitial Mn, highlighting its presence in the material. The hole density and T_c for both the as-grown and annealed samples initially increases as the Sb concentration increases from 0% to 0.80% before decreasing with further increase of Sb concentration. By determining the effective Mn concentration from magnetometry data, the authors suggest that the initial increase in T_c with Sb concentration occurs as the addition of Sb to the lattice changes its structure in a way that promotes substitutional Mn incorporation, but that higher Sb concentrations introduce more lattice defects, including interstitial Mn which reduces T_c.

In this chapter (Ga,Mn)(As,Sb) with 10% Sb concentration, i.e. (Ga,Mn)($As_{0.9}$,$Sb_{0.1}$), is investigated. Going by the trends shown in reference [114], the relatively large Sb concentration should severely reduce T_c from that of (Ga,Mn)As, however the larger Sb concentration should also induce stronger SOC and therefore more prominent SOC phenomena such as AMR, as is considered in chapter 3.

2.3 Experimental results and discussion

This section presents and discusses the results of experimental measurements made on as-grown and annealed (Ga,Mn)Sb and (Ga,Mn)($As_{0.9}$,$Sb_{0.1}$) samples. Details on experimental methods are given in section 1.3.

2.3.1 Sample growth and preparation

Both (Ga,Mn)Sb and (Ga,Mn)($As_{0.9}$,$Sb_{0.1}$) samples were grown by Dr Richard Campion in the Nottingham MBE system at a growth temperature at 220^{o}C. For the (Ga,Mn)Sb sample (Mn691), a 150nm thick GaSb buffer layer was deposited on a InAs (001), upon which a 25nm, 6% Mn-doped (Ga,Mn)Sb layer was grown. For the (Ga,Mn)($As_{0.9}$,$Sb_{0.1}$) sample (Mn692) a 25nm, 6% Mn-doped (Ga,Mn)($As_{0.9}$,$Sb_{0.1}$) sample was grown directly onto a GaAs (001) substrate. For both growths the heated Sb source yielded elemental Sb_4 which was found to be

extremely deleterious to electron multiplier on the MBE system's mass spectrometer (which cannot be shut off on the Nottingham system).

Different pieces of the sample taken from a similar part of the wafer were used for as-grown and annealed measurements for both SQUID magnetometry and transport. For the annealed measurements, samples were annealed in air at 180^oC for 48 hours.

XRD measurements were made on the as-grown Mn691 (Ga,Mn)Sb and Mn692 (Ga,Mn)($As_{0.9}$,$Sb_{0.1}$) samples by Dr Pete Wadley, revealing that the (Ga,Mn)Sb layer is fully relaxed whereas the (Ga,Mn)($As_{0.9}$,$Sb_{0.1}$) layer is fully strained. Using a Vegard's law calculation to obtain the lattice parameter of $GaAs_{0.9}Sb_{0.1}$, the lattice mismatch of $GaAs_{0.9}Sb_{0.1}$ on GaAs substrate is -0.78%. The negative sign indicates a compressive strain. The lattice mismatch of (Ga,Mn)($As_{0.9}$,$Sb_{0.1}$) on GaAs is more difficult to estimate due to the different effects that substitutional and interstitial Mn can have on expanding the host lattice[115].

2.3.2 (Ga,Mn)Sb

2.3.2.1 SQUID magnetometry

SQUID magnetometry measurements were performed on the as-grown and annealed (Ga,Mn)Sb Mn691 sample by Dr Mu Wang. The results are shown in figures 2.1-2.2:

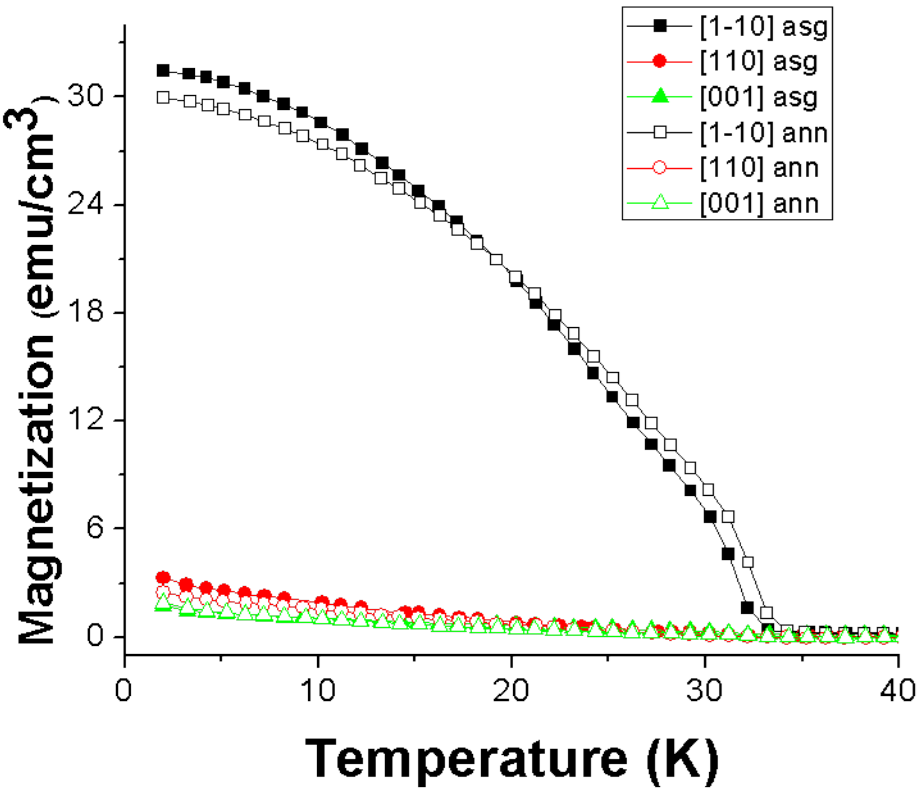

Figure 2.1: Remnant magnetization of as-grown (closed symbols) and annealed (open symbols) (Ga,Mn)Sb with increasing temperature after field-cooling along the $[1\bar{1}0]$, [110], and [001] crystalline axes in a field of 1kOe.

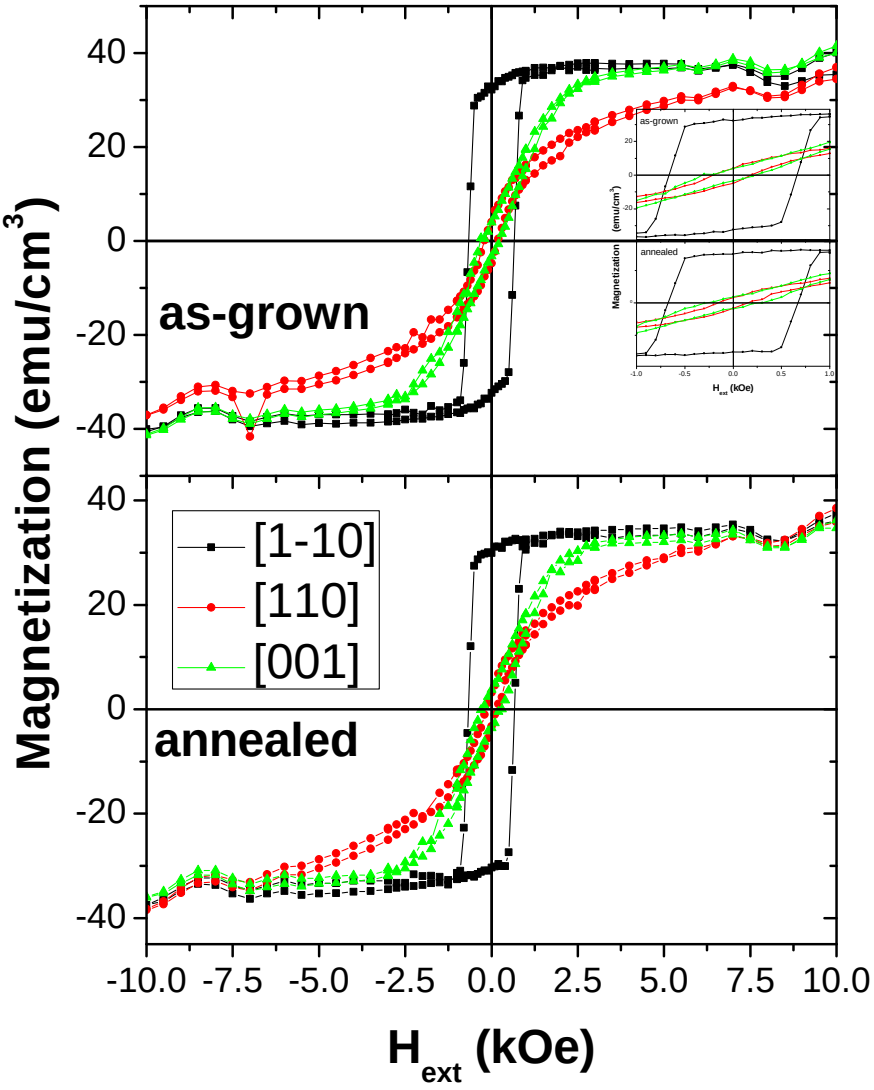

Figure 2.2: Magnetization along various crystalline axes of as-grown (top) and annealed (bottom) (Ga,Mn)Sb against external field for a field sweep loop at 2K. Inset shows the same data plotted for a narrower region of external field.

Several key observations can be made from figures 2.1 and 2.2. Firstly, T_c of the (Ga,Mn)Sb sample is 34K for both the as-grown and annealed samples. Secondly, both the as-grown and annealed samples have a dominant $[1\bar{1}0]$ uni-axial magnetic anisotropy across the whole temperature range up to T_c. Thirdly, the strength of the magnetization at 2K corresponds to a moment of $3.8\mu_B$ per nominal Mn atom for the as-grown sample and $3.6\mu_B$ per nominal Mn atom for the annealed sample (the slight decrease of this value upon annealing is likely to arise due to surface oxidation during the annealing and/or a slightly different size of sample). The inset of figure 2.2 shows that at 2K the coercive field for both the as-grown and annealed samples is roughly 670Oe. For comparison, the magnetic properties of the as-grown and annealed (Ga,Mn)Sb sample are listed in the table in figure 2.3 along with those of similarly doped (Ga,Mn)As[53] and (Ga,Mn)($As_{0.9}$,$Sb_{0.1}$) (see section 2.3.3) samples:

DMS	State	Tc (K)	Magnetic anisotropy	Moment per Mn (μ_B per Mn)	Coercive Field (Oe)
(Ga,Mn)Sb	as-grown	34	uni-axial at all temperatures	3.8	670
(Ga,Mn)Sb	annealed	34	uni-axial at all temperatures	3.6	670
(Ga,Mn)As	as-grown	80	bi-axial to uni-axial transition or uni-axial at all temperatues	2.8	30
(Ga,Mn)As	annealed	135	bi-axial to uni-axial transition or uni-axial at all temperatues	3.4	19
(Ga,Mn)($As_{0.9}Sb_{0.1}$)	as-grown	28	bi-axial to uni-axial transition	1.7	440
(Ga,Mn)($As_{0.9}Sb_{0.1}$)	annealed	55	bi-axial to uni-axial transition	2.6	210

Figure 2.3: Table of magnetic properties of 6% Mn-doped, 25nm thick (Ga,Mn)Sb, (Ga,Mn)As, and (Ga,Mn)($As_{0.9}$,$Sb_{0.1}$) samples. (Ga,Mn)Sb and (Ga,Mn)($As_{0.9}$,$Sb_{0.1}$) data is that obtained from this investigation, (Ga,Mn)As data is taken from reference [53].

It is clear that annealing the (Ga,Mn)Sb sample at 180^{o}C for 48 hours does not change its magnetic properties, which indicates that either there is very little formation of interstitial Mn during the sample growth, or that the 180 ^{o}C annealing temperature does not provide sufficient energy for the removal of interstitial Mn. Given the relatively high value of moment per Mn atom, the former argument seems more likely to be the case. The fact that the moment per Mn atom is still below the ideal case ($\approx 4.5\mu_B$ per Mn atom) suggests that some amount of the nominal Mn dopant atoms are magnetically inactive, and/or that the nominal Mn concentration inferred from the MBE flux rates is not fully accurate. One possible reason that interstitial Mn do not form in (Ga,Mn)Sb may be that the self-compensation of carriers needed to stabilise the Fermi level position is largely achieved through Sb antisite defects rather than interstitial Mn (both of these defects act as donors). GaSb has a narrower band gap than GaAs and so its antisite defects have shallower ionization levels[116], and the shallow ionization level of the mobile Sb antisite may make its formation a more energetically favourable way of compensating holes than the formation of interstitial Mn. If the relative flux of Ga to Sb during the growth was slightly imbalanced this would further help the formation of Sb antisties. Other factors such as the size of the Sb atom and the smaller volume of the interstitial site in GaSb may also play a role in the lack of interstitial Mn.

The measured T_c is the highest ever recorded for a (Ga,Mn)Sb sample. Part of the reason for this is probably due to the relatively high Mn concentration (6%) compared with the (Ga,Mn)Sb samples of previous investigations (2%). As it appears that for the (Ga,Mn)Sb sample studied here most of the Mn go into substitutional positions, increasing Mn doping should increase both the effective Mn concentration and the hole density, unlike the case of optimally annealed (Ga,Mn)As where the effective Mn concentration and hole density are relatively stable with increasing nominal Mn concentration from about 5% upwards[42][62]. An increased effective Mn concentration and hole density will promote a higher T_c as the average distance between substitutional Mn and itinerant holes decreases, so the strength of the hole-mediated ferromagnetic exchange coupling between Mn moments increases, and therefore requires a higher temperature to overcome. As expected, the measured T_c is still significantly lower than similarly doped (Ga,Mn)As samples, and while this is most likely a result the factors suggested in section 2.2.1, no real insight or firm conclusions with regard as to why the

lower T_c of (Ga,Mn)Sb is lower than (Ga,Mn)As can be gained from the SQUID magnetometry data presented here alone.

Previous studies have shown the magnetic anisotropy of (Ga,Mn)Sb to be highly sensitive to the choice of substrate and buffer layer(s)[89], and so it is important to consider the whole sample structure when analysing the magnetic anisotropy of the (Ga,Mn)Sb sample in this investigation. InAs was chosen as a substrate as it is well lattice matched to GaSb (lattice constants of 0.606nm and 0.610nm respectively), and the XRD measurements indicate that the GaSb buffer maintains its lattice shape rather than adopt that of InAs which would lead to compressive strain of the layer (buffer layer is fully relaxed). As discussed in section 1.2.2.5, strain anisotropy in (III,Mn)V DMSs generally dictates the form of the magnetic anisotropy, with compressive/tensile lattice strains yielding an in-plane/out of plane easy axis, however magnetocrystalline and shape anisotropies can also be important in some cases. For the (Ga,Mn)Sb sample in this investigation a dominant in-plane uni-axial magnetic anisotropy at all temperatures is observed, and this may simplistically lead one to conclude that the layer is under compressive strain. Given the XRD findings, such a compressive strain would not be due to the InAs substrate, and would have to arise from some other mechanism that expands the (Ga,Mn)Sb lattice with respect to the GaSb buffer, such as Sb antisites (but not interstitial Mn as it appears not to be present in (Ga,Mn)Sb). The in-plane uni-axial anisotropy across the whole temperature range up to T_c is in akin to some similarly doped (Ga,Mn)As samples, and therefore like (Ga,Mn)As may be related to the formation of Mn dimers during sample growth[41], while anisotropic relaxation of the GaSb host lattice may also be a factor[117]. However, it must also be noted that, as seen in figure 2.2, the [001] axis is magnetically easier than the [110] axis, and so perhaps relating the magnetic anisotropy of the (Ga,Mn)Sb sample to lattice strain is not so straight forward, and that the intrinsic magnetocrystalline anisotropy and perhaps even shape anisotropy also play a role in determining the overall magnetic anisotropy. It is also unclear why the (Ga,Mn)Sb sample has a significantly higher coercivity than similarly doped (Ga,Mn)As, but it could pertain to lattice defects or a reduced carrier density which can hinder domain wall nucleation and propagation.

2.3.2.2 Transport

Transport measurements were not able to be made on the as-grown or annealed (Ga,Mn)Sb Mn691 sample due to the dominating effects of parallel conduction through the InAs substrate, which is apparent from the sample's n-type conduction (as judged by ordinary Hall effect measurements) and relatively very high conductivity. Samples bonded with silver epoxy or ball bonding techniques were also tested but were still parallel conducting, confirming that the issue is not solely caused by wedge bonds punching through the (Ga,Mn)Sb layer to the substrate, indicating that the GaSb buffer layer is ineffective at preventing current leakage to the substrate. Tests of the sample conduction were made at 4.2K and room temperature in case of any significant variation of the relative InAs and (Ga,Mn)Sb conductivities with temperature, but substrate conduction dominates at both temperatures.

2.3.3 (Ga,Mn)($As_{0.9}$,$Sb_{0.1}$)

2.3.3.1 SQUID magnetometry

SQUID magnetometry measurements were performed on the as-grown and annealed (Ga,Mn)($As_{0.9}$,$Sb_{0.1}$) Mn692 sample by Dr Mu Wang. The results are shown in figures 2.4-2.2:

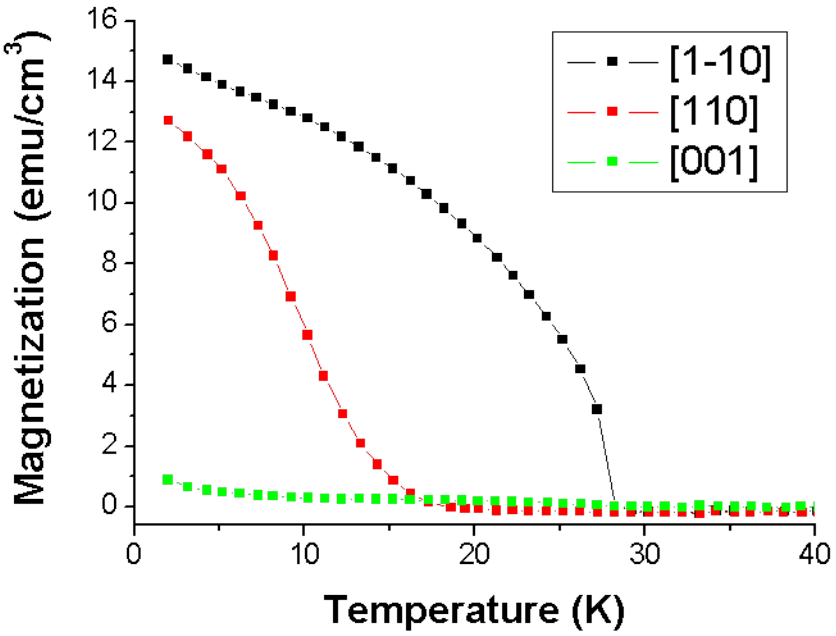

Figure 2.4: Remnant magnetization of as-grown (Ga,Mn)($As_{0.9}$,$Sb_{0.1}$) with increasing temperature after field-cooling along the [1$\bar{1}$0], [110], and [001] crystalline axes in a field of 1kOe.

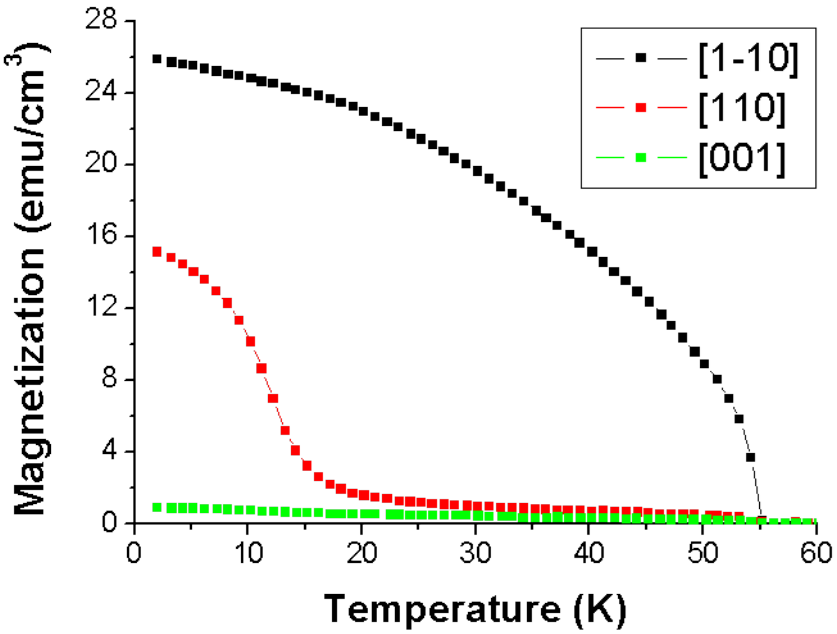

Figure 2.5: Remnant magnetization of annealed (Ga,Mn)($As_{0.9}$,$Sb_{0.1}$) with increasing temperature after field-cooling along the [1$\bar{1}$0], [110], and [001] crystalline axes in a field of 1kOe.

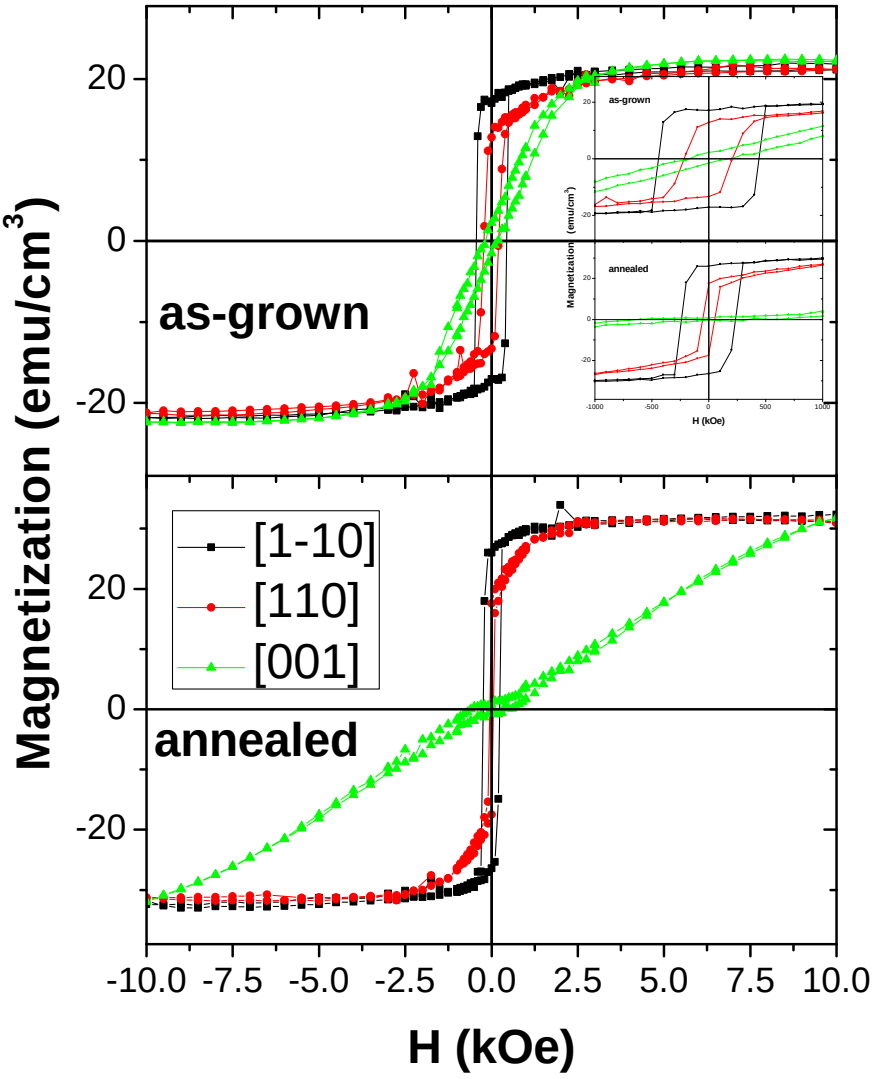

Figure 2.6: Magnetization along various crystalline axes of as-grown (top) and annealed (bottom) (Ga,Mn)($As_{0.9}$,$Sb_{0.1}$) against external field for a field sweep loop at 2K. Inset shows the same data plotted for a narrower region of external field.

Again, several key observations can be made from figures 2.4 and 2.5. Firstly, T_c of (Ga,Mn)($As_{0.9}$,$Sb_{0.1}$) is 28K for the as-grown sample and 55K for the annealed sample. Secondly, both the as-grown and annealed samples have a bi-axial magnetic anisotropy that becomes more uni-axial-like with increasing temperature from 2K up to around 15K where it becomes fully uni-axial in the $[1\bar{1}0]$ direction and remains so as temperature increases up to the respective values of T_c. The ratio of the uni-axial (K_U) to cubic (K_C) magnetic anisotropy constants in the regime of $K_C > K_U$ can be obtained from equation 1.8, and it is found that for the as-grown sample K_C is nearly 7 times greater than K_U at 2K, but only 2 times greater than K_U at 2K in the annealed sample. Thirdly, the strength of the magnetization at 2K corresponds a moment of $1.7\mu_B$ per Mn atom for the as-grown sample and $2.6\mu_B$ per Mn atom for the annealed sample. At 2K the coercive field for the as-grown

sample is 440Oe along the $[1\bar{1}0]$ direction and 210Oe along the [110] direction, whereas for the annealed sample it is 240Oe along the $[1\bar{1}0]$ direction and 55Oe along the [110] direction. These properties are summarised in the table in figure 2.3.

Annealing the (Ga,Mn)($As_{0.9}$,$Sb_{0.1}$) sample changes its magnetic properties, indicating that the annealing removes interstitial Mn from the material. The presence of interstitial Mn in (Ga,Mn)($As_{0.9}$,$Sb_{0.1}$) is a characteristic shared with (Ga,Mn)As, but not (Ga,Mn)Sb, which is perhaps not surprising given the stoichiometry of the sample. Enhancement of the magnetic properties upon annealing (Ga,Mn)(As,Sb) is also observed in reference [114]. The strength of the moment per Mn for optimally annealed (Ga,Mn)($As_{0.9}$,$Sb_{0.1}$) is less than similarly doped (Ga,Mn)As samples, and while this could be due to some degree of compensation of the Mn moments even after annealing in (Ga,Mn)($As_{0.9}$,$Sb_{0.1}$), a more likely explanation is that a greater percentage of the Mn dopants enter the lattice as interstitial or random Mn in (Ga,Mn)($As_{0.9}$,$Sb_{0.1}$) compared with (Ga,Mn)As. As mentioned in section 2.2.2, reference [114] reports that increases of the Sb concentration of (Ga,Mn)(As,Sb) beyond 0.8% lead to an increase of the number of interstitial Mn compared with (Ga,Mn)As, and so for the (Ga,Mn)($As_{0.9}$,$Sb_{0.1}$) sample in this investigation the low moment per Mn compared with (Ga,Mn)As may well be due to an increased number of interstitial Mn. Reference [118] suggests that interstitial Mn are less likely to form in (Ga,Mn)(As,P) than (Ga,Mn)As as the Mn acceptor level lies deeper in the valence band of the wider band gap (Ga,Mn)(As,P), and so the opposite logic may apply for (Ga,Mn)(As,Sb) which should have a narrower band gap than (Ga,Mn)As.

T_c of the annealed (Ga,Mn)($As_{0.9}$,$Sb_{0.1}$) (55K) is less than that of similarly doped optimally annealed (Ga,Mn)As samples (135K), but greater than that of (Ga,Mn)Sb (34K). The fact that the (Ga,Mn)($As_{0.9}$,$Sb_{0.1}$) T_c lies between (Ga,Mn)As and (Ga,Mn)Sb is not surprising from a highly simplistic point of view, but given the 9:1 ratio of Ga to Sb in (Ga,Mn)($As_{0.9}$,$Sb_{0.1}$), one may expect a T_c somewhat closer to (Ga,Mn)As than (Ga,Mn)Sb. However, it is known that for (Ga,Mn)As and (Ga,Mn)Sb, T_c depends on the hole density (by different factors), and as discussed ln section 2.3.3.2, the hole density in the annealed (Ga,Mn)($As_{0.9}$,$Sb_{0.1}$) sample is 5 times less than similarly doped (Ga,Mn)As samples, so the relatively low T_c of (Ga,Mn)($As_{0.9}$,$Sb_{0.1}$) compared to (Ga,Mn)As may well be related to the significantly reduced hole density. The T_c's of the three DMSs are summarised in figure 2.7 where T_c of (Ga,Mn)($As_{0.9}$,$Sb_{0.1}$) is shown as a function of saturation magnetization and plotted with data sets for 50nm thick (Ga,Mn)As samples taken from reference [53], as well as for the Mn691 (Ga,Mn)Sb sample. At the saturation magnetization, all substitutional Mn should be aligned, and therefore the value of the saturation magnetization should only depend on the effective Mn concentration. It is clear from figure 2.7 that T_c of (Ga,Mn)($As_{0.9}$,$Sb_{0.1}$) is less than (Ga,Mn)As and more than (Ga,Mn)Sb for a given saturation magnetization (and therefore effective Mn concentration).

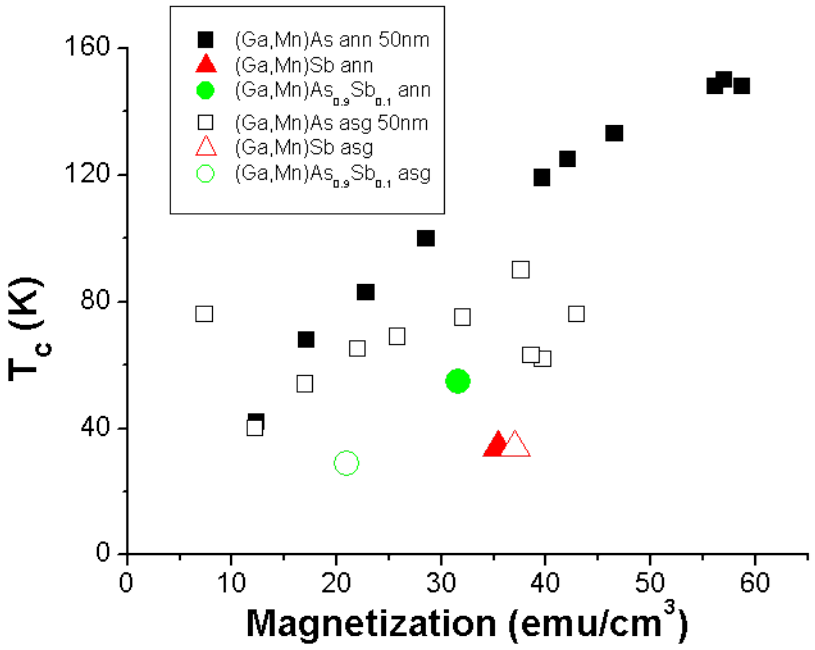

Figure 2.7: T_c of as-grown and annealed (Ga,Mn)As, (Ga,Mn)($As_{0.9}$,$Sb_{0.1}$), and (Ga,Mn)Sb samples as a function of saturation magnetization.

The magnetic anisotropy is bi-axial in-plane for the as-grown and annealed (Ga,Mn)($As_{0.9}$,$Sb_{0.1}$) samples, which usually suggests a compressive strain of the layer. A compressive strain will arise if (Ga,Mn)($As_{0.9}$,$Sb_{0.1}$) has a larger lattice constant than GaAs, and this may be occur due to the larger size of the Sb atom than the As atom and/or the presence of interstitial Mn and/or As or Sb antisites. The bi-axial magnetic anisotropy at low temperatures and uni-axial magnetic anisotropy at higher temperatures of the as-grown and annealed (Ga,Mn)($As_{0.9}$,$Sb_{0.1}$) samples is dissimilar to that of the Mn691 (Ga,Mn)Sb sample where a uni-axial magnetic anisotropy dominates at all temperatures, but is comparable to the magnetic anisotropy of some similarly doped (Ga,Mn)as samples[119][120], though it should be noted that other similarly doped (Ga,Mn)As samples show a uni-axial magnetic anisotropy at all temperatures[53]. The enhancement of the uni-axial anisotropy to cubic anisotropy ratio with annealing is also reported for some similarly doped (Ga,Mn)As samples[121]. Overall, the behaviour of the magnetic anisotropy is more resemblant of (Ga,Mn)As than (Ga,Mn)Sb, which is again simplistically consistent with sample stoichiometry. The reduction of the (Ga,Mn)($As_{0.9}$,$Sb_{0.1}$) coercivity upon annealing is another property similar to (Ga,Mn)As, however, like (Ga,Mn)Sb, the (Ga,Mn)($As_{0.9}$,$Sb_{0.1}$) coercivity is more than an order of magnitude greater than similarly doped (Ga,Mn)As samples, and again may also be related to lattice defects and/or a reduced hole density.

2.3.3.2 Transport

Unlike the Mn691 (Ga,Mn)Sb sample, transport and magneto-transport measurements were able to be made on the Mn692 (Ga,Mn)($As_{0.9}$,$Sb_{0.1}$) sample as

conduction through the (Ga,Mn)($As_{0.9}$,$Sb_{0.1}$) layer dominates (as indicated by p-type conduction from Hall measurements). Figures 2.8-2.11 show the variation of the longitudinal and transverse resistances of the as-grown and annealed (Ga,Mn)($As_{0.9}$,$Sb_{0.1}$) sample for 4kOe field sweeps along the [1$\bar{1}$0], [110], and [100] directions and current flow along the [1$\bar{1}$0] direction at 4K:

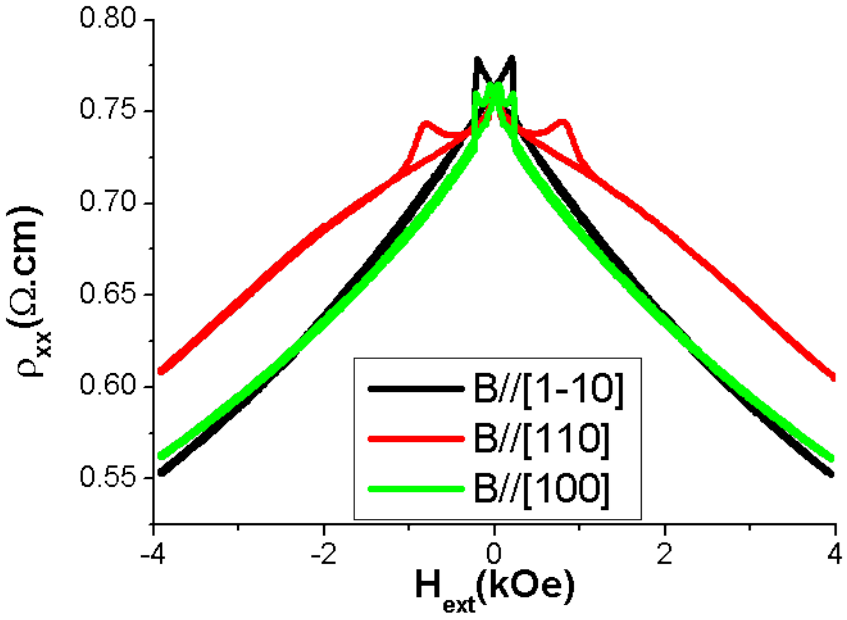

Figure 2.8: Longitudinal resistivity of as-grown (Ga,Mn)($As_{0.9}$,$Sb_{0.1}$) sample against external field for field sweeps along various directions, with current along the [1$\bar{1}$0] direction at 4K.

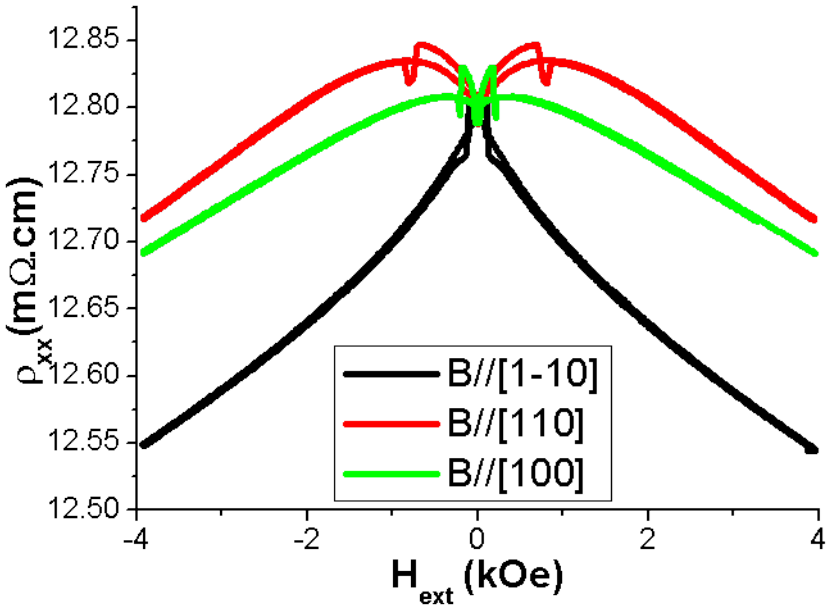

Figure 2.9: Longitudinal resistivity of annealed (Ga,Mn)($As_{0.9}$,$Sb_{0.1}$) sample against external field for field sweeps along various directions, with current along the [1$\bar{1}$0] direction at 4K.

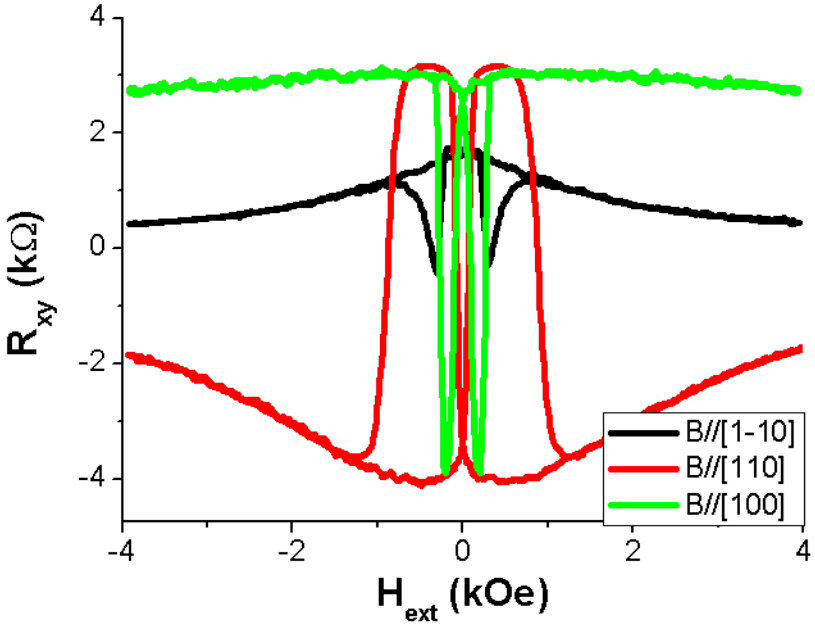

Figure 2.10: Transverse resistance of as-grown (Ga,Mn)($As_{0.9}$,$Sb_{0.1}$) sample against external field for field sweeps along various directions, with current along the [1$\bar{1}$0] direction at 4K.

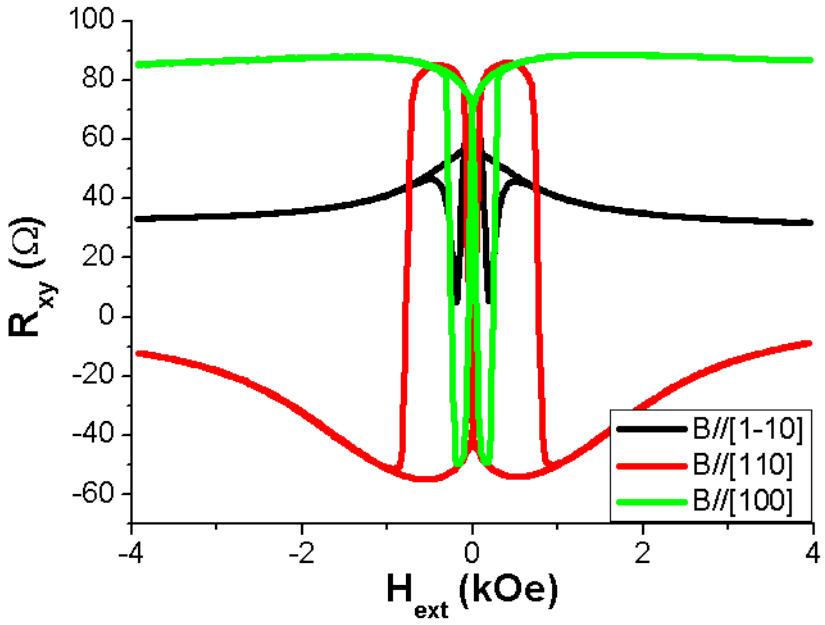

Figure 2.11: Transverse resistance of annealed (Ga,Mn)($As_{0.9}$,$Sb_{0.1}$) sample against external field for field sweeps along various directions, with current along the [$1\bar{1}0$] direction at 4K.

The variation in the longitudinal and transverse resistances in the external field sweeps is given by the variation in the orientation of the magnetization through the longitudinal AMR and PHE respectively. A more detailed study of the AMR of the (Ga,Mn)($As_{0.9}$,$Sb_{0.1}$) sample is presented in chapter 3. The general character of the magnetic anisotropy that can be inferred from the field sweep data is in agreement with the SQUID magnetometry data shown in section 2.3.3.1. For all data sets in figures 2.8-2.11 there is a 3-step switching behaviour at low fields that would not be present in a strongly uni-axial sample, but can be explained by a bi-axial anisotropy where the magnetization jumps between the [100], [$1\bar{1}0$], and [010] axes. The switching happens at smaller fields for the annealed sample than the as-grown sample, which is consistent with the coercivity of (Ga,Mn)($As_{0.9}$,$Sb_{0.1}$) reducing upon annealing. Additionally it can be seen from figures 2.8 and 2.9 that both the as-grown and annealed (Ga,Mn)($As_{0.9}$,$Sb_{0.1}$) have a negative magnetoresistance, which is also observed in (Ga,Mn)As and (Ga,Mn)Sb, and is assumed to arise from reduced spin-scattering as field strength increases but may also have a contribution from suppression of localization with increasing field strength[122].

Out of plane 140kOe field sweeps were performed on the annealed (Ga,Mn)($As_{0.9}$,$Sb_{0.1}$) sample in order to determine its hole density. Further details of the out of plane field sweep method are given in sections 1.3.2.3 and 1.3.3.2. The variation in the longitudinal and transverse resistances of annealed (Ga,Mn)($As_{0.9}$,$Sb_{0.1}$) with out of plane field for current along the [$1\bar{1}0$] direction at 2K are shown in figures 2.12 and 2.13 respectively:

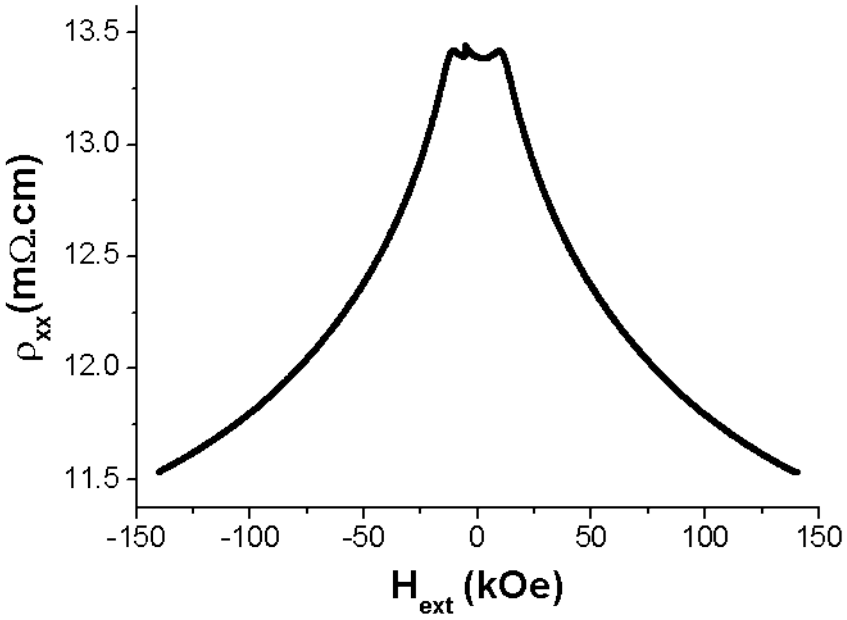

Figure 2.12: ρ_{xx} of annealed (Ga,Mn)($As_{0.9}$,$Sb_{0.1}$) sample against external field for out an of plane field sweep, with current along the $[1\bar{1}0]$ direction at 2K.

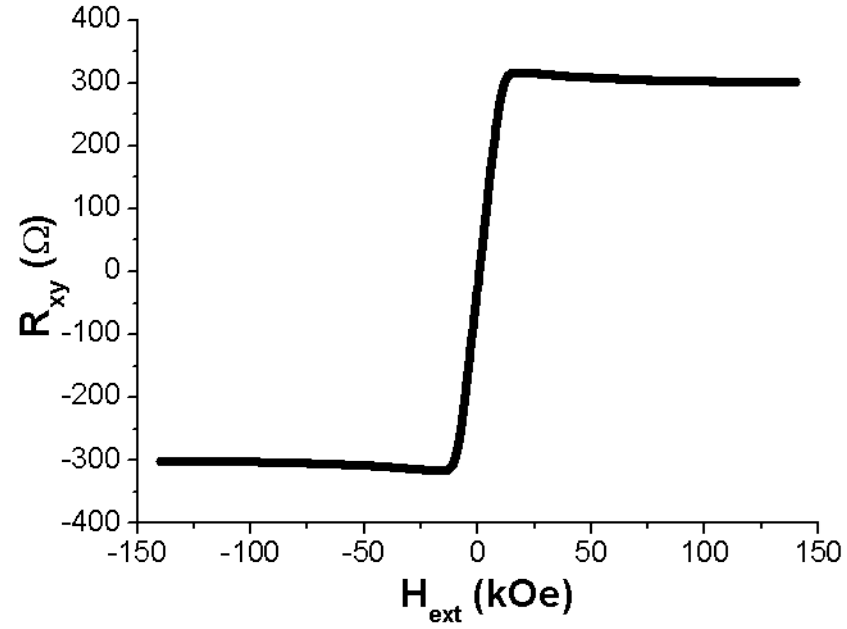

Figure 2.13: R_{xy} of annealed (Ga,Mn)($As_{0.9}$,$Sb_{0.1}$) sample against external field for out an of plane field sweep, with current along the $[1\bar{1}0]$ direction at 2K.

A negative magnetoresistance is observed for the out of plane field sweep in figure 2.12 with a magnitude of 14% at 140kOe, which is considerably larger than similarly doped (Ga,Mn)As samples[123]. The negative sign of the magnetoresistance is

expected given that the in-plane field sweeps also show a negative magnetoresistance. The variation of R_{xy} with out of plane field, shown in figure 2.13, has strikingly different slopes at low and high fields and is fairly typical of a ferromagnet with SOC. At low fields, the slope is dominated by the AHE which is proportional to the component of the magnetization out of plane (which varies with H_{ext}), with a smaller AHE contribution from the variation of R_{xx} as well as a small OHE contribution. At high fields, the magnetization lies fully along the out of plane direction, so the slope is determined by the interplay of the AHE component which varies with R_{xx} (which in turn varies with H_{ext}) and the OHE component. The relative size of the AHE contribution to the high field slope is perhaps larger than in similarly doped (Ga,Mn)As materials due to the relatively large magnetoresistance of (Ga,Mn)($As_{0.9}$,$Sb_{0.1}$). The theory of the OHE and AHE are presented in greater detail in section 1.3.3.2, along with a discussion of how to separate their contributions to the R_{xy} signal and obtain a carrier density from the OHE, so a detailed method will not be given here. R_{xy} from the AHE is proportional to R_{xx}^n, where n is assumed to take the value of 1 or 2, therefore the following equations are used to try and fit to the high field regions (+50kOe to +140kOe and -50kOe to -140kOe where the magnetization is assumed to lie fully out of plane) of the R_{xy} against H_{ext} data set in order to obtain the ordinary Hall coefficient and hence the carrier density:

$$R_{xy} = C_1 B + C_2 R_{xx} \tag{2.1}$$

$$R_{xy} = C_1 B + C_2 R_{xx}^2 \tag{2.2}$$

$$R_{xy} = C_1 B + C_2 R_{xx}^n \tag{2.3}$$

$$R_{xy} = C_1 B + C_2 R_{xx} + C_3 R_{xx}^2 \tag{2.4}$$

where C_1, C_2, C_3, and n are variable fitting parameters. Examples of the fits to the +50kOe to +140kOe R_{xy} against H_{ext} data set using equations 2.1-2.4 are shown in figures 2.14-2.17:

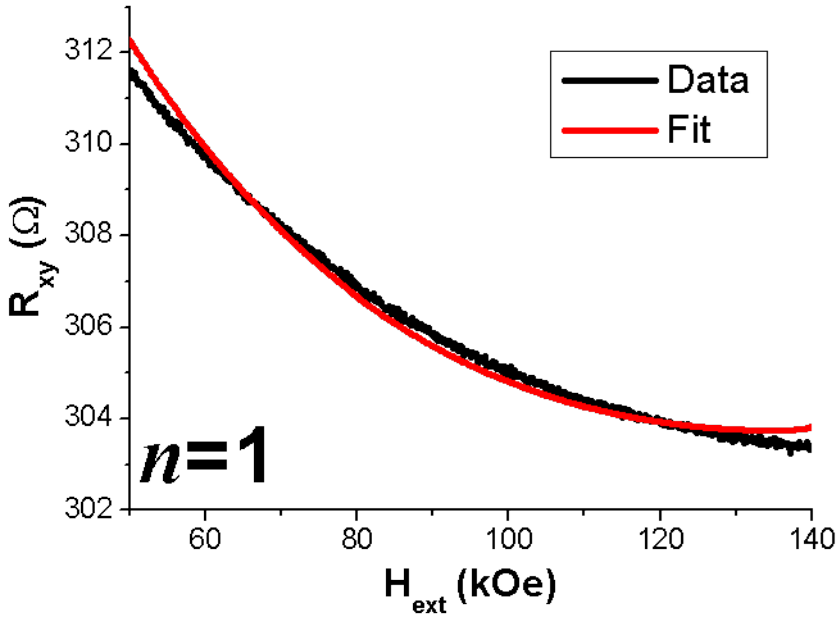

Figure 2.14: Data (black) and fit using equation 2.1 (red) for R_{xy} against out of plane field for annealed (Ga,Mn)($As_{0.9}$,$Sb_{0.1}$), with current along the $[1\bar{1}0]$ direction at 2K.

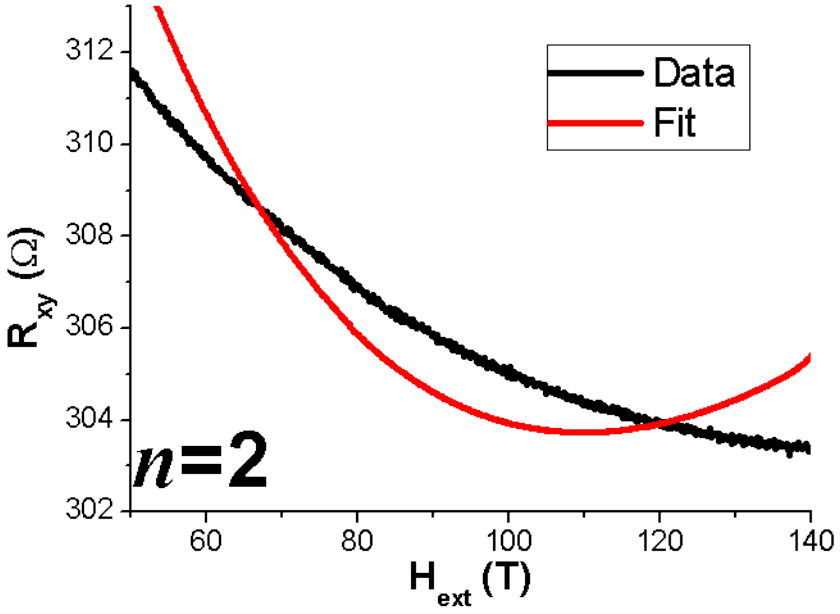

Figure 2.15: Data (black) and fit using equation 2.2 (red) for R_{xy} against out of plane field for annealed (Ga,Mn)($As_{0.9}$,$Sb_{0.1}$), with current along the $[1\bar{1}0]$ direction at 2K.

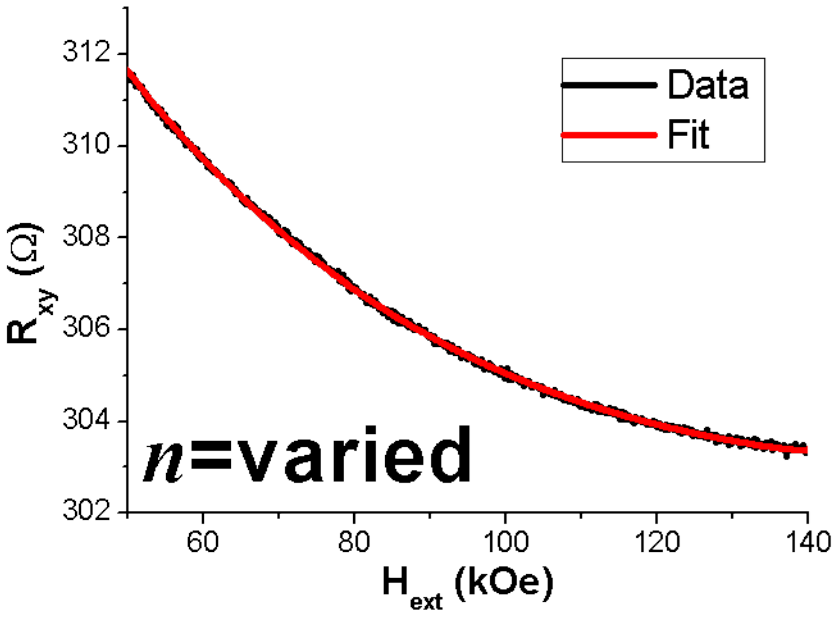

Figure 2.16: Data (black) and fit using equation 2.3 (red) for R_{xy} against out of plane field for annealed (Ga,Mn)($As_{0.9}$,$Sb_{0.1}$), with current along the $[1\bar{1}0]$ direction at 2K. Note that the equation 2.3 fit is made across the entire external field range for a single value of n, i.e. n does not vary with external field.

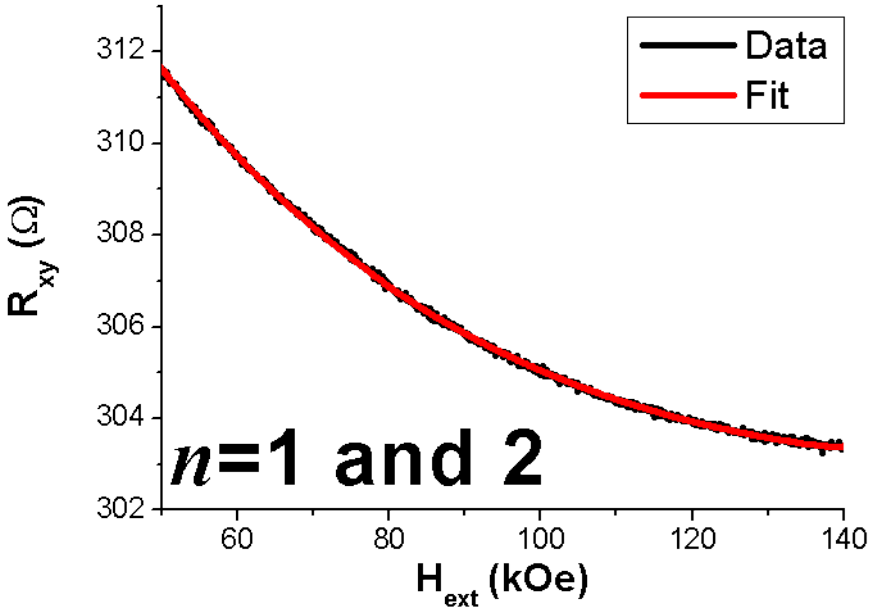

Figure 2.17: Data (black) and fit using equation 2.4 (red) for R_{xy} against out of plane field for annealed (Ga,Mn)($As_{0.9}$,$Sb_{0.1}$), with current along the $[1\bar{1}0]$ direction at 2K.

It is clear from figures 2.14-2.17 that equations 2.1 and 2.2 do not adequately capture the data, but that equations 2.3 and 2.4 do. As discussed in section 1.3.3.2, when n=1 ($R_{xy} \propto R_{xx}$) the AHE is associated with a skew scattering contribution, whereas when n=2 ($R_{xy} \propto R_{xx}^2$) it is associated with a side-jump and/or intrinsic Berry phase contribution. The fact that equations 2.1 and 2.2 do not fit the data but equation 2.4 does suggests that no one mechanism dominates the AHE in the annealed (Ga,Mn)($As_{0.9}$,$Sb_{0.1}$) sample. Equation 2.3 also fits well, and interestingly n, which is a free fitting parameter, takes a value of around 0.73 (see figure 2.18), i.e. not in between 1 and 2, an observation that has previously been made for low-conductivity (Ga,Mn)As samples[124]. Given the low conductivity of the (Ga,Mn)($As_{0.9}$,$Sb_{0.1}$) sample (detailed further on in this section), the less than 1 value of n obtained from the equation 2.3 fit is plausible. Unfortunately it is impossible to make any further comment about the relative size of the contributions to the AHE from the skew-scattering/side-jump/intrinsic mechanisms from the data and the fits.

The hole density is obtained from the C_1 fitting parameter as C_1 represents the ordinary Hall coefficient, i.e. $C_1 = R_H = 1/pet$. The values of the hole density obtained from the fits to the out of plane field sweep data in the ranges +50kOe to +140kOe and -50kOe to -140kOe for both the constant flux and constant heat methods (see section 1.3.2.2) using equations 2.3 and 2.4 are given in the table in figure 2.18, along with the other relevant fitting parameters:

Fitting Equation	Field Range (kOe)	Method	C_1	n	Carrier Density (x10^{20} cm^{-3})
$C_1B + C_2R_{xx} + C_3R_{xx}^2$	50 to 140	flux	0.804 (±0.005)	-	2.0 (±0.2)
$C_1B + C_2R_{xx} + C_3R_{xx}^2$	50 to 140	heat	0.966 (±0.007)	-	2.4 (±0.2)
$C_1B + C_2R_{xx} + C_3R_{xx}^2$	-140 to -50	flux	0.807 (±0.004)	-	2.0 (±0.2)
$C_1B + C_2R_{xx} + C_3R_{xx}^2$	-140 to -50	heat	0.890 (±0.005)	-	2.2 (±0.2)
$C_1B + C_2R_{xx}^n$	50 to 140	flux	0.761 (±0.005)	0.725 (±0.002)	1.9 (±0.2)
$C_1B + C_2R_{xx}^n$	50 to 140	heat	0.951 (±0.009)	0.774 (±0.004)	2.4 (±0.2)
$C_1B + C_2R_{xx}^n$	-140 to -50	flux	0.764 (±0.005)	0.728 (±0.002)	1.9 (±0.2)
$C_1B + C_2R_{xx}^n$	-140 to -50	heat	0.855 (±0.005)	0.727 (±0.003)	2.1 (±0.2)

Figure 2.18: Table of fitting coefficients and carrier densities of obtained from various fits to out of plane field sweep data of (Ga,Mn)($As_{0.9}$,$Sb_{0.1}$).

The errors on C_1 and n are the errors from the fit, and the error on the carrier density is the combination of the error on C_1 and sample thickness (estimated to be 10%). With the exception of the +50kOe to +140kOe constant heat data sets, the obtained hole densities all agree within error which suggests that the experimental

data has been well captured by the fitting equations 2.3 and 2.4. The carrier density of the annealed (Ga,Mn)($As_{0.9}$,$Sb_{0.1}$) of approximately 2x10^{20}cm^{-3} is considerably smaller than similarly doped (Ga,Mn)As samples where it is around 1x10^{21}cm^{-3}[53].

Using the simplistic assumptions that i) annealing removes all interstitial Mn in (Ga,Mn)($As_{0.9}$,$Sb_{0.1}$), and ii) the nominal Mn doping concentrations are accurate, the 2.6μ_B per Mn atom for (Ga,Mn)($As_{0.9}$,$Sb_{0.1}$) obtained from SQUID magnetometry measurements in section 2.3.3.1 suggests that around half of the nominal Mn dopants enter the (Ga,Mn)($As_{0.9}$,$Sb_{0.1}$) lattice in substitutional positions. If a rough upper estimate of the lattice constant for annealed (Ga,Mn)($As_{0.9}$,$Sb_{0.1}$) is taken as 0.575nm[114], and assuming there are 0.12 substitutional Mn contributed per unit cell (4 Ga atoms contributed per unit cell x 0.03 substitutional Mn concentration), a very rough estimate of the hole density for the case of 1 substitutional Mn providing 1 hole can be calculated as 0.12/(5.75x10^{-8}cm)^3 = 6x10^{20}cm^{-3}, which is three times larger than the measured hole density. It must be stressed again that this calculated ideal hole density is a very loose estimate, but even so it seems to suggest that there must be some mechanism that compensates carrier holes but not Mn moments in (Ga,Mn)($As_{0.9}$,$Sb_{0.1}$). The likely explanation for this is the presence of donor-like defects that act to reduce the hole density. As antisites, i.e. an As atom that sits in a Ga lattice position and acts as a donor, are known to occur in higher Mn doped (Ga,Mn)As samples[125][43] and are stable against 180^{o}C annealing temperatures[126], and it is certainly possible that As antisites are present in the 6% Mn doped (Ga,Mn)($As_{0.9}$,$Sb_{0.1}$) sample and may well explain the lower than expected hole density. Sb antisites, which would have the same effect as As antisites, may also occur in (Ga,Mn)($As_{0.9}$,$Sb_{0.1}$). For the growth of the (Ga,Mn)($As_{0.9}$,$Sb_{0.1}$) the group V flux was increased from that normally used for (Ga,Mn)As samples (same Ga and As ratios as for (Ga,Mn)As growth but with Sb also added), and so given the greater group V to group III atomic ratio during the growth it is believable that group V antisites could form.

In (Ga,Mn)As, the As sublattice is found to be free from defects[125], but it is worth considering if trying to alloy two different group V atoms into the same sublattice, as in the case of (Ga,Mn)($As_{0.9}$,$Sb_{0.1}$), might lead to defects of the group V sublattice which also compensate holes. Group V sublattice defects could include Ga antisites (Ga atom in a group V position) and a vacancy at the group V atom position, however, both of these defects would act as acceptors and therefore should not explain the reduced hole density of (Ga,Mn)($As_{0.9}$,$Sb_{0.1}$) (additionally their acceptor like nature would make their formation energetically unfavourable in (Ga,Mn)($As_{0.9}$,$Sb_{0.1}$)). Unless there is some additional hole compensating defect that has not been considered here, it would seem that group V antisites are the most likely cause of the reduced hole density, but it is not clear why this defect would be more prevalent in (Ga,Mn)($As_{0.9}$,$Sb_{0.1}$) than (Ga,Mn)As.

The relatively low hole density of (Ga,Mn)($As_{0.9}$,$Sb_{0.1}$) suggests a relatively low conductivity/high resistivity also. The resistivity of as-grown and annealed (Ga,Mn)($As_{0.9}$,$Sb_{0.1}$) as a function of temperature for current along various Hall bar directions is shown in figures 2.19 and 2.20 respectively:

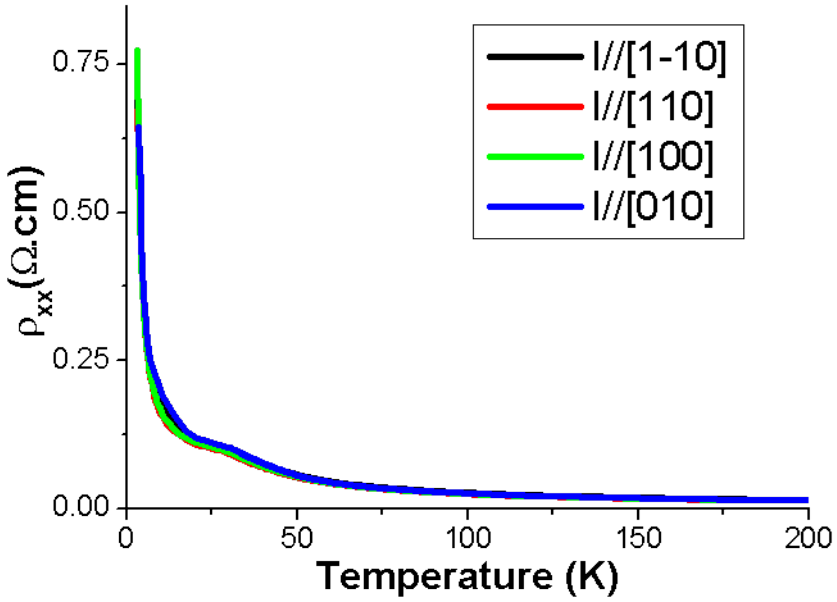

Figure 2.19: Resistivity against temperature for as-grown (Ga,Mn)($As_{0.9}$,$Sb_{0.1}$) with current flow along various Hall bar directions.

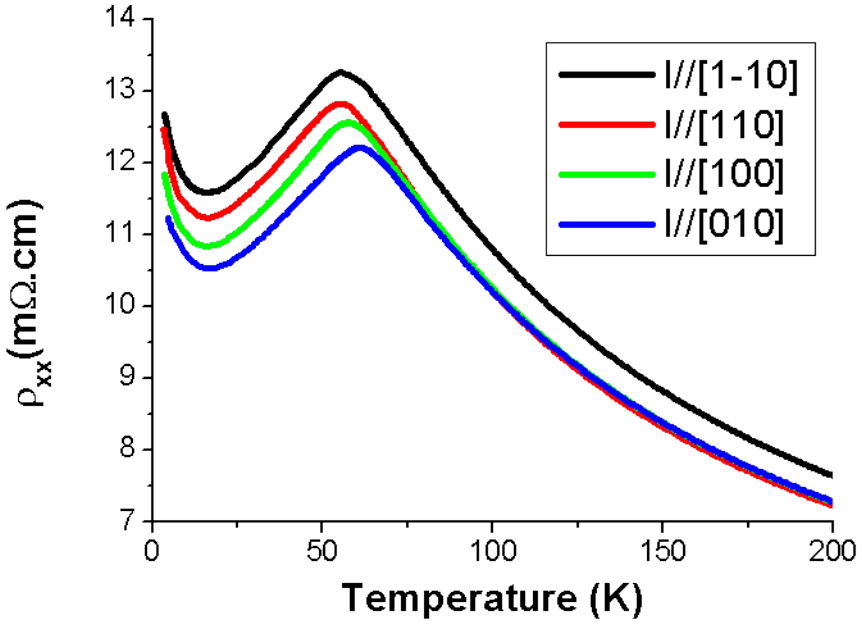

Figure 2.20: Resistivity against temperature for annealed (Ga,Mn)($As_{0.9}$,$Sb_{0.1}$) with current flow along various Hall bar directions.

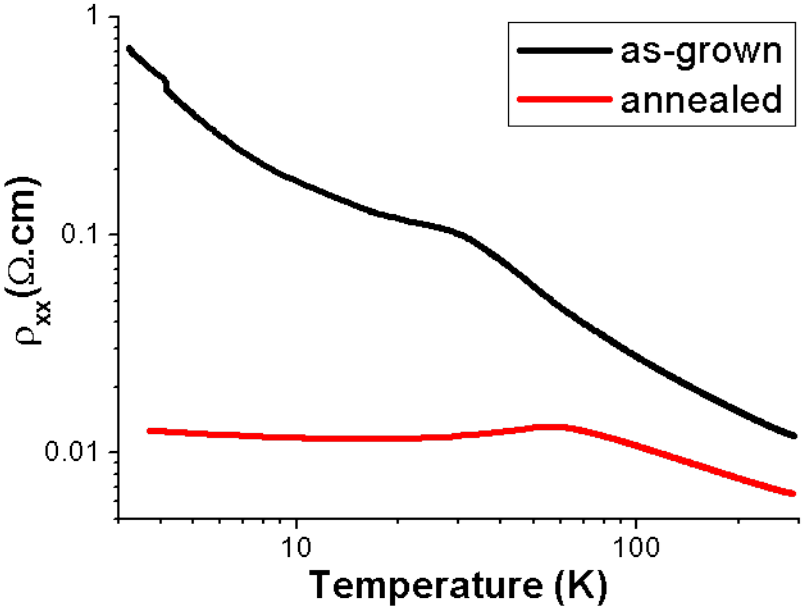

Figure 2.21: Resistivity against temperature for as-grown (black) and annealed (red) (Ga,Mn)($As_{0.9}$,$Sb_{0.1}$) with current flow along the [1$\bar{1}$0] direction, plotted on a log-log scale for ease of comparison.

The corresponding conductivity of the as-grown (Ga,Mn)($As_{0.9}$,$Sb_{0.1}$) is $1.3\Omega^{-1}cm^{-1}$ at 4K and $80\Omega^{-1}cm^{-1}$ at room temperature, and the conductivity of the annealed (Ga,Mn)($As_{0.9}$,$Sb_{0.1}$) is $80\Omega^{-1}cm^{-1}$ at 4K and $160\Omega^{-1}cm^{-1}$ at room temperature. By comparison similarly doped as-grown (Ga,Mn)As has a conductivity of $325\Omega^{-1}cm^{-1}$ at 4K and $300\Omega^{-1}cm^{-1}$ at room temperature, and similarly doped annealed (Ga,Mn)As has a conductivity of $700\Omega^{-1}cm^{-1}$ at 4K and $500\Omega^{-1}cm^{-1}$ at room temperature[53]. The difference in the magnitude of the resistivity against temperature plots for the different Hall bar directions in figure 2.20 is likely to be due to the different Hall bars unintentionally having slightly different dimensions (the same dimensions were assumed when calculating the resistivity), and the difference in the shape of the plots, namely the temperature at which the resistance peak occurs, is probably because of inconsistent rates of cooling of the sample temperature and/or slight variation in the sample wafer for the different Hall bars.

Both the size of the conductivity/resistivity of (Ga,Mn)($As_{0.9}$,$Sb_{0.1}$) and its relationship with temperature change greatly upon annealing the sample. The as-grown (Ga,Mn)($As_{0.9}$,$Sb_{0.1}$) displays an insulating-like character at low temperatures where ρ_{xx} drastically increases as temperature decreases. The conductivity at 4K is very low, more than 2 orders of magnitude less than similarly doped (Ga,Mn)As samples and nearly 3 orders of magnitude lower than lesser doped (Ga,Mn)Sb samples[88][89]. It is unclear as to exactly why the as-grown sample has such a low conductivity. No hole density measurements were made on the sample, but as the as-grown sample contains hole and moment compensating interstitial Mn (as seen from the SQUID magnetometry data where the moment increases from $1.7\mu_B$ per Mn atom to $2.6\mu_B$ per Mn atom upon annealing), the hole density of

the as-grown sample will clearly be lower than the relatively small $2x10^{20}cm^{-3}$ hole density of the annealed sample. However, the 4K conductivity of the as-grown sample is more than 60 times less than the annealed sample, and bearing in mind that conductivity is proportional to both carrier density and mobility, and that it is highly unlikely that the as-grown sample's hole density is more than 60 times less than the annealed sample, the low carrier density alone should not explain the extremely low 4K conductivity of the as-grown (Ga,Mn)($As_{0.9}$,$Sb_{0.1}$). This suggests that as-grown (Ga,Mn)($As_{0.9}$,$Sb_{0.1}$) also has an extremely low mobility. Such a low mobility may arise in (Ga,Mn)($As_{0.9}$,$Sb_{0.1}$) if the Fermi level lies at the valence band edge where carriers are strongly localised. In disordered lattices, the random potential resulting from the non-periodic lattice experienced by carrier waves can act to suppress tunnelling transport from one lattice site to another due to decoherence, the result of which is localisation of the carriers (Anderson localisation[127]). Replacing Ga atoms in the GaSb lattice with Mn dopants introduces disorder into the lattice, while the presence of interstitial Mn, antisites and other lattice defects will all also act to increase lattice disorder. If the carrier density is significantly low (which is perhaps the case for as-grown (Ga,Mn)($As_{0.9}$,$Sb_{0.1}$)) then the transport becomes dominated by localised carriers and so the mobility and hence conductivity become extremely small. The increase in conductivity with temperature is likely be due to the greater thermal energy of carriers giving them a higher probability of tunnelling between lattice sites. Similar insulating trends to that of as-grown (Ga,Mn)($As_{0.9}$,$Sb_{0.1}$) have also been seen in the ρ_{xx} against temperature plots in ultra-thin (<5nm) 5% Mn doped as-grown (Ga,Mn)As layers[128][129], where a hole density of $1.6x10^{20}cm^{-3}$ is reported[130], as well as in 25nm 9% Mn doped as-grown (Ga,Mn)($As_{0.9}$,$P_{0.1}$)[112], and as-grown (Ga,Mn)As samples of both low and high Mn concentrations grown during the early stages of the material's development[131].

Upon annealing, (Ga,Mn)($As_{0.9}$,$Sb_{0.1}$) goes through a insulator to metal transition, as indicated by the shape of the annealed (Ga,Mn)($As_{0.9}$,$Sb_{0.1}$) ρ_{xx} against temperature plot, which resembles that for similarly doped (Ga,Mn)As samples which have metallic character. Annealing the (Ga,Mn)($As_{0.9}$,$Sb_{0.1}$) increases the carrier density, pushing the Fermi level deeper into the valence band where the carrier states significantly overlap, thus the transport is dominated by delocalised carriers which brings about the metallic behaviour. The shape of the ρ_{xx} against temperature plot can be explained by considering the behaviour at different temperature ranges as temperature is decreased from 200K downwards: Initially, ρ_{xx} increases with decreasing temperature due to a non-magnetic contribution until the shoulder-like feature slightly above T_c, then decreases as temperature decreases down to around 17K due to reduced uncorrelated spin-scattering as the magnetization strength increases, and finally from 17K downwards ρ_{xx} increases, which is believed to be a result of weak localisation and electron-electron interactions[132][133]. The lower conductivity of as-grown (Ga,Mn)($As_{0.9}$,$Sb_{0.1}$) compared to as-grown (Ga,Mn)As can be largely ascribed to its extremely low mobility, however, for the annealed (Ga,Mn)($As_{0.9}$,$Sb_{0.1}$), the ratios of its 4K conductivity and hole density compared to annealed (Ga,Mn)As (1:8 and 1:5 respectively) are reasonably similar, and therefore difference in hole density between the two DMSs plays a much more significant role in explaining the differences in their conductivities.

The SQUID magnetometry and transport measurements of annealed (Ga,Mn)($As_{0.9}$,$Sb_{0.1}$) show it to be a material with generally similar characteristics to annealed (Ga,Mn)As (metallic transport behaviour, bi-axial to uni-axial magnetic anisotropy, removal of interstitial Mn with annealing), but with a reduced T_c, conductivity, and hole density. To illustrate this point, figure 2.22 plots the T_c against conductivity at 4K and room temperature of annealed (Ga,Mn)($As_{0.9}$,$Sb_{0.1}$) and various (Ga,Mn)As samples at different stages of annealing for different annealing temperatures:

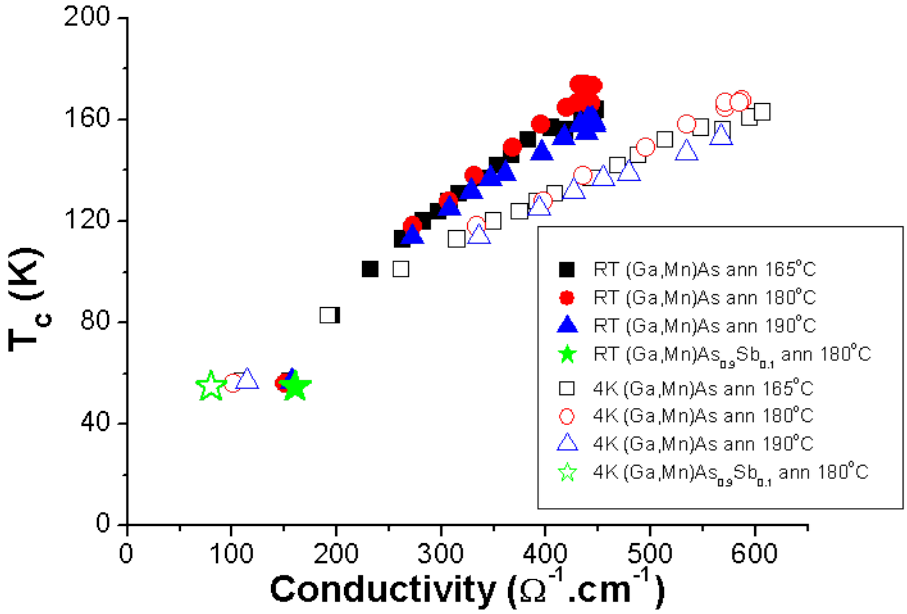

Figure 2.22: T_c against conductivity at 4K (open symbols) and room temperature (closed symbols) for step-annealed (Ga,Mn)($As_{0.9}$,$Sb_{0.1}$) and various annealed (Ga,Mn)As samples (data taken from reference [65]).

It can be seen in figure 2.22 that the annealed (Ga,Mn)($As_{0.9}$,$Sb_{0.1}$) follows the same trend as (Ga,Mn)As in the relationship between T_c and conductivity for both 4K and room temperature conductivities. As (Ga,Mn)As is increasingly annealed, its effective Mn concentration and hence also its hole density increase, which explains the positive correlation between T_c and conductivity. The fact that the (Ga,Mn)($As_{0.9}$,$Sb_{0.1}$) data points fit into the (Ga,Mn)As trends suggests that the relationship between T_c and conductivity is the same for (Ga,Mn)($As_{0.9}$,$Sb_{0.1}$) as it is for (Ga,Mn)As, and assuming that mobility is reasonably similar for (Ga,Mn)($As_{0.9}$,$Sb_{0.1}$) and (Ga,Mn)As, then the relationship between T_c and hole density can also be considered to be similar to (Ga,Mn)As.

2.4 Conclusions and future work

This chapter reported on the characterisation of the Sb-based DMSs (Ga,Mn)Sb and (Ga,Mn)($As_{0.9}$,$Sb_{0.1}$). It is known from previous studies that (Ga,Mn)Sb is

a DMS with a high conductivity and low T_c, and it is an appealing choice of (III,Mn)V material for spintronics research as the large Sb atom suggests it should have a strong SOC. (Ga,Mn)($As_{0.9}$,$Sb_{0.1}$) is in the class of the seldom studied (III,Mn)(V_A,V_B) quaternary DMSs, which are interesting systems as varying the relative alloy compositions can affect both the electrical and magnetic material properties, adding another dimension to the already rich DMS tunability.

SQUID magnetometry measurements were made on as-grown and annealed (Ga,Mn)Sb and revealed that the magnetic properties do not change upon annealing, presumably as interstitial Mn do not form in (Ga,Mn)Sb. The (Ga,Mn)Sb sample has a T_c of 34K (the highest recorded value), an in-plane uni-axial magnetic anisotropy at all temperatures up to T_c, a moment of $3.8\mu_B$ per Mn atom, and a coercive field of 670Oe. The SQUID magnetometry measurements show that (Ga,Mn)Sb is a material with some similar and some different magnetic properties to (Ga,Mn)As. XRD measurements indicated that the (Ga,Mn)Sb layer is fully relaxed, but the observed strong in-plane uni-axial magnetic anisotropy and weak in-plane cubic magnetic anisotropy make it somewhat difficult to link the overall magnetic anisotropy to strain alone. No transport measurements were able to be made on the (Ga,Mn)Sb sample as the majority of the conduction is through the InAs substrate.

(Ga,Mn)($As_{0.9}$,$Sb_{0.1}$) is shown to be a unique material, distinct from (Ga,Mn)As in its own right but also with some similarities. Like (Ga,Mn)As but unlike (Ga,Mn)Sb, the magnetic and electrical properties of (Ga,Mn)($As_{0.9}$,$Sb_{0.1}$) change upon annealing, indicating the removal of interstitial Mn; T_c increases from 28K to 55K, its bi-axial magnetic anisotropy becomes more uni-axial, its magnetization increases from $1.7\mu_B$ per Mn atom to $2.6\mu_B$ per Mn atom, and its conductivity at 4K increases from $1.3\Omega^{-1}cm^{-1}$ to $80\Omega^{-1}cm^{-1}$. When compared to the magnetization data, the low measured hole density of $2x10^{20}cm^{-3}$ of the annealed sample is incompatible with being caused solely from a low number of substitutional Mn, suggesting that hole compensating defects such as As antisites are present in the material. The low hole density can largely explain the relatively low 4K conductivity of the annealed sample, however, it is unlikely to be able to explain the ultra-low 4K conductivity of the as-grown sample, which suggests a very low carrier mobility at this temperature, likely as as result of strong carrier localisation. XRD measurements show the as-grown sample to be fully strained, which could be because of the larger size of the Sb atom compared to the As atom, and/or the presence of interstitial Mn, and/or the presence of As antisites.

The characterisation of (Ga,Mn)Sb and (Ga,Mn)($As_{0.9}$,$Sb_{0.1}$) has shown them to be interesting and unique DMSs. While many of the basic material properties of the two samples are revealed by the measurements presented in this chapter, much of the underlying physics responsible for those material properties is only speculated upon, demonstrating that there is far from a full fundamental understanding of these DMSs. Additionally, with the exception of the AMR study of (Ga,Mn)($As_{0.9}$,$Sb_{0.1}$) presented in chapter 3, no investigations have been carried out looking at spintronic phenomena in these presumably strongly spin-orbit coupled Sb-based DMSs, largely owing to the parallel conduction in the (Ga,Mn)Sb sample

and the low conductivity of the (Ga,Mn)($As_{0.9}$,$Sb_{0.1}$) sample. These reasons are motivating factors for further study of Sb-based DMS, including more work on the existing (Ga,Mn)Sb and (Ga,Mn)($As_{0.9}$,$Sb_{0.1}$) samples, but also by growing a variety of additional samples. However, in order to grow more Sb-based DMS samples in the Nottingham MBE machine, the issues discussed in section 2.3.1 of growing with elemental Sb_4 would need to be circumvented. One route for doing this is to use a cracker cell in the growth to reduce Sb_4 molecules to less detrimental Sb_2 molecules, but as cracker cells are very costly there would need to be an extremely strong motivation for continued MBE growth of Sb samples at Nottingham. There are currently no further (Ga,Mn)Sb growths planned in Nottingham in the immediate future.

If at some point growth of further Sb-based DMSs samples were to be made possible in Nottingham, first and foremost a (Ga,Mn)Sb sample without the parallel conduction issues of the Mn691 (Ga,Mn)Sb sample investigated in this chapter would be an important material to grown and investigate. One approach to obtain such a material would be to grow the (Ga,Mn)Sb on a GaSb substrate with an AlSb buffer layer, which should prevent parallel conduction. AlSb has a lattice constant of 0.614nm compared to 0.610nm for GaSb, but it is not clear how the GaSb/AlSb buffer substrate would strain the (Ga,Mn)Sb layer; if the AlSb layer takes the GaSb shape then a compressive strain of the (Ga,Mn)Sb layer may be expected (as defects in (Ga,Mn)Sb should expand the lattice), but if the AlSb layer relaxes on the GaSb and maintains its own shape then a tensile strain of the (Ga,Mn)Sb layer may be expected (due to the larger AlSb lattice constant). Assuming a (Ga,Mn)Sb sample without parallel conduction could be achieved, it would be interesting to see how the magnetic and transport properties vary as the Mn concentration is increased. Interstitial Mn seemingly do not form in the 6% Mn doped Mn691 (Ga,Mn)Sb sample, leading to a relatively large moment per Mn atom, but it is not immediately obvious if this would still be the case at high Mn concentrations of 12%-14%. If interstitial Mn were still absent at these concentrations a high saturation magnetization could be achieved for (Ga,Mn)Sb. Additionally, measuring the hole density and conductivity of (Ga,Mn)Sb over a range of Mn concentrations would help to build up a picture of hole compensating defects in (Ga,Mn)Sb such as Sb antisites, and give a clearer idea as to whether they are responsible for the lack of interstitial Mn observed in the 6% sample in this investigation. A range of (Ga,Mn)Sb samples with different Mn concentrations would also allow the relationship between T_c and hole density, reported to be $T_c \propto p^{1.4}$ in reference [91], to be determined without the need for a gated device structure. High-field hole density measurements in (Ga,Mn)Sb would also be intriguing in terms of investigating the contributions to the AHE in the strongly spin-orbit coupled, high conductivity DMS, and even how those contributions evolve with Mn concentration.

As well providing an insight into material characteristics, future (Ga,Mn)Sb samples could also be used as a test-bed material to investigate SOC phenomena. The high conductivity and strong SOC would make (Ga,Mn)Sb an ideal material to investigate spin-orbit torque, and it would be interesting to see how the relative size of the Dresselhaus and Rashba style current induced fields compare with similarly doped (Ga,Mn)As samples. AMR has been well investigated in

(Ga,Mn)As where a non-crystalline contribution is dominant, but as shown in chapter 3, AMR in (Ga,Mn)($As_{0.9}$,$Sb_{0.1}$) has more balanced contributions from non-crystalline, crystalline, and crossed terms, and therefore investigating the AMR of (Ga,Mn)Sb should lead to further understanding of the origin and relative importance of the various contributions to AMR in DMSs. Tunnelling anisotropic magnetoresistance (TAMR) is another SOC-phenomenon that has not been well studied in DMSs other than (Ga,Mn)As[6][134][135] and therefore an investigation of TAMR with (Ga,Mn)Sb as the ferromagnetic electrode may be helpful. Such a (Ga,Mn)Sb TAMR structure could be realised by using n-type InAs substrate as the non-magnetic electrode and AlSb as the tunnel barrier. Similarly thermal SOC phenomena such as the planar Nernst effect[136], anomalous Nernst effect[85], and anisotropic magnetothermopower[137] have all only been observed in one type of DMS to date - (Ga,Mn)As, and while information of these thermal SOC phenomena in other DMSs would be valuable, achieving the required controllable temperature gradients in (Ga,Mn)Sb devices would be time-consuming and difficult compared with SOT/AMR/TAMR experiments.

Reference [114] investigated (Ga,Mn)(As,Sb) for very low concentrations of Sb, but perhaps a more useful study would be to explore the properties of (Ga,Mn)(As,Sb) over the full range of As:Sb ratios. Due to the different lattice constants of As and Sb, the choice of substrate and buffer layer would be an important factor for fair comparisons between samples of different As:Sb ratios in such an investigation. InP has a lattice constant that is approximately in-between that of GaAs and GaSb and therefore might be a suitable substrate. It is probable that T_c will continually decrease with increasing Sb content across the whole range of As:Sb ratios due to the increasing distance between Mn moments and holes, but it is not so clear how transport properties such as carrier density and conductivity would vary, or perhaps more fundamentally how the concentration of interstitial Mn and antisite defects would vary. It appears that there is less substitutional Mn in (Ga,Mn)($As_{0.9}$,$Sb_{0.1}$) than both (Ga,Mn)As and (Ga,Mn)Sb, and it would be instructive to determine at which As:Sb ratio the substitutional Mn concentration reaches a minimum. From a fundamental point of view it would also be illuminating to determine the location of the substitutional and interstitial Mn within (Ga,Mn)(As,Sb). For example, as there are no interstitial Mn in (Ga,Mn)Sb, but there are interstitial Mn in (Ga,Mn)As, would interstitial Mn in (Ga,Mn)(As,Sb) be more likely to sit at positions adjacent to As lattice sites rather than Sb lattice sites? Similarly, as (Ga,Mn)Sb seems to have more substitutional Mn than (Ga,Mn)As, would substitutional Mn be more likely to sit at lattice sites near to Sb atoms rather than As atoms? The latter question should be able to answered by cross section scanning electron microscopy (X-STM) which should be able to resolve the relative positions of As atoms, Sb atoms, and substitutional Mn within (Ga,Mn)(As,Sb). However, X-STM is a technique that is insensitive to interstitial Mn[138]. Nevertheless, a good idea of the answer to the former question could be gained by using an electron emission channelling technique[139] that is capable of detecting radioactive interstitial Mn that are crudely implanted into a DMS.

A recent report claims that doping GaSb with Fe yields a p-type DMS with single phase magnetic behaviour and a significantly higher T_c than (Ga,Mn)Sb (140K

for a 13.7% Fe-doped sample)[140]. The T_c of (Ga,Fe)Sb is predicted to increase further with higher Fe doping concentrations than those which are studied in the report. It is therefore worthwhile examining the properties of (Ga,Fe)Sb in more depth to reveal if the DMS has potential for use as material for device applications, or even simply as another test-bed material with unique characteristics. Beyond DMSs, non-magnetic Sb-based semiconductors may also be intriguing systems for spintronics research. The spin Hall effect (SHE)[141] is a SOC phenomenon that can be viewed as the non-magnetic equivalent to the AHE, and has previously been observed in the semiconductors GaAs[17] and (In,Ga)As[142], but seemingly not in GaSb or InSb where the greater strength of SOC and different material properties may reveal a SHE with a larger spin Hall angle and/or with different relative intrinsic and extrinsic contributions. Additionally there has been interest in investigating the quantum spin Hall effect (QSHE)[143] in inverted InAs/GaSb quantum wells[144] where the relative band alignment between InAs and GaSb allows for unique hybridization of electron and hole states that can be tuned by an external electric field, which provides a useful platform to study the QSHE. Finally the giant spin Seebeck effect (GSSE) was recently discovered in the non-magnetic semiconductor InSb[145]. The GSSE is still not fully understood so further investigation of this phenomenon is required, and the large SOC and phonon-electron drag in InSb makes it an ideal material choice for any future GSSE experiments.

Chapter 3

AMR studies of (Ga,Mn)($As_{0.9}$,$Sb_{0.1}$)

3.1 Introduction

Spintronics is an area of physics research that looks to simultaneously exploit the charge and spin degrees of freedom of an electron (or hole), and one macroscopic manifestation of this is the coupling of a spintronic material's electrical and magnetic properties. In the 1850's Lord Kelvin showed what was arguably the first demonstration of spintronic physics when he noted that the resistance of Fe and Ni change with both the strength and orientation of an externally applied magnetic field[4], with the former and latter observations relating to what are now referred to as ordinary/isotropic magnetoresistance (O/IMR) and anisotropic magnetoresistance (AMR) respectively. While it took the research field of spintronics as we know it nearly another 150 years to arrive, the fundamental discoveries of spintronic phenomena that Kelvin made are still of great interest today as O/IMR and AMR have found use in multiple applications, notably in sensing devices and recording technologies. O/IMR is the dependence of a conducting material's resistance on the magnitude of an external magnetic field, and is a phenomenon which can arise due to contributions from several factors such as spin-disorder scattering, localization effects, and modification of electron orbitals at the Fermi level due to the Lorentz force. AMR is the dependence of a conducting magnetic material's resistance on the orientation of its magnetization (which can be experimentally varied with a magnetic field) and is understood to arise, at heart, as a result of spin-orbit coupling (SOC). However, despite its longevity and practical functionality, there still lacks a complete fundamental understanding of the origins of AMR, and this is a motivating factor in its continued research by both the scientific community and the technological industries.

For films of magnetic material, AMR measurements are generally made by passing current along a given direction laterally in the sample plane and recording the longitudinal resistance (R_{xx}) during the course of either i) rotating an external magnetic field in the sample plane and/or out of the sample plane, or ii) sweeping an external field at various in-plane and/or out of plane angles with respect to the current direction. Some experiments also simultaneously measure the transverse resistance (R_{xy}), though it should be noted that this scenario becomes more

complex when the magnetization has an out of plane component as R_{xy} gains a large contribution from the anomalous Hall effect (AHE). AMR manifests itself as a change in R_{xx} and R_{xy} of the magnetic material as its magnetization orientation changes, and is commonly defined by the difference in R_{xx} for the cases of the magnetization lying parallel to and perpendicular in-plane to the current direction, geometries which also often correspond to the largest difference in R_{xx}. The term 'positive AMR' describes the situation where R_{xx} is larger when the magnetization is parallel to the current than when it is perpendicular to it, whereas the term 'negative AMR' describes the opposite case. These terms are an appropriate classification for materials where the AMR is largely a function of the angle between the magnetization and current direction (ϕ), which is known as non-crystalline AMR. There are also a range of materials which have an ordered crystalline structure where the AMR is largely a function of the angle between the magnetization and crystalline axes (ψ), which is known as crystalline AMR, and in which case the 'positive AMR' and 'negative AMR' terminology becomes less meaningful. In the case of magnetization being constrained to within the sample plane, for non-crystalline AMR, the magnetization dependent component of R_{xx} varies as +/-$cos(2\phi)$, while for crystalline AMR the situation is somewhat more complicated as the magnetization dependent component of R_{xx} can vary as +/-$cos(2\psi)$ and/or +/-$cos(4\psi)$, as well as with more complex and higher order symmetries. The strength and signs of the different contributions to AMR vary for individual magnetic materials, and so by studying a wide range of materials a detailed understanding can be gained as to the sources of the AMR contributions, and in particular how they relate to various material properties.

In the 140 years or so that followed Lord Kelvin's initial observations of AMR in Fe and Ni, the phenomenon was further investigated in pure metals[146], 3d transition metal alloys[147][148][149], and perovskite oxides[150][151]. The advent of the diluted magnetic semiconductor (DMS) (Ga,Mn)As in the early 1990's provided another system in which to study AMR, though it wasn't until the early 2000's that in-depth reports of AMR in (Ga,Mn)As began to appear[152][153][154]. (Ga,Mn)As is seen as an ideal material for understanding the various mechanisms that contribute to AMR as it has a high crystal quality, as well as a strong SOC and simple band-structure at the Fermi level, while its tunability allows AMR to be investigated in samples with a range of electrical and magnetic properties. Generally (Ga,Mn)As is shown to have a negative AMR, which is opposite to most metals where a positive AMR is observed, and phenomenologically this is due to the negative sign of the non-crystalline AMR contribution, the magnitude of which is larger than the crystalline AMR contributions. However, unlike amorphous and polycrystalline metal ferromagnets, crystalline contributions in (Ga,Mn)As are often non-negligible, and in some cases even dominate the AMR, and this gives the AMR in (Ga,Mn)As a rich make-up that is both interesting and insightful to explore and understand.

This chapter presents an experimental and analytical study of the contributions to the AMR of the as-grown and annealed DMS (Ga,Mn)($As_{0.9}$,$Sb_{0.1}$). As shown in chapter 2, (Ga,Mn)($As_{0.9}$,$Sb_{0.1}$) is a DMS with unique properties compared with (Ga,Mn)As; it has a lower Curie temperature (T_c), a lower magnetization strength,

a lower conductivity, and a lower hole density, however it is also expected to have a larger intrinsic and strain-induced SOC than (Ga,Mn)As owing to the size of the Sb atom. Additionally, there is a considerable change in some of the properties of (Ga,Mn)($As_{0.9}$,$Sb_{0.1}$) upon annealing, and therefore the distinct and semi-tunable characteristics of (Ga,Mn)($As_{0.9}$,$Sb_{0.1}$) make it an excellent material to try and uncover the origins of the various contributions to AMR, building upon previous understanding gained from (Ga,Mn)As.

To measure the AMR of (Ga,Mn)($As_{0.9}$,$Sb_{0.1}$), Hall bars were patterned along the $[1\bar{1}0]$, [110], [100], and [010] crystalline directions as well as a Corbino disk, as shown in figure 3.1. For each measurement, the magnetization was rotated 360^o in the plane of the sample by a saturating external magnetic field, and R_{xx} and R_{xy} were recorded as a function of ϕ and ψ. Applying current along different crystalline directions allows non-crystalline and crystalline AMR contributions to be separated through phenomenological analysis, and thus yields specific evidence as to how they relate to the material properties which evolve with annealing, which can be used in a more general discussion regarding the fundamental comprehension of AMR.

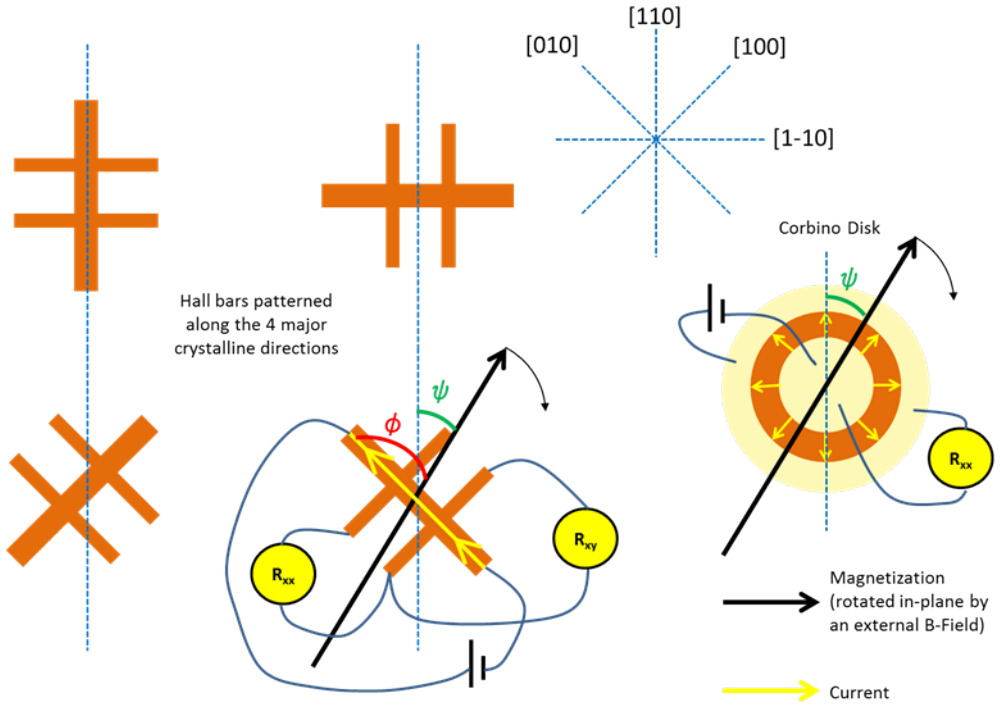

Figure 3.1: Diagram of the Hall bars and Corbino disk used in this investigation to measure AMR. The principles of the measurement are shown for the [010] Hall bar only but are the same for the other directions. Note that Hall bars and Corbino disk are not to scale.

3.2 Theory

3.2.1 Formal definition and phenomenology of AMR

The term 'AMR' is often used in literature to refer to the change in R_{xx} with magnetization orientation, an effect here which shall be referred to as 'AMR_{xx}', but in Hall bar geometry R_{xy} also changes with magnetization orientation, and this shall be referred to here as 'AMR_{xy}'. AMR_{xy} shares exactly the same common origin as AMR_{xx} and can be thought of as the off-diagonal component of an AMR resistivity tensor. Simplistically, a voltage will exist between the transverse voltage probes if, due to AMR_{xx}, a straight line parallel to the bar length is not the path of least resistance for current travelling along the bar, which thus leads to a transverse electric field building up due to charge accumulation along the bar edge. The term 'planar Hall effect' (PHE) is regularly used to describe the change in transverse voltage/resistance with magnetization orientation of a magnetic material, and in most cases the PHE arises entirely due to the off-diagonal component of the AMR and so is equivalent to AMR_{xy}[155], but it should be noted that in some ferromagnetic systems with reduced symmetry there can be additional contributions to the PHE that do not arise from the same origins as AMR_{xx}[156][157][158]. For the case of the DMSs studied in this thesis it is assumed that the PHE is entirely due to AMR_{xy} and therefore 'PHE' and 'AMR_{xy}' are interchangeable terms.

AMR_{xx} has been defined in several different ways in previous studies, and this can lead to inconsistencies when reporting the magnitude of the effect. This thesis will use the definition for the magnitude of AMR adopted in references [159], [160], and [161]:

$$\begin{aligned}\text{AMR}_{xx}(\%) &= \left(\frac{\rho_{xx}-\rho_{ave}}{\rho_{ave}} - \left(\frac{\rho_{xx}-\rho_{ave}}{\rho_{ave}}\right)_{min}\right)\times 100 \\ &= \left(\frac{\Delta\rho_{xx}}{\rho_{ave}} - \left(\frac{\Delta\rho_{xx}}{\rho_{ave}}\right)_{min}\right)\times 100\end{aligned} \tag{3.1}$$

$$\text{AMR}_{xy}(\%) = \left(\frac{\rho_{xy}}{\rho_{ave}} - \left(\frac{\rho_{xy}}{\rho_{ave}}\right)_{min}\right)\times 100 \tag{3.2}$$

where ρ_{ave} is the average value of resistivity (ρ_{xx}) for magnetization rotated over 360^o in-plane and $\left(\frac{\rho_{xx}-\rho_{ave}}{\rho_{ave}}\right)_{min}$ is the minimum value of $\frac{\rho_{xx}-\rho_{ave}}{\rho_{ave}}$.

In amorphous and polycrystalline metals where crystalline AMR should average out to zero, as well as in certain crystalline materials where the crystalline AMR is small, only the non-crystalline AMR contribution is significant. In these systems AMR_{xx} is assumed to take the form $\rho_{xx} = \frac{1}{2}(\rho_{\parallel}+\rho_{\perp}) + \frac{1}{2}(\rho_{\parallel}-\rho_{\perp})cos(2\phi)$, where $\rho_{\parallel}$ and $\rho_{\perp}$ are the resistivities for magnetization parallel and perpendicular to the current direction, and this definition is commonly used in literature. Investigating AMR in these materials is relatively straightforward as only one Hall bar is required (with current along any direction), only two measurements need to be made (R_{xx} for the magnetization parallel and perpendicular to the current direction), and phenomenological fitting analysis is not necessary to infer the size of the effect.

However, in materials where crystalline contributions to AMR can be significant, a more detailed approach and phenomenological model is required that accounts for the various allowed symmetries of the observed AMR. In the pioneering work of reference [159], four different contributions to AMR in (Ga,Mn)As were identified, each with a unique symmetry that depends on the magnetization orientation with respect to the current direction and/or the crystalline axes. The phenomenological model of AMR presented in reference [159] shall be used in this investigation of AMR in (Ga,Mn)($As_{0.9}$,$Sb_{0.1}$), and is given as:

$$\frac{\Delta\rho_{xx}}{\rho_{ave}} = C_I cos(2\phi) + C_U cos(2\psi) + C_C cos(4\psi) + C_{I,C} cos(4\psi - 2\phi) \tag{3.3}$$

$$\frac{\rho_{xy}}{\rho_{ave}} = C_I sin(2\phi) + C_{I,C} sin(4\psi - 2\phi) \tag{3.4}$$

where C_I is the non-crystalline coefficient, C_U is the uni-axial crystalline coefficient, C_C is the cubic crystalline coefficient, and $C_{I,C}$ is the crossed non-crystalline/cubic-crystalline coefficient. Higher order AMR terms are ignored. ϕ is defined as the in-plane angle between the current direction and the magnetization and ψ is defined as the angle between the [110] crystalline direction and the magnetization. Symmetry dictates that the purely crystalline contributions are excluded from AMR_{xy}. It is easier to picture how these symmetries described in the above equations appear in an actual magnetization rotation AMR experiment by considering only the ϕ coordinate system, where for a given current direction equations 3.3 and 3.4 become:

$$[1\bar{1}0]_{xx} = \frac{\Delta\rho_{xx}}{\rho_{ave}} = (C_I + C_{I,C} - C_U)cos(2\phi) + C_C cos(4\phi) \tag{3.5}$$

$$[110]_{xx} = \frac{\Delta\rho_{xx}}{\rho_{ave}} = (C_I + C_{I,C} + C_U)cos(2\phi) + C_C cos(4\phi) \tag{3.6}$$

$$[100]_{xx} = \frac{\Delta\rho_{xx}}{\rho_{ave}} = (C_I - C_{I,C})cos(2\phi) + C_U sin(2\phi) - C_C cos(4\phi) \tag{3.7}$$

$$[010]_{xx} = \frac{\Delta\rho_{xx}}{\rho_{ave}} = (C_I - C_{I,C})cos(2\phi) - C_U sin(2\phi) - C_C cos(4\phi) \tag{3.8}$$

$$[1\bar{1}0]_{xy} = [110]_{xy} = \frac{\Delta\rho_{xy}}{\rho_{ave}} = (C_I - C_{I,C})sin(2\phi) \tag{3.9}$$

$$[100]_{xy} = [010]_{xy} = \frac{\Delta\rho_{xy}}{\rho_{ave}} = (C_I + C_{I,C})sin(2\phi) \tag{3.10}$$

where $[1\bar{1}0]_{xx}$ is AMR_{xx} for current along the $[1\bar{1}0]$ direction etc. The origins of the four AMR contributions considered in this analysis are discussed further in sections 3.2.2 and 3.4, but here the focus is the nature of how they affect R_{xx} and R_{xy}. The strength and sign of each AMR contribution is represented by its respective AMR coefficient, and so for simplicity 'uni-axial crystalline AMR' shall now be referred to as 'C_U' etc. For all four current directions considered in this investigation C_I and $C_{I,C}$ give a $cos(2\phi)$ and $sin(2\phi)$ contribution to AMR_{xx} and AMR_{xy} respectively, where the sign of the C_I contribution is independent of current

direction, but the sign of the $C_{I,C}$ contribution is different for $[1\bar{1}0]_{xx(y)}/[110]_{xx(y)}$ and $[100]_{xx(y)}/[010]_{xx(y)}$. Similarly, C_C gives a $cos(4\phi)$ contribution to AMR_{xx} for all four current directions that also varies in sign between $[1\bar{1}0]_{xx}/[110]_{xx}$ and $[100]_{xx}/[010]_{xx}$. C_U is the only AMR contribution which is itself unique for AMR_{xx} of each current direction, appearing as another $cos(2\phi)$ contribution of opposite signs for $[1\bar{1}0]_{xx}$ and $[110]_{xx}$, and as a distinct $sin(2\phi)$ contribution of opposite signs for $[100]_{xx}$ and $[010]_{xx}$.

It is also possible to allow current to flow radially rather than along a specific direction by processing samples into Corbino disk geometry (which is shown in figure 3.1). Radial current flow will average out any AMR from contributions which depend on current direction, meaning that C_I and $C_{I,C}$ go to zero, and therefore AMR in Corbino disk geometry is given solely by crystalline terms:

$$\mathrm{AMR}_{Corbino} = \frac{\Delta\rho_{xx}}{\rho_{ave}} = C_U cos(2\psi) + C_C cos(4\psi) \tag{3.11}$$

3.2.2 Literature review of theory of AMR in DMSs

The microscopic physics of AMR in DMSs, or more specifically (Ga,Mn)As, was first investigated in depth in reference [159]. In this work, two possible mechanisms were modelled that could lead to magnetization-dependent anisotropic carrier lifetimes (and hence AMR) in (Ga,Mn)As. The first considers the combined effect of unpolarized carriers in a spin-orbit coupled carrier band and randomly distributed, polarized magnetic impurity scatterers, while the second considers a polarized carrier band which leads to an anti-symmetric band spin-texture. By theoretically turning off and on these individual mechanisms and comparing to experimental data, it was found that while both act simultaneously in (Ga,Mn)As, the former mechanism dominates the AMR. In this mechanism, the spin-orbit coupled carrier band was modelled as having a pure 'spin parallel to momentum' ($\mathbf{s}\|\boldsymbol{k}$) spin-texture. The effects of other spin-textures such as Rashba and Dresselhaus were not included as the $\mathbf{s}\|k$ model replicated the experimental data well. The $\mathbf{s}\|k$ spin-texture or style of SOC ultimately arises from the same atomic spin-orbit interaction as Rashba and Dresselhaus SOCs, and appears in the valence band of GaAs (and other zincblende semiconductors) as a result of the $\boldsymbol{L.S}$ splitting of the Bloch states composed dominantly of the p-orbital ($l = 1$) As atoms. However, unlike the intrinsic Rashba and Dressellhaus SOCs, $\mathbf{s}\|k$ SOC is linear in k and does not originate from a broken inversion symmetry. Reference [159] goes on to specifically focus on C_I, which is known from experiments to commonly be positive for metals and negative for (Ga,Mn)As. It was shown that for the model used, the sign of C_I varies with the ratio of the non-magnetic to magnetic impurity scattering potentials, α, which for $\alpha \ll 1$ gives a positive AMR, $\alpha > 1/\sqrt{20}$ gives a negative AMR, and that AMR is maximum when $\alpha = 1/2$ and disappears when $\alpha \gg 1$. As α is known to be greater than $1/\sqrt{20}$ in (Ga,Mn)As[153], the sign of the AMR predicted from the microscopic model of reference [159] agrees with experiment. Furthermore, reference [159] goes on to perform numerical simulations of non-crystalline and crystalline AMR by assuming a spherical and band-warped Fermi surface respectively, and yields model results that are consistent with experimental measurements also presented within the paper. The experimental measurements of reference [159] are discussed

in more detail in section 3.3 of this chapter, but in short they reveal that for a 25nm, as-grown, 5% Mn-doped (Ga,Mn)As sample, C_I mostly dominates the AMR, but that contributions from C_U, C_C, and $C_{I,C}$ are non-negligible, while for a similar sample of 5nm thickness C_U becomes the largest term and dominates the AMR.

Reference [162] extended the investigation of non-crystalline AMR in (Ga,Mn)As. In this paper, ways in which magnetization orientation can lead to an anisotropic conductivity are further examined, and in addition to the two anisotropic carrier lifetime mechanisms discussed in reference [159], an additional distinct mechanism is postulated that considers the magnetization distorting the shape of the Fermi surface which leads anisotropic group velocities at the Fermi level. It is again shown that the mechanism of unpolarized spin-orbit coupled carriers scattering off polarized magnetic impurities dominates, but that quantitative corrections to the AMR due to the anisotropic group velocity and polarized carrier band mechanisms arise as all three mechanisms act simultaneously, though acting alone the latter two would give a negligible AMR. Calculations show that the magnitude of C_I increases with (ideal) Mn doping concentration up to around 5% before reducing as doping further increases, and this is as a result of α approaching a value of 1/2 for 5% doping. The paper stresses that (Ga,Mn)As is an excellent material for investigating AMR for two main reasons. Firstly, from a practical viewpoint, in ferromagnetic metals where s-state carriers scatter off d-state spin-orbit coupled magnetic impurities, magnetization and SOC, the two key ingredients for AMR, compete with one another which leads to a small AMR effect. This is not the case for (Ga,Mn)As where the SOC is strong in the current carrying p-states at the top of the valence band where the Fermi level lies and so the d-states only need to provide the magnetization 'ingredient' for AMR, thus both SOC and magnetization can both be large, therefore giving a large AMR. Secondly, from a theoretical viewpoint, the fact that there are only a few bands present at the Fermi level in (Ga,Mn)As makes modelling the effects of AMR a much simpler task, and it is demonstrated that numerical calculations with only the two heavy hole bands yields an AMR that is in complete qualitative agreement with a full band calculation, thus making numerical study of (Ga,Mn)As even less demanding. The methods used in the study are suggested to be useful in other DMSs which have a metallic conductivity and an AMR largely dominated by C_I, with (In,Mn)As and (In,Mn)Sb, which have a more isotropic Fermi surface than (Ga,Mn)As, suggested as promising additional DMSs to study.

A more detailed theoretical examination of how the Fermi surface spin-texture, which is determined by the SOC style of the carrier bands, affects AMR in non-specific systems is given in reference [163]. Using the approximation that the only contribution to transport lifetimes is backscattering to states with opposite group velocities, reference [163] evaluates the allowed backscattering channels for given combinations of various spin-textures, current directions, magnetization orientations, values of α, ranges of impurity potential, and relative strengths of SOC and Fermi energy. The sign of the AMR is inferred from the available backscattering channels; resistance is minimum when there are no available backscattering channels, small for majority band to minority band and/or minority band to majority band transitions, and maximum for majority band to majority band and/or minor-

ity band to minority band transitions. It is shown that for the case of a pure Rashba style spin-texture, a short range impurity potential, and for all values of α, C_I is positive, and that there is no crystalline AMR. For a pure Dresselhaus style spin-texture, a short range impurity potential, and for all values of α, the AMR changes sign for current along the [110] and [100] directions as a result of the different relative spin orientations, and this corresponds to a finite crystalline AMR contribution, whereas C_I is zero. It must be stressed that while the Dresselhaus spin-texture does yield a crystalline AMR component, in (Ga,Mn)As the crystalline AMR is well modelled by assuming a non-spherical Fermi surface rather than a Dresselhaus spin-texture[159], indicating that crystalline AMR originating from Dresselhaus SOC may be small in such systems. The case of the strengths of the Rashba and Dresselhaus style SOCs being of equal strengths is also considered, and here it is demonstrated that AMR disappears for a short range impurity potential but is finite for a long range impurity potential, which implies the possible importance of the range of the impurity potential in certain situations. For both pure Rashba and Dresselhaus spin-textures the AMR is maximum when the minority band is depleted. Reference [163] also confirms the findings of reference [159] that for the $\mathbf{s}\|k$ spin texture, the sign of C_I changes from positive to negative as α increases.

3.3 Experiment and Results

3.3.1 Experimental and analytical method

For both the as-grown and annealed samples, measurements were made on Hall bars processed with dimensions of 50μm wide and 320μm between adjacent arms, with individual bars allowing current flow along the [1$\bar{1}$0], [110], [110], and [010] crystalline directions. The Hall bar width is not expected to induce significant strain relaxation, which has been shown to vary C_U[164]. Separate Hall bars were used for the as-grown and annealed measurements, i.e. the as-grown Hall bars were not annealed and then re-measured, however the as-grown and annealed Hall bars did come from a similar region of the sample wafer. For the annealed samples only, measurements were also made for the Corbino disk geometry, with disk samples processed with the dimensions of an inner radius of 780μm and outer radius of 830μm. The Corbino disks were also processed from a similar (but not the same) part of the wafer as the annealed Hall bars. To make the AMR measurements, a constant dc current was applied through the Hall bar being measured, and an external magnetic field that saturates the (Ga,Mn)($As_{0.9}$,$Sb_{0.1}$) magnetization orientation (i.e. the magnetization orientation perfectly tracks the external field) was applied in the plane of the sample and rotated 360° in-plane, with R_{xx} and R_{xy} simultaneously recorded in 5° steps. It was found that a 5kOe external field was sufficient to saturate the magnetization of the annealed samples, but did not fully saturate the magnetization of the as-grown samples. A 20kOe external field proved to be sufficient for the as-grown samples, and therefore 20kOe and 5kOe external fields were used for the as-grown and annealed AMR measurements respectively. The applied current was 10μA for the as-grown measurements and 100μA for the annealed measurements, where the larger current was used for the annealed measurements due to the sample's lower resistivity.

Each AMR measurement yields R_{xx} and R_{xy} as a function of ϕ over a 360° range. Numerical fitting to these datasets gives fitting coefficients that correspond either directly to AMR coefficients or to combinations of AMR coefficients. Given the expected symmetries of AMR_{xx} and AMR_{xy} for the different current directions (see equations 3.5 - 3.10), the following equations were used to fit to the experimental data:

$$\mathrm{AMR}_{xx} = P_1 cos(2\phi) + P_2 cos(4\phi) + P_3 sin(2\phi) \tag{3.12}$$

$$\mathrm{AMR}_{xy} = P_4 sin(2\phi) \tag{3.13}$$

where P_1, P_2, P_3, and P_4 are variable fitting coefficients that correspond to combinations of C_I, C_U, C_C, and $C_{I,C}$ for the various current directions as shown in the table in figure 3.2. Note that for the Corbino disk measurement, equation 3.12 uses the ψ rather than ϕ coordinate system.

	Current Direction			
Coefficient	**1-10**	**110**	**100**	**010**
P1	$C_I + C_{I,C} - C_U$	$C_I + C_{I,C} + C_U$	$C_I - C_{I,C}$	$C_I - C_{I,C}$
P2	C_C	C_C	$-C_C$	$-C_C$
P3	0	0	C_U	$-C_U$
P4	$C_I - C_{I,C}$	$C_I - C_{I,C}$	$C_I + C_{I,C}$	$C_I + C_{I,C}$

Figure 3.2: Table of AMR coefficients corresponding to fitting coefficients of equations 3.12 and 3.13 for given current directions.

As figure 3.2 shows, C_C can be extracted for each individual current direction alone, and C_U can be extracted alone for the [100] and [010] current directions. The other AMR coefficients require measurements along either two or three current directions to be able to obtained by solving simultaneous equations. All coefficients can be obtained by more than one specific data set, either from different combinations of current direction measurements or from R_{xx} and R_{xy} for a given combination of current directions.

3.3.2 Results

Selected AMR polar plots for the as-grown and annealed (Ga,Mn)($As_{0.9}$,$Sb_{0.1}$) are shown in figures 3.3 - 3.11:

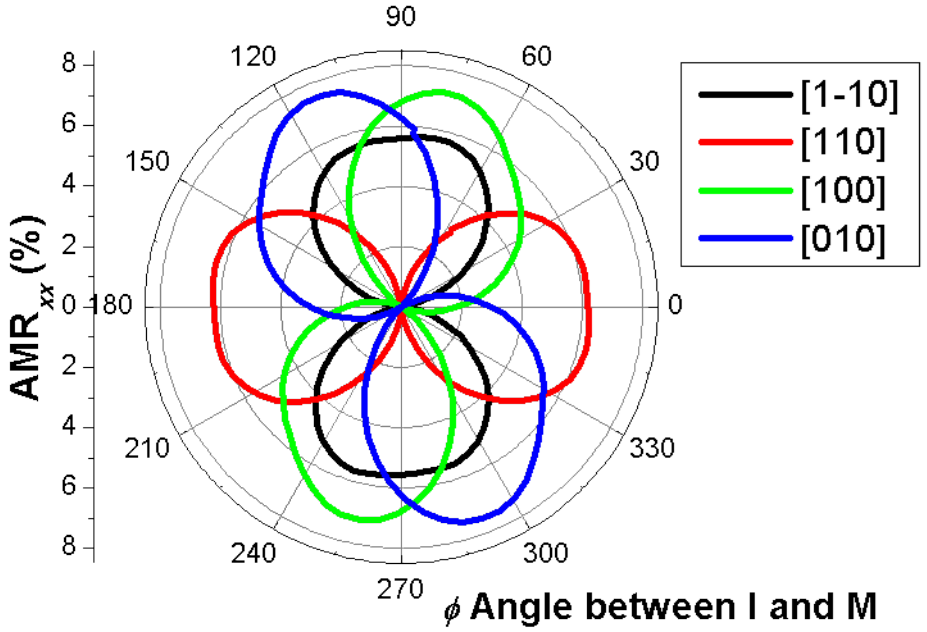

Figure 3.3: AMR$_{xx}$ of as-grown (Ga,Mn)(As$_{0.9}$,Sb$_{0.1}$) for current along various crystalline directions at 4.2K.

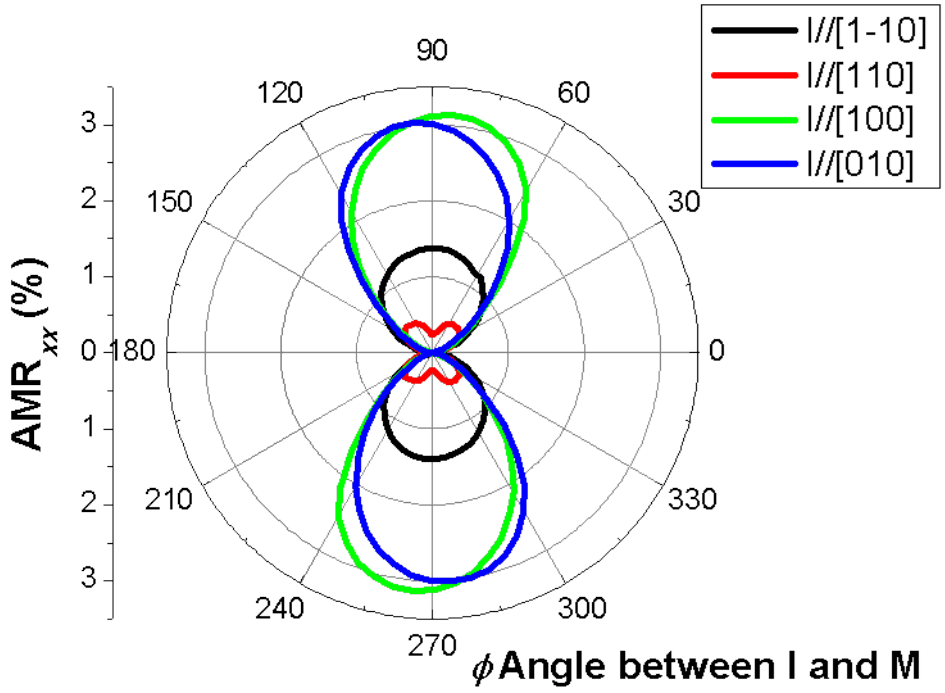

Figure 3.4: AMR$_{xx}$ of annealed (Ga,Mn)(As$_{0.9}$,Sb$_{0.1}$) for current along various crystalline directions at 4.2K.

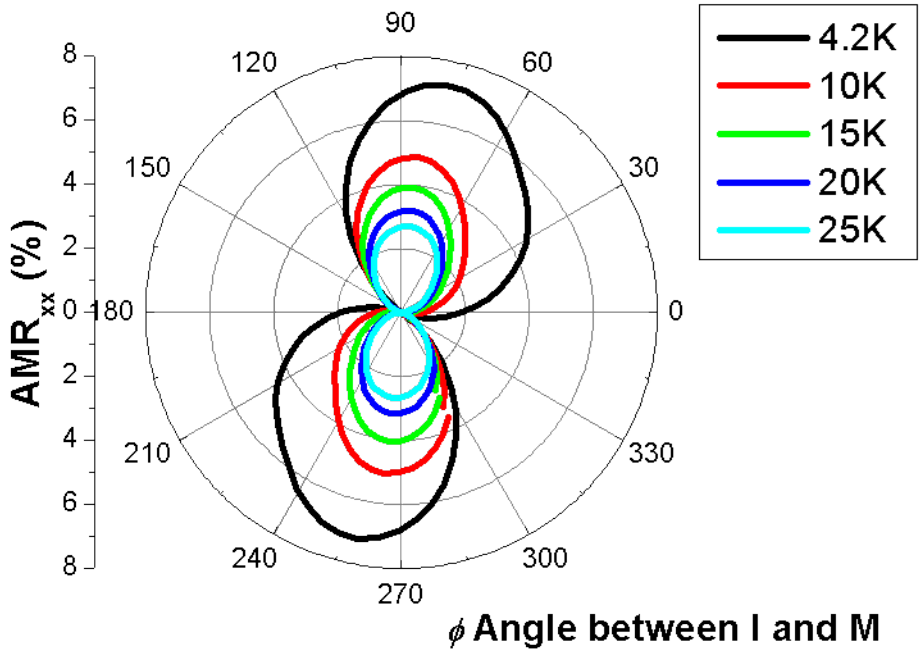

Figure 3.5: AMR$_{xx}$ of as-grown (Ga,Mn)(As$_{0.9}$,Sb$_{0.1}$) for current along the [100] crystalline direction at various temperatures.

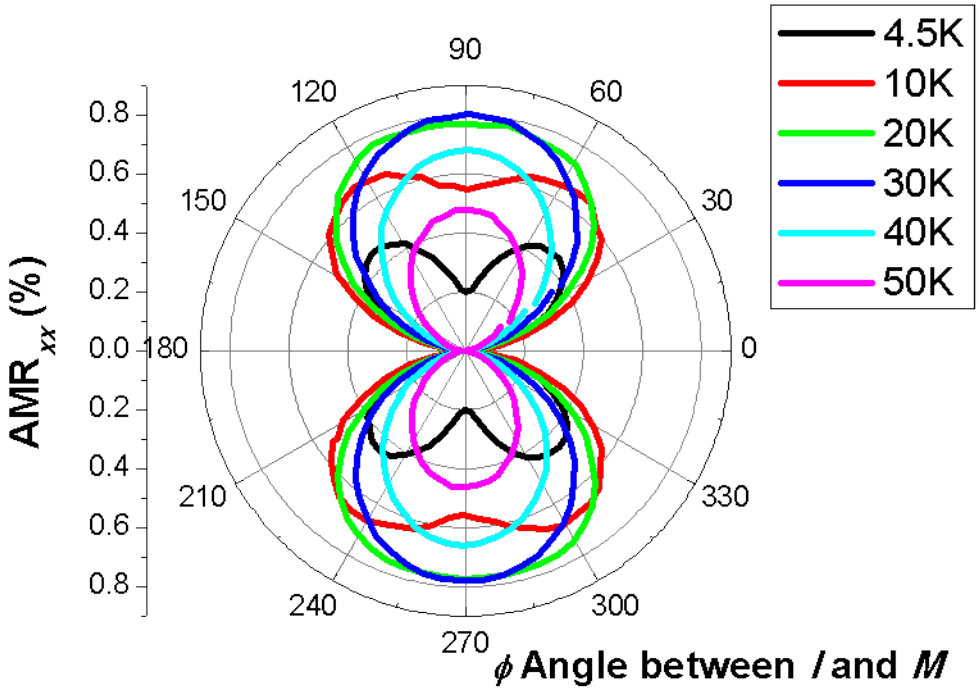

Figure 3.6: AMR$_{xx}$ of annealed (Ga,Mn)(As$_{0.9}$,Sb$_{0.1}$) for current along the [110] crystalline direction at various temperatures.

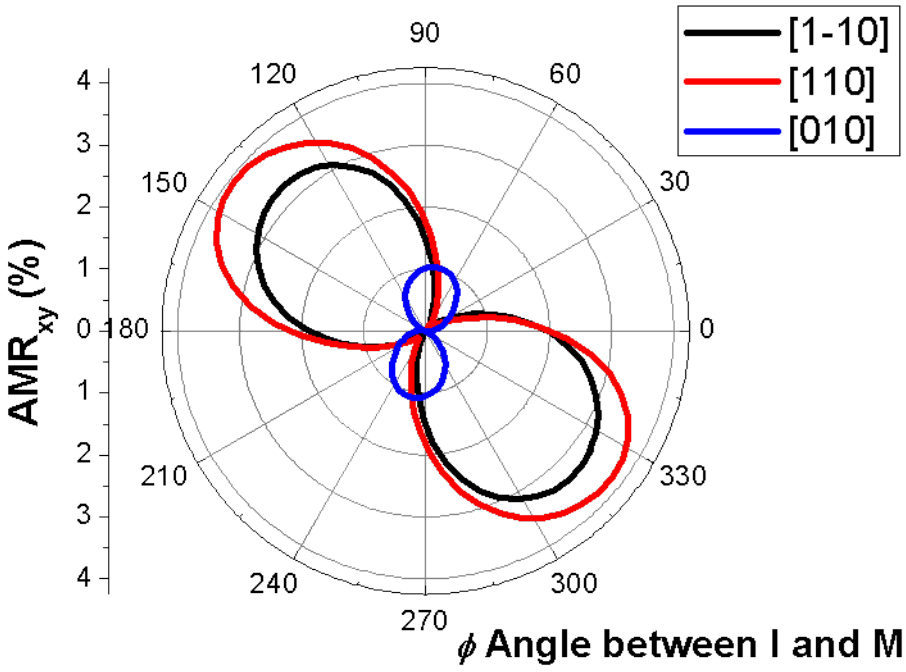

Figure 3.7: AMR$_{xy}$ of as-grown (Ga,Mn)(As$_{0.9}$,Sb$_{0.1}$) for current along various crystalline directions at 4.2K. Note [100] data is missing due to an issue with the measurement.

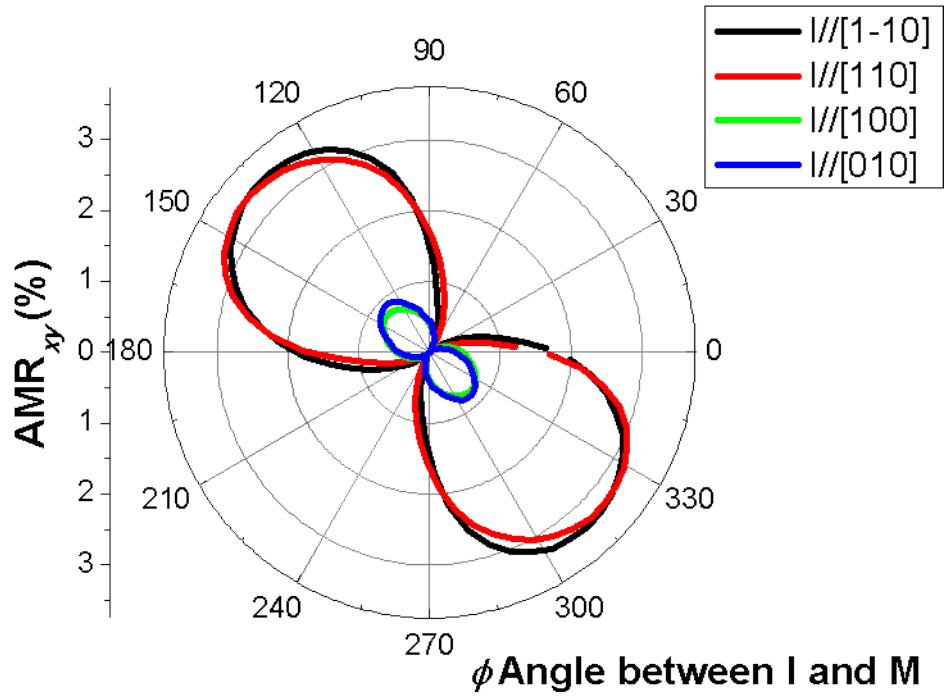

Figure 3.8: AMR$_{xy}$ of annealed (Ga,Mn)(As$_{0.9}$,Sb$_{0.1}$) for current along various crystalline directions at 4.2K.

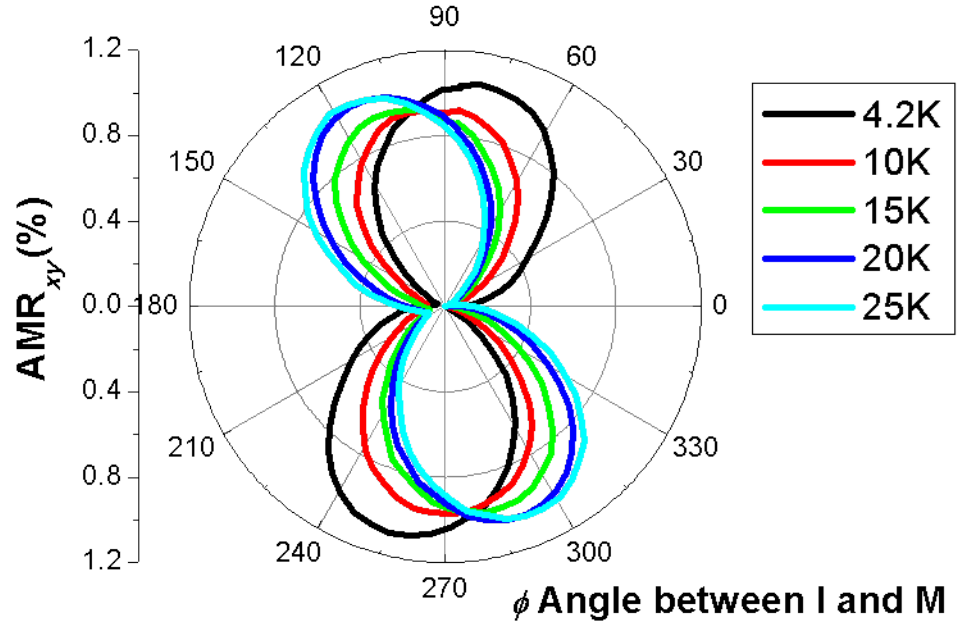

Figure 3.9: AMR$_{xy}$ of as-grown (Ga,Mn)(As$_{0.9}$,Sb$_{0.1}$) for current along the [010] crystalline direction at various temperatures.

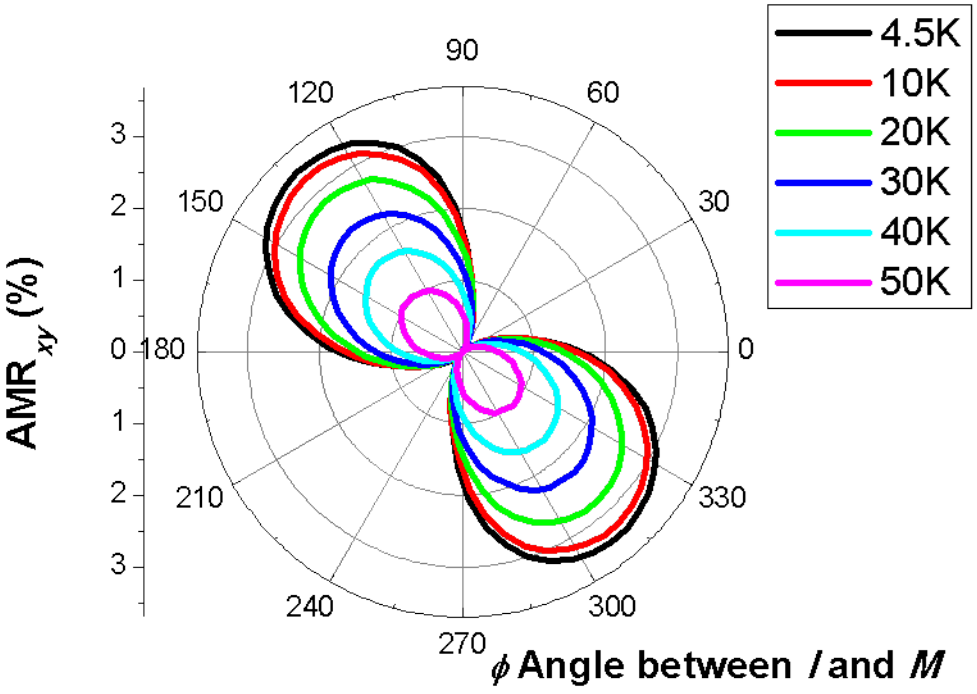

Figure 3.10: AMR$_{xy}$ of annealed (Ga,Mn)(As$_{0.9}$,Sb$_{0.1}$) for current along the [1$\bar{1}$0] crystalline direction at various temperatures.

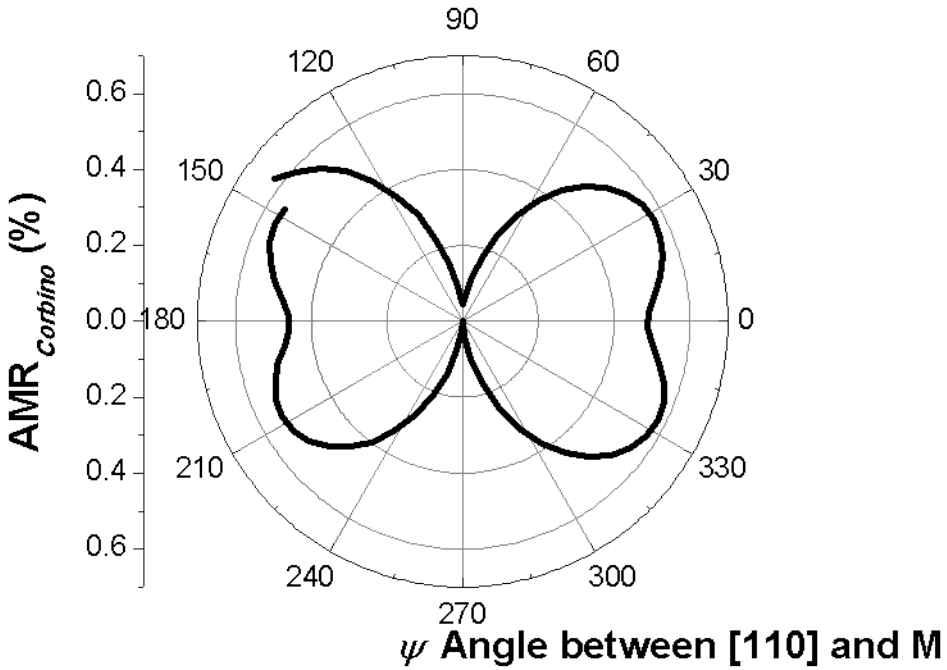

Figure 3.11: $AMR_{Corbino}$ of annealed (Ga,Mn)($As_{0.9}$,$Sb_{0.1}$) for radial current in Corbino disk geometry at 4.2K.

The AMR coefficients (and combinations of coefficients) of as-grown and annealed (Ga,Mn)($As_{0.9}$,$Sb_{0.1}$) at various temperatures were extracted from the AMR_{xx} and AMR_{xy} data sets by fitting with equations 3.12 and 3.13. The size of the coefficients as a function of temperature are shown in figure 3.12 and 3.13:

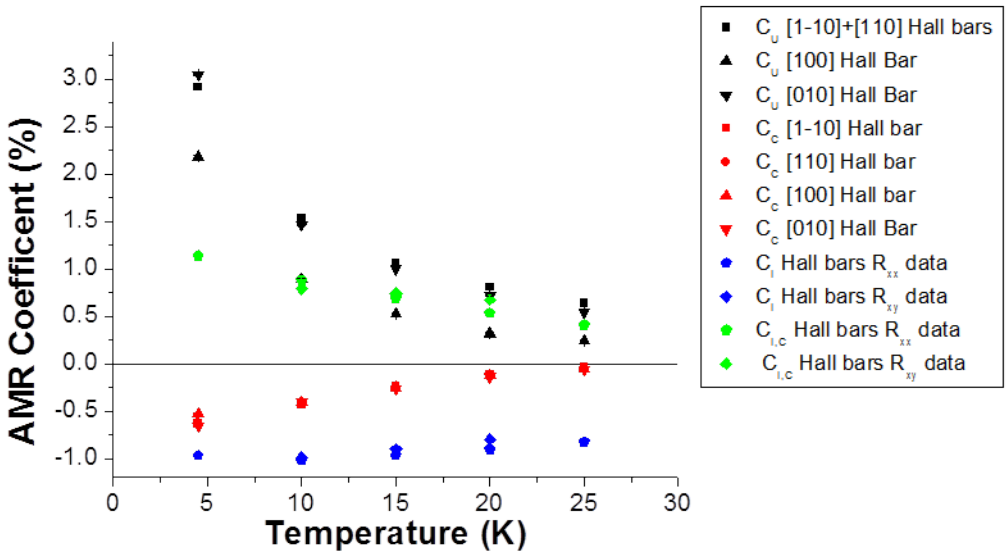

Figure 3.12: AMR coefficients of as-grown (Ga,Mn)($As_{0.9}$,$Sb_{0.1}$) obtained from AMR_{xx} and AMR_{xy} data fitted to with equations 3.12 and 3.13.

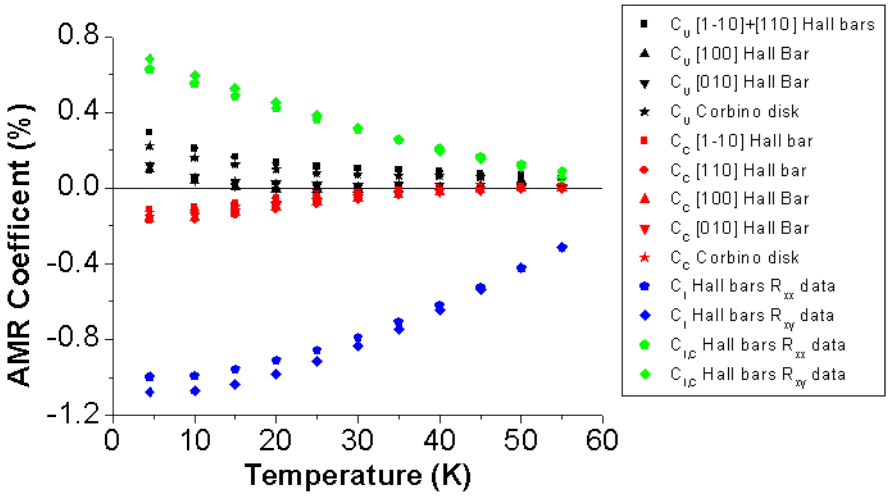

Figure 3.13: AMR coefficients of annealed (Ga,Mn)($As_{0.9}$,$Sb_{0.1}$) obtained from AMR_{xx}, AMR_{xy}, and $AMR_{Corbino}$ data fitted to with equations 3.12 and 3.13.

3.3.3 Experimental uncertainties

3.3.3.1 Filamentary Conduction in as-grown Hall bars

Equations 3.12 and 3.13 are able to fit well to all of the annealed and the majority of the as-grown (Ga,Mn)($As_{0.9}$,$Sb_{0.1}$) AMR_{xx} and AMR_{xy} data, but for a few individual cases of the as-grown sample, fitting with these equations proves unsatisfactory. In order to improve the fitting, a 8-term fitting equation was used for both AMR_{xx} and AMR_{xy} data that allows for up to 8-fold symmetries:

$$\begin{aligned} AMR_{xx/xy} = P_1 cos(\phi) + P_2 sin(\phi) + P_3 cos(2\phi) + P_4 sin(2\phi) + P_5 cos(4\phi) \\ + P_6 sin(4\phi) + P_7 cos(8\phi) + P_8 sin(8\phi) \end{aligned} \quad (3.14)$$

Examples of the advantages of fitting with equation 3.14 are demonstrated in figures 3.14 and 3.15. Figure 3.14 displays the fitting parameters for the 8 trigonometric terms of equation 3.14 for the temperature dependent AMR_{xy} data for current in the [010] direction (which is plotted in figure 3.9), showing the importance of the $cos(2\phi)$ term that is absent in equation 3.13. Figure 3.15 shows the fittings to the data for AMR_{xx} at 15K for current in the [110] direction using equation 3.12 and equation 3.14. It can be seen that while fitting with equation 3.12 accounts fairly well for the overall shape of the AMR, fitting with equation 3.14 is required to fully capture the subtleties of the data.

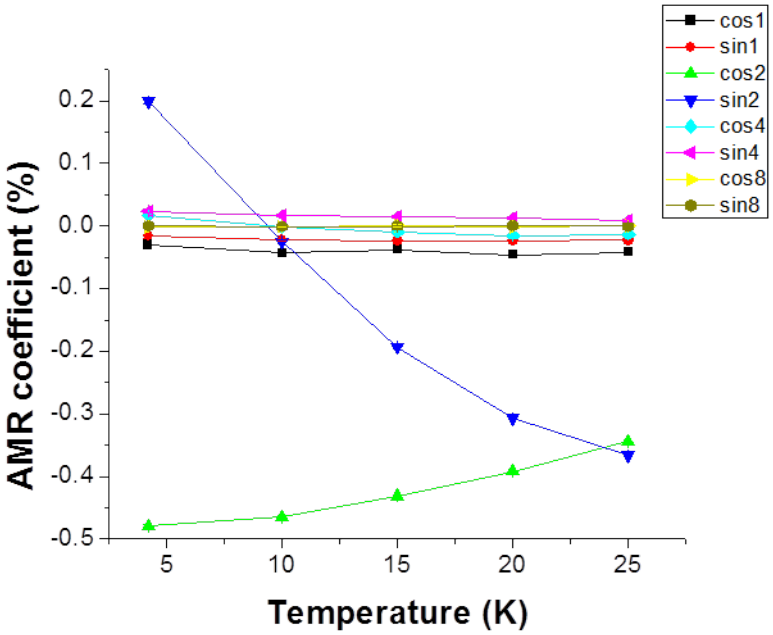

Figure 3.14: Size of fitting parameters for the various terms in equation 3.14 when fitting to the data of AMR_{xy} as a function of temperature for current in the [010] for as-grown $(Ga,Mn)As_{0.9}Sb_{0.1}$.

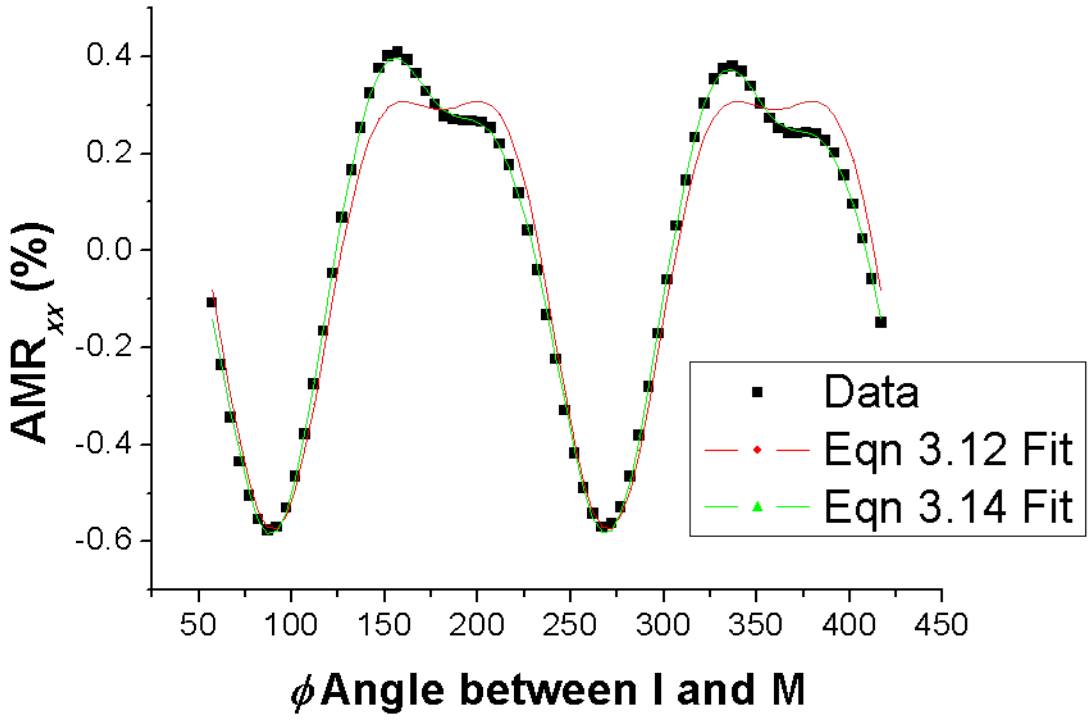

Figure 3.15: Fit using equation 3.12 (red curve) and equation 3.14 (green curve) to data (black squares) of AMR_{xx} at 15K for current in the [110] direction for as-grown $(Ga,Mn)As_{0.9}Sb_{0.1}$.

It is clear that for the specific cases shown in figures 3.14 and 3.15 terms from outside the standard AMR phenomenology are required to fully fit the data. It can be seen from figure 3.14 that for $[010]_{xy}$ at lower temperatures, the magnitude of the unexpected $cos(2\phi)$ term is more than twice the magnitude of the $sin(2\phi)$ term, which oddly is positive at 4K and near zero at 10K. The magnitude of the $sin(2\phi)$ term from $[010]_{xy}$ (and also $[100]_{xy}$) is much smaller than the $sin(2\phi)$ term from $[1\bar{1}0]_{xy}$ and $[110]_{xy}$ (data not shown), which is consistent with the similarly sized C_I and $C_{I,C}$ terms either adding to or subtracting from one another, and this exaggerates the effect of the $cos(2\phi)$ term on the shape of $[010]_{xy}$. The $cos(2\phi)$ term is, however, still non-negligible compared to (C_I - $C_{I,C}$), being more than a quarter of the magnitude of it. The mostly likely explanation for the presence of the $cos(2\phi)$ term in $[010]_{xy}$ is not that it is a real additional AMR contribution from outside the standard phenomenology, but rather that it arises due to filamentary conduction. Filamentary conduction, i.e. current not flowing in a straight line along the Hall bar length but rather following a path of minimum resistance, can give an R_{xx} contribution to the R_{xy} signal which would allow for the observed $cos(2\phi)$ AMR between transverse voltage probes of the [010] orientated bar. Filamentary conduction in the [010] Hall bar may arise from the random distribution of Mn in the (Ga,Mn)$As_{0.9}Sb_{0.1}$ layer giving regions of varying conductivity along the bar and would be expected to have a more noticeable effect in the higher resistivity as-grown sample where carriers appear to be strongly localised. The temperature dependence of the relative sizes of the $cos(2\phi)$ and $sin(2\phi)$ terms may be governed by any temperature dependence of the filamentary conduction and/or the interplay of the respective AMR coefficients that govern the $cos(2\phi)$ and $sin(2\phi)$ terms with temperature. For the data and fits in figure 3.15, the superior fit with equation 3.14 is largely brought about by the $sin(2\phi)$ and $sin(4\phi)$ terms of equation 3.14, which are around 6.6% and 2.9% of the magnitude of the largest $cos(2\phi)$ term respectively. The $sin(4\phi)$ contribution can be explained by a misalignment of the current with the crystalline axes of around 2° for the specific case of the data in figure 3.15 (as estimated from the magnitudes of the $cos(4\phi)$ and $sin(4\phi)$ terms), a misalignment that may stem from processing error or filamentary conduction. For measurements at different temperatures and for different Hall bars, the estimated misalignment needed to explain the $sin(4\phi)$ term varies between around 1° - 3°. This variation may be due to analytical uncertainty, but otherwise would indicate that filamentary conduction plays some role as processing misalignment with temperature is constant. A misalignment would also lead to the $sin(2\phi)$ term, though as there are two possible sources for this (R_{xy} mixing into R_{xx} as well as from the $[100]_{xx}/[010]_{xx}$ C_U term) it is more difficult to estimate the misalignment needed to account for the $sin(2\phi)$ term. Finally, it must be noted that fitting to include the $sin(2\phi)$ and $sin(4\phi)$ terms has essentially a negligible effect on the expected $cos(2\phi)$ and $cos(4\phi)$ terms, i.e. they are the same for fitting with equation 3.12 or equation 3.14.

3.3.3.2 Estimation of errors

The only source of error on the obtained AMR coefficients that can be quantified is the (cumulative) error on the numerical fit(s) to the experimental data. These fitting errors are most significant in the case of the annealed C_U values obtained

from the [100] and [010] bars where they are around 0.02% in magnitude at 4.2K, which is roughly 20% the magnitude of the C_U value itself. However, for the majority of the coefficients obtained by the various methods, the numerical fitting error is typically around 1%-2% the coefficient magnitude across the temperature range for both the as-grown and annealed samples, and in most cases these errors are not sufficiently large to account for the discrepancy in coefficient values. As the values of a given coefficient obtained by different methods should ideally be the same, it is clear that there are further uncertainties associated with the obtained coefficient values other than just fitting errors.

3.3.3.3 Possible sources of inconsistencies between AMR constants

It is clear from figures 3.12 and 3.13 that there is inconsistency between the magnitude of some of the individual AMR coefficients obtained by different methods. For the as-grown (Ga,Mn)$As_{0.9}Sb_{0.1}$, C_U obtained directly from the [100] Hall bar is only 40% - 75% the magnitude of C_U obtained from either the [010] or [1$\bar{1}$0]/[110] Hall bars across the measured temperature range. Similarly for the annealed (Ga,Mn)$As_{0.9}Sb_{0.1}$, there is poor agreement between the various C_U values, in this case with the [100] and [010] values being less than 30% of the [1$\bar{1}$0]/[110] and Corbino values. The agreement of the other AMR coefficients obtained from different methods is significantly better for both the as-grown and annealed samples; the values of both C_I and $C_{I,C}$ obtained from the respective AMR_{xx} and AMR_{xy} data agree within 90% of one another while the C_C values from the four bar directions (as well as the Corbino disk for the annealed sample) generally agree within 75% of one another except at higher temperatures where C_C drops quickly towards zero. For the annealed sample, C_U from the [1$\bar{1}$0]/[110] bars and Corbino disk perhaps seem more believable values than from the [100] and [010] bars as the former remain positive and continually decrease with increasing temperature (behaviour which is seen in references [129], [164], and [165]), whereas the latter fall to zero and even become negative at a low temperature before increasing again (behaviour which has only previously been seen in reference [159]). A plausible explanation for the spurious [100] C_U term for both the as-grown and annealed samples is that, due to limitations of the mask-set used for processing the Hall bar devices, only the [1$\bar{1}$0], [110], and [010] bars could be processed on the same wafer chip, which not only gives as little wafer variation as possible for the different bars, but also ensures that any unintentional misalignment with the crystalline axes is consistent between the three bars. The [100] bars were processed separately from the other direction bars using a similar but not the same section of the sample wafer, and are likely to have a different degree of misalignment to the crystalline axes compared to the other direction bars. It has previously been shown that the AMR of MBE grown (Ga,Mn)As can vary across an individual sample wafer, particularly between sections at the centre and edge of the wafer[166], and so wafer inhomogeneity could, in principle, be an explanation for the as-grown [100] (as well as the annealed [100] and Corbino) C_U values being different from those obtained from the other direction bars, even if the size of the disagreement seems severe for bars made from pieces of the sample wafer that were in close proximity to one another. If this is the case it is not clear why the as-grown and annealed C_C values obtained from the [100] bar are not also significantly different from those obtained from the other bar directions.

The AMR fitting analysis makes the assumption that the bar and hence current direction is perfectly aligned with the crystalline axes which greatly simplifies the fitting procedure. However, a very crude estimate suggests that C_U should not vary significantly for different relative current misalignments of several degrees and so inconsistent alignment between the [100] bar and other bar directions with the crystalline axes seems unlikely to be the main cause of the disagreeing C_U values.

An unintentional out of plane component of the external magnetic field that is ϕ dependent (e.g. if the sample is not mounted perfectly in-plane) would act to give an additional contribution to AMR_{xx} that, like C_U, is two-fold symmetric with respect to the crystalline axes (though it would be symmetric about the axes of misalignment rather than the [110] axes as is the case for C_U). An out of plane external field would also give a one-fold symmetric in ϕ contribution to R_{xy} due to the anomalous Hall effect. Fitting equation 3.14 to 4.2K annealed AMR_{xy} data reveals small but finite $cos(\phi)$ and $sin(\phi)$ terms, and comparison with the Hall sweep data presented in chapter 2 suggests and out of plane misalignment of around 1° can account for these terms. However, comparing the AMR_{xx} data to that of the out of plane field sweep R_{xx} data of chapter 2, a 1° out of plane misalignment does not come close to accounting for the discrepancies in the magnitude of the C_U terms from the $cos(2\phi)$ and $sin(2\phi)$ fitting constants from the different Hall bars. Therefore, while it seems believable that there is an unintentional out of plane component of the external field for the AMR measurements that can explain the $cos(\phi)$ and $sin(\phi)$ terms in AMR_{xy}, it is unlikely that it is the reason for the disagreeing C_U values.

Strain-relaxation, which is known to alter C_U in bars of sub micrometer widths[164], also seems an unlikely explanation for the inconsistent C_U values as all Hall bars were processed with widths of approximately 50μm, i.e. much larger than where stain relaxation becomes significant.

3.4 Discussion

3.4.1 General observations from AMR polar plots

Before doing any fitting analysis, two of the key findings of this investigation of the AMR of (Ga,Mn)$As_{0.9}Sb_{0.1}$ are visually apparent in the experimental AMR polar plots of the as-grown and annealed (Ga,Mn)$As_{0.9}Sb_{0.1}$ presented in figures 3.3 - 3.11: 1) The AMR is not dominated by a single contribution, and 2) The AMR changes strongly upon annealing. It can be seen in figure 3.3 that while AMR_{xx} of the as-grown (Ga,Mn)$As_{0.9}Sb_{0.1}$ has a largely two-fold style symmetry for all current directions, it has a different shape relative to the ϕ axes for different current directions which indicates a large crystalline contribution to the AMR. With the exception of current along the [110] direction, AMR_{xx} of the annealed (Ga,Mn)$As_{0.9}Sb_{0.1}$ also has a largely two-fold style symmetry, as seen in figure 3.4, but in this case the shape relative to the ϕ axes is less dependent on current direction, which suggests that the relative importance of the C_I contribution is greater in the annealed sample than in the as-grown sample. Furthermore,

comparing figures 3.3 and 3.4 it is clear that the magnitude of AMR_{xx} decreases for all current directions upon annealing. Figures 3.5 and 3.10 display a trend commonly observed in temperature dependent AMR studies, where the magnitude of the AMR decreases with increasing temperature (which is usually a result of the magnetization becoming weaker), however figures 3.6 and 3.9 show a more anomalous temperature dependence, not only in the magnitude of the AMR but also its shape. This anomalous behaviour with temperature suggests that the AMR of (Ga,Mn)$As_{0.9}Sb_{0.1}$ is not dominated by a single AMR contribution, and that the sizes of the various AMR contributions relative to one another are not constant with temperature, i.e. some AMR contributions fall quicker with increasing temperature than others. With the exception of the case of current along the [010] direction for the as-grown sample where filamentary conduction effects are suspected to be large, AMR_{xy} for the as-grown and annealed samples shown in figures 3.7 and 3.8 has the expected $sin(2\phi)$ symmetry. However, the difference in the magnitude of AMR_{xy} for the $[1\bar{1}0]$/[110] and [100]/[010] current directions again suggests that the AMR is not totally dominated by C_I. By comparing figures 3.7 and 3.8 it is not immediately evident whether AMR_{xy} generally decreases upon annealing, unlike the AMR_{xx} polar plots where the trend is far more clear-cut. Finally, the relatively small magnitude of $AMR_{Corbino}$ shown in figure 3.11 illustrates that there are finite pure crystalline contributions to the AMR of the annealed (Ga,Mn)$As_{0.9}Sb_{0.1}$, but that these are smaller than the non-crystalline contributions.

3.4.2 Phenomenological description of observed AMR

The size and shapes of the observed AMRs in figures 3.3 - 3.11 can be phenomenologically explained by considering the sizes of the analytically extracted AMR coefficients and their temperature variation (which is shown in figures 3.12 and 3.13), along with equations 3.5 - 3.10 which determine the AMR for a given current direction.

For the as-grown (Ga,Mn)$As_{0.9}Sb_{0.1}$ at 4.2K, the largest AMR coefficient is C_U, which is approximately 2.5 times larger in magnitude than both C_I and $C_{I,C}$, and 4.5 times larger than C_C. C_I and $C_{I,C}$ are of a similar magnitude but opposite sign to one another which means that (C_I + $C_{I,C}$) is small, and therefore the $cos(2\phi)$ term of $[1\bar{1}0]_{xx}$ and $[110]_{xx}$ is mostly determined by C_U, hence why $[1\bar{1}0]_{xx}$ and $[110]_{xx}$ are similar in magnitude but are shifted by 90 degrees in ϕ with respect to one another; $[1\bar{1}0]_{xx}$ has a large negative $cos(2\phi)$ term whereas $[110]_{xx}$ has a large positive $cos(2\phi)$ term. For both $[1\bar{1}0]_{xx}$ and $[110]_{xx}$ the magnitude of the $cos(2\phi)$ term is more than 4 times larger than the $cos(4\phi)$ term (which is given by C_C only), and so the shapes of $[1\bar{1}0]_{xx}$ and $[110]_{xx}$ are largely -/+$cos(2\phi)$ like but with a slightly apparent -$cos(4\phi)$ component. The shapes of $[100]_{xx}$ and $[010]_{xx}$ are a hybrid of predominantly -$cos(2\phi)$ and +/-$sin(2\phi)$ style symmetries. (C_I - $C_{I,C}$) is only slightly smaller in magnitude than C_U, and so the -$cos(2\phi)$ component of $[100]_{xx}$ and $[010]_{xx}$ is only slightly less than the +/-$sin(2\phi)$ component, while the +$cos(4\phi)$ contribution from C_C is also just about evident.

An example of how the change in AMR coefficients with temperature changes the

AMR can be seen in the temperature evolution of the shape of as-grown $[100]_{xx}$ (figure 3.5), which reflects the evolution of the individual and relative magnitudes of (C_I - $C_{I,C}$) and C_U (obtained from $[100]_{xx}$) with temperature, as shown in figure 3.16. As temperature increases, the magnitudes of both (C_I - $C_{I,C}$) and C_U decrease, and so the magnitude of $[100]_{xx}$ decreases. However, as C_U drops more rapidly than (C_I - $C_{I,C}$), $[100]_{xx}$ takes more of a -$cos(2\phi)$ shape and less of a +$sin(2\phi)$ shape as temperature increases, and in fact at 25K the magnitude of (C_I - $C_{I,C}$) is approximately 5 times greater than C_U.

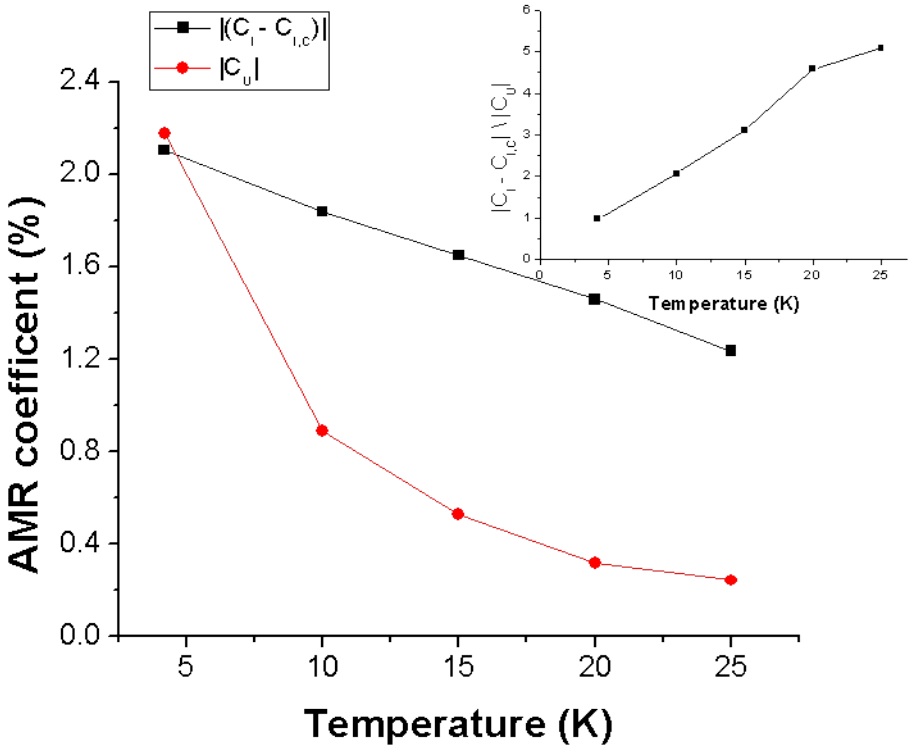

Figure 3.16: Magnitude of (C_I - $C_{I,C}$) (black) C_U (red) of as-grown (Ga,Mn)$As_{0.9}Sb_{0.1}$ as a function of temperature. Inset: Relative magnitude of (C_I - $C_{I,C}$) and C_U as a function of temperature.

The phenomenological decomposition of the annealed (Ga,Mn)$As_{0.9}Sb_{0.1}$ is also instructive. At 4.2K, C_I is now the largest coefficient, but again like the as-grown sample, the AMR is not dominated by a single term. C_I is approximately 1.5 times the magnitude of $C_{I,C}$, 4 times the magnitudes of C_U, and 7 times the magnitude of C_C. The magnitude of $C_{I,C}$ is sufficient that alone it can heavily compensate or add to C_I, and this can be seen in comparing $[1\bar{1}0]_{xx}$ to $[100]_{xx}$ and $[010]_{xx}$ as well as comparing $[1\bar{1}0]_{xy}$ and $[110]_{xy}$ to $[100]_{xy}$ and $[010]_{xy}$ where the magnitudes of the AMRs that feature a (C_I - $C_{I,C}$) contribution to the $cos(2\phi)$ or $sin(2\phi)$ terms are much larger than the AMRs that feature a (C_I + $C_{I,C}$) contribution to those terms. The presence of the C_U term is evident in $[100]_{xx}$ and $[010]_{xx}$ as the maximum in the AMR_{xx} is shifted +/- in ϕ due to the finite +/-$sin(2\phi)$ contribution.

The most interesting and illuminating example of how the interplay of the AMR coefficients phenomenologically accounts for the observed AMR is the case of the

annealed $[110]_{xx}$ and its temperature dependence (shown in figure 3.6). At 4.2K, $(C_{I,C} + C_U)$ has a similar magnitude to C_I but is of opposite sign, and therefore $(C_I + C_{I,C} + C_U)$ is small, even smaller in magnitude than C_C. $[110]_{xx}$ is thus unique from AMR_{xx} for the other current directions as its magnitude is considerably smaller and it has a largely fourfold symmetry. As temperature increases, all the AMR coefficients individually decrease, but not at the same rate as one another, and so the relative differences in the sizes of the coefficients is not constant with temperature. The shape and magnitude of $[110]_{xx}$ is determined by the sizes of $(C_I + C_{I,C} + C_U)$ and C_C, which are plotted in figure 3.17. As temperature increases from 4.2K to 25K, $(C_I + C_{I,C} + C_U)$ actually increases in magnitude as C_I drops less sharply than $C_{I,C}$ and C_U before decreasing as temperature further increases. The manifestation of this can be seen in figure 3.6, where the magnitude of $[110]_{xx}$ increases and its shape becomes less cubic and more -$cos(2\phi)$-like as temperature initially increases before decreasing and becoming nearly entirely -$cos(2\phi)$-like as temperature increases towards T_c.

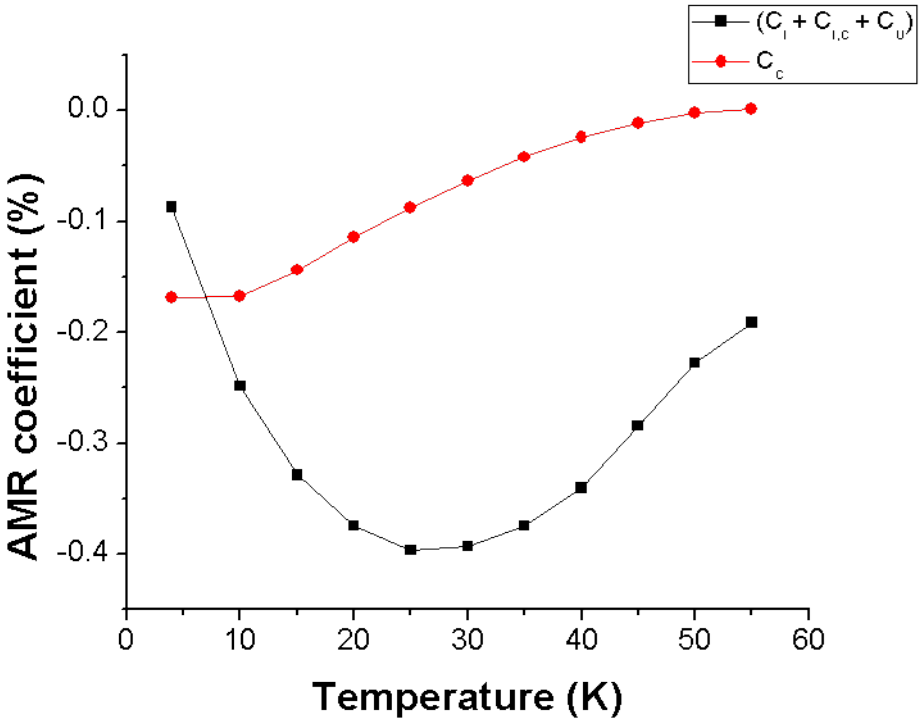

Figure 3.17: $(C_I + C_{I,C} + C_U)$ (black) and C_C (red) of annealed (Ga,Mn)$As_{0.9}Sb_{0.1}$ as a function of temperature. Note that the C_U is obtained from the $[1\bar{1}0]/[110]$ Hall bars only and C_C is obtained from the [110] Hall bar only.

3.4.3 Behaviour of individual AMR coefficients

This section focuses the discussion on to the significance and behaviour of the individual AMR contributions to (Ga,Mn)$As_{0.9}Sb_{0.1}$, compares the AMR to previously published experimental results in other DMSs, and examines what can be learned generally about the AMR contributions from the experimental investigation presented in this chapter. The average values of the AMR coefficients as well as their

contribution to the total AMR of both as-grown and annealed (Ga,Mn)$As_{0.9}Sb_{0.1}$ at 4.2K are shown in the table in figure 3.18:

(Ga,Mn)($As_{0.9}Sb_{0.1}$)	C_I (%)	C_U (%)	C_C (%)	$C_{I,C}$ (%)
as-grown	-0.76 (14.6%)	2.91 (55.7%)	-0.63 (12.1%)	0.92 (17.6%)
annealed	-1.00 (47.8%)	0.26 (12.5%)	-0.15 (7.2%)	0.68 (32.5%)

Figure 3.18: Table of AMR coefficients (black text) and the relative proportion of the sum of the coefficients magnitudes (red text) for as-grown and annealed (Ga,Mn)($As_{0.9}$,$Sb_{0.1}$) at 4.2K.

In order to help consider possible origins of the AMR coefficients as well as for ease of comparison between coefficients themselves, figures 3.19 and 3.20 plot resistivity (ρ_{xx}), remnant ($\mathbf{M}[1\bar{1}0]$:Rem and $\mathbf{M}[110]$:Rem) and 5kOe field cooled ($\mathbf{M}[110]$:5kOe) magnetizations, and the relative magnitude of each AMR coefficient (C/C_{max}), all as a function of temperature for as-grown and annealed (Ga,Mn)$As_{0.9}Sb_{0.1}$ respectively. The relative magnitude of an AMR coefficient is defined as its value at a given temperature divided by its maximum value within the measured temperature range.

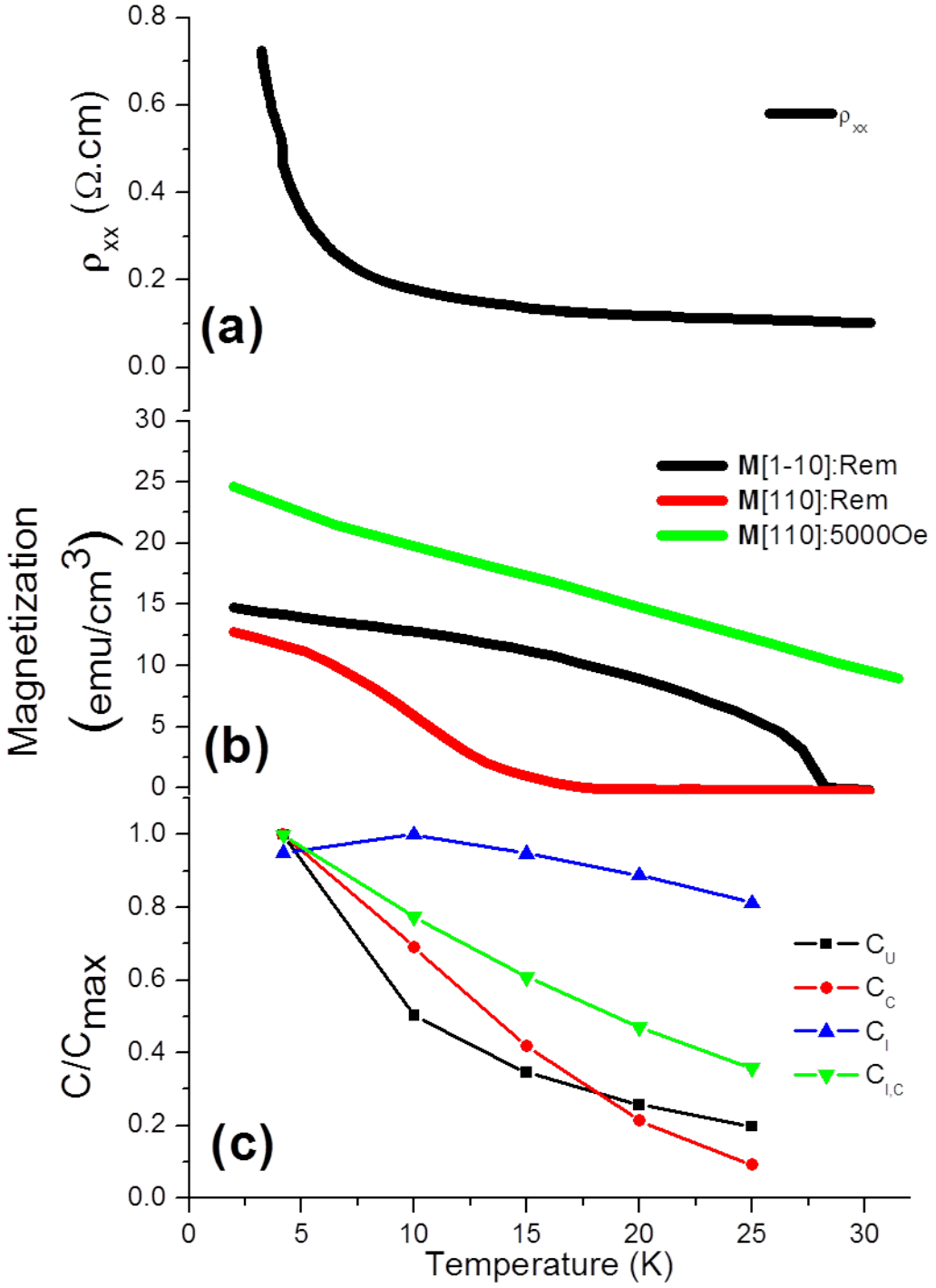

Figure 3.19: **(a)** Resistivity, **(b)** Remnant magnetization along the $[1\bar{1}0]$ (black) and [110] (red) crystalline axes after field cooling in a 1kOe field, as well as magnetization along the [110] crystalline axes during a 5kOe field cool (green), and **(c)** Relative magnitude of AMR coefficients, all as a function of temperature for as-grown (Ga,Mn)($As_{0.9}$,$Sb_{0.1}$).

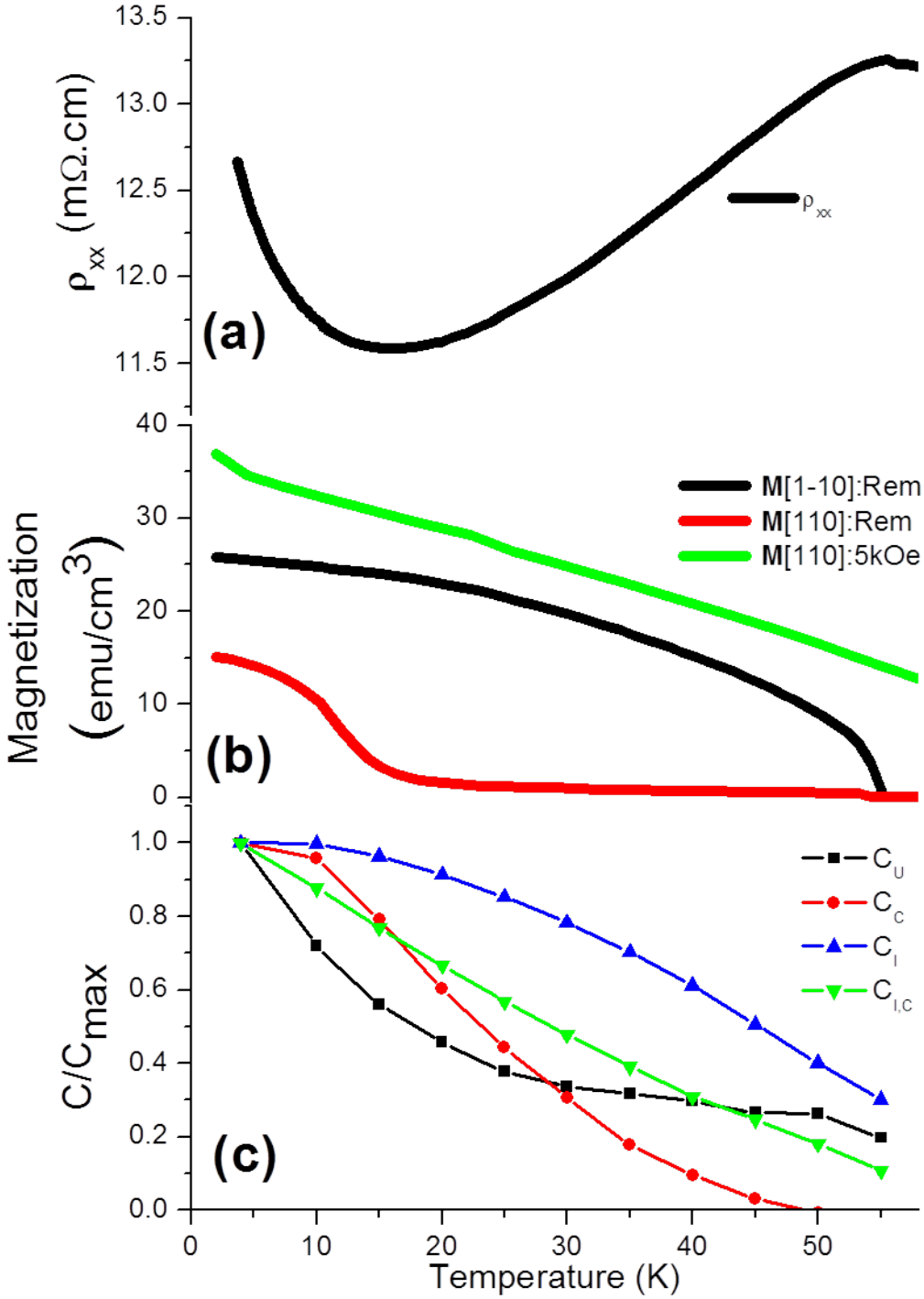

Figure 3.20: **(a)** Resistivity, **(b)** Remnant magnetization along the $[1\bar{1}0]$ (black) and [110] (red) crystalline axes after field cooling in a 1kOe field, as well as magnetization along the [110] crystalline axes during a 5kOe field cool (green), and **(c)** Relative magnitude of AMR coefficients, all as a function of temperature for annealed (Ga,Mn)($As_{0.9}$,$Sb_{0.1}$).

Phenomenologically the C_I term encapsulates any contribution to AMR that varies as $cos(2\phi)$ for all current directions, and experimentally several studies of the DMS (Ga,Mn)As have indicated that C_I is the dominant contribution to

its AMR[159][152][154][167]. While C_I is the largest AMR contribution to the annealed (Ga,Mn)($As_{0.9}$,$Sb_{0.1}$) at 4.2K, it does not alone dominate its AMR, and for the as-grown (Ga,Mn)($As_{0.9}$,$Sb_{0.1}$) sample C_I is only the third largest AMR contribution. Like (Ga,Mn)As, C_I for (Ga,Mn)($As_{0.9}$,$Sb_{0.1}$) is negative, however none of the previous (Ga,Mn)As AMR studies explicitly obtain and present a value for C_I, and so a direct comparison of C_I for (Ga,Mn)($As_{0.9}$,$Sb_{0.1}$) and (Ga,Mn)As is not possible. Nevertheless, given the overall magnitude of the AMR of the 5% Mn-doped, 25nm thick, as-grown (Ga,Mn)As sample of reference [159] and the fact that it appears to be mostly dominated by C_I, it seems that its value of C_I may not be too dissimilar from that of the 6% Mn-doped, 25nm thick, as-grown (Ga,Mn)($As_{0.9}$,$Sb_{0.1}$) sample of this investigation. Therefore, while it is clear that the relative contribution of C_I to the AMR is considerably smaller in (Ga,Mn)($As_{0.9}$,$Sb_{0.1}$) than in similar (Ga,Mn)As samples, its actual size may be comparable in the two DMSs. This would suggest that alloying 10% Sb to (Ga,Mn)As increases the strength of the other AMR coefficients, but does not seem to have such a strong effect on C_I. As shown in figures 3.19 **(c)** and 3.20 **(c)**, for both as-grown and annealed (Ga,Mn)($As_{0.9}$,$Sb_{0.1}$) C_I is the AMR coefficient that reduces the least as temperature increases. As temperature initially increases from 4.2K, the rate of decrease of C_I is actually its slowest across the measured temperature ranges, which is in contrast to the pure crystalline AMR coefficients whose values drop most sharply in this region. The increase of the as-grown C_I value from 4.2K to 10K is assumed to not be a real result, and that there is likely to be some error on C_I obtained at 4.2K that has noticeably reduced its magnitude. C_I decreases more rapidly as temperature further increases, but for both the as-grown and annealed cases as the temperature approaches T_c, C_I is still the largest AMR coefficient in terms of relative magnitude, and is also the largest AMR coefficient in terms of overall magnitude. Above 10K and 20K for the as-grown and annealed samples respectively, the reasonably linear decrease of C_I with increasing temperature is similar to the temperature dependent behaviour of $\mathbf{M}$[110]:5kOe, and so it seems likely that C_I depends largely on magnetization strength. As temperature approaches T_c, both the as-grown and annealed C_I values do not drop to zero, having a relative magnitude of around 0.8 and 0.3 respectively at T_c, and this is a result of the 20kOe and 4kOe external fields that are used in the respective AMR measurements inducing and strengthening a single-phase magnetization at temperatures approaching and beyond T_c[168]. C_I is the only AMR coefficient of (Ga,Mn)($As_{0.9}$,$Sb_{0.1}$) whose magnitude becomes larger upon annealing, increasing by a factor of 1/3. Annealing removes moment compensating interstitial Mn, and given the apparent link between C_I and magnetization strength it seems probable that the increase of C_I with annealing is related to the strengthening of the magnetization.

At 4.2K, C_U is the largest AMR coefficient of the as-grown (Ga,Mn)($As_{0.9}$,$Sb_{0.1}$), being more than 3 times larger than the next largest coefficient $C_{I,C}$ and accounting for more than half of the sum of the AMR coefficients. Annealing reduces the 4.2K value of C_U by more than an order of magnitude, leaving it the third largest AMR coefficient that accounts for only 12.5% of the sum of the AMR coefficients. For both as-grown and annealed (Ga,Mn)($As_{0.9}$,$Sb_{0.1}$), C_U is the AMR coefficient whose magnitude drops most significantly as temperature initially increases from

4.2K, dropping to a relative magnitude of around 0.4 at temperatures of 15K and 30K for the as-grown and annealed samples respectively. In both cases, the rate of decrease of C_U with increasing temperature slows as temperature continues to increase, and as temperature approaches T_c C_U still has a finite value with a relative magnitude of around 0.3. A decreasing magnetization strength is most likely largely responsible for the overall decrease of C_U with increasing temperature, however the different shape of the temperature dependencies of C_U and C_I hint that there may be an additional temperature dependent factor(s) that play a role in the magnitude of C_U. The resistivity of the as-grown (Ga,Mn)($As_{0.9}$,$Sb_{0.1}$) is high (conductivity low), and the shape of its temperature dependence is quite similar to that of C_U. Furthermore, C_U is also the largest AMR coefficient in the 5% Mn-doped, 5nm thick, as-grown (Ga,Mn)As sample studied in references [130] and [159] which also has a high resistivity, and these observations suggest that C_U may be related to resistivity/conductivity in some capacity. To investigate such a possible link, the table in figure 3.21 displays the conductivities and C_U values at 4.2K of several similarly doped DMSs grown in the Nottingham MBE system, both from this investigation and from literature.

DMS	4.2K Conductivity $\Omega^{-1}cm^{-1}$	C_U (%)
(Ga,Mn)As – 25nm, 5%, as-grown	≈ 350*	0.125
(Ga,Mn)($As_{0.9}Sb_{0.1}$) – 25nm, 6%, annealed	80	0.29
(Ga,Mn)($As_{0.9}Sb_{0.1}$) – 25nm, 6%, as-grown	1.3	2.9
(Ga,Mn)As – 5nm, 5%, as-grown	0.04	5.4

Figure 3.21: Table of conductivities and values of C_U of (Ga,Mn)As and (Ga,Mn)($As_{0.9}$,$Sb_{0.1}$) samples at 4.2K. *Conductivity value of a similar but different sample[53] to that from which C_U is taken[159].

For the limited number of data points given in the table in figure 3.21, there is a general trend that C_U increases as conductivity decreases. Unfortunately no further reports in literature could be found of C_U values in other DMSs, and so there is insufficient data to claim that this trend exits more generally in various DMSs. The suggested trend from data points is very non-linear, which begs the question as to whether, if at all, C_U is directly related to conductivity or whether it is related to another factor upon which conductivity also depends. It is worth noting that the higher resistivity 5% Mn-doped, 5nm thick, as-grown (Ga,Mn)As and as-grown (Ga,Mn)($As_{0.9}$,$Sb_{0.1}$) samples both have insulating-like resistance against temperature profiles, and both have a C_U value that is an order of magnitude or more greater than the annealed (Ga,Mn)($As_{0.9}$,$Sb_{0.1}$) and 5% Mn-doped, 25nm thick, as-grown (Ga,Mn)As samples, both of which have metallic-like resistance against temperature profiles. This may suggest that it is the nature of the transport behaviour which plays some role in the magnitude of C_U. Previous reports have proposed that strong crystalline AMR observed in (Ga,Mn)As is linked to localisation of carriers[169][170]. As discussed in chapter 2, the low conductivity and insulating-like behaviour of the as-grown (Ga,Mn)($As_{0.9}$,$Sb_{0.1}$) may well be a result of Anderson localisation of the carriers, while the sample passes through the insulator to metal transition upon annealing which may also be due to carriers

becoming delocalised. If such carrier behaviour is true in (Ga,Mn)($As_{0.9}$,$Sb_{0.1}$) then the corresponding C_U values in the as-grown and annealed states would agree with the idea that C_U is large in systems where carriers are localised. Besides magnetization and carrier localisation dependencies, C_U has also previously been shown to vary with in-plane uni-axial tensile strain introduced or relaxed by micro-processing techniques as well as gaining a different temperature dependence in the samples where strain has been altered[164][165]. However, as previously stated, uni-axial tensile strain manipulation should not be a factor in the devices used in this investigation, and while the presence of Sb in (Ga,Mn)($As_{0.9}$,$Sb_{0.1}$) should increase its tetragonal growth strain in comparison to similarly doped (Ga,Mn)As samples, it is not clear whether this should have any bearing on C_U.

C_C is the smallest AMR coefficient for both the as-grown and annealed (Ga,Mn)($As_{0.9}$,$Sb_{0.1}$), having a magnitude of around 5% and 15% of the largest AMR coefficients in these samples respectively at 4.2K. The 4.2K value of C_C decreases by a factor of 4 upon annealing, however its contribution to the sum of the AMR coefficients only decreases by less than a factor of 2 as the overall AMR also decreases. For both the as-grown and annealed (Ga,Mn)($As_{0.9}$,$Sb_{0.1}$), C_C steadily drops with increasing temperature until it has a relative magnitude of around 0.2, after which its value continues to decrease with increasing temperature but at a slower rate. A comparable temperature dependence has previously been observed for C_C of different (Ga,Mn)As samples[164][165]. As well as being the AMR coefficient with the lowest magnitude at all temperatures, C_C also has the lowest relative magnitude from around 15K and 30K upwards for the as-grown and annealed samples respectively, and for the annealed sample it drops to zero below T_c despite $\mathbf{M}$[110]:5kOe still having a finite value. Overall C_C decreases with increasing temperature which indicates that like all the AMR coefficients C_C depends on magnetization strength. Interestingly reference [170] shows that for low temperatures and external magnetic fields greater than around 20kOe, for a given temperature C_C actually decreases with increasing magnetic field (and thus magnetization) for reasons that are not known, however, as this investigation uses 4kOe and 20kOe magnetic fields for the AMR measurements the results of the general magnetization dependence of C_C of this investigation and reference [170] are in agreement with one another. As C_C is the only AMR contribution that has a $cos(4\phi)$ symmetry it is easy to distinguish and measure, and therefore there have been several reports of its appearance and magnitude in previous AMR investigations of various DMSs which allows for further insight into its origins. In reference [171], 7% Mn-doped, 50nm thick (Ga,Mn)As is subject to partial annealing and hydrogenation in order to vary the hole density, and it is found that C_C increases non-linearly with decreasing hole density. A similar trend is reported in reference [172] where the hole density of 6% Mn-doped, 25nm thick (Ga,Mn)($As_{0.9}$,$P_{0.1}$) is modulated by electrical gating, and at 15K C_C is reported to have a magnitude of 0.3% when in depletion mode and 0% when in accumulation mode. The microscopic physics underpinning the relationship between C_C and hole density is not entirely clear, but it may be related to the effects of carrier localisation becoming increasingly significant as hole density decreases. The hole density of the as-grown (Ga,Mn)($As_{0.9}$,$Sb_{0.1}$) was not measured, but as annealing removes hole compensating interstitial Mn it is highly likely that the hole density

of (Ga,Mn)($As_{0.9}$,$Sb_{0.1}$) increases upon annealing, and this may be (partially) responsible for the subsequent decrease of C_C. While it appears that C_C does vary with hole density for a given DMS, when comparing different DMSs it is unlikely that hole density is the only factor that affects C_C, for example the 5% Mn-doped, 25nm thick, as-grown (Ga,Mn)As sample of reference [159] has an almost identical C_C value at 4.2K to the annealed (Ga,Mn)($As_{0.9}$,$Sb_{0.1}$) of this investigation, however its hole density is likely to be twice as big[53][65]. Finally, unlike C_U, C_C has been shown to not be affected by uni-axial tensile strain variations induced by microprocessing[164][165], but like C_U it is not clear if tetragonal growth strain should have any effect on C_C.

The $C_{I,C}$ contribution to AMR in DMSs is often overlooked, however the results of this investigation show it to play a key role in the make up of the AMR of (Ga,Mn)($As_{0.9}$,$Sb_{0.1}$). For both the as-grown and annealed (Ga,Mn)($As_{0.9}$,$Sb_{0.1}$) at 4.2K, $C_{I,C}$ is the second largest AMR coefficient, and while its magnitude decreases by a factor of 1/4 upon annealing, its relative contribution to the sum of the AMR nearly doubles which is a result of the pure crystalline coefficients reducing more severely. The magnitude of $C_{I,C}$ decreases with increasing temperature in a loosely linear manner which is a somewhat distinct temperature dependence from the other AMR coefficients, but like C_I and C_U, $C_{I,C}$ still has a finite value at T_c. The linear-like decrease of $C_{I,C}$ with increasing temperature is akin to that of $\mathbf{M}$[110]:5kOe which is evidence that the temperature dependence of $C_{I,C}$ is largely determined by magnetization strength. The decrease of $C_{I,C}$ with annealing goes against its general trend with magnetization shown in the temperature dependence and so must be brought about by some other factor that changes with annealing. The only previous reports of $C_{I,C}$ in DMSs are for 5% Mn-doped, as-grown (Ga,Mn)As of thickness 5nm[129] and 25nm[159], where values of 0.55% (at 10K) and 0.16% (at 4.2K) respectively are found. $C_{I,C}$ for the as-grown and annealed (Ga,Mn)($As_{0.9}$,$Sb_{0.1}$) of this investigation is larger than for the previously reported (Ga,Mn)As samples. In the as-grown, 25nm (Ga,Mn)($As_{0.9}$,$Sb_{0.1}$) and (Ga,Mn)As samples, $C_{I,C}$ is nearly 6 times larger in the former, but the reason for this large value of $C_{I,C}$ in (Ga,Mn)($As_{0.9}$,$Sb_{0.1}$) is not clear. As chapter 2 reports, alloying 10% Sb into (Ga,Mn)As reduces the hole density, conductivity, carrier delocalisation, and magnetization, but given the size of the Sb atom, SOC strength and growth strain should increase. Unlike C_U and to a lesser extent C_C, $C_{I,C}$ does not decrease drastically upon annealing, and given that the resistivity and (presumably) carrier localisation of (Ga,Mn)($As_{0.9}$,$Sb_{0.1}$) do decrease significantly with annealing, it may be the case the large value of $C_{I,C}$ in (Ga,Mn)($As_{0.9}$,$Sb_{0.1}$) is not attributable to either of these factors. AMR does ultimately stem from SOC and so the large values of $C_{I,C}$ and (presumably) SOC in (Ga,Mn)($As_{0.9}$,$Sb_{0.1}$) may be related, however no conclusions can be drawn from the limited data obtained in this investigation. The pure crystalline coefficient C_U is known to vary with induced uni-axial strain, but the variation of AMR coefficients with growth strain has not been investigated. Growth strain would alter the strength of the Dresselhaus-like SOC, but as shown in reference [159], AMR in (Ga,Mn)As can be well modelled without accounting for Dresselhaus SOC, and so therefore growth strain may not play a significant role in the size of AMR generally or indeed $C_{I,C}$.

3.5 Conclusions and future work

This chapter presented measurements, analysis, and discussion of AMR in as-grown and annealed (Ga,Mn)($As_{0.9}$,$Sb_{0.1}$). Previous studies have shown that DMSs have a non-crystalline AMR contribution that varies with the angle between magnetization and current direction and is opposite in sign to most metals, but that they also have crystalline AMR contributions that vary with the angle between magnetization and crystalline axes that can be of considerable size. The motivation behind the study in this chapter was to further understand the origins of the different AMR contributions and observe how they change for DMSs of different material properties.

The AMR of both the as-grown and annealed (Ga,Mn)($As_{0.9}$,$Sb_{0.1}$) has a rich make-up and is not dominated by one single contribution, unlike most magnetic materials where it is generally assumed to be dictated by C_I, and this results in the AMR being strongly dependent on the current direction. For the as-grown sample, a two-fold AMR_{xx} is observed for all current directions, however its magnitude and its symmetry with respect to the current flow is different for measurements across the four Hall bar orientations as a result of the significantly large crystalline AMR contributions. For the annealed sample, a fourfold AMR_{xx} is seen for current along the [110] direction which is strikingly different to the two-fold AMR for the other current directions, and again the magnitude of the AMR is different for each direction, with both observations a result of the interplay between the various AMR contributions.

When placed in the context of the transport and magnetic properties of (Ga,Mn)($As_{0.9}$,$Sb_{0.1}$) presented in chapter 2, as well as with the results of previous experimental studies of AMR in DMSs, the sizes and temperature dependencies of the AMR coefficients obtained in this investigation allow some further insight into their possible origins, though more DMSs would be needed to be studied to make any certain conclusions. The pure crystalline AMR contributions can be theoretically modelled by assuming a band-warped Fermi surface, and experimentally there is evidence to suggest they depend on the carrier properties of the DMS. The large value of C_U in the insulating-like as-grown (Ga,Mn)($As_{0.9}$,$Sb_{0.1}$), the observation of a similarly large C_U in insulating-like (Ga,Mn)As[129], as well as the small value of C_U in the metallic-like annealed (Ga,Mn)($As_{0.9}$,$Sb_{0.1}$) all suggest a possible link between C_U and carrier localisation. C_C has previously been shown to increase with decreasing hole density in (Ga,Mn)As[171][172], and this may explain why the value of C_C for (Ga,Mn)($As_{0.9}$,$Sb_{0.1}$) decreases with annealing, however it is likely that C_C also depends other factors. Unlike the pure crystalline AMR contributions, the temperature dependencies of C_I and $C_{I,C}$ of (Ga,Mn)($As_{0.9}$,$Sb_{0.1}$) are similar to that of its magnetization, which is evidence that magnetization strength is the dominant temperature dependent factor in their size. C_I is the only AMR contribution that increases with annealing, which may be a result of the magnetization becoming stronger. $C_{I,C}$ is larger in (Ga,Mn)($As_{0.9}$,$Sb_{0.1}$) than in (Ga,Mn)As, but further study would be needed to elucidate why this may be the case.

This investigation has shown that there are several pathways to tune both the size and make-up of AMR in DMSs. It is apparent that alloying 10% Sb with (Ga,Mn)As generally enhances the size of the total AMR and the relative contribution of the crystalline terms, confirming that doping can have a significant effect on AMR. The evolution of the strength and relative importance of the individual AMR contributions with annealing is remarkable and allows the AMR of (Ga,Mn)($As_{0.9}$,$Sb_{0.1}$) to be tailored by post-growth sample treatment alone. The somewhat different temperature dependencies of the various AMR coefficients means that the shape of the AMR can be varied with temperature, and this is most apparent for the annealed $[110]_{xx}$ case where a 25K change in temperature can significantly alter the shape as well as the magnitude of the AMR.

There is much scope for further AMR study in DMSs, particularly in order to more accurately relate the AMR contributions to various material properties so that DMSs with customizable AMR characteristics can be realised. It would be interesting to see how varying the thickness of (Ga,Mn)($As_{0.9}$,$Sb_{0.1}$) changes its AMR. It is known that in thinner (Ga,Mn)As samples the crystalline AMR becomes significantly stronger[129], possibly as a result of increased carrier localisation, and it would be helpful to demonstrate if this would also be true of (Ga,Mn)($As_{0.9}$,$Sb_{0.1}$), especially in the as-grown state where the crystalline terms are already strong at the moderate 25nm thickness which has insulating-like transport characteristics. Furthermore, it has recently been postulated that there is an AMR contribution in ferromagnetic/non-magnetic metallic bi-layers that arises from a magnetization dependent scattering at the interface[173][174][175] and therefore becomes more significant to the total AMR as layer thicknesses are reduced. It would be intriguing to determine if such an effect could also exist at a magnetic semiconductor/non-magnetic semiconductor interface by studying various heterostructures of relatively thin layer thicknesses. At the other end of the thickness scale, lattice strain in notably thick ($>$ 200nm) (Ga,Mn)($As_{0.9}$,$Sb_{0.1}$) should on average be more relaxed across the layer than the 25nm sample, and so observing how AMR differs in thicker samples may give some indication as to what, if any, effect growth strain has on AMR. Varying the choice of substrate would be an alternative method to change the growth strain of (Ga,Mn)($As_{0.9}$,$Sb_{0.1}$) to search for its effect on AMR. Another possible investigation would be to vary the Mn concentration of optimally annealed (Ga,Mn)($As_{0.9}$,$Sb_{0.1}$) and/or (Ga,Mn)As. Increasing the Mn doping should increase the hole density, saturation magnetization, and T_c, while keeping the conductivity fairly constant for the higher Mn concentrations[62], and so performing AMR measurements on a range of samples of varying Mn concentrations would help to shed light on the relationship between C_C and hole density, as well as how all the AMR terms evolve with magnetic properties. Step annealing and AMR measurements of an individual (Ga,Mn)($As_{0.9}$,$Sb_{0.1}$) would allow for a similar study. Replicating the investigation of reference [164] but using (Ga,Mn)($As_{0.9}$,$Sb_{0.1}$) instead of (Ga,Mn)As, i.e. varying uni-axial tensile strain in (Ga,Mn)($As_{0.9}$,$Sb_{0.1}$) through micro-pattering and use of an external piezoelectric transducer may reveal higher order crystalline AMR contributions and/or significantly alter C_U, particularly as the standard crystalline contributions are already stronger in (Ga,Mn)($As_{0.9}$,$Sb_{0.1}$) than (Ga,Mn)As for unpatterned material. Finally, reference [170] shows variation of C_C and (presumably) C_U with magnetic field/magnetization strength for a given

temperature, and it would be interesting to see if the strong C_U and C_C values of (Ga,Mn)($As_{0.9}$,$Sb_{0.1}$) behave similarly in such measurements.

This chapter has shown that alloying only 10% of Sb into (Ga,Mn)As drastically alters the AMR, and so it would be fascinating to observe how the AMR varies across the whole Sb concentration range in (Ga,Mn)(As,Sb) samples. The motivating factor of such a study would be that SOC strength should increase with Sb concentration, but care would need to be taken to disentangle any SOC induced AMR changes from those from other factors that would also change as a result of varying the Sb concentration such as hole density, carrier localisation, and magnetization strength. Using different annealing procedures may be an approach to controlling these factors. Growth strain, which may or may not affect AMR, would also change with Sb concentration, and ways to compensate for this could include varying the thickness of the (Ga,Mn)(As,Sb) layer, growing the (Ga,Mn)(As,Sb) on buffer layers, and using different substrates.

Beyond Sb-based DMSs, more insight could be gained by investigating AMR in other systems. A full study of AMR in various (III,Mn)V DMSs as well as quaternary Mn doped DMSs would provide more data on how the various AMR contributions change with material properties (which would vary greatly with the choice of group III and V elements). The AMR of the n-type DMS (In,Fe)As has already been studied, showing dominant crystalline contributions[176], and the emergence of additional III-V n-type DMSs materials[177] provides an excellent platform for further exploring AMR in these systems. There has also been some interest of AMR in oxide-based DMSs[178][179][180] which show both non-crystalline and crystalline contributions, and so it would be useful to apply the phenomenological analysis technique used in this chapter to these oxide-based DMSs to see how the individual AMR coefficients differ in this distinctive class of materials.

There are other magnetoresistance type effects that exist in magnetic/non-magnetic bilayers that are fundamentally distinct from the intrinsic AMR of a single ferromagnetic layer, but are interesting in their own right and measurable in a similar way to AMR, i.e. by rotating an external field and measuring the change in resistance. The resistance of the non-magnetic metal Pt deposited on the ferromagnetic insulator YIG is seen to vary with the angle of an external field, and there are two possible mechanisms postulated for this. The first suggests that magnetic ordering is induced in the Pt as a result of its proximity to YIG, and therefore due to the inherent spin-orbit coupling in Pt a conventional type of AMR arises[181]. The second suggests that a spin current generated in the Pt reflects off the YIG interface by an amount that depends on the YIG magnetization angle. This reflected spin current is then converted into an electrical current in the Pt by the inverse spin Hall effect that changes the sample resistance, an effected dubbed 'spin Hall magnetoresistance'[8]. The relative importance of each mechanism remains unclear[182] which motivates further research in similar systems with different non-magnetic metals, thickness, and layer structures, while it should also possible for the effect to be explored in the insulating DMS/non-magnetic semiconductor structure (Ga,Mn)N/n-GaN. There is also scarce study of AMR in magnetic metal/non-magnetic metal bi-layers. There are experimental[183] and theoretical[184] reports

that a spin current generated in a Pt layer could alter the AMR of an adjacent ferromagnetic layer, while at the same time the effects caused by such an interface on the Rashba SOC and its contribution to the AMR in the non-magnetic layer also need to be considered[163], as well as any contribution from the previously mentioned interface scattering AMR. Therefore there is sufficient motivation for more investigation in order to characterise and understand AMR in such bi-layer systems.

Chapter 4

Spin-orbit torque in (Ga,Mn)As

4.1 Introduction

Processors and memory are essential for the functionality of personal computers. In today's computers, processing is carried out by microprocessors - integrated circuits made up of charge based transistors. Computer memory can be subdivided into two classifications: primary and secondary memories. Primary memory is directly accessible to a computer's central processing unit (CPU), allowing for fast reading and writing of data regardless of its storage location. Random access memory (RAM) is the primary memory in modern computers, and like microprocessors, RAM is made up from integrated circuits which largely limits it to volatile operation only, i.e. it needs to be constantly refreshed as it loses its memory when power is removed. Secondary memory is non-volatile (retains memory when powered down) and can store a higher density of data than primary memory, but as it is detached from the CPU, accessing the data is slow. The most common form of secondary memory is the hard disk drive (HDD), which stores data in the state of a ferromagnet's magnetization. Solid state drives (SSDs), which store data as charge in floating gate transistor based integrated circuits, are another common form of secondary memory with several advantages and disadvantages over HDDs[185].

The realisation of a 'universal memory' that offers the speed of primary memory and the non-volatility of secondary memory would facilitate major advances in computing technology. One promising candidate for a universal memory is magnetoresistive RAM (MRAM)[186]. Like HDDs, data in MRAM is encoded in the polarity of a magnetic layer (in the case of MRAM the free layer of a spin valve), but unlike HDDs there is no mechanical motion needed to write the data. Writing in MRAM is conventionally performed by passing current through 'write lines' to generate Oersted magnetic fields strong enough reorientate the magnetization of the spin valve ('toggle MRAM'). This writing mechanism does not scale favourably with reduced device dimensions as the magnitude of the Oersted field per unit current decreases with write line diameter, meaning that larger currents are needed to write data. Furthermore the presence of write lines add complexity to device design which can increase fabrication costs as well as reduce packing densities due to overlapping stray fields. Alternative mechanisms of writing data in MRAM (i.e. switching magnetization of a spin valve) are therefore being keenly investigated to

help MRAM match and better RAM and HDD/SDD technologies and hence find more widespread uses than its current relatively niche applications.

Spin transfer torque (STT) is the leading alternative MRAM writing mechanism[187]. In STT-MRAM, electrical current is passed through the spin valve's fixed layer to gain a spin polarisation and then injected into the free layer. This spin polarised current transfers its angular momentum to the local moments in the free layer which can bring about their reorientation. For the reverse operation, current is passed from the free layer to the fixed layer with spins of opposite orientation to the fixed layer being reflected back into the free layer which causes a reorientation of the moments. As the free layer is internally torqued by the spin-polarised current rather than externally torqued by an Oersted field, switching occurs at a given current density rather than at given current magnitude, as is the case in Oersted switching. STT-MRAM is therefore scalable, and for small device dimensions it requires lower writing currents than toggle MRAM. This is not only beneficial for lower device power consumption, but as it also gives smaller associated stray fields it also allows for tighter packing of devices. A major drawback to STT-writing is that a large voltage needs to be applied across the spin valve causing damage to the tunnel barrier and thus reduces the number of write cycles that the device can withstand. A writing mechanism where current only needs to be laterally passed through the spin valve's free layer is therefore desirable.

The notion of spin-orbit torque (SOT) was first pointed in the mid 2000's[188][189] which is perhaps surprisingly late given the simplicity of the phenomenon and material structures needed to observe it. The SOT mechanism relative to this investigation can be summarised as follows: When current flows through ferromagnetic material that lacks inversion symmetry, the carrier spins gain a non-equilibrium polarisation. If these spins are exchange coupled to the local moments of the ferromagnet they will exert a torque on the moments, which if strong enough can lead to magnetization switching. Note that a separate polarising fixed magnetic layer is not required here; all that is needed for SOT is a single ferromagnetic layer with broken inversion symmetry (such as a zincblende diluted magnetic semiconductor (DMS) like (Ga,Mn)As or a thin magnetic layer interfaced with a non-magnetic layer such as CoFeB/Pt). There have recently been many experimental and theoretical studies of SOT in a variety of material systems, mostly DMSs[190][191] and magnetic multilayers[192][193], but also topological insulators[194] and antiferromagnets[195]. Fully understanding the underlying mechanisms behind the SOT phenomenon and characterising it in different materials and under different conditions will help to optimise the effect for repeatable low energy magnetic switching, therefore making SOT an attractive writing mechanism to be used in MRAM.

As discussed in chapter 1, (Ga,Mn)As is a DMS that is unlikely to find practical applications due to its low Curie temperature (T_c), but its electrical, magnetic, and structural tunability, along with its large spin-orbit coupling (SOC) and simple band structure make it an ideal system with which to characterise new phenomena. For these reasons the first experimental demonstration of SOT was made using (Ga,Mn)As[190], and there have since been multiple investigations of SOT in the material[191][196][119][197][198][199]. The investigation presented in this chapter

further experimentally investigates the nature of SOT in (Ga,Mn)As, or more specifically the current induced fields (CIFs) that can be considered to parametrise the phenomenon. The investigation has two major aims: Firstly to develop a simple experimental technique that is distinct from and holds some advantages over other methods previously used to measure CIFs in (Ga,Mn)As. Secondly, to use this technique to study how the CIFs in (Ga,Mn)As vary with temperature, a relationship that has previously been investigated but not definitively confirmed. Establishing an experimental technique that can measure the size of CIFs that act along different directions, and can be used to study how those CIFs vary as a function of an external parameter (current density, temperature etc) could prove useful for future SOT studies with the goal of characterising and optimising the SOT effect.

4.2 Theory

There is debate in literature about the origins of SOT in magnetic multilayer structures, whereas the origins of SOT in (Ga,Mn)As are more broadly agreed upon. This chapter investigates SOT in (Ga,Mn)As only, and as such, further references to terms like 'SOT' and 'CIFs' in this chapter are made in the context of the SOT mechanism in single layer (Ga,Mn)As and not metallic magnetic multilayers unless specifically stated. The majority of the theory presented in this section describes the physics behind SOT in (Ga,Mn)As (or III-V DMSs more generally), with the specific physics behind SOT in magnetic multilayers being briefly discussed in section 4.2.5.

4.2.1 Spin-orbit coupling from broken inversion symmetry

As discussed in more depth in section 1.2.2.4, at an atomic level, SOC is a relativistic effect that couples the spin and orbital angular momenta of an electron, and is at the heart of many spintronic phenomena. This type of intrinsic SOC scales with atomic number, and so heavy elements such as Pt are often regarded as excellent spintronic materials. In materials that are not inversion symmetric, additional types of SOC can arise that allow for novel spintronic effects and functionalities.

The concept of inversion symmetry can be thought of by considering the electric confining potential of a lattice (a periodic array of unit cells). If an observer placed in the lattice were to see the structure and composition of the surrounding lattice as being the same in all directions, then the electric potential would also be the same in all directions. A material with such a symmetric structure would be known as 'inversion symmetric', for example bulk Pt and Si.

Inversion symmetry can be broken in bulk structures without the requirement of an interface. The zincblende lattice of GaAs is an example of such bulk inversion asymmetry (BIA), where the symmetry breaking arises because the unit cell of the lattice structure lacks a centre of inversion symmetry. The zincblende lattice has the same structure as the diamond lattice of Si with the exception that all lattice sites are not occupied by atoms of the same charge. An observer at the centre of each bond in the Si unit cell would see the same arrangement of the same atoms in

all directions, i.e. the unit cell is invariant under inversion. However, an observer at the same point in a GaAs unit cell would see a different arrangement of the Ga and As atoms in different directions, and therefore would experience a different electric potential in different directions. This BIA causes a type of SOC known as Dresselhaus SOC. Dresselhaus SOC has two intrinsic forms, one that is linear with respect to momentum and one that is cubic with respect to momentum. Here the focus is only on the linear form as previous studies have shown it to be the dominant Dresselhaus term in SOT experiments[190][191].

As discussed in section 1.2.2.2, the growth strain of (Ga,Mn)As, which corresponds to the diagonal elements of its strain tensor, results in a tetragonal distortion of the lattice along the growth direction. This distortion exaggerates the asymmetric electric potential of the zincblende lattice which leads to an enhancement of the linear Dresselhaus SOC. In SOT experiments, the contribution of linear Dresselhaus SOC attributable to growth strain is believed to be more significant than the intrinsic contribution of linear Dresselhaus SOC from the symmetry of the unstrained zincblende lattice. The evidence for this assumption is that the CIFs associated with linear Dresselhaus SOC are along opposite directions for compressive and tensile strained DMSs[196] - this sign change agrees with theoretical models for growth strain contributions to linear Dresselhaus SOC but not intrinsic ones.

In multilayer structures that have a non-symmetric layer arrangement, e.g. CoFeB/Pt, thin crystalline layers of bulk inversion symmetric materials such as Pt can become inversion asymmetric near an interface. At such a position, an observer would see a different structure when looking towards the interface than when looking away from the interface, and thus there is a gradient in the electric potential in the growth direction of the structure. This type of breaking of inversion symmetry is known as structural inversion asymmetry (SIA) and causes a type of SOC known as Rashba SOC. This mechanism of Rashba SOC tends to only be significant in spatial regions a few nm's either side of an interface, and so while the mechanism can give observable effects in ≈nm thick magnetic multilayers, it may not be expected to be significant in (Ga,Mn)As layers of tens of nm thickness' like the one used in this investigation. However, CIFs with Rashba symmetry have been previously observed in (Ga,Mn)As[190][196]. It has been shown theoretically that (Ga,Mn)As under shear strain can yield SOC with Rashba symmetry. Shear strain is represented by the off diagonal elements of the strain tensor, and physically it corresponds to compression along one diagonal of a unit cell and elongation along the other. In model calculations a shear strain of 0.01% is sufficient to generate Rashba CIFs comparable to those measured in experiment. It must be noted that shear strain has never been experimentally detected in (Ga,Mn)As[200], however shear strains of around 0.01% have also been previously used to model uni-axial magnetic anisotropies[71] and magnetotransport[159] effects that are not expected by crystalline symmetry. It has been experimentally shown that, like linear Dresselhaus CIFs, the orientation of Rashba CIFs are also opposite in DMSs with compressive and tensile growth strain[196].

The physical manifestation of both Rashba and Dresselhaus SOC is an orientation of the spin of an electron (or hole) in a direction that depends on its momentum

with respect to the crystalline axes. For Rashba SOC the electron spin is always orientated perpendicular to is momentum. For linear Dresselhaus SOC the electron spin is orientated perpendicular to momentum along the <110> axes and parallel to momentum along the <100> axes[201]. Figure 4.1 shows the spin orientations given by the Rashba and linear Dresselhaus SOCs.

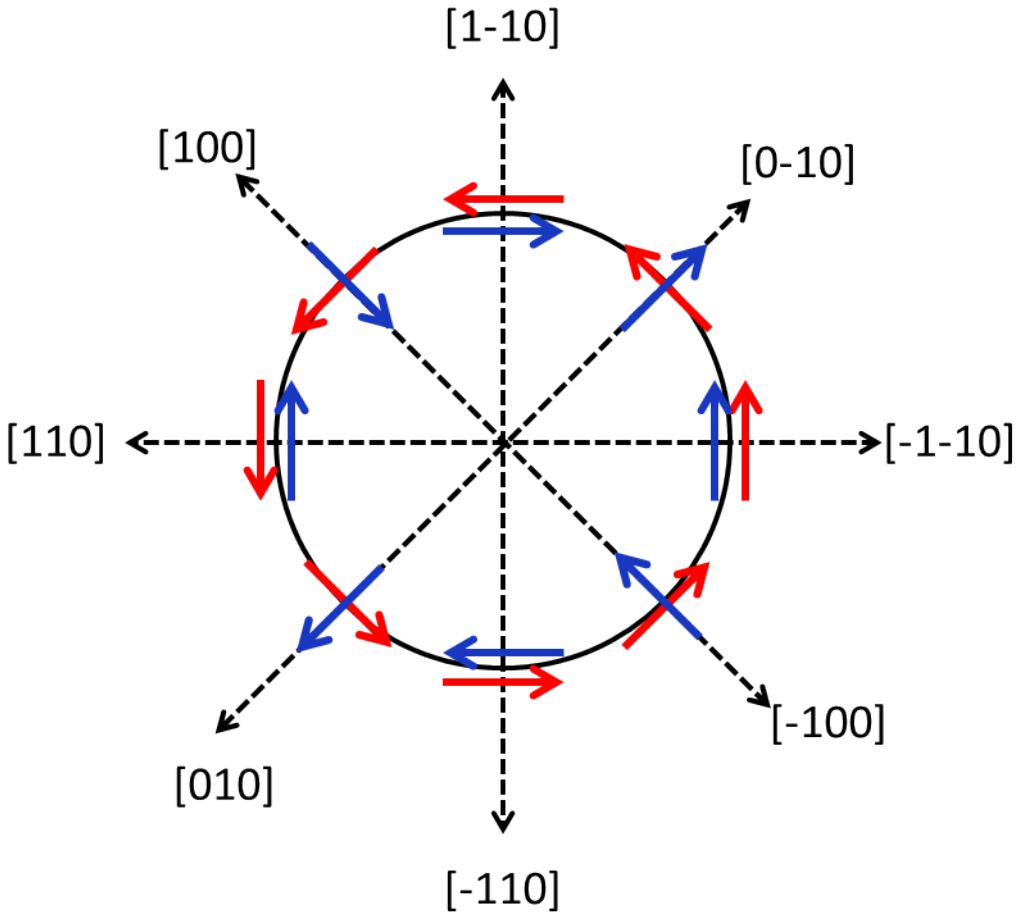

Figure 4.1: Spin orientations with respect to momentum direction for Rashba (red) and linear Dresselhaus (blue) SOC.

4.2.2 Non-equilibrium spin polarization

In (Ga,Mn)As, hybridisation of the $4p$ valence band states with the $3d$ Mn impurity states results in an antiferromagnetic alignment between the carrier holes and Mn moments. Under equilibrium conditions and below T_c, carriers in (Ga,Mn)As therefore have a finite net steady state spin polarisation. Similarly, the imbalanced populations of spin sub-bands at the Fermi level in other ferromagnetic materials have allowed the passing of current through a ferromagnetic layer to become a well established method of generating a spin polarised current[202][203][204][205].

As Dresselhaus and Rashba SOCs align spins in a direction that depends on their momentum, they too can lead to a spin polarised current even in the absence of magnetic ordering. This phenomenon is known as the inverse spin galvanic

effect (ISGE), sometimes also referred to as the Edelstein effect[206]. Consider a non-magnetic material which has Rashba SOC (Dresselhaus SOC is ignored for simplicity) where the carrier spins are aligned according to their momentum, as per figure 4.1. Under equilibrium conditions there is no net current flow and so carriers are evenly distributed across all momentum directions on the Fermi surface. As Rashba SOC is symmetrical with respect to the crystalline axes, the net steady state spin polarisation of the carriers averages to zero. Applying an electric field to the material induces a current flow of carriers along a given direction, which can be considered as a redistribution of carriers on the Fermi surface as they gain a net momentum. The resulting uneven occupation of the spin-orbit coupled carrier states means that the net carrier steady state spin polarisation is non-zero. This scenario describes the intraband contribution to the ISGE which is dominant in good conductors. In more disordered systems, an interband ISGE contribution can also play a significant role. In the case of the interband ISGE, a finite net steady state spin polarisation arises as the electric field polarizes the states on the Fermi surface so that they are no longer symmetric across it. In real systems the intraband and interband ISGE contributions act simultaneously, and as both lead to the same result of a net steady state carrier spin polarisation of the same symmetry they cannot be experimentally separated.

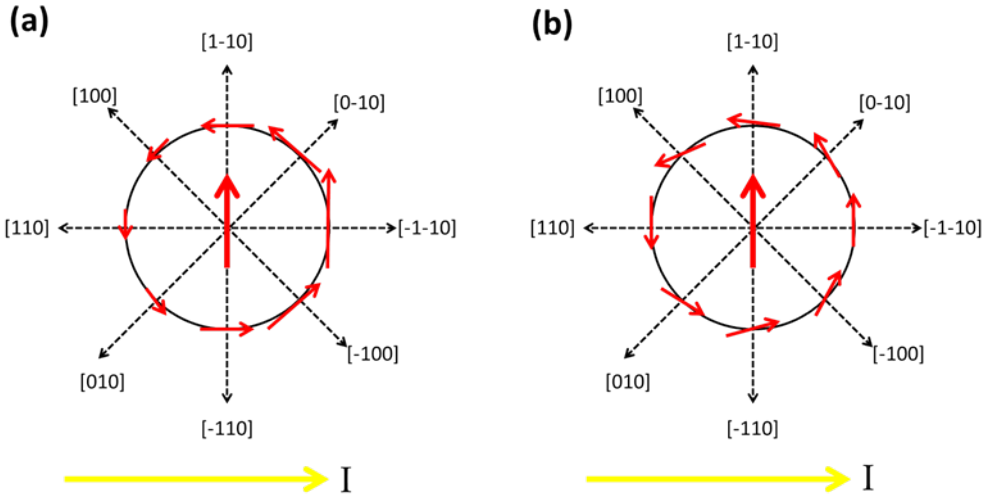

Figure 4.2: Spin orientations and occupancies of Fermi surface states for a non-magnetic material with Rashba SOC and current flow along the $[\bar{1}10]$ direction. Direction of arrows on Fermi surface represent the spin orientation of the state, magnitude of arrows represents the relative occupancy. Arrow at the centre represents the net steady state spin polarisation. **(a)** Intraband ISGE: States along the $[\bar{1}10]$ direction are more heavily occupied due to momentum shift of carriers induced by electric field, **(b)** Interband ISGE: Electric field modifies states so they are no longer symmetric about the Fermi surface (spin orientation not always perpendicular to momentum).

For the case of a ferromagnetic material with Dresselhaus/Rashba SOC such as (Ga,Mn)As, the effect of applying an electric field across the material and the subsequent ISGE is that the net carrier steady state spin polarisation is no longer

necessarily aligned in a parallel direction to the magnetization as it is under equilibrium conditions. This non-equilibrium spin polarisation is illustrated in figure 4.3**(d)** for the simplified case of a ferromagnet with Rashba SOC only, and where only the intraband ISGE is considered.

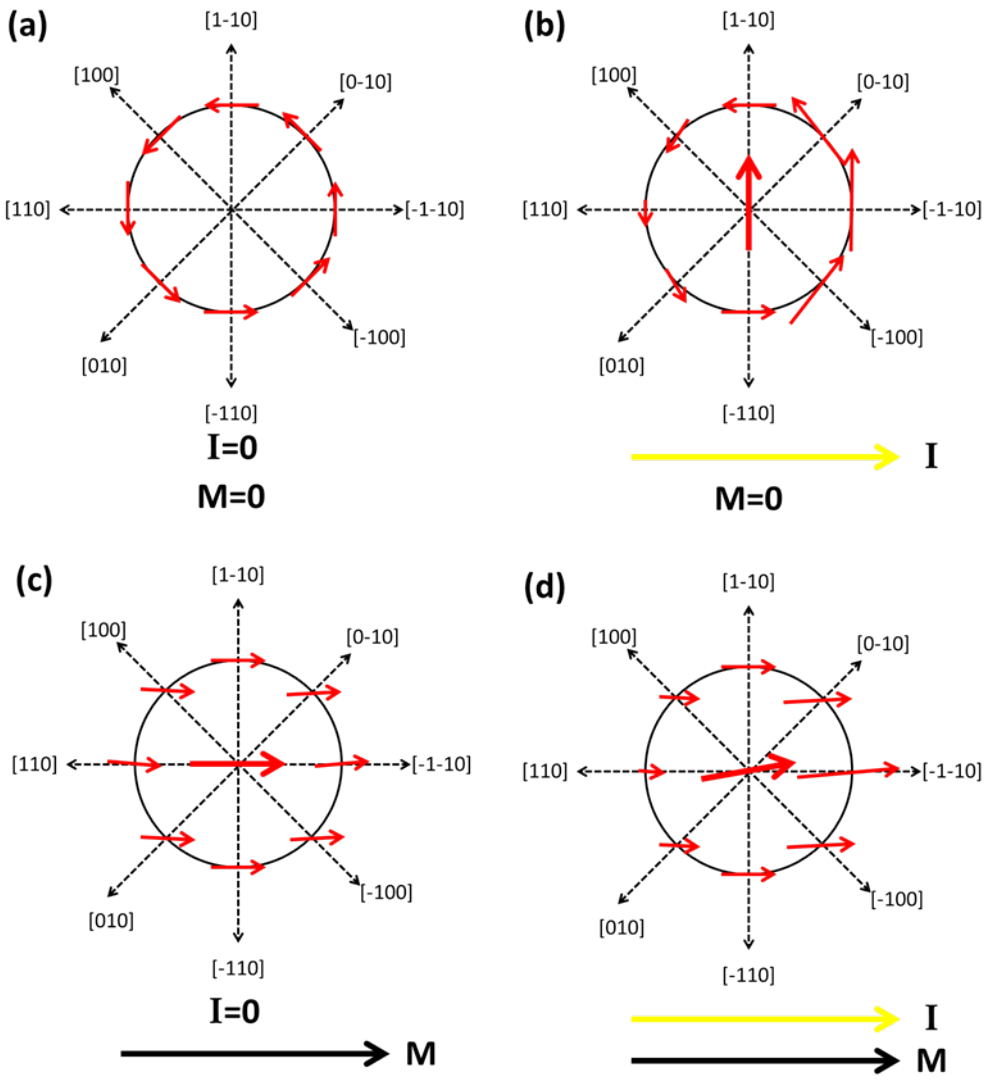

Figure 4.3: Spin orientations and occupancies of Fermi surface states for a material with Rashba SOC and in some cases current flow and/or magnetization along the $[\bar{1}10]$ direction. Only intraband ISGE is considered. Direction of arrows on Fermi surface represent the spin orientation of the state, magnitude of arrows represents the relative occupancy. Arrow at the centre represents the net steady state spin polarisation. **(a)** Non-magnetic system under equilibrium conditions, **(b)** Non-magnetic system with ISGE, **(c)** Magnetic system under equilibrium conditions, **(d)** Magnetic system with ISGE - note in this case the net steady state spin polarisation is misaligned with the magnetization.

Given its origins, the non-equilibrium spin polarisation from the ISGE should scale linearly with both SOC strength and current density, the latter having been previously observed in optical experiments on non-magnetic materials[207][208].

4.2.3 Torque from non-equilibrium spin polarisation

In (Ga,Mn)As, carrier spin relaxation occurs on a much faster time-scale than magnetization relaxation[199]. Given that the carrier spins are exchange coupled to the localised moments, the magnetization can be considered to respond to the steady state position of the carrier spins. In this scenario the magnetization dynamics are described by the Landau-Lifshitz-Gilbert equation:

$$\frac{d\mathbf{M}}{dt} = -\gamma\mathbf{M} \times \mathbf{H} + \alpha\mathbf{M} \times \frac{d\mathbf{M}}{dt} + \frac{J_{ex}}{g\mu_B}\mathbf{M} \times \delta\mathbf{S} \tag{4.1}$$

where $\mathbf{M}$ is the magnetization, γ is the gyromagnetic ratio, $\mathbf{H}$ is any external field, α is the Gilbert damping parameter, J_{ex} is the exchange coupling between carrier holes and local moments, g is the g-factor of the localised d-electrons (g=2), μ_B is the Bohr magneton, and $\delta\mathbf{S}$ is the non equilibrium component of the carrier spin density. The final term in equation 4.1 indicates that when the net steady state spin polarisation is not aligned parallel or anti-parallel to the magnetization, a torque will be exerted on the magnetization. This torque is classified as a 'field-like' torque as its effect on the magnetization dynamics is analogous to the application of an external magnetic field. On the pico-second time scale the magnetization will precess around the spin polarisation (which can be observed in optical spin-orbit torque experiments[52]) before damping causes it to lie along some new steady state position. The magnetization can be considered to have been acted on by a 'SO effective magnetic field', referred to in this thesis as a current induced field (CIF), resulting from the non-equilibrium carrier spin-polarisation and the exchange interaction and parametrised by:

$$H_{\mathrm{CIF}} = -\frac{J_{ex}}{g\mu_B}\delta\mathbf{S} = -\frac{J_{pd}N_{Mn}S_{Mn}}{g\mu_B}\delta\mathbf{S} \tag{4.2}$$

where J_{pd} is the antiferromagnetic coupling constant of (Ga,Mn)As, N_{Mn} is the concentration of Mn atoms, and S_{Mn} is the spin of the Mn atom ($S = 5/2$). The direction of the CIF lies along the direction of the non-equilibrium component of the spin polarisation, which in turn is determined by the Dresselhaus and Rashba SOCs. Therefore, the CIF acting on the magnetization can be considered to consist of two independent CIFs, a Dresselhaus CIF (H_D) and a Rashba CIF (H_R) which take the same symmetry as displayed in figure 4.1.

Terms like 'CIF', 'spin-orbit field', 'effective field' etc are used inconsistently across literature. In this thesis a 'CIF' does not describe the momentum dependent internal field that aligns carrier spins due to the spin-orbit interaction, nor does it describe an external magnetic field that would be needed generate a (non-equilibrium) spin polarisation equivalent to that from the ISGE. Here a CIF is the external magnetic field that would be required to cause the equivalent torque on the magnetization as that which arises from the non-equilibrium spin polarisation generated from the ISGE. Without the non-equilibrium spin polarisation or exchange coupling, the torque on the magnetization would be zero, and so as zero external field would be needed to produce the equivalent torque, the CIFs as defined in this thesis are zero without either of these factors.

4.2.4 Factors affecting CIFs

As the ISGE scales linearly with SOC strength and current density, and the size of the CIFs acting on the magnetization are linear with the non-equilibrium spin polarisation generated from the ISGE, the CIFs themselves will therefore also vary linearly with SOC strength and current density. While the dependence of CIFs with SOC strength has only been examined theoretically[197][199], the linear relationship between CIFs and current density in (Ga,Mn)As has been previously demonstrated in multiple experiments (see section 4.3.1).

Reference [199] predicts that the CIFs in (Ga,Mn)As will be largely independent of the angle between the magnetization and the current direction, while reference [197] suggests that the CIFs' dependence on the angle between magnetization and current direction increases with increasing warping of the Fermi surface. In previous experimental measurements of CIFs in (Ga,Mn)As, the size of the CIF has always been assumed to be independent of magnetization orientation[190][191][196], an assumption also used in this investigation.

The size of CIFs in (Ga,Mn)As have also been experimentally shown to vary with temperature[191][209]. These observations and the possible origins of the relationship between CIFs and temperature are discussed in more depth in sections 4.3.1 and 4.4 respectively.

4.2.5 Additional SOT effects

The discussion so far has related to the field-like CIFs in (Ga,Mn)As that can be modeled from growth and shear strains as these are the only CIFs relevant to this investigation. In the interest of completeness, additional types of CIFs that are associated with SOT will briefly be introduced.

Reference [198] reports the existence of a further type of CIF in (Ga,Mn)As that acts in the direction out of the sample plane. This CIF is distinct from field-like CIFs as it produces an anti-damping rather than field-like torque on the magnetization, and its origins lie with the same quantum mechanical Berry curvature mechanism that is responsible for the intrinsic anomalous and spin Hall effects. The out of plane anti-damping CIF requires the generation of an interband type non-equilibrium spin polarisation that is non-collinear with the magnetization orientation, and so both in-plane field-like and out of plane anti-damping-like CIFs can occur simultaneously in (Ga,Mn)As.

SOT has been extensively investigated in magnetic multilayer systems, typically consisting of a heavy non-magnetic metal interfaced with a ferromagnetic metal[192][193][210][211][212]. These systems have several advantages over (Ga,Mn)As for use in SOT experiments, including their high conductivities which allow for large current densities to be achieved, and a greater ability to tailor magnetic properties to enhance switching efficiency. However, the structure of such multilayers makes it difficult to uncover the microscopic origin of the SOT effect. Two main contributions are usually considered. Firstly, due to the structural asymmetry an intrinsic Rashba SOC arises at the interface between the magnetic

and non-magnetic layers which can penetrate into a significant portion of the thin ferromagnetic layer, allowing for the ISGE and associated CIF on the magnetization. Secondly, current flowing through the non-magnetic layer generates a transverse spin current due to the spin Hall effect (SHE) which is injected to the ferromagnetic layer, causing a STT on its magnetization. In this investigation (and generally in (Ga,Mn)As samples), current only flows through the single (Ga,Mn)As layer and so a SHE-STT type CIF is not possible.

4.3 Experiment

This section presents the experimental method used in this investigation to measure CIFs in (Ga,Mn)As. A brief overview of previous experimental studies of CIFs in (Ga,Mn)As is given to outline existing measurement techniques and the results established from these measurements. The experimental technique in this investigation is then described in detail and compared to the existing measurement techniques, and Hall bar design and sample choice are considered. Finally, an anomalous Nernst effect signal detected in the CIF measurements is presented and characterised.

4.3.1 Previous experimental studies of CIFs in (Ga,Mn)As

4.3.1.1 Measurement techniques

In addition to the present study, there have been to date five published experimental studies of CIFs in (Ga,Mn)As using two distinct experimental techniques. The first of these is the 'weak field rotation technique' used in references [190], [191], and [119]. Here a large current density is applied to a (Ga,Mn)As sample to generate CIFs, and a non-saturating external field is rotated in the sample plane, so the magnetization orientation depends on the strength and orientations of the external field, anisotropy field, and CIFs. Magnetization orientation is tracked by the planar Hall effect (PHE), and at some angle of external field the magnetization will begin to switch from one easy direction to another. By comparing the switching angles for positive and negative applied current, the size of the CIFs can be inferred from a geometrical relation between the angle of the external field at the start of the magnetization switching, the angle of the magnetization at the start of the magnetization switching, and the external field strength. The strength of the magnetic anisotropy is indirectly considered within this geometrical relation. The magnetization switching used to infer the CIFs appears to be domain-like switching in references [190] and [119], whereas it is claimed to be single-domain coherent switching in reference [191], achieved by ensuring the external field strength is greater than the anisotropy field.

The second technique, named 'spin-orbit ferromagnetic resonance (SO-FMR)', utilizes resonant excitation of the magnetization of the (Ga,Mn)As sample by passing a microwave-frequency current through it, and is used in references [196] and [198]. SO-FMR differs from conventional FMR experiments in that it is the CIFs from the SOT mechanism that drive the magnetization precession as

opposed to an external time-varying field, while the magnetization dynamics are detected through anisotropic magnetoresistance (AMR) rather than microwave absorption. Microwave frequency ac current is passed through the (Ga,Mn)As sample, which generates time varying CIFs that drive magnetization precession, resulting in a time-varying longitudinal resistance due to AMR. The frequency of the longitudinal resistance is equal to that of the ac current and so a dc voltage is generated across the sample, the magnitude of which depends on the amplitude of the magnetization precession and its phase with respect to the ac current. The resonant frequency of the magnetization and therefore magnitude of the dc voltage across the sample varies as an external field is swept, resulting in a lineshape profile, the peak of which consists of symmetric and antisymmetric Lorentzian components that depend on out of plane and in-plane CIFs respectively. A fitting procedure can then be applied consistently to the field sweep lineshapes across several external field orientations to obtain the magnitude and orientations of the CIFs generated by the ac current (see supplementary information of reference [196]).

4.3.1.2 Experimental findings

References [190], [191], [196], and [119] investigate (Ga,Mn)As samples with Mn concentration in the range of 5%-8%, and all confirm a linear relation between CIF magnitude and current density, with a CIF per current density ratio of the order 1Oe per MA/cm^2. In references [190] and [191] the Dresselhaus and Rashba fields cannot be separated, whereas in references [196] and [119] they are independently evaluated by the nature of the SO-FMR measurement and the use of Hall bars along different current directions respectively. In both cases it is seen that Dresselhaus to Rashba field ratio is around 3:1. Reference [191] measures a linear combination of the Dresselhaus and Rashba fields as a function of temperature and observes that the CIFs increase with increasing temperature by a factor of around 3 from 30K-110K. An unpublished study[209] of the variation of the Dresselhaus and Rashba fields assessed independently with temperature as measured by SO-FMR shows both fields increase with increasing temperature, again by a factor of around 3 over a 5K-130K temperature range. Reference [196] also measures the CIFs in a tensile-strained (Ga,Mn)(As,P) sample, and it is seen that both the Dresselhaus and Rashba CIFs take opposite orientations as to the case of compressively-strained (Ga,Mn)As, the magnitude of the CIFs are larger than in (Ga,Mn)As, and that the Rashba fields are much closer in magnitude to the Dresselhaus fields than they are for (Ga,Mn)As. Finally, in reference [198] the anti-damping like out of plane CIF is identified using SO-FMR and is seen to have a comparable magnitude to the field like in-plane CIFs, as well as the expected symmetry with respect to the Dresselhaus and Rashba fields.

4.3.2 Method

The technique used in this investigation to obtain the CIFs in (Ga,Mn)As, referred to as the 'field sweep technique', consists of two components: PHE experimental measurements while sweeping an external field, and numerical fitting to the ex-

perimental data using a single magnetic domain model. This section describes the measurement procedure in the context of measurements made on the 12% Mn doped, optimally annealed, 25nm thick (Ga,Mn)As Hall bar sample studied in this investigation, but the principles are applicable to a range of DMS samples.

4.3.2.1 Experimental measurement

At a given temperature, a constant dc current of density 1.26MA/cm^2 was passed from the source to drain contact of the (Ga,Mn)As Hall bar ('positive' current), and both the longitudinal (R_{xx}) and transverse (R_{xy}) resistances were measured using a standard 4-probe configuration. The magnitude of this current density is similar to those reported in references[190][191] and is sufficient to produce CIFs of detectable sizes in the (Ga,Mn)As sample. With the positive current applied and R_{xy} being recorded continuously, an external field was swept in the plane of the sample from -4kOe to +4kOe at angles of 0^o, 45^o, 90^o, and 135^o to the direction of the Hall bar channel in separate measurements. The current direction was then reversed ('negative' current), and the field sweeps along the four in-plane directions were repeated. Unlike other measurements in this thesis where the angle of the in-plane external field is varied by rotating the magnetic field around the sample, in these measurements the sample itself is rotated (by a rotatable sample probe header) in the plane of the field, the direction of which is held constant. This allows the component of the external field applied out of the sample plane to be minimised by rotating the external magnet. Overall this approach allows less control of the in-plane field direction, but greater control of the out-of-plane field direction.

As discussed in more detail in chapter 3, R_{xy} that arises from the PHE is sensitive to the orientation of the magnetization with respect to the current direction, i.e. the PHE is a probe of the magnetization orientation. The PHE can therefore be used to detect magnetic fields that act on the magnetization. An example of the variation of R_{xy} as the external field is swept along the four in-plane directions is shown in figure 4.4.**(a)**. Here positive current flows along the [100] direction. The figure is typical of the PHE behaviour of a ferromagnet with in-plane uni-axial anisotropy rotating its magnetization to an opposite orientation, and can be described in the six stages indicated on the figure by considering the different fields that act on the magnetization: H_{ext} (external field), H_U (uni-axial anisotropy field), H_C (cubic anisotropy field), H_R (Rashba CIF), and H_D (Dresselhaus CIF). In the experimental set up used, the earth's magnetic field (H_{earth}) also acts on the sample during measurements, with its component in the plane of the sample always being perpendicular to H_{ext}, however for reasons discussed in section 4.3.2.2 it is ignored in this analysis. For a given measurement, H_{ext} varies while H_U, H_C, H_R, and H_D remain constant. At any point in a field sweep the magnetization orientation depends on the relative sizes and directions of the five different fields. From the subsequent fitting analysis it is found that H_U is around 1 order of magnitude larger than H_C and around 2 orders of magnitude larger than H_D and H_R across the measured temperature range, but within the limits of this experiment contributions from all of the fields are detectable. Consider the case of field being swept along the [110] hard axis (135^o/315^o to the current direction), shown by the

red markings and arrows in figure 4.4, for different stages in the sweep indicated by the red numbers in the figure.

• **1.** H_{ext} is much larger than all the other fields, and so the magnetization is saturated in the direction of H_{ext}.

• **2.** As H_{ext} is swept from -4kOe towards zero, H_U, and to a lesser extent H_C, H_R, and H_D become increasingly important, and the magnetization orientation depends on the relative sizes and directions of all of the fields, but H_{ext} and H_U are most significant.

• **3.** H_{ext} is nearly at zero and the magnetization lies nearly parallel to the $[1\bar{1}0]$ direction of the easy axis, but contributions from H_R and H_D do cause a measurable tilt on the magnetization.

• **4.** As H_{ext} passes through zero, the magnetization rotates in-plane across the hard axis and towards the opposite easy axis direction, $[\bar{1}10]$, with H_R and H_D again making a measurable contribution to its orientation.

• **5. and 6.** H_{ext} goes towards +4kOe and becomes the increasingly dominant factor in the magnetization orientation as tilts from H_R and H_D become more suppressed.

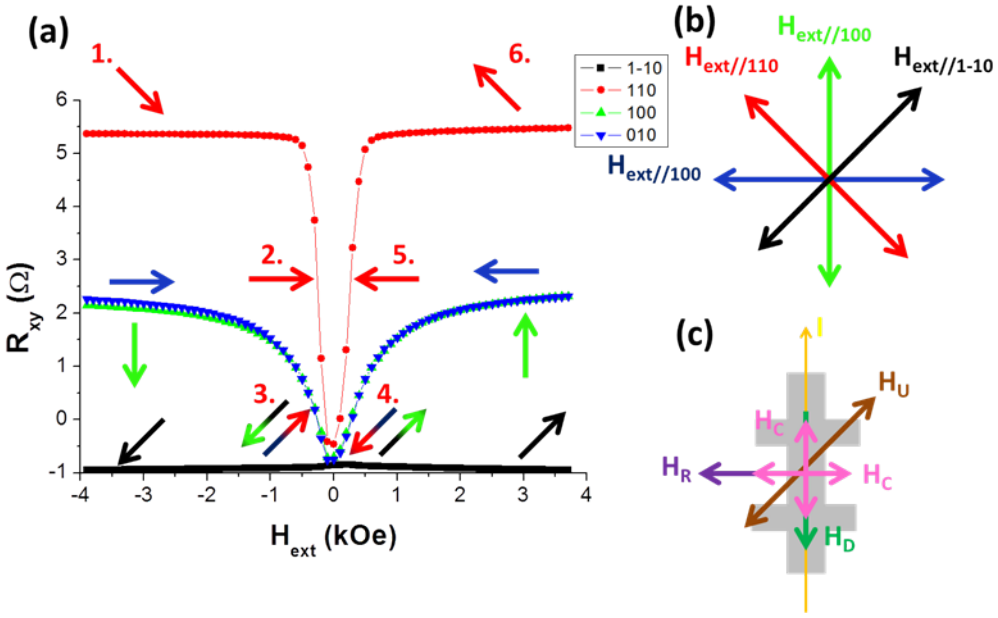

Figure 4.4: **(a)** R_{xy} against H_{ext} for current along the [100] crystalline direction and H_{ext} along various in-plane crystalline directions. Arrows indicate direction of magnetization at given point during the field sweep. **(b)** Direction of crystalline axes/field sweep directions, **(c)** Direction of current as well as anisotropy and current induced fields.

In order to extract the CIF contributions to the magnetization switching behaviour it is necessary to repeat the same field sweep measurement for positive and negative currents. While H_{ext}, H_U, and H_C are all independent of current direction, both H_R and H_D act in opposite directions for opposite directions of current flow. The PHE has a 180^o symmetry, and so the effects of H_{ext}, H_U, and H_C give identical contributions to R_{xy} for both positive and negative current directions, whereas

H_R and H_D can give opposite contributions to R_{xy} for opposite current directions. Ignoring thermal voltages that can be factored out (see section 4.3.6), for a given field sweep, subtracting the negative current R_{xy} data from the positive current R_{xy} data gives a difference in R_{xy} (ΔR_{xy}) that depends only on H_R and H_D.

ΔR_{xy} due to the CIFs is more apparent in some geometries than others for two reasons. Firstly, if the CIFs are parallel/anti-parallel to the magnetization they will not cause a tilt in its orientation that would give a direct contribution to ΔR_{xy}, though they will make it easier or harder for other fields to reorientate the magnetization. Secondly, if the magnetization is at a $45^o/135^o/225^o/315^o$ angle to the current, a small tilt either side of this orientation will give the same change in R_{xy} due to the symmetry of the PHE, i.e. ΔR_{xy} is zero. Nevertheless, the effects of the CIFs on ΔR_{xy} are sufficiently distinguishable when the whole sweep is considered for all geometries, and this allows for the consistent fitting across all four external field sweep directions in the second part of the field sweep technique of this investigation.

4.3.2.2 Numerical fitting

The second part of the field sweep technique to measure CIFs in (Ga,Mn)As is numerical fitting to the field sweep data sets. For the fitting procedure, (Ga,Mn)As is assumed to have single domain ferromagnetism, and its magnetic free energy density is modelled by the equation:

$$U = H_U sin^2\theta - \frac{H_C}{4} sin^2 2\theta - H_{ext} cos(\theta - \theta_H) - H_{eff1} cos(\theta - \theta_I - \frac{\pi}{2}) - H_{eff2} cos(\theta - \theta_I) \tag{4.3}$$

where U is the magnetic energy density, H_U is the in-plane uni-axial anisotropy field, H_C is the in-plane cubic anisotropy field, H_{ext} is the external field, H_{eff1} is the CIF perpendicular to the magnetization, H_{eff2} is the CIF parallel to the magnetization, θ is the magnetization angle with respect to the uni-axial easy axis $[1\bar{1}0]$, θ_H is the external field angle with respect to the uni-axial easy axis $[1\bar{1}0]$, and θ_I is the current direction angle with respect to the uni-axial easy axis $[1\bar{1}0]$. The equilibrium position of the magnetization will be that with the lowest associated energy cost when all the fields acting on it are considered, i.e. θ which minimises equation 4.3.

The magnetization orientation of the (Ga,Mn)As sample during the field sweep measurements can be inferred from the PHE, which varies as $sin(2\theta - 2\theta_I)$. The R_{xy} signal contains contributions from the PHE, the anomalous Nernst effect (ANE - again see section see section 4.3.6), and R_{xx} due to an unintentional misalignment of the transverse Hall probes, and is given by:

$$R_{xy} = A_{PHE} sin(2\theta - 2\theta_I) + A_{ANE} cos(\theta - \theta_I) + R_{mis} \tag{4.4}$$

where A_{PHE} is the PHE amplitude, A_{ANE} is the ANE amplitude, and R_{mis} is the R_{xx} contribution to R_{xy} from misalignment. For a given set of input fields, equation 4.3 is minimised at discreet steps for a varying H_{ext} to obtain the magnetization orientation, and the corresponding R_{xy} value is generated from equation 4.4. This

process yields model R_{xy} field sweep plots which are then compared with those obtained from experiment. This is the basis of the procedure used to fit to the experimental data. All fits were performed using the 'Rashbatorque' MATLAB code edited by Dr Kevin Edmonds.

For a given current direction and temperature there are four experimental R_{xy} ΔR_{xy} and against H_{ext} plots corresponding to the four field sweep directions. The key to the fitting procedure is to establish a fixed value for each of the free variables from a trial and error style method so that when all variables are fixed the model R_{xy} and ΔR_{xy} against H_{ext} plots for all four field sweep directions have the best least squares agreement with the experimental plots. To obtain some of the variables in the fitting procedure it is preferable to discard the effects of the CIFs. This is done in the model plots by setting H_{eff1} and H_{eff2} to zero, while for the experimental data it is necessary to average the positive and negative current R_{xy} against H_{ext} plots. The variables of A_{PHE}, R_{mis}, and θ_H and θ_I (which will both be subject to a slight experimental misalignment) are relatively easy to obtain from fitting to the R_{xy} against H_{ext} plots. With these variables set a more rigorous simultaneous variation of H_U and H_C is performed to determine their values. A_{ANE} is found by a simple fit to high field regions of the ΔR_{xy} against H_{ext} plots. Finally, H_{eff1} and H_{eff2} are determined by rigorously fitting to the ΔR_{xy} against H_{ext} plots. For the $[1\bar{1}0]$ and [110] current directions H_{eff2} is set to zero in accordance with the expected symmetry of the CIFs and thus only H_{eff1} needs to be varied, while for the [100] current direction H_{eff1} and H_{eff2} are varied simultaneously. The fitting procedure makes three key assumptions:
1. The magnetization remains single domain throughout the field sweep (which is valid for all regions except $H_{ext} \approx 0$ where domain switching takes place[213]).
2. The sizes of the CIFs do not vary with angle between magnetization and current.
3. Any out of plane CIF does not influence the magnetization dynamics during the field sweep, so out of plane CIFs can be ignored in the fitting.

The magnitude of H_{earth} that acts in the sample plane during the field sweep technique was measured with a Gaussmeter to be around 0.2Oe, a magnitude comparable to the values of H_R obtained in this experiment, but 1 and 2 orders of magnitude smaller than the obtained values H_C, and H_U respectively. The component of H_{earth} acting out of the sample plane is negligible and not large enough to affect the magnetization orientation given the strong in-plane anisotropy of the (Ga,Mn)As sample used in the experiment. While the effects of H_R on magnetization are distinguishable in the R_{xy} against H_{ext} data sets (for a single current direction), H_R cannot be accurately obtained through fitting to these plots as the shape of R_{xy} is dominated by the much larger H_{ext}, H_U, and H_C fields (hence why H_R is obtained from fits to the ΔR_{xy} against H_{ext} data). H_{earth} does not change with current polarity, and therefore its effects on magnetization are only apparent in the R_{xy} against H_{ext} data sets. However, like H_R, the small magnitude of H_{earth} means that a satisfactory fit of R_{xy} against H_{ext} can be achieved without including a H_{earth} term in equation 4.3. As H_{ext}, H_U, and H_C can be consistently obtained without accounting for H_{earth}, this justifies the neglect of H_{earth} in the fitting and analysis of this experiment.

4.3.3 Comparison with existing techniques

The field sweep technique has some similarities to the weak field rotation technique used in references [190], [191], and [119]. Both techniques apply large positive and negative currents to generate oppositely orientated CIFs and use the PHE to monitor their effects on the magnetization orientation, and in both techniques the magnetization orientation depends on the interplay of H_{ext}, H_U, H_C, H_R, and H_D. There are also differences between the two techniques. Firstly, in the weak field rotation technique the CIFs are inferred from a geometrical argument relating to various angles between magnetization, current, and H_{ext} at the starting point of domain switching of the magnetization, whereas in field sweep technique the CIFs are inferred from consistent fits to experimental data over a finite ($\approx$ 2kOe) field range where coherent magnetization rotation is observed. Secondly, in the weak field rotation technique, the strength of the magnetic anisotropy appears to only be indirectly considered within the geometrical formulation to obtain the CIFs, however in the field sweep technique the it is evaluated independent of the CIFs for each measurement. As the magnetic anisotropy of (Ga,Mn)As changes with temperature, as well as the strength of domain pinning fields, the field sweep technique therefore seems a more appropriate method to use to study the temperature dependence of the CIFs.

The field sweep technique is more distinct when compared to SO-FMR, but again it does have a few similarities, namely the use of AMR to track the magnetization dynamics, as well as the use of experimental field sweeps along several in-plane orientations and consistent numerical fits to the data sets to obtain the value of the CIFs. However, SO-FMR is fundamentally different to the field sweep technique; in SO-FMR the time-varying CIFs drive a continuous magnetization precession - the amplitude and phase of which is measured via a frequency mixing effect of the supply current and AMR signals, whereas in the field sweep technique the static CIFs torque the magnetization to a steady state equilibrium position (as the magnetization precession is damped) which is detected by long time-scale PHE measurements. In SO-FMR all orientations of CIFs must be considered as these can lead to magnetization precession around a constant vector position, but in the field sweep technique only CIFs in directions that will give a steady state change in magnetization orientation need to be accounted for. For a sample with strong in-plane magnetic anisotropy, SO-FMR is capable of detecting out of plane CIFs while the field sweep technique is not. Additionally, the requirement of magnetization precession rather than reorientation means that SO-FMR is capable of detecting CIFs an order of magnitude smaller than the field sweep technique. The advantage of the field sweep technique over SO-FMR is in the greater simplicity of the experimental measurement method and numerical fitting procedure.

4.3.4 Choice of sample

As discussed in section 1.2, there are several ways in which the properties of (Ga,Mn)As can be tuned, and so there is a degree of control in selecting a (Ga,Mn)As sample with characteristics appropriate to a given experiment. The three most important characteristics of the (Ga,Mn)As sample to consider for a SOT experiment

are the sample conductivity, magnetic anisotropy, and the strength of SOC.

• **Conductivity:** CIFs are known to scale linearly with current density, and so in most cases a relatively high conductivity is desirable in order to perform measurements with higher current densities, thus yielding larger CIFs which should be easier to detect without the experimental issues that arise from Joule heating. Generally conductivity increases with increasing Mn doping up to concentrations of around 5%[55], while annealing (Ga,Mn)As from an as-grown state is also a well established technique to increase conductivity[123].
• **Magnetic anisotropy:** In principle the field sweep technique should be equally applicable to samples with in-plane uni-axial or bi-axial magnetic anisotropy as both uni-axial and cubic anisotropy fields are included in equation 4.3. However, in the case of strong uni-axial anisotropy, the magnetic switching behaviour becomes simpler to model, and so H_U and H_C are easier to determine from the trial and error style fitting method. Having a strong in-plane anisotropy is also beneficial when considering the influence that any out of plane CIF could have on the magnetization. If the in-plane anisotropy is sufficiently large, an out of plane CIF should not influence the magnetization reorientation process, and hence it can be neglected from the fitting analysis which greatly simplifies the procedure. Optimally annealed (Ga,Mn)As samples with higher Mn doping concentrations grown on GaAs (or any other substrate/buffer that promotes compressive strain in the layer) tend to favour an in-plane uni-axial anisotropy[73][71][62].
• **SOC:** Stronger SOC should lead to a larger ISGE, and hence larger CIFs that act on the magnetization. Linear Dresselhaus SOC varies with tetragonal strain, while shear strain can theoretically account for Rashba SOC. Straining the (Ga,Mn)As sample can therefore potentially increase the strength of the CIFs. In (Ga,Mn)As, strain can be manipulated by choice of substrate[214] or use of an external transducer[76], but varying the Mn concentration can be another (less drastic) method of varying the strain, owing to the different sizes of the Ga and Mn atoms[115].

Taking the above mentioned factors into consideration, an optimally annealed, 12% Mn doped, 25nm thick (Ga,Mn)As sample (Mn440) was chosen for the experiment due to its relatively high conductivity, uni-axial magnetic anisotropy at all temperatures up to T_c, and large Mn doping which may lead to an increased Dresselhaus style SOC. The high T_c of the sample (170K) also allows for a wide-ranging temperature dependence study.

4.3.5 Hall bar design and temperature control

Preliminary measurements in this investigation were performed on 50μm wide, 1140μm long Hall bars of the Mn440 sample. A relatively large current needed to be applied through the bar to achieve a current density of the order of 1MA/cm^2, and this caused significant Joule heating, as indicated by the increase in R_{xx}. As discussed in section 4.3.6, current-induced heating is detrimental SOT experiments. To reduce the applied current needed to achieve a 1MA/cm^2 current density, new Hall bar structures were fabricated to reduce the conducting channel width and length within the limits of optical lithography and wet etching. Hall bars of various dimensions were designed using the Wavemaker software package, and etch and

contact photomasks were produced by JD Phototools. After processing and testing multiple Hall bars, it was found that a 'two arm' Hall bar of width 10μm and length between contacts of 10μm was the most suitable for the SOT investigation due to the combination of significantly reduced sample heating and reasonably small contact misalignment.

The sample temperature can be inferred from the value of R_{xx}, and reflects the temperature of the carriers rather than the lattice. When applying a 1.26MA/cm^2 current density to the 10μm dimension Hall bars, the sample temperature immediately increased by around 10K-15K but quickly saturated. A slow calibration temperature sweep was performed on the sample with a low current density applied where the effects of sample heating are negligible. The cryostat sample space temperature, given by a thermocouple placed next to the sample, was varied and R_{xx} of the sample recorded. The slow scan speed and low applied current give confidence that the temperature of the thermocouple is approximately the same as that of the sample, and thus the sample resistance can be used as a sample temperature gauge. The sample temperature could then be varied by controlling the cryostat sample space temperature, bearing in mind that for high applied current density there will always be an offset between the sample and cryostat temperatures.

4.3.6 Vertical temperature gradient and anomalous Nernst effect

Observing the effects of the CIFs in the field sweep technique experiment relies on the PHE contribution to the R_{xy} signal being different for positive and negative applied currents. Ideally the PHE should be the only contribution to the R_{xy} signal, and the combination and symmetry of the PHE and CIFs should be the only contribution to the ΔR_{xy} signal. Experimentally there is another contribution to the ΔR_{xy} signal which can be seen in the field sweep data, the size of which is larger than that from the PHE/CIFs. Further study of this additional ΔR_{xy} signal shows that it arises due to the ANE.

The ANE is the thermoelectric counterpart of the AHE (see section 1.3.3.2), and has been observed in (Ga,Mn)As[85] and various ferromagnetic metals[215][216], multilayer structures[217], spinel materials[218][219], and perovskites[220]. It is a SOC phenomenon, and the microscopic physics behind the effect is similar to the AHE (asymmetric deflection and/or scattering of spins), however in the ANE the charge separation is induced by a temperature gradient (thermoelectric effect) rather than an electrical current. The ANE has the same symmetry as the AHE but with the temperature gradient replacing the current flow, i.e. in conducting ferromagnetic material with significant SOC, a temperature gradient will generate a voltage that varies with the cross product of the magnetization orientation and the direction of the temperature gradient. While the AHE is nearly always measured experimentally in a 'current in-plane/magnetization out of plane' geometry, the ability to establish sizeable temperature gradients both in and out of the sample plane have lead to reports of the ANE in both 'temperature gradient in-plane/magnetization out of plane'[85] and 'temperature gradient out of

plane/magnetization in-plane' geometries[216].

4.3.6.1 Appearance of non-PHE signal in field sweep data

From symmetry considerations, it is clear that PHE/CIFs are not the only contribution to the ΔR_{xy} signal observed in the experimental field sweep data. For example, consider the ΔR_{xy} against H_{ext} plots, where H_{ext} is swept along the $[1\bar{1}0]$ direction, shown in figures 4.5 and 4.6 for the cases of current along the $[1\bar{1}0]$ and [100] directions respectively. Each plot shows evidence of the behaviour of the ΔR_{xy} signal that is inconsistent with the expected PHE/CIFs contribution, confirming the presence of an additional contribution to the ΔR_{xy} signal. For the geometry of the figure 4.5 plot, the magnetization remains parallel/antiparallel to the $[1\bar{1}0]$ direction at all points during the field sweep, and so the effect of the CIFs is always to tilt the magnetization either side of the $[1\bar{1}0]$ direction for positive/negative applied current. Due to the PHE symmetry, this should increase/decrease R_{xy}, and hence give a finite ΔR_{xy} signal. As H_{ext} increases, the tilt on the magnetization from the CIFs will be reduced, thus also reducing ΔR_{xy}, and this behaviour is seen as H_{ext} is swept between -1kOe to +1kOe. As H_{ext} increases further, ΔR_{xy} would be expected to continue to decrease to zero as the magnetization becomes fully saturated by H_{ext}. Instead ΔR_{xy} approximately saturates to a finite value at H_{ext} $\approx$ 1kOe, and remains constant as the magnitude of H_{ext} increases, suggesting that the PHE/CIF contribution is not responsible for the ΔR_{xy} signal in the high field limit. For the geometry of the figure 4.6 plot, again the magnetization remains parallel/antiparallel to the $[1\bar{1}0]$ direction at all points during the field sweep, but in this case the current is at a 45^o angle to the magnetization. While the CIFs should tilt the magnetization either side of the $[1\bar{1}0]$ direction for positive/negative current, the symmetry of the PHE is such that the opposite tilts will give the same change in the R_{xy} signal, and so there should be no ΔR_{xy} signal from the PHE. The observed presence of a finite ΔR_{xy} signal across the entire field range again indicates that there is an additional contribution to the ΔR_{xy} signal besides PHE/CIFs.

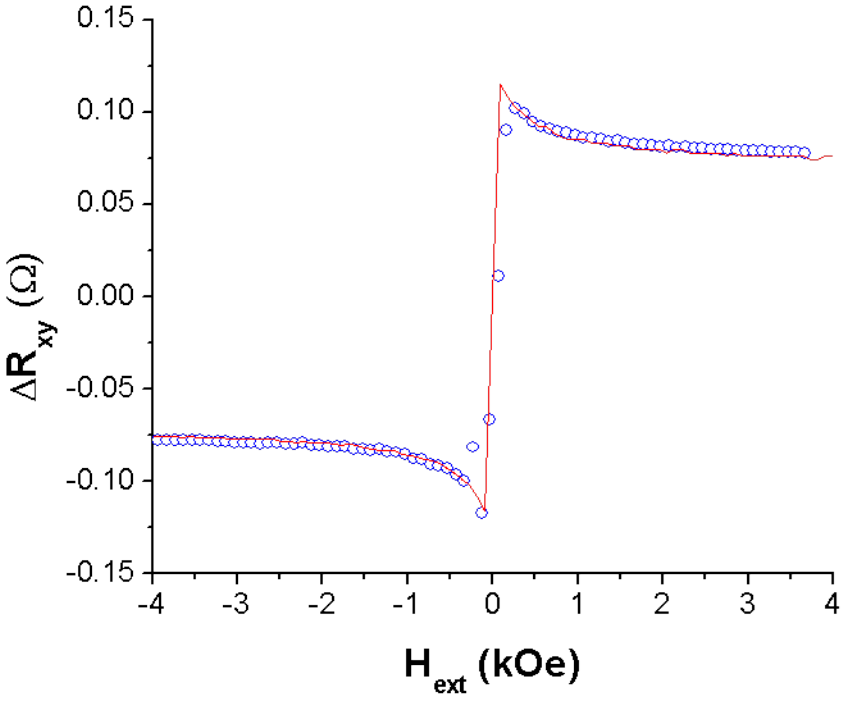

Figure 4.5: ΔR_{xy} against H_{ext} for current along the $[1\bar{1}0]$ direction and H_{ext} along the $[1\bar{1}0]$ direction at a sample temperature of 71K. Red circles are measured data points, blue line is the fit.

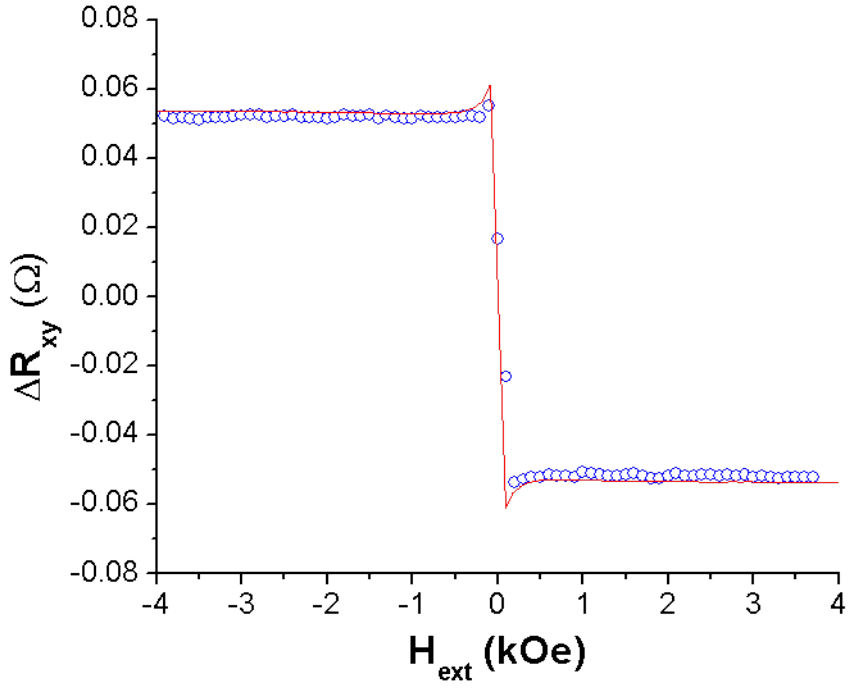

Figure 4.6: ΔR_{xy} against H_{ext} for current along the [100] direction and H_{ext} along the $[1\bar{1}0]$ direction at a sample temperature of 101K. Red circles are measured data points, blue line is the fit.

4.3.6.2 Characterisation of ANE signal

In order to identify the source of the additional ΔR_{xy} signal and characterise its behaviour, field rotation measurements were performed on the Mn440 (Ga,Mn)As sample as a function of current density, external field magnitude, current direction, and temperature. For the majority of the these measurements the magnitude of the external field used is 20kOe as this is sufficient to ensure the magnetization tracks the external field as well as negating any effects the CIFs have on it. The external field was rotated 360° in the plane of the sample in 5° steps, with positive current applied and R_{xy} and R_{xx} being recorded. The process was then repeated but with negative current applied, and so the difference of the positive and negative current field sweep data sets gives ΔR_{xy} and ΔR_{xx} as a function of the angle between current and magnetization. The ΔR_{xy} results are shown in figures 4.7-4.10:

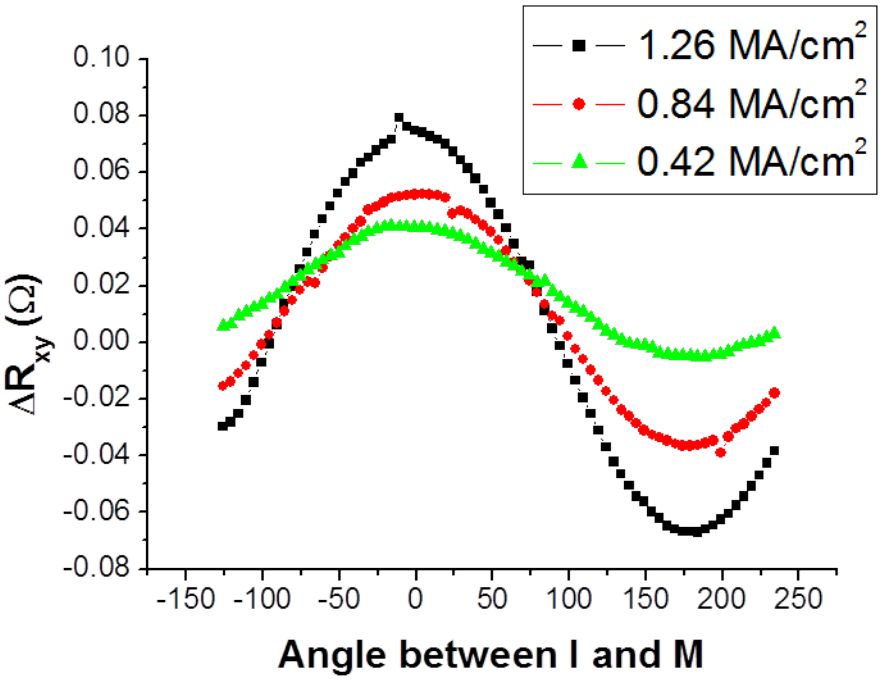

Figure 4.7: ΔR_{xy} as a function of angle between current and magnetization for various current densities. Measurements are for the Mn440 sample with current along the [110] direction, at a sample temperature 119K, and with an external field magnitude of 20kOe.

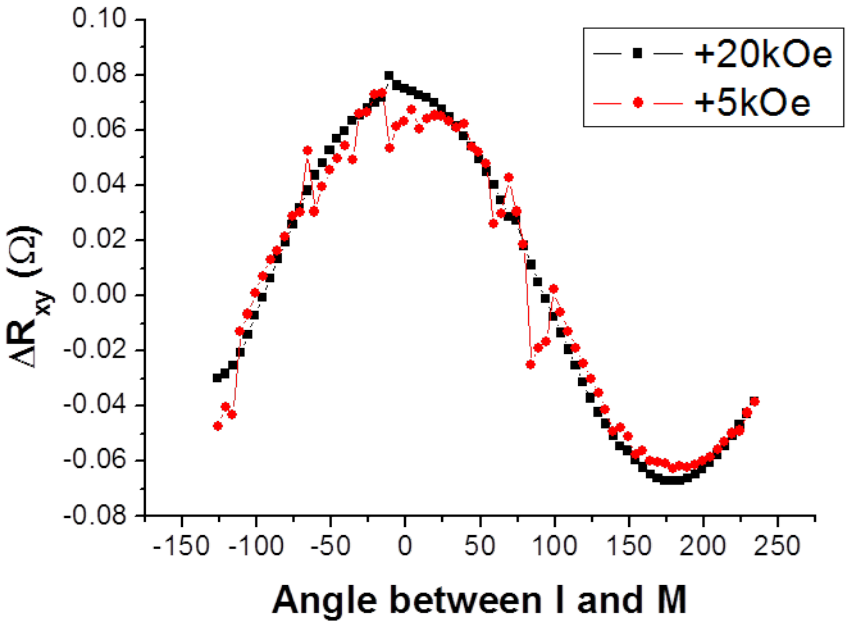

Figure 4.8: ΔR_{xy} as a function of angle between current and magnetization for external fields of magnitude 20kOe (black) and 5kOe (red). Measurements are for the Mn440 sample with current along the [110] direction, at a sample temperature 119K, and a current density of 1.26MA/cm^2.

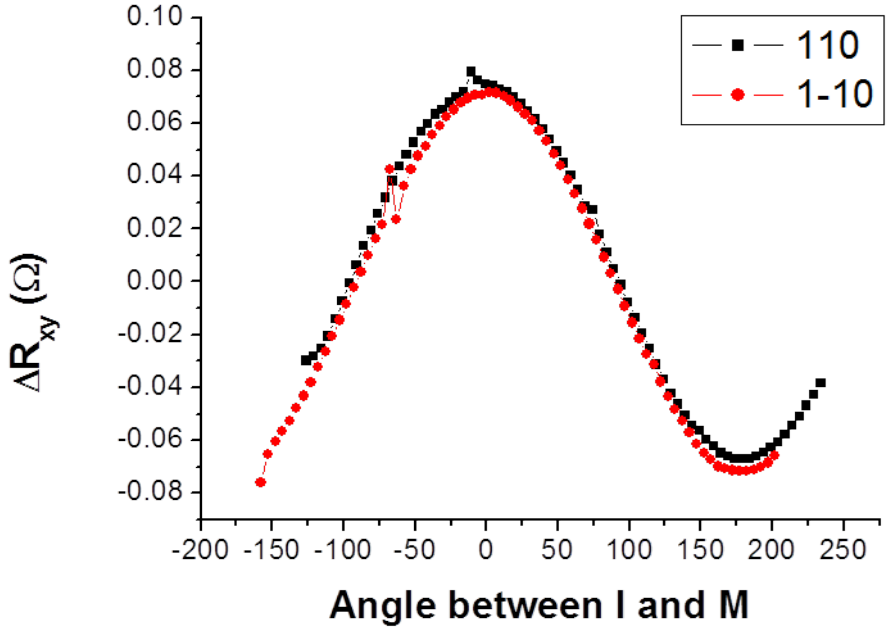

Figure 4.9: ΔR_{xy} as a function of angle between current and magnetization for current along the [110] (black) and [1$\bar{1}$0] (red) directions. Measurements are for the Mn440 sample at a sample temperature 119K, a current density of 1.26MA/cm^2, and with an external field magnitude of 20kOe.

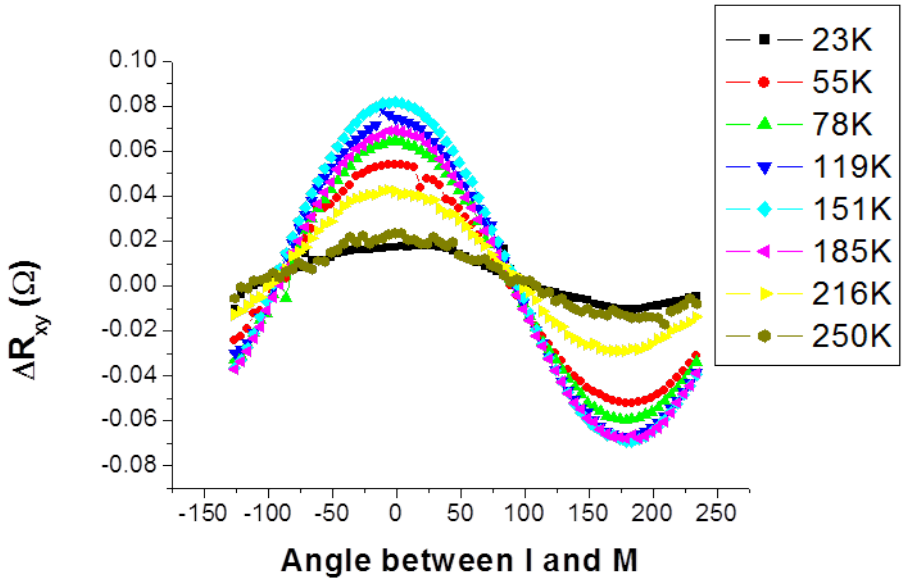

Figure 4.10: ΔR_{xy} as a function of angle between current and magnetization for various sample temperatures. Measurements are for the Mn440 sample at a sample temperature with current along the [110] direction, a current density of 1.26MA/cm^2, and with an external field magnitude of 20kOe.

For the following analysis, the ΔR_{xy} contribution from PHE/CIFs is assumed to be suppressed by the large external magnetic field. The main findings from the characterisation measurements are:
• Figures 4.7-4.10 all show the general trend that ΔR_{xy} varies as $\cos(\phi)$, where ϕ is the angle between the current and magnetization.
• Figure 4.7 demonstrates that the magnitude of ΔR_{xy} increases approximately linearly with increasing current density.
• Figure 4.8 confirms that ΔR_{xy} remains constant with external field magnitude, which is consistent with the high field regions of the field sweep technique data.
• The data for the $[1\bar{1}0]$ and [110] current directions measured in figure 4.9 along with [100] and [010] current directions (measured separately and not shown) show that ΔR_{xy} is independent of current direction with respect to the crystalline axis.
• The magnitude of ΔR_{xy} has an anomalous temperature dependence as seen in figure 4.10.

To investigate the temperature dependence more closely, field rotations at various sample temperatures were also performed on a 2% Mn doped, 50nm thick, optimally annealed (Ga,Mn)As sample (Mn250). The magnitude of ΔR_{xy} as a function of temperature for both Mn440 and Mn250 samples is displayed in figure 4.11:

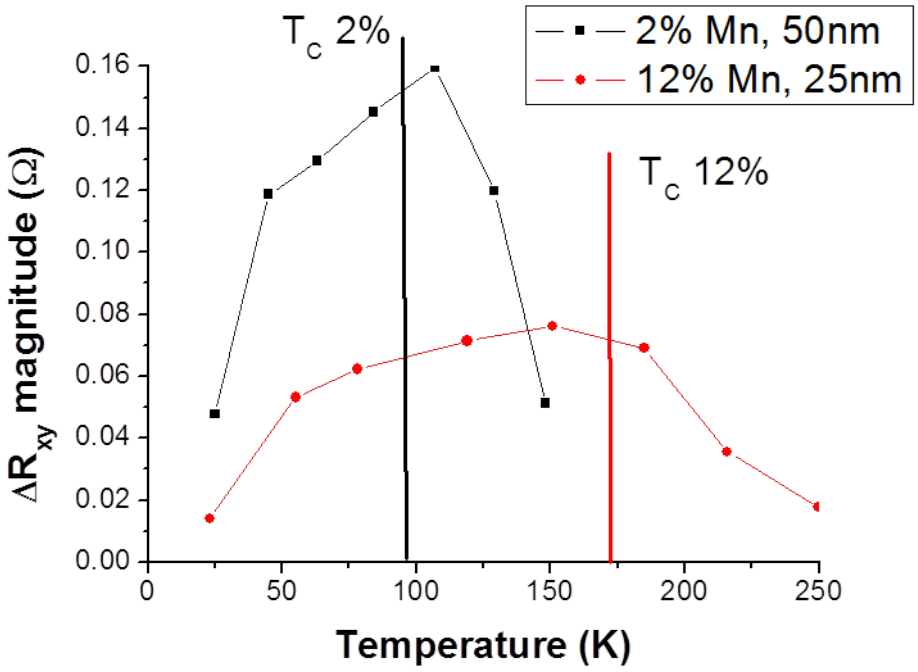

Figure 4.11: Magnitude of ΔR_{xy} as a function of temperature for Mn250 (black) and Mn440 (red).

Figure 4.11 shows that the anomalous temperature dependence of ΔR_{xy} follows a similar trend for both samples: An initial sharp increase in ΔR_{xy} with temperature, followed by a slower increase in ΔR_{xy} with temperature up to a point around T_c, and finally a fairly sharp decrease in ΔR_{xy} to zero with temperature from the point around T_c. It is also apparent from figure 4.11 that the magnitude of ΔR_{xy} in Mn250 is roughly double that of Mn440. As ΔR_{xy} remains present above T_c, to gain further insight into its origin field rotation measurements were performed on Mn250 at a sample temperature above T_c for external fields of magnitudes 20kOe and 5kOe, as shown in figure 4.12:

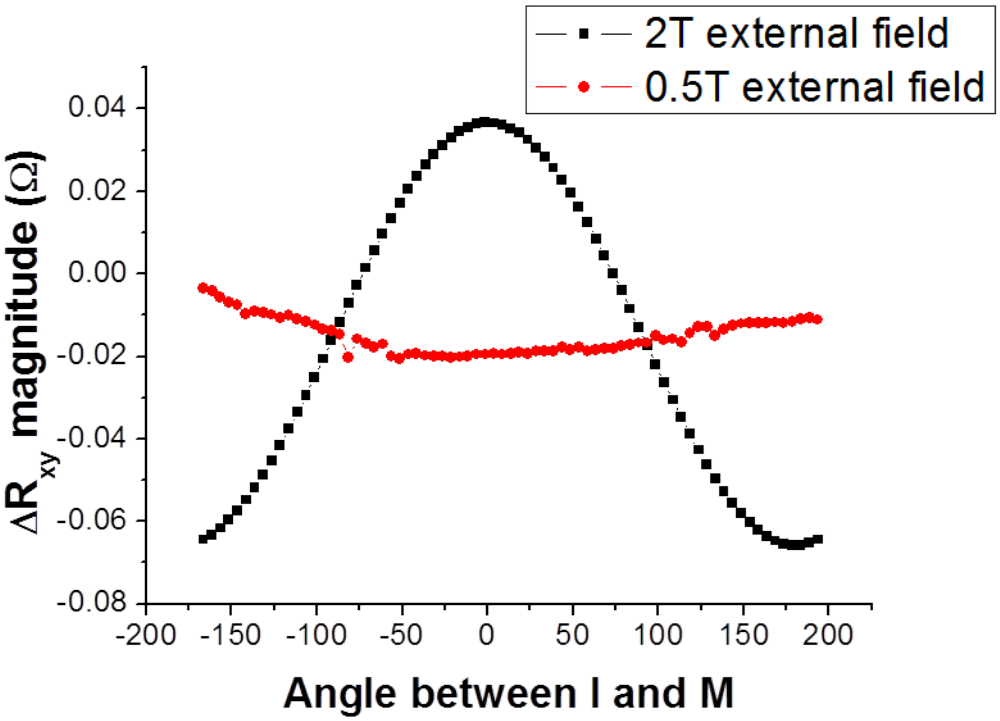

Figure 4.12: ΔR_{xy} as a function of angle between current and magnetization for external fields of magnitude 20kOe (black) and 5kOe (red). Measurements are for the Mn250 sample with current along the [110] direction, at a sample temperature 148K, and a current density of 1.26MA/cm^2.

Unlike measurements below T$_c$, above T$_c$ it can be seen that the size of ΔR_{xy} does depend on the magnitude of the external field.

All of the above trends relate to the ΔR_{xy} signal, but in some of the field rotation measurements a $\sin(\phi)$ trend in the ΔR_{xx} signal (that is the difference between R_{xx} for positive and negative current) is also seen. This trend in the ΔR_{xx} signal is harder to observe than trends in the ΔR_{xy} signal as R_{xx} is more susceptible to drift of the sample temperature than R_{xy}. Only in measurements with a very stable sample temperature does the $\sin(\phi)$ trend become apparent. An example of the ΔR_{xx} signal compared with the ΔR_{xy} signal is shown in figure 4.13:

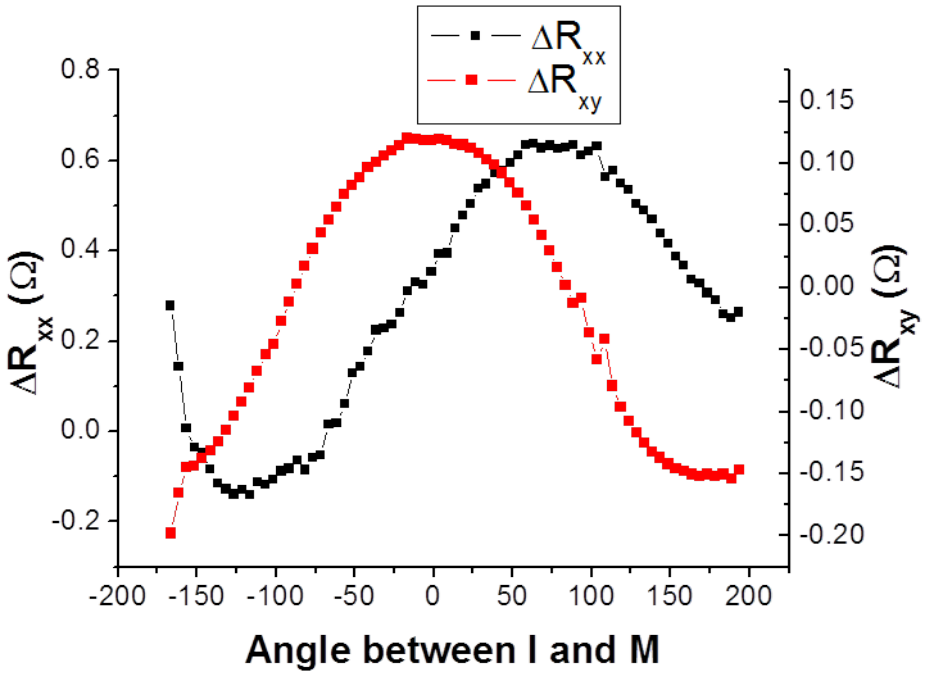

Figure 4.13: ΔR_{xx} (black) and ΔR_{xy} (red) as a function of angle between current and magnetization for an external field of magnitude 20kOe. Measurements are for the Mn250 sample with current along the [110] direction, at a sample temperature 84K, and a current density of 1.26MA/cm^2.

All the observations from the field rotation measurements are consistent with ΔR_{xy} and ΔR_{xx} arising due to the ANE, i.e. an induced voltage (V_{ANE}) that is orthogonal to both the magnetization and a temperature gradient, where in this case the temperature gradient is out of the plane of the sample (vertical temperature gradient). The temperature gradient, and therefore V_{ANE}, are independent of current polarity and so as $R = V/I$, R_{xy} and R_{xx} will change sign with changing current polarity, giving finite ΔR_{xy} and ΔR_{xx} values. V_{ANE} is orthogonal to the magnetization in the sample plane, and so the component of the V_{ANE} sensed by the transverse and longitudinal voltage probes varies sinusoidally (with a 90° phase shift) with the angle between the magnetization and Hall bar (current) direction.

The evidence for the observed ΔR_{xy} signal arising from the ANE/vertical temperature gradient mechanism is the existence of a ΔR_{xx} signal and the respective symmetries of the ΔR_{xy} and ΔR_{xx} signals. Additionally, the trends shown in figures 4.8, 4.9 and 4.12 can also support an ANE explanation for ΔR_{xy} as they show that ΔR_{xy} depends on magnetization and not external field, and that it does not depend on crystalline orientation. The similarity in the temperature dependence of ΔR_{xy} to the transverse Seebeck coefficient of (Ga,Mn)As in reference [85] would also be convincing evidence for the ANE if the size of the temperature gradient is independent of the lattice temperature, however there is insufficient data to determine whether this is the case. The fact that the Mn250 sample, which is twice the thickness of the Mn440 sample, gives a ΔR_{xy} signal that is approximately twice as large may support the involvement of the vertical temperature gradient in the explanation of ΔR_{xy} (reference [85] shows that the magnitude of the ANE is

relatively independent of Mn concentration so only the different thicknesses of the samples is considered in this suggestion).

4.3.6.3 Vertical temperature gradient

A very rough estimate of the size of the vertical temperature gradient can be obtained by assuming a maximum transverse Seebeck coefficient for the (Ga,Mn)As layer of 8μV/K (see reference [85]) and a maximum ANE voltage generated across the 10μm wide Hall bar of the 25nm thick Mn440 (Ga,Mn)As sample of 210μV (V=0.07Ω/3mA). Using the equation ΔT_z = -($\Delta V_{xy} \times dz$)/($S_{xy} \times dy$), where ΔT_z is the temperature difference, S_{xy} the transverse Seebeck coefficient, dz is the length along which the temperature difference occurs (sample thickness), and dy is the length across which the voltage is generated (sample width), a temperature difference is obtained of 0.07K across the 25nm thick layer, so a temperature gradient of 3x10^{6}K/m. A temperature difference of tens of mK over only tens of nanometres may seem unrealistically large. Intentional lateral temperature differences of up to 4K over the several millimetres have previously been reported in (Ga,Mn)As layers[221][222][136], i.e. temperature gradients that are around 4 orders of magnitude less than those inferred from this experiment, while intentional vertical temperature gradients of "a few" K/m to 8000K/m have been reported in Py on MgO substrate[216], Py on Si substrate[223], $Y_3Fe_5O_{12}$[224], graphene on SiO_2[225], and (Mn,Zn)Fe_2 O_4[226], again all significantly less than the estimated vertical temperature gradient in (Ga,Mn)As reported in this experiment.

The striking difference in the size of the vertical temperature gradient in this experiment compared with the vertical and horizontal temperature gradients from the above referenced literature can be explained by their different origins. The referenced temperature gradients are all established by a similar method of thermally contacting one side of the material to a heat source and the other to a heat sink. The material's lattice temperature at the heat source contact is greater than its lattice temperature at the heat sink contact, and so there exists a thermal gradient in the lattice temperature across the material. Thermoelectric phenomena depend upon the temperature of the charge carriers ($T_{carrier}$) rather than the temperature of the host lattice ($T_{lattice}$). Considering lattice heating only, the carriers are approximately in thermal equilibrium with the lattice, $T_{carrier} \approx T_{lattice}$, and so a gradient in $T_{carrier}$ simply reflects a gradient in $T_{lattice}$.

In this chapter's experiment, carriers in the (Ga,Mn)As samples are directly heated by the applied electric field as well as by the lattice. The induced current flow gives the carriers additional kinetic energy, i.e. they are hot carriers that are out of thermal equilibrium with the lattice. For measurements at all temperatures, the (Ga,Mn)As sample either sits in liquid He or is immersed in a liquid He flow, and this allows any Joule heating of the lattice to be quickly dissipated to the surrounding environment. At all temperatures $T_{lattice}$ is therefore assumed to be close to the cryostat sample space temperature despite the large applied current density. It is also assumed there is no significant gradient in the lattice temperature across the (Ga,Mn)As layer. If not a gradient in $T_{lattice}$, what causes the vertical

gradient in $T_{carrier}$ needed to explain the ANE signal? The assumed mechanism is as follows: The hot hole carriers can lose energy via interactions with the lattice, thereby emitting phonons. Carriers can also scatter off phonons or reabsorb them. As one side of the (Ga,Mn)As layer is a free surface, and the other is epitaxially bonded to the substrate, the phonon distribution within the (Ga,Mn)As layer will be non-isotropic, and on average phonons will be propagated towards the substrate. As the degree to which carriers emit, scatter off, and reabsorb phonons is dependent on their vertical position in the lattice, $T_{carrier}$ will also vary with vertical lattice position, and so there will be a vertical gradient in $T_{carrier}$ in the (Ga,Mn)As layer. The significantly lower energy scales needed to heat a carrier compared to heating an atom may then cause larger variations in $T_{carrier}$ across the layer than would be achievable in $T_{lattice}$ though direct lattice heating.

4.3.6.4 Implications on field sweep technique

Given the extent of carrier heating during measurements, one may question if the planar Nernst effect (PNE)[136] also makes any contribution to the ΔR_{xy} signal due to an in-plane temperature gradient. Unlike the ΔR_{xy} signal which is antisymmetric about 180^o, the PNE is symmetric about 180^o, and so any PNE contribution to the ΔR_{xy} signal must be negligible as it is not apparent in the experimental data. Furthermore, the lateral symmetry of the Hall bar structure should make it difficult to establish an unintentional but repeatable in-plane temperature gradient across the multiple devices measured.

The unintentional vertical temperature gradient and the resulting ANE contribution to the ΔR_{xy} signal characterised and discussed in this section is a hindrance to the 'field sweep technique' CIF measurements, but its well defined symmetry allows it to be accounted for when fitting to the data by adding the $A_{ANE}cos(\theta - \theta_I)$ term to equation 4.4. While the contribution to the ΔR_{xy} signal from the ANE is larger than that from the PHE/CIFs, at low fields there is still a significant portion of the ΔR_{xy} signal from PHE/CIFs, which thus allows the 'field sweep technique' experiment to still be a viable way of measuring the CIFs.

4.4 Results and discussion

4.4.1 Field sweep data and fits

An example of the typical R_{xy} against H_{ext}, and ΔR_{xy} against H_{ext} plots for the experimentally measured data and the corresponding fits is shown in figure 4.14. The plots are for field sweeps along all four directions, with current along the $[1\bar{1}0]$ direction, and at a sample temperature of 101K.

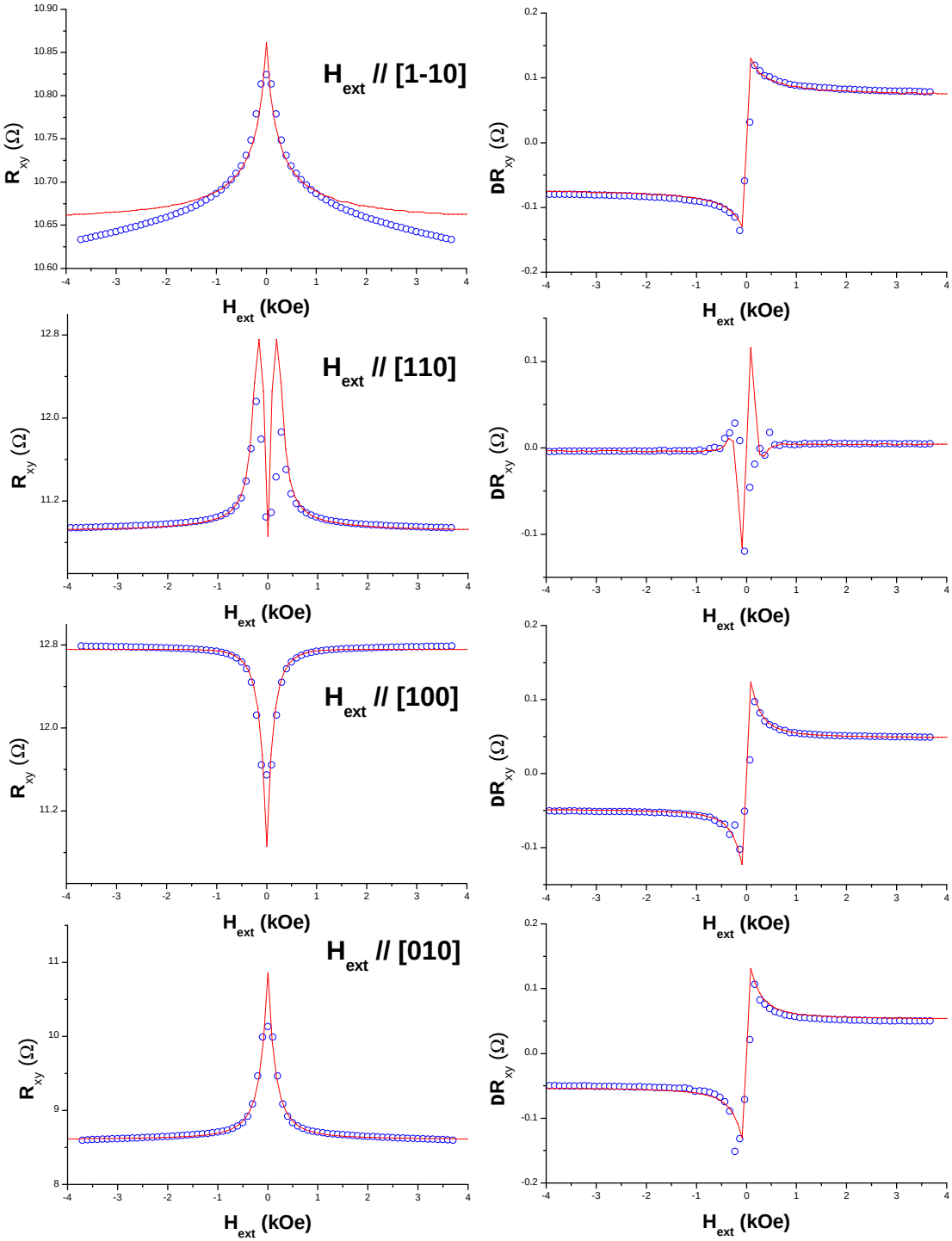

Figure 4.14: R_{xy} (left hand column) and ΔR_{xy} (right hand column) against H_{ext} for current along the $[1\bar{1}0]$ crystalline direction and H_{ext} along various crystalline directions at a sample temperature of 101K. Blue circles are measured data points, red line is the fit.

The R_{xy} against H_{ext} plots in the left hand column of figure 4.14 are consistent with the switching behaviour of a uni-axial ferromagnet. The disagreement between experimental data and fit seen for the H_{ext} along $[1\bar{1}0]$ sweep at the higher field ($>$ 1kOe) magnitudes is likely to arise from an R_{xx} isotropic magnetoresistance contribution to R_{xy} due to the Hall bar arm misalignment. This contribution will

also be present for the other field sweep directions but is only noticeable on the small R_{xy} scale of the $[1\bar{1}0]$ sweep. For all four field sweep directions the fit does not capture the experimental data at $H_{ext} \approx 0$ because the fit assumes coherent magnetization rotation but experimentally domain switching occurs. Overall the fit to the experimental data is good for all four field sweep directions, giving confidence in the obtained fitting parameters of H_U, H_C, A_{PHE}, R_{mis}, and θ_H and θ_I. The corresponding ΔR_{xy} against H_{ext} plots in the right hand column of figure 4.14 again show a good fit to the data across the entire field range. A_{ANE} and H_{eff1} are assumed to be well determined by the quality of the fits in the high and low external field regions respectively.

The importance of CIFs (H_{eff1}) in the fitting is shown in figure 4.15 which displays the fits when H_{eff1} is set to zero. It is clear from the disagreement of the fit and data points in the low field regions that H_{eff1} needs to be accounted for in order to accurately fit to the ΔR_{xy} against H_{ext} data.

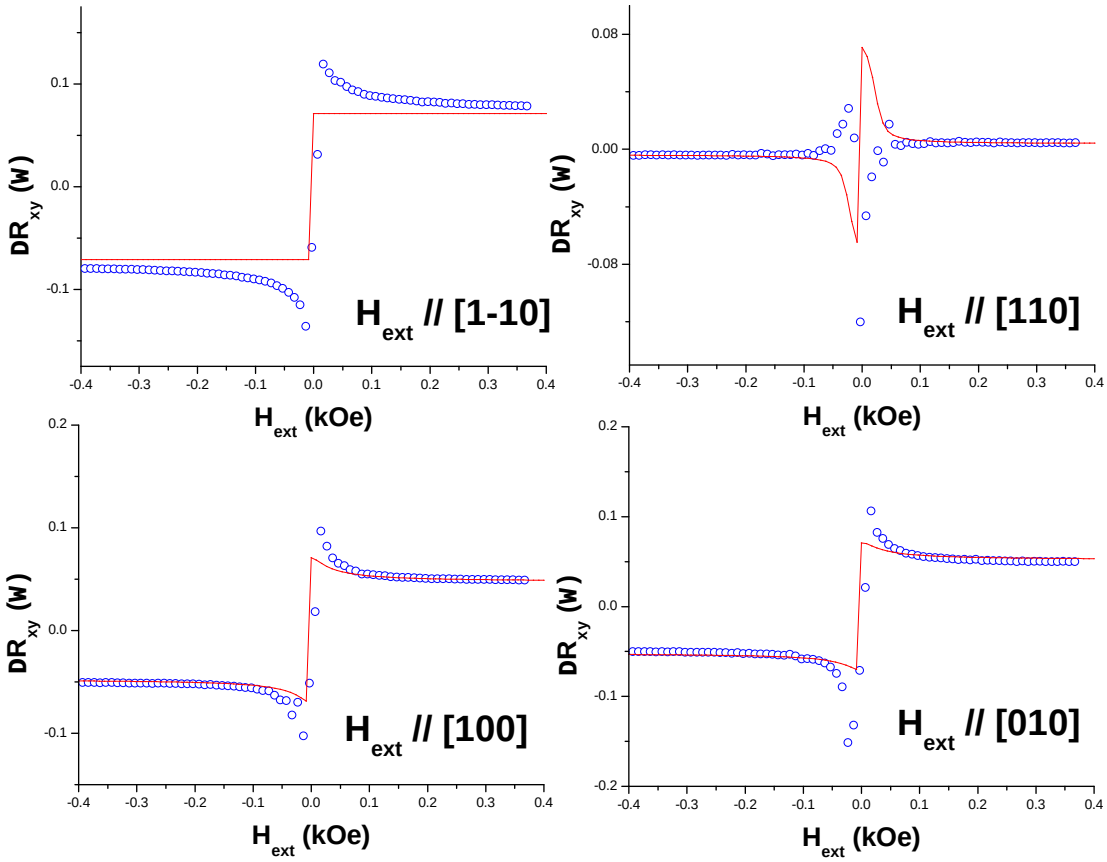

Figure 4.15: ΔR_{xy} against H_{ext} for current along the $[1\bar{1}0]$ crystalline direction and H_{ext} along various crystalline directions at a sample temperature of 101K. Blue circles are measured data points, red line is the fit but with H_{eff1} set to zero.

4.4.2 Size and temperature dependence of CIFs

As explained in section 4.3.2, H_{eff1} and H_{eff2} are fitting parameters for the component of the CIFs parallel and perpendicular to the current direction respectively. The relation between H_{eff1} and H_{eff2}, and H_D and H_R, is defined by the symmetry

of the CIFs with respect to current direction (see figure 4.1):

- **For current along [1$\bar{1}$0]:** $H_{eff1} = H_R$ - H_D, $H_{eff2} = 0$
- **For current along [110]:** $H_{eff1} = H_R + H_D$, $H_{eff2} = 0$
- **For current along [100]:** $H_{eff1} = H_R$, $H_{eff2} = H_D$

H_D and H_R can be extracted from the [100] Hall bar measurements alone, whereas for the [1$\bar{1}$0] and [110] current directions both Hall bars are needed to obtain H_D and H_R. The three Hall bar directions therefore allow for two separate measurements of H_D and H_R. Attempts were also made to measure current along the [010] direction to get a third set of CIF values, however problems with the Hall bar device prevented this. The magnitude of the obtained CIFs as a function of temperature are displayed in figure 4.16, with the errors generated from the least squares fitting procedure:

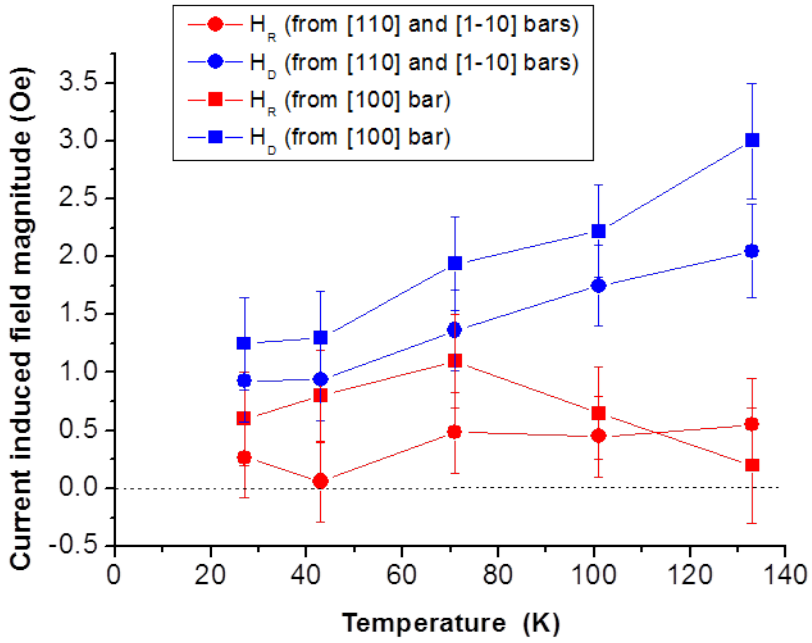

Figure 4.16: Magnitude of H_R (red) and H_D (blue) as obtained from the [1$\bar{1}$0] and [110] Hall bars (circles) and the [100] Hall bar (squares) against sample temperature.

The average values of H_R and H_D as a function of temperature from the [1$\bar{1}$0]+[110] and [100] data are plotted in figure 4.17.

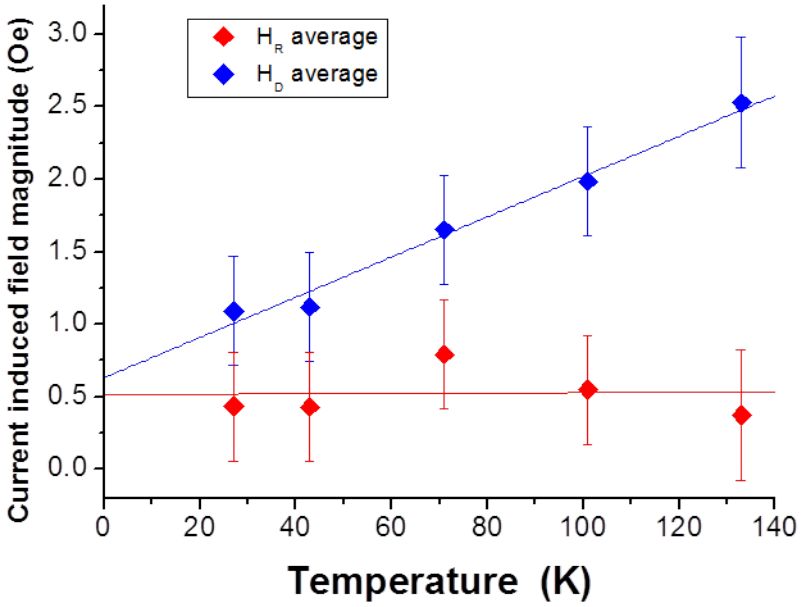

Figure 4.17: Magnitude of average H_R (red) and H_D (blue) against sample temperature. Red and blue lines are linear lines of best fit for the averaged H_R and H_D values respectively.

4.4.3 Discussion of CIFs

4.4.3.1 Oersted field contribution

The averaged CIFs vary between 1.1Oe and 2.5Oe for H_D and 0.4Oe and 0.8Oe for H_R across the measured temperature range. The sign (direction) of the CIFs is consistent with previous experiments for compressively strained (Ga,Mn)As[196][119]. The CIF per current density ratio for H_D is of the order 1Oe per MA/cm^2, which is comparable to values from other (Ga,Mn)As SOT experiments[190][191][196][119]. The magnitude of the CIF values obtained from the field sweep technique experiment and their agreement with those from literature obtained by weak field rotation technique and SO-FMR is an indication that the observed fields are indeed the CIFs associated with SOT rather than Oersted fields. The in-plane component of an Oersted field should sum to zero assuming even current distribution through the layer, but this may not necessarily be the case due to sample inhomogeneity, and so a net in-plane Oersted field could be present in the measurements. A sufficiently large net in-plane Oersted field could, in principle, be detectable by the field sweep technique, as like H_R it would act perpendicular to the current and reverse direction as current direction reverses. The maximum Oersted field at an in-plane sample edge in units of A/m is given by (current density $\times$ sample thickness)/2, which for this experiment corresponds a value in Oe of 0.2Oe, i.e. less than the measured CIFs. Assuming a slight non-isotropic current distribution within the layer, as the net Oersted field through the sample should be considerably less than 0.2Oe, it is clear that the Oersted field is not large enough to account for the magnitude of the measured CIFs.

4.4.3.2 Comparison to CIFs in magnetic multilayers

The measured CIF per current density ratio for the (Ga,Mn)As sample in this investigation is generally around 5 to 20 times smaller than those obtained in various magnetic multilayer structures[192][227][228][229][230]. The measured ratio is, however, also similar to and larger than the values obtained in Co/Pt[210] and Pt/CoFeB/MgO[231] structures respectively. The variation in the measured CIFs between different magnetic multilayer structures is likely to depend upon multiple factors, and from an applications perspective the CIF magnitude is not the only characteristic of interest as magnetic anisotropy, switching current density, sample heating are also important. An in-depth comparison between the measured CIFs in (Ga,Mn)As in this investigation and those in magnetic multilayers from literature is beyond the scope of this discussion, and so only the following comment shall be made: Generally, but not in all cases, CIFs in magnetic multilayers originating from interfacial Rashba SOC and/or SHE-STTs are larger than CIFs in (Ga,Mn)As that can be theoretically modelled as originating from strain.

4.4.3.3 Relative sizes of H_D and H_R

The ratio between H_D and H_R across the measured temperature range is plotted in figure 4.18. Note that the 133K data point, which gives a H_D/H_R ratio of 6.7 +/- 8 (the large error coming from the small value of H_R), has been omitted to allow a reasonable scale on the plot.

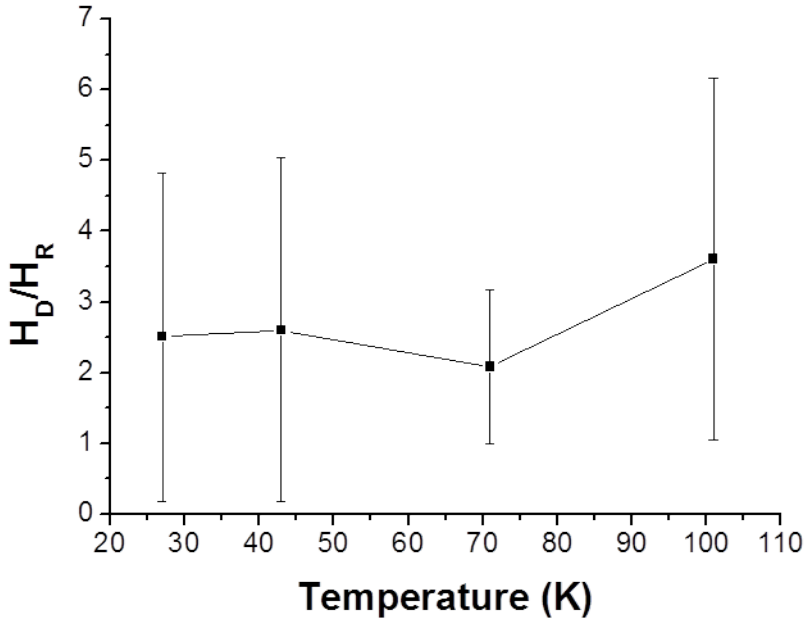

Figure 4.18: Ratio of averaged H_D to H_R against sample temperature.

The H_D/H_R ratio is between 2.1 and 3.6 in the 27K-101K temperature range, which is in agreement with the observations of references [196] and [119]. Furthermore,

the values of H_D and H_R averaged over all temperatures from both data sets are 1.7Oe and 0.5Oe respectively which again gives a ratio of H_D to H_R that agrees with the previous reports. There is insufficient information available from literature to explain the measured H_D/H_R ratio.

4.4.3.4 Temperature dependence

The obtained H_D from both the $[1\bar{1}0]/[110]$ and [100] Hall bars follows the general trend that it increases with increasing temperature. For the averaged data, H_D increases by factor of 2.3 from 27K to 133K which a significant temperature dependence that is within the measurement uncertainty. The relationship of H_R with temperature is slightly different for the $[1\bar{1}0]+[110]$ and [100] Hall bar values, the former being relatively temperature independent and the latter initially slightly increasing with temperature up to the 71K data point before decreasing. The averaged H_R varies by a factor of 2.1 within the measured temperature range, but is also independent of temperature within the reported error. Definitive trends cannot be claimed for the H_R data, however it is fair to comment that H_R does not follow the same temperature dependence as H_D as there is no significant temperature dependence within the measurement uncertainty.

Previously it has been observed that $(H_D + H_R)$[191], and H_D and H_R individually[209] increase with increasing temperature in (Ga,Mn)As as measured using the weak field rotation and SO-FMR techniques respectively. The temperature dependence of H_D in (Ga,Mn)As measured using the field sweep technique in this investigation is consistent with the above references, both in terms of the general trend and the magnitude of the variation. The agreement in the variation of H_D with temperature as measured with three distinct experimental techniques lends credibility to the result that H_D increases with increasing temperature. The temperature dependence of H_R obtained in this investigation disagrees with that of reference [209]. The reasons for this disagreement are not clear, and it would be useful to perform further measurements on a DMS with a larger H_R such as (Ga,Mn)(As,P)[196] to gain further insight into its temperature dependence.

There is currently no definitive explanation for the temperature dependencies of the CIFs observed in the investigation. Temperature should have no significant effect on any strains in a III-V semiconductor thin film, nor should it alter the strength of the intrinsic SOC, and therefore one may expect it would have little effect on the ISGE in a non-magnetic system. The most obvious way that temperature may influence the size of the CIFs in (Ga,Mn)As is through its effect on the strength of the exchange coupling or magnetization, both of which get weaker with increasing temperature. These factors can influence band splitting and the relative position of the Fermi level, which can then affect the non-equilibrium spin polarisation from the ISGE. Reference [197] investigates theoretically, as a function of exchange coupling, the size of the torque (i.e. the cross product of magnetization and CIF) in (Ga,Mn)As where only the intraband Dresselhaus CIF is considered. It is predicted that the magnitude of the SOT varies non-linearly with exchange coupling strength due to the competition between magnetic and non-magnetic scattering. At interme-

diate strengths of exchange coupling (around the known J_{pd} value for (Ga,Mn)As of ≈55meV nm^{-3}[232]), magnetic scattering dominates and the SOT increases with decreasing exchange coupling strength (increasing temperature), a trend that agrees with the temperature dependence of H_D obtained in this investigation. An alternate set of theoretical calculations are made in reference [199] where it is suggested that for both Dresselhaus and Rashba CIFs, the intraband contributions have a negligible dependence on the magnetization strength (which is determined by Mn doping concentration and hence exchange coupling strength) whereas for the interband CIFs the dependence is sizeable. The Dresselhaus interband CIF generally decreases with increasing magnetization strength (consistent with the field sweep technique results here), while the Rashba interband CIF increases with increasing magnetization. The inherent disorder in (Ga,Mn)As means that it is possible that both intraband and interband contributions to the CIFs measured in this investigation are significant, but given their experimental indistinguishability as well as the somewhat inconsistent theoretical predictions in literature, it is not possible to firmly relate the observed temperature dependencies to any microscopic theory. However, it is fair to comment that the two sets of theoretical calculations presented in references [197] and [199] can allow for H_D to increase with increasing temperature as is consistently seen experimentally.

4.4.3.5 Dependence of H_D and H_R on current direction

Figure 4.16 shows that there is a systematic difference in H_D and H_R when inferred from the $[1\bar{1}0]$/[110] and [100] Hall bars. The likely explanation for this is experimental uncertainty. Experimental uncertainty may arise in the measurement stage of the field sweep technique from unintentional factors such as variation in Hall bar dimensions and hence current density, variation in the region of the wafer used to process the different bars, variation of sample temperatures between measurements on different bars, noise on the small PHE contribution ΔR_{xy} signal, or even a non-negligible Oersted field contribution. However, it is more likely that the experimental uncertainty originates from the fitting procedure. This procedure requires multiple fitting parameters, many of which depend on one another, and so despite the least squares minimisation method there will always be a degree of uncertainty when inferring H_D and H_R from the fits. The difference in the CIF values from the $[1\bar{1}0]$/[110] and [100] Hall bars may therefore be due to measurement uncertainty, and this is reflected in the CIF values for the respective Hall bars agreeing within error.

The possibility that CIFs depend on current direction must also be considered. The analysis of reference [119] assumes that the size of H_D and H_R are independent of current direction, an assumption that seems to be generally accepted in other investigations[190][196], and there are no reports of CIFs in DMSs that do have a dependence on current direction. However, reference [233] suggests that the size of the non-equilibrium spin polarisation from the ISGE in the non-magnetic semiconductor (In,Ga)As does vary with current direction. If H_D and H_R were to depend on current direction then the $[1\bar{1}0]$/[110] Hall bar combination cannot be used to extract their values individually, and only in the [100] and [010] Hall bars,

where H_D and H_R are antiparallel, would this be possible.

4.5 Conclusions and future work

Section 4.2 presented a theoretical description of the SOT phenomenon, with particular focus on SOT in the DMS (Ga,Mn)As. In (Ga,Mn)As, linear-Dresselhaus SOC is known experimentally to be enhanced by tetragonal growth strain while Rashba SOC is also detectable experimentally and can be modelled theoretically by including a shear strain. The application of an electric field redistributes carriers on the Fermi surface and polarises their states which yields a non-equilibrium steady state net spin polarisation, the orientation of which depends on the symmetry of the Dresselhaus and Rashba SOCs and their relative strengths. The p-d exchange allows the non-equilibrium spin polarisation to torque the local moments, a process which is evaluated as CIFs acting on the magnetization. The requirements of only a single layer ferromagnetic material with broken space inversion symmetry and relatively low current densities make SOT and attractive writing mechanism for MRAM.

Section 4.3 described the experimental method used in this investigation to measure CIFs in (Ga,Mn)As and identified and characterised the ANE contribution to the measurements. The field sweep technique comprises of experimental measurements and a data fitting procedure. In the experimental measurements, CIFs are generated by applying a large current density through a (Ga,Mn)As sample, and their effect on the magnetization is detected though the PHE as an external field is swept along multiple in-plane directions for positive and negative current. For the data fitting procedure a free energy equation is minimised to model the magnetization switching behaviour from the field sweep measurements consistently for all field sweep directions, allowing the CIFs to be extracted as fitting parameters. The field sweep technique is distinct from previous experimental techniques used to measure CIFs in (Ga,Mn)As. A signal from the ANE appears in the field sweep measurements. This occurs due to a vertical gradient in the temperature of the carrier holes in the (Ga,Mn)As layer that is present due to a non-isotropic phonon distribution as the holes are heated out of equilibrium from the lattice by the large applied current. The ANE signal has a well defined symmetry which allows it to be accounted for in the data fitting procedure, therefore preventing it from obscuring the effects of the CIFs.

Section 4.4 presented the results from the field sweep technique for a 12% Mn doped, 25nm, optimally annealed (Ga,Mn)As sample. Both Dresselhaus and Rashba CIFs are observed, with magnitudes per current density that agree with previous reports. H_D is around 2-3.5 times bigger than H_R across the measured temperature range, also in agreement with previous reports. H_D increases by a factor of 2.3 as temperature increases from 27K-133K, but the trend for H_R is not clear. The increase of H_D with temperature agrees with well with observations using other experimental techniques, and may be related to the change in the strength of the exchange coupling or magnetization with temperature. A difference

in the CIFs inferred from current along different Hall bar directions is seen, but it is not clear whether this is simply due to experimental uncertainty or is a real result.

The field sweep technique has been shown in this chapter to be capable of measuring in-plane CIFs with Dresselhaus or Rashba symmetry. It can be viewed as a complimentary method to the weak field rotation technique and SO-FMR, with several advantages and disadvantages in comparison, and there are ways in which it could be improved. One of the simplest improvements is to reduce the misalignment of the current and external field angle with respect to the crystalline axes. The latter could be done by having a more reliable adjustable sample probe for measurements, as well as a flatter sample holder to avoid out of plane field misalignment. The fitting procedure does not account for out of plane field misalignment, and though it does account for current and in-plane field misalignment, reducing these fitting values should help to achieve more accurate values of H_U and H_C (and thus H_D and H_R too) as there is less freedom in the fit. Another possible improvement would be to do field sweeps in more than four directions which would give more confidence to the fitting values as they would need to consistently fit to more data sets. Reducing the ANE signal may also be beneficial for detecting smaller CIFs whose ΔR_{xy} signal from the PHE is small compared to the ANE background. The best way to do this would be to reduce the vertical temperature gradient, and this could be achieved by reducing Hall bar dimensions by using e-beam lithography processing or using a thinner sample so that a smaller current is needed to obtain the required 1MA/cm^2 current densities. This would therefore give reduced current-heating of the carriers.

The field sweep technique has been used to measure CIFs as a function of temperature, and it could be used to measure CIFs as a function of other material parameters. Given the potential strain-based origins of the CIFs, it would be interesting to apply strain to a (Ga,Mn)As sample (for example by thinning the substrate and bonding to a piezoelectric transducer) and see if any change in H_D and H_R corresponds directly to applied tetragonal and sheer strains. Additionally, processing Hall bars of sub-μm width allows for strain relaxation along the bar width and this could also generate a shear strain. As mentioned in section 4.3.4, changing the Mn concentration should have an effect on growth strain, but reference [199] suggests it will also have a significant effect on the CIFs as it will change both the magnitude of the exchange splitting and the carrier concentration. Investigating how the CIFs vary with Mn concentration and comparing the results to the calculations of reference [199] could help in understanding the importance of the different factors that determine the CIFs. Annealing is another method of varying effective Mn and carrier concentration, and so seeing how the CIFs evolve in a step-annealing study would be insightful. Annealing may also alter the SOC strength in the carrier bands as an increase in the number of carriers should give a more even distribution of carriers in the SO-split carrier sub-bands, which would help to average out the effects of SOC. Another way of varying the SOC strength is to change the semiconductor host lattice composition. GaSb should have larger strain-related and intrinsic SOC than GaAs due to the larger mismatch in size of the group III and V atoms, and so comparing the sizes of CIFs in similar (Ga,Mn)Sb and (Ga,Mn)As samples would be a useful study. Finally, sample

thickness is known to affect the magnetic anisotropy and AMR of (Ga,Mn)As[159]. The field sweep technique could be used on (Ga,Mn)As samples of varying thickness to see if CIFs in (Ga,Mn)As also vary with thickness.

Chapter 5

Magnetic gating of a 2DEG

5.1 Introduction

Electrical gating of semiconductors (also known as the field effect) is one of the most important physical techniques harnessed by the electronics industries as it enables the functionality of multiple types of transistors. Electrical gating can be described by considering a field effect transistor (FET). A simplistic diagram of a basic FET is shown in figure 5.1.

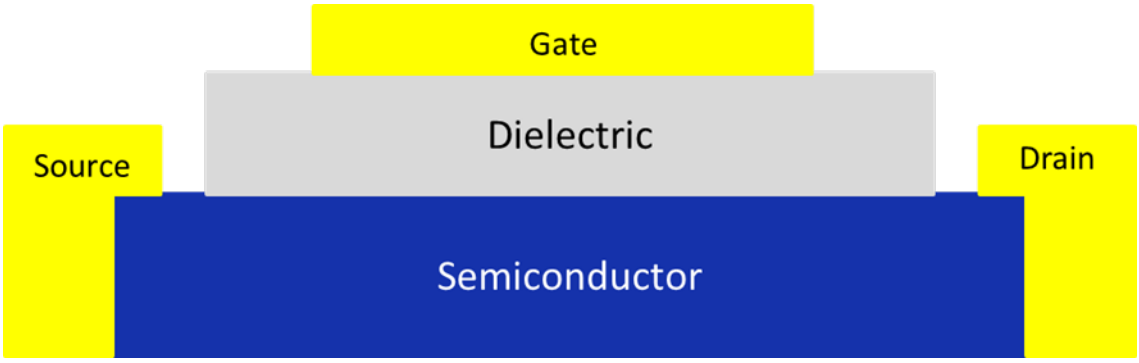

Figure 5.1: Diagram of a basic FET device.

For operation of a FET, a voltage is applied between the source and drain contacts, and this induces a current flow between them in the semiconductor layer. A voltage is then also applied between the gate and drain contacts. As a dielectric is electrically insulating, no current flows between these contacts, however the electric field from the applied voltage can pass through the dielectric and act on the semiconductor. As semiconductors have a relatively low carrier density, the electric field can penetrate a significant depth into the semiconducting channel, causing the energies of the electronic bands to change (which prevents further penetration of the field). Changing the band energies results in a change of the number of free carriers, and hence a change in conductivity. A FET can therefore amplify or suppress the current flowing between the source and drain contacts by varying the gate voltage.

Electrical gating has also found use in spintronics research. Applying a gate voltage gives rise to a gradient of the electric potential in the carrier channel, and this

results in a structural inversion asymmetry. Electrical gating can therefore be used to tune the strength of Rashba spin-orbit coupling (SOC), which could be particularly important for the realisation of a spin transistor[15][13]. Applying a gate voltage to very thin (Ga,Mn)As layers alters their carrier concentration[94], as would be expected of a semiconductor (though the high carrier concentration of (Ga,Mn)As makes gate action harder to achieve than in normal semiconductor gated structures). As the magnetic easy axis of (Ga,Mn)As is dependent on carrier concentration, it has been shown that the magnetization orientation can be controlled via electrical gating[77][234][235]. Therefore, while electrical gating has widespread application in fully electronic devices, there is also the possibility it can be used in spintronic logic and memory devices.

The spin transistor and gated (Ga,Mn)As devices are examples of electrically manipulating the spin degree of freedom in the carrier channel through a gating effect. This chapter reports on an attempt to magnetically manipulate the charge degree of freedom in the carrier channel through a gating effect. Such magnetic gating is made possible by the fact that the electrochemical potential of a ferromagnet varies with its magnetization orientation as a result of SOC[236]. Successfully demonstrating this novel effect would be fundamentally interesting, but it would also show the possibility of an alternative approach to gating electrical currents. With significant effort being made to find ways of controlling the magnetic state at a low energy cost, magnetic gating could one day have a chance of emerging as an appealing and different method to gate electrical current. One possible benefit may be that transistors could be made without an electrical contact to the gate (as the gate could be controlled by write lines producing an external magnetic field). This would allow for the prospect of novel structural transistor chip designs that could offer a route to increasing packing density.

The progress of the work in this study was somewhat disjointed, and that is reflected in the layout of this chapter. The initial part of the study involved the design of a suitable 2D electron gas (2DEG) heterostructure, and this is reported on in section 5.3.2. Section 5.4 details experimental characterisation of this 2DEG structure. Due to issues with the Nottingham MBE machine, the project was put on hold for a couple of years as growth of a new device was required. Measurements of the new device are shown in section 5.5. The new device did not demonstrate the magnetic gating effect that was hoped for, and due to time limitations no further time could be committed to the investigation. This chapter is therefore somewhat weighted towards the initial development work of the project.

5.2 Theory

5.2.1 Concept of the experiment

Figure 5.2 shows a digram of the device used for this investigation. The idealised concept of its operation for the magnetic gating experiment is as follows. The 2DEG heterostructure consists of AlGaAs and GaAs layers of various doping concentrations. The 2DEG heterostructure is designed such that the whole of

heterostructure is insulating, except at the bottom AlGaAs/GaAs interface where two dimensional conduction is possible. A voltage is applied between the source and drain contacts, and this induces a current flow along the 2DEG channel. The ferromagnetic gate is electrically insulated from the 2DEG channel and is not in contact with the source and drain contacts, and therefore no current is shunted through it. A saturating external field is rotated in the plane of the device, and this rotates the magnetization of the ferromagnetic gate. Due to SOC, the ferromagnetic gate's electrochemical potential varies with its magnetization orientation. The electrochemical potential of the 2DEG heterostructure must line up with that of the ferromagnetic gate at their interface. To achieve this the bands of the 2DEG heterostructure change their energy level ('band-bending') so that the electrochemical potential throughout the heterostructure matches up with the ferromagnetic gate's electrochemical potential. Moving the electrochemical potential therefore alters the carrier concentration of the 2DEG channel, and hence its conductivity. Rotating the magnetization of the ferromagnetic gate therefore varies the current flowing between the source and drain contacts for a given applied voltage.

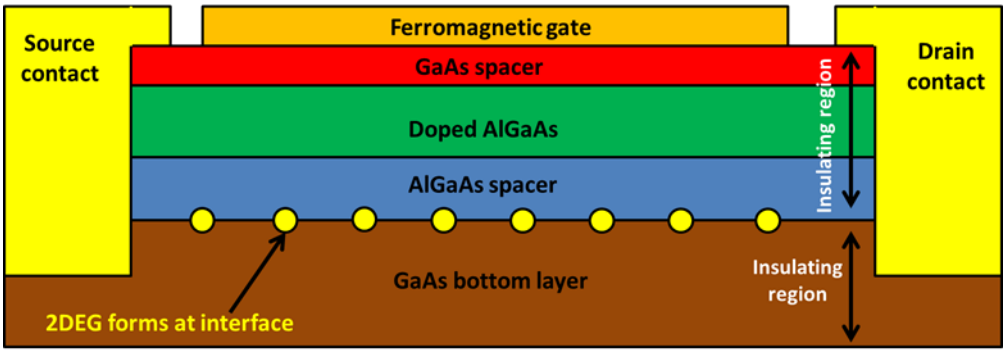

Figure 5.2: Diagram of device used in investigation. Yellow circles indicate the interface at which the 2DEG forms.

5.2.2 2DEG

A 2DEG is a sheet of electrons that can move freely in two dimensions, but not the third, often as the electrons only occupy a single energy sub-band within a triangular or square confining potential. 2DEGs can occur at dielectric/semiconductor interfaces[237], insulating oxide/oxide interfaces[238], interfaces with a superconductor[239], and in single layer materials such as graphene[240] and on the surface of 2D topological insulators[241], but in this investigation it is 2DEGs in multi-layered semiconductor structures (heterostructures) that will be considered.

In semiconductor heterostructures, 2DEGs occur at the interface between two different semiconducting materials where there is scope for carrier migration across the interface. A common example is the AlGaAs/GaAs interface, displayed simplistically in figure 5.3(a) before any carrier migration. Doping the AlGaAs layer with Si at low temperatures (either over a finite region or as a single sheet layer within the AlGaAs) provides electrons to the conduction band as the Si atoms

tend to dope the group III lattice site[242]. In order to minimise their energy, these electrons will try and cross the interface to the lower energy GaAs conduction band. Those electrons that move across the interface leave behind positively ionized Si donor atoms in the AlGaAs layer, which creates an electric field that attracts the electrons in the GaAs layer, causing them to accumulate at the interface where the large conduction band offset between the AlGaAs and GaAs stops them from re-crossing back to the AlGaAs layer. This accumulation of electrons bends the GaAs conduction band down from its equilibrium position, and hence the electrons are confined in a triangular potential between the interface and the rising GaAs conduction band (therefore the confining potential goes through the Fermi level). If the number of electrons trapped at the interface is such that it is enough to bend the conduction band through the Fermi level but not enough to occupy more than one quantised energy level within the confining potential, the electrons are confined to two dimensions and so hence are a 2DEG. Fig 5.3(b) illustrates the n-AlGaAs/GaAs interface 2DEG after carrier migration:

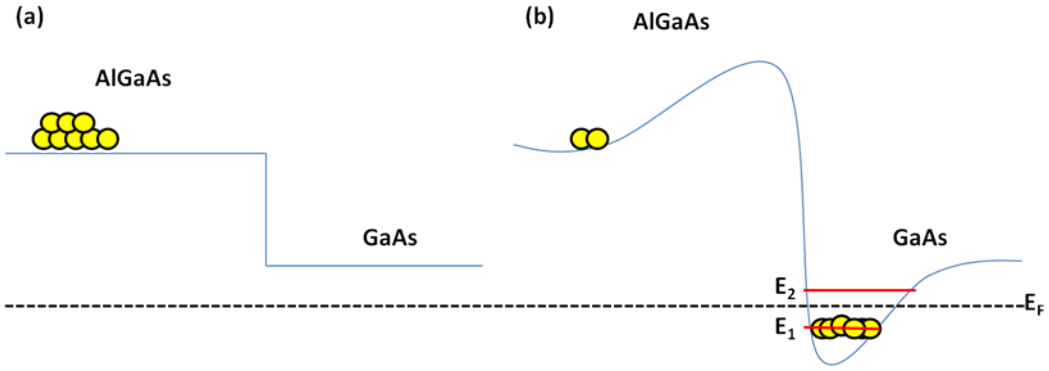

Figure 5.3: Diagram of AlGaAs/GaAs conduction band interface before (a) and after (b) carrier migration. Note a 2DEG is formed in (b) as electrons are confined to the first quantised energy level only. Energy levels are not to scale.

In terms of the magnetic gating device, using a 2DEG heterostructure as opposed to a bulk semiconductor layer (such as GaAs) as the material for the semiconducting channel has several advantages. Firstly, for the device to be successful, the current flowing from the source to drain contacts of the semiconducting channel must be electrically insulated from the ferromagnetic gate. If current were to get shunted through the ferromagnetic gate it would be detrimental to the experiment not only as it would reduce the current flowing through the semiconductor channel, but also as it would introduce an AMR signal to the measurement which would make detecting gating-induced changes in resistance more difficult. By designing a 2DEG heterostructure where the conduction band only passes through the Fermi level at one point which is well separated from the ferromagnet/semiconductor interface, there should be no channel for charge current to pass from the semiconductor to the ferromagnet. It should be noted that this would also be true of a single layer of semiconductor separated from the ferromagnetic gate by a dielectric layer or insulating layer. In terms of insulating the conducting channel from the ferromagnetic gate, GaAs heterostructure layers are preferable to oxide dielectric layers, at least for samples grown in Nottingham. This is because the ferromagnetic gate needs to be grown with high quality for its role in the experiment, and

several ferromagnetic materials are known to grow well on GaAs. The Nottingham MBE machine is capable of depositing ferromagnetic metals, such as Fe, on GaAs layers all in one growth run. On the other hand, depositing oxide dielectric layers would need to be done by magnetron sputtering, which would not only require transporting the sample between equipment, but it may also not be able to achieve high crystalline layer quality. In terms of the conducting channel properties, a 2DEG layer is also favourable over a single semiconducting layer. A 2DEG is essentially a single sheet, and so the carrier density of the 2DEG heterostructure should be relatively small compared to a single semiconductor layer. This should mean that the relative/percentage change in carrier concentration upon magnetic gating should be greater for the 2DEG than the single semiconductor layer. The 2DEG should have a higher mobility than a single semiconductor layer, and this coupled with the unique 2D nature of the carriers can bring about quantum effects not seen in normal semiconductors, such as the quantum Hall effect[243] (QHE). Additionally the resistance minima from Shubnikov-De Haas effect[244](SDHE) will only be zero in 2DEGs, unlike in bulk semiconductors. Though these effects are not directly related or important to this particular investigation, they may provide unique functionality in future experiments. They also allow a more in-depth characterisation of the 2DEG (for example the Shubnikov-De Haas oscillations allows the carrier density to be inferred from the longitudinal resistance as well as the transverse resistance).

5.2.3 Chemical potential variation in ferromagnets

In many conventional electrical gating devices, a voltage is applied to a non-magnetic metallic gate electrode (such as Pt, Au, Ti etc) which is separated from a semiconducting (or even metallic) channel by a dielectric solid[77] or ionic liquid[245], creating an electric field that acts on the channel. In the magnetic gating device detailed in this chapter, the gate electrode is a ferromagnetic metal, and the gating mechanism is controlled by rotation of the ferromagnetic gate's magnetization orientation.

The underlying physics which allows for the magnetic gating mechanism is that the magnitude of electrochemical potential of a spin-orbit coupled ferromagnet varies with respect to its magnetization orientation. Here this effect will be known as 'electrochemical potential anisotropy', although it should be noted that the electrochemical potential is a scalar. In solid state physics, the electrochemical potential is defined as the change in free energy when an electron is added to a system, i.e. the energy at which the Fermi-Dirac distribution is 0.5. When describing band structures, the electrochemical potential is often referred to as the Fermi level in literature as the two are loosely interchangeable terms.

The anisotropy of the electrochemical potential in spin-orbit coupled ferromagnets has received little attention through either experimental or theoretical studies and so a full understanding of the effect is not complete. In reference [246], the electrochemical potential variation with magnetization orientation in (Ga,Mn)As was directly measured using a single electron transistor (SET) device with a (Ga,Mn)As

back-gate. It was shown that upon magnetization rotation the electrochemical potential varies by 81μeV, 30μeV, and 6μeV for uni-axial out of plane, uni-axial in-plane, and cubic in-plane components respectively, and that the two uni-axial components increase in magnitude in more heavily Mn-doped samples while the cubic component becomes smaller . The three symmetries identified in the angular electrochemical potential datasets and their trend with doping are reminiscent of the magnetic anisotropy constants in (Ga,Mn)As[71]. This is not surprising as both effects are believed to be caused by the band-structure of (Ga,Mn)As being perturbed with change in magnetization direction due to SOC. It was also noted in reference [246] that electrochemical potential variation increases (to around 200μeV), saturates, and finally decreases with increasing out of plane external field strength (behaviour that is not replicated in a Au back-gate reference SET). This trend was ascribed to an increase in the local kinetic exchange field due to greater moment saturation at the lower external fields and increased Zeeman coupling/reduced spin splitting of hole bands at the higher external fields. The experimental results of reference [246] were supported by theoretical calculations of the electrochemical potential variation that agreed quantitatively.

The electrochemical potential also varies with the orientation of the spin axis in antiferromagnets, though this has yet to be directly verified by experiment. In reference [236], the difference in the electrochemical potential of the antiferromagnetic metallic alloys Mn_2Au and IrMn between the cases of their spin axes lying in plane and out of plane was calculated. A difference of -2.5meV for Mn_2Au and +3.2meV for IrMn was found, indicating that the electrochemical magnetic anisotropy effect is not limited to ferromagnets.

Finally, it should be noted that the electrochemical potential magnetic anisotropy effect is the source of similar transport phenomena such as Coulomb-blockade AMR[7], magneto-Coulomb oscillations[247], and magnetization dependent resonant tunnelling in semiconductor heterostructures with a (Ga,Mn)As gate electrode[248]. However, unlike reference [246], these phenomena are not a direct experimental measure of the electrochemical potential anisotropy. This is also the case for the magnetic gating experiment in this investigation.

5.3 Design of device

There are two main components that will govern the function and performance of the device; the choice material of ferromagnetic gate and the choice of material/structure of the conducting channel. In principle any electrical class (metal, semiconductor, insulator) of ferromagnetic material can be used for the gate as long as its electrochemical potential is dependent on its magnetization orientation. As reference [236] suggests, an antiferromagnetic gate could also be deployed, assuming the antiferromagnetic spin axis could be manipulated. A desirable property of the ferromagnetic gate is for the electrochemical potential anisotropy to be as large as possible, and as the electrochemical potential anisotropy is a SOC effect, it is likely that having a ferromagnet with stronger SOC will help in this regard. Other factors such as band structure and conductivity may also have

an influence on the magnitude of the electrochemical potential anisotropy. More practical considerations also need to be made such as the strength of the magnetic anisotropy fields of the ferromagnet (need to be weak enough to be saturated by the available experimental external fields), the quality of its growth upon a semiconductor surface, and the ease of processing. The reasons for choosing a 2DEG over a single semiconductor layer are highlighted in section 5.2.2. There are three factors to consider when designing a 2DEG heterostructure for the device. First and foremost, 2DEG conduction must be achieved, as opposed to insulating or 3D conduction behaviour. Secondly, there must be no additional carrier channels in the heterostructure, i.e. the depletion region must be a true depletion region. Finally, the depletion region between the ferromagnetic gate and the 2DEG needs to be sufficiently thin so that electrochemical potential changes in the gate give significant changes in carrier density at the 2DEG, i.e. the changing of the chemical potential in the heterostructure is not wholly brought about by band bending and charge redistribution in the depletion region. Generally, the closer the 2DEG is to the gate the larger the effects of changing the gate electrochemical potential are on it, however it is also more difficult to obtain a true depletion region. A near surface 2DEG is therefore desired.

5.3.1 Shape of device

A cross sectional diagram of the device design is shown in figure 5.2, and it can be seen that the device is designed so that the ferromagnetic gate is not in electrical contact with the source and drain electrode. The device needs to take some sort of Hall bar geometry to allow simultaneous longitudinal and transverse resistance measurements to be made. It is important that the gate covers as much of the surface of the Hall bar as possible for two reasons. Firstly, a larger area of the 2DEG heterostructure under the gate will give a larger area of the 2DEG heterostructure that experiences an electrochemical potential change from the gate magnetization rotation. This should mean that the overall change in the device resistance upon rotating the gate will be larger. Secondly, covering more of the 2DEG heterostructure channel with the gate means that the edge of the gate layer is closer to the source, drain, and arm contacts, and so further away from region of the Hall bar channel that is probed in 4-terminal measurements. This is important for minimising the effects that stray fields from the ferromagnetic gate can have on the 4-terminal measurements. Stray fields that are out of plane to a 2DEG channel are known to cause a magnetic barrier to carrier transport in 2DEG systems with a magnetic top layer[249][250] as they deflect the motion of electrons via the Lorentz force. For a magnetic top layer with in-plane magnetization, uniformly distributed effective monopoles on the two magnetic layer faces that are parallel to the out of plane direction and perpendicular to the magnetization orientation (i.e. in the y-z plane of figure 5.4) generate out of plane stray fields.

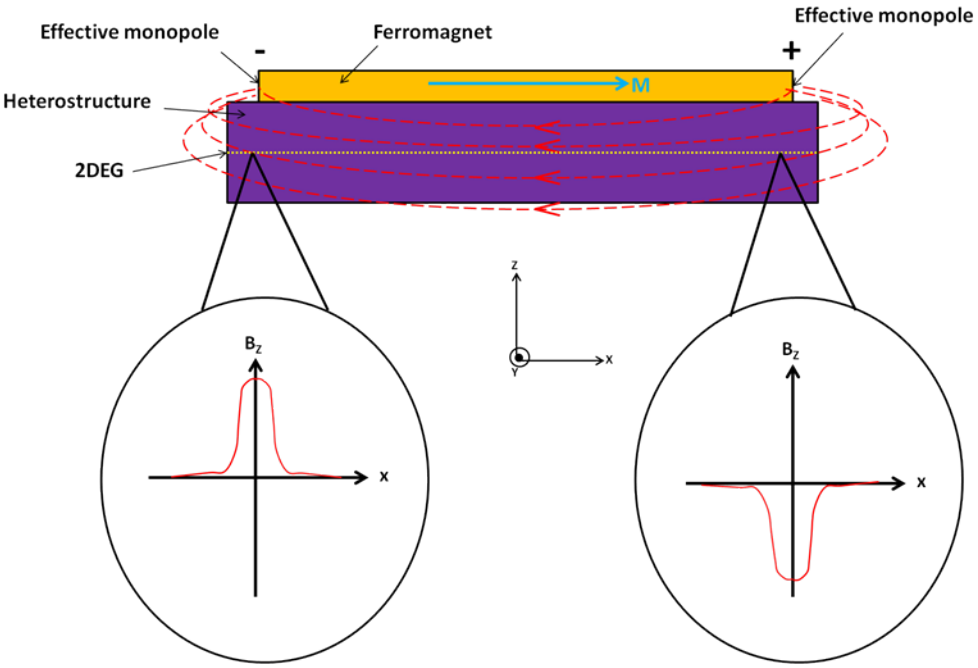

Figure 5.4: Cartoon side view of a 2DEG heterostructure with top magnetic layer. Blown-up graphs indicate a not to scale representation of the out of plane stray field distribution along the x-axis at the 2DEG underneath the top magnetic layer y-z plane faces.

The out of plane stray fields at the y-z plane faces are maximum when the in-plane magnetization is along the x-direction and minimum when the magnetization is along the y-direction. For magnetization along the x-direction the out of plane fields at the 2DEG are largest directly beneath the magnetic layer y-z plane faces and decrease rapidly either side along the x-directions (typically on the length scale of a few microns[251]). For the y-z plane face(s) of a relatively thick magnetic top layer being located in-between the 4-point measurements probes/Hall bar arms (the measurement geometry in references [249] and [250]) the change in 4-point longitudinal resistance from in-plane magnetization rotation is significantly larger than what may be expected in this experiment from the chemical potential anisotropy effect. However, in the device geometry for this investigation's experiment, the magnetic gate layer's y-z plane faces are not located in-between the Hall bar arms (and are relatively far away from the Hall bar arms) which will vastly reduce the effect of stray fields on the measurements. Additionally the magnetic gate in this experiment will be very thin (a few nm's) and so the size of the stray fields it generates should also be much smaller than the thicker magnetic top layers of references [249] and [250]. Despite these factors, stray fields may still influence the measurements and need to be accounted for. Once way of doing this is to use an L-shape Hall bar in the measurement geometry shown in figure 5.5.

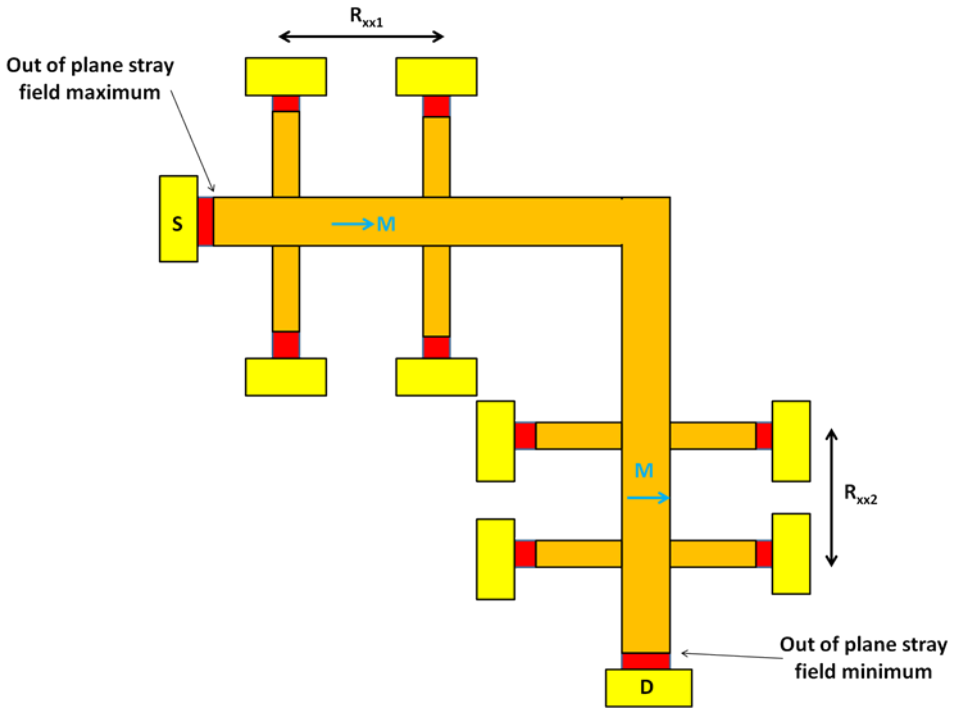

Figure 5.5: Cartoon top-down view of L-shape Hall bar geometry for magnetic gating device. Colour scheme is same as for figure 5.2.

As the chemical potential anisotropy effect should only be dependent on magnetization direction, and not on current direction (with respect to either the magnetization or crystallographic axes), the contribution to the longitudinal resistance from chemical potential anisotropy should be the same for both R_{xx1} and R_{xx2} in the figure 5.5 geometry. However, as the magnetic barrier to current flow arising from out of plane stray fields is maximum for magnetization along the current direction and minimum for magnetization perpendicular in-plane to the current direction, the out of plane stray field contribution to longitudinal resistance should be maximally different for R_{xx1} and R_{xx2}. Therefore, the difference between R_{xx1} and R_{xx2} (after probe misalignment etc has been accounted for) from such an L-shape Hall bar measurement should allow the effects of out of plane stray fields to be quantified and thus removed from further measurements of the chemical potential anisotropy induced change in longitudinal resistance.

5.3.2 Design of heterostructure and choice of gate

The heterostructure designs considered in this section all follow a similar simple layer structure to that illustrated in figure 5.2. Beneath the ferromagnetic gate is an undoped GaAs spacer layer whose function is to protect the doped AlGaAs layer and separate it from the ferromagnet. It is important that the carrier density in this region is essentially zero to prevent charge transfer between the heterostructure and the gate. Beneath the GaAs spacer layer is the doped AlGaAs layer. AlGaAs is chosen as it is well lattice matched to GaAs but has a larger band gap (which can be tuned by varying the proportion of Al to Ga). The doped AlGaAs provides the charge that forms the 2DEG, and the doping needs to be fairly heavy (around

$1x10^{18}cm^{-3}$) to allow the formation of the 2DEG. In '1D Poisson' models (see below paragraph) the doping concentration is just an input parameter, but in the actual heterostructure it is provided by Si dopants. Beneath the doped AlGaAs layer is an undoped AlGaAs layer which acts as another spacer. This spacer layer serves two purposes, firstly to limit the carrier transfer from the doped AlGaAs to the bottom GaAs layer so that just enough to form a 2DEG is allowed, and secondly increase the mobility of the carriers in the 2DEG. Mobility increases with spacer thickness as 2DEG carriers are further away from the Coulomb potential that arises from the positively ionized Si donor atoms in the doped AlGaAs layer and so do not experience as strong scattering. Finally, beneath the spacer AlGaAs layer is the bottom undoped GaAs layer, with the 2DEG forming at the interface between the two layers. Besides its compatibility with AlGaAs, GaAs is chosen as it is easy to grow on GaAs substrates (which are relatively cheap and easy to get a hold of).

In order to model carrier distribution for various heterostructure designs, the '1D Poisson' program written by Greg Snider of the University of Notre Dame was employed[252]. '1D Poisson' calculates semiconductor energy bands, carrier concentrations, and quantized energy levels for user-defined heterostructure designs, with the ability to mimic applied bias voltages (through Schottky barrier contacts voltages), as well as the degree of dopant ionization (to semi-model the effect of DX centres) within the calculations. Effects of current flow are not considered so the calculations are for thermal equilibrium. Energy bands, carrier concentrations, and quantized energy levels are calculated by self consistently simultaneously solving the 1D Poisson equation for electrostatic potential (equation 5.1) alongside the 1D Schrödinger equation (equation 5.2), which are given as:

$$\frac{d}{dx}\Big(\varepsilon(x)\frac{d}{dx}\phi(x)\Big) = \frac{-q(N_D(x) - n(x))}{\varepsilon_0} \tag{5.1}$$

where x is the heterostructure depth (from the surface), $\varepsilon(x)$ is the material permittivity, $\phi(x)$ is the electrostatic potential, q is the electron charge, $N_D(x)$ is the electron donor concentration, and $n(x)$ is the electron concentration.

$$\Big[-\frac{\hbar^2}{2}\frac{d}{dx}\Big(\frac{1}{m^*(x)}\frac{d}{dx}\Big) + V(x)\Big]\Psi(x) = E\Psi(x) \tag{5.2}$$

where

$$V(x) = -q\phi(x) + \Delta E_c(x) \tag{5.3}$$

where $V(x)$ is the potential energy, $m^*(x)$ is the electron effective mass, $\Psi(x)$ is the electron wavefunction, E is the electron energy eigenvalue, and $\Delta E_c(x)$ is a pseudopotential to account for screening effects.

Simplistically, '1D Poisson' works by the following routine:

- Use a trial potential, $\phi_1(x)$, and solve equation 5.2
- Use the obtained wavefunctions and eigenenergies to calculate $n(x)$
- Putting $n(x)$ and $N_D(x)$ (an input parameter) into equation 5.1, calculate a new

trial potential, $\phi_2(x)$
• Put $\phi_2(x)$ into equation 5.3 to give a new value of $V(x)$
• Keep iterating the above sequence until the magnitude of $\phi_i(x)$ - $\phi_{i-1}(x)$ is less than some pre-set value

'1D Possion' is an excellent program to use to get an idea of the energy bands, carrier densities, and quantized energy levels within a heterostructure design, but it should be noted that it is a purely mathematical tool, and that the calculated results should only be used as an estimate of their true values in a real heterostructure.

One device design considered was to use (Ga,Mn)As as the ferromagnetic gate on top of a 2DEG or 2 dimensional hole gas (2DHG) heterostructure. (Ga,Mn)As was considered as the gate material as it is a well understood ferromagnet with strong SOC that can be easily grown with high quality on a GaAs based heterostructure. In terms of including its non-magnetic effects on carrier distribution throughout the 2DEG or 2DHG heterostructure, (Ga,Mn)As can be modelled in '1D Possion' as a GaAs layer that is doped with $1\text{x}10^{20}\text{cm}^{-3}$ fully ionized acceptors as the top layer of the heterostructure. The conduction band (defined relative to the Fermi level) and electron density of an example (Ga,Mn)As/2DEG heterostructure as calculated by '1D Poisson' are shown in figure 5.6. The heterostructure layers are as follows, where $\text{N}_{A/D}$ is the acceptor/donor dopant density:
• (Ga,Mn)As gate layer, 7nm thick, $\text{N}_A = 1\text{x}10^{20}\text{cm}^{-3}$
• GaAs spacer layer, 10nm thick, un-doped
• $\text{Al}_{0.4}\text{Ga}_{0.6}\text{As}$ doped layer, 21nm thick, $\text{N}_D = 2.3\text{x}10^{18}\text{cm}^{-3}$
• $\text{Al}_{0.3}\text{Ga}_{0.7}\text{As}$ spacer layer, 10nm thick, un-doped
• GaAs bottom layer, 300nm thick, un-doped

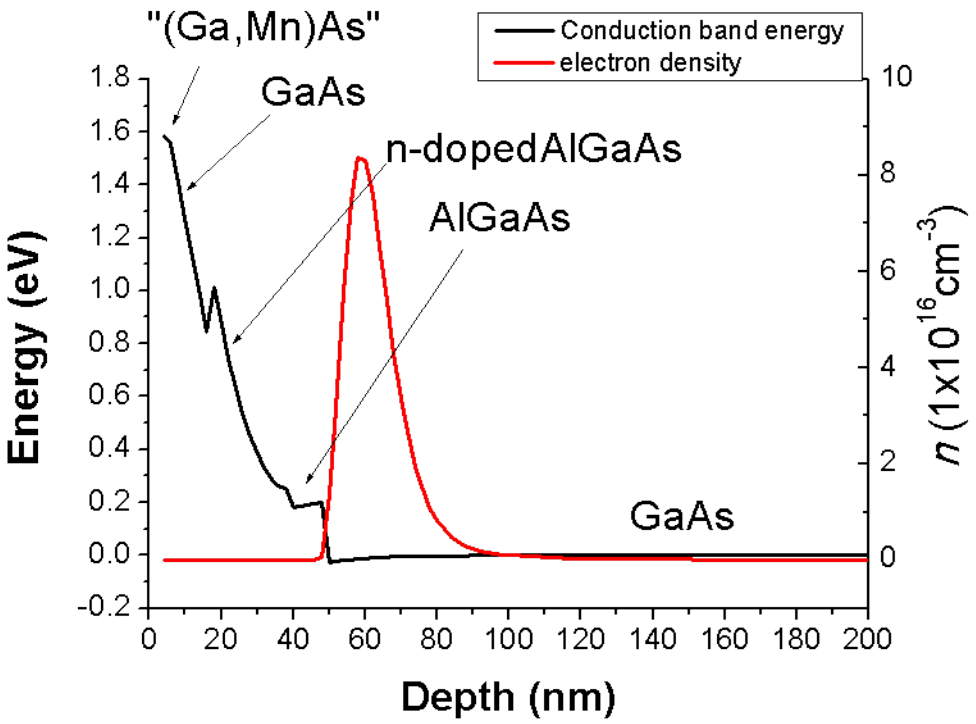

Figure 5.6: Conduction band structure (black) and electron density (red) for an example (Ga,Mn)As/2DEG heterostructure.

For the heterostructure design in figure 5.6 there is only one quantised energy level for the electron accumulation at the AlGaAs/GaAs interface, and hence a 2DEG is formed. The vast majority of the electron density within the heterostructure is confined to the bottom GaAs layer (with a negligible amount in the AlGaAs spacer layer), while the vast majority of the hole density within the heterostructure is confined to the (Ga,Mn)As layer (with a negligible amount in the top GaAs layer - hole density not shown on plot). There should therefore not be a channel for conduction from the 2DEG to the (Ga,Mn)As. For the geometry of the gated Hall bar structure used in this experiment, source and drain contacts are made to regions of the 2DEG heterostructure where the top gate layer has been removed in order to ensure that the source current is not shorted through the gate. Ideally the 2DEG should therefore form within the heterostructure regardless of whether the top gate layer is present or not. Figure 5.7 shows conduction band and electron density of figure 5.6 heterostructure design with the top (Ga,Mn)As layer removed.

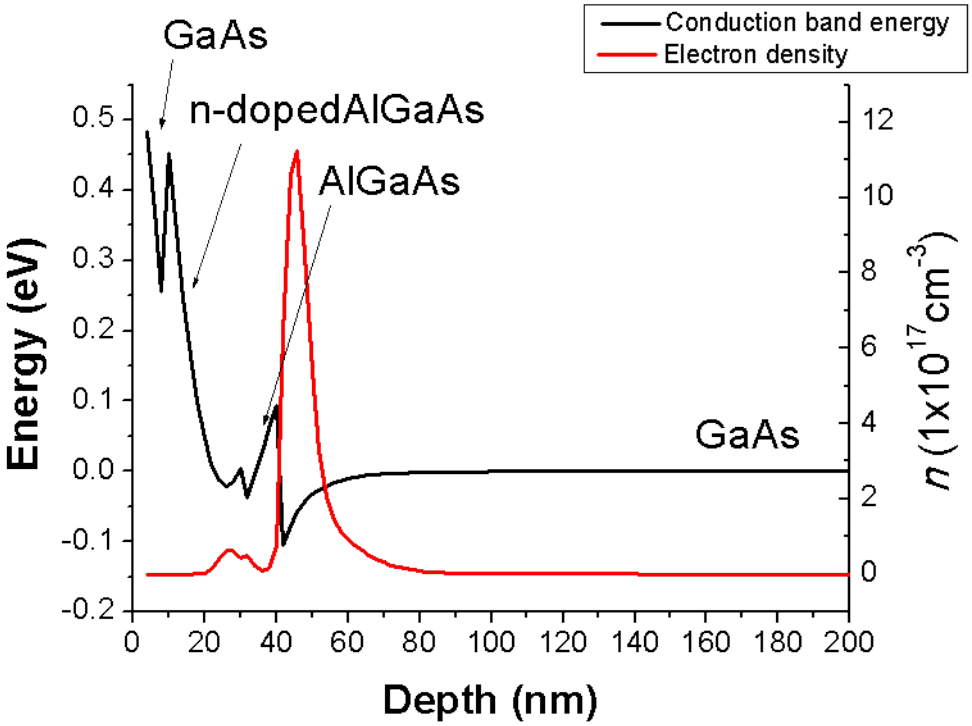

Figure 5.7: Conduction band structure (black) and electron density (red) for 2DEG heterostructure of figure 5.6 without the top (Ga,Mn)As layer.

Comparing figure 5.7 to figure 5.6, it can be seen that removing the (Ga,Mn)As layer increases the electron density at the AlGaAs/GaAs interface by an order of magnitude, and the result of this is that the number of quantized energy levels at the interface increases from one to three, hence the electrons can no longer be considered two dimensional. This could be an advantage as it would make contacting directly to the gated 2DEG region easier, but it may also be a disadvantage if it were to provide a channel for current leakage to the gate. There is also a non-negligible electron density in both the doped AlGaAs and AlGaAs spacer layers for the heterostructure without the top (Ga,Mn)As layer. The increase in electron density within the device is brought about by the large number of positively charged holes in the (Ga,Mn)As layer that significantly deplete electrons no longer being present. Without a 2D Poisson solver it is hard to predict exactly how electron density and quantized energy levels at the AlGaAs/GaAs interface in the heterostructure would behave across the device (from the region of the heterostructure channel under the source contact, through the region under the gate, and to the region under the drain contact), and this makes the (Ga,Mn)As/2DEG device an un-appealing starting point for this experiment. However, with more thought and a better heterostructure design, it may well be possible to make a working (Ga,Mn)As/2DEG device, but it is more logical to start developing an in-depth insight of the experiment (and especially the differences between Poisson models and real experimental results) with a simpler and more easy to understand device.

Designing a 2DHG heterostructure with top (Ga,Mn)As layer proved to be very difficult. Attempted designs were similar to the (Ga,Mn)As/2DEG in figure 5.6, but

with a p-doped instead of n-doped AlGaAs layer. Despite varying different aspects of the heterostructure, a design that produced a 2DHG at the AlGaAs/GaAs interface when modelled with '1D Poisson' could not be found, with the designs either giving no hole accumulation or a huge hole accumulation (with many energy levels) at the interface, as well as drastic changes with the removal of the top (Ga,Mn)As layer. Therefore a (Ga,Mn)As/2DHG device seems highly unsuitable for this experiment.

Due to the complications associated with using a (Ga,Mn)As gate, it was decided a better approach would be to use a metallic ferromagnetic gate on top of 2DEG heterostructure. The main requirements for the ferromagnetic gate material of having high quality crystalline growth on GaAs, reasonable SOC strength, and a sufficiently low coercivity make Fe an outstanding candidate. Thick Fe films (on the order or 100's of nm) are ferromagnetic up to temperatures well above room temperature and have a cubic crystalline magnetic anisotropy, as well as some non-negligible degree of intrinsic SOC owing to the size of the Fe atom. However, when thin Fe layers (10nm or less) are grown on GaAs, the mixing of the spin-polarised Fe atoms and GaAs atoms at the interface can lead to a significant enhancement of the SOC strength throughout the first few monolayers of the Fe, and hence hopefully a significant enhancement of chemical potential anisotropy at the interface too. Fe films can be well grown on GaAs due to the excellent compatibility of the two materials' lattices; Fe has a lattice parameter that is very close to half of that of GaAs, and the growth can take place in the Nottingham MBE system without breaking vacuum. Fe/GaAs structures have been well studied both in terms of the electronic and magnetic properties of the Fe film[253] and the physics of the interface[254][255]. They have also played host to many spin injection/detection experiments[256][257][258]. Thin Fe films on GaAs are known to have a strong in-plane magnetic anisotropy (which is usually uni-axial for thicknesses of 2nm and lower[259]), and form a Schottky barrier to the GaAs, the height of which varies with the atomic structure of the interface but generally falls between 0.2eV-0.9eV[254].

Schottky barriers arise at most metal/n-semiconductor interfaces as electrons flow from the semiconductor to the metal so that the electrochemical potential aligns in the two materials. This leads to a depletion of electrons at the semiconductor side of the interface, and the resulting Coulomb potential causes upwards bending of the semiconductor conduction band, giving an increased finite potential difference between the electrochemical potential and conduction band at the interface that any charge transfer from the metal to semiconductor must overcome. This potential difference is known as the Schottky barrier height. If the electrochemical potential of the metal is varied, the Schottky barrier height would also be expected to vary. '1D Poisson' only models semiconductor bands, and therefore to capture the effects of a metallic gate layer on the semiconductor heterostructure bands a Schottky barrier needs to be added to the calculations (instead of the top of the heterostructure being terminated with vacuum). The effects of varying the electrochemical potential in ferromagnetic metallic gate on the semiconductor heterostructure can then be approximately modelled by varying the Schottky barrier height.

As mentioned previously, for good magnetic gating device performance the percentage change in the electron density of the 2DEG needs to be as large as possible for a given change in ferromagnetic gate electrochemical potential. To optimize the heterostructure design in this regard, '1D Poisson' was used calculate the 2DEG electron density for a given heterostructure design with a Schottky barrier of xeV, with the calculation then repeated for the same heterostructure design but with a Schottky barrier of xeV + 100μeV (this Schottky barrier height variation is a loose estimate of the electrochemical potential change that may be expected for rotating the magnetization in Fe). Various parameters of the heterostructure design were individually varied over a range of relevant Schottky barrier values[254], and the percentage change in electron density calculated. The results are displayed in figures 5.8-5.13.

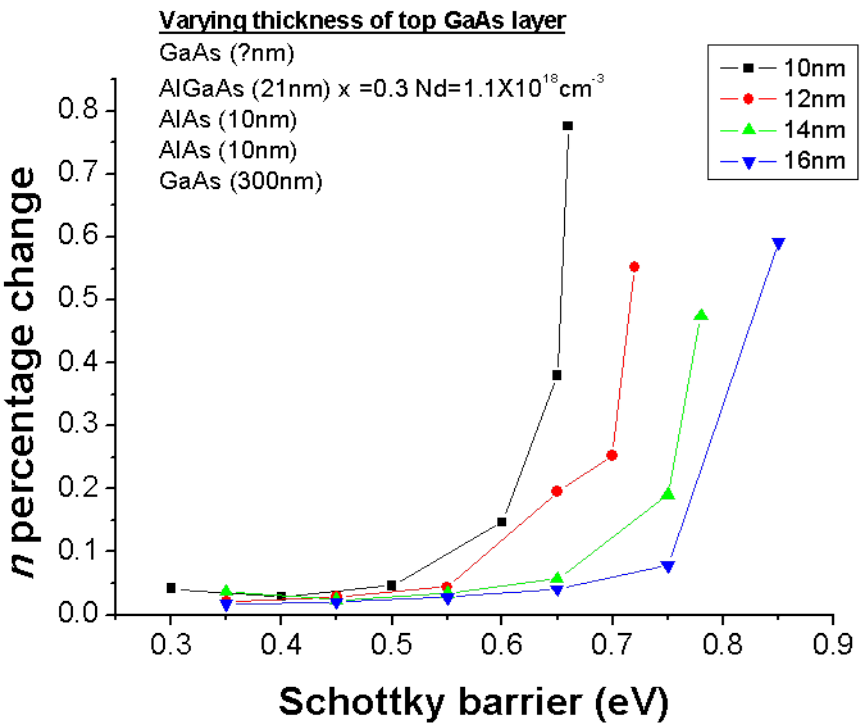

Figure 5.8: Percentage change in 2DEG electron density with Schottky barrier height for different thicknesses of top GaAs layer.

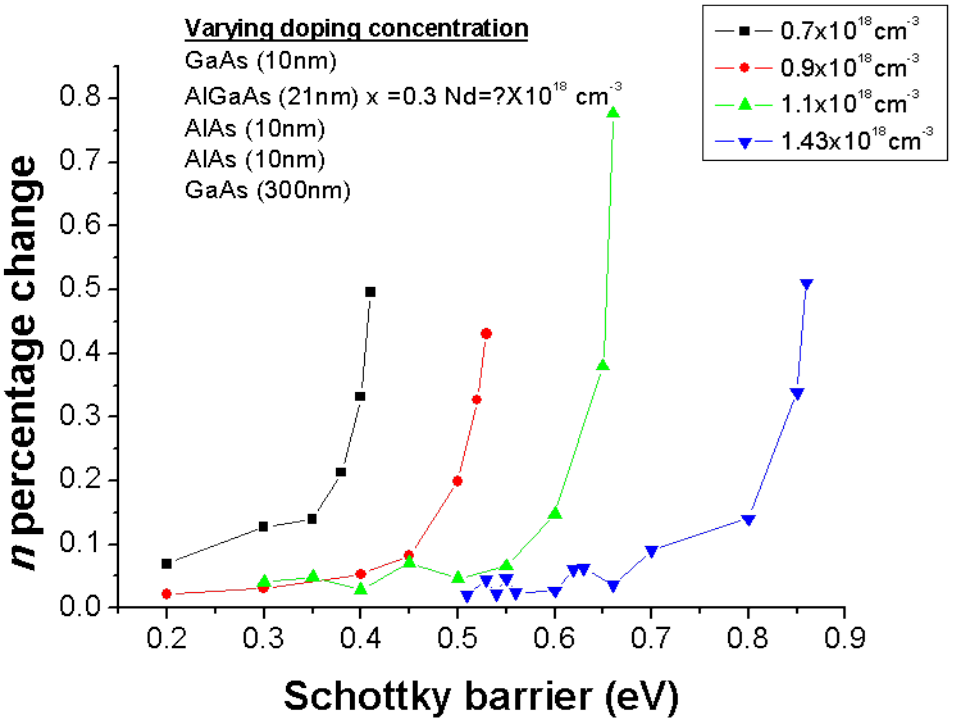

Figure 5.9: Percentage change in 2DEG electron density with Schottky barrier height for different doping concentrations of doped AlGaAs layer.

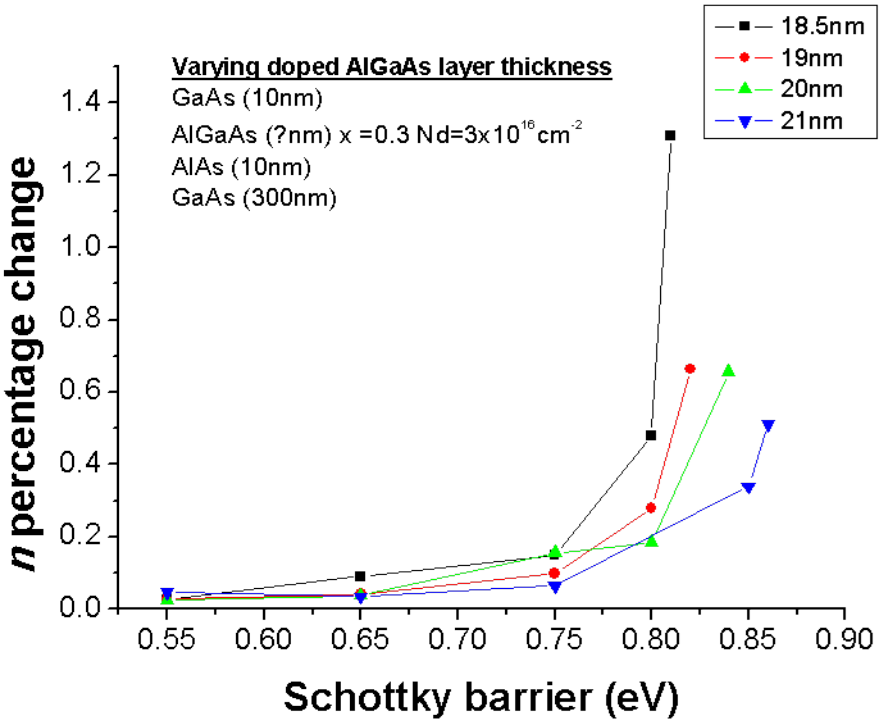

Figure 5.10: Percentage change in 2DEG electron density with Schottky barrier height for different thicknesses of doped AlGaAs layer.

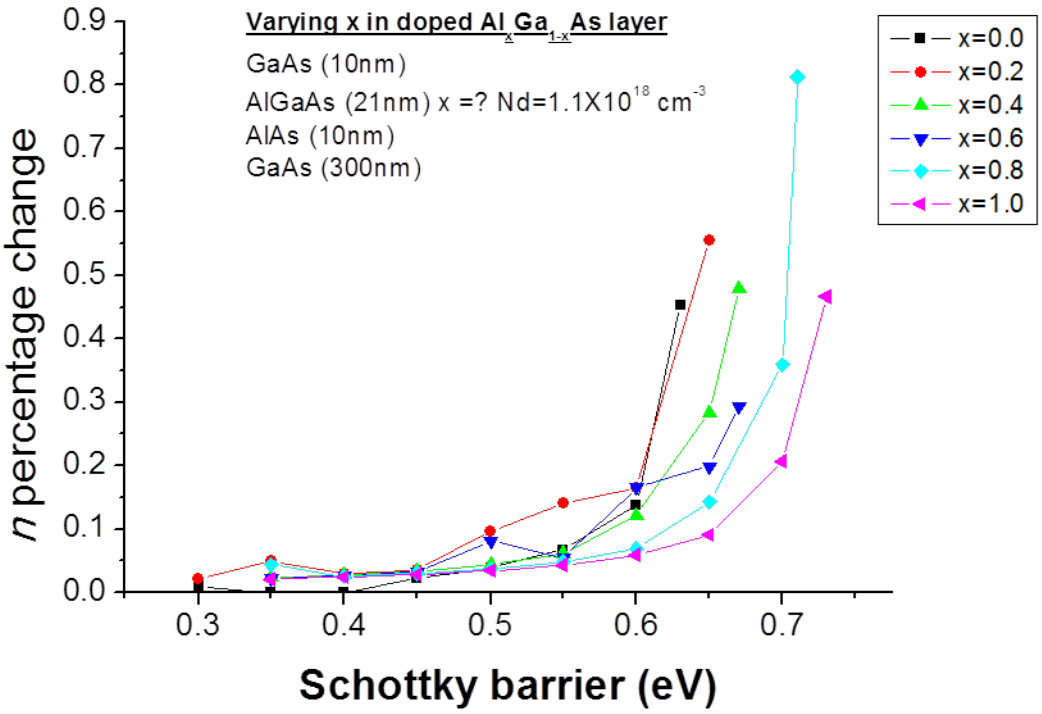

Figure 5.11: Percentage change in 2DEG electron density with Schottky barrier height for different stoichiometric compositions of doped AlGaAs layer.

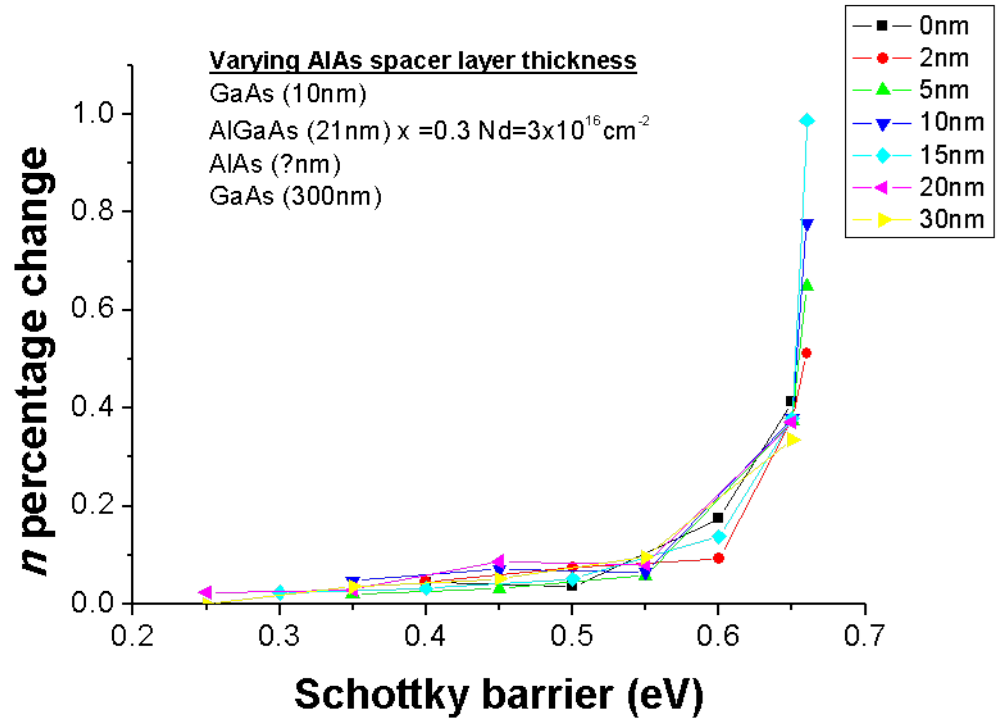

Figure 5.12: Percentage change in 2DEG electron density with Schottky barrier height for different thicknesses of AlGaAs spacer layer.

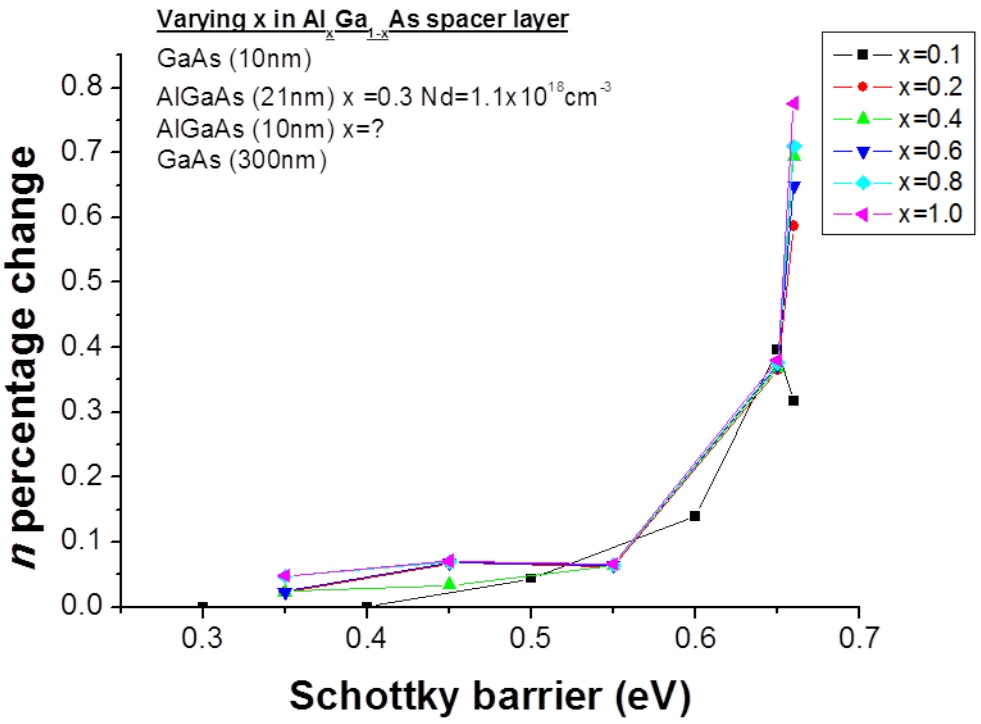

Figure 5.13: Percentage change in 2DEG electron density with Schottky barrier height for different stoichiometric compositions of AlGaAs spacer layer.

All the plots in figures 5.8-5.13 show a similar trend. At lower Schottky barrier heights the percentage change in electron density is small (around 0.05%) and remains so with increasing Schottky barrier height up until some critical value where the percentage change in electron density dramatically increases with increasing Schottky barrier height. The maximum percentage change in electron density is around 1%. The data plotted in the graphs in figures 5.8-5.13 encompasses the range of Schottky barrier heights where a 2DEG exists. At the Schottky barrier heights greater than those where the peak in electron density percentage change occurs, the 2DEG does not exist as there is no electron density at the AlGaAs/GaAs interface. At the lower Schottky barrier heights the data is not plotted where there is more than one quantized energy level occupied at the AlGaAs/GaAs interface. Generally for the heterostructure designs the 2DEGs occur over a range of Schottky barrier values of roughly 0.3eV-0.9eV, which coincides well with the range of Schottky barrier heights expected for the Fe/GaAs interface. The effect of changing parameters in the 2DEG design is largely to alter the region of Schottky barrier values where a 2DEG exists, and to alter the Schottky barrier height where the maximum percentage change in electron density occurs. There is also some effect on the magnitude of the maximum percentage change in electron density, though this is not as clear due to the large step size in Schottky barrier heights calculated. Changing some parameters also has more of an effect than changing others. For example, changing the thickness and stoichiometric composition of the AlGaAs spacer layer only gives slight changes in the percentage change in electron density.

When deciding the final 2DEG design it is desirable to have heterostructure parameters that enable the formation of a 2DEG over a wide range of Schottky barrier heights, and for the maximum percentage change in electron density to be as large as possible. It is also worth bearing in mind the effects that DX centres in the doped AlGaAs layer may have on the number of effective donors in the heterostructure. DX centres cause donor electrons to become deeply bound to their Si dopant atom due to lattice relaxation[260]. All the data in figures 5.8-5.13 was obtained using '1D Poisson' with the condition of donors being fully ionized. However, in real semiconductor materials DX centres will reduce the number of effective donors. Fortunately for the intended experiment of this investigation, trapped electrons can be released from DX centres by illumination with light of energy greater than the trapping potential energy (such as white light) and then continue to remain unbound at lower temperatures, an effect called persistent photo-conductivity. This allows some control of effective doping density after the heterostructure has been grown and during a measurement[261]. Assuming that DX centres will form in the real heterostructure, it is sensible use a relatively high doping density for the heterostructure design as the effective doping density will likely be considerably lower, but can be increased to values towards the nominal doping density via illumination. This will then give a range of accessible effective doping densities, some of which should lead to the formation in the heterostructure of a 2DEG.

After further tweaking of the various heterostructure parameters (not shown), the final heterostructure designs decided upon were:

Mn782
- GaAs spacer layer, 17nm thick, un-doped
- $Al_{0.3}Ga_{0.3}As$ doped layer, 22nm thick, $N_D = 1x10^{18}cm^{-3}$
- $Al_{0.3}Ga_{0.7}As$ spacer layer, 20nm thick, un-doped
- GaAs bottom layer, 500nm thick, un-doped

Mn781
- GaAs spacer layer, 17nm thick, un-doped
- $Al_{0.3}Ga_{0.3}As$ doped layer, 13nm thick, $N_D = 2x10^{18}cm^{-3}$
- $Al_{0.3}Ga_{0.7}As$ spacer layer, 20nm thick, un-doped
- GaAs bottom layer, 500nm thick, un-doped

Conduction bands and electron densities for the two designs for vacuum terminated heterostructure surface (no gate) and 0.6eV Schottky contacts (Fe gate) assuming a full ionization of the donor atoms are shown in figures 5.14-5.17:

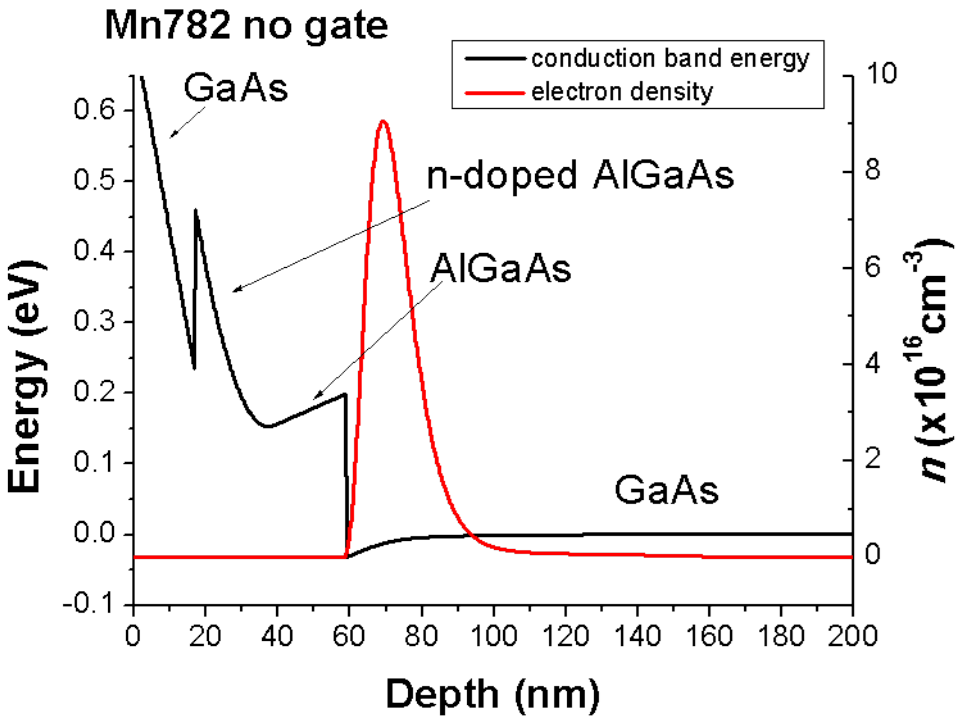

Figure 5.14: Conduction band structure (black) and electron density (red) for Mn782 2DEG heterostructure with vacuum terminated surface.

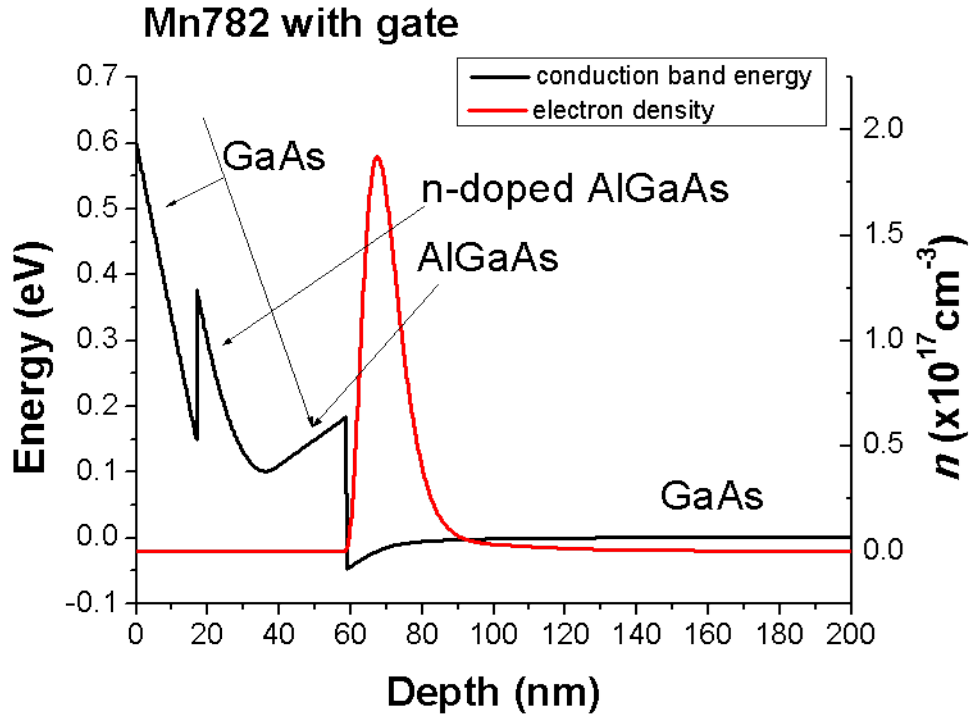

Figure 5.15: Conduction band structure (black) and electron density (red) for Mn782 2DEG heterostructure with Schottky contacts of size 0.6eV.

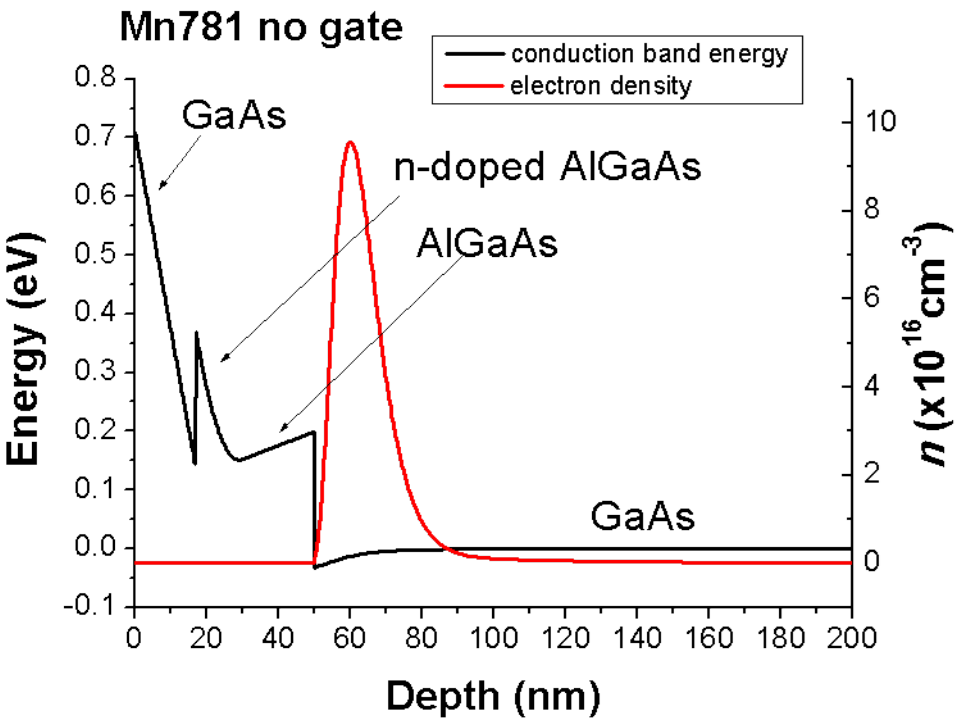

Figure 5.16: Conduction band structure (black) and electron density (red) for Mn781 2DEG heterostructure with vacuum terminated surface.

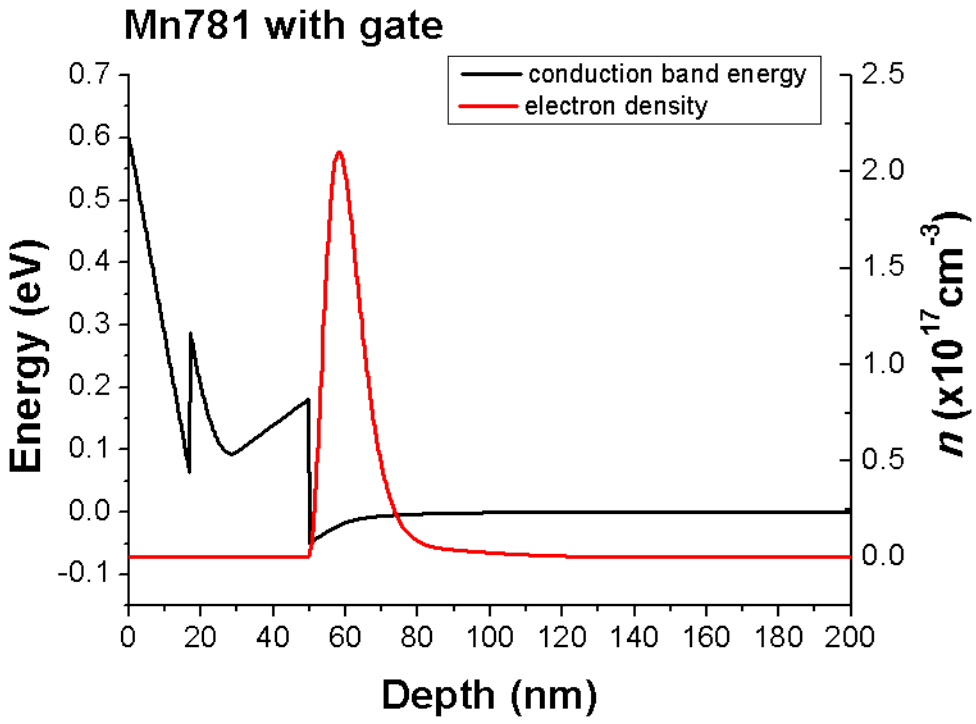

Figure 5.17: Conduction band structure (black) and electron density (red) for Mn781 2DEG heterostructure with Schottky contacts of size 0.6eV.

From the '1D Poisson' models for both the Mn782 and Mn781 heterostructure designs, single quantised energy level occupation at the AlGaAs/GaAs interface

is achieved for ohmic contacts, but double quantised energy level occupation at the AlGaAs/GaAs interface is observed for the 0.6eV Schottky contacts. However, again for both Mn782 and Mn781, using a higher Schottky barrier value (0.8eV) or a slightly lower doping density ($0.9\text{x}10^{20}\text{cm}^{-3}$/$1.8\text{x}10^{20}\text{cm}^{-3}$ respectively) gives single quantised energy level occupation for both ohmic and Schottky contacts. Given the possibility to tune effective doping density downwards from the nominal doping density due to the combination of DX centres and persistent photo-conductivity, the heterostructure designs of Mn782 and Mn781 are fairly sensible for trying to achieve a 2DEG for the purposes of the investigation.

5.4 Measurement of Mn782 sample without Fe gate

At the time of the initial sample growths, it was not possible to grow the Fe gate due to issues with the Fe source of the Nottingham MBE machine. It was decided to grow the Mn782 and Mn781 heterostructures without the Fe top layer, but with a As capping layer. Part of the wafer was used to process Hall bars to make characterisation measurements on the sample. The rest was retained so that at a later date the As cap could be removed and the Fe layer grown on the heterostructure. As stray fields did not need to be accounted for without the top Fe layer, the Mn782 and Mn781 heterostructures were processed into a normal Hall bar geometry, with length between contacts of 390μm and width between contacts of 200μm. N-type Ge/Au/Ni/Au finger-contacts were thermally evaporated onto the Hall bars and then annealed in at 390^{o}C for 10 seconds in a H_2/Ar environment in a rapid thermal annealer system. The measurements on the Mn782 sample presented in this section were carried out in the Nottingham vector magnet system at 4.2K unless otherwise stated.

It was found that the Mn781 sample was insulating at all temperatures and various levels of photo-illumination, and so transport measurements could not be made. To confirm that the insulating behaviour of the sample was as a result of the heterostructure design and not faulty contacts, several different contact recipes were tried to contact to Mn781 Hall bars, however all were still non-conducting. The behaviour of Mn781 highlights the fact that '1D Poisson' only models idealised heterostructures, and that the properties of real heterostructures may vary significantly from its calculated values. Sample Mn782 was found to be conducting with the initial contact recipe, and so it was decided to focus the characterisation measurements on this sample.

Upon cooling Mn782 to 4.2K and prior to illuminating it, the sample has a sheet resistance of 21.5kΩ/sq. A light bulb placed on the sample rod next to the Mn782 Hall bar was used to illuminate the sample with white light for 20s. The intensity of the illumination was not directly quantified, but was assumed to vary non-linearly with the voltage put through the bulb, which for the measurements in this section was 21V. Immediately after the illumination was complete the sheet resistance of the sample decreased to 28.7Ω/sq, which is nearly three orders of magnitude smaller than the pre-illumination value. The drastic decrease in the sheet resistance

upon illumination at 4.2K is the result of the white light providing enough energy for trapped electrons to become freed from DX centres (and possibly other types of defects), increasing the sample's free electron density and hence reducing its sheet resistance. As shown in figure 5.18, the sheet resistance increases quite significantly with time after illumination (an increase of about 25% in 65 minutes - note there is a slight time delay between the removal of the light and the start of the measurement shown in the figure).

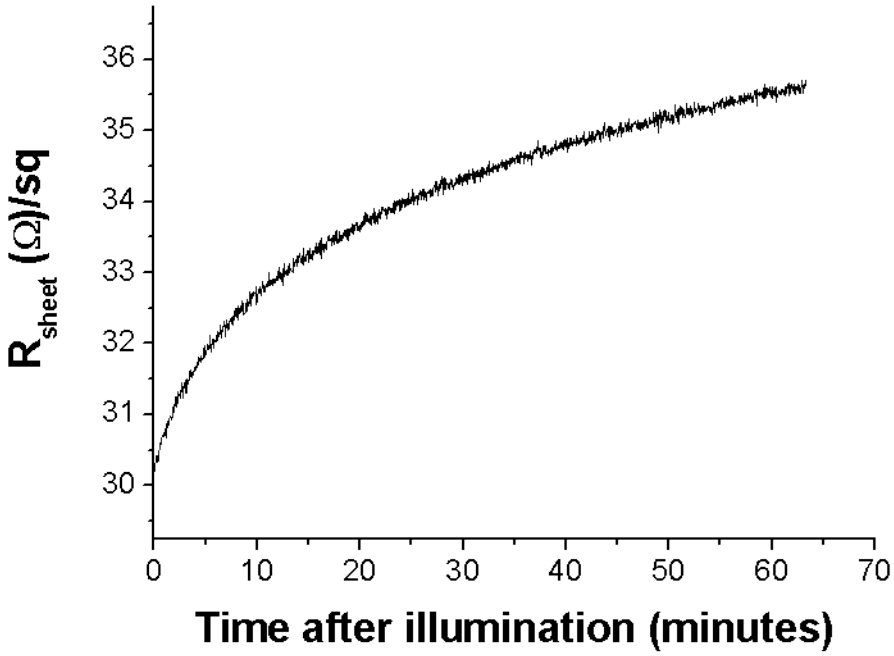

Figure 5.18: Sheet resistance against time after the removal of a 30s white light illumination for Mn782.

The increase in sheet resistance with time after illumination is perhaps somewhat surprising. It has been previously shown that below around 150K (and in the absence of illumination - only thermal effects are considered) that the occupation of DX centres 'freezes' (remains constant) as a result of large energy barriers stopping electrons escaping from or becoming trapped in DX centres[262]. The observed increase in sheet resistance with time after illumination of the Mn782 sample in figure 5.18 suggests that a small number of the liberated electrons become re-trapped by the DX centres, and that while this process is more rapid in the first 10 minutes after illumination, it continues for more than an hour (effect was only measured for 65 minutes). In order to minimise the effects of the increasing sheet resistance, the measurements presented in this section were made 2 hours or more after the illumination as the increase in resistance with time is less severe at this point.

To further characterise Mn782, out of plane sweeps with a 6T external magnetic field were performed on the sample for both non-illuminated and illuminated conditions, with the sheet and transverse resistance plotted in figures 5.19-5.22.

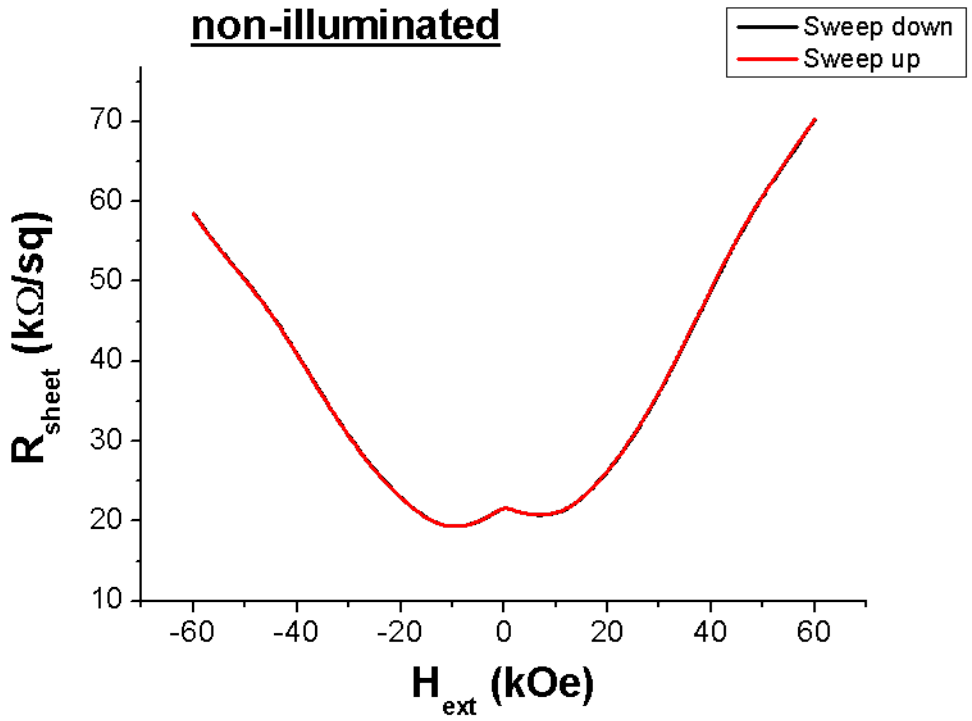

Figure 5.19: Sheet resistance against out of plane external field for non-illuminated Mn782 at 4.2K.

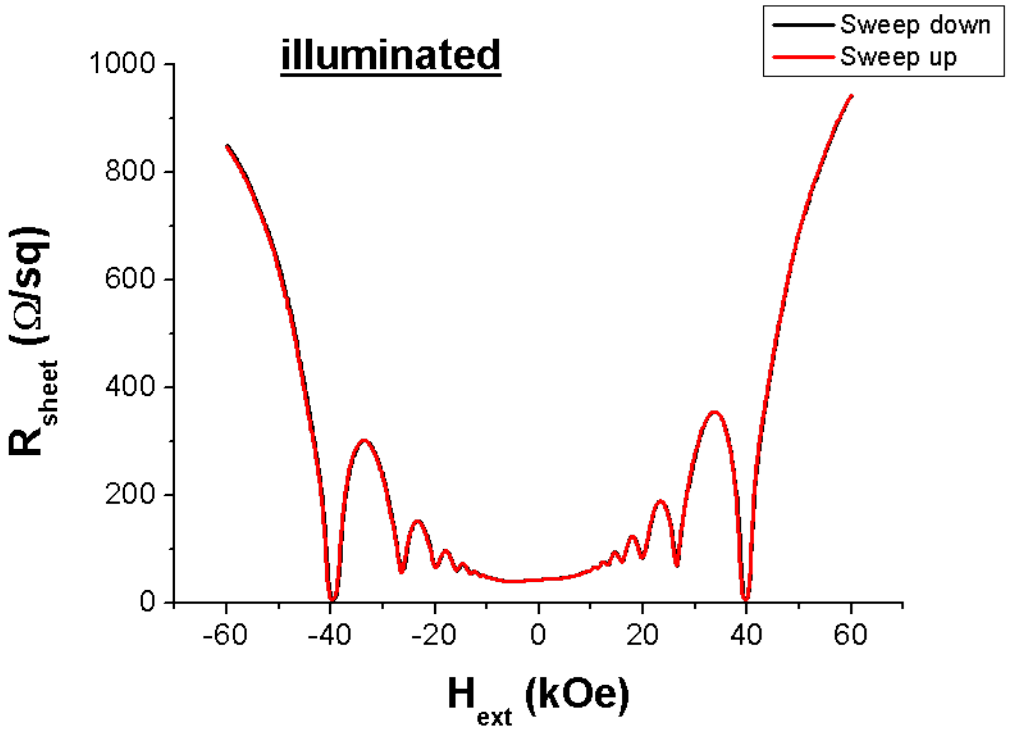

Figure 5.20: Sheet resistance against out of plane external field for illuminated Mn782 at 4.2K.

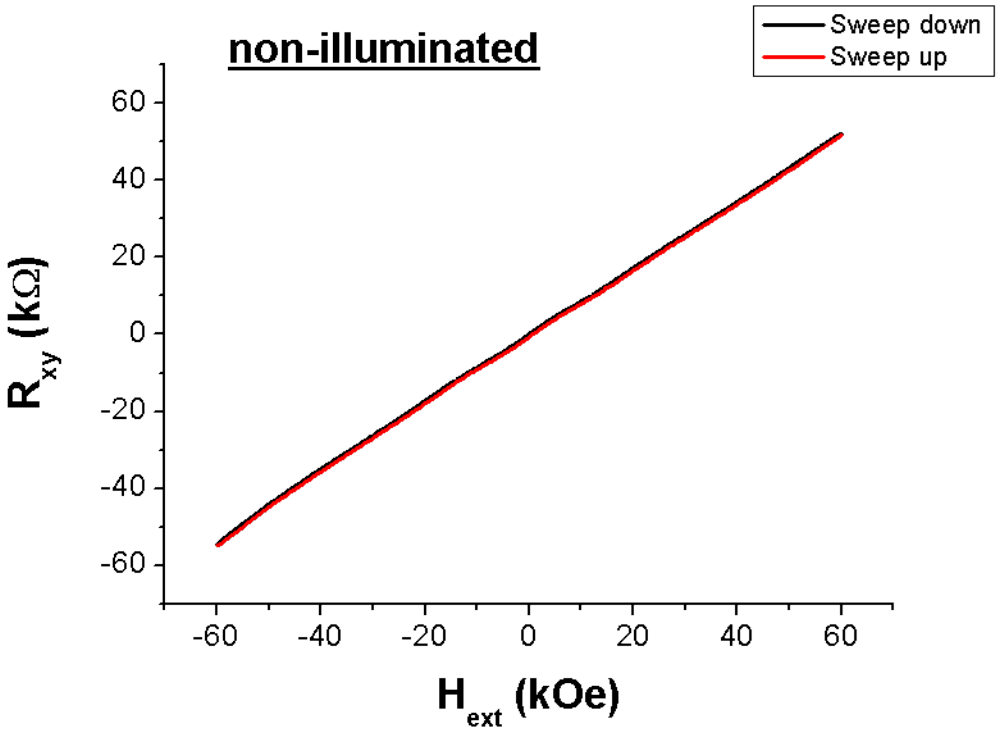

Figure 5.21: Transverse resistance against out of plane external field for non-illuminated Mn782 at 4.2K.

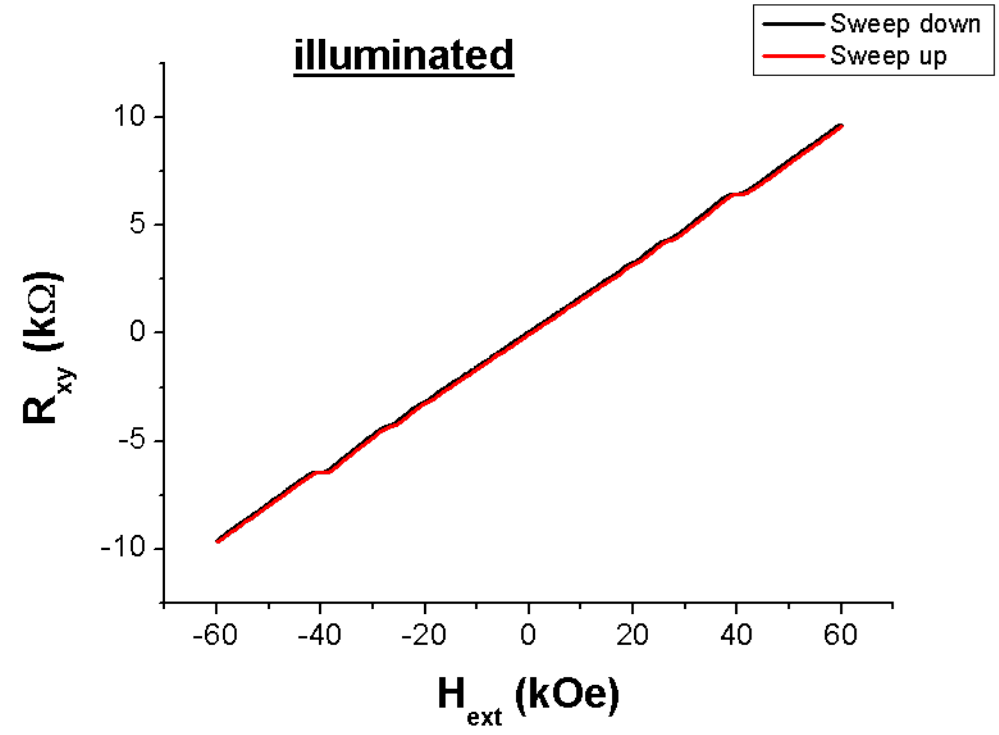

Figure 5.22: Transverse resistance against out of plane external field for illuminated Mn782 at 4.2K.

The striking comparison between the shape of the plots in figures 5.19 and 5.20

suggests that high mobility 2D transport is achieved for the post-illuminated sample, but not for the pre-illuminated sample. The oscillations in the sheet resistance with external field strength for the illuminated measurements are a signature of the SDHE[263], a quantum mechanical effect which occurs in 2D systems as a result of the density of states at the Fermi level dropping to zero at external magnetic field values where the occupied Landau level is completely filled. If the density of states at the Fermi level is zero then the sheet resistance should go to zero, and so the fact that the sheet resistance does not totally drop to zero at the oscillation minima in the illuminated sample suggests there is a small parallel conduction channel in the sample heterostructure. One possibility for this is a small population of free electrons in the doped AlGaAs layer. The 2D transport behaviour of the illuminated sample is confirmed in figure 5.22 where plateaus in the Hall resistance can be seen (these are highlighted in figure 5.23). The plateaus are a signature of the integer quantum Hall effect (IQHE)[264], which like the SDHE occurs when the occupied Landau level is completely full and so the Fermi level lies between Landau levels in 2D systems.

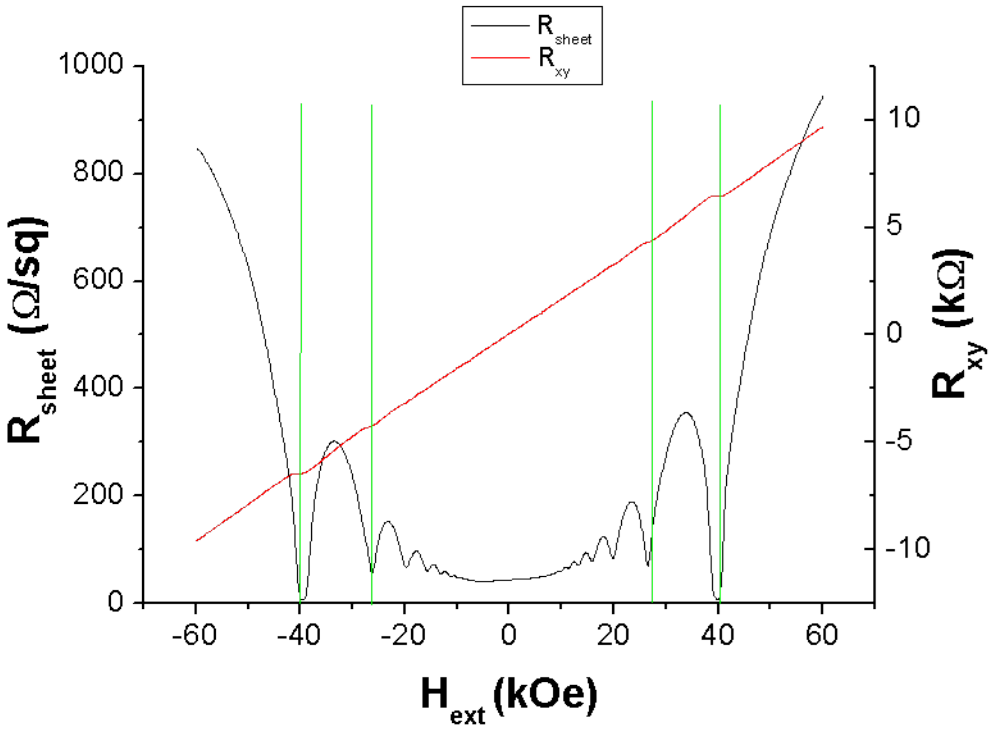

Figure 5.23: Sheet resistance (black) and transverse resistance (red) against out of plane external field for illuminated Mn782 at 4.2K. Green lines are a guide to highlight sheet resistance minima and transverse resistance plateaus.

The high sheet resistance and absence of the SDHE and IQHE in the sample for the non-illuminated measurements may suggest that a 2DEG does not form in the heterostructure, and that perhaps the low but non-zero conductivity arises from conduction in the doped AlGaAs layer by low mobility carriers. However, as the onset of the SDHE occurs at a value inversely proportional to carrier mobility it may instead be the case that the mobility is very low in the non-illuminated measurements and that the SDHE could be observed if a larger field were applied.

The observations of the SDHE and IQHE in the illuminated measurements are good indicators that a 2DEG has formed at the AlGaAs/GaAs interface. The SDHE is also useful for measuring the sheet electron density of the 2DEG by using the formula:

$$n_s = \frac{g_s e}{h(\Delta\frac{1}{B})} \tag{5.4}$$

where n_s is the sheet electron density, g_s is the spin degeneracy (in this case $g_s = 2$), e is the charge of an electron, h is the Planck constant, and $\Delta\frac{1}{B}$ is the period of oscillations when the SDHE data is plotted as sheet resistance against $\frac{1}{B}$.

Additionally the sheet electron density of the 2DEG can also be obtained from the slope of the ordinary Hall effect (the effect of the IQHE plateaus on the OHE average out) via the formula:

$$n_s = \frac{1}{e(\Delta\frac{R_{xy}}{B})} \tag{5.5}$$

For the illuminated sample, n_s is calculated to be 3.8x10^{11}cm^{-2} and 3.9x10^{11}cm^{-2} from equations 5.4 and 5.5 respectively. The good agreement is another indication of the formation of a high quality 2DEG in the heterostructure. The value of n_s for the Mn782 heterostructure calculated using '1D Poisson' under fully ionized conditions is 1.6x10^{11}cm^{-2}, which is less than half that of the measured values. This again highlights that '1D Poisson' should only be used as a general guide for heterostructure design, and should not be expected to perfectly predict electron densities and energy bands of heterostructure designs. Possible reasons for the discrepancy between experiment and model values of n_s include the doping in the AlGaAs layer not being exactly the intended amount or the presence of other defects in the heterostructure that donate electrons. The measured n_s is also nearly an order of magnitude smaller than the sheet doping density (N$_D$ = 1x10^{18}cm^{-3} in a 22nm thick AlGaAs layer gives a sheet doping density of 2.2x10^{12}cm^{-2}). The main reason for this difference between doping and electron sheet densities is that the majority of electrons from the Si donor atoms do not end up in the 2DEG formed at the AlGaAs/GaAs interface. Instead they move to the heterostructure surface to bring about the band-bending required to pin the Fermi level to that of the GaAs surface states; the free electrons from the heterostructure migrate to the surface leaving a positive charge on the heterostructure side of the heterostructure/surface interface which causes upwards bending of the heterostructure bands at the interface required to pin the Fermi level.

As well as increasing the sheet electron density, illumination of a 2DEG heterostructure can also increase the electron mobility. Electron mobility could potentially be another useful parameter to be able to tune when optimising the heterostructure for the magnetic gating experiment. The mobility can be obtained simply from the sheet resistance and the gradient of the Hall slope as such:

$$\mu = \frac{\Delta R_{xy}}{\Delta B}\frac{1}{R_{sheet}} \tag{5.6}$$

where μ is the mobility, and R_{sheet} is the sheet resistance.

To demonstrate the ability of illumination to tune n_s and μ, Mn782 was illuminated with the same intensity of white light for different periods of time, ranging from 0s to around 40s, with a 1 hour wait between each illumination and subsequent measurement. R_{sheet} was recorded and out of plane field sweeps were performed in order to obtain both n_s and μ. The results are plotted in figure 5.24:

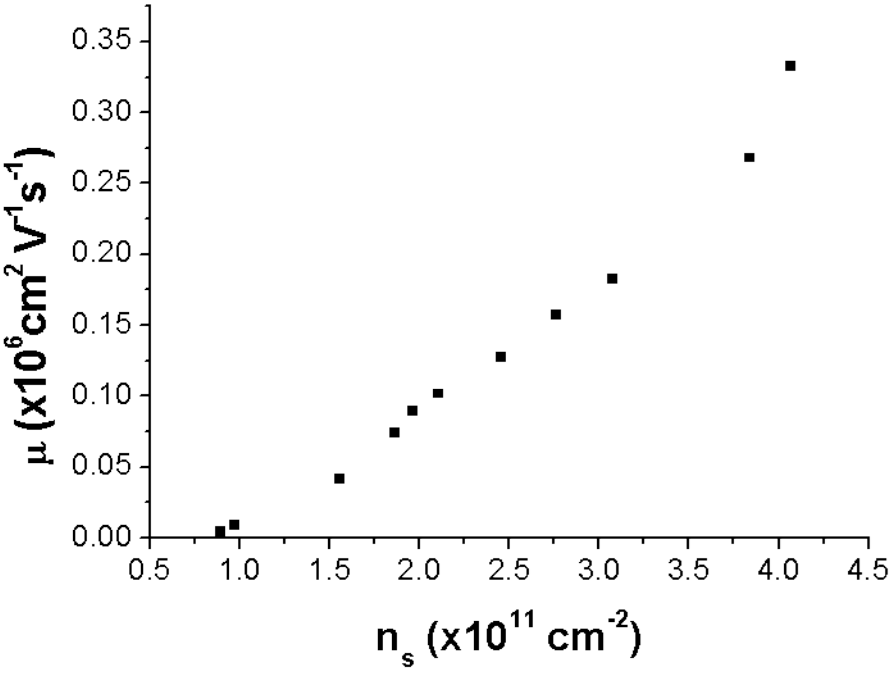

Figure 5.24: Sheet electron density against electron mobility for Mn782 at 4.2K.

As figure 5.24 shows, for Mn782 there is a fairly linear relationship between n_s and μ (there is also apparent localisation at low n_s, as μ tends to zero at a finite value of n_s). Considering that R_{sheet} depends linearly on both n_s and μ, this result highlights why the increase in R_{sheet} with illumination is so drastic. Simply by illuminating the sample n_s can be varied by a range of about $4\text{x}10^{11}\text{cm}^{-2}$ while μ can be varied by a range of nearly $0.35\text{x}10^{6}\text{cm}^{2}\text{V}^{-1}\text{s}^{-1}$. Additionally, the relationship between n_s and μ can be used to gain information about the scattering mechanisms present in the heterostructure[265][266], though this is out of the scope of the investigation in this chapter.

It is desirable that the 2DEG does not have any type of AMR-style effect, i.e. change in resistance when an external field is rotated in the plane of the sample. If the 2DEG, or the heterostructure as a whole, were to show some relatively large change in resistance with in-plane external field direction, this change in resistance could swamp the signal of the change in the 2DEG resistance that results from the electrochemical potential anisotropy with magnetization orientation effect (magnetic gating effect) in the device with the ferromagnetic gate layer. To

investigate whether the 2DEG heterostructure without the gate displayed any type of AMR signal, an in-plane field rotation measurement were performed with a 2T external field, the results of which are shown in figure 5.25.

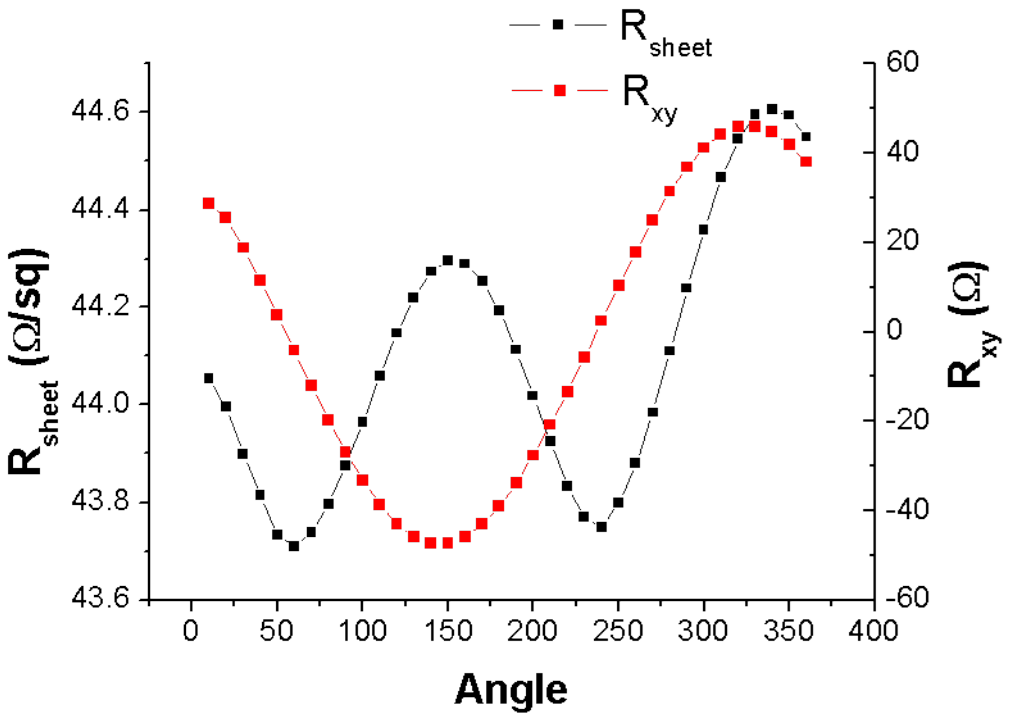

Figure 5.25: Sheet resistance (black) and transverse resistance (red) against angle of in-plane 2T external magnetic field. Note that the angle of external field is not defined with respect to any reference point of the sample.

The variation in R_{sheet} and R_{xy} with the angle of the in-plane external field shown in figure 5.25 can be explained by the in-plane field having an out of plane misalignment of around 1.7°. Ignoring a rising background drift in R_{sheet} and R_{xy} which can be ascribed to the behaviour shown in figure 5.18, R_{sheet} varies with a $\cos(2\phi)$ symmetry and R_{xy} varies with a $\cos(\phi)$ symmetry (where in this case ϕ is the angle between the in-plane external field and an arbitrarily defined reference point). The maxima and minima of the R_{xy} variation occur at approximately the same point as R_{sheet} maxima (though this is slightly obscured by the drift). These observations are consistent with an out of plane component of the external magnetic field causing a Lorentz force on the carriers to give ordinary magnetoresistance and ordinary Hall effect contributions to R_{sheet} and R_{xy} respectively. R_{sheet} varies by around 1% (in terms of an AMR style definition and accounting for the drift), and this percentage change is of a similar magnitude to what may be maximally expected of the change in carrier density from the magnetic gating effect. However, for the device with the ferromagnetic gate on, changes in R_{sheet} with external field angle due to out of plane misalignment and due to the magnetic gating effect should be relatively straightforward to separate. For the magnetic gating effect, changes in R_{sheet} should be symmetric about the angle between the Fe crystalline axes and the external field (assuming a saturating field), and there should be no variation in R_{xy}. For the misalignment effect, the variation R_{sheet} should be

symmetric about some point of misalignment at a certain in-plane angle, and the variation in R_{xy} should also be defined with respect to the same point. Fitting to the R_{xy} data should give the angle of misalignment, which can then be used in a fit to the R_{sheet} data using a $\cos(2\phi)$ function defined with respect to the angle of misalignment, and $\cos(2\phi)$ and $\cos(4\phi)$ functions defined with respect to the Fe crystalline axes (assuming in-plane uni-axial and cubic contributions to the electrochemical potential variation). Varying the magnitude of the external field may also further separate magnetic gating and misalignment contributions to R_{sheet}.

The characterisation measurements shown in this section indicate that Mn782 is a promising sample to be used as the heterostructure for the magnetic gating experiment. The SDHE and QHE measurements show that a 2DEG does form, electron density and mobility can be varied with illumination, and the only apparent AMR-style effect is caused by a field misalignment that can be accounted for with fitting. Therefore, when the Fe source on the Nottingham MBE machine became available (nearly 2 years after Mn782 was grown), it was decided to initially grow the Fe gate layer onto the Mn782 sample rather than grow a whole new heterostructure.

The Mn782 sample wafer was heated in the MBE machine to remove the As cap. Several layers of GaAs were then grown onto the sample to recover the quality of the surface, before an approximately 2nm layer of Fe was grown followed by a 5nm Al cap. To check the properties of the 2DEG heterostructure, Hall bars were processed with the Al and Fe layers completely removed (by photo-developer solution and HCl respectively), i.e. no gate. For the first Hall bar tested the same contact recipe as the previous Mn782 devices was used with the same annealing conditions. However, for transport measurements made on the Hall bar, the transport characteristics observed for the original Mn782 device were not present. Most notably, the sheet resistance at 4K and after illumination was more than 100kΩ/sq. This suggests that either contact was not made to the 2DEG channel, or that the 2DEG no longer formed in the sample. While the former is probably more likely, both scenarios seem strange given that this device was made from the same wafer as the initial Mn782 device that did show 2DEG conduction. It is not clear why leaving the sample for 2 years, heating of the initial As capping layer, growing a few more GaAs layers, or growing the Fe gate and Al layers (which were then removed by etching) would prevent contact being made to the 2DEG channel when the same contact recipe as before is used. Measurements were also made on other Hall bars from the same processing batch where the contacts had been laser annealed or not annealed at all (the same contact recipe was used), and in both cases again no contact to the 2DEG was made. Without being able to pinpoint exactly why the contact problems occurred it was decided to not pursue any further measurements with the Mn782 sample.

5.5 Measurement of RC023 sample with and without Fe gate

With the problems contacting to Mn782 after the deposition of the Fe gate layer, a new sample was grown. RC023 has exactly the same 2DEG heterostructure layer design as Mn782, but unlike Mn782 the top Fe layer was deposited in the same growth run as the 2DEG heterostructure, as was the capping Al layer. SQUID field sweep measurements of the sample indicated that the thickness of the Fe layer is 2.6nm. The SQUID measurements also show that the Fe has a strong in-plane magnetic anisotropy. The in-plane magnetic anisotropy is bi-axial, with the easy axes closer to the [110] crystalline axis than the [1-10] crystalline axis. The magnetization saturates along the [1-10] axis with an external field of 2kOe, and therefore the 4.4kOe field of the Nottingham small cryostat system should be sufficient to saturate the magnetization along all in-plane directions for the magnetic gating experiment.

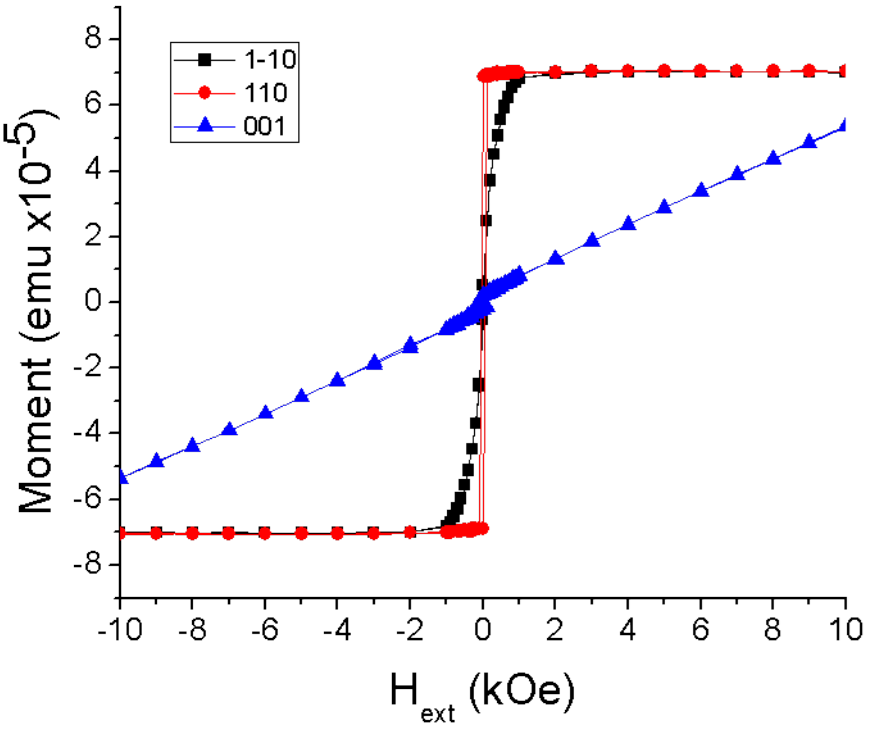

Figure 5.26: SQUID field sweep measurement of RC023 sample for field along the [1-10] (black), [110] (red), and [001] (blue) crystalline directions at 300K.

Gated L-shaped Hall bars with length between contacts of 410μm and width between contacts of 100μm were processed. The same n-type Ge/Au/Ni/Au contact recipe as for Mn782 was thermally evaporated onto the bars. An optical image of a gated L-shape Hall bar used in this investigation is shown in figure 5.27.

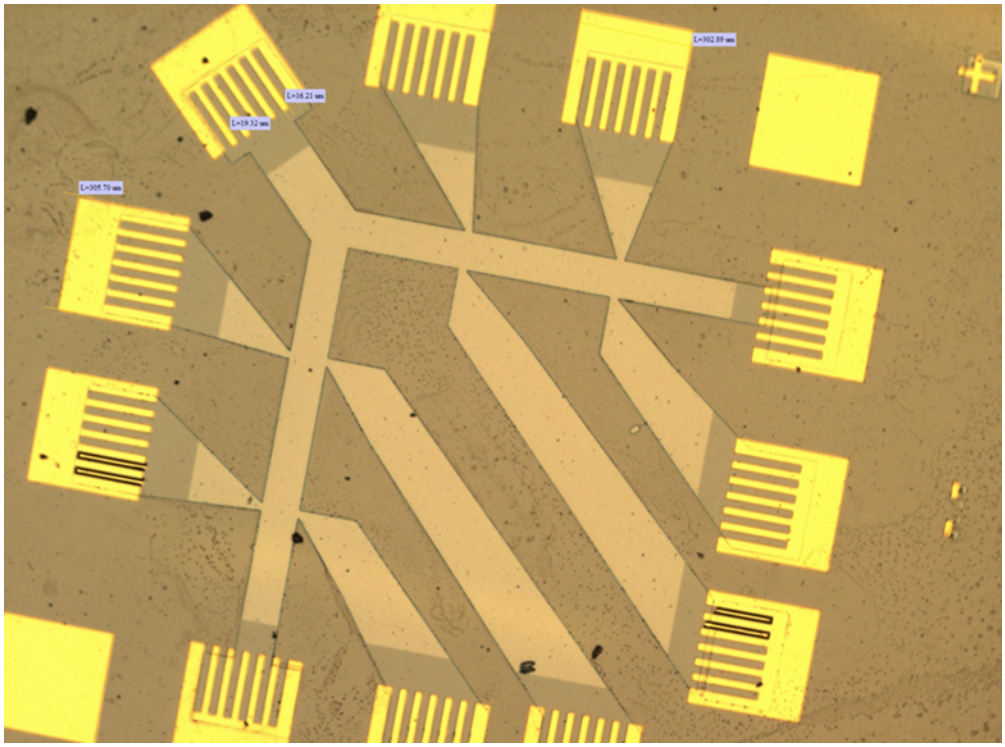

Figure 5.27: Image of L-shape Hall bar of RC023 sample with Fe gate.

Several of the bars were re-etched in photo-developer and HCl in order to remove the Fe gate so that there were ungated Hall bars for reference measurements. One of these ungated L-shaped Hall bars had its contacts annealed in at 390^{o}C for 10 seconds in a rapid thermal annealer, just as for the Mn782 devices. Subsequent transport measurements at 4.2K and roughly 1 hour after illumination of 21V through the bulb for approximately 10s showed a value of R_{sheet} of 120Ω/sq along one current direction (this R_{sheet} value was 50kΩ/sq at 4.2K before illumination), and 165Ω/sq along the orthogonal direction, values 3-4 times larger than for the original Mn782 sample. An 0.44kOe out of plane field sweep measurement was made, and the corresponding value of n_s obtained from equation 5.5 was calculated to be 4.8x10^{11}cm^{-2}, a value around 25% larger than that for the original Mn782 sample. Neither SDHE oscillations nor IQHE plateaus were observed in out of plane field sweep measurements, and this is not surprising given that the original Mn782 out of plane field sweep measurements also did not show these features in the 0.44kOe external field range. Without higher field out of plane sweep measurements it is difficult to say for sure whether a 2DEG had formed in the heterostructure, but unfortunately 0.44kOe was the maximum field available at the time of the measurement. Despite the values of R_{sheet} and n_s being larger in the ungated RC023 sample compared to the ungated Mn782 sample, the similarities in their magnitudes gave sufficient evidence that the RC023 sample was worth investigating further for the magnetic gating effect.

In order to anneal the contacts in on the devices with the Fe gate on, laser annealing was required. Fe is known to react with GaAs at the temperatures needed for the contact annealing[253][267], and this would be detrimental for the magnetic gating device. Laser annealing is simply the shining of a laser onto an area of

the sample to heat it locally. For the laser annealing in this investigation, a laser spot size of diameter 1μm was shone onto each contact (usually in the middle of one of the fingers). It was hoped that the heating at the spot was sufficient to allow the contact metal to diffuse to the 2DEG channel, but that it also would also be sufficiently dissipated at the region of the sample where the Fe gate begins so that it does not cause the Fe to degrade. For reference another ungated device also had it contacts laser annealed in order to check that the effects on the contacts of laser annealing and annealing in the rapid thermal profiler were similar. A device without any type of annealing of the contacts was also measured and showed essentially insulating behaviour even after illumination at 4.2K - this confirms that contacts do need to be annealed in. All laser annealing of devices for the work done in this investigation was kindly carried out by Dr. Oleg Makarovskiy.

5.5.1 Measurement of laser annealed RC023 sample without Fe gate

5.5.1.1 Magnetotransport characterisation

R_{sheet} of the ungated laser annealed RC023 device at 4.2K before illumination is 43kΩ/sq and 36kΩ/sq for current along the two orthogonal directions (named here as the 'Bar 1' and 'Bar 2' directions respectively). Roughly 1 hour after illumination (with 21V through the light bulb applied for approximately 10s) these values of R_{sheet} reduced to 250Ω/sq and 265Ω/sq respectively. The values are roughly double those for the ungated RC023 device with rapid thermal annealed contacts. As the R_{sheet} measurements are 4-probe measurements they should not be especially sensitive to contact resistance, and so the increased R_{sheet} values for the laser annealed contacts should not necessarily be a result of the quality of the contacts. Nevertheless, an IV measurement was made on the contacts and confirmed approximately linear behaviour up to the value of the source current used for the measurements in this investigation (10μA), and therefore the contacts are approximately ohmic for the measurements in this investigation. It should be noted that an IV measurement made on the ungated rapid thermal annealed RC023 showed similar behaviour (data not shown).

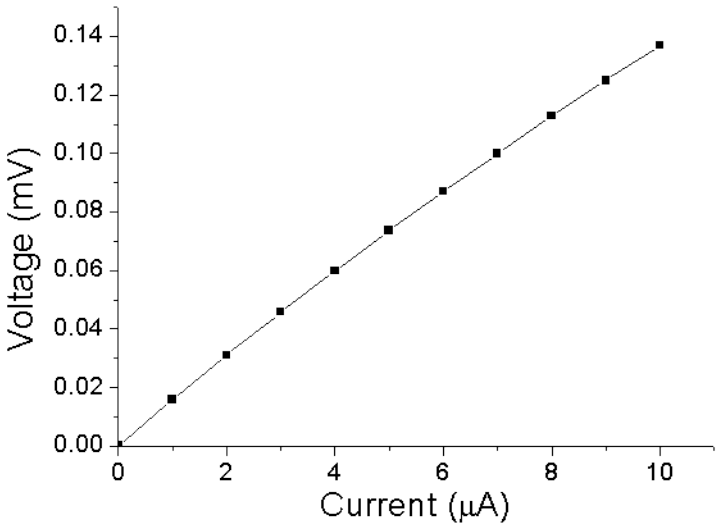

Figure 5.28: 2-probe IV measurement between two contacts of the ungated laser annealed RC023 device.

It is possible that the higher R_{sheet} for the laser annealed sample is due to a lack of precision in the duration of time that the illumination was carried out over, as well as in the duration of time between the illumination and the measurement. This part of the measurement procedure was not carried out with the degree of repeatability that it should have been, and more care should be taken in future measurements.

The values of R_{xy} under zero magnetic field at 4.2K after illumination of the laser annealed L-shape Hall bar are extraordinarily large, 315Ω for Bar 1 and 358Ω for Bar 2. These are larger than the R_{sheet} values, and it is impossible that they are caused by a misalignment of the Hall bar arms. For the rapid thermal annealed sample the R_{xy} values are also large, being around 50% and 5% of the corresponding R_{sheet} values for the two different current directions. It is unclear what is causing the large R_{xy} values in the sample. While the issue is more severe in the laser annealed device, it still appears in the rapid thermal annealed device and so is not exclusively brought about by laser annealing, though large R_{xy} values were not observed for the Mn782 sample. Given time constraints, it was decided not to further investigate the cause of the large R_{xy} values, but instead proceed with the main investigation with the hope that they would not severely affect the magnetic gating experiment.

Out of plane field sweep measurements were also made on the ungated laser annealed sample. The results for current along one of the bar directions are shown in figure 5.29.

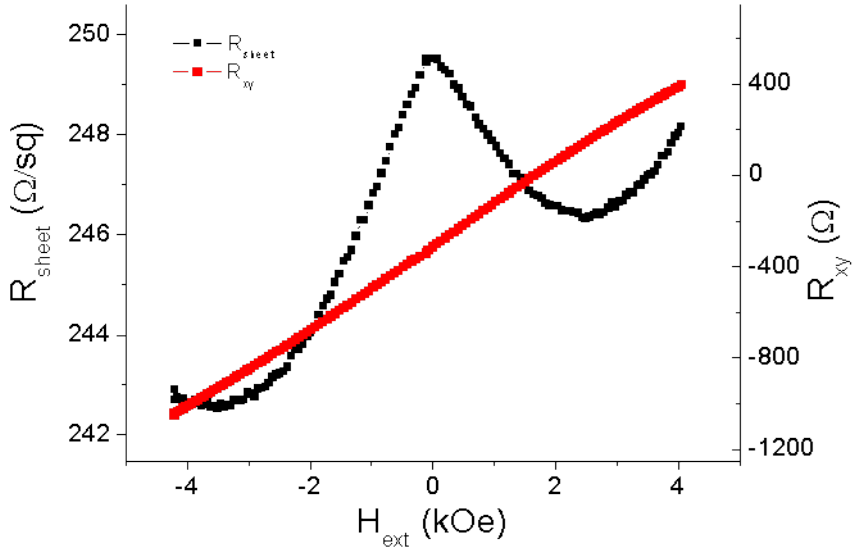

Figure 5.29: R_{sheet} (black) and R_{xy} (red) for current along the same direction of an ungated laser annealed RC023 L-shape Hall bar at 4.2K after illumination.

The low field negative magnetoresistance feature in the R_{sheet} field sweep data could be related to weak localisation[268]. The asymmetric slant on the R_{sheet} with external field suggests that the current flow is not perfectly parallel to the bar direction. This may also be a factor in the large R_{xy} values. If this were to be the case it is not clear why it is happening. The current does have to bend 90° to go from the source to drain contact of the L-shape Hall bar, but devices of the same geometry made from a different material have previously not shown such spurious R_{sheet} and R_{xy} behaviour.

From the R_{xy} Hall measurements for current along both directions, a value of n_s of 3.5x10^{11}cm^{-2} was obtained, which is lower than the value of n_s from the rapid thermal annealed device. Again this discrepancy may be due to carelessness in the illumination procedure (indeed the lower n_s would be expected to coincide with a higher R_{sheet}, as is the case). The fact that n_s is not significantly different to the ungated Mn782 device (which did not have large R_{xy} values) suggests that obtaining n_s from Hall measurements appears to still be a valid technique despite the large R_{xy} values.

5.5.1.2 Field rotation measurements

With the R_{sheet} and R_{xy} values of the ungated laser annealed RC023 device not looking ideal, in-plane field rotation measurements were made in order to see whether there were any additional AMR-style contributions to the measurements, other than the out of plane misalignment of the field observed for the Mn782 sample. Identifying and defining such contributions in the ungated sample is important for trying to separate them from possible magnetic gating effect contributions in the gated device. Figures 5.30-5.32 show the measured variation in R_{sheet} and R_{xy}

for the orthogonal Bar 1 and Bar 2 current directions on the L-shaped Hall bar device as a function of the angle between an in-plane external magnetic field and an in-plane arbitrary direction of the sample's crystalline axes. Measurements were made for different temperatures, magnitudes of external field, and intensities of illumination. The variation in R_{sheet} and R_{xy} is plotted as AMR_{xx} and AMR_{xy} as defined in equations 3.1 and 3.2 respectively in chapter 3. For all measurements the drift in R_{sheet} and R_{xy} with time after illumination is approximately accounted for by measuring its rate in a static field and subtracting a linear fit from the raw field rotation data. This procedure to remove drift was not as effective for measurements at higher temperatures.

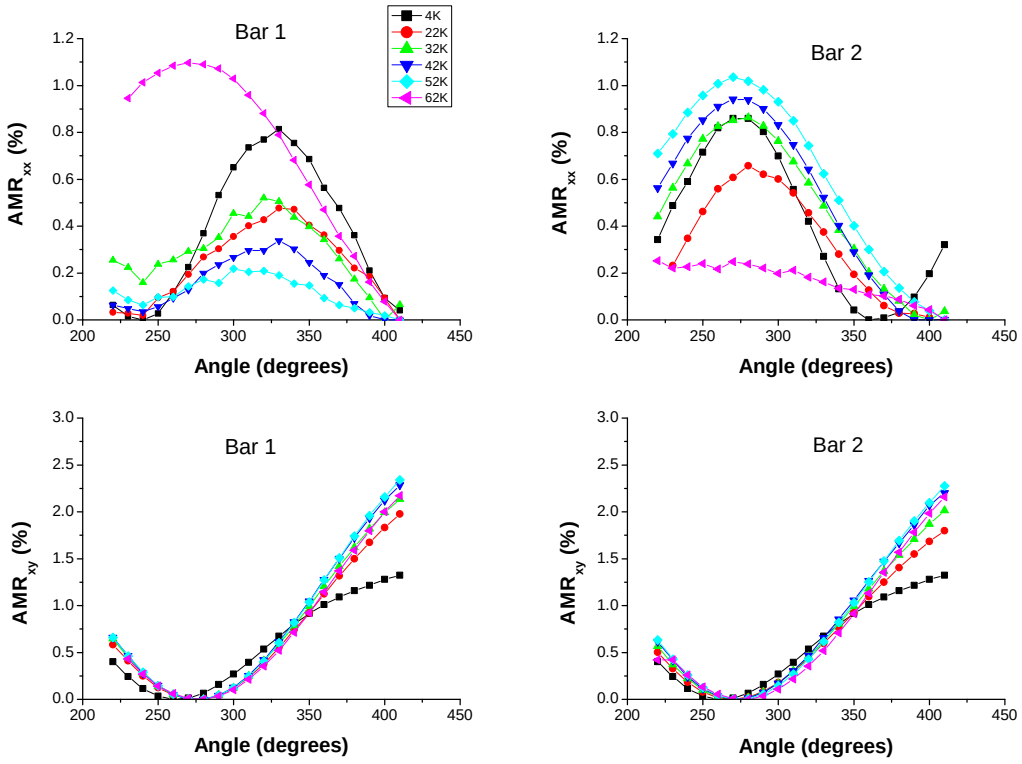

Figure 5.30: AMR_{xx} (upper plots) and AMR_{xy} (lower plots) of the ungated RC023 device for current along orthogonal directions (left and right columns for Bar 1 and Bar 2 respectively) as a function of the angle between the in-plane external magnetic field and an arbitrary direction of the sample's crystalline axes. Plots are for various temperatures, with an external field of 4.4kOe and after a 27V illumination.

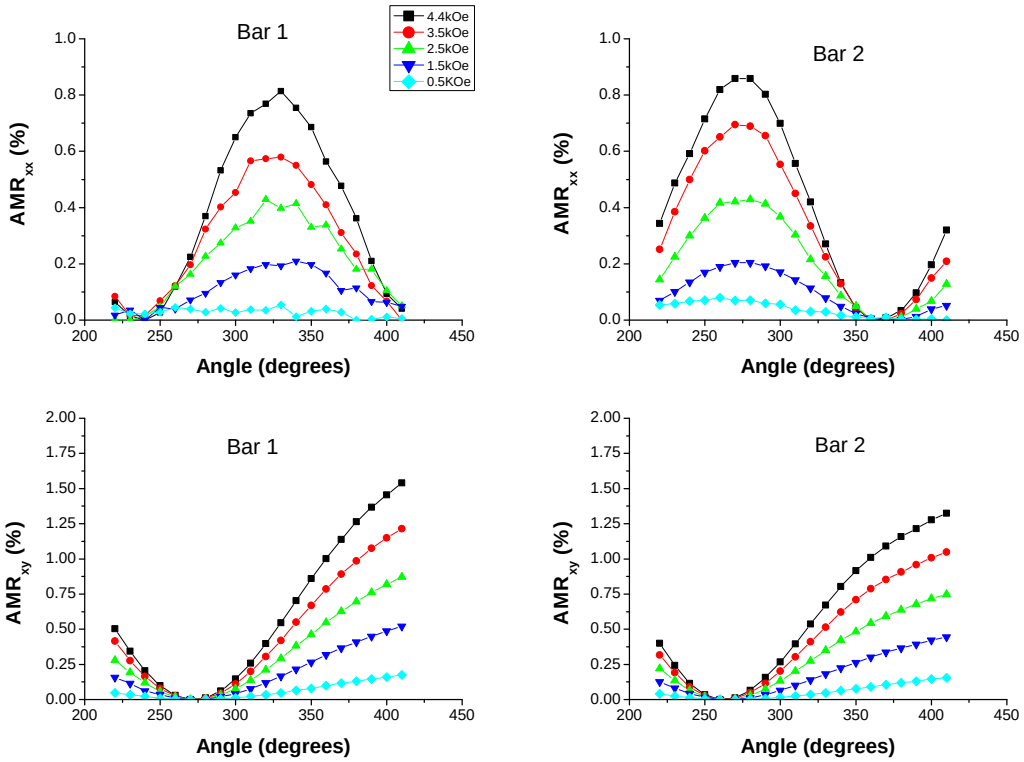

Figure 5.31: AMR_{xx} (upper plots) and AMR_{xy} (lower plots) of the ungated RC023 device for current along orthogonal directions (left and right columns for Bar 1 and Bar 2 respectively) as a function of the angle between the in-plane external magnetic field and an arbitrary direction of the sample's crystalline axes. Plots are for various magnitudes of external field, at a temperature of 4.2K and after a 27V illumination.

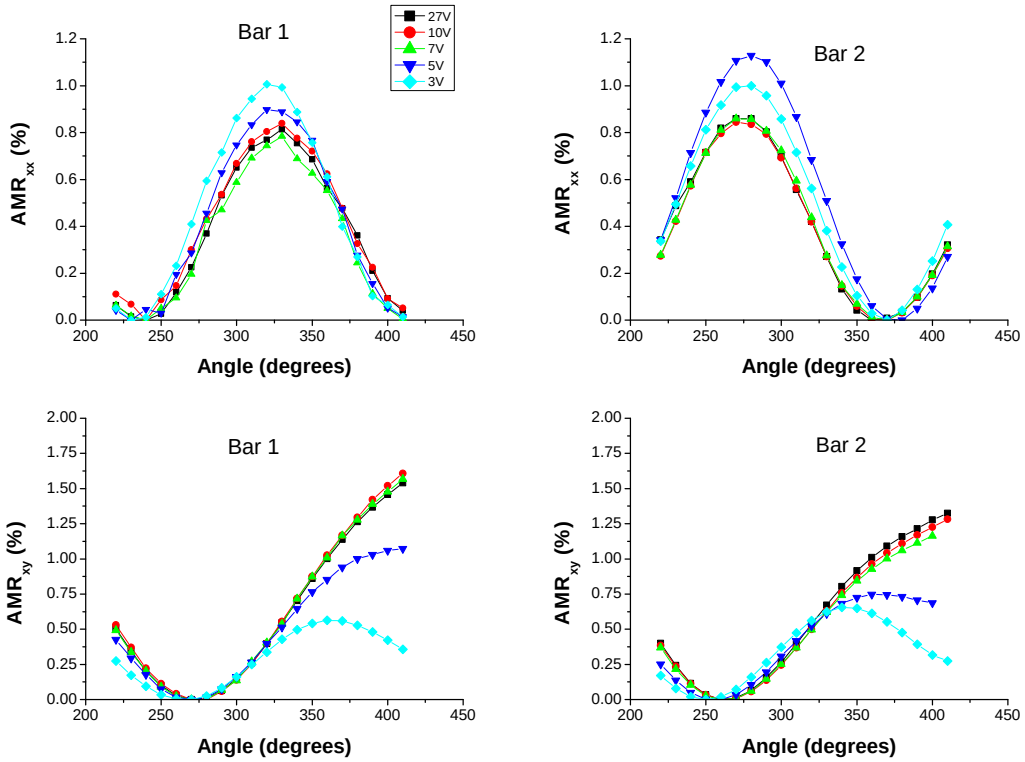

Figure 5.32: AMR$_{xx}$ (upper plots) and AMR$_{xy}$ (lower plots) of the ungated RC023 device for current along orthogonal directions (left and right columns for Bar 1 and Bar 2 respectively) as a function of the angle between the in-plane external magnetic field and an arbitrary direction of the sample's crystalline axes. Plots are for various intensities of illumination (27V being the most intense, 3V being the least intense), with an external field of 4.4kOe and at a temperature of 4.2K.

All of the AMR$_{xx}$ and AMR$_{xy}$ data in figures 5.30-5.32 can be well fitted to with the equation:

$$\text{AMR} = P_1 cos(\phi - \phi_1) + P_2 cos(2(\phi - \phi_2)) \tag{5.7}$$

where ϕ is the angle between the in-plane external field and the arbitrary direction of the crystalline axes, ϕ_1 and ϕ_2 are variable fitting parameters to adjust the angle of symmetry of the $cos(\phi)$ and $cos(2\phi)$ contributions respectively, and P_1 and P_2 are variable fitting parameters representing the magnitude of the $cos(\phi - \phi_1)$ and $cos(2(\phi - \phi_2)$ terms respectively.

The ratio of the magnitude of the $cos(2\phi)$ to $cos(\phi)$ contributions to the temperature, external field, and illumination AMR$_{xx}$ and AMR$_{xy}$ data sets are plotted in figure 5.33.

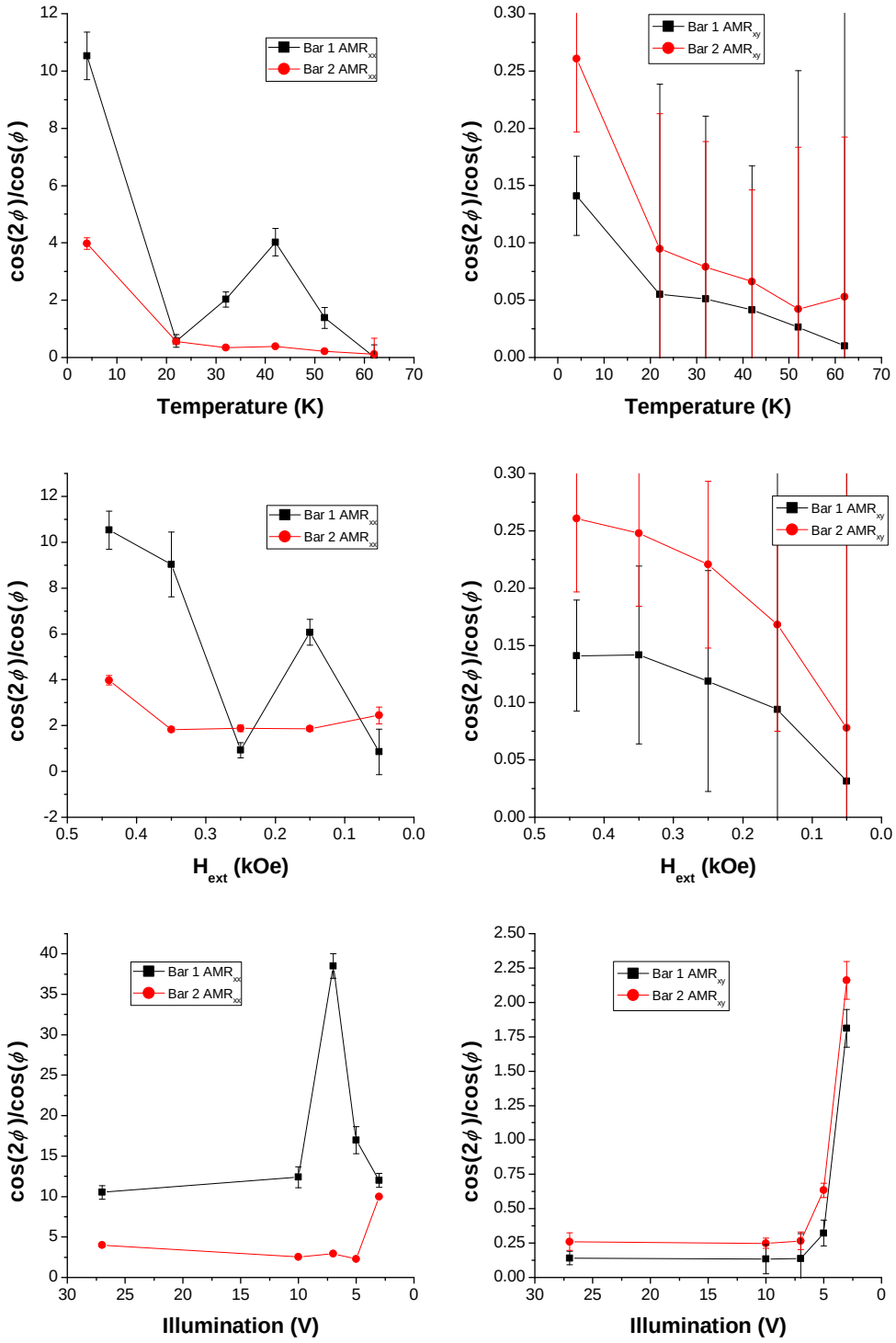

Figure 5.33: Ratio of the magnitude of the $cos(2\phi)$ to $cos(\phi)$ contributions to the fits of the AMR$_{xx}$ (left column plots) and AMR$_{xy}$ (right column plots) data in figures 5.30-5.32 made using the fitting equation 5.7.

Figures 5.30-5.32 show that some type of AMR-style signal does exist in the ungated RC023 sample. Focusing on the case for the conditions of 4.2K temperature, 4.4kOe external field, and 27V illumination (the black data points in all of the

figure 5.30-5.32 plots), the magnitude of AMR_{xx} is around 0.8%, which is a similar size to what may be expected for any possible magnetic gating effect in the gated sample. As shown in figure 5.33, the symmetry of the 4.2K temperature, 4.4kOe external field, and 27V illumination AMR_{xx} for both current directions is largely $cos(2\phi)$, though does require a smaller $cos(\phi)$ term to fit accurately. The equivalent AMR_{xy} has a largely $cos(\phi)$ symmetry that also requires a smaller $cos(2\phi)$ term to fit accurately. The mostly $cos(2\phi)$ and $cos(\phi)$ symmetries of AMR_{xx} and AMR_{xy} respectively may at first glance suggest that the AMR effects are caused largely by an out of plane misalignment of the external field, similar to the case for the Mn782 field rotation measurement shown in figure 5.25. However, the relative angular dependence between AMR_{xx} and AMR_{xy} for a given current direction as well as the relative angular dependence between AMR_{xx} for the orthogonal current directions and AMR_{xy} for the orthogonal current directions suggest this not be the case. For example, for the conditions of 4.2K temperature, 4.4kOe external field, and 27V illumination, the angle between the $cos(2\phi)$ term minima for AMR_{xx} and the $cos(\phi)$ term minima for AMR_{xy} is 39° for the Bar 1 current direction and 93° for the Bar 2 current direction. For an out of plane misalignment of an external field, the $cos(2\phi)$ term minima for AMR_{xx} should be offset by 90° from the $cos(\phi)$ term minima for AMR_{xy}; this is case for the Bar 2 current direction, but not for the Bar 1 direction. Furthermore, the angle at which the AMR_{xx} $cos(2\phi)$ term is maximum should be the same for both the Bar 1 and Bar 2 current directions, however again for the 4.2K temperature, 4.4kOe external field, and 27V illumination conditions there is a 36° difference. Similarly the angle at which the AMR_{xy} $cos(2\phi)$ term is minimum should also be the same for both current directions, but there is a 15° difference. All of these observations are evidence that an out of plane misalignment of the external magnetic field is at least not simplistically responsible for the observed AMR-style signal.

The trends of the $cos(2\phi)$ to $cos(\phi)$ ratio with increasing temperature and decreasing illumination also add further complexity when considering origin of the AMR-style signal. AMR_{xx} of the Bar 2 current direction becomes more $cos(\phi)$ like than $cos(2\phi)$ like at temperatures of 22K and higher. AMR_{xy} also becomes even more $cos(\phi)$ like at higher temperatures. Additionally, as illumination is decreased to 3V, AMR_{xy} for both current directions becomes more $cos(2\phi)$ like than $cos(\phi)$ like. These observations could indicate that there are several conduction channels in the device (with different AMR-style characteristics), and that the relative contribution of these channels to conduction varies with temperature and illumination. Again these observations are not compatible with an out of plane misalignment of the external field being the major source of the observed AMR.

Trying to uncover the origins of the observed AMR-style variations in R_{sheet} and R_{xy} of the ungated RC023 sample would be a very difficult task that is beyond the scope of this investigation, and it is certainly not possible with the limited measurements presented in this section. Indeed there is very little study in literature documenting AMR in non-magnetic semiconductor 2DEG heterostructures[269]. In terms of the overall goal of this investigation, i.e. to observe the magnetic gating effect, the AMR-style variation in R_{sheet} and R_{xy} for the ungated RC023 device is very problematic. Unlike for the case of the ungated Mn782 device where the

misalignment-induced AMR signal should be accountable for by fits, the poorly defined and inconsistent symmetries of both AMR_{xx} and AMR_{xy} for the ungated RC023 device would be much more difficult to separate from any magnetic gating effect in the gated device. This problem is compounded by the size of the ungated AMR effects being comparable to what may be expected for the magnetic gating effect.

5.5.2 Measurement of laser annealed RC023 sample with Fe gate

With its huge R_{xy} offsets, possibly spurious current directions, and non-systematic and substantial AMR effects, RC023 is in principle a significantly worse sample to use for a magnetic gating experiment than Mn782. However, unlike Mn782, Fe-gated devices with seemingly good contact to the relevant conduction channel were able to be made for RC023. Therefore, measurements were made on the Fe-gated RC023 sample in the hope that the magnetic gating effect may be present and still detectable despite the various problems with the ungated sample.

5.5.2.1 Magnetotransport characterisation

R_{sheet} of the laser annealed Fe-gated RC023 device at 4.2K before illumination is 25kΩ/sq and 42kΩ/sq for current along the Bar 1 and Bar 2 directions of the device respectively. Roughly 1 hour after illumination (with 21V through the light bulb applied for approximately 10s) these values of R_{sheet} reduce to 385Ω/sq and 490Ω/sq respectively. The R_{sheet} values are approximately 50%-90% larger than the corresponding values for the laser annealed ungated RC023 device. Given that R_{sheet} of the Fe-gated device varies by around 25Ω/sq in an out of plane external magnetic field of 4.4kOe (see figure 5.34), an even larger stray field from the Fe gate layer would be needed to account for the 105Ω/sq difference between R_{sheet} for the orthogonal current directions. At 4.2K and after illumination R_{xy} for Bar 1 is 10Ω and for Bar 2 is 882Ω. R_{xy} for the other Bar 2 set of transverse contact probes was even higher than 882Ω (though the actual value was not recorded). While the Bar 1 R_{xy} value seems somewhat reasonable, the huge R_{xy} of Bar 2 is considerably larger than for the R_{xy} values of the ungated RC023 device. Again the origin of the large R_{xy} is not known, but may be caused current not flowing perfectly along the bar direction.

Out of plane field sweeps were made on the sample. The R_{sheet} and R_{xy} data for Bar 1 are shown in figure 5.34.

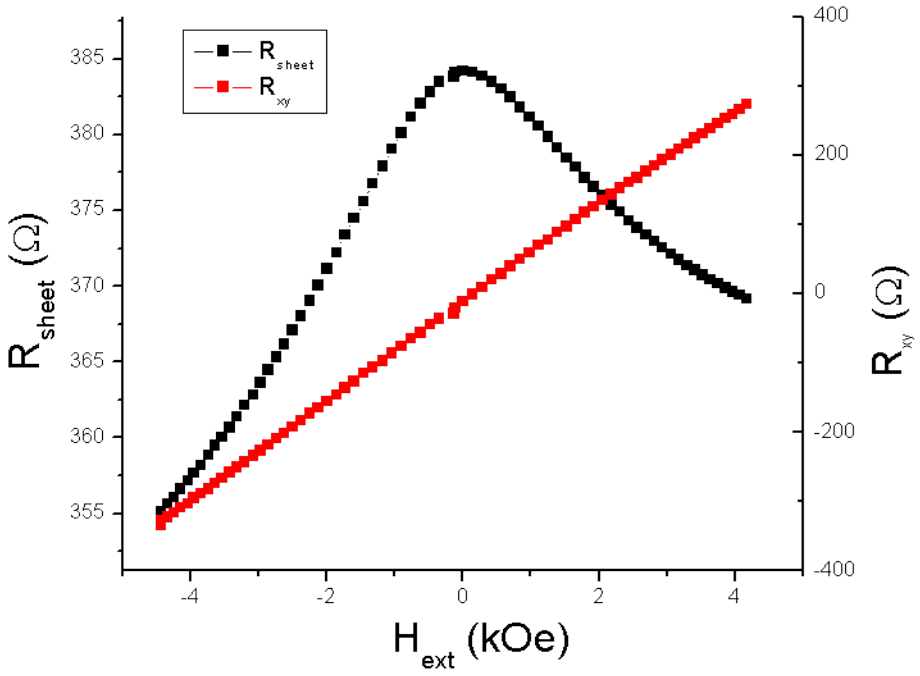

Figure 5.34: R_{sheet} (black) and R_{xy} (red) for current along the same direction of a Fe-gated laser annealed RC023 L-shape Hall bar at 4.2K after illumination.

R_{sheet} of the Fe-gated RC023 device displays a negative magnetoresistance across the whole ±4.4kOe measurement range, unlike the ungated device which has a positive magnetoresistance at field magnitudes of greater than 2.5kOe. The R_{sheet} field sweep data has an asymmetric slant, like that of the ungated device, which again may be caused by current not flowing perfectly along the bar direction.

From the R_{xy} Hall measurements for current along both directions, a value of n_s of 8.8x10^{11}cm^{-2} was obtained, which is 1.6 times bigger than the value of n_s for the ungated device. The size of n_s for the Fe-gated and ungated devices is in good agreement with the '1D Poisson' calculations used to generate figures 5.14 and 5.15, which give n_s to be 1.7 times larger for the case of the heterostructure having a 0.6eV Schottky barrier height as opposed to a vacuum terminated surface (though it should be noted that the actual calculated values of n_s are around 3 times less than the values measured in the RC023 devices). Given the larger n_s of the Fe-gated device compared to the ungated device, it is surprising that its R_{sheet} values are also larger.

5.5.2.2 Field rotation measurements

In order to try and observe the magnetic gating effect, field rotation measurements were made on the Fe-gated RC023 device in the same way as they were for the ungated device documented in section 5.5.1.2. The results are shown in figures 5.35-5.37.

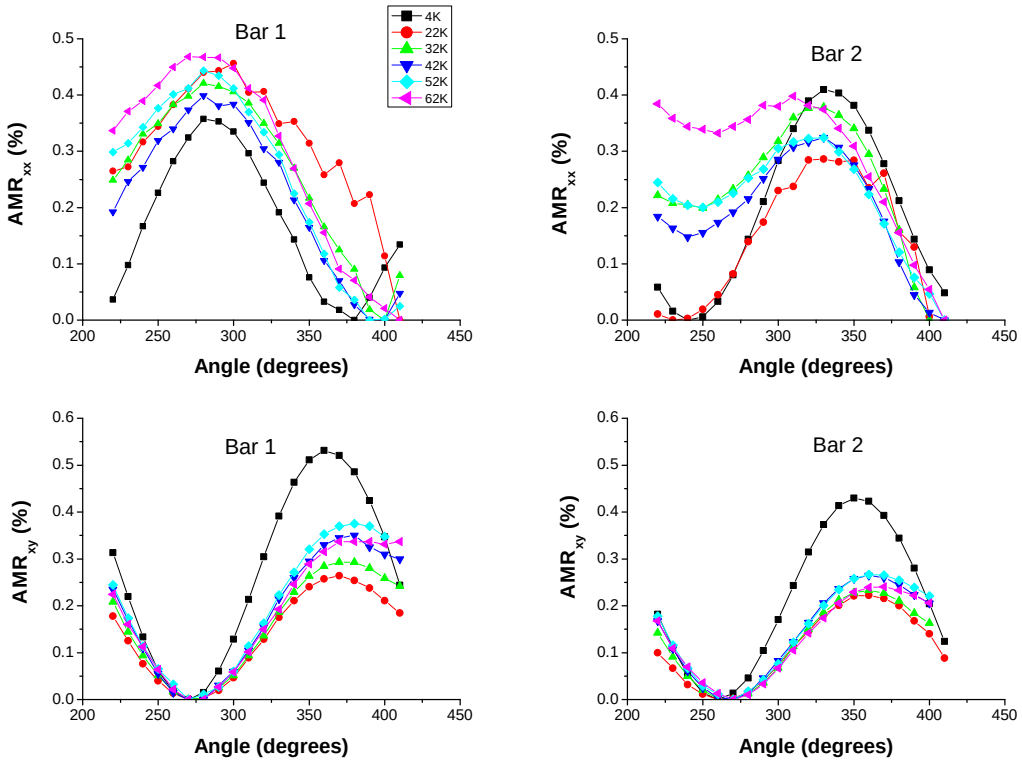

Figure 5.35: AMR_{xx} (upper plots) and AMR_{xy} (lower plots) of the Fe-gated RC023 device for current along orthogonal directions (left and right columns for Bar 1 and Bar 2 respectively) as a function of the angle between the in-plane external magnetic field and an arbitrary direction of the sample's crystalline axes. Plots are for various temperatures, with an external field of 4.4kOe and after a 27V illumination.

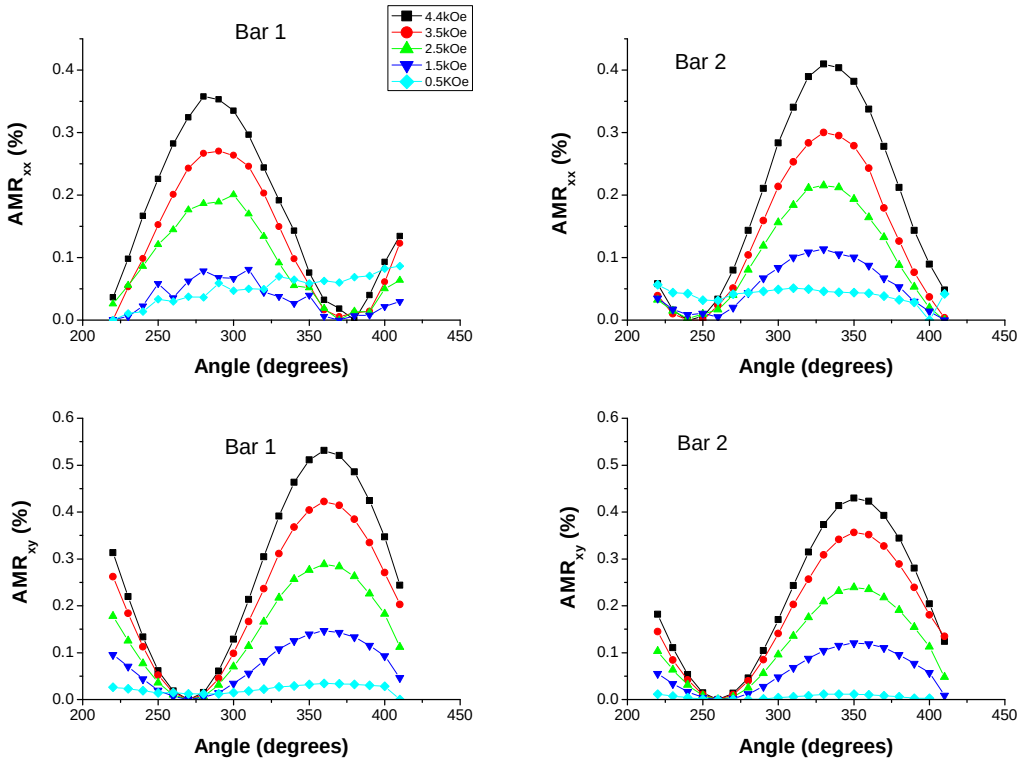

Figure 5.36: AMR$_{xx}$ (upper plots) and AMR$_{xy}$ (lower plots) of the Fe-gated RC023 device for current along orthogonal directions (left and right columns for Bar 1 and Bar 2 respectively) as a function of the angle between the in-plane external magnetic field and an arbitrary direction of the sample's crystalline axes. Plots are for various magnitudes of external field, at a temperature of 4.2K and after a 27V illumination.

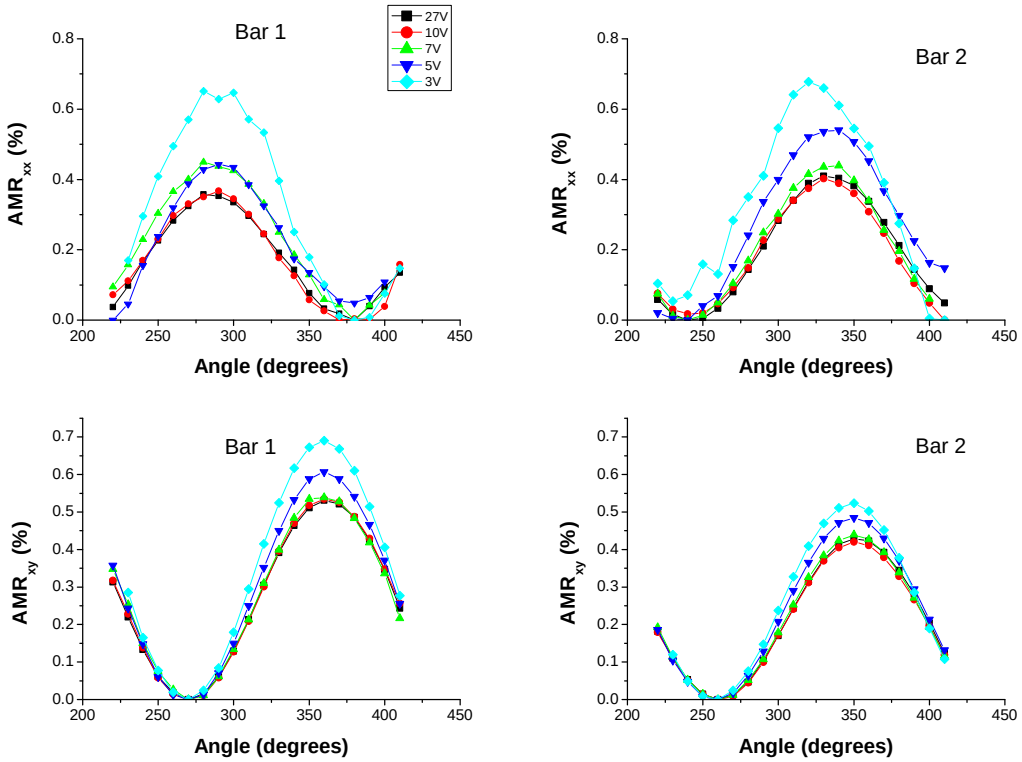

Figure 5.37: AMR$_{xx}$ (upper plots) and AMR$_{xy}$ (lower plots) of the Fe-gated RC023 device for current along orthogonal directions (left and right columns for Bar 1 and Bar 2 respectively) as a function of the angle between the in-plane external magnetic field and an arbitrary direction of the sample's crystalline axes. Plots are for various intensities of illumination (27V being the most intense, 3V being the least intense), with an external field of 4.4kOe and at a temperature of 4.2K.

The AMR$_{xx}$ and AMR$_{xy}$ data for the Fe-gated 2DEG were fitted to with equation 5.7, and the ratio of the magnitude of the $cos(2\phi)$ to $cos(\phi)$ fitting terms for the whole data set are plotted in figure 5.38.

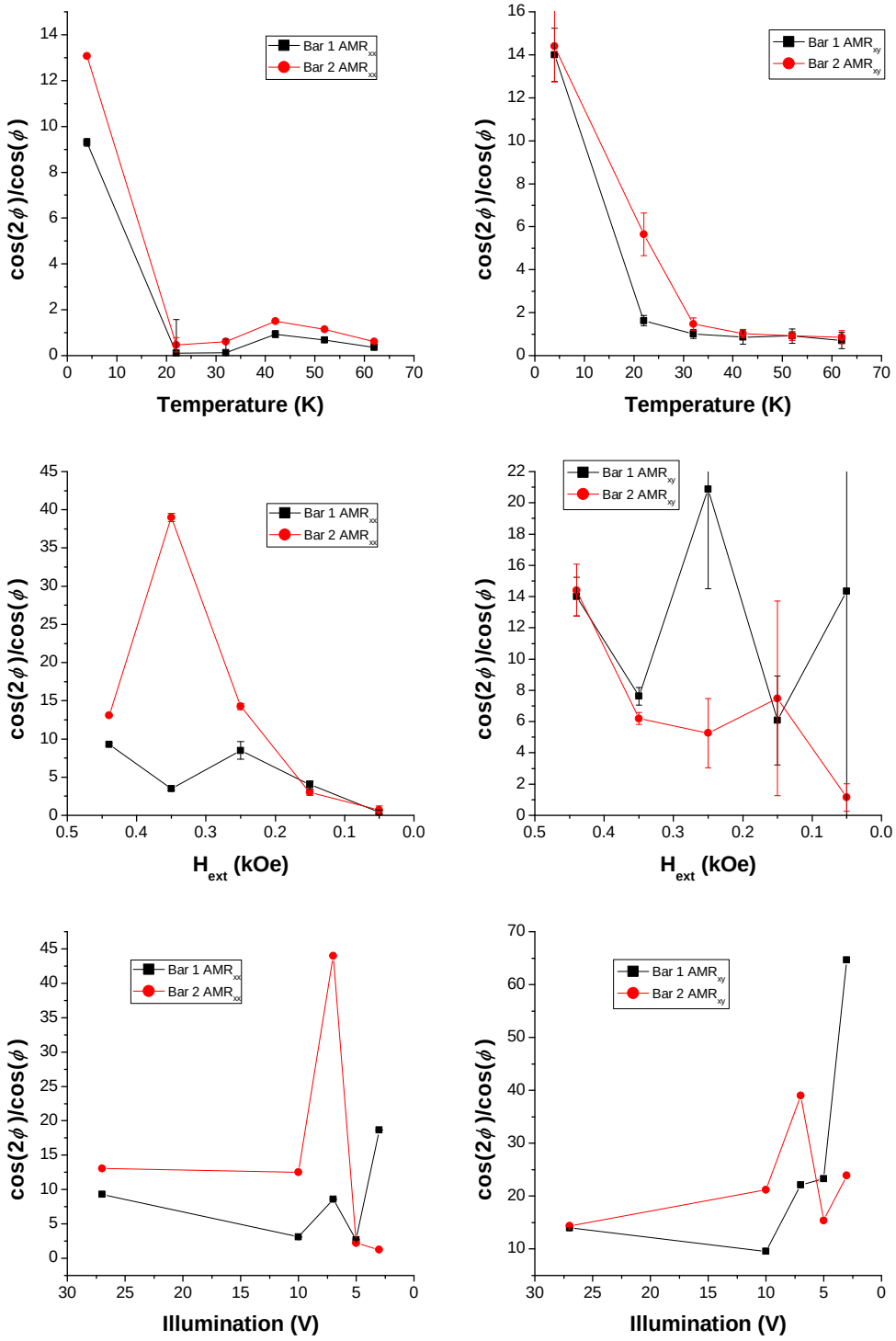

Figure 5.38: Ratio of the magnitude of the $cos(2\phi)$ to $cos(\phi)$ contributions to the fits of the AMR$_{xx}$ (left column plots) and AMR$_{xy}$ (right column plots) data in figures 5.30-5.32 made using the fitting equation 5.7.

As shown in figures 5.35-5.37, both AMR$_{xx}$ and AMR$_{xy}$ are observed in the Fe-gated RC023 device. Both are smaller in magnitude in the Fe-gated device than in the ungated device. The magnitudes of corresponding AMR$_{xx}$ and AMR$_{xy}$

values are closer to one another in the Fe-gated device, possibly suggesting their origins are more similar than in the ungated device. For the conditions of 4.2K temperature, 4.4kOe external field, and 27V illumination, the relative strength of the $cos(2\phi)$ term in AMR_{xx} is stronger for the Fe-gated sample than the ungated device. Interestingly, while the $cos(\phi)$ term dominates AMR_{xy} of the ungated device except for at 3V illumination, the $cos(2\phi)$ term dominates AMR_{xy} of the Fe-gated sample, except for at temperatures of 22K and higher (though for these conditions it still remains a similar size to the $cos(\phi)$ term which itself may be brought about by the drift in the data not being fully accounted for).

The fact that AMR_{xy} of the Fe-gated device has a mostly $cos(2\phi)$ symmetry is evidence against an out of plane misalignment of the external field being largely responsible for it (as AMR_{xy} from an out of plane misalignment would be expected to have a $cos(\phi)$ symmetry). Just as for the ungated device, the difference between the angle of the $cos(2\phi)$ term maximum for AMR_{xx} of the Bar 1 and Bar 2 directions provides further evidence against an out of plane field misalignment being significant. At 4.2K temperature, 4.4kOe external field, and 27V illumination, this difference is 48°, not the 0° difference that would be expected for an out of plane misalignment. For the same conditions, the difference in the angle of maximum of the $cos(2\phi)$ of AMR_{xy} terms for the orthogonal bar directions is 9°, while the difference between the maximum angle of the $cos(2\phi)$ term for AMR_{xx} and AMR_{xy} is 75° for Bar 1 and 18° for Bar 2. All of these various relative differences in angles of maxima are largely similar as temperature, field magnitude, and illumination are varied.

There is no evidence for the existence of the magnetic gating effect in the Fe-gated RC023 sample. Given the magnetic anisotropy of the Fe layer, if the magnetic gating effect were to exist it seems most likely that it would have $cos(4\phi)$ and/or $cos(2\phi)$ contributions to AMR_{xx}, similar to those observed in the electrochemical potential variation with magnetization orientation in (Ga,Mn)As[246]. For the measured AMR_{xx} data, any significant $cos(4\phi)$ contribution can be ruled out because equation 5.7, which does not include a $cos(4\phi)$ term, fits to the data extremely well. A magnetic gating contribution to AMR_{xx} would be expected to have the same angular dependence with respect to the device's crystalline axis for current along any direction (as is also the case for an out of plane misalignment contribution). The fact that the maxima in the $cos(2\phi)$ AMR_{xx} terms for Bar 1 and Bar 2 of the Fe-gated device have a difference of 48° is therefore evidence against a $cos(2\phi)$ magnetic gating contribution to AMR_{xx}. Furthermore, magnetic gating would give no contribution to AMR_{xy}. While the observation in AMR_{xy} cannot be used as direct evidence against magnetic gating, the possibility that it may originate from the same source as AMR_{xx} (due to the similar sizes of the AMRs) would again hint that the observed AMR_{xx} is not brought about by magnetic gating.

An attempt was made to electrically gate the Fe-gated 2DEG in order to try and tune the observed AMR effects and possibly induce the magnetic gating effect by varying the carrier density to a more favourable level. A contact was made to the Fe gate on the device, and voltage applied between the gate and drain contacts. However, the application of this voltage induced a current flow that passed through the gate layer to the 2DEG heterostructure. This leaky gate is

presumably caused by some channel for conduction in the upper layers of the 2DEG heterostructure that was not predicted with the '1D Poisson' models. The effect of applying the gate voltage on the dc transport measurements for the normal measurement geometry was therefore to add an additional signal with a distorted current path to the 4-probe measurements of R_{sheet} and R_{xy}. This was of course not helpful for the magnetic gating experiment, and so no further electrical gating measurements were made.

5.6 Conclusions and future work

Section 5.2 of this chapter proposed the possibility of magnetically gating a 2DEG. Such an effect would be brought about by the combination of the SOC-induced variation of the electrochemical potential of a ferromagnetic gate layer, and the redistribution of charge carriers in the 2DEG heterostructure to ensure its electrochemical potential matches that of the gate.

Section 5.3 detailed the design of the magnetic gating device for this investigation. An L-shape Hall bar geometry was suggested to account for the effects of stray magnetic fields from the gate layer. While this turned out not to be a significant factor in the actual experiment, the L-shape Hall bar did prove to be useful for ruling out certain AMR effects due to their relative symmetries for current along orthogonal directions. '1D Poisson' was used to model the electronic properties of various GaAs/AlGaAs heterostructure designs, and to see how the 2DEG carrier density varied with gate electrochemical potential. Calculations for a device with a (Ga,Mn)As gate layer showed it to form a 2DEG, but it was decided that the difference between the ungated and gated devices made it an unsuitable starting point for the magnetic gating experiment. Instead Fe was chosen as the gate layer due to its ease of growth on GaAs, as well as its SOC and magnetic properties. By varying several parameters to give a maximum change in carrier density with changes in gate electrochemical potential, an optimal 2DEG heterostructure design was decided upon.

Section 5.4 presented experimental measurements that characterise the properties of the ungated Mn782 device. Out of plane field sweep measurements on the device at 4.2K after illumination showed SDHE oscillations and IQHE plateaus, evidence of 2D conduction. The measured sheet electron density is larger than what was maximally predicted from '1D Poisson' calculations, and can be tuned by varying the illumination conditions. In-plane field rotation measurements showed an AMR-style effect caused by an out of plane misalignment of the external magnetic field. While the size of the AMR was significant in the context of the magnetic gating experiment, its well defined symmetry means that it can be accounted for by fitting. An attempt was made to grow a Fe gate layer onto the Mn782 sample, however contact could not subsequently be made to the 2DEG channel for reasons which are not known.

Section 5.5 showed characterisation and field rotation measurements for ungated

and Fe-gated RC023 devices. For both cases, extraordinarily large values of R_{xy} were observed which may possibly relate to current not flowing along the bar direction. The ungated device shows a sizeable AMR_{xx} and AMR_{xy} that is not caused by an out of plane misalignment. The origin of these AMRs is not known, and their poorly defined symmetries would make them more difficult to separate from magnetic gating effects when fitting. The Fe-gated device also shows a AMR_{xx} and AMR_{xy}. The AMR of the Fe-gated device is somewhat distinct from the gated device: it has a smaller magnitude and $cos(2\phi)$ symmetry for AMR_{xy}. Like the ungated device, the AMR of the Fe-gated device is not caused by an out of plane field misalignment. Disappointingly in terms of the overall goal of the investigation, there was no evidence for the existence of the magnetic gating effect in the Fe-gated device measurements.

The study was hindered by problems with both the Mn782 and RC023 samples. Ungated Mn782 has 2D conduction, reasonable R_{sheet} and R_{xy} values, and only a misalignment contribution to AMR. This make it an excellent 2DEG heterostructure for the magnetic gating device. The inability to successfully contact to Mn782 after the subsequent growth of the Fe gate layer is not understood. It is unclear whether the same issue would have arisen had the Fe layer been grown in the same growth run as the heterostructure. The large R_{xy} values of the RC023 devices and the leaky gate suggest some type of problem with the electrostatics within the structure, but it is difficult to speculate any further. The presence of AMR in the ungated device makes RC023 unsuitable for detecting the magnetic gating effect. This is confirmed as AMR that is not from the magnetic gating effect (and not exactly the same as the AMR in the ungated device) is seen in the gated device.

Another issue to consider is that the magnitude of the magnetic gating effect for the device designs of this experiment may be considerably smaller than the very loose prediction of up 1%. This prediction was made with several assumptions that may be flawed. Firstly, it was based upon idealised '1D Poisson' calculations, which have been shown in this chapter to usually not be in quantitative agreement with real measured devices. Secondly, the maximum predicted effect was only for a very narrow range of the possible Schottky barrier heights - the effect is actually predicted to be 0.05% for the majority of the possible Schottky barrier heights. Thirdly, the calculations were made for an electrochemical potential variation of 100μeV. The actual electrochemical potential variation with magnetization orientation in thin Fe films has never been measured or calculated, and may be much smaller than this value. If change in R_{sheet} from the magnetic gating effect should actually be significantly smaller than the loose 1% prediction, detecting it above other contributions to AMR_{xx} in field rotation experiments would become a considerably more difficult task.

If more time and growths were able to be committed to this project, the first step to progress would be to repeat the growth of the Mn782/RC023 heterostructure with the Fe gate layer. Mn782 and RC023 are nominally the same sample in terms of their intended structure, yet ungated Mn782 and RC023 devices show different properties. It may be the case that for some reason the RC023 sample did not grow as well as Mn782. If a future growth was able to replicate the quality of the Mn782

sample, but with the Fe gate layer and with good electrical contact to the 2DEG channel, that device may in itself provide a good enough platform to observe the magnetic gating effect. Depending on the results, the 2DEG heterostructure could also be modified in subsequent growths. For example, if the gate was still leaky, a larger spacer layer or lower doping densities could be considered. If the magnetic gating effect was absent or weak, it could be tried bringing the 2DEG interface closer to the surface which may enhance the magnitude of the magnetic gating effect.

If the magnetic gating effect could be achieved in an Fe-gated device, it may also be interesting to vary the thickness of the Fe gate layer. A thin Fe gate layer was used in this experiment as it was assumed that only the monolayers of the gate close to the GaAs interface would give a significant contribution to the magnetic gating effect, firstly as these are the layers with which the heterostructure chemical potential is sensitive to, and secondly because the SOC may be stronger in these layers. Increasing the thickness of the Fe gate layer would not be expected to significantly vary the Schottky barrier height to GaAs (and hence the carrier density of the 2DEG). Therefore it may allow a fair comparison directly via magnetic gating measurements to see how (if at all) varying the Fe thickness varies the effects at the Fe/GaAs interface responsible for the magnetic gating effect. For example, the magnetic anisotropy of Fe becomes more cubic as thickness of the Fe layer increases from 2nm, so a $cos(4\phi)$ contribution to the magnetic gating effect may become more significant.

Besides Fe, there are several other magnetic materials that could be chosen as the gate layer for a GaAs/AlGaAs 2DEG heterostructure. Changing the gate material will alter the Schottky barrier height/carrier migration in the 2DEG heterostructure, and so the heterostructure parameters may need to be varied for each sample with a different gate layer. The reasons for considering the dilute magnetic semiconductor (Ga,Mn)As as a gate were outlined in section 5.3.2 (grows well on GaAs, strong SOC), assuming that a suitable heterostructure design could be achieved for both with and without the (Ga,Mn)As layer. This situation might be somewhat simplified by instead using the metal MnAs as the gate layer. MnAs is also known to grow well on GaAs[270], with which it forms Schottky barrier[247] that like Fe could make the effects on the 2DEG of removal of the gate layer less drastic. The MnAs/GaAs interface is also sharper than the Fe/GaAs interface[271] which could also help the magnetic gating effect. Furthermore, MnAs does not degrade at 390^{o}C (its spintronic properties are in fact enhanced[272]), and this would remove the need for the time-consuming laser annealing of contacts. Spin-polarised Pt may be another interesting material to consider for the gate. Pt is a non-magnetic element with a high magnetic susceptibility, and it is known that a magnetic moment in Pt can be induced near its interface with Co[273]. As it is presumably the monolayers of the gate next to the GaAs interface that are most significant for the magnetic gating effect, a very thin ($<$ 1nm) Pt layer sandwiched between the 2DEG heterostructure and a Co layer may be sufficient to allow for the magnetic gating effect. The benefit of Pt over Fe or Co itself as the gate material is that it is a significantly heavier element, so will have stronger SOC which may also give it a stronger electrochemical potential anisotropy with the induced moment orientation. Antiferromagnetic materials could also be explored

for the role of the gate. Reference [236] demonstrated significant electrochemical potential variation with spin axis direction in IrMn and Mn_2Au, while CuMnAs can grow well on GaAs and shows SOC effects (see chapter 6). To control such antiferromagnetic gating devices, a ferromagnetic layer would need to be grown on top of the antiferromagnetic layer with substantial enough exchange coupling to rotate the spin axis throughout the whole of the antiferromagnetic layer.

Finally, it should be noted that a recent paper reported on what was dubbed "magnetic gating" of spin currents[274]. The technique (rotating the magnetization of the magnetic gate with an external magnetic field) and the measured output (a $cos(2\phi)$ variation in an electrical voltage) of the reference [274] magnetic gating of spin current experiment are similar to the magnetic gating of electrical current proposed in this investigation, however they are two completely different effects. For the magnetic gating of spin current experiment, a pure spin current is generated in the Cu layer of a Cu/YIG bilayer. The spin current is absorbed via a spin transfer torque to the YIG by an amount that depends on the relative angle between the spin current polarisation and the magnetization of the YIG. The spin current is detected as a non-local voltage referenced to a ferromagnetic electrode. This non-local voltage therefore varies with YIG magnetization orientation. The equivalent "magnetic gating" effect on electrical current is spin Hall magnetoresistance[8], though this has never been referred to as a magnetic gating effect. This is obviously distinct from the magnetic gating of electrical current in this investigation, where varying the magnetic gate's magnetization orientation varies its electrochemical potential, which alters the carrier density and hence electrical current in the 2DEG (or for a constant applied current the measured voltage across the 2DEG). Despite being fundamentally different to the work in this chapter, reference [274] and [8] do demonstrate an increasing interest in searching for alternative ways to control current in spintronic devices.

Chapter 6

Current-induced magnetic reorientation in an antiferromagnet

6.1 Introduction

Hard disk drives (HDDs) are currently the most widely used secondary computer memory. Meanwhile, magnetoresistive random access memory (MRAM) is becoming an appealing candidate for a universal memory, as documented in the introduction to chapter 4 of this thesis. In both HDDs and MRAM, data is encoded in the orientation of the magnetization of a ferromagnet. This feature allows data to be written by Oersted fields from write lines. Today Oersted fields are the dominant mechanism for writing in HDDs, and are one of the two approaches commonly used for writing in MRAM. The ability to reorientate the magnetization of a ferromagnet with an external magnetic field is therefore a benefit for ferromagnetic (FM) memory devices, but it can also be a hindrance. For example, large magnetic fields associated with medical and industrial equipment can cause data loss on phones, bank cards, and other items which have a FM memory component that may be carried on a person. There are two other major drawbacks to FM memory devices. Firstly, ferromagnets produce stray magnetic fields (it is the stray field of a magnetic disk that the read-head is sensitive to in HDDs). If neighbouring 'bits' of FM memory are in too close proximity their stray fields can interfere with the memory state of one another, which is therefore a limiting factor to the density to which they can be packed in devices. Secondly, the time scale over which the reorientation of a FM moment takes place can be longer than the time in which the process causing the reorientation is initiated. This is not so important in HDDs where slow mechanical motion of the write-head is required, but it is a significant limiting factor for the writing speed in MRAM. While MRAM is already faster than dynamic random access memory (DRAM), which is the primary memory for most commercial personal computers, it is currently slower than static random access memory (SRAM), the primary memory used for certain high speed applications. Increasing the writing speed of MRAM is therefore important for it to find application in high speed computing.

There has been recent interest in using antiferromagnets instead of ferromagnets as

the active component of magnetic memory devices, as opposed to their traditional passive role as pinning layers. Antiferromagnets are largely insensitive to magnetic fields, and this could allow for greater data stability. They do not produce their own stray fields and so antiferromagnetic (AF) memory bits could potentially be packed closer together. It has also be shown that AF magnetic moments (AF spin-axis) can be reorientated on a time scale that is nearly 3 orders of magnitude shorter than for ferromagnets[275], owing to the zero net angular momentum of AF coupled moments. On the other hand, the insensitivity of AF moments to stray fields makes manipulating their orientation a considerably more complex task than in ferromagnets, and for this reason antiferromagnets have long been discounted for potential active use in magnetic memory.

For an AF memory device to be realised, not only would there need to be some means to control the orientation of the AF spin-axis, but there would also need to be some means to electrically read its orientation, similar to the anisotropic, giant, and tunnel magnetoresistance (AMR, GMR, and TMR) mechanisms used in FM memory devices. Investigations of such magnetoresistance effects in antiferromagnets were initially restricted to theoretical study[276][277][278][236], presumably due to the difficulty in controlling the AF spin-axis. In 2011 the first experimental demonstration of such an AF magnetoresistance effect was made in a NiFe/IrMn/MgO/Pt tunnel device[279]. Tunnelling anisotropic magnetoresistance (TAMR) depends on the orientation of the magnetic moments at the interface with the tunnel barrier, and so in the reference [279] device the TAMR signal is sensitive to the orientation of the AF spin-axis of IrMn, which was controlled via the exchange spring effect[280] with the FM NiFe layer. A TAMR signal of more than 100% was achieved. An experiment in reference [281] also used the exchange spring writing mechanism to manipulate the AF spin-axis of the antiferromagnetic semiconductor Sr_2IrO_4[281]. In this case the AF spin-axis orientation was detected via AMR in ohmic measurements, with a AMR magnitude of around 1% being recorded. An AMR of a similar size was also detected in the antiferromagnetic phase of the metal FeRh[282]. For the reference [282] experiment, the AF spin-axis orientation was set via cooling through the magnetic phase transition of FeRh in the presence a 90kOe external magnetic field (see section A.3 of the appendix of this thesis for more details). Finally, spin Hall magnetoresistance (SMR) was observed in a Pt/$SrMnO_3$ bilayer[283], where $SrMnO_3$ is an antiferromagnetic insulator. For this experiment, the AF spin-axis of $SrMnO_3$ was partially canted with a 1kOe external magnetic field.

The reference [279], [282], and [283] experiments show AF magnetoresistance effects in tunnelling, ohmic, and gating-style transport regimes respectively. It is therefore now accepted magnetoresistance effects can exist in antiferromagnets just as they do in ferromagnets, and with similar sizes, and hence there are various possible reading mechanisms for an AF memory device. However, the exchange spring, field cooling, and field application writing techniques used to manipulate the AF spin axis in the respective references are all not wholly satisfactory for an AF memory device. For the exchange spring mechanism the AF spin-axis depends on the magnetization orientation of the FM layer, and therefore the major benefits of an AF memory device (insensitivity to and lack of associated stray fields, ultra-fast

reorientation) are lost. The direct field application mechanism of reference [283] loses the benefit of insensitivity to stray fields, and is only made possible anyway as $SrMnO_3$ is an unusual AF material where the AF spin-axis can be canted by a 1kOe field. The FeRh field cool mechanism retains the stray field benefits when operating at or below room temperature, and has the possibility to allow for ultra-fast reorientation if a quick enough heating mechanism could be found (for example a laser pulse[275]). However, the 9kOe external field needed to set the AF spin-axis orientation is huge, albeit this value could probably be reduced with material optimisation. Even if the switching field could be lowered to a more realistic magnitude, write lines would still be required for an actual FeRh memory device. As discussed in the introduction to chapter 4, write lines can be problematic in MRAM due to unfavourable scaling of write currents at lower device dimensions which leads to reduced energy efficiency, as well as greater device complexity which leads to reduced packing densities. Due to the various shortcomings of the reference [279], [283], and [282] AF writing mechanisms, alternative approaches are being explored.

It has recently been pointed out that the spin-orbit torque (SOT) mechanism, which is an established method of switching the magnetization orientation of a ferromagnet (see chapter 4), can act in antiferromagnets in such a way as to switch the AF spin-axis[195]. This AF type of SOT is dubbed 'Neel order spin-orbit torque' (NSOT), and is only possible in antiferromagnetic materials where each spin sublattice has a broken inversion symmetry. NSOT could be extremely advantageous for the development of magnetic memory devices as it can control the AF spin-axis orientation, which would then allow the benefits of an AF memory device without the difficulty of writing, while also offering better scalability and packing densities compared to any Oersted field writing mechanism (such as the FeRh field cool writing). This chapter introduces the concept of NSOT, and shows preliminary experimental evidence for its existence in the AF semimetal CuMnAs, as measured by AMR. The work in this chapter was cut short due to time constraints, and so a full experimental study is not provided. However, if the findings of this chapter are later confirmed, they will not only show the first experimental measurements of AMR in CuMnAs, but also the first experimental observations of NSOT in any material.

6.2 Theory

6.2.1 CuMnAs

The increasing interest in AF spintronics comes hand in hand with an increased focus on developing AF materials with suitable spintronic properties. Inspiration can be taken from the development of FM spintronic materials over the last 25 years or so. Factors such as room temperature magnetic ordering, high quality thin film crystalline growth on commonly used substrates, electronic properties suitable for integration with established technologies, and strong spin-orbit coupling (SOC) can be just as important for an AF spintronic material as they are for a FM spintronic material. (Ga,Mn)As fulfilled all of the above criteria with the exception of room temperature magnetic ordering, and while this meant it could never find real world

application, it is still an outstanding FM spintronic material for discovering and characterising new phenomena. (Ga,Mn)As is therefore an interesting reference point for developing an AF material which can act as a test-bed for characterising AF spintronic phenomena, as well as having the potential to find real device application.

CuMnAs is an antiferromagnet which has recently emerged as a candidate material for AF spintronics[25]. Bulk CuMnAs preprepared by chemical synthesis had previously been investigated[284][285], but it is the epitaxially grown thin film form introduced in reference [25] that is of most interest for AF spintronics. Like (Ga,Mn)As, it is the Mn atoms with their half filled $3d$ subshells which provide the source of magnetic moments in CuMnAs. However, whereas Mn is a dopant in a III-V semiconductor lattice in (Ga,Mn)As, in CuMnAs it is of equal stoichiometry to Cu and As and maintains its own lattice site. In terms of valency, CuMnAs is a I-II-V material as Cu is a group Ib transition metal. Cu is chosen over group I elements as it allows for a more stable compound that can be grown with greater ease.

When grown epitaxially by MBE on a GaAs or GaP (001) substrate, CuMnAs assumes a tetragonal lattice structure, i.e. $a{=}b{\neq}c$. The CuMnAs film grows on GaAs and GaP with an in-plane distortion of 45° to the substrate, i.e. the [1-10]/[110] axes of CuMnAs lie along the [100]/[010] axes of GaAs and GaP. CuMnAs grown on GaAs is fully relaxed, with an in-plane lattice constant of 0.382nm. This lattice constant is close to being half that of the diagonal GaP plane, and so CuMnAs grown on GaP is fully strained. The relaxed lattice constant of CuMnAs is even better matched to Si, suggesting it can also be grown well on Si substrates, though this has yet to have been reported on experimentally. The lattice arrangement of tetragonal CuMnAs is shown in figure 6.1.

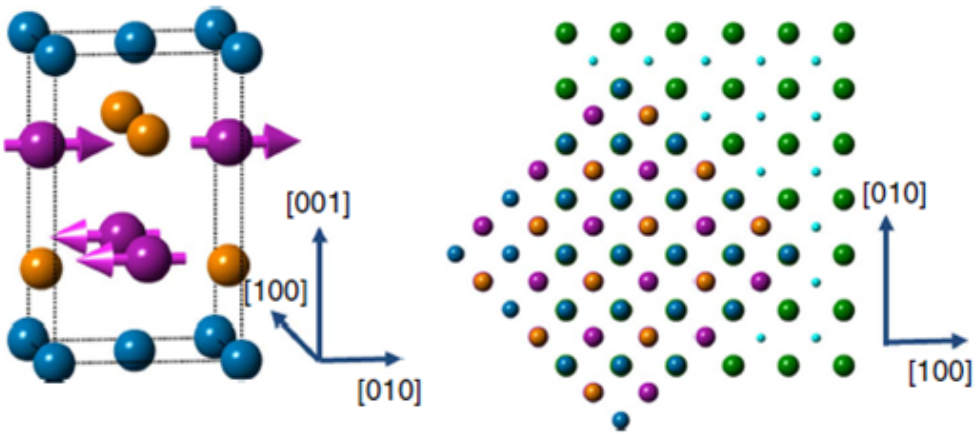

Figure 6.1: **(Left hand figure)** Unit cell of tetragonal CuMnAs. Blue circles represent Cu atoms, purple circles Mn atoms, and orange circles As atoms. The purple arrows on the Mn atoms represent their associated magnetic moment. **(Right hand figure)** Top down view of tetragonal CuMnAs on GaAs/GaP substrate. Green circles represent the As/P atoms of the substrate, small light blue circles the Ga atoms of the substrate. Both diagrams are taken from reference [25].

Tetragonal CuMnAs generally has a resistivity of around 160$\mu\Omega$.cm at 300K which reduces to around 90$\mu\Omega$.cm at 4K, with a metallic like resistivity against temperature profile. Calculations of the band structure of CuMnAs suggest it to be on the semimetal side of the semiconductor/semimetal transition. The calculations also suggest that there is both significant electron and hole conduction, and if this is the case it makes experimentally obtaining the carrier density from Hall slopes a considerably more complex task.

Tetragonal CuMnAs is a collinear antiferromagnet where the moments of the Mn atom order ferromagnetically in the *ab* plane for a given layer, and ferromagnetically in the opposite direction for the adjacent layers. These so called spin sublattices are exchange coupled to and perfectly compensate one another, and so tetragonal CuMnAs has no net magnetic moment. While neutron diffraction studies have confirmed that the moments lie in the *ab* plane[25], they cannot distinguish their exact crystalline orientation. A recent x-ray linear dichroism (XMLD) investigation[286] suggested that in thin ($\approx$ 10nm) CuMnAs films grown on GaP, the AF spin-axis lies along either the CuMnAs [100] or [010] plane (one is preferred over the other though the exact direction was not determined)[286], while for thicker ($\approx$ 50nm) films AF domains are formed along two orthogonal (or close to orthogonal) in-plane directions. The domains are expected to be approximately equally populated, however the exact crystalline directions along which they form could again not be determined. It is not clear why a uni-axial AF spin-axis is favoured in the thinner samples. It has also been shown in SQUID measurements[25] that an exchange bias can be induced in CuMnAs/Fe bilayer samples, and that in thinner CuMnAs ($\approx$ 5nm) samples the Fe can act as an exchange spring to rotate the CuMnAs AF spin-axis throughout the entire CuMnAs layer (which is detected by XMLD[286]). The Neel temperature (T_N), i.e. the temperature up to which AF ordering persists, of CuMnAs can be determined by neutron diffraction or by a peak in the derivative of the resistivity against temperature curve[287], similar to determining T_c of (Ga,Mn)As. For tetragonal CuMnAs samples grown in Nottingham, T_N is generally around 485K.

With its high quality growth on GaAs, GaP, and possibly Si substrates, conductivity that could be compatible with existing semiconductor electronics structures, above room temperature AF ordering, and possibility to exhibit spintronic phenomena (exchange spring, SOC - see section 6.2.2), CuMnAs demonstrates appealing characteristics for use as both a test-bed material, but also a possible AF spintronics material for device applications.

6.2.2 Neel order spin-orbit torque

Chapter 4 introduced the concept of field-like SOT in the ferromagnet (Ga,Mn)As. The mechanism for this SOT is briefly as follows: (Ga,Mn)As has a broken inversion symmetry, owing to its zincblende lattice structure and lattice strain from substrate mismatch. This causes current flowing through (Ga,Mn)As to gain a non-equilibrium spin polarisation in a phenomenon know as the inverse spin galvanic effect (ISGE). The carrier spins are exchange coupled to the local Mn moments,

and if there is a non-collinear alignment between them, they will exert a torque on one another, which causes the magnetization of (Ga,Mn)As to reorientate from its equilibrium position. This type of SOT is parametrised by effective fields which represent an external magnetic field that would generate the equivalent torque on the local moment, and hence the effective fields depend on crystal symmetry and current direction.

A logical question to ask is whether such a mechanism could also torque antiferromagnetic moments. Consider the case shown diagrammatically in figure 6.2 of two magnetic atoms on adjacent lattice sites to one another, with exchange coupling between their moments. In case **(a)**, the exchange coupling aligns the moments ferromagnetically. If the effective field experienced by each moment is in the same direction, both moments will reorientate towards the effective field direction, therefore retaining their parallel alignment with one another. In case **(b)**, the exchange coupling aligns the moments antiferromagnetically. If the effective field experienced by each moment is again in the same direction, the moments would again want to reorientate towards the effective field direction. However, to do so they would need to break their antiparallel alignment with one another. This would require the effective field to be larger than the exchange field between the moments (which is unlikely to be the case in most systems), making any magnetic reorientation extremely difficult. Finally, in case **(c)**, the exchange coupling again aligns the moments antiferromagnetically. In this case the effective field acts in opposite orientations on the adjacent lattice sites. This allows the moments to reorientate whilst maintaining their antiparallel alignment, and so no exchange field has to be overcome.

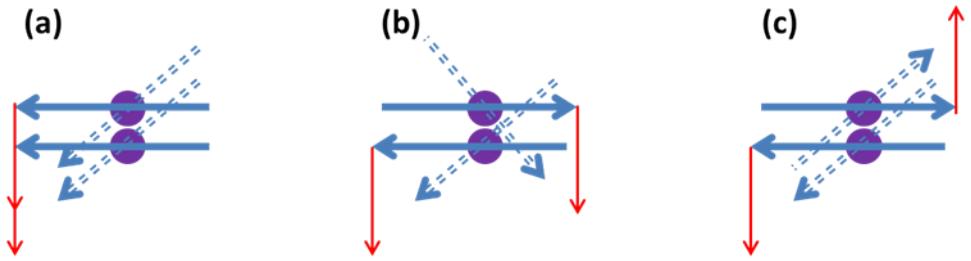

Figure 6.2: Simplistic diagrams of effective fields torquing exchange coupled magnetic moments. Purple circles are lattice sites of magnetic atoms, solid blue arrows represent magnetic moments in equilibrium, dashed blue arrows represent magnetic moments when acted on by an effective magnetic field that is bigger than the exchange field, and red arrows represent effective magnetic fields. **(a)** FM exchange coupling and same effective fields at each lattice site, **(b)** AF exchange coupling and the same effective fields at each lattice site, **(c)** AF exchange coupling and opposite effective fields at adjacent lattice sites.

As figure 6.2 demonstrates, for rotation of the AF spin axis that maintains the antiferromagnetic alignment of the moments, oppositely orientated moments need to experience oppositely orientated effective magnetic fields. Until recently, effective magnetic fields have only been considered for the cases of materials where the lattice has a broken inversion symmetry (non-centrosymmetric lattice). However, it

was noted in reference [288] that in certain materials where the lattice has inversion symmetry (centrosymmetric lattice), the lattice can be divided into to sublattices, each of which is by itself non-centrosymmetric. These non-centrosymmetric sublattices can therefore generate spin polarisations through Rashba and Dresselhaus SOC effects in the same way that a non-centrosymmetric lattice can. The sublattices have an inverted atomic arrangement with respect to one another (and hence are known as 'inversion partners'), and therefore an opposite confining electrical potential. The result of this is that the spin polarisations from Rashba and/or Dresselhaus SOC will be in opposite directions in the two sublattices. The opposite spin polarisations in the inversion partner sublattices perfectly compensate each other in the unit cell lattice, and so sublattice spin polarisations had always gone undetected experimentally. After the publication of reference [288], such a sublattice spin polarisation was confirmed experimentally in the non-magnetic transition-metal dichalcogenide WSe_2 via spin and angle resolved photoemission spectroscopy[289].

It was shown in reference [195] that the centrosymmetric lattice of the layered collinear antiferromagnet Mn_2Au can be split into inversion partner sublattices that coincide with the sublattices for the Mn layers with oppositely orientated moments (the spin sublattices). Current flowing through these two sublattices will gain an opposite non-equilibrium spin polarisation to one another as the sublattices have opposite inversion symmetry breaking (and so an opposite ISGE). Because the local Mn moments are exchange coupled to the non-equilibrium carrier spins they will experience an opposite field-like torque in the two sublattices that can be parametrised as opposite effective magnetic fields. The moments, which are coupled antiferromagnetically between adjacent Mn layers, can therefore reorientate towards the direction of the effective field, and so the AF spin-axis is reorientated towards the effective field axis. This is the NSOT phenomenon. The convenient and fortuitous atomic and magnetic arrangement of Mn_2Au means that the effects of the opposite spin polarisations for inversion partner sublattices do not cancel one another out in the full lattice, unlike in non-magnetic materials. The work in reference [195] therefore indicates that 1. SOT is not limited to FM materials, and 2. SOT is not limited to inversion asymmetric materials. Calculations for Mn_2Au show that for current along the [100] crystalline direction the NSOT effective magnetic field acts in a direction that is in-plane and perpendicular to the current direction, and in opposite directions for the adjacent spin sublattices. The magnitude of the NSOT effective field is predicted to be comparable to the equivalent SOT effective fields in FM transition metal materials. This field-like NSOT arises from an intraband non-equilibrium spin polarisation. Reference [195] goes on to further introduce the concept of an antidamping NSOT in an idealised 2D Rashba AF system where the whole lattice is inversion asymmetric and the two spin sublattices experience the same symmetry breaking field. This antidamping NSOT arises from an interband non-equilibrium spin density, and its mechanism is related to the same Berry curvature understanding of the intrinsic anomalous[9] and spin[14] Hall effects, as well as the out of plane antidamping SOT in (Ga,Mn)As[198].

The unit cell of tetragonal CuMnAs is centrosymmetric as it has a centre of inversion symmetry. This point is indicated by the yellow circle in the unit cell in

figure 6.3**(a)**, which is a known inversion centre for the space group p4/nmm[290]. The symmetry about this point is not obvious from figure 6.3**(a)**, but becomes more apparent view of the cell is translated by (0.5,0.5,0) (which would place the centre of inversion at (0,0,0)) combined with shifting the centre of inversion to the equivalent (0.5,0.5,0.5) position, as shown in figure 6.3**(b)**. It can be seen more clearly from this viewpoint that an observer at the yellow circle would see the same atomic arrangement when looking in opposite directions of various planes. It can also be seen that an observer at the purple Mn atom would see an inverted atomic arrangement to that which an observer at the red Mn atom would see. As these atomic arrangements are perfectly inverted (as opposed to just different), the spin sublattices form inversion partners and would hence experience the perfectly opposite effective fields required for a field-like NSOT. Tetragonal CuMnAs therefore has a suitable lattice symmetry to allow an AF spin-axis reorientation through the NSOT mechanism.

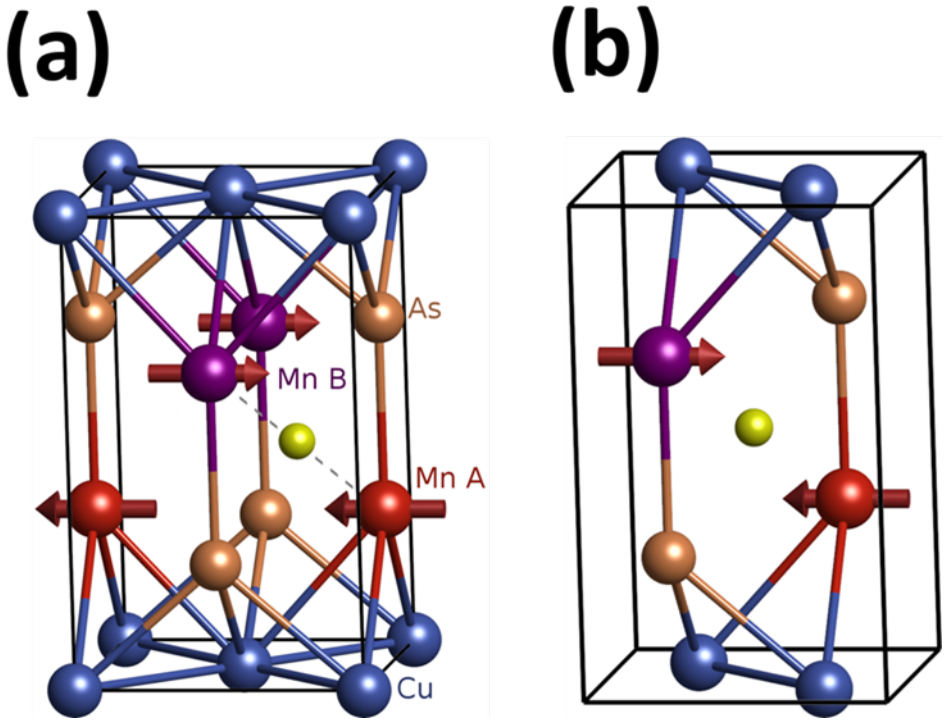

Figure 6.3: **(a)** Unit cell of tetragonal CuMnAs. Yellow circle is an indicator of the centre of inversion rather than an atomic position. Blue circles are Cu atoms, orange circles are As atoms, purple circles are Mn atoms for one spin sublattice, red circles are Mn atoms for the other spin sublattice. **(b)** View from a different plane of the same centre of inversion. Figures are produced by Jakub Zelezny.

6.3 Experimental results

With the NSOT in CuMnAs being shown to be possible by symmetry arguments relating to the CuMnAs lattice structure, this section reports on experimental efforts to generate and detect NSOT in CuMnAs.

6.3.1 Experimental design

In principle, the NSOT mechanism is an incredibly simple method of reorientating an AF spin-axis of CuMnAs. All that is required is the application of a suitably large current along an appropriate direction. Detection of the AF spin-axis orientation could potentially be made by spectroscopic techniques such as XMLD[291], XMLD photoemission electron microscopy (XMLD-PEEM)[292], or magneto-optical effects[293]. However, electrical detection via AMR seems an experimentally much simpler starting point. The fact that AMR exists in other antiferromagnets gave sufficient hope that AMR would be present and strong enough in CuMnAs to distinguish between different AF spin-axis orientations. It should be noted that the first experimental detection of SOT in a ferromagnet was also made via AMR measurements[190]. The motivation of this investigation is to provide evidence for the existence of NSOT in CuMnAs, rather than to quantify the size of the associated effective fields (which would be considerably more difficult for NSOT than SOT). As any change in the resistance of CuMnAs with applied current (presumably due to NSOT) does not need to be converted into an effective field in this investigation, the all-electrical AF spin-axis setting and detection techniques therefore make the experiment in this chapter extremely simple; the only equipment required are sourcemeters and multimeters in order to generate current and measure voltages.

The sample used in this investigation is Mn752, an approximately 50nm thick CuMnAs layer grown by MBE on GaP substrate by Dr. Richard Campion, Dr. Vit Novak, and Victoria Hills. Mn752 was chosen partly because of its availability, but also because its magnetic anisotropy is anticipated to consist of domains formed along at least two (orthogonal) in-plane directions, as opposed to the uni-axial magnetic anisotropy observed in thinner CuMnAs samples. Having more than one easy direction for the AF spin-axis is advantageous for an AMR detection NSOT experiment as it allows for the possibility of magnetic switching that is retained after the setting current is removed. The AMR measurements can then be made using smaller probe currents that reduce heating and sample degradation. Note that this is in contrast to the SOT experiment presented in chapter 4 where the uniaxial magnetic anisotropy of (Ga,Mn)As prevented switching of the equilibrium magnetic state, and hence the AMR measurements had to be made with the same large current used for setting the magnetic orientation, which led to issues with heating effects. The 50nm thick Mn752 sample was chosen ahead of other thicker samples which also are expected to not have uniaxial magnetic anisotropy as thinner samples require a lower source current to generate an equivalent current density. Like SOT, NSOT is expected to vary with current density rather than current, and so by reducing the current channel dimensions, less current needs to be put through bond wires, contacts pins, and other circuitry, and this should also reduce possible heating effects on measurements.

With uncertainty surrounding the easy directions of the AF spin-axis of the Mn752 sample, the most sensible measurement geometry to begin with is that of a 'Union Jack' style Hall cross device that allows for current flow along the $[1\bar{1}0]$, [110], [100], and [010] current directions. Such device geometries were designed for a new photomask ('Bryn 2014') using Tanner L-Edit CAD software. The narrowest device

on the mask has 10μm width of arms. However, the etching of the actual devices during processing was found to slightly undercut the resist, and this resulted in about 1μm been taken off the side of every feature, hence the narrowest arms are actually around 8μm wide. Furthermore, this etching also rounded the edges of the central region of the device, making it circular. Preliminary testing on a different CuMnAs sample where wedge bonds were made directly to the CuMnAs layer without any contact pads observed that the bond wire blew up at the point of contact with the CuMnAs sample at applied current values of around 0.2A. Therefore, for the devices used in this investigation, large Cr(25nm)/Au(250nm) contact pads were evaporated on to the device, with three wedge bonds made to each contact. In this configuration, no bond wire was blown up during the investigation. As shown in figure 6.4**(a)**, the contact pad runs down towards the central channel. The motivation for this was to reduce the distance through CuMnAs that current needs to travel, therefore reducing resistance and hence Joule heating effects. However, it was found during the course of this investigation that when applying voltages of around 14V-16V across the device over multiple current pulse cycles, the CuMnAs layer at the interface with the Cr/Au contact can completely and instantaneously degrade, as shown in figure 6.4**(b)**. Presumably this is related to the resistance on the CuMnAs/contact interface, and the fact that all of the current needs pass through the interface in such a narrow region, which could cause severe local heating that degrades the CuMnAs layer. All of the measurements shown in this chapter are made on devices before this severe degradation occurred.

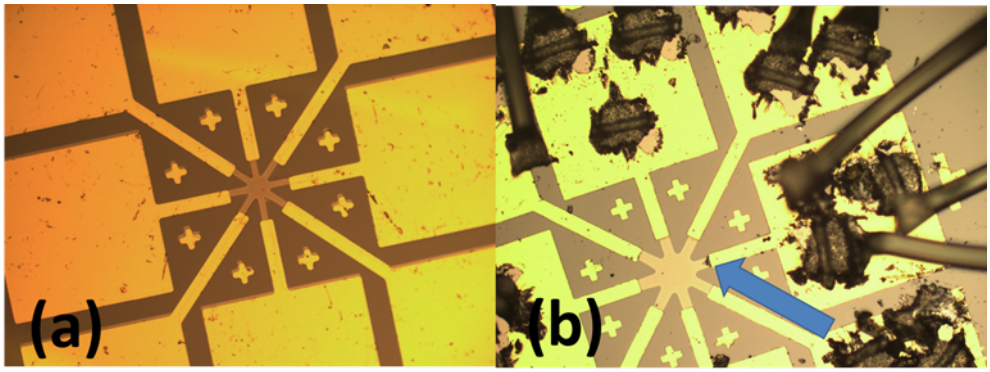

Figure 6.4: **(a)** Image of Union Jack Hall cross device with 8μm wide arms used for the majority of measurements in this chapter. **(b)** Image of a 12μm device used in preliminary testing, after degradation of the CuMnAs layer around one of the contacts (indicated by the blue arrow).

6.3.2 Measurement principle

The measurement principle is as follows, using the diagram in figure 6.5 as a guide. A short 'setting' pulse of dc current of current density of the order 10MA/cm^2 is applied along one of the major crystalline axes of the device (i.e. between contacts C1 to C5, C2 to C6, C7 to C3, or C8 to C4). After a wait of around 30s, a constant dc 'probe' current of 100μA (around 25kA/cm^2 current density) is then applied between C1 and C5, with 4-probe R_{xx} measurements being made for C2-C4, and

C8-C6, and a 4-probe R_{xy} measurement for C7-C3. The probe current is then applied between C2-C6, with 4-probe R_{xx} measurements being made for C3-C5, and C1-C7, and a 4-probe R_{xy} measurement for C8-C4. Similar measurements are also made for current between C7 and C3, and current between C8 and C4. Another setting pulse is then applied, usually in an orthogonal direction to the previous setting pulse, and again the same set of probe measurements are made.

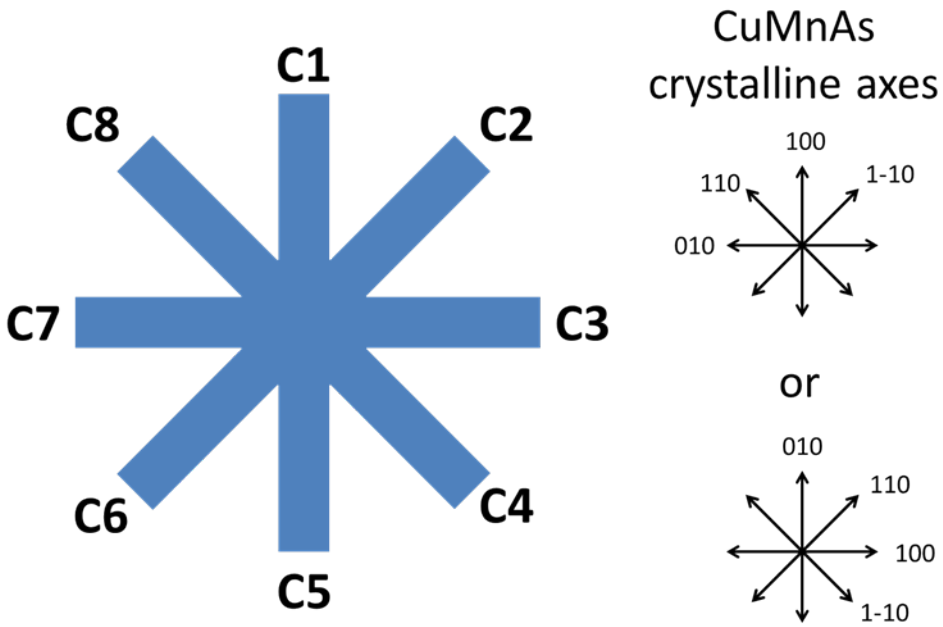

Figure 6.5: **(Left hand figure)** Diagram of Union Jack Hall cross device contacts as used in this investigation. The orientation of the contacts with respect to the CuMnAs crystalline axis is not exactly known, but is one of the two possibilities shown on the right hand side of the figure, i.e. C1-C5 is either along the [100] or [010] crystalline axis of CuMnAs etc.

Consider the possible case that under equilibrium conditions Mn752 consists of equally populated AF domains along the [100] and [010] CuMnAs crystalline directions which are equivalent easy axes. The domain populations are given by statistical thermal fluctuations. Here the focus is only on the central region of the Union Jack Hall cross device, i.e. the region which current flow along all 4 axes must pass through. If a setting current pulse is applied along the [100] direction, it may generate a large enough NSOT effective field in the [010] direction to reorientate the [100] domains to lie along [010], while leaving the [010] domains as they are. Instead of an approximately 50:50 split of [100]/[010] domains in the central device region, the AF spin-axis in the entire region would now lie along the [010] direction. If a subsequent setting current pulse was then applied along the [010] direction, it may generate a large enough NSOT effective field along the [100] direction to reorientate the AF spin axis along the [100] direction. To probe these magnetic states, consider the case of CuMnAs having a non-crystalline AMR that is given as $R_{xx} = R_0 + R_{Max}cos(2\phi)$ and $R_{xy} = R_{Max}sin(2\phi)$ (assuming a square aspect ratio), as is the case for many metallic ferromagnets, where now ϕ is the angle between the AF spin axis and current direction. Here a positive AMR is assumed. Note that

due to the 2ϕ symmetry it does not matter which spin sublattice ϕ is defined with respect to; the oppositely orientated moments give the same AMR. For the case of the AF spin-axis lying along the [010] direction, for a probe current along the [100] direction, $\phi = 90°$, and so from AMR, $R_{xx} = R_0 - R_{Max}$, and $R_{xy} = 0$. However, for the case of the AF spin-axis lying along the [100] direction, and for a probe current again also along the [100] direction, $\phi = 0°$, and so $R_{xx} = R_0 + R_{Max}$, and $R_{xy} = 0$. Therefore, for a probe current along the [100] direction, the difference in the R_{xx} measurements between the setting pulse being along the [100] and [010] directions is $2R_{Max}$, whereas the difference in the R_{xy} measurements is zero. Similarly, consider the case again of the setting pulse again being along the [100] and [010] directions, but this time the probe current is along the [110] direction. When the AF spin-axis lies along [010], $\phi = 135°$, and so $R_{xx} = R_0$ and $R_{xy} = -R_{Max}$. When the AF spin-axis lies along [100], $\phi = 45°$, and so $R_{xx} = R_0$ and $R_{xy} = +R_{Max}$. Therefore, for a probe current along the [110] direction, the difference in the R_{xx} measurements between the setting pulse being along the [100] and [010] directions is zero, whereas the difference in the R_{xy} measurements is $2R_{Max}$. In this idealised situation of NSOT setting the AF spin-axis in the central device region and CuMnAs having a simple non-crystalline AMR, evidence for NSOT can be obtained from pulse and probe current measurements if the associated differences in R_{xx} and R_{xy} values vary with the expected symmetry for setting pulses in orthogonal directions. The fact that for certain configurations no change in R_{xx} and R_{xy} is expected for orthogonal pulses will help separate any NSOT effects from other effects like heating and sample degradation that would not have such a well defined symmetry.

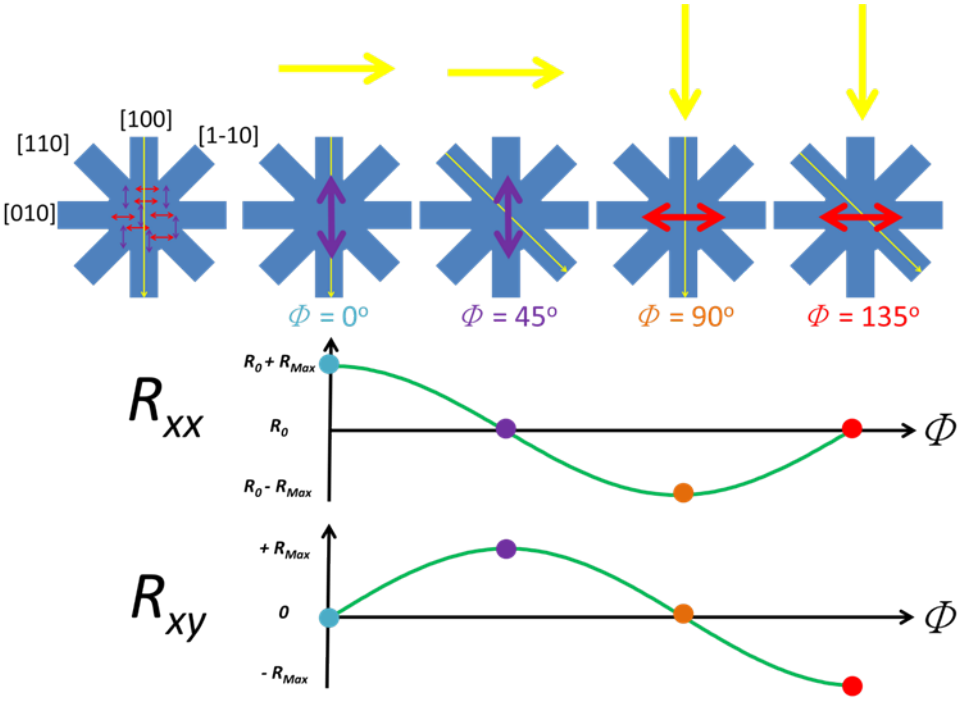

Figure 6.6: Diagrams explaining the principle of detecting NSOT through AMR measurements. For the rows of diagrams from top to bottom: Thick yellow arrows indicate direction of setting pulse. Purple and red arrows indicate the AF spin-axis within the central region of the Union Jack Hall cross, and thin yellow arrows indicate direction of probe current. Plot of $R_{xx} = R_0 + R_{Max}cos(2\phi)$ showing how R_{xx} varies for different AF spin-axis/probe current alignments. Similar plot for $R_{xy} = R_{Max}sin(2\phi)$.

The above explanation of the idealised measurement principle assumes linear current flow between contacts of a Union Jack Hall cross device, but this will not be the case in reality. To explore the distribution of current within the device, finite element models were made with the MATLAB PDE tool-kit for the 8μm Union Jack Hall cross device. As shown in figure 6.7, when current is applied from C1 to C5, it spreads out within the central region of the device. In the areas of the central region directly between the C1 to C5 arms or the C7 to C3 arms, the current flows parallel to the C1 to C5 direction. However, in regions near the C2, C4, C6, and C8 arms the current flows in a direction that is as much as 45° away from the C1 to C5 direction. Figures 6.8 and 6.9 show the corresponding component of the current densities along the C1 to C5 and C7 to C3 directions respectively within the device. In the central region of the device the current density along the C1 to C5 direction is only 20%-37.5% of its magnitude in the C1 and C5 arms. The 4-probe R_{xx} and R_{xy} measurements are sensitive to the central region of the device, but it is not straightforward to determine what is the current density sensed in each 4-probe R_{xx} and R_{xy} measurement. The current densities reported in this thesis will therefore nominally be the current density that flows along the arms of the device, i.e. the size of the applied current divided by the width of the arm. It should be noted that the current densities in the central region of the device, and hence those required for AF spin-axis reorientation, will only be around 20%-37.5% of these nominal arm current density values. The component

of the current density along the C7 to C3 direction near the C2, C4, C6, and C8 arms is around 6.25%-12.5% of the magnitude of the current density along the C1 to C5 direction in the C1 and C5 arms, and therefore around a third of the C1 to C5 direction current density in the central device region. As a different direction of current flow will give a different NSOT effective field direction, as well as different values of ϕ for the probe current, this localised non-linear current flow could impact on probe measurements made with the C2, C4, C6, and C8 arms.

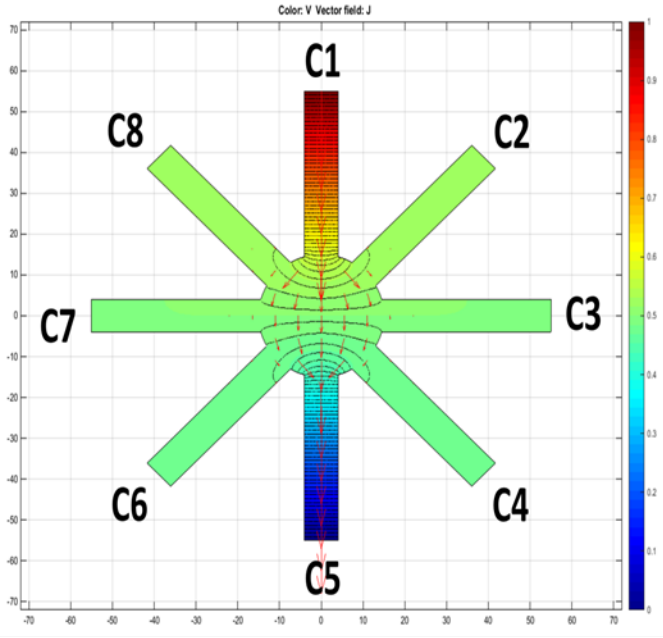

Figure 6.7: Contour plot of computed electric potential and current flow in the 8μm Union Jack Hall cross device for a voltage applied between C1 and C5. Colour chart on right hand side indicates the normalised electric potential within the device. Black lines are lines of equipotential. Each line is separated by a normalised electric potential value of 0.01. Red arrows indicate the direction of current flow within the device, with the size of the arrows being proportional to current density.

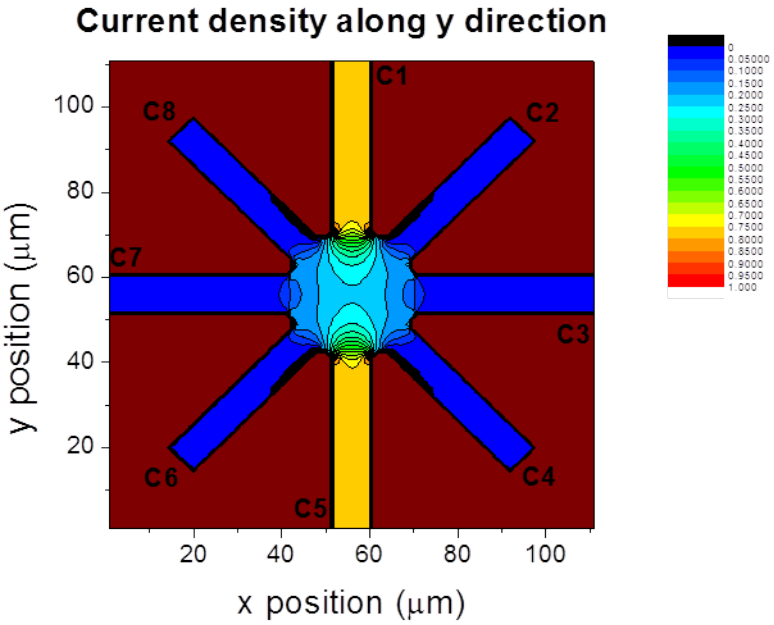

Figure 6.8: Contour plot of computed component of current density along the C1 to C5 direction in the 8μm Union Jack Hall cross device for a voltage applied between C1 and C5.

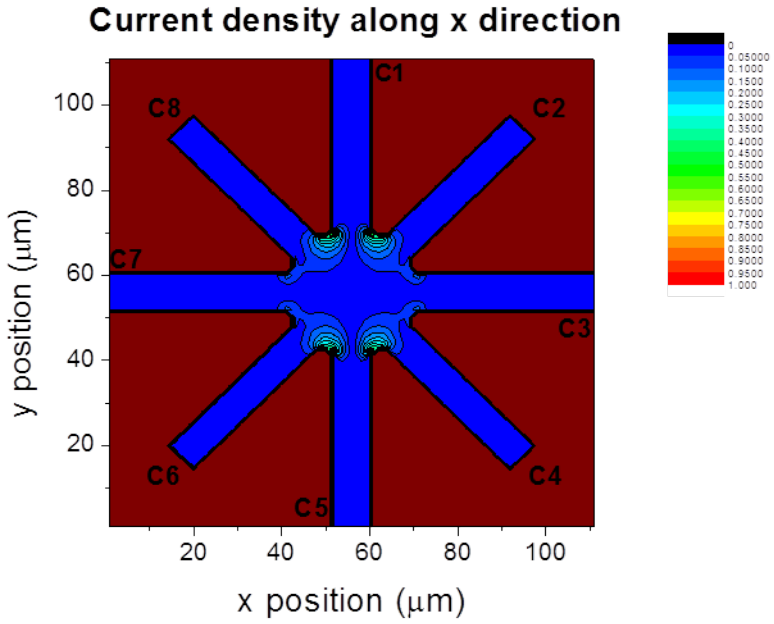

Figure 6.9: Contour plot of the magnitude of the computed component of current density along the C7 to C3 direction in the 8μm Union Jack Hall cross device for a voltage applied between C1 and C5. Note that the current density values are normalised to the same scale as for the C1 to C5 current density component in figure 6.8.

6.3.3 Results

Figure 6.10 displays R_{xx} and R_{xy} measurements for probe currents along the four major directions after 0.05s setting pulses of 12.5MA/cm^2 nominal current density applied alternatively in subsequent measurements along the C1 to C5, and C7 to C3 directions, which correspond to the [100]/[010] axes. Both setting pulses and probe measurements are performed at 298K. Note that all 298K measurements in this chapter were made in the Nottingham small cryostat system, with the combination of a He flow and heat exchanger being used to maintain a stable sample space temperature.

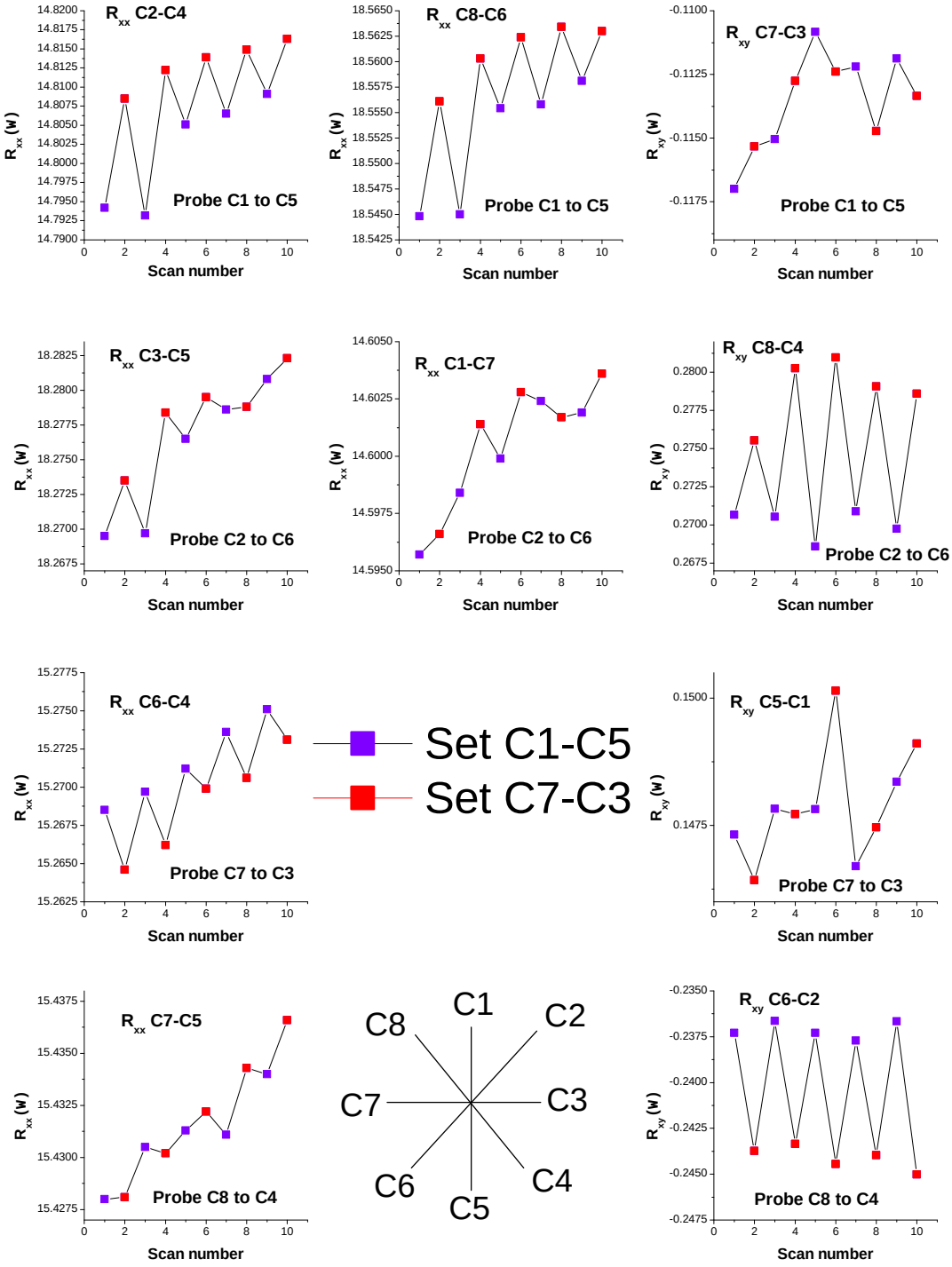

Figure 6.10: Various 4-probe R_{xx} and R_{xy} measurements after 0.05s setting pulses of 12.5MA/cm^2 current density applied along the C1 to C5 (purple), and C7 to C3 (red) directions. Both setting pulses and probe measurements are performed at 298K. Note that no data was collected for C8-C2 and C1-C3 4-probe R_{xx} measurements.

In terms of the difference between subsequent R_{xx} and R_{xy} measurements after the setting current pulse along the orthogonal C1 to C5 and C7 to C3 current directions, the data in figure 6.10 shows a general agreement with the NSOT and AMR symmetry principles described in section 6.3.2, i.e. for a given set of R_{xx}

probes, R_{xx} after the setting pulse is applied along the same direction is consistently smaller than R_{xx} after a subsequent setting pulse along an orthogonal direction. If this were to be interpreted as a NSOT effective field perpendicular to the current direction reorientating the AF spin-axis, it would correspond to CuMnAs having a positive AMR. Similarly the R_{xy} data for the cases when the setting pulse is 45° and 135° to the R_{xy} probes shows low and high values whose signs are in agreement with the R_{xx} data. There is a clear drift in all R_{xx} data, i.e. R_{xx} increases after each setting pulse, regardless of pulse polarity. This effect is largely absent from the R_{xy} datasets. Later measurements (not shown here) confirmed that the drift in R_{xx} is largely caused by Joule heating of the sample with each current pulse (a sample degradation effect had also been considered[294]). There is an approximately 5 minute time delay between subsequent setting pulses for the measurements presented here, and so the Joule heating takes more than 5 minutes to fully dissipate from the sample after each pulse is applied. Future experiments should leave an appropriate time between the application of a setting pulse and the start of probe measurements to allow a significant enough proportion of the Joule heating to dissipate so that the drift in R_{xx} is heavily reduced. Despite the increase in R_{xx} with each setting pulse measurement, the AMR-like variation of R_{xx} can still be seen on top of the non-magnetic R_{xx} increase for the appropriate measurement geometries. For the data here, the drift in R_{xx} can largely be accounted for by taking the difference between R_{xx} values for probe current directions 45° apart (i.e. where there is and is not an AMR-like variation in R_{xx}) for a given setting pulse direction, as shown in figure 6.11.

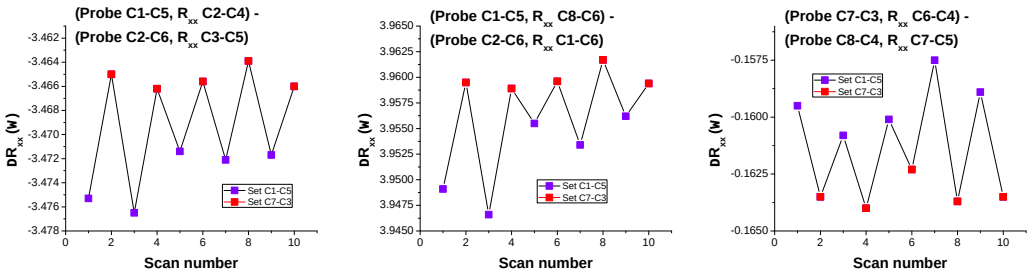

Figure 6.11: Difference in 4-probe R_{xx} measurements between the case of probe currents along directions 45° apart for the figure 6.10 data. Note that other subtraction of data combinations are possible but are not shown.

The size of the difference between subsequent R_{xx} values after orthogonal setting pulses is not consistent between the five measurement sets recorded for each measurement geometry. The same is also true for subsequent R_{xy} values. This data is shown in figure 6.12. The average difference in resistance over the five measurement sets for the five different measurement geometry combinations shown in figure 6.12 are (in order corresponding to the legend on the figure): -8(±1)mΩ, -7(±2)mΩ, +4.0(±0.7)mΩ, -9(±1)mΩ, and +7.0(±0.4)mΩ. Assuming a square aspect ratio, these correspond to AMR-like values of around 0.026% to 0.055%. The discrepancy between the difference in resistance values for a given geometry, as well as the discrepancy in the average difference in resistance values for different geometries can potentially be explained by a scenario where the setting pulses do not fully saturate the AF spin-axis of all the domains in the central region of

the Union Jack Hall cross device. In this scenario the number of domains that do saturate with each setting pulse could have somewhat of a random/statistical nature to it, and so may not be consistent between different setting pulses of the same size and direction. This idea is further explored later in this chapter. On the other hand, the inconsistencies could also be partially attributed to measurement noise from circuitry effects, thermovoltages etc..

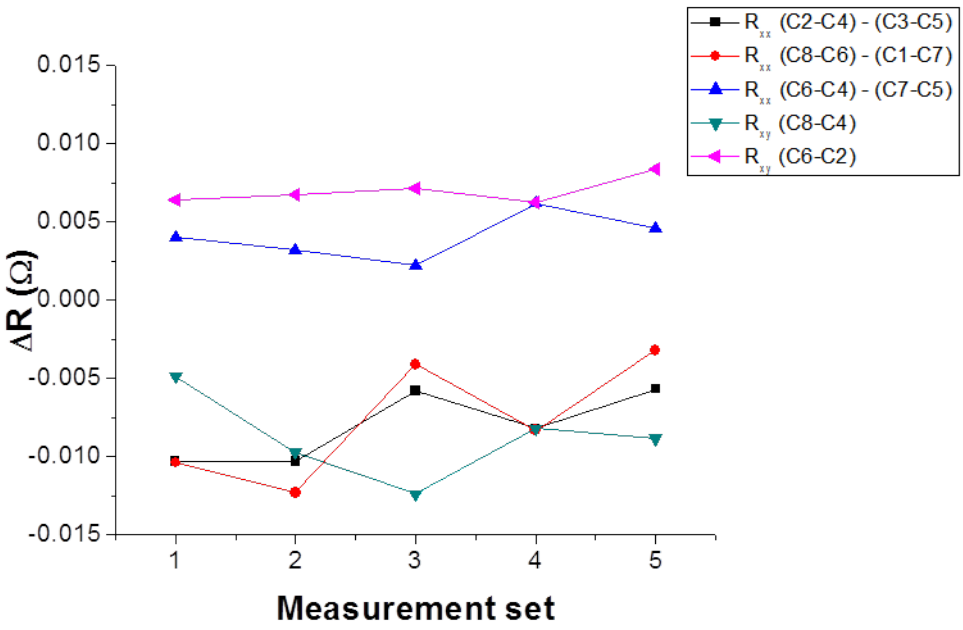

Figure 6.12: ΔR_{xx} and ΔR_{xy} for subsequent setting pulses along C1 to C5 and C7 to C3 directions. The ΔR_{xx} data is the difference between the red and purple data points in figure 6.11 while the ΔR_{xy} data is the difference between the red and purple data points for the R_{xy} plots in figure 6.10.

The measurements were repeated with the 0.05s 12.5MA/cm^2 setting pulses now applied along the C2 to C6 and C8 to C4 directions (which correspond to the CuMnAs $[1\bar{1}0]/[110]$ axes). The probe measurements were made for the same geometries as before, and again the setting pulse and probe measurements were applied at 298K. The results are shown in figures 6.13-6.15.

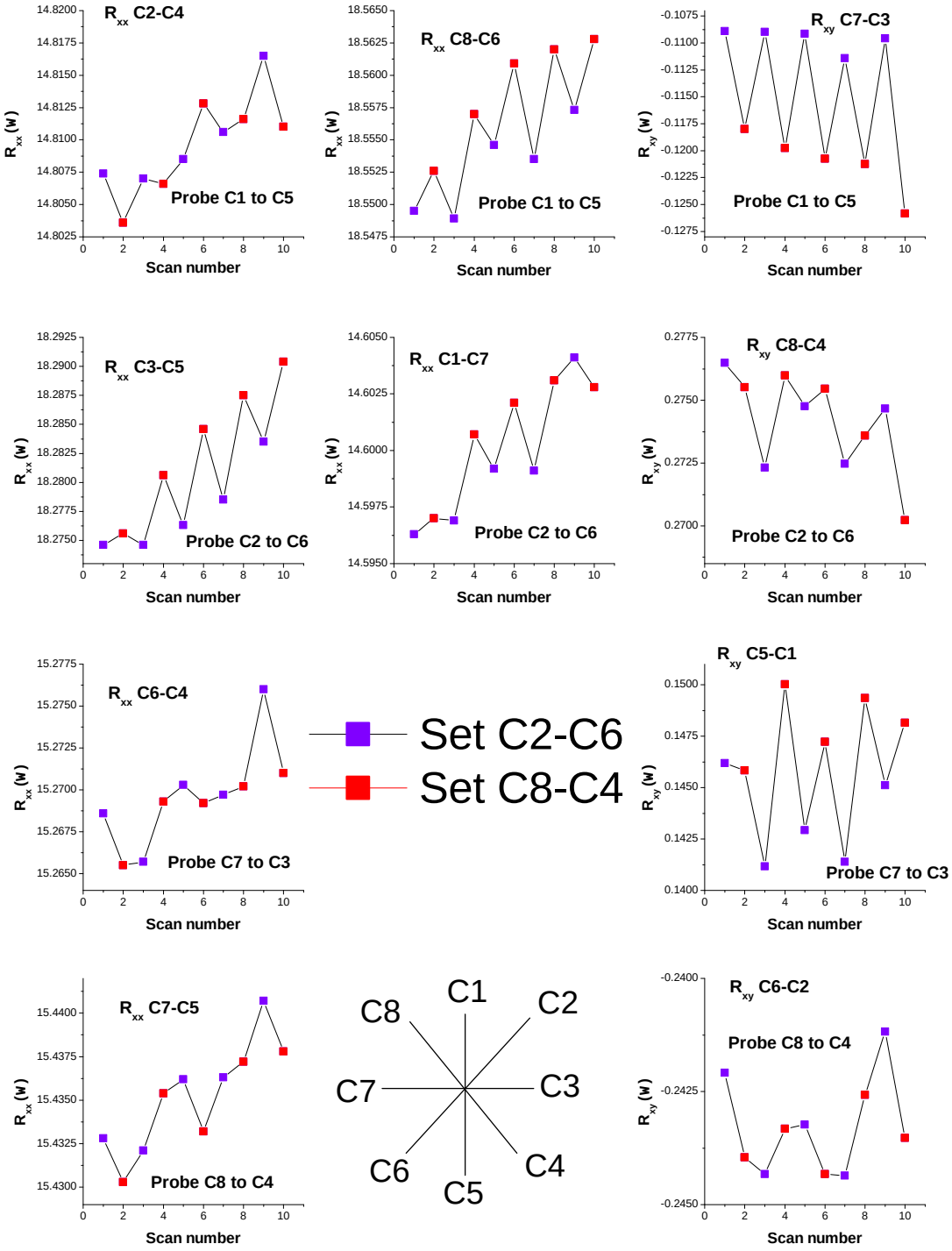

Figure 6.13: Various 4-probe R_{xx} and R_{xy} measurements after 0.05s setting pulses of 12.5MA/cm^2 current density applied along the C2 to C6 (purple), and C8 to C4 (red) directions. Both setting pulses and probe measurements are performed at 298K. Note that no data was collected for C8-C2 and C1-C3 4-probe R_{xx} measurements.

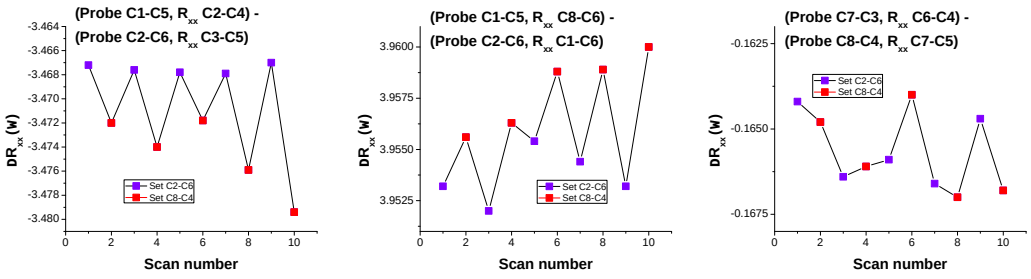

Figure 6.14: Difference in 4-probe R_{xx} measurements between the case of probe currents along directions 45° apart for the figure 6.13 data. Note that other subtraction of data combinations are possible but are not shown.

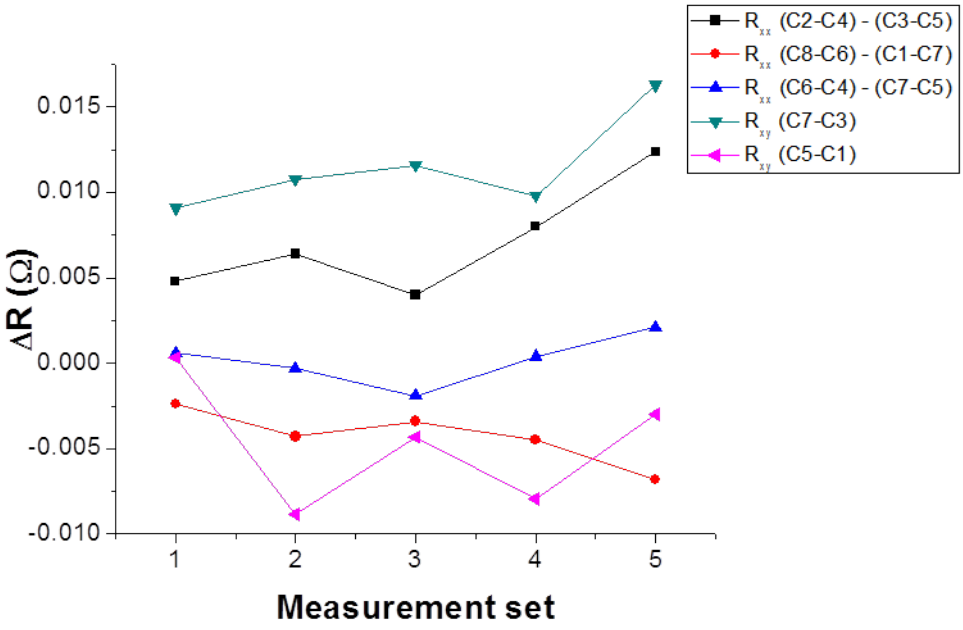

Figure 6.15: ΔR_{xx} and ΔR_{xy} for subsequent setting pulses along C2 to C6 and C8 to C4 directions. The ΔR_{xx} data is the difference between the red and purple data points in figure 6.14 while the ΔR_{xy} data is the difference between the red and purple data points for the R_{xy} plots in figure 6.13.

If the CuMnAs sample were to have no magnetic anisotropy, i.e. if there was no axis more energetically favourable than any other for the AF spin-axis to lie along, and assuming that the NSOT effective magnetic fields are of a similar magnitude for all current directions (which would be the case for Rashba symmetry), then one may expect the above data for the $[1\bar{1}0]/[110]$ setting pulses to look similar to the [100]/[010] setting pulse data but with a 45° shifted symmetry. The data in figure 6.13 shows this to partially be the case. For example, R_{xy} clearly varies with setting pulse direction for probe current along C1 to C5 (which is 45°/135° to the setting pulses), but not for probe current along C2 to C6 (which is 0°/90° to the setting pulses). Similar (but not quite as clear) trends are seen for the other R_{xy} measurements. The R_{xx} data is less consistent. For the six R_{xx} datasets, three show the behaviour that would be expected for the no magnetic anisotropy situation

and three do not. For example, for the probe along C1 to C5 R_{xx} measurements (the top left and top middle plots of figure 6.13), for the no magnetic anisotropy situation, both would not be expected to show any difference in R_{xx} for the different setting pulse directions. However, for the 4-probe C8-C6 measurement there is a clear variation (again on top of a background drift). This potentially suggests that what is being sensed at the C8-C6 probes is not the same as what is being sensed at the C2-C4 probes, which again could be consistent with the idea of domains not saturating in the central region of the device. For the C8-C6 measurements, domains would presumably have to form near the C8 and C6 probes with the AF spin-axis lying closer towards the [100]/[010] directions than the $[1\bar{1}0]$/[110] directions (to allow for the significant R_{xx} variation via AMR symmetry). This could be made possible by the direction of current flow near these probes being close to the [100]/[010] directions (as shown in figure 6.7), combined with a biaxial magnetic anisotropy. Another factor that could be important is that if domains do form, the domain walls could be relatively thick (say due to a strong magnetocrystalline anisotropy), and this could be responsible for the AF moments in certain regions of the device lying at 45°/135° to the AF spin-axis domains which would further complicate the situation. However, without having more information about the magnetic structure of the central region of the device (for example through XMLD-PEEM measurements), it is difficult to make any real conclusion about the dataset as a whole. As shown in figure 6.15, the size of the difference in R_{xx} and in R_{xy} for subsequent orthogonal setting pulses is again not consistent for the different measurement sets for a given probe geometry, nor are the magnitudes of ΔR_{xx} and ΔR_{xy} for different geometries consistent with one another (the average difference in resistance over the five measurement sets for the five measurement geometries in figure 6.15 are $+7(\pm1)$mΩ, $-4.3(\pm0.7)$mΩ, $+0.2(\pm0.7)$mΩ, $+12(\pm1)$mΩ, and $-5(\pm2)$mΩ). All in all, the $[1\bar{1}0]$/[110] setting pulse measurements do not give sufficiently clear evidence to support the NSOT/AMR picture, but nor do they provide sufficiently clear evidence that the observed variations in R_{xx} and R_{xy} are caused by a completely different mechanism (magnetic or non-magnetic). The situation is quite possibly complicated by non-saturated domains forming in the central region of the device, as well as the magnetic anisotropy of the CuMnAs sample potentially being more complex than a simple [100]/[010] easy axes situation.

To further investigate the possibility that the change in R_{xx} and R_{xy} in the figure 6.10 and figure 6.13 datasets is related to AMR, repeat measurements for these data sets were made at 4.2K. For these measurements, the setting pulse was still applied at 298K, before the sample was cooled down to 4.2K and probe measurements made. The results are shown in figures 6.16 and 6.17.

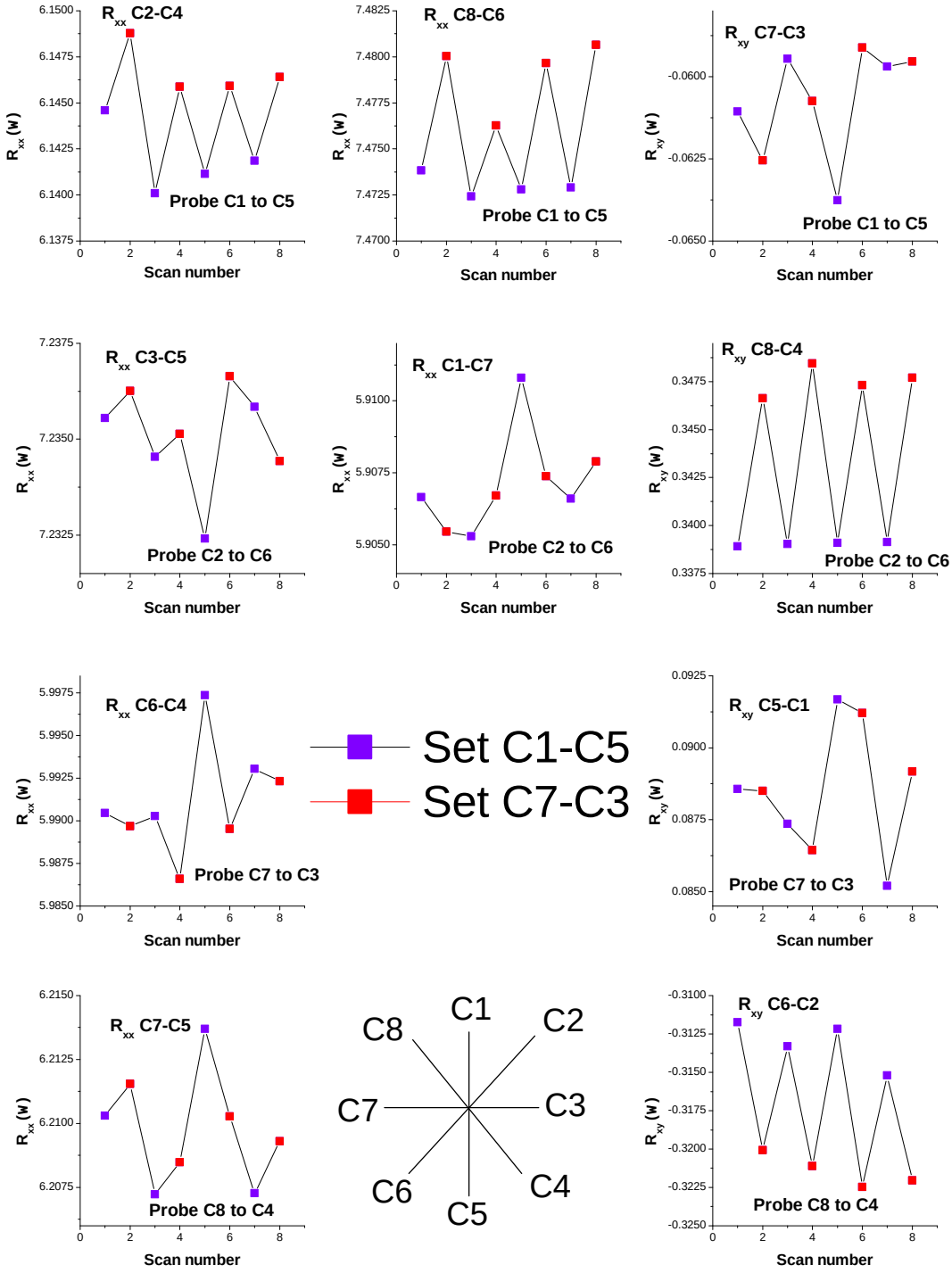

Figure 6.16: Various 4-probe R_{xx} and R_{xy} measurements after 0.05s setting pulses of 12.5MA/cm^2 current density applied along the C1 to C5 (purple), and C7 to C3 (red) directions. Setting pulses are applied at 298K and probe measurements are made at 4.2K. Note that no data was collected for C8-C2 and C1-C3 4-probe R_{xx} measurements.

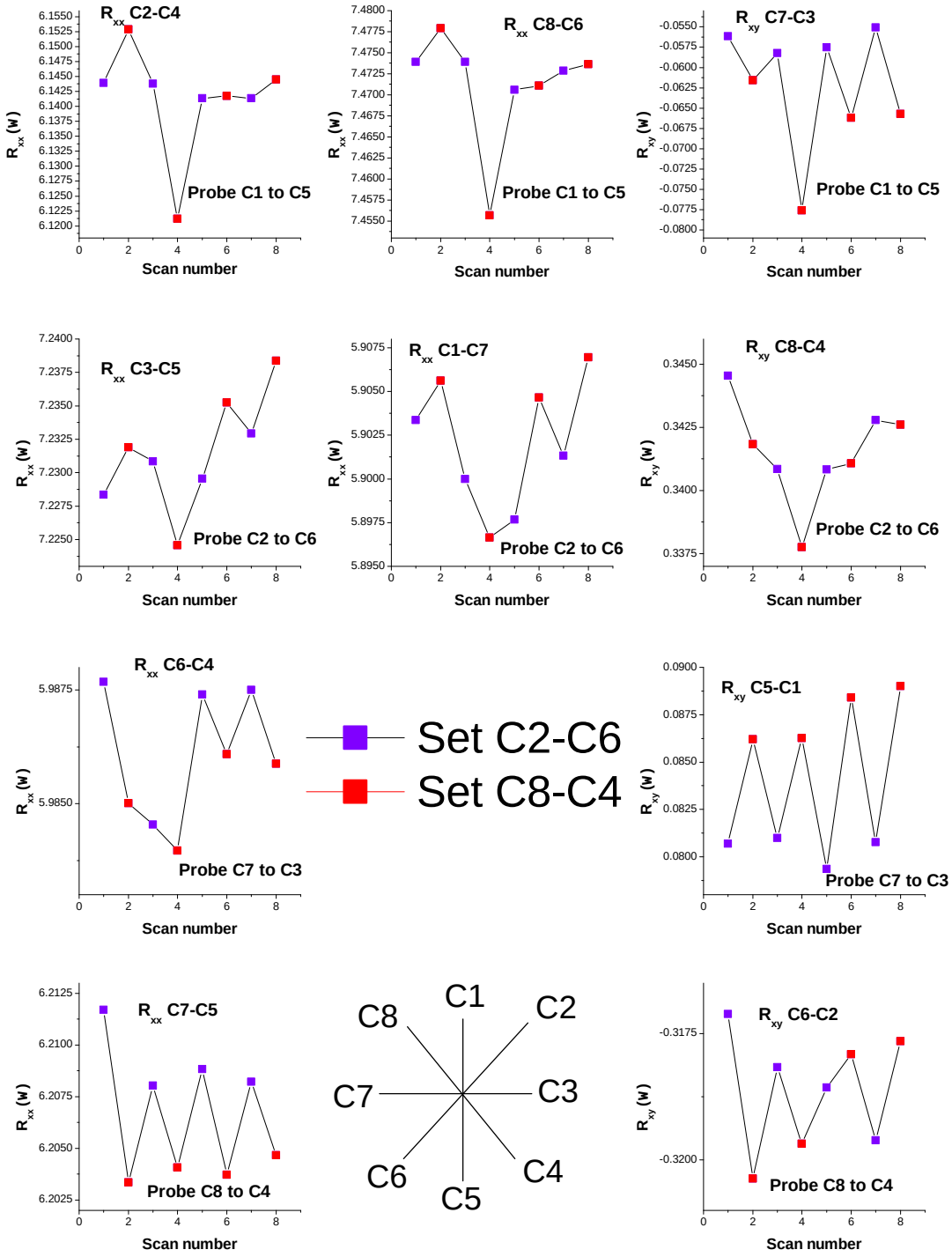

Figure 6.17: Various 4-probe R_{xx} and R_{xy} measurements after 0.05s setting pulses of 12.5MA/cm^2 current density applied along the C2 to C6 (purple), and C8 to C4 (red) directions. Setting pulses are applied at 298K and probe measurements are made at 4.2K. Note that no data was collected for C8-C2 and C1-C3 4-probe R_{xx} measurements.

In terms of the appearance of high and low R_{xx} and R_{xy} states, the data shown in figure 6.16 for [100]/[010] setting pulses measured at 4.2K looks similar to that in figure 6.10 for [100]/[010] setting pulses measured at 298K, i.e. both give the high and low resistance states for the same geometries of probe current (though this is

not as clearly defined for the R_{xx} C6-C4 4.2K measurement). One obvious difference between the datasets is that the 4.2K measurements do not have an upwards drift on the R_{xx} data. This suggests that the Joule heating of the sample dissipates as it is cooled from 298K to 4.2K (at which the sample sits in liquid He). If the [100]/[010] 298K dataset was to be interpreted as being caused by the NSOT/AMR mechanism, its agreement with the 4.2K dataset in terms of the geometry of the high and low resistance states would suggest that the AF spin-axis direction and hence possibly also the easy axes direction of the CuMnAs sample does not change as it is cooled from 300K to 4.2K. This is in contrast to some (Ga,Mn)As samples whose easy axes can change as a function of temperature[53]. The average ΔR_{xx} and ΔR_{xy} values at 4.2K for subsequent 298K pulses along [100]/[010] are -4($\pm$1)mΩ, -7($\pm$2)mΩ, +3.5($\pm$0.7)mΩ, -8.5($\pm$0.4)mΩ, and +8.3($\pm$0.7)mΩ. These values are of a similar magnitude to the 298K probe measurements, however as R_{xx} is lower at 4.2K than 298K they correspond to bigger AMR-like values of between 0.056%-0.145%. The fact that these AMR-like values increase as temperature decreases lends support to the ΔR_{xx} and ΔR_{xy} signals truly arising from AMR (which is known to generally increase with decreasing temperature), as opposed to some non-magnetic voltage effect. For the setting pulse applied at 298K along the [1$\bar{1}$0]/[110] directions, the 4.2K probe measurement dataset shown in figure 6.17 is also somewhat confusing like the 298K probe measurement dataset in figure 6.13. High and low R_{xy} states are again observed for probe currents along the [1$\bar{1}$0]/[110] directions but not the [100]/[010] directions, which would be in agreement with the AF spin-axis setting along directions closer to the [1$\bar{1}$0]/[110] axes than the [100]/[010] axes. However, again like the 298K datasets, the high and low R_{xx} states do not always occur in a geometry that agrees with the R_{xy} data. For example, no high and low R_{xx} states are formed for probe currents along the C2 to C6 direction. One thing that is noticeable in the R_{xx} datasets is that for probe current along the C1 to C5, and C2 to C6 directions, where in both cases two 4-probe R_{xx} measurements are made (one for either side of the central region of the device), there is a much better agreement in the two R_{xx} measurements for a given current direction at 4.2K than there is at 298K. If the central region of the device does consist of domains, this could perhaps be interpreted as greater saturation of domains across the central region at 4.2K compared with 298K, i.e. the domains at the probes at either side of the central region are more similar to one another at 4.2K. This is not as obvious for the [100]/[010] setting pulse measurements. Like the [100]/[010] setting pulse dataset, for the [1$\bar{1}$0]/[110] setting pulse dataset the ΔR_{xx} and ΔR_{xy} 4.2K values for subsequent 298K pulses along [1$\bar{1}$0]/[110] are of a similar average size (+5($\pm$5)mΩ, +7($\pm$3)mΩ, -4.9($\pm$0.8)mΩ, +11($\pm$3)mΩ, -7.0($\pm$0.9)mΩ) to the 298K probe measurements.

Measurements were also made with the 0.05s 12.5MA/cm^2 current density setting pulses applied at 4.2K along the [100]/[010] directions, and probe measurements also made at 4.2K. Over six pulses (three along each direction) there was no evidence of consistent high and low resistance states for any of the R_{xx} and R_{xy} geometries. In terms of the NSOT/AMR picture, this would infer that at 4.2K the current pulse is not strong enough to align the AF spin-axis of a significant number of domains (to be detectable by AMR). There are two possible reasons that would explain this. Firstly, the magnetic anisotropy of CuMnAs is expected to be stronger at 4.2K

than 298K, and therefore a larger effective field would be needed to reorientate it away from an easy axis to another direction. Secondly, as shown in chapter 4 of this thesis, Dresselhaus FM SOT effective fields can decrease in magnitude with decreasing temperature, and hence the magnitude of the NSOT effective field may also have a similar temperature dependence. The observed lack of variation in R_{xx} and R_{xy} when applying the setting pulses at 4.2K can therefore be used as evidence in support of the NSOT/AMR mechanism for the 298K setting pulse data.

The dependence of how R_{xx} and R_{xy} vary with the magnitude of the setting pulses was initially briefly investigated with the 8μm Union Jack Hall cross device for 298K setting pulse and probe measurements. A full investigation was not done on the 8μm Union Jack Hall cross device and as care was taken not to completely degrade any of the contacts (as discussed in section 6.3.1). Later on a full investigation of setting pulse current density was done on a separate device of the same sample, and the results are shown at the end of this results section. The results of the brief 8μm Union Jack Hall cross device current density investigation (not shown) indicated that the size of the variation in R_{xx} and R_{xy} with setting pulses direction increases with increasing setting pulse current density (for the three different current densities used) as well as with increasing setting pulse length. These results could be consistent with the larger/longer setting pulses reorientating more domains in the central region of the device, similar to previous observations of the behaviour FM domains with the application of spin polarised current[295][296]. Ideally larger/longer setting pulses could have been applied to this device to see if the variation in R_{xx} and R_{xy} could be saturated. However, to avoid degrading contacts, measurements were instead made where a 0.05s 12.5MA/cm^2 setting pulse was applied along the C1 to C5 direction, the usual series of probe measurements performed, and the same pulse applied again along the same direction with the usual probe measurements made again and so on. The time between the application of each pulse was around 5 minutes, which is the time it takes to make the probe measurements. After 10 of these measurements the next pulse was applied along the C7 to C3 direction and the process repeated for 40 of these pulses. The pulse direction was then changed back to C1 to C5 for another 55 measurements, and then back once more for another 50. All measurements were made nominally at 298K, though the sample space temperature drifted upwards by about 0.4K over the course of the whole set of measurements. The results are plotted in figures 6.18 and 6.19.

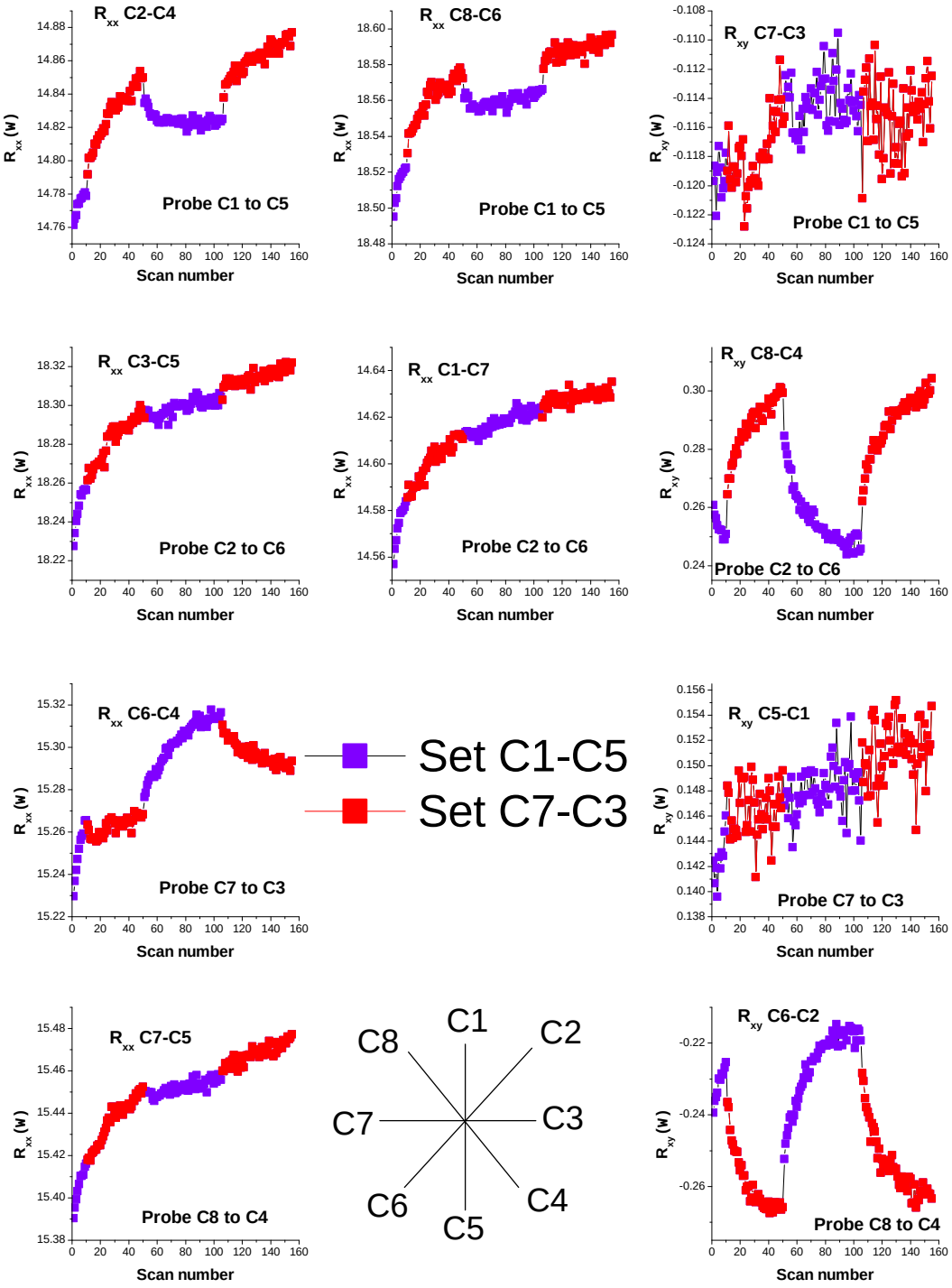

Figure 6.18: Various 4-probe R_{xx} and R_{xy} measurements after 0.05s setting pulses of 12.5MA/cm^2 current density applied along the C1 to C5 (purple), and C7 to C3 (red) directions. Setting pulses are applied and probe measurements are made at 298K.

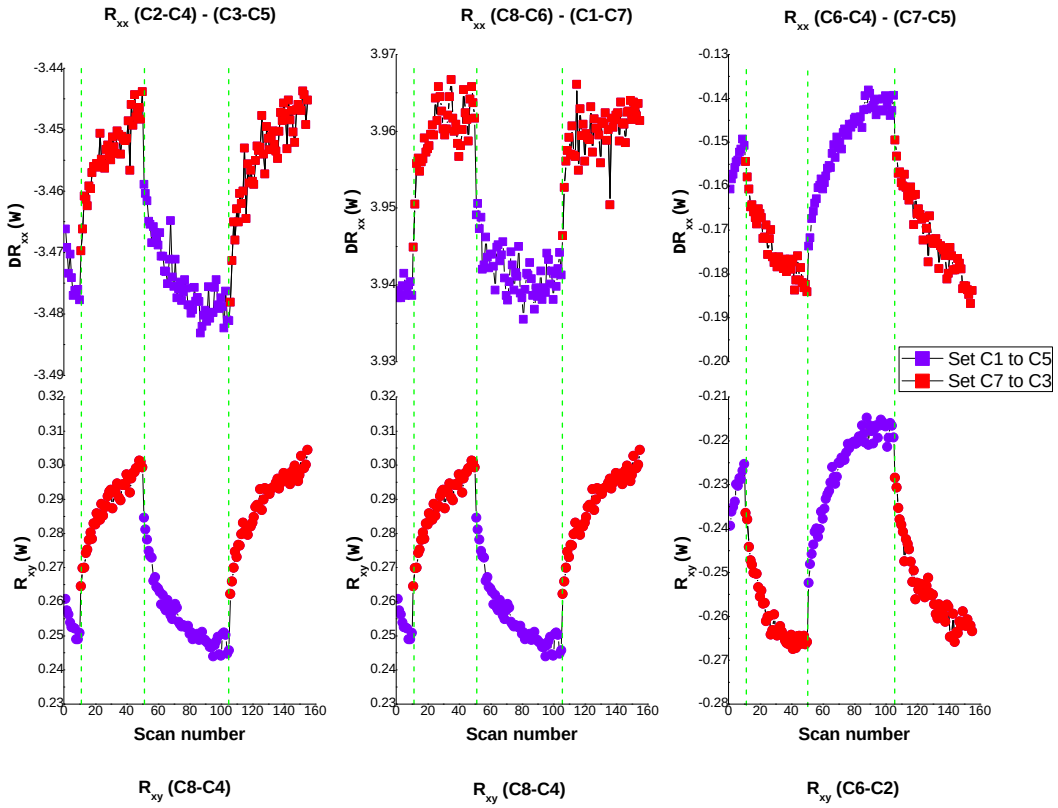

Figure 6.19: **Upper plots:** Difference in 4-probe R_{xx} measurements between the case of probe currents along directions 45° apart for the figure 6.18 data for setting pulse along the C1 to C5 (purple squares), and C7 to C3 (red squares) directions. **Lower plots:** R_{xy} data plots from the figure 6.18 data for setting pulse along the C1 to C5 (purple circle), and C7 to C3 (red circles) directions. Dashed green lines are a visual guide as to when the setting pulse direction is changed.

The R_{xx} data in figure 6.18 shows that R_{xx} continues to drift upwards with subsequent pulses over the course of 155 pulses. The size of the drift is most severe in the initial 30 or so pulses, but reduces as the number of pulses increases further. Over the 150 pulses the drift is around 0.08Ω, which when converted to a resistivity and compared with resistivity against temperature data for other CuMnAs samples, roughly corresponds to a 1K temperature increase. In figure 6.19 where the drift in R_{xx} is accounted for via plotting the difference in R_{xx} for different current geometries after the same setting pulse, the effect of the setting pulses becomes apparent. For subsequent setting pulses applied in the same direction, ΔR_{xx} and R_{xy} continuously increase/decrease in size. The largest change in size in ΔR_{xx} and R_{xy} is for the first pulse along a new direction, with the size of the change being approximately consistent with the data in figure 6.10 where only one pulse is applied in each direction at a time. The increase/decrease in the size of ΔR_{xx} and R_{xy} generally gets smaller with continuing pulses in the same direction, but there is significant variation within this general trend. Importantly, with the possible exception of the case of ΔR_{xx} for (C8-C6) - (C1-C7), the change in ΔR_{xx} and R_{xy} with continuing pulses along the same direction does not obviously saturate, generally increasing by around 30mΩ over the duration of the

pulses applied for a given direction. The maximum difference in the ΔR_{xx} data (i.e. between the final measurements for pulses along each direction) is around 25mΩ-45mΩ for the three different geometries. For the R_{xy} data this maximum difference of high and low states is around 50mΩ. It should be noted that these values are somewhat of a moot point as the high and low resistance states are not saturated, and hence they could be increased further by applying more pulses along the same direction. The figure 6.19 data is again compatible with the idea of NSOT setting the AF spin-axes of domains in the central region of the device, and AMR giving the high and low resistance states. In this situation, the total amount of the domains aligned in the same direction in the central region of the device would generally increase with every setting pulse, but would not saturate to form a single domain state in the central region. One reason for this could be that the setting current density is not consistent across the central device region, as shown in figure 6.8. Domains further away from the middle of the central region experience a lower magnitude of current density flowing through them and thus it would be much more difficult for these areas to reorientate their AF spin-axis via NSOT. Other effects could also be taking place that are not related to NSOT. For example, if each setting pulse heats up the central region of the device, domains could potentially flip their AF spin-axis from one easy axis to another through thermal fluctuation. AF domains are a complex and not particularly well-studied topic[297][298][299], and it is hard to picture exactly what may be occurring in terms of the magnetic structure of the central device region without using a spectroscopic technique like XMLD-PEEM. Nevertheless, figure 6.19 shows that with sufficiently large or long current pulses, enough domains in the central device region can be saturated to give well-separated high and low resistance states.

As the resistance of CuMnAs at 300K is known to permanently increase after heating to 500K, the Union Jack Hall cross device was annealed at 500K for 2 hours in vacuum to see whether it had any effect on its behaviour with the application of setting pulses. Repeat measurements of the figure 6.10 dataset were made (single 0.05s, 12.5MA/cm^2 setting pulses along [100]/[010] applied and measured at 298K). As shown in figure 6.20, the variation in resistances with setting pulse is very similar to the measurements on the sample before annealing. The R_{xx} values are around 1Ω larger after annealing. The size of the drift in R_{xx} is larger after annealing, but this may be in-part because the temperature of the sample space happened to be less stable during these measurements than for the measurements before annealing. The average size in the variation in ΔR_{xx} and R_{xy} for the various geometries after setting pulses along orthogonal directions are -7.2(±0.6)mΩ, -9(±1)mΩ, +6(±2)mΩ, -12.2(±0.6)mΩ, +8(±1)mΩ, which are similar in size to the measurements on the sample before annealing. The same measurements were also made for setting pulses along the $[1\bar{1}0]$/[110] directions, and the annealed data (not shown) looks similar to that of the measurements before annealing (figure 6.13). Annealing the device therefore seems to have little effect on its magnetic properties and AMR-like response to setting current pulses.

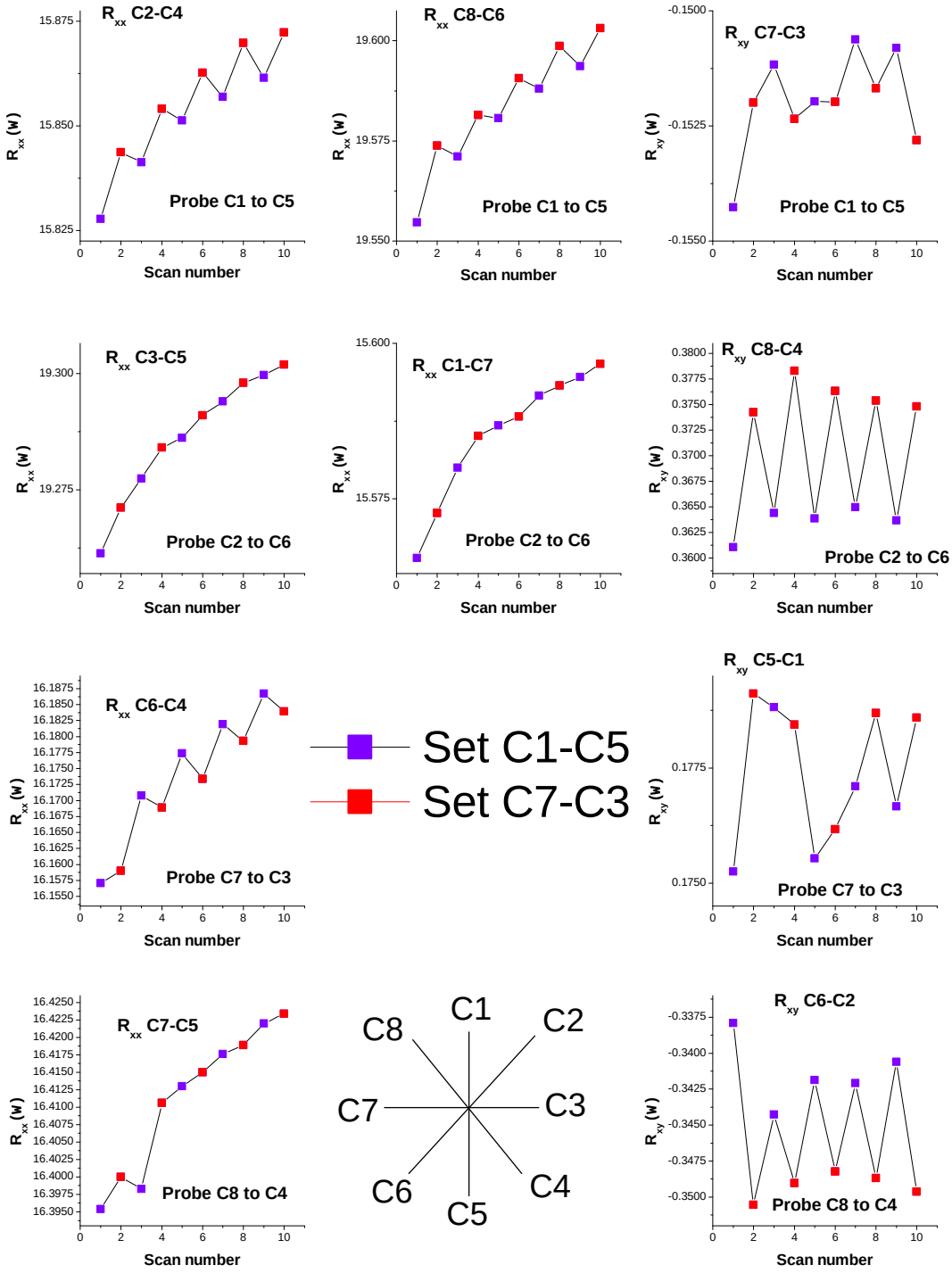

Figure 6.20: Various 4-probe R_{xx} and R_{xy} measurements after 0.05s setting pulses of 12.5MA/cm^2 current density applied along the C1 to C5 (purple), and C7 to C3 (red) directions on the device after 500K annealing. Both setting pulses and probe measurements are performed at 298K.

A brief study was made on the annealed sample of the effects of reversing the polarity of the setting pulse. Immediately after making the 0.05s, 12.5 MA/cm^2 [100]/[010] setting pulse measurements of figure 6.20, measurements were made for applying the setting pulses along the opposite directions, i.e. C5 to C1 and C3 to C7. It was observed that for these setting pulses, the change in both ΔR_{xx}

(difference in R_{xx} for different probe geometries to account for drift) and R_{xy} for the orthogonal pulses was considerably smaller than for the C1 to C5 and C7 to C3 pulses (this is especially true in the ΔR_{xx} data). Similar measurements were then made with the setting pulses along the $[1\bar{1}0]/[110]$ directions. For the R_{xy} geometries where the high and low states were fairly well defined, similar behaviour upon reversing pulse polarity was observed, i.e. the size in the change in R_{xy} became considerably smaller when the orthogonal setting pulse direction was reversed from C2 to C6 and C8 to C4, to C6 to C2 and C8 to C4. Finally, measurements were made once again for the setting pulse along the [100]/[010] directions, but this time only for the C5 to C1 and C3 to C7 pulse directions (i.e. the 'reverse' directions that previously gave significantly smaller changes in ΔR_{xx} and R_{xy}). The size of the difference in ΔR_{xx} and R_{xy} for the orthogonal pulses now becomes similar to the size of the difference in ΔR_{xx} and R_{xy} for the C1 to C5 and C7 to C3 directions in the initial [100]/[010] measurements, i.e. much larger than the initial C5 to C1 and C3 to C7 measurements. It seems that when applying pulses only along the [100]/[010] directions, the change in resistance is not the same for forward and reverse current. In the domain picture, this could infer a unidirectional or chiral element to the magnetic state, as torquing the AF domains with opposite effective fields (generated by opposite current directions) gives inequivalent effects on the domains. The fact that the size of the reverse current effect for the [100]/[010] setting pulse directions then becomes much larger after pulses have been applied along the $[1\bar{1}0]/[110]$ directions is difficult to explain. An example of the effects of reversing the current polarity is shown in figure 6.21.

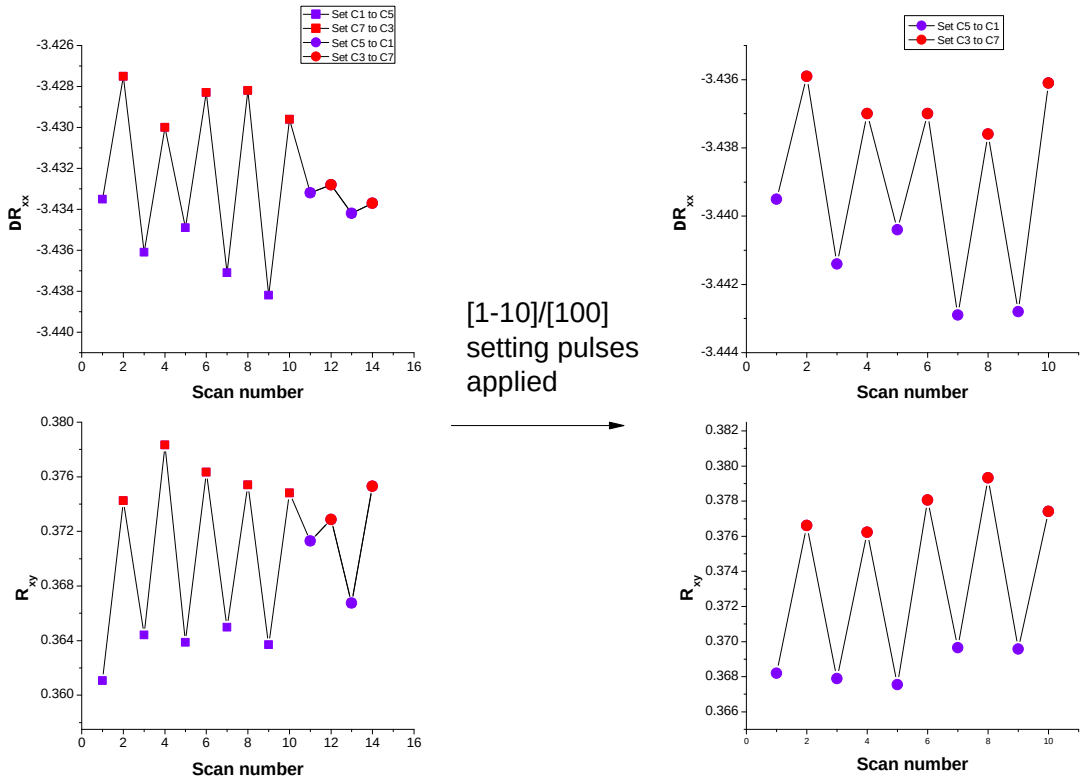

Figure 6.21: 4-probe ΔR_{xx} and R_{xy} for setting pulses applied along the [100]/[010] directions for forwards (square data points) and reverse current (circle data points). After the measurements in the plots on the left-hand side of the figure, setting pulses were applied along the $[1\bar{1}0]/[110]$ directions (data not shown), before reverse setting pulses only were applied again along the [100]/[010] directions (right-hand side plots).

To complete the experimental measurements presented in this chapter, the dependence of the variation in R_{xx} and R_{xy} with setting pulse direction for different setting pulse current densities was investigated more thoroughly. For these measurements, a new device of the same Mn752 sample was processed with more favourable dimensions for reorientating domains in the central region. The new device is still a Union Jack Hall cross, however the arms along the [100]/[010] directions are around 28μm wide whereas the arms along the $[1\bar{1}0]/[110]$ directions are around 8μm wide. For setting pulses along the C1 to C5 direction, finite element calculations for this geometry show that the current density in the C1 to C5 direction in the central device region is around 50%-65% of that in the arms, as opposed to 20%-37.5% for the 8μm Union Jack Hall cross device. Once more the stated current densities reported here for this new device are nominally the current densities for the 28μm device arms, and so care should be taken when comparing setting pulse current densities between the two devices as the current densities in the central regions will not be the same. With a greater percentage of current flowing in the desired direction in the central region of the new device, a greater percentage of domains in this region should be able to reorientate their AF spin-axis via NSOT.

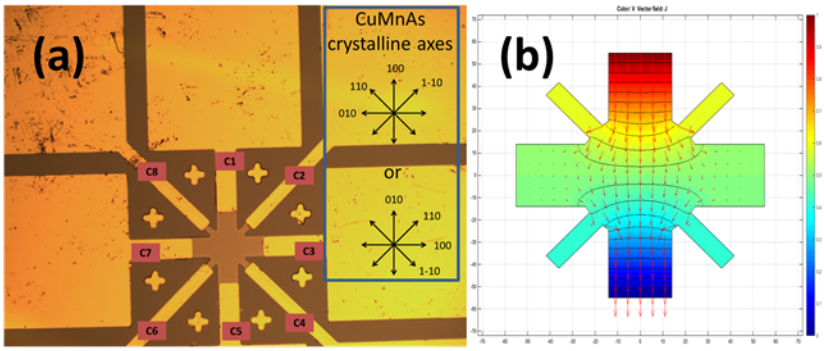

Figure 6.22: **(a)** Image of new 28μm Union Jack Hall cross device used for the setting pulse current density measurements shown in figure 6.24. The orientation of the device with respect to the crystalline axes is not known exactly, but is one of the two possibilities shown on the right hand side of the figure, i.e the wider arms are along the [100]/[010] directions. **(b)** Contour plot of computed electric potential and current flow in the 28μm Union Jack Hall cross device for a voltage applied between C1 and C5. Colour chart on right hand side indicates the normalised electric potential within the device. Black lines are lines of equipotential. Each line is separated by a normalised electric potential value of 0.01. Red arrows indicate the direction of current flow within the device, with the size of the arrows being proportional to current density.

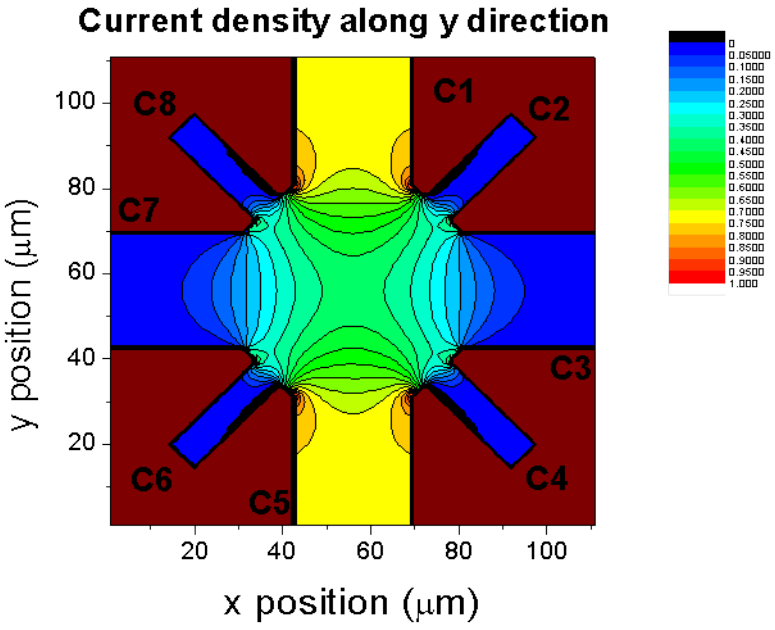

Figure 6.23: Contour plot of computed component of current density along the C1 to C5 direction in the new 28μm Union Jack Hall cross device for a voltage applied between C1 and C5.

For the setting pulse current density investigation, 0.05s setting pulses were applied along the [100]/[010] directions of the 28μm Union Jack Hall cross device at 298K, and the usual R_{xx} and R_{xy} measurements made after a 8 minute wait (though this turned out to not be long enough to completely remove the R_{xx} drift) also at

298K sample space temperature. The magnitude of the setting pulses varied from 5MA/cm^2 to 7.86MA/cm^2. For each setting pulse magnitude, three pulses were applied along the [100] and [010] directions, thus giving three sets of ΔR_{xx} and ΔR_{xy} values from which an average was taken. The results were obtained with the help of Carl Andrews and Dr. Peter Wadley and are plotted in figure 6.24.

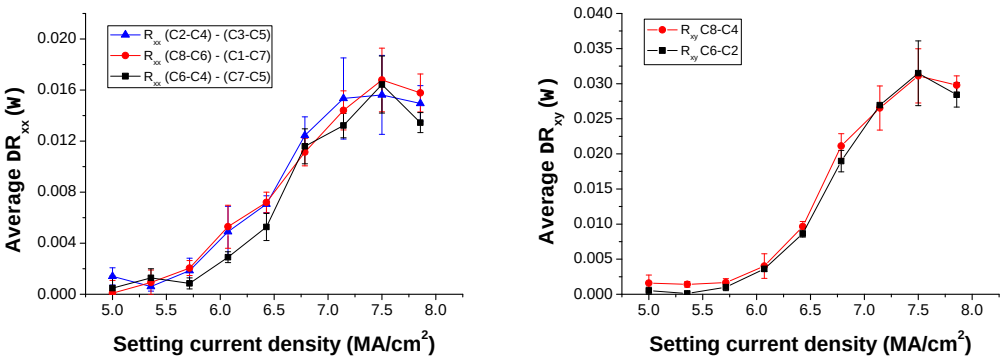

Figure 6.24: **(a)** Magnitude of average variation for setting pulses along the [100] and [010] directions in the difference in 4-probe R_{xx} measurements between the case of probe currents along directions 45° apart (to account for Joule heating) as a function of setting pulse current density. **(b)** Magnitude of average variation in 4-probe R_{xy} measurements for setting pulses along the [100] and [010] directions as a function of setting pulse current density. All setting pulses and probe measurements are applied at 298K, and are made for the 28μm device.

For the 28μm device, ΔR_{xy} is larger than ΔR_{xx} as the device geometry does not give a square aspect ratio, unlike the 8μm Union Jack Hall cross device. Both ΔR_{xx} and ΔR_{xy} for all the datasets in figure 6.24 increase with increasing current density up until the 7.50MA/cm^2 data points. In the domain picture, this would suggest that more domains reorientate their AF spin-axis with increasing current density. If a given domain within the device needs to experience a critical current density to reorientate its AF spin-axis, the calculated profile of current density through the device shown in figure 6.23 indicates that the domains in the middle of the central device region will switch for a lower value of the nominal applied current density than the domains at the edge of the central device region. With increasing nominal applied current density, domains that are increasingly further away from the middle of the central device region will experience the critical current density, and so in total more domains in the central device region will reorientate their AF spin-axis in the same direction with each setting pulse. For all data sets the 7.86MA/cm^2 ΔR_{xx} and ΔR_{xy} values are smaller than the 7.50MA/cm^2 values. The fact that they are not larger could be interpreted as the 7.86MA/cm^2 setting pulses not switching a greater amount of domains in the central device region than the 7.50MA/cm^2 setting pulses, possibly because a 7.50MA/cm^2 setting pulse is sufficient to switch all of the domains. In this interpretation is not clear why the larger 7.86MA/cm^2 pulses would give smaller ΔR_{xx} and ΔR_{xy} values than the 7.50MA/cm^2 pulses, but it should be noted that all the ΔR_{xx} and ΔR_{xy} values for the 7.50MA/cm^2 and 7.86MA/cm^2 measurements agree within error. No measurements for setting pulses of current densities larger than 7.86MA/cm^2 were

taken to avoid possible contact degradation.

After the completion of the work presented in this chapter, further measurements made by Dr. Peter Wadley and Carl Andrews showed that the high and low resistance state effect with setting pulse direction is insensitive to the application of a 4.4kOe external magnetic field applied along various directions. Along with a SQUID measurement of the sample which showed no FM signal, these findings rule out the possibility that the high and low resistance state effect is related to FM inclusions in the CuMnAs sample.

6.4 Conclusions and future work

Section 6.1 of this chapter outlined the basic structural, electronic, and magnetic properties of tetragonal CuMnAs. It also introduced the concept of NSOT as an approach to manipulating the spin-axis of an antiferromagnet. Field-like NSOT can arise in antiferromagnets whose centrosymmetric lattice can be split into two non-centrosymmetric sublattices that coincide with the spin sublattices. CuMnAs was shown to have this unique lattice arrangement, and as it is a fairly well characterised AF material it is a good starting point to try and observe and investigate NSOT.

Section 6.3 of this chapter reported on experimental measurements to try and detect NSOT in CuMnAs via AMR. A 50nm thick CuMnAs sample grown on GaP was chosen as it was believed to lack a significant uniaxial magnetic anisotropy which would otherwise hinder switching between different stable AF spin-axis orientations. Measurements were made with a Union Jack Hall cross device in order to allow current flow and R_{xx} and R_{xy} 4-probe sensing along the major in-plane crystalline axes. Large current pulses were applied to the device in order to try and set the AF spin-axis via the NSOT mechanism. Detection of AF spin-axis switching relied upon the principle that R_{xx} and R_{xy} would vary with AF spin-axis orientation for certain probe measurement geometries given by AMR symmetry. The key findings of the experimental measurements were:
• For setting pulses along the [100]/[010] directions applied at 298K, R_{xx} and R_{xy} vary with setting pulse direction for the expected probe geometries from AMR symmetry. No variation in R_{xx} and R_{xy} with setting pulse direction is seen in geometries where it is not expected from AMR symmetry.
• The size of the AMR-like signal for the variation in R_{xx} and R_{xy} with setting pulse direction is larger for probe measurements made at lower temperatures. For 0.05s 12.5MA/cm^2 setting pulses applied at 298K to the 8μm Union Jack Hall cross device, the AMR-like signal when probed at 298K is around 0.04%, whereas when probed at 4.2K it is around 0.1%.
• For the same setting pulses applied at 4.2K, probe measurements also made at 4.2K show no variation in R_{xx} and R_{xy} in any probe geometry.
• For multiple setting pulses applied sequentially along the same [100] or [010] direction, R_{xx} and R_{xy} continually increase/decrease for the same probe geometries as the single pulse measurements. The size of the increase/decrease in R_{xx} and R_{xy} with each current pulse gets smaller as more pulses are applied, but the effect

does not saturate for the number of pulse applied in this experiment.
• The variation in R_{xx} and R_{xy} with setting pulse direction gets bigger with increasing setting pulse current density and length. For the 28μm device, the variation appears to saturate for a large enough setting pulse magnitude.
• The variation in R_{xx} and R_{xy} with setting pulse direction is unaffected by the application of an external magnetic field.
• For setting pulses applied along the [1$\bar{1}$0]/[110] directions, the observed changes in R_{xx} and R_{xy} for the various probe geometries are less consistent and more confusing than for setting pulses along the [100]/[010] directions.

The most plausible explanation for the above observations is as follows: The magnetic structure of the Mn752 sample (and more importantly the central region of the device) is split into sub-μm AF domains. The domains are likely to be aligned along or near to the [100] and [010] crystalline axes. Setting pulses along the [100]/[010] directions generate an NSOT effective field that acts to reorientate the domains in the direction of the field. For the 8μm device the setting pulses reorientate a significant enough amount of the domains to be detectable by AMR, but do not reorientate all of the domains. Further domains can be reorientated with the application of further setting pulses, but it is difficult to saturate all the domains in the central device region, possibly due to the path taken by and spread of current density in this region.

The above mechanism cannot be verified through transport measurements alone. It is crucial to perform XMLD-PEEM measurements (which can image AF domains to a resolution of around 50nm[300]) on a similar device of the same sample in order to resolve the magnetic structure. There are several vital observations that would need to be made. Firstly, does the sample contain domains, what are their size, and along which directions do they lie? Secondly, how does the domain picture look immediately after the application of a setting pulse? It would be important here to also observe areas of the device where there would be significantly less current to flow through. Thirdly, does the domain picture change with time after the application of a setting pulse? Finally, how does the domain picture change for applying the setting pulses along the [100]/[010] and [1$\bar{1}$0]/[110] directions? Only through direct observation of the magnetic behaviour of the sample can its indirect observation through AMR measurements be clarified. Nevertheless, it is difficult to postulate any other mechanism that would increase the sample conductivity along the setting pulse direction other than an AMR effect. If the R_{xx} and R_{xy} variations with setting pulse direction are confirmed to be caused by the AF spin-axis reorientating, the work in this investigation will be the first demonstration of AMR in CuMnAs. The sign of the AMR cannot be clarified without knowing whether the setting pulses align the AF spin-axis perpendicular or parallel to the current direction. The maximum size of the AMR cannot be known without fully saturating the domains in the region of the device which the given detection probes are sensitive to.

The creation of AF domains as opposed to a saturated AF spin-axis throughout the CuMnAs device may be due to local defect sites or strains pinning the AF spin-axis in certain regions of the device. For characterising the NSOT phenomenon it would be ideal for the magnetic ordering of the device to be single domain as it would

make the AMR measurements much more easy to interpret. However, the existence of domains could also offer additional functionality for an AF memory device. For example, consider a current flow from the C8 contact to C6 contact of the 8μm Union Jack Hall cross device. The calculated current density distribution for this situation is shown in figures 6.25 and 6.26. The current density in the C1 to C5 direction in the left hand side of central device region is roughly double that of the middle of the central device region, and triple that of the right hand side of the central device region. The magnitude of this current density is also roughly at least double that of the current density in the C7 to C3 direction for the majority of the central device region. It could be possible to apply such a magnitude of setting current from the C8 to C6 contacts that the C1 to C5 direction current density in the left hand side of the central device region is sufficient to reorientate the magnetic domains in that area, but the C1 to C5 direction current density in the rest of the central device region is not sufficiently large to reorientate the domains there, nor is the C7 to C3 direction current density sufficiently large to reorientate domains in the vast majority of the central device region. If the domains were able to be locally saturated in this way, given the right geometry the central region of a Union Jack Hall cross device could be split into multiple magnetic states by passing current between different sets of contacts. A cartoon of such idealised behaviour is shown in figure 6.27. Consider, for example, probe current from C1 to C5, and R_{xx} sensed at C2-C4. Depending on the how far into the central region of the device the C2 and C4 probes are sensitive to, the eight scenarios in depicted in figure 6.27 may all give different R_{xx} values. This simplified cartoon assumes a cubic magnetic anisotropy, that the effects of current flow in the orthogonal direction (to the yellow arrow in the central device region in figure 6.27) on domain switching are negligible, that the large domain states would be stable, that probes are sensitive across most of the central region etc, and so more consideration would be needed to actually create any device with more than two well defined R_{xx} states. Nevertheless, it would be worth applying setting pulses along C8 to C6, C6 to C4 etc of one of the 8μm devices in this investigation just to get a feel for how the various probe geometry measurements of R_{xx} and R_{xy} vary with setting current path.

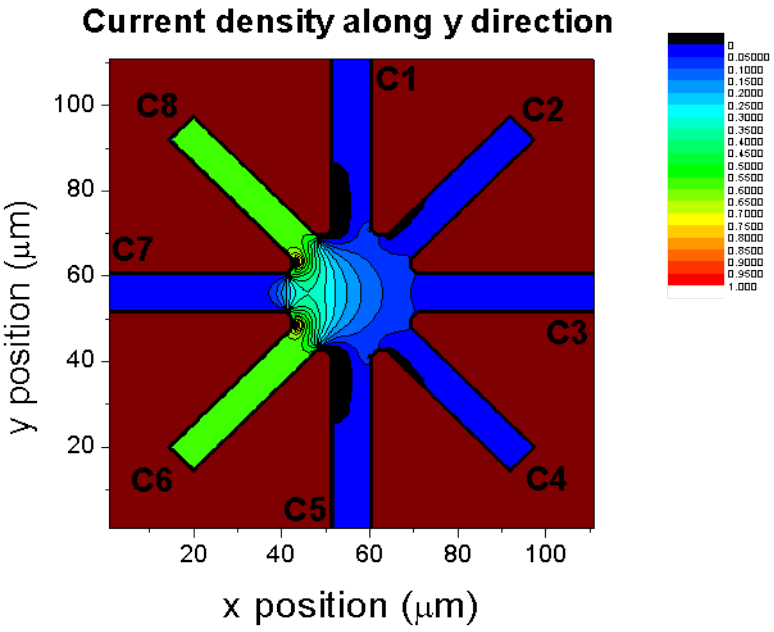

Figure 6.25: Contour plot of computed component of current density along the C1 to C5 direction in the 8μm Union Jack Hall cross device for a voltage applied between C8 and C6.

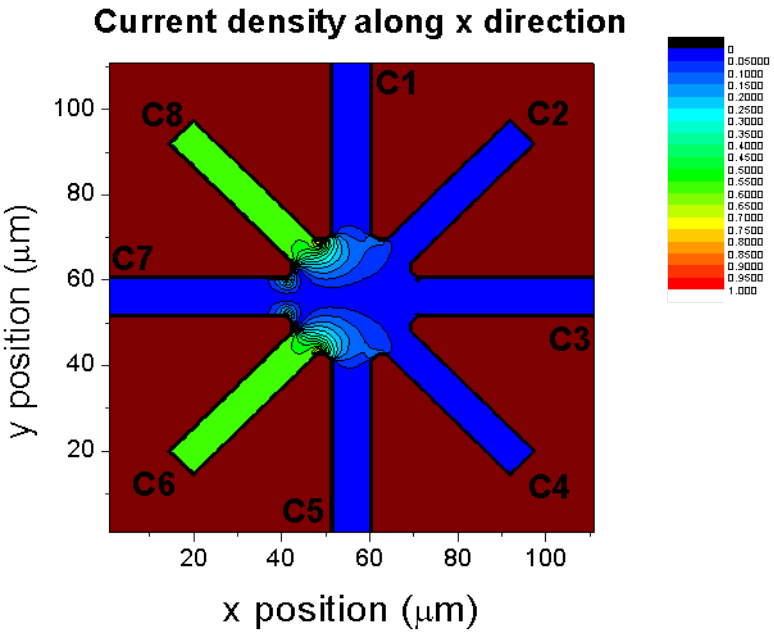

Figure 6.26: Contour plot of computed component of current density along the C7 to C3 direction in the 8μm Union Jack Hall cross device for a voltage applied between C8 and C6. Note that the current density values are normalised to the same scale as for the C1 to C5 current density component in figure 6.25.

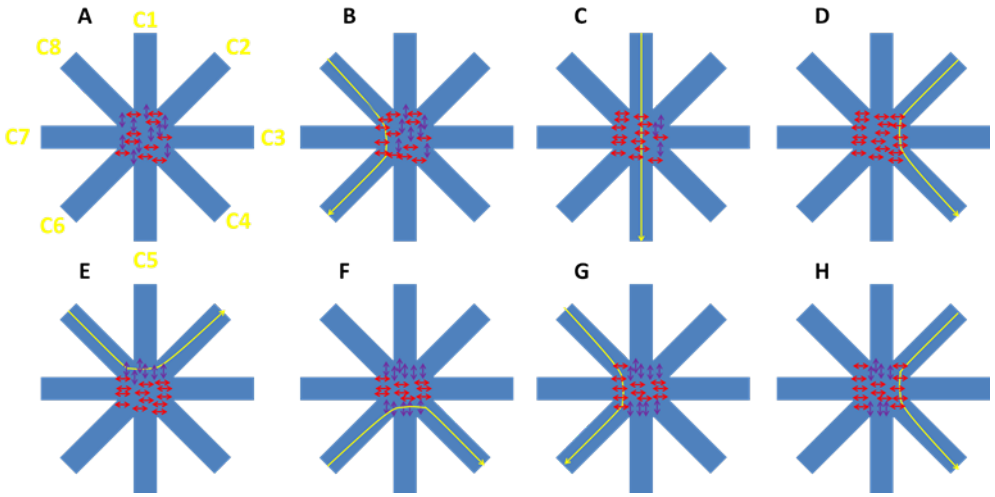

Figure 6.27: Cartoon of how applying current along specific paths of a Union Jack Hall cross device could lead to creation of multiple possible magnetic states in the central region of the device. An example sequence of setting current pulses (yellow arrows) is shown for steps **A**-**H**.

For a nominal setting pulse current density of 7.5MA/cm^2 applied to the 28μm device, the AMR-like signal from the variation in R_{xx} and R_{xy} is around 0.1%. As shown in figure 6.8, the current density in the central device region (the area which the probe measurements are sensitive to) will be less than 7.5MA/cm^2. No real quantitative comment can be made on these values of AMR and current density as the AMR/nominal current density could be further increased/decreased with longer current pulses, better device geometry etc. However, it is worth noting that this nominal current density is of the same order of magnitude as the switching current density for STT-MRAM[301][302] (though the pulses are much shorter in the STT-MRAM references). Given the general properties of CuMnAs outlined in section 6.2.1 (high quality growth on standard semiconductor substrates, above room temperature T_N, compatible conductivity for semiconductor electronics), the demonstration of high and low resistance states for setting pulses of the order of MA/cm^2 suggests that CuMnAs may have sufficient properties to be more than a test-bed material to explore NSOT, and that it can be considered as a candidate material for a real-world AF memory device. A significant amount of material development work, as well as greater understanding and characterisation of NSOT and AMR in CuMnAs would be needed to be achieved to reach such real-world applications, however the work in this investigation does provide a solid starting point that highlights the potential of CuMnAs as a useful AF spintronic material.

There is much scope for further work in this CuMnAs NSOT project, particularly if XMLD-PEEM measurements on the CuMnAs sample confirm that the setting current pulses do reorientate AF domains as would be expected of a NSOT mechanism. It would be ideal to be able to saturate all the AF domains in the central region of a Union Jack Hall cross device with a single setting pulse. This would allow the AMR and switching current density (for a given pulse length) of the CuMnAs sample to be well-defined. Having high and low resistance states that are consistently separated by the same percentage value over multiple switches

of the AF spin-axis is important for good stability and performance of a memory device. One factor that is likely to have prevented such domain saturation in this investigation is that the size and length of the setting pulses is limited by the instantaneous degradation of the CuMnAs layer next to the contact as discussed in section 6.3.1. It is therefore worth investigating different contact designs and recipes that will allow for larger current densities to pass from the contact to the CuMnAs layer without degradation. For example, finger contacts would give a larger area over which current could pass from the contact to the CuMnAs for a given CuMnAs channel width, and this may prevent bottle necking of current and localised heating next to the contact which could lead to degradation. Another method of saturating more domains in the central device region would simply be to make the C2, C4, C6, and C8 arms even narrower relative to the C1, C3, C5, and C7 arm width. This would allow an even greater percentage area of the central device to experience a critical switching current density (flowing in the desired direction). The magnetic structure of other CuMnAs layers (different thicknesses, substrates etc) should also be imaged with XMLD-PEEM to see if there is any layer with more suitable magnetic properties for NSOT switching. For example, a sample with equivalent [100] and [010] easy axes but in which domains form on the scale of several μm's or more would be ideal for coherent switching of the AF spin-axis in the central region of a device of μm dimensions.

If single domain switching of the AF spin-axis could be achieved, a full temperature investigation of the size of the AMR could be possible. It would be interesting to see whether the temperature dependence of the AF AMR of CuMnAs is similar to that of a non-crystalline FM AMR for a FM thin film with a similar T_c to the T_N of CuMnAs. Ideally the setting pulses could be applied at whatever temperature the AMR R_{xx} and R_{xy} probe measurements are made, but this would practically difficult to achieve. For example, the results in this investigation have shown that it is much harder to create the high/low resistance states when setting at 4.2K compared to setting at 300K. Furthermore, as R_{xx} increases with temperature, setting measurements at higher temperatures would require larger voltages to be applied across the device, which would give a larger chance of contacts blowing. The best approach would therefore be to always apply the setting pulses at 300K and then to decrease/increase the temperature and make various probe measurements. Care would need to be taken to achieve the same device temperature between different temperature cycles (i.e. after different setting pulses), and this could be done with the aid of a resistance thermometer, as was shown for the experiment documented in section A.3 in the appendix. The experiment could be repeated on other CuMnAs samples to see how the AMR varies as a function of strain (from different substrates), conductivities etc.

As a starting point to further investigate the $[1\bar{1}0]/[110]$ setting pulse data, it may be helpful to see if the variation in R_{xx} and R_{xy} when applying setting pulses along the $[1\bar{1}0]$ and [110] directions becomes any more clear and consistent when larger setting pulses and a more favourable device geometry (wide arms along $[1\bar{1}0]/[110]$, narrow along [100]/[010]) are used. For any probe geometry where R_{xx} or R_{xy} do vary with setting pulse direction, it would be worth applying multiple setting pulses along the same $[1\bar{1}0]$ or [110] direction to see if the increase/decrease

in R_{xx} or R_{xy} per setting pulse is lesser with increasing numbers of pulses applied, similar to the behaviour for [100]/[010] setting pulses shown in figure 6.19. If the NSOT mechanism in CuMnAs yields effective fields with both Rashba and Dresselhaus symmetry, setting pulses along the $[1\bar{1}0]$ and [110] directions would not give effective fields perpendicular to the current direction that are the same magnitude as one another, and this could further complicate interpreting any AMR measurements. Once again XMLD-PEEM is crucial for understanding what effect $[1\bar{1}0]$ and [110] setting pulses have on the magnetic ordering of CuMnAs.

The suppression of the variation in R_{xx} and R_{xy} when reversing the current direction of the [100]/[010] setting pulses shown in figure 6.21 is somewhat unexpected. The subsequent increase in the variation for the reverse current direction setting pulses along [100]/[010] after the application of pulses along $[1\bar{1}0]$/[110] only adds further confusion to the situation. Reversing the setting current direction should reverse the direction of the effective field that acts on each spin sublattice, and thus reverse the direction in which the spin sublattices reorientates (assuming the effective field is not parallel/antiparallel to the moments). From a top-down view this could be pictured as the AF coupled spin sublattices rotating clockwise in the plane for one setting current direction, and anticlockwise in the plane for the opposite setting current direction. If the setting current was able to switch the AF spin-axis from one easy direction to the other (say [100] to [010]), the magnetic arrangement of the CuMnAs lattice would look different depending on the setting current polarity (and thus whether the moments rotated clockwise or anticlockwise), as shown in figure 6.28.

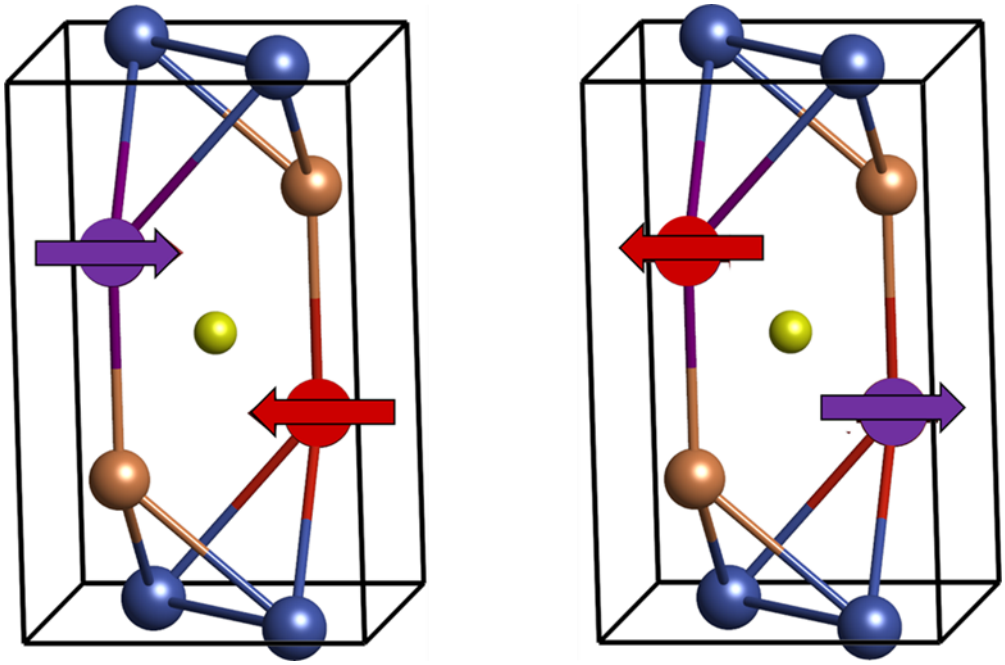

Figure 6.28: Two possible magnetic arrangements of the CuMnAs lattice. Yellow circle is an indicator of the centre of inversion rather than an atomic position. Blue circles are Cu atoms, orange circles are As atoms, purple circles are Mn atoms for one spin sublattice, red circles are Mn atoms for the other spin sublattice.

One would expect the two magnetic arrangements of the CuMnAs lattice to give the same AMR change in R_{xx} and R_{xy} as AMR has a 180° symmetry and is experimentally measured over many unit cells. This appears to be the case when comparing the initial figure 6.21 measurements for forward [100]/[010] setting current pulses to the final figure 6.21 measurements for reverse [100]/[010] setting current pulses, after the pulses along $[1\bar{1}0]$/[110]. It seems more likely therefore that the discrepancy between the initial figure 6.21 measurements for forward and reverse [100]/[010] setting current pulses is related to the number of domains reorientating with each of the orthogonal reverse [100]/[010] setting current pulses being less than for the forward [100]/[010] setting current pulses. It is not clear why this would be the case, or why applying pulses along $[1\bar{1}0]$/[110] in between the forward and reverse [100]/[010] would make a difference. This forward/reverse current effect should therefore be investigated further. Firstly, the same measurement procedure should be performed on various Mn752 devices to confirm that it is not exclusive to the 8μm device used in this investigation, i.e. it is not just caused by some defect in this device. Secondly, the measurements should be repeated for the reverse setting pulses applied first, immediately followed by the forward setting pulses. If the suppression of the variation of R_{xx} and R_{xy} is apparent for the forward setting pulses in this scenario, it would show that this unidirectional-like effect is related to the initial current direction (and thus magnetic orientation) rather than the crystalline axes. Thirdly, it should be observed what happens when the current is reversed for only one of the setting pulse directions, e.g. forward pulses are applied along [100]/[010], and then forward pulses along [100] but reverse pulses along [010]. Finally, it should be seen whether the suppressed variation in R_{xx} and R_{xy} for a given polarity can be recovered by applying setting pulses with a larger magnitude (and then going back to the magnitude of setting pulse current density that previously gave the suppressed R_{xx} and R_{xy} variation). This may indicate some sort of frustration of the domains that can be overcome with bigger setting pulses (like as it seems to be overcome with setting pulses along $[1\bar{1}0]$/[110]). These simple experiments may provide some further insight into the seeming inequivalence between the two possible magnetic lattice arrangements in terms of reorientation of their AF spin-axis.

If XMLD-PEEM or other spectroscopic measurement techniques confirm that the setting current pulses are reorientating the AF spin-axes of domains in the CuMnAs sample, NSOT should be investigated in other AF materials which have the correct spin sublattice inversion asymmetry. The only other candidate material which has so far been identified is Mn_2Au[195]. The growth of high quality single crystalline thin film Mn_2Au is a challenge[303], however there is significant motivation as, owing to the large Au atom, Mn_2Au may be expected to have larger SOC than CuMnAs. Indeed, calculations have shown that the electrochemical potential anisotropy, which is a SOC effect, is relatively large in Mn_2Au[236]. Depending on the strength and form of its magnetic anisotropy, Mn_2Au may be able to switch its AF spin-axis orientation via the NSOT mechanism at lower current densities than for CuMnAs. Similarly the size of the AMR may be larger in Mn_2Au which would also be beneficial for an AF memory device. Other AF materials with the correct spin sublattice inversion asymmetry should also be searched for, particularly materials with a cubic magnetic anisotropy where the average domain size is of the

order of or larger than several μm's to allow for coherent AF spin-axis switching.

Chapter 7

Conclusions

The motivation of this thesis was to study spin-orbit coupling (SOC) phenomena that can set or detect magnetic orientation via the application of electrical current. These phenomena were investigated in semiconducting materials whose conductivity is with commercial electronic devices.

Chapter 1 presented a short history of electronics and computing technology, and pointed out why spintronics can have a role in its continuing development. An outline was given of some of the major and relevant aspects and findings in spintronics which have occurred since the late 1980's Nobel prize winning work of Fert and Grunberg. There has been much progress in the field of spintronics in the past 25 years, but it is now time to increase its real world application beyond that of just magnetic read head technologies in hard disk drives. Chapter 1 also gave a more in-depth overview of the structural, electronic, and magnetic properties of the diluted magnetic semiconductor (DMS) (Ga,Mn)As, which is in many ways a model spintronic system. The underlying physics behind (Ga,Mn)As is especially relevant for the work in chapters 2, 3, and 4. Finally, chapter 1 set out the microfabrication, electrical transport, and SQUID magnetometry techniques used for the work in this thesis.

The DMSs (Ga,Mn)Sb and (Ga,Mn)($As_{0.9}$,$Sb_{0.1}$) were characterised in chapter 2. The motivation for growing Sb-based DMSs was that the heavy Sb atom should allow for these materials to host larger SOC effects than (Ga,Mn)As. The Curie temperature (T_c) of the (Ga,Mn)Sb sample was found to be 34K, which is higher than any other (Ga,Mn)Sb sample previously recorded in literature. The magnetic properties of the (Ga,Mn)Sb sample did not change upon annealing which indicated a lack of interstitial Mn in the material. Transport measurements could not be made on the (Ga,Mn)Sb sample to due dominant parallel conduction through the InAs substrate. Both the magnetic and transport properties of the (Ga,Mn)($As_{0.9}$,$Sb_{0.1}$) sample changed with annealing: Its T_c increased from 28K to 55K, while its conductivity against temperature profile went from insulating to metallic. The T_c of the annealed (Ga,Mn)($As_{0.9}$,$Sb_{0.1}$) sample lies between the respective values for similarly doped annealed (Ga,Mn)Sb and (Ga,Mn)As samples.

The anisotropic magnetoresistance (AMR) of (Ga,Mn)($As_{0.9}$,$Sb_{0.1}$) was investigated in chapter 3. Through field rotation measurements and analytical fittings for current

flow along the four major in-plane crystalline axes, the AMR of (Ga,Mn)($As_{0.9}$,$Sb_{0.1}$) was decomposed into four different contributions with unique symmetries. Unlike in many ferromagnets where the non-crystalline contribution dominates the AMR, crystalline contributions were found to be significant in both as-grown and annealed (Ga,Mn)($As_{0.9}$,$Sb_{0.1}$), and this accounted for the anomalous temperature dependence of the AMR for current along the [110] direction of the annealed sample. It was postulated that the uni-axial crystalline AMR contribution is related to carrier localisation in DMSs. (Ga,Mn)($As_{0.9}$,$Sb_{0.1}$) was shown to be a DMS with more balanced non-crystalline and crystalline AMR contributions than (Ga,Mn)As, and in some cases also a stronger AMR than (Ga,Mn)As, and so Sb-based DMSs are a useful testbed material to further study the origins of contributions to AMR. While AMR signals are typically much smaller than tunnel and giant magnetoresistance signals, the fact that AMR requires ohmic current flow through a single layer is a possible advantage for its use as a read mechanism in magnetic memory devices.

The combination of experimental AMR measurements (in this case field sweep measurements of the transverse AMR) and analytical fitting were once again used in chapter 4 to measure effective magnetic fields associated with the SOT mechanism in (Ga,Mn)As. There has been much recent interest in SOT as a potential writing mechanism for MRAM as it offers scalability and does not require a polarising layer. The study in chapter 4 revealed that in (Ga,Mn)As the size of SOT effective magnetic fields arising from Dresselhaus SOC increase with increasing temperature, whereas those arising from Rashba SOC show no significant temperature dependence within experimental uncertainty. The magnitude of the effective field per unit of current density for the Dresselhaus and Rashba fields was found to be comparable with previous investigations using different experimental techniques.

Chapter 5 suggested the concept of magnetic gating of a 2DEG. Unlike the other samples studied in this thesis, for this investigation the semiconductor material of the device through which current was conducted in the experiment was non-magnetic, with the magnetic functionality provided by the device's gate material whose electrochemical potential varies with its magnetization orientation, a SOC effect. Such a device could be viewed as a way to electrically read the magnetic state of the gate layer, however the motivation behind it here is to offer a transistor-like structure that can suppress or amplify electrical current through magnetic rather than electrical means. A GaAs/AlGaAs 2DEG heterostructure was designed with the aid of 1D Poisson models of band structure and carrier density. While the initially grown 2DEG heterostructure without a Fe gate layer displayed promising characteristics for the magnetic gating experiment, subsequent growth runs of the same heterostructure design with and without a Fe gate layer yielded materials with significant AMR-like effects that hampered the intended investigation. The source of the AMR in the ungated and gated heterostructure was not able to be determined. The concept of magnetically gating a semiconducting channel is fundamentally interesting, and it is worth revisiting this experiment if the issue of the unaccountable AMR in the 2DEG heterostructure can be resolved.

Evidence for Néel order SOT (NSOT) in the antiferromagnet CuMnAs was presented in chapter 6. There are several advantages of using an antiferromagnet over

a ferromagnet as the active component in a magnetic memory device, however to realise these an efficient and practical method of setting the antiferromagnetic (AF) spin-axis direction needs to be found. NSOT is predicted to be the leading contender, but occurs only in AF materials whose spin sublattices form inversion partners with one another, as is the case for CuMnAs. The experimental measurement principle used in the chapter 6 investigation was that the AF spin-axis of CuMnAs could be switched by applying large setting current that generates NSOT effective magnetic fields, and its orientation detected via probe AMR measurements. The unique symmetry predicted of such setting and probe measurements was demonstrated experimentally. The results also suggested that the magnetic structure of the CuMnAs sample studied consisted of sub-μm AF domains, and that the number of domains which switched depended on the setting current density magnitude and current path. Spectroscopic measurements may be required to unequivocally confirm the suggested NSOT mechanism, but the transport results presented in chapter 6 lend strong support to what would be the first demonstration of electrically writing an antiferromagnet.

There is much more to the field of spintronics than just electrical reading and writing of the magnetic state which is the main focus of this thesis. However, in the next 5 to 10 years this topic may prove to be the most exciting in terms of providing applications that will have a major real world impact. There is now significant industrial and public funding to study and develop MRAM for the next generation of computer memory devices. Despite having several advantages, MRAM is still some way off replacing DRAM and SRAM, in part due to a lack of commitment to mass-scale fabrication. The commercial availability of STT-MRAM is, however, a promising start. Harnessing previously ignored relativistic writing (and possibly even reading) mechanisms may help to accelerate the advancement of MRAM technologies. Hopefully some of the topics studied in this thesis may be further developed to one day increase MRAM performance.

Appendix A

Side Projects

This section briefly introduces and discusses several additional projects that I worked on during my PhD. While I did play an active role in all of these projects, I was not the principal investigator in them.

A.1 XMCD study of (Ga,Mn)Sb

(Ga,Mn)Sb is a Mn-doped III-V diluted magnetic semiconductor (DMS) which is discussed in detail in chapter 2. Similar to (Ga,Mn)As, Mn atoms in (Ga,Mn)Sb provide a finite magnetic moment due to uncompensated spins in their half-filled $3d$ shell. Also similar to (Ga,Mn)As, the Fermi level in (Ga,Mn)Sb lies within the top of the valence band, which is composed mainly of anion p states, and it is the delocalised carrier holes that mediate the net magnetic ordering between the localised Mn moments. Owing to the larger atomic number of Sb compared to As, the spin-orbit splitting of the valence band states is larger in (Ga,Mn)Sb than (Ga,Mn)As. Therefore, (Ga,Mn)Sb is an interesting test-bed material for exploring spintronic phenomena that are associated with spin-orbit coupling.

X-ray magnetic circular dichroism (XMCD) is a spectroscopic technique that can yield elemental specific information on a material's electronic structure, chemical environment, and magnetic properties. The technique can be briefly summarised as follows: A film of the magnetic material under investigation is exposed to a flux of circularly polarised x-rays of varying energy. Core electrons can absorb an x-ray to get excited to a higher energy level if 1. The energy of the x-ray corresponds to the energy of the transition, and 2. The transition obeys the dipole selection rules. By reversing the polarity of the x-rays and/or sample magnetization and applying sum rules[304][305] to the resulting XMCD spectra, the spin and orbital magnetic moments of individual elements within the material can be obtained. Previous XMCD investigations of (Ga,Mn)As have provided insight into the nature of its magnetic and electronic structure[306][307][308]. The aim of the experiment detailed here was to gain similar insight into (Ga,Mn)Sb, in particular with respect to the states which are responsible for its ferromagnetism.

Measurements were made on the 25nm thick, 6% Mn-doped (Ga,Mn)Sb Mn691 sample (see chapter 2 for further sample details) as well as a similarly doped (Ga,Mn)As reference sample, and were performed at the I10 end-station of Di-

amond Light Source. The investigation was led by Dr. Kevin Edmonds, with support from Prof. Gerrit van der Laan, Dr. Peter Wadley, and myself. XMCD was performed at the Mn $L_{2,3}$ edges ($2p$ to $3d$ transitions) and Sb $M_{4,5}$ edges ($3d$ to $5p$ transitions) at a temperature of 6K (below T_c of the sample) and in a saturating in-plane magnetic field. Both total electron yield (TEY) and fluorescent yield (FY) signals were used for detection.

As shown in figure A.1, the TEY x-ray absorption at the Mn L_3 edge (639eV) is smaller for (Ga,Mn)Sb than it is for the (Ga,Mn)As reference sample. The (Ga,Mn)Sb TEY Mn L_3 edge absorption also shows a multiplet structure in the post-edge region. In contrast, the FY XMCD is similar for (Ga,Mn)Sb and (Ga,Mn)As, and the multiplet structure is not evident. As FY is a less surface sensitive detection technique than TEY, this suggests the presence of an oxide layer on the surface of (Ga,Mn)Sb. The (Ga,Mn)Sb sample was dipped in HCl to remove such a layer immediately before being loaded into the measurement apparatus, but unlike (Ga,Mn)As, the HCl etch was presumably either ineffective or the oxide layer quickly reformed. Despite the existence of the oxide layer, the Mn L_3 edge XMCD is still significant enough for both TEY and FY detection to reveal the absence of a peak at 640eV in the (Ga,Mn)Sb spectra which is present in the (Ga,Mn)As spectra, as shown in figure A.2. Furthermore, the general features of the (Ga,Mn)Sb spectra are broader than the (Ga,Mn)As spectra, which suggests a more metallic environment for the Mn atoms in (Ga,Mn)Sb.

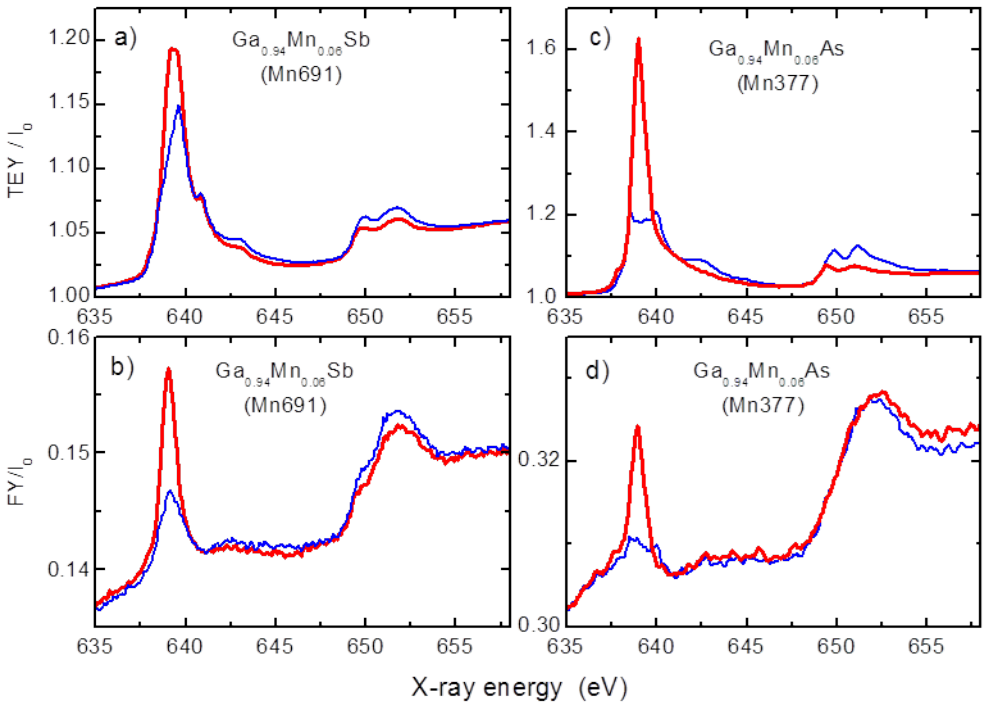

Figure A.1: Mn $L_{2,3}$ x-ray absorption spectra. X-ray helicity and magnetization orientation are parallel for blue lines, antiparallel for red lines. **(a)** TEY detection and **(b)** FY detection of (Ga,Mn)Sb. For comparison, **(c)** TEY and **(d)** FY detection of the reference (Ga,Mn)As sample are also shown.

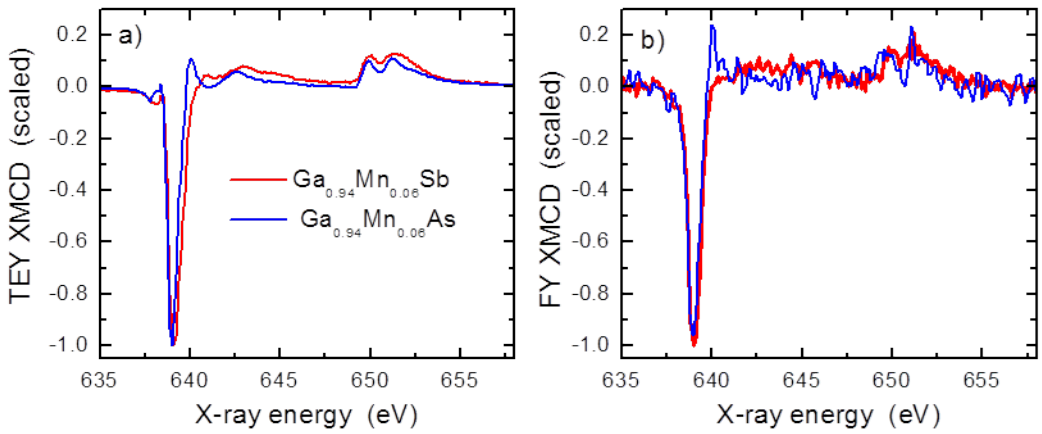

Figure A.2: Mn $L_{2,3}$ XMCD spectra for (Ga,Mn)Sb (red) and (Ga,Mn)As (blue) as measured with **(a)** TEY and **(b)** FY detection, normalised to the 639eV peak.

The surface oxidation of the (Ga,Mn)Sb sample proved more detrimental to measurements at the Sb $M_{4,5}$ edges. As shown in figure A.3, the TEY x-ray absorption at the Sb $M_{4,5}$ edges is dominated by the rising background signal caused by the oxygen K-edge which peaks at 540eV. Any features in the XMCD spectra from the Sb $M_{4,5}$ edges were insufficiently large to be seen over the measurement noise, possibly as a result of the presence of the surface oxide layer and the sensitivity of TEY detection to the surface. While FY detection is less surface sensitive than TEY, it generally has a worse signal to noise ratio, and any XMCD features from the Sb $M_{4,5}$ edges could also not be resolved with FY detection.

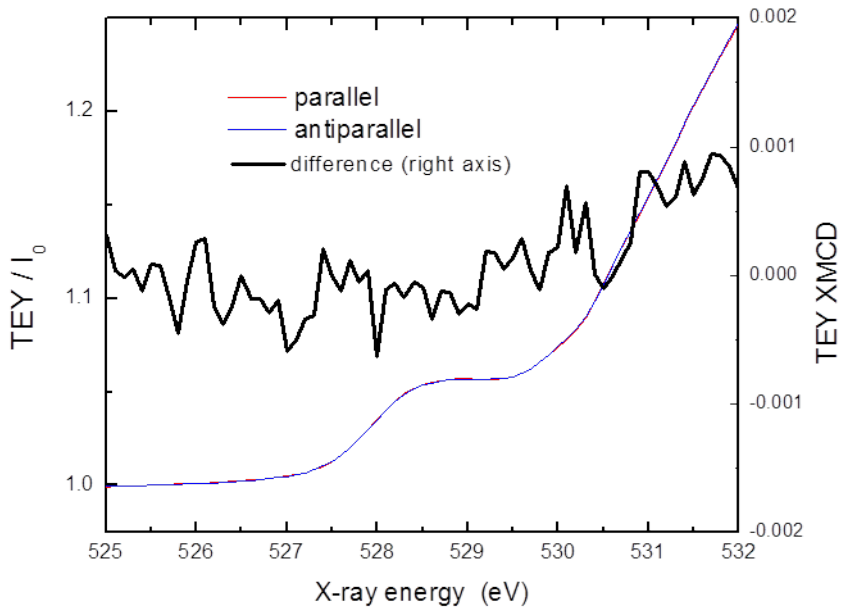

Figure A.3: X-ray absorption of (Ga,Mn)Sb sample at Sb $M_{4,5}$ edges for x-ray helicity and magnetization parallel (blue) and antiparallel (red), as well as the resulting XMCD (black), all for TEY detection.

While some qualitative information was gained from the measurements at Mn $L_{2,3}$ edges, the investigation as a whole was significantly hindered by the oxide layer on the (Ga,Mn)Sb surface. This issue would need to be overcome (for example by capping the (Ga,Mn)Sb or *in-situ* cleaning) if more revealing XMCD measurements of (Ga,Mn)Sb are to be made at a future date.

A.2 Investigation of high T_c of (In,Mn)Sb

The most significant factor that has limited (Ga,Mn)As from finding practical application in electronic devices is the fact that its T_c is below room temperature. There has therefore been considerable interest in finding a DMS with similar electronic and magnetic properties to (Ga,Mn)As, but which remains ferromagnetic well above room temperature. Two papers published in 2010[309][310] reported on a (In,Mn)Sb sample which was claimed to show a single phase, carrier mediated ferromagnetism with a T_c higher than room temperature. The aim of the side-project investigation reported on here was to determine whether the high T_c of the (In,Mn)Sb from references [309] and [310] was associated with a single magnetic phase within the bulk of the sample. The investigation was carrier out in collaboration with Dr. Juanita Bocquel and Dr. Paul Koenraad from Eindhoven University, with the sample provided by Dr. Bruce Wessels from Northwestern University. My role was to perform some of the SQUID magnetometry measurements as well as wet etching on the sample.

The sample investigated was a 500nm thick, 1.5% Mn-doped as-grown (In,Mn)Sb

layer grown on a GaAs (100) substrate by metal-organic vapour phase epitaxy (MOVPE). The sample was not one of the samples reported on in references [309] and [310], but it was grown by the same grower under the same conditions and so is assumed to have similar characteristics to those referenced samples. A SQUID field sweep measurement was made on the sample along the $[1\bar{1}0]$ axis at 2K, and the measured saturation magnetization corresponds to a magnetic moment of around $0.5\mu_B$ per Mn atom. This value is far below the ideal case for Mn substituting at In lattice positions ($\approx 4.5\mu_B$ per Mn atom), and is also smaller than the moments per Mn obtained in the reference [309] and [310] samples ($1.6\mu_B$ and $4.6\mu_B$ per Mn atom for 2% and 3.5% Mn-doping concentrations respectively). A SQUID remnant measurement was made also along the $[1\bar{1}0]$ axis after a field cool in a 10kOe field. It was observed that the sample's remnant magnetization does not fall to zero within the temperature range of the SQUID measurement system, and so in order to obtain a rough estimate of T_c, the measured data was fitted with equation A.1 (see reference [311]). The results are plotted in figure A.4.

$$\frac{M(T)}{M(0)} = \left[1 - s\left(\frac{T}{T_c}\right)^{1.5} - (1-s)\left(\frac{T}{T_c}\right)^{p}\right]^{\frac{1}{3}} \tag{A.1}$$

Where M is magnetization, T is temperature, s is a free variable which is greater than 0, and p is a free variable that is greater than 1.5.

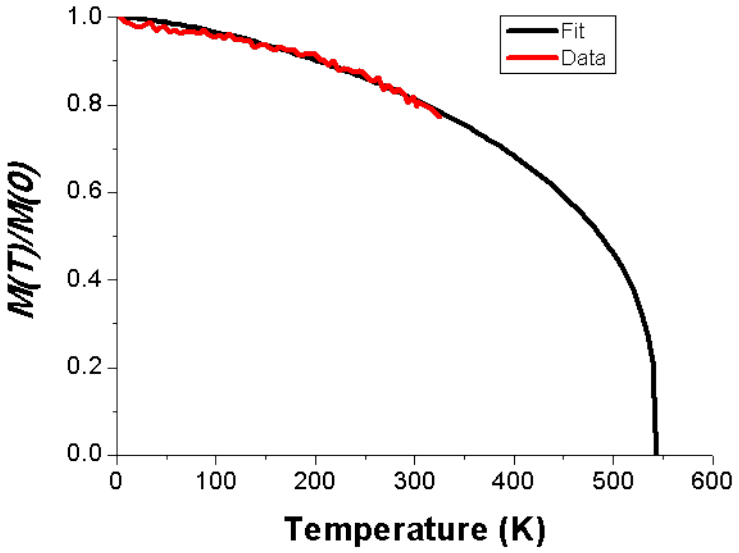

Figure A.4: Relative remnant magnetization of (In,Mn)Sb sample. Experimental data (red line) and extrapolated fit to data using equation A.1 (black line).

From the equation A.1 fit, the inferred value of T_c is 540K. However, the quality of the fit is not ideal, and so this inferred T_c should not be taken as an exact value, but rather as a fair indication that the actual T_c of the sample is expected to lie well above 330K (i.e. the highest temperature measurement made on the sample).

Judging by eye, there is no clear evidence of a secondary phase in the experimental SQUID remnant data. This is in agreement with (In,Mn)Sb samples of references

[309] and [310]. That being said, previous studies of MBE grown (In,Mn)Sb samples show T_c values of only around 7-8K[312][313]. It is possible that the large step size of the SQUID remnant measurement performed here (≈8.5K per step) combined with the poor signal to noise on the measurement could allow a magnetic phase similar to that observed in references [312] and [313] to go undetected. Even if a more accurate measurement were to confirm the SQUID remnant data for this sample to be a single magnetic phase, the vast difference in its T_c value to that of the reference [309] and [310] MBE samples raises questions about the origin of the magnetic ordering within the sample. One possibility is that MnSb forms on the surface of the material and is the source of the dominating magnetic phase detected in the SQUID measurements (thin MnSb films can have T_c values of well over 500K[314]). A Mn-rich surface layer could also lead to the same result. In order to confirm or rule these possibilities out, an etching study was attempted on the (In,Mn)Sb sample.

The methodology for the etching study was as follows. Firstly, half of a (In,Mn)Sb chip is covered in resist and etched in a given solution. Secondly, the resist is removed and the etch depth is checked by atomic force microscopy (AFM) measurements. If the etch is successful, the (In,Mn)Sb chip used for the SQUID measurements is etched in the same solution. Finally, a remnant SQUID measurement is made on the etched SQUID chip.

The first etch used was an HCl dip followed by 10s in buffered oxide etch (BOE). This etch was intended to remove any Mn-rich layers from the surface without etching the (In,Mn)Sb. The AFM detected no step height from the etch, confirming that it does not touch the bulk of the sample. The SQUID remnant measurement of the etched (In,Mn)Sb chip showed no difference to that of the pre-etched chip. This suggests two possibilities: 1. The magnetic signal does not originate from the surface, or 2. The etch is not effective at removing any Mn surface layer. From this measurement alone neither possibility can be confirmed or ruled out.

In order to determine the role of the surface, a second etch was performed that was intended to remove the top 50nm of the 500nm thick (In,Mn)Sb sample, and therefore remove the surface for sure. If the magnetic signal disappeared completely following the etch then the surface would be shown to be its source. However, if the magnetic signal remained (well above room temperature), but reduced in magnitude by around 10% from that of the un-etched sample then it would be attributable to the bulk of the sample (note this would not rule out magnetic clusters within the bulk). Following an HCl dip, the sample was etched in a 10:1 lactic acid (85%) : nitric acid (70%) solution, a known etchant for InSb[315], for 12s. Somewhat surprisingly the AFM showed that the etch had not worked on the (In,Mn)Sb sample as no step height was detected. The (In,Mn)Sb was instead etched in another known InSb etchant, citric acid (50%) : hydrogen peroxide (30%) at a 10:1 ratio for 5 minutes[315]. Again, the AFM showed that this etch did not work at all on the (In,Mn)Sb sample.

A final etch was attempted, this time using an etch recipe provided by the grower of the sample: deionized water : hydrogen peroxide (3%) : lactic acid (85%) :

hydrogen fluoride (3%) at the ratio 100:6:1:3, with an etch rate of 200nm/minute. This recipe was claimed to have been used effectively on similar (In,Mn)Sb samples. The (In,Mn)Sb sample of this investigation was initially etched for 20s (which should have removed around 66nm), however the resulting AFM measurement indicated that, yet again, the etch had not touched the sample. The sample was then etched for a further 2 minutes. This time the etch had some effect on the sample, but not that which was intended. As shown in figure A.5, instead of etching the surface uniformly, the etch left craters of around 200nm depth. Furthermore, these craters occurred not only on the uncovered half of the surface, but also on the half that was covered in resist. There was also no measurable step height between the covered and uncovered areas of the chip.

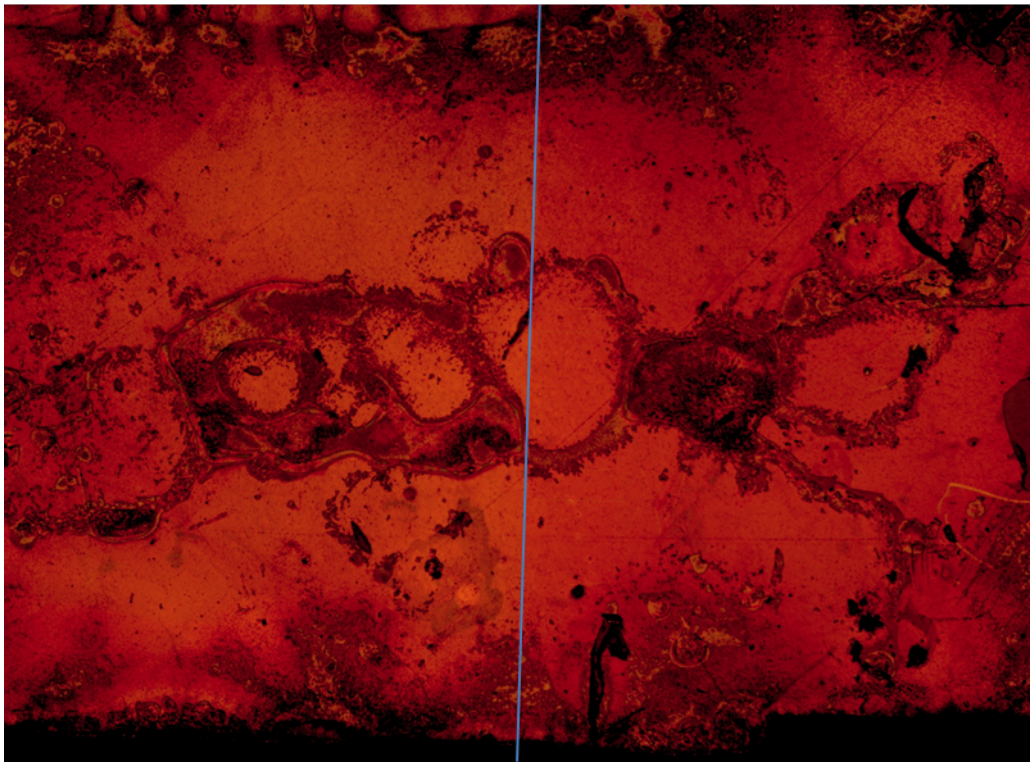

Figure A.5: Optical image of the surface of the (In,Mn)Sb chip after etching with final etchant solution and with the resist removed. The area to the right of the blue line had been covered with resist, the area to the left had been left exposed. The etch left craters of around 200nm depth on the previously smooth surface.

With the attempted etches proving to be either ineffective or uncontrollable, the investigation was stopped. Therefore, no conclusion can be drawn as to the source of the high T_c magnetic phase of the sample. The fact that three different types of etching solutions that have been reported to be effective on similar samples were unsuccessful at etching the sample raises some concerns about the quality of the sample. In order to complete the etching study, a more effective etching method (potentially ion milling) would be needed to be utilised, or another sample would need to be obtained.

A.3 AMR in FeRh

As discussed in chapter 6, one of the major benefits of using antiferromagnetic materials as the active component in a magnetic memory device is their insensitivity to stray fields. This property can also be a hindrance as it means that the magnetic (spin-axis) orientation of an antiferromagnet cannot be set by applying a magnetic field, as is the case for toggle MRAM. Therefore, there is increasing interest in finding other paths to manipulating the spin axis of an antiferromagnet, including Neel order spin-orbit torque[195] and the use of an exchange coupled ferromagnet[279].

FeRh is a well studied metal with unique magnetic properties[316][317][318][319]. At low temperatures FeRh is antiferromagnetic, but at a certain temperature named the transition temperature (T_t) it undergoes a structural phase transition which results in a magnetic phase transition, with its magnetic ordering becoming ferromagnetic until its temperature is further increased to T_c. It has recently been shown that this magnetic phase transition can be exploited to set the antiferromagnetic spin axis orientation via cooling through T_t in the presence of an external magnetic field[282]. It was also simultaneously shown in reference [282] that reorientating the spin-axis of FeRh is accompanied by a change in its resistance, i.e. an antiferromagnetic AMR (AF-AMR). These dual effects could make FeRh a possible material for use in a memory device, using techniques similar to current heat assisted magnetic recording technologies[320].

The goal of this side project was to cool FeRh through T_t while an external field is applied at various angles in a 360° range in the sample plane, and see how this was reflected in the subsequent AF-AMR. If the spin-axis were able to be set along any in-plane direction then one may expect the AF-AMR to have a $cos(2\phi)$ dependence (where ϕ is the angle between the spin-axis and the current direction), similar to many metallic ferromagnets. If the spin-axis were only able to set along certain preferential orientations then the experiment could still provide insight into the magnetic anisotropy of FeRh. The work for this project was done in partnership with Dr. Ryan Beardsley.

Two different FeRh-based samples were provided by Sophie Morley and Prof. Chris Marrows from Leeds University. Both samples were grown by dc sputtering on MgO substrates. The first sample was 25nm Fe(Rh,Cu), and the second sample was a 20nm Fe(Rh,Cu)/5nm Au bilayer. In both cases the Cu doping was around 2% of the Rh concentration, and served the purpose of lowering T_t[321] to within the limits of the Nottingham small cryostat system's temperature range. The purpose of the 5nm Au capping layer in the bilayer sample was to suppress the formation of ferromagnetic phases below T_t[322]. The samples were processed into L-shaped Hall bars to allow simultaneous measurements of R_{xx} and R_{xy} for current along orthogonal directions. For the field cool measurements, the sample was heated to 400K (above T_t for both samples) and cooled in the presence of a 4.4kOe external field applied along a given in-plane angle. The sample was cooled to a certain temperature below T_t (which was very carefully controlled), the field removed, and the resistance recorded. Additional field sweep and field rotation measurements

were also made at various temperatures. SQUID remnant measurements were also made after applying a 10kOe field along the measurement direction at 365K/390K.

Some of the results for the 25nm Fe(Rh,Cu) sample are shown in figures A.6 - A.9.

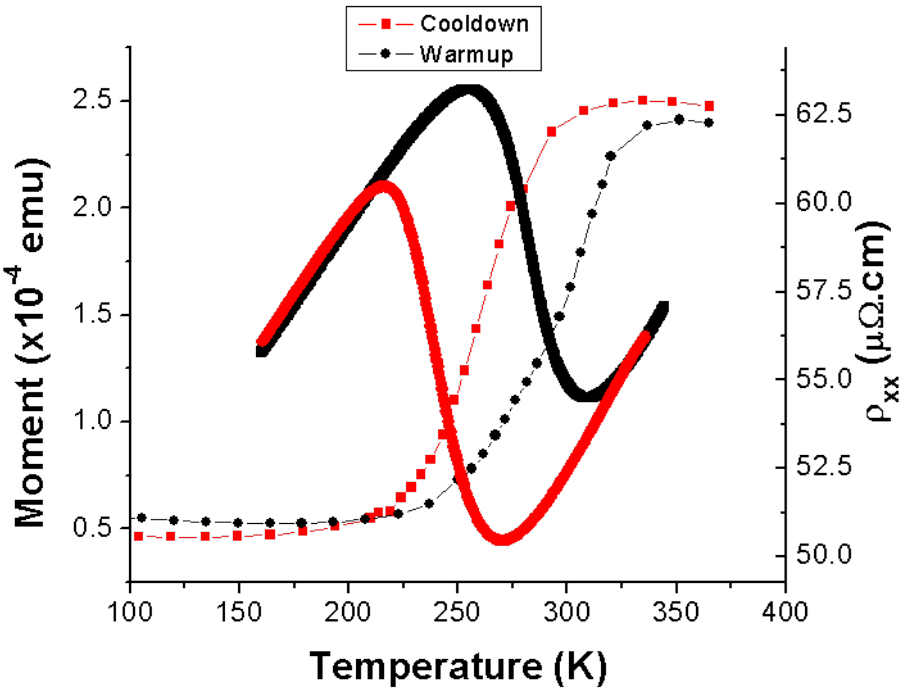

Figure A.6: Remnant magnetization along the $[1\bar{1}0]$ crystalline axis after applying and removing a field of 10kOe at 365K (data points separated by line) and longitudinal resistivity also along the $[1\bar{1}0]$ crystalline axis (thick solid lines) of 25nm Fe(Rh,Cu) sample as a function of temperature (note longitudinal resistivity measurements are only made in the 160K-350K range). For recorded measurements, sample is initially cooled down (red) before being warmed up (black). Note that a SQUID field sweep measurement was performed at 4K in between the remnant cool-down and warm-up measurements, and this is the source of the discrepancy between the cool-down and warm-up moments at low temperatures.

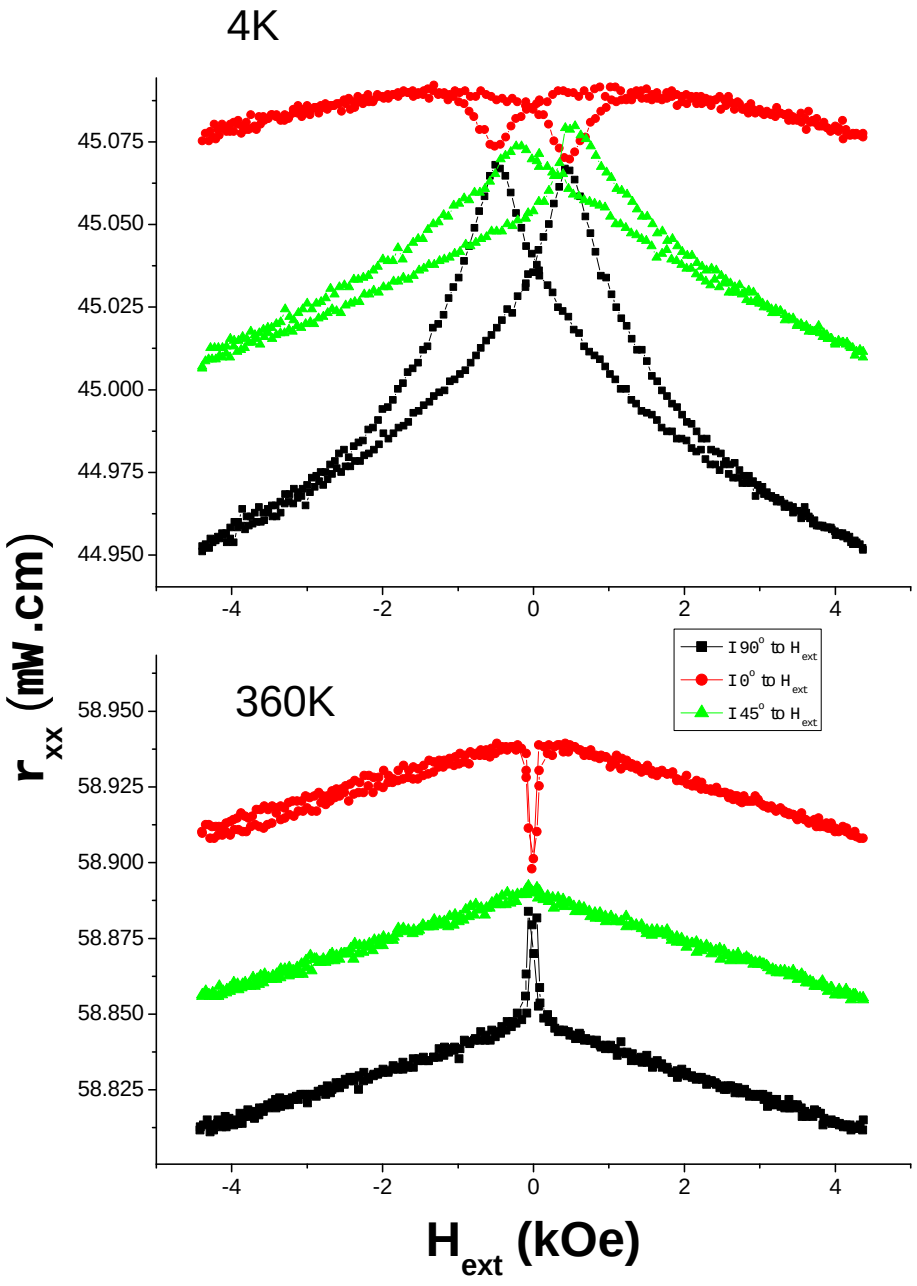

Figure A.7: Longitudinal resistivity along the $[1\bar{1}0]$ crystalline axis of 25nm Fe(Rh,Cu) for forward and reverse field sweeps along various directions at 4K (upper plot) and 360K upon warming the sample up (lower plot).

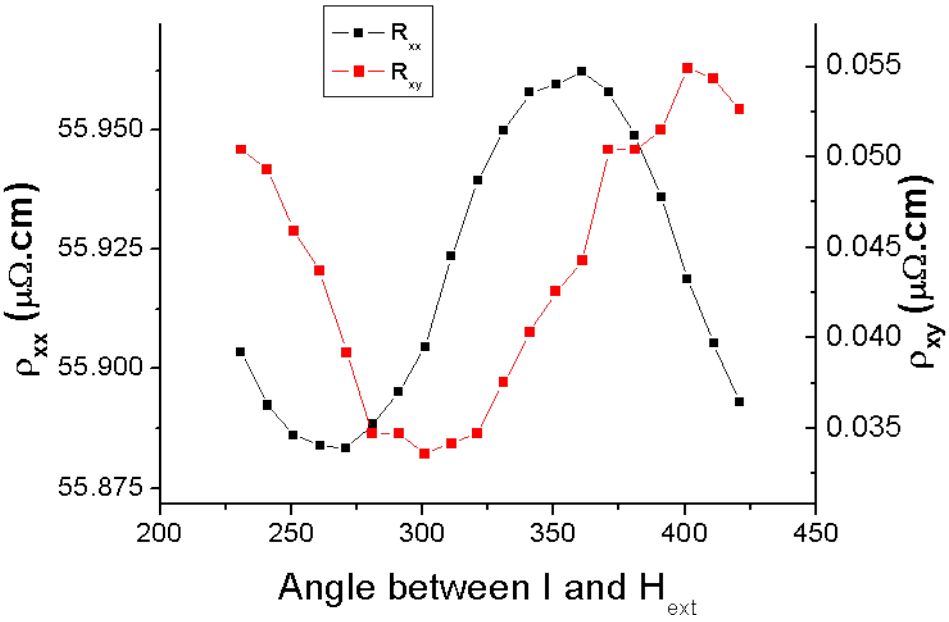

Figure A.8: Longitudinal (black data points) and transverse (red data points) resistivity along the $[1\bar{1}0]$ crystalline axis of 25nm Fe(Rh,Cu) as a function of angle between current and an external 4.4kOe external field at 160K upon cooling the sample.

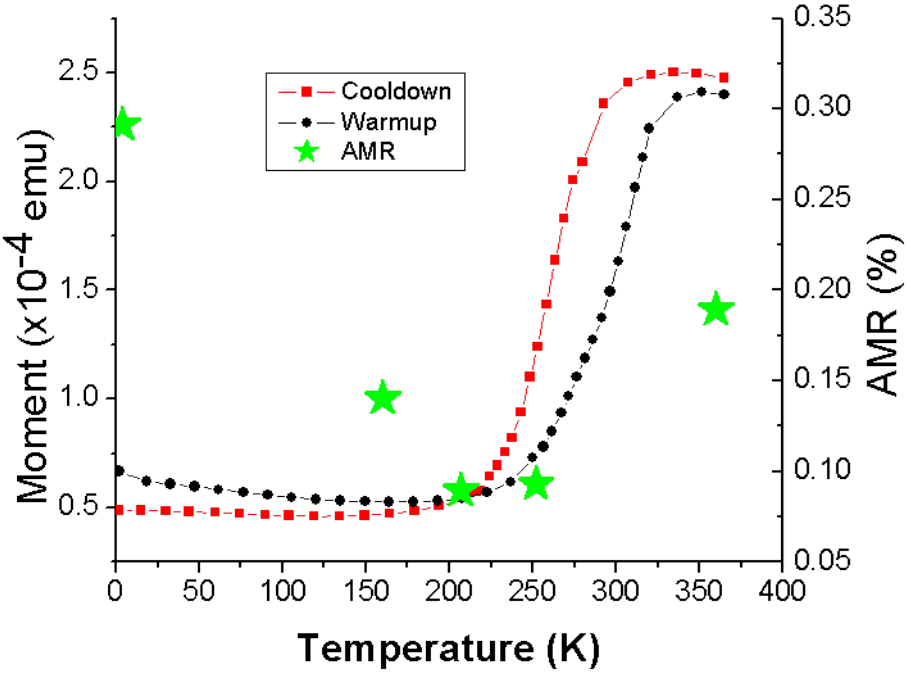

Figure A.9: Same remnant SQUID data as shown in figure A.6 (red and black data points) and magnitude of measured the FM-AMR$_{xx}$ from field rotation measurements (green data points) of 25nm Fe(Rh,Cu) upon warming up as a function of temperature.

Figures A.6 - A.9 all show evidence of the 25nm Fe(Rh,Cu) sample having some degree of ferromagnetic ordering below T_t. The remnant SQUID data in A.6 shows that the measured moment falls to around 20% of its maximum value as the sample is cooled down below T_t. This is somewhat surprising as in an ideal case the moment should drop to zero here as the sample becomes completely antiferromagnetic. Figure A.7 shows that a ferromagnetic AMR (FM-AMR) persists in the sample below T_t, and that the sample also has magnetic anisotropy at this temperature. Interestingly the ferromagnetic anisotropy seems to change somewhat above T_t, as the [100] axis appears to become an easier axis, while also the anisotropy field of all axes decreases. Figure A.8 again shows that a FM-AMR exists below T_t, with a $+cos(2\phi)$ symmetry similar to many ferromagnetic metals. Finally, figure A.9 shows that the magnitude of the FM-AMR does not scale linearly with the strength of the moment, and is in fact stronger at 4K (below T_t) than at 360K (above T_t) despite the ferromagnetic moment being considerably smaller.

The presence of ferromagnetism and a FM-AMR (that is of a similar size to the AF-AMR of FeRh reported in reference [282]) below T_t make the intended field cooling AF-AMR difficult with this sample. It is unclear if the FeRh antiferromagnetic spin axis has any preferential orientation, and so separating any possible AF-AMR from FM-AMR contributions is a complex task. Ferromagnetic ordering in the sample below T_t has previously been observed in other FeRh-based samples[322], and it was decided to focus instead on the 20nmFe(Rh,Cu)/5nm Au bilayer sample. Results for this sample are shown in figures A.10 and A.11. The transport data in these figures was collected by Dr. Ryan Beardsley.

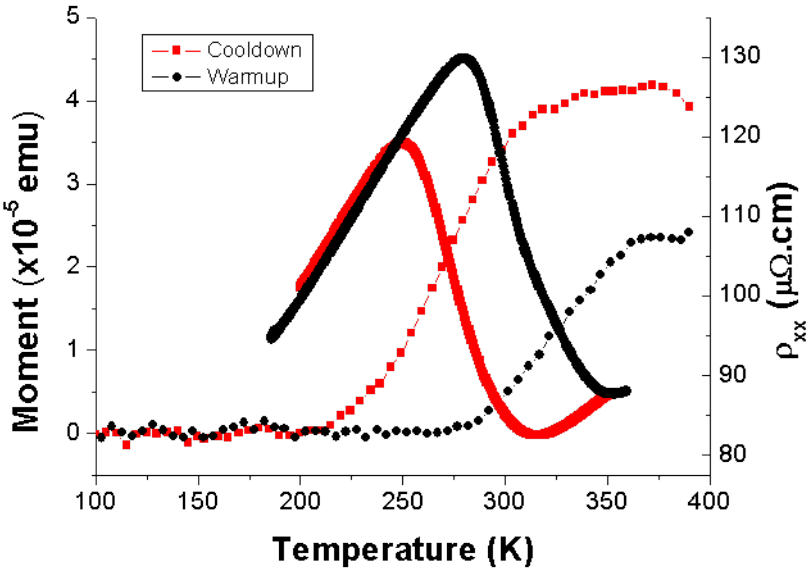

Figure A.10: Remnant magnetization after along the $[1\bar{1}0]$ crystalline axis after applying and removing a 10kOe field at 390K (data points separated by line) and longitudinal resistivity also along the $[1\bar{1}0]$ crystalline axis (thick solid lines) of 20nm Fe(Rh,Cu)/5nm Au bilayer sample as a function of temperature (note longitudinal resistivity measurements are only made in the 160K-350K range). For recorded measurements, sample is initially cooled down (red) before being warmed up (black). Note that unlike the data in figure A.6, no field was applied and removed at 4.2K before the warm up measurement.

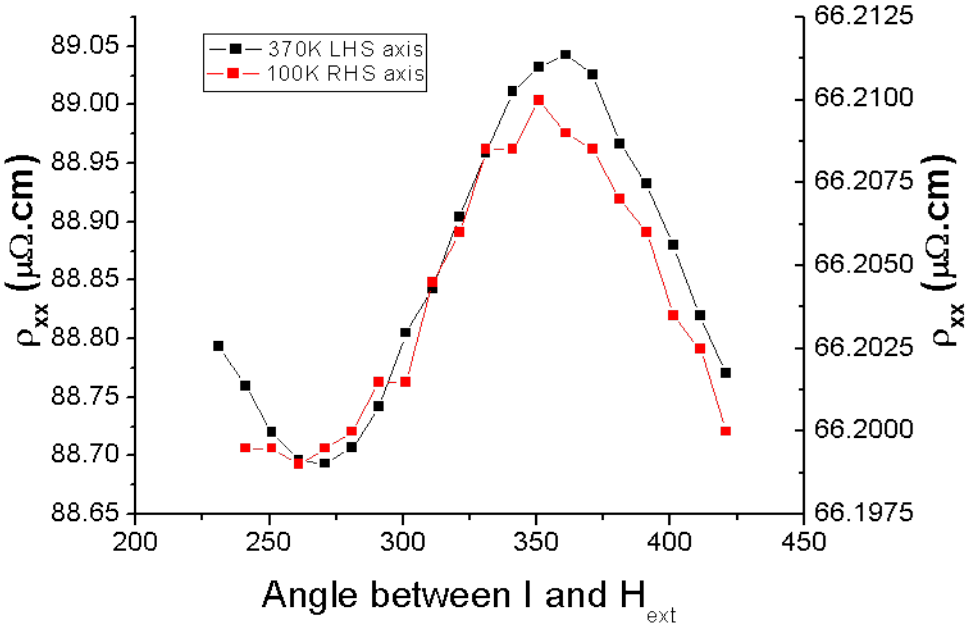

Figure A.11: Longitudinal resistivity along the $[1\bar{1}0]$ crystalline axis of 20nm Fe(Rh,Cu)/5nm Au bilayer sample as a function of angle between current and an external 4.4kOe external field at 370K upon heating the sample (black data points) and 100K upon cooling the sample (red data points).

The measured moment in the SQUID data in figure A.10 is assumed to originate almost entirely from the 20nm Fe(Rh,Cu) layer, with negligible contribution from the 5nm Au layer. The fact that the measured moment along the $[1\bar{1}0]$ crystalline axis is smaller on the warm up measurement can be attributed to the fact that no field was applied at 2K before warming up (unlike the SQUID measurement of the 25nm Fe(Rh,Cu) sample), and therefore domains along multiple easy axes may form as the ferromagnetism is regained. It should also be noted that the calibration of this particular SQUID measurement was not ideal, and so despite the size of the chip used in the SQUID measurement being of a similar size to that of the 25nm Fe(Rh,Cu) SQUID measurement (and 80% of the thickness of the magnetic layer), it is not prudent to compare magnitudes of the measured moments of the two sample. However, it is fair to make the observation that for the bilayer sample the measured moment below T_t is less than 0.5% of the maximum moment above T_t. This confirms that the Au capping layer is effective at suppressing ferromagnetism below T_t.

The resistivity of the bilayer sample is approximately double that of the 25nm Fe(Rh,Cu) sample, which is surprising given that Au has a lower resistivity than FeRh. There is evidence that much of the current is shunted through the 20nm Fe(Rh,Cu) layer of the bilayer sample: The magnitude of the sample's FM-AMR at 370K is 0.4%, which is larger than the AMR of the 25nm Fe(Rh,Cu) sample at a similar temperature (presumably any current that passes through the 5nm Au layer in the bilayer sample makes no contribution to AMR). Furthermore, the relative change in resistance in the transition region is larger for the bilayer sample than it is for the 25nm Fe(Rh,Cu) sample (and again, current passing through the 5nm Au

layer of a bilayer will not make a contribution to this feature). The fact that seemingly a considerable proportion of the current flows through the 20nm Fe(Rh,Cu) layer of the bilayer sample is hugely beneficial for the intended AF-AMR field cool experiment. A 0.015% FM-AMR persists at 160K for the bilayer sample, and this can be attributed to the tiny ferromagnetism that still persists below T_t. This FM-AMR is an order of magnitude smaller than the AF-AMR of FeRh observed in reference [282], and is assumed to not be significant in the scope of the investigation.

As the bilayer showed suitable transport behaviour, multiple field cooling measurements were performed, with fields applied along angles of 0° and 90° to the current direction, and with resistance measurements after the cool down being made mostly at 100K, but also at 4K. A resistance thermometer connected in series to the sample was used to accurately monitor the sample temperature, and great care was taken to ensure the inferred temperature from the resistance thermometer was the same for each measurement after each field cool cycle. A maximum temperature variation of 0.07K for the 100K measurements was achieved. Measurements were made using a quasi-ac current so as to negate any thermoelectric contributions to the measured resistances. As shown in the upper plots of figure A.12, the measured longitudinal resistances for the $[1\bar{1}0]$ and [110] current directions do not consistently vary with the direction of the applied field, and the mean values for the different field cool orientations for a given current direction agree within standard error. As the maximum variation in the measured resistances within different field cool cycles was 0.036%, this suggests that no AF-AMR was induced that was greater than this percentage. As shown in the lower plots of figure A.12, the measured transverse resistances show a more consistent variation with the direction of the applied field for a given current direction, and the mean values for field cooling along a given orientation do not agree within standard error. However, these variations are inconsistent between the orthogonal current directions, e.g. for the $[1\bar{1}0]$ direction, transverse resistance is minimum for field cools along the current direction, whereas for the [110] direction transverse resistance is maximum for field cools along the current direction. This is significant as transverse AF-AMR should only depend on non-crystalline contributions. The variation in the transverse resistance only gives an AMR-like value of around 0.0012% anyway (which is an order of magnitude less than the FM-AMR in figure A.11), less than the 0.036% detection limit for which AF-AMR is ruled out from the longitudinal measurements.

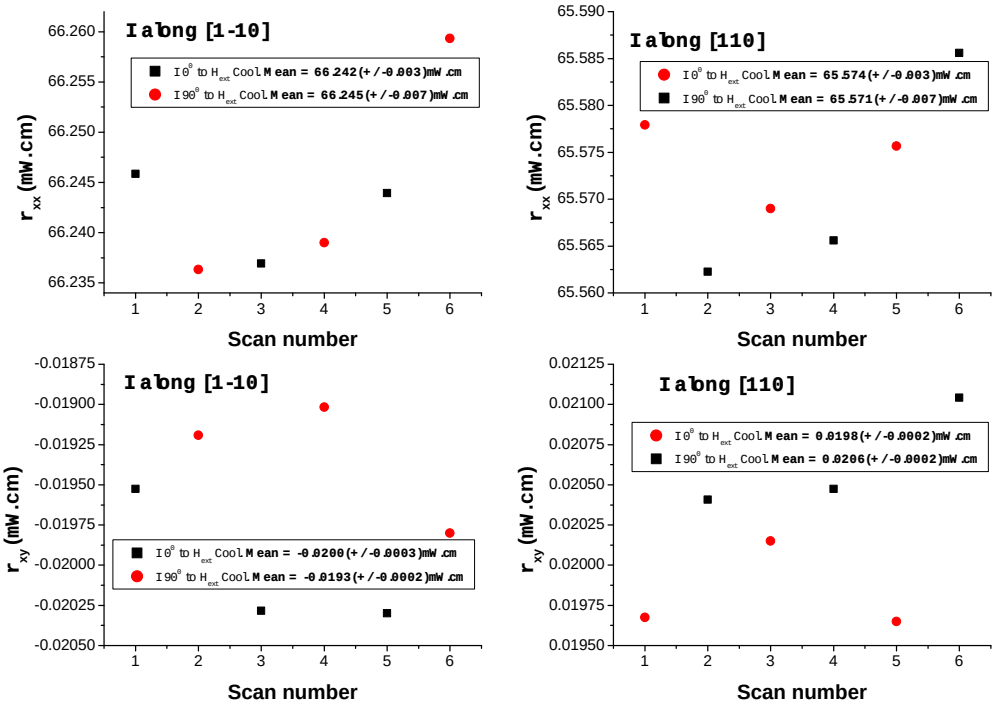

Figure A.12: Longitudinal (upper plots) and transverse (lower plots) resistivity for current along the [1$\bar{1}$0] (left column plots) and [110] (right column plots) crystalline direction of the 20nm Fe(Rh,Cu)/5nm Au bilayer sample after field cooling from 400K to 100K with an 4.4kOe external field parallel to (black square) or perpendicular to (red circles) the current direction. Mean values and their standard error for each dataset are given within the legend.

The lack of observed AF-AMR does not necessarily reflect the fact that it does not exist in the bilayer sample. It is quite possible that the 4.4kOe field was not large enough to set the AF spin-axis upon cooling. This would probably be because it is not strong enough to fully orientate the ferromagnetic moments just above T_t, and the problem would be exaggerated as the weaker the field is, the higher T_t becomes (T_t is known to reduce with increasing external field in FeRh[317]). Indeed, for the observation of AF-AMR in FeRh in reference [282], fields of up to 90kOe were used when cooling through T_t. Therefore, in order to increase the chance of observing AF-AMR in the bilayer sample, further experiments should use a larger field that begins to be applied at a higher temperature in order to fully saturate the ferromagnetic magnetization orientation for when the sample is cooled through T_t. Such high fields and temperatures were not accessible with the equipment used in this investigation. It is hoped further AF-AMR studies of the bilayer sample can be carried out in the future, while there are also interesting preliminary results of a (anomalous) Hall effect study of the same sample which suggests unique behaviour.

Appendix B

List of acronyms

- AF = antiferromagnetic
- AHE = anomalous Hall effect
- AMR = anisotropic magnetoresistance
- ANE = anomalous Nernst effect
- BIA = bulk inversion asymmetry
- CBAMR = Coulomb blockade anisotropic magnetoresistance
- CIF = current induced field
- CPU = central processing unit
- DC = direct current
- DMS = diluted magnetic semiconductor
- DRAM = dynamic random access memory
- FET = field effect transistor
- FM = ferromagnetic
- FMR = ferromagnetic resonance
- FY = fluorescent yield
- GMR = giant magnetoresistance
- GSSE = giant spin Seebeck effect
- HDD = hard disk drive
- IMR = isotropic magnetoresistance
- IQHE = integer quantum Hall effect
- ISGE = inverse spin galvanic effect
- LT-MBE = low temperature molecular beam epitaxy
- MBE = molecular beam epitaxy
- MOVPE = metal-organic vapour phase epitaxy
- MRAM = magnetoresistive random access memory
- NSOT = Néel order spin-orbit torque
- OHE = ordinary Hall effect
- OMR = ordinary magnetoresistance
- PEEM = photoelectron emission microscopy
- PHE = planar Hall effect
- PNE = planar Nernst effect
- QHE = quantum Hall effect
- QSHE = quantum spin Hall effect
- RAM = random access memory
- RHEED = reflection high-energy electron diffraction

- SDHE = Shubnikov-De Haas effect
- SET = single electron transistor
- SHE = spin Hall effect
- SIA = structural inversion asymmetry
- SMR = spin Hall magnetoresistance
- SOC = spin-orbit coupling
- SOI = spin-orbit interaction
- SQUID = superconducting quantum interference device
- SRAM = static random access memory
- SSD = solid state drive
- STT = spin transfer torque
- TAMR = tunnel anisotropic magnetoresistance
- TEY = total electron yield
- TMR = tunnel magnetoresistance
- UHV = ultra high vacuum
- XMCD = x-ray magnetic circular dichroism
- XMLD = x-ray magnetic linear dichroism
- X-STM = cross-sectional scanning tunneling microscopy

Appendix C

Publication list

• B Howells, M Wang, KW Edmonds, P Wadley, RP Campion, AW Rushforth, CT Foxon, and BL Gallagher. Crystalline anisotropic magnetoresistance in quaternary ferromagnetic semiconductor (Ga,Mn)(As,Sb). *Applied Physics Letters*, 102:052407, 2013

• B Howells, KW Edmonds, RP Campion, BL Gallagher. Temperature dependence of spin-orbit torque effective fields in the diluted magnetic semiconductor (Ga,Mn)As. *Applied Physics Letters*, 105:012402, 2014

• P Wadley & B Howells, J Zelezny, C Andrews, V Hills, RP Campion, V Novak, F Freimuth, Y Mokrousov, AW Rushforth, KW Edmonds, B Gallagher, T Jungwirth. Electrical switching of an antiferromagnet. *Submitted to Science, March 2015*

Bibliography

[1] G.E. Moore. Cramming more components onto integrated circuits. *Electronics*, 86:114–117, 1965.

[2] Mario Norberto Baibich, JM Broto, Albert Fert, F Nguyen Van Dau, F Petroff, P Etienne, G Creuzet, A Friederich, and J Chazelas. Giant magnetoresistance of (001) fe/(001) cr magnetic superlattices. *Physical Review Letters*, 61(21):2472, 1988.

[3] Grünberg Binasch, Peter Grünberg, F Saurenbach, and W Zinn. Enhanced magnetoresistance in layered magnetic structures with antiferromagnetic interlayer exchange. *Physical review B*, 39(7):4828, 1989.

[4] William Thomson. On the electro-dynamic qualities of metals:–effects of magnetization on the electric conductivity of nickel and of iron. *Proceedings of the Royal Society of London*, 8:546–550, 1856.

[5] Michel Julliere. Tunneling between ferromagnetic films. *Physics Letters A*, 54(3):225–226, 1975.

[6] C Gould, C Rüster, T Jungwirth, E Girgis, GM Schott, R Giraud, K Brunner, G Schmidt, and LW Molenkamp. Tunneling anisotropic magnetoresistance: a spin-valve-like tunnel magnetoresistance using a single magnetic layer. *Physical review letters*, 93(11):117203, 2004.

[7] J Wunderlich, T Jungwirth, B Kaestner, AC Irvine, AB Shick, N Stone, K-Y Wang, U Rana, AD Giddings, CT Foxon, et al. Coulomb blockade anisotropic magnetoresistance effect in a (ga, mn) as single-electron transistor. *Physical review letters*, 97(7):077201, 2006.

[8] H Nakayama, M Althammer, Y-T Chen, K Uchida, Y Kajiwara, D Kikuchi, T Ohtani, S Geprägs, M Opel, S Takahashi, et al. Spin hall magnetoresistance induced by a nonequilibrium proximity effect. *Physical Review Letters*, 110(20):206601, 2013.

[9] Naoto Nagaosa, Jairo Sinova, Shigeki Onoda, AH MacDonald, and NP Ong. Anomalous hall effect. *Reviews of Modern Physics*, 82(2):1539, 2010.

[10] T. Jungwirth, J. Wunderlich, V. Novak, K. Olejnik, B.L. Gallagher, R.P. Campion, K.W. Edmonds, A.W. Rushforth, A.J. Ferguson, and P. Nemec. Spin-dependent phenomena and device concepts explored in (ga,mn)as. *Rev. Mod. Phys.*, 86:855896, Jul 2014.

[11] DC Ralph and Mark D Stiles. Spin transfer torques. *Journal of Magnetism and Magnetic Materials*, 320(7):1190–1216, 2008.

[12] Philippe Debray, SMS Rahman, J Wan, RS Newrock, M Cahay, AT Ngo, SE Ulloa, ST Herbert, M Muhammad, and M Johnson. All-electric quantum point contact spin-polarizer. *Nature nanotechnology*, 4(11):759–764, 2009.

[13] Pojen Chuang, Sheng-Chin Ho, LW Smith, F Sfigakis, M Pepper, Chin-Hung Chen, Ju-Chun Fan, JP Griffiths, I Farrer, HE Beere, et al. All-electric all-semiconductor spin field-effect transistors. *Nature nanotechnology*, 10(1):35–39, 2015.

[14] Tomas Jungwirth, Jörg Wunderlich, and Kamil Olejník. Spin hall effect devices. *Nature materials*, 11(5):382–390, 2012.

[15] Supriyo Datta and Biswajit Das. Electronic analog of the electro-optic modulator. *Applied Physics Letters*, 56:665, 1990.

[16] Srinivasan Krishnamurthy, Mark Van Schilfgaarde, and Nathan Newman. Spin lifetimes of electrons injected into gaas and gan. *Applied physics letters*, 83(9):1761–1763, 2003.

[17] Markus Ehlert, Cheng Song, Mariusz Ciorga, Martin Utz, Dieter Schuh, Dominique Bougeard, and Dieter Weiss. All-electrical measurements of direct spin hall effect in gaas with esaki diode electrodes. *Physical Review B*, 86(20):205204, 2012.

[18] Ron Jansen. Silicon spintronics. *Nature materials*, 11(5):400–408, 2012.

[19] Mingzhong Wu and Axel Hoffmann. Preface. In Mingzhong Wu and Axel Hoffmann, editors, *Recent Advances in Magnetic Insulators From Spintronics to Microwave Applications*, volume 64 of *Solid State Physics*, pages xiii – xvi. Academic Press, 2013.

[20] Dmytro Pesin and Allan H MacDonald. Spintronics and pseudospintronics in graphene and topological insulators. *Nature Materials*, 11(5):409–416, 2012.

[21] V Alek Dediu, Luis E Hueso, Ilaria Bergenti, and Carlo Taliani. Spin routes in organic semiconductors. *Nature materials*, 8(9):707–716, 2009.

[22] Jacob Linder and Klaus Halterman. Superconducting spintronics with magnetic domain walls. *arXiv preprint arXiv:1401.5806*, 2014.

[23] Fedor Jelezko and Jörg Wrachtrup. Focus on diamond-based photonics and spintronics. *New Journal of Physics*, 14(10):105024, 2012.

[24] AH MacDonald and M Tsoi. Antiferromagnetic metal spintronics. *Philosophical Transactions of the Royal Society A: Mathematical, Physical and Engineering Sciences*, 369(1948):3098–3114, 2011.

[25] P Wadley, V Novák, RP Campion, C Rinaldi, X Martí, H Reichlová, J Železnỳ, J Gazquez, MA Roldan, M Varela, et al. Tetragonal phase of epitaxial room-temperature antiferromagnet cumnas. *Nature communications*, 4, 2013.

[26] Jacek K Furdyna. Diluted magnetic semiconductors. *Journal of Applied Physics*, 64(4):R29–R64, 1988.

[27] Jacek K. Furdyna and Jacek Kossut. *Semiconductors and Semimetals: Volume 25 Diluted Magnetic Semiconductors*. Academic Press, 1988.

[28] A Haury, A Wasiela, A Arnoult, J Cibert, S Tatarenko, T Dietl, and Y Merle d'Aubigné. Observation of a ferromagnetic transition induced by two-dimensional hole gas in modulation-doped cdmnte quantum wells. *Physical Review Letters*, 79(3):511, 1997.

[29] D Ferrand, C Bourgognon, J Cibert, A Wasiela, S Tatarenko, Y Merle d'Aubign, A Bonnani, D Stifter, H Sitter, Le Van Khoi, S Kolenik, J Jaroszyski, M Sawicki, T Andrearczyk, and T Dietl. Indication of ferromagnetic ordering in p-zn1xmnxte. *Physica B: Condensed Matter*, 284288, Part 2(0):1177 – 1178, 2000.

[30] Ram Seshadri. Zinc oxide-based diluted magnetic semiconductors. *Current Opinion in Solid State and Materials Science*, 9(1):1–7, 2005.

[31] Michael Snure, Dhananjay Kumar, and Ashutosh Tiwari. Progress in zno-based diluted magnetic semiconductors. *JOM*, 61(6):72–75, 2009.

[32] H Ohno, H Munekata, T Penney, S Von Molnar, and LL Chang. Magnetotransport properties of p-type (in, mn) as diluted magnetic iii-v semiconductors. *Physical Review Letters*, 68(17):2664, 1992.

[33] H Ohno, A Shen, F Matsukura, A Oiwa, A Endo, S Katsumoto, and Y Iye. (ga, mn) as: A new diluted magnetic semiconductor based on gaas. *Applied Physics Letters*, 69:363, 1996.

[34] K Olejník, MHS Owen, V Novák, J Mašek, AC Irvine, J Wunderlich, and T Jungwirth. Enhanced annealing, high curie temperature, and low-voltage gating in (ga, mn) as: A surface oxide control study. *Physical Review B*, 78(5):054403, 2008.

[35] Mu Wang, RP Campion, AW Rushforth, KW Edmonds, CT Foxon, and BL Gallagher. Achieving high curie temperature in (ga, mn) as. *Applied Physics Letters*, 93(13):132103–132103, 2008.

[36] Tomasz Dietl and Hideo Ohno. Dilute ferromagnetic semiconductors: physics and spintronic structures. *Reviews of Modern Physics*, 86(1):187, 2014.

[37] H Munekata, H Ohno, S Von Molnar, Armin Segmüller, LL Chang, and L Esaki. Diluted magnetic iii-v semiconductors. *Physical Review Letters*, 63(17):1849, 1989.

[38] AY Cho and JR Arthur. Molecular beam epitaxy. *Progress in Solid State Chemistry*, 10:157–191, 1975.

[39] RP Campion, VA Grant, KW Edmonds, BL Gallagher, and CT Foxon. The growth of high quality gamnas layers and heterostructures by molecular beam epitaxy. *physica status solidi (b)*, 244(8):2944–2949, 2007.

[40] M Kodzuka, T Ohkubo, K Hono, F Matsukura, and H Ohno. 3dap analysis of (ga, mn) as diluted magnetic semiconductor thin film. *Ultramicroscopy*, 109(5):644–648, 2009.

[41] M Birowska, C Śliwa, JA Majewski, and T Dietl. Origin of bulk uniaxial anisotropy in zinc-blende dilute magnetic semiconductors. *Physical review letters*, 108(23):237203, 2012.

[42] Tomasz Dietl. *Spintronics*. Academic Press, 2008.

[43] Janusz Sadowski and JZ Domagala. Influence of defects on the lattice constant of gamnas. *Physical Review B*, 69(7):075206, 2004.

[44] KY Wang, KW Edmonds, RP Campion, BL Gallagher, NRS Farley, CT Foxon, M Sawicki, P Boguslawski, and T Dietl. Influence of the mn interstitial on the magnetic and transport properties of (ga, mn) as. *Journal of applied physics*, 95(11):6512–6514, 2004.

[45] KW Edmonds, P Bogusławski, KY Wang, RP Campion, SN Novikov, NRS Farley, BL Gallagher, CT Foxon, M Sawicki, T Dietl, et al. Mn interstitial diffusion in (g a, m n) a s. *Physical review letters*, 92(3):037201, 2004.

[46] D Chiba, KM Yu, W Walukiewicz, Y Nishitani, F Matsukura, and H Ohno. Properties of ga 1-x mn x as with high x (¿ 0.1). *Journal of Applied Physics*, 103(7):07D136–07D136, 2008.

[47] Safa Kasap and Peter Capper. *Springer handbook of electronic and photonic materials*. Springer, 2007.

[48] M Wang, KW Edmonds, BL Gallagher, AW Rushforth, O Makarovsky, A Patanè, RP Campion, CT Foxon, V Novak, and T Jungwirth. High curie temperatures at low compensation in the ferromagnetic semiconductor (ga, mn) as. *Physical Review B*, 87(12):121301, 2013.

[49] KM Yu, W Walukiewicz, T Wojtowicz, I Kuryliszyn, X Liu, Y Sasaki, and JK Furdyna. Effect of the location of mn sites in ferromagnetic ga 1-x mn x as on its curie temperature. *Physical Review B*, 65(20):201303, 2002.

[50] M. J. Seong, S. H. Chun, H. M. Cheong, N. Samarth, and A. Mascarenhas. Spectroscopic determination of hole density in the ferromagnetic semiconductor $ga_{1-x}mn_xAs$. *Phys. Rev. B*, 66:033202, Jul 2002.

[51] B. C. Chapler, S. Mack, L. Ju, T. W. Elson, B. W. Boudouris, E. Namdas, J. D. Yuen, A. J. Heeger, N. Samarth, M. Di Ventra, R. A. Segalman, D. D. Awschalom, F. Wang, and D. N. Basov. Infrared conductivity of hole accumulation and depletion layers in (ga,mn)as- and (ga,be)as-based electric field-effect devices. *Phys. Rev. B*, 86:165302, Oct 2012.

[52] N Tesařová, P Němec, E Rozkotová, J Zemen, T Janda, D Butkovičová, F Trojánek, K Olejník, V Novák, P Malỳ, et al. Experimental observation of the optical spin-orbit torque. *Nature Photonics*, 7(6):492–498, 2013.

[53] Kaiyou Wang. *Magnetotransport and magnetic properties of (Ga,Mn)As thin-films*. PhD thesis, University of Nottingham, 2005.

[54] J Daeubler, M Glunk, W Schoch, W Limmer, and R Sauer. Lattice parameter and hole density of (ga, mn) as on gaas (311) a. *Applied physics letters*, 88(5):051904, 2006.

[55] T Jungwirth, Jairo Sinova, AH MacDonald, BL Gallagher, V Novák, KW Edmonds, AW Rushforth, RP Campion, CT Foxon, L Eaves, et al. Character of states near the fermi level in (ga, mn) as: Impurity to valence band crossover. *Physical Review B*, 76(12):125206, 2007.

[56] Roland Winkler. *Spin-orbit coupling effects in two-dimensional electron and hole systems*. Number 191. Springer, 2003.

[57] M Cardona, NE Christensen, and G Fasol. Relativistic band structure and spin-orbit splitting of zinc-blende-type semiconductors. *Physical Review B*, 38(3):1806, 1988.

[58] JS Kasper and BW Roberts. Antiferromagnetic structure of α-manganese and a magnetic structure study of β-manganese. *Physical Review*, 101(2):537, 1956.

[59] Clarenece Zener. Interaction between the d shells in the transition metals. *Physical Review*, 81(3):440, 1951.

[60] T Jungwirth, J Mašek, KY Wang, KW Edmonds, M Sawicki, M Polini, Jairo Sinova, AH MacDonald, RP Campion, LX Zhao, et al. Low-temperature magnetization of (ga, mn) as semiconductors. *Physical Review B*, 73(16):165205, 2006.

[61] KW Edmonds, NRS Farley, TK Johal, G van der Laan, RP Campion, BL Gallagher, and CT Foxon. Ferromagnetic moment and antiferromagnetic coupling in (ga, mn) as thin films. *Physical Review B*, 71(6):064418, 2005.

[62] P Němec, V Novák, N Tesařová, E Rozkotová, H Reichlová, D Butkovičová, F Trojánek, K Olejník, P Malỳ, RP Campion, et al. The essential role of carefully optimized synthesis for elucidating intrinsic material properties of (ga, mn) as. *Nature communications*, 4:1422, 2013.

[63] T Dietl, H Ohno, F Matsukura, J Cibert, and D Ferrand. Zener model description of ferromagnetism in zinc-blende magnetic semiconductors. *Science*, 287(5455):1019–1022, 2000.

[64] H Ohno. Bridging semiconductor and magnetism. *Journal of Applied Physics*, 113(13):136509, 2013.

[65] M Wang. *Studies of III-V ferromagnetic semiconductors*. PhD thesis, University of Nottingham, 2012.

[66] A. M. Alsmadi, Y. Choi, D. J. Keavney, K. F. Eid, B. J. Kirby, X. Liu, J. Leiner, K. Tivakornsasithorn, M. Dobrowolska, and J. K. Furdyna. Interfacial exchange coupling in fe/(ga,mn)as bilayers. *Phys. Rev. B*, 89:224409, Jun 2014.

[67] X Liu, WL Lim, Z Ge, S Shen, M Dobrowolska, JK Furdyna, T Wojtowicz, KM Yu, and W Walukiewicz. Strain-engineered ferromagnetic in 1-x mn x as films with in-plane easy axis. *Applied Physics Letters*, 86(11):112512–112512, 2005.

[68] C Bihler, M Kraus, H Huebl, MS Brandt, STB Goennenwein, M Opel, MA Scarpulla, PR Stone, R Farshchi, and OD Dubon. Magnetocrystalline anisotropy and magnetization reversal in ga 1- x mn x p synthesized by ion implantation and pulsed-laser melting. *Physical Review B*, 75(21):214419, 2007.

[69] T Dietl, H Ohno, and F Matsukura. Hole-mediated ferromagnetism in tetrahedrally coordinated semiconductors. *Physical Review B*, 63(19):195205, 2001.

[70] M Sawicki, K-Y Wang, KW Edmonds, RP Campion, CR Staddon, NRS Farley, CT Foxon, E Papis, E Kamińska, A Piotrowska, et al. In-plane uniaxial anisotropy rotations in (ga, mn) as thin films. *Physical Review B*, 71(12):121302, 2005.

[71] J Zemen, J Kučera, K Olejník, and T Jungwirth. Magnetocrystalline anisotropies in (ga, mn) as: Systematic theoretical study and comparison with experiment. *Physical Review B*, 80(15):155203, 2009.

[72] Sunjae Chung, H.C. Kim, Sanghoon Lee, X. Liu, and J.K. Furdyna. The effect of carrier density on magnetic anisotropy of the ferromagnetic semiconductor (ga, mn)as. *Solid State Communications*, 149(4142):1739 – 1742, 2009.

[73] M Glunk, J Daeubler, L Dreher, S Schwaiger, W Schoch, R Sauer, W Limmer, A Brandlmaier, STB Goennenwein, C Bihler, et al. Magnetic anisotropy in (ga, mn) as: Influence of epitaxial strain and hole concentration. *Physical Review B*, 79(19):195206, 2009.

[74] M Sawicki, F Matsukura, A Idziaszek, T Dietl, GM Schott, C Ruester, C Gould, G Karczewski, G Schmidt, and LW Molenkamp. Temperature dependent magnetic anisotropy in (ga, mn) as layers. *Physical Review B*, 70(24):245325, 2004.

[75] K-Y Wang, M Sawicki, KW Edmonds, RP Campion, S Maat, CT Foxon, BL Gallagher, and T Dietl. Spin reorientation transition in single-domain (ga, mn) as. *Physical review letters*, 95(21):217204, 2005.

[76] AW Rushforth, E De Ranieri, J Zemen, J Wunderlich, KW Edmonds, CS King, E Ahmad, RP Campion, CT Foxon, BL Gallagher, et al. Voltage control of magnetocrystalline anisotropy in ferromagnetic-semiconductor-piezoelectric hybrid structures. *Physical Review B*, 78(8):085314, 2008.

[77] D Chiba, M Sawicki, Y Nishitani, Y Nakatani, F Matsukura, and H Ohno. Magnetization vector manipulation by electric fields. *Nature*, 455(7212):515–518, 2008.

[78] Brian David Josephson. Possible new effects in superconductive tunnelling. *Physics Letters*, 1(7):251–253, 1962.

[79] John Clarke and Alex I Braginski. The squid handbook: Applications of squids and squid systems, volume ii, 2004.

[80] MI D'yakonov and VI Perel. Possibility of orienting electron spins with current. *Soviet Journal of Experimental and Theoretical Physics Letters*, 13:467, 1971.

[81] Saburo Takahashi and Sadamichi Maekawa. Spin current, spin accumulation and spin hall effect. *Science and Technology of Advanced Materials*, 9(1):014105, 2008.

[82] Robert Karplus and JM Luttinger. Hall effect in ferromagnetics. *Physical Review*, 95(5):1154, 1954.

[83] SH Chun, YS Kim, HK Choi, IT Jeong, WO Lee, KS Suh, Y S Oh, KH Kim, ZG Khim, JC Woo, et al. Interplay between carrier and impurity concentrations in annealed ga 1-x mn x as: Intrinsic anomalous hall effect. *Physical review letters*, 98(2):026601, 2007.

[84] KW Edmonds, KY Wang, RP Campion, AC Neumann, CT Foxon, BL Gallagher, and PC Main. Hall effect and hole densities in ga 1-x mn x as. *Applied physics letters*, 81(16):3010–3012, 2002.

[85] Yong Pu, Daichi Chiba, Fumihiro Matsukura, Hideo Ohno, and Jing Shi. Mott relation for anomalous hall and nernst effects in ga_ {1-x} mn_ {x} as ferromagnetic semiconductors. *Physical review letters*, 101(11):117208, 2008.

[86] T Jungwirth, KY Wang, J Mašek, KW Edmonds, Jürgen König, Jairo Sinova, M Polini, NA Goncharuk, AH MacDonald, M Sawicki, et al. Prospects for high temperature ferromagnetism in (ga, mn) as semiconductors. *Physical Review B*, 72(16):165204, 2005.

[87] M. Wang, R. A. Marshall, K. W. Edmonds, A. W. Rushforth, R. P. Campion, and B. L. Gallagher. Determining curie temperatures in dilute ferromagnetic semiconductors: High curie temperature (ga,mn)as. *Applied Physics Letters*, 104(13):–, 2014.

[88] F Matsukura, E Abe, and H Ohno. Magnetotransport properties of (ga, mn) sb. *Journal of Applied Physics*, 87(9):6442–6444, 2000.

[89] WL Lim, T Wojtowicz, X Liu, M Dobrowolska, and JK Furdyna. Mbe growth and magnetotransport studies of ferromagnetic ga¡ sub¿ 1- x¡/sub¿ mn¡ sub¿ x¡/sub¿ sb semiconductor layers on hybrid znte/gaas substrates. *Physica E: Low-dimensional Systems and Nanostructures*, 20(3):346–349, 2004.

[90] Y Nishitani, M Endo, F Matsukura, and H Ohno. Magnetic anisotropy in a ferromagnetic (ga, mn) sb thin film. *Physica E: Low-dimensional Systems and Nanostructures*, 42(10):2681–2684, 2010.

[91] Hsiao Wen Chang, Shingo Akita, Fumihiro Matsukura, and Hideo Ohno. Hole concentration dependence of the curie temperature of (ga, mn) sb in a field-effect structure. *Applied Physics Letters*, 103(14):142402, 2013.

[92] V Šestáková, P Hubik, B Štěpánek, and J Krištofik. Gasb single crystals doped with manganese. *Journal of crystal growth*, 132(1):345–347, 1993.

[93] M. Linnarsson, E. Janzén, B. Monemar, M. Kleverman, and A. Thilderkvist. Electronic structure of the gaas:mn. *Phys. Rev. B*, 55:6938–6944, Mar 1997.

[94] Y Nishitani, D Chiba, M Endo, M Sawicki, F Matsukura, T Dietl, and H Ohno. Curie temperature versus hole concentration in field-effect structures of ga 1-x mn x as. *Physical Review B*, 81(4):045208, 2010.

[95] T Slupinski, H Munekata, and A Oiwa. Ferromagnetic semiconductor (in, ga, mn) as with curie temperature above 100 k. *Applied physics letters*, 80(9):1592–1594, 2002.

[96] Shinobu Ohya, Hideo Kobayashi, and Masaaki Tanaka. Magnetic properties of heavily mn-doped quaternary alloy ferromagnetic semiconductor (ingamn) as grown on inp. *Applied physics letters*, 83(11):2175–2177, 2003.

[97] M Yokoyama, S Ohya, and M Tanaka. Magnetic anisotropy of ferromagnetic semiconductor [(inga) mn] as thin films. *physica status solidi (c)*, 5(9):2901–2903, 2008.

[98] Shinobu Ohya, Iriya Muneta, Yufei Xin, Kenta Takata, and Masaaki Tanaka. Valence-band structure of ferromagnetic semiconductor (in, ga, mn) as. *Physical Review B*, 86(9):094418, 2012.

[99] K Takamura, F Matsukura, D Chiba, and H Ohno. Magnetic properties of (al, ga, mn) as. *Applied physics letters*, 81(14):2590–2592, 2002.

[100] AW Rushforth, NRS Farley, RP Campion, KW Edmonds, CR Staddon, CT Foxon, BL Gallagher, and KM Yu. Compositional dependence of ferromagnetism in (al, ga, mn) as magnetic semiconductors. *Physical Review B*, 78(8):085209, 2008.

[101] M Wang, AW Rushforth, AT Hindmarch, RP Campion, KW Edmonds, CR Staddon, CT Foxon, and BL Gallagher. Magnetic and structural properties of (ga, mn) as/(al, ga, mn) as bilayer films. *Applied Physics Letters*, 102(11):112404, 2013.

[102] O Maksimov, BL Sheu, P Schiffer, and N Samarth. Molecular-beam epitaxial growth and characterization of (in 0.5 al 0.5) 1-x mn x as-(in 0.5 ga 0.5) 1-x mn x as: Thin films and superlattices. *Journal of Vacuum Science & Technology B: Microelectronics and Nanometer Structures*, 23(3):1304–1307, 2005.

[103] R.A. Oliver, M.J. Kappers, J. Sumner, R. Datta, and C.J. Humphreys. Highlighting threading dislocations in movpe-grown gan using an in situ treatment with sih4 and {NH3}. *Journal of Crystal Growth*, 289(2):506 – 514, 2006.

[104] WN Lee, YF Chen, JH Huang, XJ Guo, CT Kuo, and HC Ku. Mbe growth and structural and magnetic properties of (in¡ sub¿ 1-¡/sub¿¡ i¿ y¡/i¿ al¡ i¿ y¡/i¿)¡ sub¿ 1-¡/sub¿¡ i¿ x¡/i¿ mn¡ i¿ x¡/i¿ as-diluted magnetic semiconductors. *Journal of crystal growth*, 289(2):502–505, 2006.

[105] Tsuyoshi Kondo, Jun-ji Hayafuji, Akira Oiwa, and Hiro Munekata. A quaternary magnetic alloy semiconductor (ga, in, mn) n. *Japanese journal of applied physics*, 43(7A):L851, 2004.

[106] R Kling, A Köder, W Schoch, S Frank, M Oettinger, W Limmer, R Sauer, and A Waag. Influence of nitrogen incorporation on structural, electronic and magnetic properties of ga¡ sub¿ 1- x¡/sub¿ mn¡ sub¿ x¡/sub¿ as. *Solid state communications*, 124(5):207–210, 2002.

[107] I Oshiyama, T Kondo, and H Munekata. Effect of nitrogen incorporation in ferromagnetic (ga, mn) as epilayers. *Journal of applied physics*, 98(9):093906, 2005.

[108] Genki Kobayashi, Takahiro Mori, Takashi Kato, Takashi Hanada, Hisao Makino, and Takafumi Yao. Molecular beam epitaxy and magnetic properties of gamnnas. *Journal of Crystal Growth*, 301:642–646, 2007.

[109] AW Rushforth, M Wang, NRS Farley, RP Campion, KW Edmonds, CR Staddon, CT Foxon, and BL Gallagher. Molecular beam epitaxy grown (ga, mn)(as, p) with perpendicular to plane magnetic easy axis. *Journal of Applied Physics*, 104(7):073908–073908, 2008.

[110] Aristide Lemaître, Audrey Miard, Laurent Travers, Olivia Mauguin, Ludovic Largeau, Catherine Gourdon, Vincent Jeudy, Michael Tran, and J-M George. Strain control of the magnetic anisotropy in (ga, mn)(as, p) ferromagnetic semiconductor layers. *Applied Physics Letters*, 93(2):021123, 2008.

[111] A Casiraghi, AW Rushforth, M Wang, NRS Farley, P Wadley, JL Hall, CR Staddon, KW Edmonds, RP Campion, CT Foxon, et al. Tuning perpendicular magnetic anisotropy in (ga, mn)(as, p) by thermal annealing. *Applied Physics Letters*, 97(12):122504, 2010.

[112] Arianna Casiraghi. *Manipulating the magnetic anisotropy in the ferromagnetic semiconductor Gallium Manganese Arsenide*. PhD thesis, University of Nottingham, 2012.

[113] O Yastrubchak, J Sadowski, L Gluba, JZ Domagala, M Rawski, J Żuk, M Kulik, T Andrearczyk, and T Wosinski. Ferromagnetism and the electronic band structure in (ga, mn)(bi, as) epitaxial layers. *Applied Physics Letters*, 105(7):072402, 2014.

[114] JJ Deng, JT Che, J Chen, WJ Wang, B Hu, HL Wang, and JH Zhao. Effect of sb incorporation on structure and magnetic properties of quaternary ferromagnetic semiconductor (ga, mn)(as, sb) thin films. *Journal of Applied Physics*, 114(24):243901, 2013.

[115] J Mašek, J Kudrnovskỳ, and F Máca. Lattice constant in diluted magnetic semiconductors (ga, mn) as. *Physical Review B*, 67(15):153203, 2003.

[116] M Hakala, MJ Puska, and RM Nieminen. Native defects and self-diffusion in gasb. *Journal of applied physics*, 91(8):4988–4994, 2002.

[117] Brian R Bennett. Strain relaxation in inas/gasb heterostructures. *Applied physics letters*, 73(25):3736–3738, 1998.

[118] J Mašek, J Kudrnovskỳ, F Máca, Jairo Sinova, AH MacDonald, RP Campion, BL Gallagher, and T Jungwirth. Mn-doped ga (as, p) and (al, ga) as ferromagnetic semiconductors: Electronic structure calculations. *Physical Review B*, 75(4):045202, 2007.

[119] Yuanyuan Li, Y. F. Cao, G. N. Wei, Yanyong Li, Y. Ji, K. Y. Wang, K. W. Edmonds, R. P. Campion, A. W. Rushforth, C. T. Foxon, and B. L. Gallagher. Anisotropic current-controlled magnetization reversal in the ferromagnetic semiconductor (ga,mn)as. *Applied Physics Letters*, 103(2):022401, 2013.

[120] Jungbum Yoon Younghun Jo Myung-Hwa Jung H. K. Choi Y. D. Park S. K. Jerng Y. S. Kim, Z. G. Khim and S. H. Chun. Magnetic anisotropy and ac susceptibility of (ga,mn)as. *J. Korean Phys.Soc*, 50:839, 2007.

[121] V Stanciu and P Svedlindh. Annealing-induced changes of the magnetic anisotropy of (ga, mn) as epilayers. *Applied Physics Letters*, 87(24):242509, 2005.

[122] Y Iye, A Oiwa, A Endo, S Katsumoto, F Matsukura, A Shen, H Ohno, and H Munekata. Metal–insulator transition and magnetotransport in iii–v compound diluted magnetic semiconductors. *Materials Science and Engineering: B*, 63(1):88–95, 1999.

[123] KW Edmonds, KY Wang, RP Campion, AC Neumann, NRS Farley, BL Gallagher, and CT Foxon. High-curie-temperature gamnas obtained by resistance-monitored annealing. *Applied Physics Letters*, 81:4991, 2002.

[124] M. Glunk, J. Daeubler, W. Schoch, R. Sauer, and W. Limmer. Scaling relation of the anomalous hall effect in (ga,mn)as. *Phys. Rev. B*, 80:125204, Sep 2009.

[125] F Tuomisto, K Pennanen, K Saarinen, and Janusz Sadowski. Ga sublattice defects in (ga, mn) as: Thermodynamical and kinetic trends. *Physical review letters*, 93(5):055505, 2004.

[126] DE Bliss, W Walukiewicz, JW Ager III, EE Haller, KT Chan, and S Tanigawa. Annealing studies of low-temperature-grown gaas: Be. *Journal of applied physics*, 71(4):1699–1707, 1992.

[127] Philip W Anderson. Absence of diffusion in certain random lattices. *Physical review*, 109(5):1492, 1958.

[128] Brian Sorenson. *Electric and Magnetic Properties of Ultra Thin (Ga,Mn)As Epilayers*. PhD thesis, University of Copenhagen, 2004.

[129] Chris King. *Magnetotransport and Magnetocrystalline Anisotropy Studies of Gallium Manganese Arsenide Thin Films*. PhD thesis, University of Nottingham, 2008.

[130] AW Rushforth, AD Giddings, KW Edmonds, RP Campion, CT Foxon, and BL Gallagher. Amr and magnetometry studies of ultra thin gamnas films. *physica status solidi (c)*, 3(12):4078–4081, 2006.

[131] F Matsukura, H Ohno, A Shen, and Y Sugawara. Transport properties and origin of ferromagnetism in (ga, mn) as. *Physical Review B*, 57(4):R2037, 1998.

[132] LP Rokhinson, Y Lyanda-Geller, Z Ge, S Shen, X Liu, M Dobrowolska, and JK Furdyna. Weak localization in ga 1- x mn x as: Evidence of impurity band transport. *Physical Review B*, 76(16):161201, 2007.

[133] Daniel Neumaier, Konrad Wagner, Stefan Geißler, Ursula Wurstbauer, Janusz Sadowski, Werner Wegscheider, and Dieter Weiss. Weak localization in ferromagnetic (ga, mn) as nanostructures. *Physical review letters*, 99(11):116803, 2007.

[134] C Rüster, C Gould, T Jungwirth, J Sinova, GM Schott, R Giraud, K Brunner, G Schmidt, and LW Molenkamp. Very large tunneling anisotropic magnetoresistance of a (g a, m n) a s/g a a s/(g a, m n) a s stack. *Physical review letters*, 94(2):027203, 2005.

[135] AD Giddings, MN Khalid, T Jungwirth, J Wunderlich, S Yasin, RP Campion, KW Edmonds, J Sinova, K Ito, K-Y Wang, et al. Large tunneling anisotropic magnetoresistance in (ga, mn) as nanoconstrictions. *Physical review letters*, 94(12):127202, 2005.

[136] Yong Pu and Jing Shi. Anisotropic thermopower and planar nernst effect in ga1-xmnxas. *Bulletin of the American Physical Society*, 2006.

[137] Ts Naydenova, P Dürrenfeld, K Tavakoli, N Pégard, L Ebel, K Pappert, K Brunner, C Gould, and LW Molenkamp. Diffusion thermopower of (ga, mn) as/gaas tunnel junctions. *Physical review letters*, 107(19):197201, 2011.

[138] Samuel Mauger. *Atomic-scale study of Mn- and Sb-containing III-V semiconductor nanostructures*. PhD thesis, Technische Universiteit Eindhoven, 2013.

[139] TAL Lima, Ulrich Wahl, Valérie Augustyns, DJ Silva, A Costa, K Houben, KW Edmonds, BL Gallagher, RP Campion, MJ Van Bael, et al. Identification of the interstitial mn site in ferromagnetic (ga, mn) as. *Applied Physics Letters*, 106(1):012406, 2015.

[140] Nguyen Thanh Tu, Pham Nam Hai, Masaaki Tanaka, et al. (ga, fe) sb: A p-type ferromagnetic semiconductor. *Applied Physics Letters*, 105(13):132402, 2014.

[141] MI Dyakonov and AV Khaetskii. Spin hall effect. In *Spin physics in semiconductors*, pages 211–243. Springer, 2008.

[142] ES Garlid, QO Hu, MK Chan, CJ Palmstrøm, and PA Crowell. Electrical measurement of the direct spin hall effect in fe/in x ga 1-x as heterostructures. *Physical review letters*, 105(15):156602, 2010.

[143] Xiao-Liang Qi and Shou-Cheng Zhang. The quantum spin hall effect and topological insulators. *Physics Today*, 63(1):33–38, 2010.

[144] Ivan Knez and Rui-Rui Du. Quantum spin hall effect in inverted inas/gasb quantum wells. *Frontiers of Physics*, 7(2):200–207, 2012.

[145] CM Jaworski, RC Myers, E Johnston-Halperin, and JP Heremans. Giant spin seebeck effect in a non-magnetic material. *Nature*, 487(7406):210–213, 2012.

[146] LW McKeehan. Electrical resistance of nickel and permalloy wires as affected by longitudinal magnetization and tension. *Physical Review*, 36(5):948, 1930.

[147] J Smit. Magnetoresistance of ferromagnetic metals and alloys at low temperatures. *Physica*, 17(6):612–627, 1951.

[148] O Jaoul, IA Campbell, and A Fert. Spontaneous resistivity anisotropy in ni alloys. *Journal of Magnetism and Magnetic Materials*, 5(1):23–34, 1977.

[149] TR McGuire and RI Potter. Anisotropic magnetoresistance in ferromagnetic 3d alloys. *IEEE Transactions on Magnetics*, 11(4), 1975.

[150] JN Eckstein, I Bozovic, J ODonnell, M Onellion, and MS Rzchowski. Anisotropic magnetoresistance in tetragonal la1- xcaxmnoδ thin films. *Applied physics letters*, 69(9):1312–1314, 1996.

[151] J ODonnell, JN Eckstein, and MS Rzchowski. Temperature and magnetic field dependent transport anisotropies in la 0.7 ca 0.3 mno 3 films. *Applied Physics Letters*, 76(2):218–220, 2000.

[152] David V Baxter, Dmitry Ruzmetov, Julia Scherschligt, Y Sasaki, X Liu, JK Furdyna, and CH Mielke. Anisotropic magnetoresistance in ga 1-x mn x as. *Physical Review B*, 65(21):212407, 2002.

[153] T Jungwirth, M Abolfath, Jairo Sinova, J Kucera, and AH MacDonald. Boltzmann theory of engineered anisotropic magnetoresistance in (ga, mn) as. *Applied physics letters*, 81(21):4029–4031, 2002.

[154] KY Wang, KW Edmonds, RP Campion, LX Zhao, CT Foxon, and BL Gallagher. Anisotropic magnetoresistance and magnetic anisotropy in high-quality (ga, mn) as films. *Physical Review B*, 72(8):085201, 2005.

[155] KM Seemann, F Freimuth, H Zhang, S Blügel, Y Mokrousov, DE Bürgler, and CM Schneider. Origin of the planar hall effect in nanocrystalline co 60 fe 20 b 20. *Physical review letters*, 107(8):086603, 2011.

[156] HT He, XC Cao, T Zhang, YQ Wang, and JN Wang. Systematic study of anisotropic magnetoresistance effect in (311) a gamnas films. *Journal of Applied Physics*, 107(6):063902, 2010.

[157] KJ Friedland, M Bowen, J Herfort, HP Schönherr, and KH Ploog. Intrinsic contributions to the planar hall effect in fe and fe3si films on gaas substrates. *Journal of Physics: Condensed Matter*, 18(9):2641, 2006.

[158] K-J Friedland, J Herfort, PK Muduli, H-P Schönherr, and KH Ploog. Planar hall effect in epitaxial fe layers on gaas (001) and gaas (113) a substrates. *Journal of superconductivity*, 18(3):309–314, 2005.

[159] AW Rushforth, K Vỳbornỳ, CS King, KW Edmonds, RP Campion, CT Foxon, J Wunderlich, AC Irvine, P Vašek, V Novák, et al. Anisotropic magnetoresistance components in (ga, mn) as. *Physical review letters*, 99(14):147207, 2007.

[160] AW Rushforth, K Vỳbornỳ, CS King, KW Edmonds, RP Campion, CT Foxon, J Wunderlich, AC Irvine, V Novák, K Olejník, et al. The origin and control of the sources of amr in (ga, mn) as devices. *Journal of Magnetism and Magnetic Materials*, 321(8):1001–1008, 2009.

[161] B Howells, M Wang, KW Edmonds, P Wadley, RP Campion, AW Rushforth, CT Foxon, and BL Gallagher. Crystalline anisotropic magnetoresistance in quaternary ferromagnetic semiconductor (ga, mn)(as, sb). *Applied Physics Letters*, 102(5):052407–052407, 2013.

[162] Karel Vỳbornỳ, Jan Kučera, Jairo Sinova, AW Rushforth, BL Gallagher, and T Jungwirth. Microscopic mechanism of the noncrystalline anisotropic magnetoresistance in (ga, mn) as. *Physical Review B*, 80(16):165204, 2009.

[163] Maxim Trushin, Karel Vỳbornỳ, Peter Moraczewski, Alexey A Kovalev, John Schliemann, and Tomas Jungwirth. Anisotropic magnetoresistance of spin-orbit coupled carriers scattered from polarized magnetic impurities. *Physical Review B*, 80(13):134405, 2009.

[164] E De Ranieri, AW Rushforth, K Vỳbornỳ, U Rana, E Ahmad, RP Campion, CT Foxon, BL Gallagher, AC Irvine, J Wunderlich, et al. Lithographically and electrically controlled strain effects on anisotropic magnetoresistance in (ga, mn) as. *New Journal of Physics*, 10(6):065003, 2008.

[165] Junichi Shiogai, Dieter Schuh, Werner Wegscheider, M Kohda, J Nitta, and Dieter Weiss. Magnitude and sign control of lithography-induced uniaxial anisotropy in ultra-thin (ga, mn) as wires. *Applied physics letters*, 98(8):083101–083101, 2011.

[166] C Gould, S Mark, K Pappert, RG Dengel, J Wenisch, RP Campion, AW Rushforth, D Chiba, Z Li, X Liu, et al. An extensive comparison of anisotropies in mbe grown (ga, mn) as material. *New Journal of Physics*, 10(5):055007, 2008.

[167] W Limmer, M Glunk, J Daeubler, T Hummel, W Schoch, R Sauer, C Bihler, H Huebl, MS Brandt, and STB Goennenwein. Angle-dependent magnetotransport in cubic and tetragonal ferromagnets: Application to (001)-and (113) a-oriented (ga, mn) as. *Physical Review B*, 74(20):205205, 2006.

[168] JA Haigh, AW Rushforth, CS King, KW Edmonds, RP Campion, CT Foxon, and BL Gallagher. A low field technique for measuring magnetic and magnetoresistance anisotropy coefficients applied to (ga, mn) as. *Applied Physics Letters*, 95(23):232102, 2009.

[169] RR Gareev, A Petukhov, Markus Schlapps, Janusz Sadowski, and Werner Wegscheider. Giant anisotropic magnetoresistance in insulating ultrathin (ga, mn) as. *Applied Physics Letters*, 96(5):052114, 2010.

[170] D Wu, Peng Wei, E Johnston-Halperin, DD Awschalom, and Jing Shi. High-field magnetocrystalline anisotropic resistance effect in (ga, mn) as. *Physical Review B*, 77(12):125320, 2008.

[171] P Vašek, P Svoboda, V Novák, M Cukr, Z Vỳbornỳ, V Jurka, J Stuchlík, M Orlita, and DK Maude. Anisotropic magnetoresistance of gamnas ferromagnetic semiconductors. *Journal of superconductivity and novel magnetism*, 23(6):1161–1163, 2010.

[172] E Mikheev, I Stolichnov, Z Huang, AW Rushforth, JA Haigh, RP Campion, KW Edmonds, BL Gallagher, and N Setter. Non-volatile ferroelectric gating of magnetotransport anisotropy in (ga, mn)(as, p). *Applied Physics Letters*, 100(26):262906–262906, 2012.

[173] A Kobs, S Heße, W Kreuzpaintner, G Winkler, D Lott, P Weinberger, A Schreyer, and HP Oepen. Anisotropic interface magnetoresistance in pt/co/pt sandwiches. *Physical review letters*, 106(21):217207, 2011.

[174] YF Liu, JW Cai, and L Sun. Large enhancement of anisotropic magnetoresistance and thermal stability in ta/nife/ta trilayers with interfacial pt addition. *Applied Physics Letters*, 96(9):092509, 2010.

[175] S. Jaiswal A.W. Rushforth B.L. Gallagher D. Atkinson M. Tokac, M. Wang and A.T. Hindmarch. Interfacial origin of thickness dependent in-plane anisotropic magnetoresistance.

[176] Pham Nam Hai, Daisuke Sasaki, Masaaki Tanaka, et al. Crystalline anisotropic magnetoresistance with two-fold and eight-fold symmetry in (in, fe) as ferromagnetic semiconductor. *Applied Physics Letters*, 100(26):262409, 2012.

[177] Nguyen Thanh Tu, Pham Nam Hai, Masaaki Tanaka, et al. Epitaxial growth and characterization of n-type magnetic semiconductor (in, co) as. *Japanese Journal of Applied Physics*, 53(4S):04EM05, 2014.

[178] AJ Behan, A Mokhtari, HJ Blythe, M Ziese, AM Fox, and GA Gehring. Magnetoresistance of magnetically doped zno films. *Journal of Physics: Condensed Matter*, 21(34):346001, 2009.

[179] JW Lee, S Kuroda, F Takano, H Akinaga, and K Takita. Anisotropy of magnetization and magnetoresistance of (zn, co) o films grown by pulsed laser deposition. *physica status solidi (c)*, 3(12):4098–4101, 2006.

[180] Isaschar Genish, Yevgeny Kats, Lior Klein, James W Reiner, and MR Beasley. Paramagnetic anisotropic magnetoresistance in thin films of srruo3. *Journal of applied physics*, 95(11):6681–6683, 2004.

[181] YM Lu, Y Choi, CM Ortega, XM Cheng, JW Cai, SY Huang, L Sun, and CL Chien. Pt magnetic polarization on y 3 fe 5 o 12 and magnetotransport characteristics. *Physical Review Letters*, 110(14):147207, 2013.

[182] Tao Lin, Chi Tang, Hamad M Alyahayaei, and Jing Shi. Experimental investigation of the nature of the magnetoresistance effects in pd-yig hybrid structures. *Physical review letters*, 113(3):037203, 2014.

[183] S.-H. Yang, P. Barba, K.-S. Ryu, L. Thomas, A. Manchon, and S. Parkin. Anomalous Hall effect (AHE) and anisotropy magnetoresistance (AMR) in perpendicularly magnetized Co/Ni multilayers on Pt and Au underlayers. In *APS Meeting Abstracts*, page 15009, March 2013.

[184] P. Gonzalez Barba, S.-H. Yan, L. Thomas, K.-S. Ryu, S. Parkin, and A. Manchon. Spin Hall Effect induced Anisotropic Magnetoresistance. In *APS Meeting Abstracts*, page 15010, March 2013.

[185] Feng Chen, David A Koufaty, and Xiaodong Zhang. Understanding intrinsic characteristics and system implications of flash memory based solid state drives. In *ACM SIGMETRICS Performance Evaluation Review*, volume 37, pages 181–192. ACM, 2009.

[186] Ricardo C Sousa and I Lucian Prejbeanu. Non-volatile magnetic random access memories (mram). *Comptes Rendus Physique*, 6(9):1013–1021, 2005.

[187] Takayuki Kawahara, Kenchi Ito, Riichiro Takemura, and Hideo Ohno. Spin-transfer torque ram technology: review and prospect. *Microelectronics Reliability*, 52(4):613–627, 2012.

[188] B Andrei Bernevig and Shou-Cheng Zhang. Intrinsic spin hall effect in the two-dimensional hole gas. *Physical review letters*, 95(1):016801, 2005.

[189] A Manchon and S Zhang. Theory of nonequilibrium intrinsic spin torque in a single nanomagnet. *Physical Review B*, 78(21):212405, 2008.

[190] Alexandr Chernyshov, Mason Overby, Xinyu Liu, Jacek K Furdyna, Yuli Lyanda-Geller, and Leonid P Rokhinson. Evidence for reversible control of magnetization in a ferromagnetic material by means of spin–orbit magnetic field. *Nature Physics*, 5(9):656–659, 2009.

[191] M Endo, F Matsukura, and H Ohno. Current induced effective magnetic field and magnetization reversal in uniaxial anisotropy (ga, mn) as. *Applied Physics Letters*, 97(22):222501–222501, 2010.

[192] Ioan Mihai Miron, Gilles Gaudin, Stéphane Auffret, Bernard Rodmacq, Alain Schuhl, Stefania Pizzini, Jan Vogel, and Pietro Gambardella. Current-driven spin torque induced by the rashba effect in a ferromagnetic metal layer. *Nature materials*, 9(3):230–234, 2010.

[193] Luqiao Liu, Chi-Feng Pai, Y Li, HW Tseng, DC Ralph, and RA Buhrman. Spin-torque switching with the giant spin hall effect of tantalum. *Science*, 336(6081):555–558, 2012.

[194] Yabin Fan, Pramey Upadhyaya, Xufeng Kou, Murong Lang, So Takei, Zhenxing Wang, Jianshi Tang, Liang He, Li-Te Chang, Mohammad Montazeri, et al. Magnetization switching through giant spin–orbit torque in a magnetically doped topological insulator heterostructure. *Nature materials*, 2014.

[195] J Železnỳ, H Gao, K Vỳbornỳ, J Zemen, J Mašek, Aurélien Manchon, J Wunderlich, Jairo Sinova, and T Jungwirth. Relativistic néel-order fields induced by electrical current in antiferromagnets. *Physical review letters*, 113(15):157201, 2014.

[196] D Fang, H Kurebayashi, J Wunderlich, K Vỳbornỳ, LP Zârbo, RP Campion, A Casiraghi, BL Gallagher, T Jungwirth, and AJ Ferguson. Spin-orbit-driven ferromagnetic resonance. *Nature Nanotechnology*, 6(7):413–417, 2011.

[197] Hang Li, Xuhui Wang, Fatih Dogan, and Aurelien Manchon. Tailoring spin-orbit torque in diluted magnetic semiconductors. *Applied Physics Letters*, 102(19):192411, 2013.

[198] H Kurebayashi, Jairo Sinova, D Fang, AC Irvine, TD Skinner, J Wunderlich, V Novák, RP Campion, BL Gallagher, EK Vehstedt, et al. An antidamping spin-orbit torque originating from the berry curvature. *Nature nanotechnology*, 2014.

[199] Ion Garate E. K. Vehstedt A. Cejchan Jairo Sinova D. Fang H. Kurebayashi J. Wunderlich A. J. Ferguson L. P. Zarbo, K. Vyborny and T. Jungwirth1. Spin-orbit current induced torque in uniform ferromagnets: A detailed study in (ga,mn)as.

[200] G Woltersdorf, J Stigloher, HS Körner, F Hoffmann, M Kiessling, V Novak, J-Y Chauleau, and CH Back. Spatial constraints on the source of uniaxial anisotropy in (ga, mn) as films. *Journal of Physics D Applied Physics*, 47(19):5001, 2014.

[201] M Studer, MP Walser, S Baer, H Rusterholz, S Schön, D Schuh, W Wegscheider, K Ensslin, and G Salis. Role of linear and cubic terms for drift-induced dresselhaus spin-orbit splitting in a two-dimensional electron gas. *Physical Review B*, 82(23):235320, 2010.

[202] Mark Johnson and R. H. Silsbee. Interfacial charge-spin coupling: Injection and detection of spin magnetization in metals. *Phys. Rev. Lett.*, 55:1790–1793, Oct 1985.

[203] Mark Johnson. Spin accumulation in gold films. *Physical review letters*, 70(14):2142, 1993.

[204] PR Hammar, BR Bennett, MJ Yang, and Mark Johnson. Observation of spin injection at a ferromagnet-semiconductor interface. *Physical Review Letters*, 83(1):203, 1999.

[205] R Fiederling, M Keim, Get al Reuscher, W Ossau, G Schmidt, A Waag, and LW Molenkamp. Injection and detection of a spin-polarized current in a light-emitting diode. *Nature*, 402(6763):787–790, 1999.

[206] Victor M Edelstein. Spin polarization of conduction electrons induced by electric current in two-dimensional asymmetric electron systems. *Solid State Communications*, 73(3):233–235, 1990.

[207] Yuichiro Kato, RC Myers, AC Gossard, and DD Awschalom. Coherent spin manipulation without magnetic fields in strained semiconductors. *Nature*, 427(6969):50–53, 2004.

[208] Y. K. Kato, R. C. Myers, A. C. Gossard, and D. D. Awschalom. Electrical initialization and manipulation of electron spins in an l-shaped strained n-ingaas channel. *Applied Physics Letters*, 87(2):–, 2005.

[209] Hidekazu Kurebayashi. Spin orbit torques in (ga,mn)as, lanna 2012 presentation.

[210] Luqiao Liu, OJ Lee, TJ Gudmundsen, DC Ralph, and RA Buhrman. Current-induced switching of perpendicularly magnetized magnetic layers using spin torque from the spin hall effect. *Physical review letters*, 109(9):096602, 2012.

[211] Junyeon Kim, Jaivardhan Sinha, Masamitsu Hayashi, Michihiko Yamanouchi, Shunsuke Fukami, Tetsuhiro Suzuki, Seiji Mitani, and Hideo Ohno. Layer thickness dependence of the current-induced effective field vector in ta— cofeb— mgo. *Nature materials*, 12(3):240–245, 2013.

[212] Xin Fan, Halise Celik, Jun Wu, Chaoying Ni, Kyung-Jin Lee, Virginia O Lorenz, and John Q Xiao. Quantifying interface and bulk contributions to spin–orbit torque in magnetic bilayers. *Nature communications*, 5, 2014.

[213] HX Tang, RK Kawakami, DD Awschalom, and ML Roukes. Giant planar hall effect in epitaxial (ga, mn) as devices. *Physical review letters*, 90(10):107201, 2003.

[214] KY Wang, KW Edmonds, LX Zhao, M Sawicki, RP Campion, BL Gallagher, and CT Foxon. (ga, mn) as grown on (311) gaas substrates: Modified mn incorporation and magnetic anisotropies. *Physical Review B*, 72(11):115207, 2005.

[215] Masaki Mizuguchi, Satoko Ohata, Ken-ichi Uchida, Eiji Saitoh, and Koki Takanashi. Anomalous nernst effect in an l10-ordered epitaxial fept thin film. *Applied Physics Express*, 5(9):093002, 2012.

[216] Maximilian Schmid, Sasmita Srichandan, Daniel Meier, Timo Kuschel, J-M Schmalhorst, Michael Vogel, Günter Reiss, Christoph Strunk, and Christian H Back. Transverse spin seebeck effect versus anomalous and planar nernst effects in permalloy thin films. *Physical review letters*, 111(18):187201, 2013.

[217] O Kelekci, HN Lee, TW Kim, and H Noh. Anomalous nernst effects of [cosib/pt] multilayer films. *arXiv preprint arXiv:1308.5485*, 2013.

[218] Wei-Li Lee, S. Watauchi, V. L. Miller, R. J. Cava, and N. P. Ong. Anomalous hall heat current and nernst effect in the cucr2se4xbrx ferromagnet. *Phys. Rev. Lett.*, 93:226601, Nov 2004.

[219] N Hanasaki, K Sano, Y Onose, T Ohtsuka, S Iguchi, I Kézsmárki, S Miyasaka, S Onoda, N Nagaosa, and Y Tokura. Anomalous nernst effects in pyrochlore molybdates with spin chirality. *Physical review letters*, 100(10):106601, 2008.

[220] T Miyasato, N Abe, T Fujii, A Asamitsu, S Onoda, Y Onose, N Nagaosa, and Y Tokura. Crossover behavior of the anomalous hall effect and anomalous nernst effect in itinerant ferromagnets. *Physical review letters*, 99(8):086602, 2007.

[221] CM Jaworski, J Yang, S Mack, DD Awschalom, JP Heremans, and RC Myers. Observation of the spin-seebeck effect in a ferromagnetic semiconductor. *Nature materials*, 9(11):898–903, 2010.

[222] V Osinniy, K Dybko, A Jedrzejczak, M Arciszewska, W Dobrowolski, T Story, MV Radchenko, VI Sichkovskiy, GV Lashkarev, SM Olsthoorn, et al. Thermoelectric studies of electronic properties of ferromagnetic gamnas layers. *Semiconductor Physics, Quantum Electronics and Optoelectronics*, 11(2):257–265, 2008.

[223] SY Huang, WG Wang, SF Lee, J Kwo, and CL Chien. Intrinsic spin-dependent thermal transport. *Physical review letters*, 107(21):216604, 2011.

[224] Ken-ichi Uchida, Hiroto Adachi, Takeru Ota, Hiroyasu Nakayama, Sadamichi Maekawa, and Eiji Saitoh. Observation of longitudinal spin-seebeck effect in magnetic insulators. *Applied Physics Letters*, 97(17):172505, 2010.

[225] Joseph G Checkelsky and NP Ong. Thermopower and nernst effect in graphene in a magnetic field. *Physical Review B*, 80(8):081413, 2009.

[226] Ken-ichi Uchida, Tatsumi Nonaka, Takeru Ota, and Eiji Saitoh. Longitudinal spin-seebeck effect in sintered polycrystalline (mn, zn) fe 2 o 4. *Applied Physics Letters*, 97(26):262504–262504, 2010.

[227] Kevin Garello, Ioan Mihai Miron, Can Onur Avci, Frank Freimuth, Yuriy Mokrousov, Stefan Blügel, Stéphane Auffret, Olivier Boulle, Gilles Gaudin, and Pietro Gambardella. Symmetry and magnitude of spin-orbit torques in ferromagnetic heterostructures. *Nature nanotechnology*, 8(8):587–593, 2013.

[228] Satoru Emori, Uwe Bauer, Sung-Min Ahn, Eduardo Martinez, and Geoffrey SD Beach. Current-driven dynamics of chiral ferromagnetic domain walls. *Nature materials*, 12(7):611–616, 2013.

[229] Can Onur Avci, Kevin Garello, Corneliu Nistor, Sylvie Godey, Belén Ballesteros, Aitor Mugarza, Alessandro Barla, Manuel Valvidares, Eric Pellegrin, Abhijit Ghosh, Ioan Mihai Miron, Olivier Boulle, Stephane Auffret, Gilles Gaudin, and Pietro Gambardella. Fieldlike and antidamping spin-orbit torques in as-grown and annealed ta/cofeb/mgo layers. *Phys. Rev. B*, 89:214419, Jun 2014.

[230] Tim Yang, Makoto Kohda, Takeshi Seki, Koki Takanashi, and Junsaku Nitta. Platinum layer thickness dependence of spin-hall induced effective magnetic field in pt/co/pt structures. *Japanese Journal of Applied Physics*, 53(4S):04EM06, 2014.

[231] Masamitsu Hayashi, Junyeon Kim, Michihiko Yamanouchi, and Hideo Ohno. Quantitative characterization of the spin-orbit torque using harmonic hall voltage measurements. *Physical Review B*, 89(14):144425, 2014.

[232] Jun Okabayashi, Akio Kimura, Oliver Rader, Takashi Mizokawa, Atsushi Fujimori, Toshiaki Hayashi, and Masaaki Tanaka. Core-level photoemission study of ga 1-x mn x as. *Physical Review B*, 58(8):R4211, 1998.

[233] Benjamin Norman, Christopher Trowbridge, David Awschalom, and Vanessa Sih. Current-induced spin polarization in anisotropic spin-orbit fields. *Bulletin of the American Physical Society*, 2014.

[234] D Chiba, T Ono, F Matsukura, and H Ohno. Electric field control of thermal stability and magnetization switching in (ga, mn) as. *Applied Physics Letters*, 103(14):142418, 2013.

[235] M Cormier, V Jeudy, T Niazi, D Lucot, M Granada, J Cibert, and A Lemaître. Electric-field-induced magnetization reorientation in a (ga, mn) as/(ga, mn)(as, p) bilayer with out-of-plane anisotropy. *Physical Review B*, 90(17):174418, 2014.

[236] Alexander B Shick, Sergii Khmelevskyi, Oleg N Mryasov, Joerg Wunderlich, and Tomas Jungwirth. Spin-orbit coupling induced anisotropy effects in bimetallic antiferromagnets: A route towards antiferromagnetic spintronics. *Physical Review B*, 81(21):212409, 2010.

[237] K Janicka. *TWO DIMENSIONAL ELECTRON GAS AT OXIDE INTERFACES*. PhD thesis, University of Nebraska, 2011.

[238] HY Hwang, Y Iwasa, M Kawasaki, B Keimer, N Nagaosa, and Y Tokura. Emergent phenomena at oxide interfaces. *Nature materials*, 11(2):103–113, 2012.

[239] A Ohtomo and HY Hwang. A high-mobility electron gas at the laalo3/srtio3 heterointerface. *Nature*, 427(6973):423–426, 2004.

[240] Takahiro Morimoto, Yasuhiro Hatsugai, and Hideo Aoki. Optical hall conductivity in 2deg and graphene qhe systems. *Physica E: Low-dimensional Systems and Nanostructures*, 42(4):751–754, 2010.

[241] Gao Chun-Lei, Qian Dong, Liu Can-Hua, Jia Jin-Feng, and Liu Feng. Topological edge states and electronic structures of a 2d topological insulator: Single-bilayer bi (111). *Chinese Physics B*, 22(6):067304, 2013.

[242] Halldor G Svavarsson, JT Gudmundsson, GI Gudjonsson, and Hafli Petur Gislason. Potential fluctuations and site switching in si-doped gaas studied by photoluminescence. *Physica Scripta*, 2002(T101):114, 2002.

[243] AH MacDonald. Introduction to the physics of the quantum hall regime. *arXiv preprint cond-mat/9410047*, 1994.

[244] EM Lifshits and AM Kosevich. Theory of the shubnikovde haas effect. *Journal of Physics and Chemistry of Solids*, 4(1):1–10, 1958.

[245] Hongtao Yuan, Hidekazu Shimotani, Atsushi Tsukazaki, Akira Ohtomo, Masashi Kawasaki, and Yoshihiro Iwasa. High-density carrier accumulation in zno field-effect transistors gated by electric double layers of ionic liquids. *Advanced Functional Materials*, 19(7):1046–1053, 2009.

[246] C Ciccarelli, LP Zârbo, AC Irvine, RP Campion, BL Gallagher, J Wunderlich, T Jungwirth, and AJ Ferguson. Spin gating electrical current. *Applied Physics Letters*, 101(12):122411–122411, 2012.

[247] SJ Van Der Molen, N Tombros, and BJ Van Wees. Magneto-coulomb effect in spin-valve devices. *Physical Review B*, 73(22):220406, 2006.

[248] M Tran, J Peiro, H Jaffrès, J-M George, O Mauguin, L Largeau, and A Lemaître. Magnetization-controlled conductance in (ga, mn) as-based resonant tunneling devices. *Applied Physics Letters*, 95(17):172101–172101, 2009.

[249] V Kubrak, AW Rushforth, AC Neumann, F Rahman, BL Gallagher, PC Main, M Henini, CH Marrows, and BJ Hickey. The transport of 2d electrons through magnetic barriers. *Physica E: Low-dimensional Systems and Nanostructures*, 7(3):997–1000, 2000.

[250] Masahiro Hara, Akira Endo, Shingo Katsumoto, and Yasuhiro Iye. Transport in two-dimensional electron gas with isolated magnetic barriers. *Journal of the Physical Society of Japan*, 71:543, 2002.

[251] Volker Kubrak. *Transport of Two-Dimensional Electrons Through Magnetic Barriers*. PhD thesis, University of Nottingham, 2001.

[252] GL Snider. computer program 1d poisson. *Schrödinger: A band diagram calculator, University of Notre Dame, Notre Dame, IN*, 1995.

[253] A Filipe, A Schuhl, and P Galtier. Structure and magnetism of the fe/gaas interface. *Applied physics letters*, 70(1):129–131, 1997.

[254] L Fleet. *Interface and Transport Properties of Fe/GaAs(001) Heterostructures*. PhD thesis, University of York, 2012.

[255] BD Schultz, N Marom, D Naveh, X Lou, C Adelmann, J Strand, PA Crowell, L Kronik, and CJ Palmstrøm. Spin injection across the fe/gaas interface: Role of interfacial ordering. *Physical Review B*, 80(20):201309, 2009.

[256] K Olejnik, J Wunderlich, AC Irvine, RP Campion, VP Amin, Jairo Sinova, and T Jungwirth. Spin hall transistor with electrical spin injection. *arXiv preprint arXiv:1202.0881*, 2012.

[257] HJ Zhu, M Ramsteiner, H Kostial, M Wassermeier, HP Schönherr, and KH Ploog. Room-temperature spin injection from fe into gaas. *Physical Review Letters*, 87(1):016601–016601, 2001.

[258] SA Crooker, M Furis, X Lou, C Adelmann, DL Smith, CJ Palmstrøm, and PA Crowell. Imaging spin transport in lateral ferromagnet/semiconductor structures. *Science*, 309(5744):2191–2195, 2005.

[259] Günther Bayreuther, Jörg Premper, Matthias Sperl, and Dirk Sander. Uniaxial magnetic anisotropy in fe/gaas (001): Role of magnetoelastic interactions. *Physical Review B*, 86(5):054418, 2012.

[260] PM Mooney. Deep donor levels (dx centers) in iii-v semiconductors. *Journal of Applied Physics*, 67(3):R1–R26, 1990.

[261] Andrew Gannon, David Donnelly, and Billy Covington. Trapping mechanism to account for persistent photoeffects in heavily doped gaas/algaas multiple quantum wells. *Journal of applied physics*, 79(9):7169–7172, 1996.

[262] John H Davies. The physics of low-dimensional semiconductors. *Physics of Low-Dimensional Structures*, 1, 1997.

[263] Nikolai Borisovich Brandt and SM Chudinov. Shubnikov-de haas effect and its application to investigation of the energy spectrum of metals, semimetals, and semiconductors. *Physics-Uspekhi*, 25(7):518–529, 1982.

[264] Robert B Laughlin. Quantized hall conductivity in two dimensions. *Physical Review B*, 23(10):5632, 1981.

[265] A Gold. Mobility of the two-dimensional electron gas in algaas/gaas heterostructures at low electron densities. *Applied physics letters*, 54(21):2100–2102, 1989.

[266] V Umansky, R De-Picciotto, and M Heiblum. Extremely high-mobility two dimensional electron gas: Evaluation of scattering mechanisms. *Applied physics letters*, 71(5):683–685, 1997.

[267] T Zhang, M Spangenberg, N Takahashi, T-H Shen, D Greig, JAD Matthew, and EA Seddon. A photoemission study: the influence of heating process and au buffer layers on the fe/gaas (1 0 0) structure. *Applied surface science*, 191(1):211–217, 2002.

[268] A Sasaki, S Nonaka, Y Kunihashi, M Kohda, Tobias Bauernfeind, Tobias Dollinger, Klaus Richter, and J Nitta. Direct determination of spin–orbit interaction coefficients and realization of the persistent spin helix symmetry. *Nature nanotechnology*, 9(9):703–709, 2014.

[269] AV Goran, AA Bykov, and AI Toropov. Classical anisotropic magnetoresistance of a non-planar 2d electron gas in a parallel magnetic field. *Semiconductor Science and Technology*, 23(10):105017, 2008.

[270] M Tanaka, JP Harbison, MC Park, YS Park, T Shin, and GM Rothberg. Epitaxial ferromagnetic mnas thin films grown by molecular-beam epitaxy on gaas: Structure and magnetic properties. *Journal of Applied Physics*, 76(10):6278–6280, 1994.

[271] F Schippan, A Trampert, L Däweritz, and KH Ploog. Kinetics of mnas growth on gaas (001) and interface structure. *Journal of Vacuum Science & Technology B*, 17(4):1716–1721, 1999.

[272] JH Song, Y Cui, JJ Lee, MY Kim, and JB Ketterson. Postgrowth annealing effects on heteroepitaxial mnas thin films grown on gaas (001) and si (001). *Journal of applied physics*, 99(8):08D513–08D513, 2006.

[273] Focko Meier, Samir Lounis, Jens Wiebe, Lihui Zhou, Swantje Heers, Phivos Mavropoulos, Peter H Dederichs, Stefan Blügel, and Roland Wiesendanger. Spin polarization of platinum (111) induced by the proximity to cobalt nanostripes. *Physical Review B*, 83(7):075407, 2011.

[274] Estitxu Villamor, Miren Isasa, Saül Vélez, Amilcar Bedoya-Pinto, Paolo Vavassori, Luis E Hueso, F Sebastián Bergeret, and Fèlix Casanova. Modulation of pure spin currents with a ferromagnetic insulator. *Physical Review B*, 91(2):020403, 2015.

[275] AV Kimel, A Kirilyuk, A Tsvetkov, RV Pisarev, and Th Rasing. Laser-induced ultrafast spin reorientation in the antiferromagnet tmfeo3. *Nature*, 429(6994):850–853, 2004.

[276] Alvaro S Núnez, RA Duine, Paul Haney, and AH MacDonald. Theory of spin torques and giant magnetoresistance in antiferromagnetic metals. *Physical Review B*, 73(21):214426, 2006.

[277] PM Haney, D Waldron, RA Duine, AS Núñez, H Guo, and AH MacDonald. Ab initio giant magnetoresistance and current-induced torques in cr/ au/ cr multilayers. *Physical Review B*, 75(17):174428, 2007.

[278] RA Duine, PM Haney, AS Núñez, and AH MacDonald. Inelastic scattering in ferromagnetic and antiferromagnetic spin valves. *Physical Review B*, 75(1):014433, 2007.

[279] BG Park, J Wunderlich, X Marti, V Holỳ, Y Kurosaki, M Yamada, H Yamamoto, A Nishide, J Hayakawa, H Takahashi, et al. A spin-valve-like magnetoresistance of an antiferromagnet-based tunnel junction. *Nature materials*, 10(5):347–351, 2011.

[280] A Scholl, M Liberati, E Arenholz, H Ohldag, and J Stöhr. Creation of an antiferromagnetic exchange spring. *Physical review letters*, 92(24):247201, 2004.

[281] I Fina, X Marti, D Yi, J Liu, JH Chu, C Rayan-Serrao, S Suresha, AB Shick, J Železnỳ, T Jungwirth, et al. Anisotropic magnetoresistance in an antiferromagnetic semiconductor. *Nature communications*, 5, 2014.

[282] X Marti, I Fina, C Frontera, Jian Liu, P Wadley, Qing He, RJ Paull, JD Clarkson, J Kudrnovskỳ, I Turek, et al. Room-temperature antiferromagnetic memory resistor. *Nature materials*, 13(4):367–374, 2014.

[283] JH Han, C Song, F Li, YY Wang, GY Wang, QH Yang, and F Pan. Antiferromagnet-controlled spin current transport in srmno 3/pt hybrids. *Physical Review B*, 90(14):144431, 2014.

[284] J Mündelein and H-U SCHUSTER. Preparation and crystal structure of compounds mncux (x: P, as, pxas1-x). *ChemInform*, 23(42), 1992.

[285] F Máca, J Mašek, O Stelmakhovych, X Martí, H Reichlová, K Uhlířová, P Beran, P Wadley, V Novák, and T Jungwirth. Room-temperature antiferromagnetism in cumnas. *Journal of Magnetism and Magnetic Materials*, 324(8):1606–1612, 2012.

[286] Kevin Edmonds & Peter Wadley. Xmld studies of cumnas (private communication to be published at a later date).

[287] Richard Campion Vit Novak Ryan Beardsley Kevin Edmonds Bryan Gallagher Bachir Ouladdiaf Victoria Hills, Peter Wadley and Tomas Jungwirth. Paramagnetic to antiferromagnetic transition in epitaxial tetragonal cumnas. Accepted for publication in Journal of Applied Physics, 2015.

[288] Xiuwen Zhang, Qihang Liu, Jun-Wei Luo, Arthur J Freeman, and Alex Zunger. Hidden spin polarization in inversion-symmetric bulk crystals. *Nature Physics*, 10(5):387–393, 2014.

[289] JM Riley, F Mazzola, M Dendzik, M Michiardi, T Takayama, L Bawden, C Granerød, Mats Leandersson, T Balasubramanian, M Hoesch, et al. Direct observation of spin-polarized bulk bands in an inversion-symmetric semiconductor. *Nature Physics*, 10(11):835–839, 2014.

[290] Theo Hahn, Uri Shmueli, Arthur James Cochran Wilson, and Edward Prince. *International tables for crystallography*. D. Reidel Publishing Company, 2005.

[291] J Zhu, Q Li, JX Li, Z Ding, JH Liang, X Xiao, YM Luo, CY Hua, H-J Lin, TW Pi, et al. Antiferromagnetic spin reorientation transition in epitaxial nio/coo/mgo (001) systems. *Physical Review B*, 90(5):054403, 2014.

[292] Kuniaki Arai, Taichi Okuda, Arata Tanaka, Masato Kotsugi, Keiki Fukumoto, Takuo Ohkochi, Tetsuya Nakamura, Tomohiro Matsushita, Takayuki Muro, Masaki Oura, et al. Three-dimensional spin orientation in antiferromagnetic domain walls of nio studied by x-ray magnetic linear dichroism photoemission electron microscopy. *Physical Review B*, 85(10):104418, 2012.

[293] Viktor Valentinovich Eremenko, NK Kharchenko, VM Naumenko, and Yu G Litvinenko. *Magneto-optics and Spectroscopy of Antiferromagnets*. Springer, 1992.

[294] Victoria Hills. Private communication on how resistance of cumnas varies during 500k heating cycles.

[295] Julie Grollier, Pierre Boulenc, Vincent Cros, Amir Hamzić, Annie Vaures, Albert Fert, and Giancarlo Faini. Switching a spin valve back and forth by current-induced domain wall motion. *Applied Physics Letters*, 83(3):509–511, 2003.

[296] CH Marrows. Spin-polarised currents and magnetic domain walls. *Advances in Physics*, 54(8):585–713, 2005.

[297] M Bode, EY Vedmedenko, K Von Bergmann, A Kubetzka, P Ferriani, S Heinze, and R Wiesendanger. Atomic spin structure of antiferromagnetic domain walls. *Nature materials*, 5(6):477–481, 2006.

[298] OG Shpyrko, ED Isaacs, JM Logan, Yejun Feng, G Aeppli, Rafael Jaramillo, HC Kim, TF Rosenbaum, Paul Zschack, Michael Sprung, et al. Direct measurement of antiferromagnetic domain fluctuations. *Nature*, 447(7140):68–71, 2007.

[299] M García-Fernández, SB Wilkins, Ming Lu, Qing'an Li, KE Gray, H Zheng, JF Mitchell, and Daniel Khomskii. Antiferromagnetic domain structure in bilayer manganite. *Physical Review B*, 88(7):075134, 2013.

[300] A Scholl, J Stöhr, J Lüning, Jin Won Seo, J Fompeyrine, H Siegwart, J-P Locquet, F Nolting, S Anders, EE Fullerton, et al. Observation of antiferromagnetic domains in epitaxial thin films. *Science*, 287(5455):1014–1016, 2000.

[301] Yiming Huai. Spin-transfer torque mram (stt-mram): Challenges and prospects. *AAPPS Bulletin*, 18(6):33–40, 2008.

[302] Long Ying Loh. Mechanism ans assessment of spin-transfer torque (stt) based memory. Master's thesis, Massachusetts Institute of Technology, 2009.

[303] Han-Chun Wu, Zhi-Min Liao, RG Sofin, Gen Feng, Xiu-Mei Ma, Alexander B Shick, Oleg N Mryasov, and Igor V Shvets. Mn2au: Body-centered-tetragonal bimetallic antiferromagnets grown by molecular beam epitaxy. *Advanced Materials*, 24(47):6374–6379, 2012.

[304] BT Thole, Paolo Carra, F Sette, and Gerrit van der Laan. X-ray circular dichroism as a probe of orbital magnetization. *Physical review letters*, 68(12):1943, 1992.

[305] Paolo Carra, BT Thole, Massimo Altarelli, and Xindong Wang. X-ray circular dichroism and local magnetic fields. *Physical Review Letters*, 70(5):694, 1993.

[306] KW Edmonds, G van der Laan, AA Freeman, NRS Farley, TK Johal, RP Campion, CT Foxon, BL Gallagher, and E Arenholz. Angle-dependent x-ray magnetic circular dichroism from (ga, mn) as: anisotropy and identification of hybridized states. *Physical review letters*, 96(11):117207, 2006.

[307] G Van der Laan, KW Edmonds, E Arenholz, NRS Farley, and BL Gallagher. Valence-state model of strain-dependent mn l 2, 3 x-ray magnetic circular dichroism from ferromagnetic semiconductors. *Physical Review B*, 81(21):214422, 2010.

[308] KW Edmonds, G van der Laan, NRS Farley, RP Campion, BL Gallagher, CT Foxon, BCC Cowie, S Warren, and TK Johal. Magnetic linear dichroism in the angular dependence of core-level photoemission from (ga, mn) as using hard x rays. *Physical review letters*, 107(19):197601, 2011.

[309] ND Parashar, N Rangaraju, VK Lazarov, S Xie, and BW Wessels. High-temperature ferromagnetism in epitaxial (in, mn) sb films. *Physical Review B*, 81(11):115321, 2010.

[310] JA Peters, ND Parashar, N Rangaraju, and BW Wessels. Magnetotransport properties of inmnsb magnetic semiconductor thin films. *Physical Review B*, 82(20):205207, 2010.

[311] MD Kuzmin. Shape of temperature dependence of spontaneous magnetization of ferromagnets: quantitative analysis. *Physical review letters*, 94(10):107204, 2005.

[312] M Csontos, G Mihály, B Jankó, T Wojtowicz, X Liu, and JK Furdyna. Pressure-induced ferromagnetism in (in, mn) sb dilute magnetic semiconductor. *Nature materials*, 4(6):447–449, 2005.

[313] S Yanagi, K Kuga, T Slupinski, and H Munekata. Carrier-induced ferromagnetic order in the narrow gap iii–v magnetic alloy semiconductor (in, mn) sb. *Physica E: Low-dimensional Systems and Nanostructures*, 20(3):333–337, 2004.

[314] James D Aldous, Christopher W Burrows, Ian Maskery, Matt S Brewer, TPA Hase, JA Duffy, Martin R Lees, Cecilia Sanchez-Hanke, T Decoster, W Theis, et al. Depth-dependent magnetism in epitaxial mnsb thin films: effects of surface passivation and cleaning. *Journal of Physics: Condensed Matter*, 24(14):146002, 2012.

[315] Kow-Ming Chang, Jiunn-Jye Luo, Chen-Der Chiang, and Jacob Kou-Chen Liu. Mesa etching characterization of insb for high density image array applications. *Journal of the Chinese Institute of Engineers*, 30(1):11–16, 2007.

[316] JS Kouvel and CC Hartelius. Anomalous magnetic moments and transformations in the ordered alloy ferh. *Journal of Applied Physics*, 33(3):1343–1344, 1962.

[317] M Sharma, HM Aarbogh, J-U Thiele, S Maat, EE Fullerton, and C Leighton. Magnetotransport properties of epitaxial mgo (001)/ferh films across the antiferromagnet to ferromagnet transition. *Journal of Applied Physics*, 109(8):083913, 2011.

[318] C Stamm, J-U Thiele, T Kachel, I Radu, P Ramm, M Kosuth, J Minár, H Ebert, HA Dürr, W Eberhardt, et al. Antiferromagnetic-ferromagnetic phase transition in ferh probed by x-ray magnetic circular dichroism. *Physical Review B*, 77(18):184401, 2008.

[319] J. Kudrnovský, V. Drchal, and I. Turek. Physical properties of ferh alloys: The antiferromagnetic to ferromagnetic transition. *Phys. Rev. B*, 91:014435, Jan 2015.

[320] Liang Pan and David B Bogy. Data storage: Heat-assisted magnetic recording. *Nature Photonics*, 3(4):189–190, 2009.

[321] Radhika Barua. *Pathways for tailoring the magnetostructural response of FeRh-based systems*. PhD thesis, Northeastern University, 2014.

[322] C Baldasseroni, GK Pálsson, C Bordel, S Valencia, AA Unal, F Kronast, S Nemsak, CS Fadley, JA Borchers, BB Maranville, et al. Effect of capping material on interfacial ferromagnetism in ferh thin films. *Journal of Applied Physics*, 115(4):043919, 2014.